Full-Scale Testing and Progressive Damage Modeling of

Sandwich Composite Aircraft Fuselage Structure

A Thesis

Submitted to the Faculty

of

Drexel University

by

Frank A. Leone, Jr.

in partial fulfillment of the

requirements for the degree

of

Doctor of Philosophy

October 2010

DEDICATION

To Sara

for her endless support and patience

ACKNOWLEDGEMENTS

First and foremost, I would like to express my gratitude and thanks to my advisors, Professors Jonathan Awerbuch and Tein-Min Tan. Throughout my studies, their support has been constant and their advice plentiful. My time spent working with them has made me the researcher I am today. I can only hope to someday repeat this great favor.

This work was supported by a grant from the Federal Aviation Administration William J. Hughes Technical Center through the FAA-Drexel Fellowship Research Program. I consider myself most fortunate for having participated in the program, gaining priceless hands-on research experience as an undergraduate student, and, as an fellow, offering more than ample resources and opportunities to establish myself as a member of the research community. The high quality of my time in the fellowship was largely due to the tireless efforts and strong support of Dr. John G. Bakuckas, Jr. As a mentor, advisor, and friend, John stands as an example.

For her infinite generosity and support, I thank Dr. Didem Ozevin. Her ever-present advice and encouragement related to my work on acoustic emission and frequency response were instrumental for the successful completion of these tasks.

Credit is due to Mr. Curtis Davies of the FAA, who initiated the project, and Dr. Suresh Keshavanarayana of Wichita State University, for his formulation of the initial test plan. For their time and expertise in performing additional nondestructive inspections, I thank David Galella, Ciji Nelson, Jean Sena, Paul Swindell, and Kyle Thompson. I would like to thank Bao Mosinyi for sharing his experience and guidance as I began my graduate student work. His advice has proven invaluable time and time again. Many thanks are also due to Andrew Bergan for his assistance with data reduction and fractography work.

The partial support of the Department of Mechanical Engineering and Mechanics (MEM) was also highly valuable. The opportunity given to me as a teaching assistant in several undergraduate courses provided me with the needed experience for clear communication of

concepts and ideas which undoubtedly will be invaluable in my future career. A special thanks goes to Dr. Robert Koerner, for his encouragement to continue to develop as a member of the research community and for his support during my final year of study.

Also, I am deeply grateful for my thesis committee, Professors Franco Capaldi, Nicholas Cernansky, and Roger Doherty, for both their attention and their critiques, making my dissertation ever stronger.

TABLE OF CONTENTS

LIST OF TABLES

LIST OF FIGURES

ABSTRACT

Full-Scale Testing and Progressive Damage Modeling of
Sandwich Composite Aircraft Fuselage Structure
Frank A. Leone, Jr.
Advisors:
Prof. Jonathan Awerbuch and Prof. Tein-Min Tan

A comprehensive experimental and computational investigation was conducted to characterize the fracture behavior and structural response of large sandwich composite aircraft fuselage panels containing artificial damage in the form of holes and notches. Full-scale tests were conducted where panels were subjected to quasi-static combined pressure, hoop, and axial loading up to failure. The panels were constructed using plain-weave carbon/epoxy prepreg face sheets and a Nomex honeycomb core.

Panel deformation and notch tip damage development were monitored during the tests using several techniques, including optical observations, strain gages, digital image correlation (DIC), acoustic emission (AE), and frequency response (FR). Additional pretest and posttest inspections were performed via thermography, computer-aided tap tests, ultrasound, x-radiography, and scanning electron microscopy. The framework to simulate damage progression and to predict residual strength through use of the finite element (FE) method was developed.

The DIC provided local and full-field strain fields corresponding to changes in the state-of-damage and identified the strain components driving damage progression. AE was monitored during loading of all panels and data analysis methodologies were developed to enable real-time determination of damage initiation, progression, and severity in large composite structures. The FR technique has been developed, evaluating its potential as a real-time nondestructive inspection technique applicable to large composite structures.

Due to the large disparity in scale between the fuselage panels and the artificial damage, a global/local analysis was performed. The global FE models fully represented the specific geometries, composite lay-ups, and loading mechanisms of the full-scale tests. A progressive

damage model was implemented in the local FE models, allowing the gradual failure of elements in the vicinity of the artificial damage. A set of modifications to the definitions of the local FE model boundary conditions is proposed and developed to address several issues related to the scalability of progressive damage modeling concepts, especially in regards to full-scale fuselage structures. Notable improvements were observed in the ability of the FE models to predict the strength of damaged composite fuselage structures. Excellent agreement has been established between the FE model predictions and the experimental results recorded by DIC, AE, FR, and visual observations.

CHAPTER 1: INTRODUCTION

1.1. COMPOSITES IN AEROSPACE

The application of composite materials has become increasingly more commonplace in the design of military and commercial aircraft over the past several decades [1.1]. While initially only used in the design of secondary structures, major commercial aircraft manufacturers are now designing the primary structures, such as components of the wings and fuselage, of their flagship aircraft (e.g., Boeing 787, Airbus A350) with advanced composite materials. With the steady rise of fuel costs, this is a necessary adaptation and advancement by the aircraft industry. The potential weight-savings due to the superior stiffness-to-weight ratios characteristic of advanced composites is well established [1.2, 1.3]. Additional weight-savings and superior structural mechanical response are accomplished through selection of constituent materials and the optimal design of the laminate configuration and structural geometry to withstand the intended loading function.

Both solid and sandwiched laminate configurations are frequently employed in aerospace applications. Sandwich composites consist of two solid laminate face sheets and a lightweight core material. The face sheets are designed to carry the majority of the in-plane loads, while the core is designed to resist transverse shear deformation, maintain separation of the face sheets, and provide stability. The construction of sandwich composites offers increased flexural stiffness-to-weight ratios and lower lateral deformations when compared to solid laminates of comparable weight. Sandwich composites have been used in aerospace applications for several decades due to their advantages over both metallic alloys and solid laminates for certain applications. The usage of sandwich composite construction in aerospace structures has been increasing over time, as is evident by the history of sandwich composite usage for secondary structures (in terms of percent wetted surface) in Boeing commercial aircraft, as reported by Bitzer [1.4], Figure 1.1. Smaller general aviation aircraft (e.g., Beech Starship and Cirrus SR20) have adopted sandwich

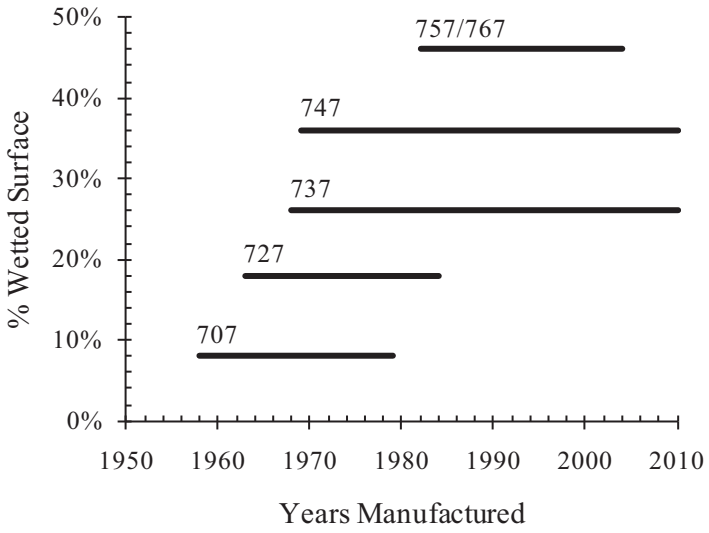

Figure 1.1. History of usage of honeycomb sandwich composites in the secondary structures of Boeing aircraft in terms of percent wetted surface. [1.4]

composites into their design even more ambitiously than commercial airliners, with sandwich composites represented in the majority of the primary and secondary structures [1.5].

The technical and financial advantages of integrating advanced composites into aircraft design are not without additional unique technical challenges. The aircraft industry and related government agencies recognize the key difficulties in taking full advantage of composites, namely: their sensitivity to foreign object impact damage, their mechanical response under harsh environments (in terms of temperature and humidity), and their propensity to contain nonvisual, internal damage due to either foreign objects or fabrication inhomogeneities. Further, there are significant differences in the overall structural design of the fuselage, (e.g., aluminum skin riveted to frame and stringers vs. sandwiched laminates which do not require a stiffening substructure). Similarly, baseline data on the mechanical properties and damage tolerance characteristics of composites are limited compared to the corresponding database readily available for metallic materials.

The design of a conventional aluminum alloy fuselage involves the riveting together of several curved sections of fuselage skin, via lap and butt joints, onto the skeletal substructure,

composed of frames, stringers, etc. These riveted joints are known sources of stress concentrations where fatigue cracks are expected to occur. A fuselage composed of a fiber-reinforced polymer laminate, such as that of the Boeing 787, consists of just three large, one-piece barrel sections, roughly 19 ft. in diameter and up to 22 ft. in length [1.6], attached to the neighboring sections with few additional components. The first barrel section of the Boeing 787 fuselage contains less than ten-thousand drilled holes, compared to the more than one-million contained in the 747 fuselage [1.7]. A key advantage in having such large composite sections is the reduction in the number of joints and, consequently, the number of required fasteners. However, the large-scale uniformity makes large regions of the fuselage equally likely to contain damage, greatly increasing the area for which regular inspections may be warranted or necessary.

Damage found in aluminum alloy fuselage structures is most often in the form of fatigue cracks emanating from known stress risers. In composite materials, however, the state-of-damage is a complex combination and interaction of multiple damage modes. For laminated fiber-reinforced composites, for example, possible damage modes include fiber fracture, fiber pull-out, fiber/matrix interfacial failure, delamination, matrix cracking, matrix splitting, and matrix crazing. Sandwiched composite structures exhibit additional possible failure modes related to their construction and to the particular core type (e.g., solid, honeycomb, corrugated) and material (e.g., aluminum, balsa wood, foam, Nomex®, etc.) used. The potential failure modes of honeycomb cores, for example, can include skin-to-core disbonding, intra-cell dimpling, face wrinkling, core crushing, core shear, and local core indentation. The early stages of damage formation in composite materials are very complex, influenced by the interactions of matrix cracking and delaminations long before more severe, visual damage develops [1.8, 1.9].

The complexity of the state-of-damage in sandwich composites renders reliable, accurate, and timely measurements and predictions of damage criticality quite difficult. Numerous modes of damage often occur at the same site, obscuring each other from the penetrating eye of the particular nondestructive inspection (NDI) technique used, making it difficult to identify and

discern individual damage modes at a particular load level or cycle number. As a result, ascertaining the criticality of the damage detected is rarely trivial. The ability to accurately measure, characterize, and quantify the severity of particular damage modes, external and internal, will further enhance the application of the principles of damage tolerance philosophy to composite aircraft design. While the damage tolerance of composite aircraft structures is an ongoing area of research, aircraft constructed using advanced composite materials in their primary and secondary structures are flying safely due to constraints put on their designs [1.10].

1.2. DAMAGE TOLERANCE

The basic principle of damage tolerant aircraft design is to ensure that structural damage does not lead to catastrophic failure of an aircraft when subjected to design limit loads, whether in flight or on the ground [1.11, 1.12]. More specifically, the structural components of an aircraft should be designed and their inspections should be planned so as to ensure that any damage within a principal structural element cannot progress from its largest undetectable size to a critical dimension. If inspection is not practical, a safe-life design approach should be adopted, in which a component must be retired and replaced before damage may form and propagate to criticality.

A principal structural element is a component whose failure would lead to catastrophic failure of the aircraft if undetected. It is critical to identify the principal structural elements and sites of potential failure initiation of an aircraft in order to establish a thorough inspection plan. Principal structural elements are not always easily accessible during regular, mandated inspections of in-use aircraft. However, redundancy in aircraft design can provide multiple load paths for certain structural components, enabling the assessment of failure of non-accessible primary components through inspection of accessible, secondary structural components. For such structural components containing single dominant fatigue cracks, a safe crack growth period, between crack size at detection and crack size at failure, can be determined using fracture

mechanics-based approaches. However, the inspectable damage in the accessible, secondary structural components is itself oftentimes nonvisual, requiring advanced inspection methods.

While the study of damage tolerance in metallic aircraft structures is well-established, the presence of widespread fatigue damage (WFD) further complicates the issue. WFD is characterized by the simultaneous presence of cracks at multiple structural details of sufficient size and density to cause the structure to no longer meet its damage tolerance requirements, sources of which include multiple site damage (MSD) and multiple element damage (MED) [1.13]. MSD is the presence and interaction of several small fatigue cracks in the same structural element, and MED is the presence and interaction of several small fatigue cracks in parallel structural elements. A set of microscopic fatigue cracks, all below the minimum detectable crack size, has the potential to link up to form a single, dominant fatigue crack of critical length in fewer cycles than any individual crack would require. Much effort has been placed in developing and verifying methods to assess the effects of MSD and MED on the fatigue and residual strength behavior of metallic fuselage structures (e.g., [1.14–1.16]). Current rule-making activities by the Federal Aviation Administration (FAA) will require actions to preclude the development of WFD within the limit of validity of an airplane's maintenance program [1.17].

While the goal of applying the principles of damage tolerance to primary aircraft structures composed of sandwich composites is the same as for metallic structures, the fundamental differences in the material composition and overall aircraft structural framework require a bottom-up revisiting of the various facets of damage tolerance philosophy. A traditional *slow growth* approach may be implemented for certain cases of damage in composite structures. The slow growth approach requires the demonstration that damage in a structure can withstand repeated loads with slow, stable, and predictable damage growth either for the life of the structure or beyond the inspection intervals associated with the detectability of damage [1.10]. For such cases, each of the following must be determined: (i) principal structures, (ii) critical failure modes, (iii) critical loading modes, (iv) optimal NDI modes for each particular failure mode, (v)

initial damage size, (vi) minimum detectable damage size, (vii) critical damage size, etc. [1.5]. However, predictable damage growth is not exhibited in most instances of damage in composite structures, and *no-growth* or *arrested growth* approaches must be implemented instead. The no-growth approach requires demonstration that a damaged structure can withstand repeated loads without detrimental damage growth for the life of the structure. The arrested growth approach requires demonstration that a damaged structure can withstand repeated loads with damage growth to be either mechanically arrested or terminated before becoming critical. [1.10]

Significant work has been performed by the aircraft industry, government, and academia on the damage tolerance characteristics of primary and secondary sandwich composite aircraft structures. However, the vast majority of this work has been performed at the coupon- and element-level, with full-scale testing being performed less often due to its increased cost and complexity [1.18]. The work presented in this thesis is an extension of coupon- and element-level research performed by the FAA and the National Institute for Aviation Research on honeycomb sandwich composites [1.19–1.24], focusing on the experimental and computational analysis of full-scale sandwich composite aircraft fuselage structures. Particular attention is paid to the application of progressive damage modeling concepts, which have been validated on the coupon-level, to full-scale engineering structures.

1.3. SUMMARY OF RESEARCH PROGRAM

The goals of this study were to:

(i) Characterize, experimentally and analytically, the effects of holes and notches on the residual strength of full-scale sandwich composite aircraft fuselage structures, monitoring the deformation of the structure and the redistribution of load as damage progressed;

(ii) Measure the state-of-damage in the structures, before, during, and after the residual strength tests, assessing the ability of various NDI methodologies to detect and discern the various modes of damage; and

(iii) Model the formation, progression, and eventual instability of damage, validating the models using the experimental data.

Six full-scale sandwich composite aircraft fuselage panels were tested at the Full-Scale Aircraft Structural Test and Research (FASTER) facility at the William J. Hughes FAA Technical Center, Atlantic City International Airport, NJ. The face sheets and core of the sandwich composite consisted of plain-weave carbon/epoxy prepreg and Nomex® honeycomb materials, respectively. The panels contained artificially inserted holes and notches, representative of common failure modes, such as impact (e.g., caused by tool drops, runway stones, etc.), debonded repair patches, and blade separation. Each panel was subjected to a combination of internal pressurization, hoop, and longitudinal loads designed to cause additional damage during loading. The testing of the panels commenced on August 17, 2006 and was completed on September 6, 2007. The deformation and strain of the panels were monitored using strain gages and a 3-D digital image correlation (DIC) system. The state-of-damage in the panels was characterized using various NDI methods, including thermography, computer-aided tap testing (CATT), ultrasound, and x-ray computed tomography (CT). The progression of damage was monitored during the test using the acoustic emission (AE) and frequency response (FR) methods, and the morphology of the fracture surfaces was evaluated via scanning electron microscopy (SEM).

The deformation and strain fields measured using the DIC method and the point-wise strain gage data collected from the panels are presented in Chapter 4. Strain gage and loader data collected from the FASTER data acquisition system provided a thorough history of the deformation of the panels in terms of in-plane strains and bending. Any differences between the intended and applied loads is noted and discussed, as well as any unexpected panel deformations. While the notched panels generally exhibited few stages of visible damage extension prior to

catastrophic failure, the full-field DIC data provided excellent data regarding the redistribution of strain with increasingly severe states-of-damage. The strain gage data correlated well with the DIC strain results, which were used to later validate finite element (FE) models of the panels.

Results from the various NDI techniques (e.g., thermography, CATT, ultrasound, and x-ray CT) and the examinations of the fracture surfaces via SEM are presented and discussed in Chapter 5. A large skin-to-core disbond was detected in one panel prior to loading. The ability of each of the NDI methods to detect and measure the disbond, in terms of both size and severity, were evaluated. Inspections were also performed in the vicinity of the various artificial holes and notches. The SEM fractography work revealed multiple coincident failure modes ahead of the artificial notches after loading.

A thorough analysis of the AE data is presented in Chapter 6. The chapter provides detailed discussions on the detection of damage initiation and its progression, the effect of various filtering schemes on the accuracy of the event source location algorithm, and anticipating the ultimate fracture load. The difficulties in using AE for distinguishing different failure mechanisms in complex, full-scale structures are discussed in detail, including thorough analyses of the distributions of waveform intensities of all accumulated AE signals and the characteristics of individual waveforms. The chapter concludes with a discussion on the effect of AE channel busyness on the distribution AE waveform characteristics and source location.

The experimental results obtained using the FR method are presented in Chapter 7. The ability of the FR method to detect nonvisual, subsurface damage is assessed and compared with the sensitivity of similar methods. The method proved to be of comparable sensitivity to the AE method, offering indications of damage prior to the occurrence of visible damage ahead of the artificial damage.

In Chapter 8, FE models capable of simulating the formation, progression, and instability of damage in full-scale sandwich composite aircraft fuselage structures using custom user subroutines are presented. A global/local FE analysis was performed for each of the panels. The

global models accurately represented the introduction of the loads to the panels by the FASTER loading fixtures and the details of the panel geometry and lay-up. The face sheets and core were treated as homogeneous orthotropic materials.

A material degradation failure model was implemented for the face sheets using three separate damage state variables, one in each principal material direction. The failure criteria and damage evolution laws were selected so as to allow for the gradual failure of the material. Due to significant transverse shear strains in the areas of interest, the application of the local model boundary conditions was modified to incorporate the global model nodal displacements and the transverse shear strains. Furthermore, an alternative method to global/local FE model co-simulation was proposed and implemented. A set of adaptive boundary conditions was defined to ensure proper driving of the local models while damage progressed, shifting the center of the predicted elevated strain field. A library of global FE model solutions was developed. The results within this library were queried and interpolated to produce a custom set of global model results corresponding to the applied loads and the severity of damage of the local model for each iteration throughout its solution.

Good correlations were found between the experimental and computational results. The formation, progression, and final extent of the modeled notch tip damage agreed with experimental observations. Both the experimental and computational results indicated that a significant portion of the damage progression process was nonvisual, with few stages of visual damage progression occurring prior to instability. It should be noted that instability occurred at loads far exceeding realistic flight loading conditions, even with severe initial artificial damage configurations.

A summary of the major findings of the experimental and computational phases of this work and the contributions to the field are detailed and listed in Chapter 9. Recommendations for future work in the field of progressive damage modeling are offered, as well.

CHAPTER 2: BACKGROUND AND LITERATURE REVIEW

2.1. MODELING DAMAGE IN COMPOSITE MATERIALS

With the increased willingness of the aircraft industry to take advantage of advanced composite materials in the design of primary and secondary aircraft structures, there is an impetus to develop more efficient designs and fabrication processes while still maintaining a thorough understanding of the expected service life and fatigue performance of aircraft. Critical to this advancement is the ability to assess the severity of damage (of various modes, shapes, and sizes) and its criticality. However, a lack of information exists concerning the fatigue and damage tolerance performance of many newer materials. The thorough material testing of composite materials composed of every possible combination of constituent materials is clearly prohibitive in terms of both time and cost. As a result, the development of effective analytical and computational tools to aid in this endeavor is crucial.

Accurately predicting the initiation, progression, and eventual instability of damage in large composite structures is a formidable task. To predict the onset of failure, the deformation field ahead of the notch tip must first be accurately calculated. Second, an appropriate failure criterion must be selected for the material, geometry, and loading configuration under investigation. Once the material is determined to have failed, the effect of the damage on the structural response of the material must be determined. Finally, a method for advancing the state-of-damage with increasing load (or number of fatigue cycles) must be formulated to allow the damage to progress in both size and severity. This process must be repeated following the occurrence of each new failure until instability is reached, and the structure ultimately fails as a whole. The problem is further complicated by the fact that each of the various failure modes requires individual consideration, yet may be influenced by additional nearby damage.

The finite element (FE) method is a powerful computational tool often used to study such complex problems. Several commercial codes (e.g., ABAQUS, LS-DYNA, etc.) now include the

ability to model damage progression for certain classes of materials. Many more progressive damage modeling concepts and techniques have been proposed throughout the literature for a much wider set of materials, geometries, and loading configurations. Several reviews are available on the key concepts of progressive damage modeling in both technical [2.1] and comparative [2.2] contexts. A brief review of the most common failure criteria, modeling techniques, and damage evolution laws as they pertain to this investigation are presented here.

2.1.1. FAILURE CRITERIA

The simplest method of obtaining the stiffness and strength properties of a new material is to perform a uniaxial tensile test. For a brittle, homogenous, isotropic material, this will yield the Young's modulus and ultimate strength. With these inputs, either the maximum stress or maximum strain failure criteria could be used to make accurate predictions for similar tests in the future. The maximum stress and maximum strain failure criteria can be written as:

$$\left|\frac{\sigma_1}{X}\right| \geq 1 \tag{2.1}$$

$$\left|\frac{C_{11}\varepsilon_1}{X}\right| \geq 1, \tag{2.2}$$

respectively, where σ_i and ε_j are the stress and strain tensors in contracted notation, X is the strength in the 1-direction, and C_{ij} is the stiffness tensor. The stress, strain, and stiffness tensors are related through the generalized Hooke's law via:

$$\sigma_i = C_{ij}\,\varepsilon_j \tag{2.3}$$

where i and j range from 1 to 6. Rewriting the maximum stress criterion for failure in the 1-direction in terms of strain yields:

$$\left|\frac{C_{11}\varepsilon_1 + C_{12}\varepsilon_2 + C_{13}\varepsilon_3}{X}\right| \geq 1, \tag{2.4}$$

which is equivalent to the maximum strain criterion for cases of uniaxial loading.

Under biaxial and triaxial loading conditions, the prediction of failure becomes more complicated, even for homogeneous, isotropic materials. While certain homogeneous, isotropic materials behave according to the predictions of the maximum stress and maximum strain failure criteria under multiaxial loading, for others the components of stress are known to interact. In such cases, failure theories such as the Tresca and von Mises yield criteria are preferable [2.3]. For composite materials, the tendency for the components of stress to interact, the orthotropic material properties, and the various failure modes of the constituent materials have led to the development of several other classes of failure criteria. In addition to the *non-interactive* maximum stress and maximum strain criteria, such classes of failure criteria include *interactive* and *failure mode-based* (i.e., partially interactive) criteria [2.2]. Here, "interactive" refers to the influence of off-axis and shear stresses on failure.

Tsai [2.4] developed an interactive, single-equation failure criterion for orthotropic materials:

$$\frac{\sigma_1^2}{X^2} - \frac{\sigma_1\sigma_2}{X^2} - \frac{\sigma_2^2}{Y^2} + \frac{\sigma_6^2}{S^2} \geq 1, \tag{2.5}$$

where Y is the strength in the 2-direction and S is the in-plane shear strength. The failure criterion is a reduced version of the more general orthotropic yield criterion proposed by Hill [2.5] for the case of a unidirectional lamina in plane stress. Hill assumed that a quadratic curve-fit could represent the failure envelope of orthotropic materials through:

$$F(\sigma_2 - \sigma_3)^2 + G(\sigma_3 - \sigma_1)^2 + H(\sigma_1 - \sigma_2)^2 + 2L\sigma_4^2 + 2M\sigma_5^2 + 2N\sigma_6^2 \geq 1, \tag{2.6}$$

where F, G, H, L, M, and N are experimentally determined constants. While the Tsai-Hill criterion does take into account the interactions of the stress components, there is no distinction between failure modes. Interestingly, the maximum stress and maximum strain criteria, while non-interactive, are capable of distinguishing between fiber and matrix failure modes by having separate criteria for each principal material direction [2.1].

Tsai and Wu [2.6] later generalized the Tsai-Hill criterion, producing a tensorial failure criterion for anisotropic materials subjected to multiaxial stresses in three dimensions:

$$F_i\sigma_i + F_{ij}\sigma_i\sigma_j \geq 1 \tag{2.7}$$

where F_i and F_{ij} are second- and fourth-rank strength tensors, respectively, where the subscripts i and j range from 1 to 6. The tensorial derivation of the criterion allows for coordinate transformations to be performed for both the stress and strength tensors. Application of the criterion to a fully three-dimensional anisotropic material would be quite demanding; the complete expansion of the Tsai-Wu criterion contains 6 linear and 21 quadratic empirical strength terms. However, for a three-dimensional orthotropic material, the criterion simplifies to:

$$\begin{aligned} F_1\sigma_1 + F_2\sigma_2 + F_3\sigma_3 + F_4\sigma_4 + F_5\sigma_5 + F_{66}\sigma_6 + F_{11}\sigma_1^2 + F_{22}\sigma_2^2 \\ + F_{33}\sigma_3^2 + F_{44}\sigma_4^2 + F_{55}\sigma_5^2 + F_{66}\sigma_6^2 + 2F_{12}\sigma_1\sigma_2 \\ + 2F_{13}\sigma_1\sigma_3 + 2F_{23}\sigma_2\sigma_3 \geq 1 \end{aligned} \tag{2.8}$$

Yet, even after simplification, the determination of the components of the strength tensors often requires extensive, difficult-to-perform mechanical testing.

The Tsai-Wu criterion maintains the assumption that the failure envelope of a material can be represented by a single smooth surface, regardless of the multiple failure modes which may be occurring in different planes. Regardless, when the terms of the strength tensors are experimentally available, the Tsai-Wu criterion often outperforms other non-interactive and interactive failure criteria, especially in cases involving compressive transverse stress [2.2].

Rather than attempting to represent the failure envelope for a composite material as a single smooth function, Hashin and Rotem [2.7] proposed to use a set of failure criteria, in which the failure modes of each constituent material are independently determined. Based on previous experimental observations, two failure modes were considered for unidirectional fiber-reinforced laminae under plane stress: fiber failure and matrix failure. The tensile fiber, compressive fiber, tensile matrix, and compressive matrix failure criteria were represented as:

$$\left|\frac{\sigma_1}{X_{\mathrm{T}}}\right| \geq 1 \tag{2.9}$$

$$\left|\frac{\sigma_1}{X_{\mathrm{C}}}\right| \geq 1 \tag{2.10}$$

$$\left(\frac{\sigma_2}{Y_{\mathrm{T}}}\right)^2 + \left(\frac{\sigma_6}{S}\right)^2 \geq 1 \tag{2.11}$$

$$\left(\frac{\sigma_2}{Y_{\mathrm{C}}}\right)^2 + \left(\frac{\sigma_6}{S}\right)^2 \geq 1 \tag{2.12}$$

Shear stresses are neglected for the fiber failure criteria, yielding the maximum stress criterion, while a quadratic relationship between the transverse normal and in-plane shear stresses form the two matrix failure criteria.

Hashin and Rotem conducted fatigue and static strength tests with unidirectional off-axis E-glass fiber-reinforced epoxy coupons. Fiber failures were observed only with off-axis angles less than 2°; matrix failures were observed throughout the remaining off-axis range. The test results correlated well with the predictions of the proposed set of failure criteria.

In a later paper, Hashin [2.8] derived the failure mode-based criteria for transversely isotropic materials, taking into account transverse shear stresses. The initially assumed shape of the failure envelope included each first- and second-order term of the stress invariants of a transversely isotropic material. Again, failure criteria were developed for the fiber and matrix materials. However, unlike Hashin's original criteria, tensile and compressive failure mechanisms were determined to depend on different components of stress. Here, the tensile fiber, compressive fiber, tensile matrix, and compressive matrix failure criteria were determined to be:

$$\left(\frac{\sigma_1}{X_{\mathrm{T}}}\right)^2 + \frac{1}{S_{\mathrm{A}}^2}\left(\sigma_5^2 + \sigma_6^2\right) \geq 1 \tag{2.13}$$

$$\left|\frac{\sigma_1}{X_{\mathrm{C}}}\right| \geq 1 \tag{2.14}$$

$$\frac{1}{Y_{\mathrm{T}}^2}(\sigma_2+\sigma_3)^2+\frac{1}{S_{\mathrm{T}}^2}(\sigma_4^2-\sigma_2\sigma_3)+\frac{1}{S_{\mathrm{A}}^2}\left(\sigma_5^2+\sigma_6^2\right)\geq 1 \tag{2.15}$$

$$\begin{aligned}\frac{1}{Y_{\mathrm{C}}}\left[\left(\frac{Y_{\mathrm{C}}}{2S_{\mathrm{T}}}\right)^2-1\right](\sigma_2+\sigma_3)+\frac{1}{4S_{\mathrm{T}}^2}(\sigma_2+\sigma_3)^2+\frac{1}{S_{\mathrm{T}}^2}(\sigma_4^2-\sigma_2\sigma_3)\\ +\frac{1}{S_{\mathrm{A}}^2}\left(\sigma_5^2+\sigma_6^2\right)\geq 1,\end{aligned} \tag{2.16}$$

where S_{A} and S_{T} are the shear strengths in the axial and transverse directions. The comparison with the experimental results reported in [2.7] was repeated, again showing improved correlation.

Hashin noted the importance for FE analyses of not only knowing at what load material fails, but in what mode the failure occurs, so as to be able to accurately continue the simulation after the onset of failure. Further, Hashin noted that the specific form of the proposed criteria is not definitive, but simply a mathematical model used to fit the available experimental data. In fact, all the failure criteria expressed above are semi-empirical.

Puck [2.9] expanded on the failure mode-based approach of Hashin, taking into further consideration the nonlinear relationships associated with the compressive normal and shear stresses of unidirectional fiber-reinforced laminae. Puck rederived the fiber failure criterion and developed several new matrix failure criteria. The rederived tensile fiber failure criterion accounted for the different material properties of the constituent materials (i.e., fibers and matrix) and the lamina, as well as the distribution of stresses between the constituent materials:

$$\frac{E_1}{X_{\mathrm{T}}}\left(\varepsilon_1+\frac{\nu_{f12}}{E_{f1}}m_{\sigma f}\,\sigma_2\right)\geq 1, \tag{2.17}$$

where ν_{f12} and E_{f1} are the Poisson ratio and Young's Modulus of the fibers, and $m_{\sigma f}$ is a stress amplification factor that takes into account the higher stresses in the fibers with respect to the matrix at the micromechanical level.

The assumption by Mohr [2.10] that only the stresses on a particular action plane can cause a failure within that plane is the basis for the matrix failure criteria proposed by Puck. As such, the matrix failure criteria were derived in a coordinate system orthogonal to the matrix

fracture plane. For cases with positive transverse stresses σ_{n}, the general form of the matrix failure criterion is:

$$\left(\frac{\sigma_{\mathrm{n}}}{R_{\mathrm{n}}}\right)^2+\left(\frac{\sigma_{\mathrm{nt}}}{R_{\mathrm{nt}}}\right)^2+\left(\frac{\sigma_{\mathrm{n1}}}{R_{\mathrm{n1}}}\right)^2\geq 1, \tag{2.18}$$

where the subscripts 1, n, and t refer to the directions parallel to the fibers, normal to the fracture plane, and perpendicular to the fibers in the fracture plane, respectively; R_{n}, R_{nt}, and R_{n1} are the strengths in the crack-oriented coordinate system. This general form is essentially the original Hashin matrix failure criterion in a crack-oriented coordinate system. Compressive stress normal to the fracture plane tends to prevent cracking rather than contribute to its onset. The shear strengths of the fracture plane are effectively increased by the compressive normal stresses through:

$$\left(\frac{\sigma_{\mathrm{nt}}}{R_{\mathrm{nt}}-p_{\mathrm{nt}}\sigma_{\mathrm{n}}}\right)^2+\left(\frac{\sigma_{\mathrm{n1}}}{R_{\mathrm{n1}}-p_{\mathrm{n1}}\sigma_{\mathrm{n}}}\right)^2\geq 1, \tag{2.19}$$

where p_{nt} and p_{n1} refer to the experimentally derived slopes of the (σ_{n},σ_{nt}) and (σ_{n},σ_{n1}) fracture envelopes. Using the matrix failure criteria resultant of transforming from the crack-oriented coordinate system to the material coordinate system, it is possible to predict the orientation of the newly formed cracks.

To assess the capability of predicting failure in fiber-reinforced epoxy laminates under biaxial loading, a study known as the World-Wide Failure Exercise (WWFE) was conducted in which the performance of several laminates was predicted by the authors of several proposed failure criteria [2.11]. Results indicated that while good agreement between predictions and experimental results were achieved in the tensile-tensile regime, the inclusion of compressive transverse stress and shear stresses led to significant prediction errors [2.12]. Similar results were achieved in a comparative study by Daniel [2.2]. Due to the appreciable variance in predictive results, Daniel recommends selecting a failure criterion from each class (i.e., non-interactive, interactive, and failure mode-based) and choosing a criterion based on the required safety factors

involved in the design; the most conservative being the interior regions of all evaluated failure envelopes. While Daniel's recommendations are sound for engineering design purposes, several researchers continue to further develop their sets of failure criteria to better represent the physical processes of damage initiation and progression.

Motivated by the results of the WWFE, Dávila and Camanho [2.13] proposed a new set of failure mode-based failure criteria for matrix and fiber failures, referred to as the LaRC03 failure criteria. Expanding on the work of Hashin and Puck, the different failure mechanisms resultant of tensile and compressive loading were considered for both the matrix and fiber failure criteria.

For cases of transverse compression, the matrix failure criterion proposed by Puck was adopted, noting that the in-situ strengths should be used for laminated composites. Cases involving transverse tension and shear, however, were identified as being a mixed mode fracture mechanics problem. The stress energy release rates for Mode I and Mode II loading were calculated for an assumed matrix crack and combined according to the mixed mode failure criterion proposed by Hahn [2.14], yielding:

$$(1-g)\frac{\sigma_2}{Y_{\mathrm{IS}}^{\mathrm{T}}}+g\left(\frac{\sigma_2}{Y_{\mathrm{IS}}^{\mathrm{T}}}\right)^2+\left(\frac{\sigma_6}{S_{\mathrm{IS}}}\right)^2\geq 1, \tag{2.20}$$

where g is the ratio of the Mode I and Mode II fracture toughness values, and $Y_{\mathrm{IS}}^{\mathrm{T}}$ and S_{IS} are the in-situ tensile transverse strength and in-situ shear strength, respectively.

In tension, the maximum strain criterion was deemed sufficient for predicting fiber fracture. Under compression, however, fiber failure was related to shear kinking and localized matrix failure. Dávila and Camanho assumed a kink band of a certain angle of misalignment, determined the local matrix stresses oriented with respect to the kind band, and related these to the known compressive strengths in the material coordinate system. Solving for the angle of misalignment, the compressive fiber failure criteria are determined by solving either the tensile or

compressive matrix failure criteria, using the local matrix stresses of the misaligned coordinate system as inputs.

The predictive capability of the LaRC03 failure criteria was compared with the experimental results used in the WWFE. Improved correlation was observed for both the σ_1-σ_2 failure envelope, as well as the compressive strength as a function of lamination angle. Pinho et al. [2.15] later expanded on the work of Dávila and Camanho, proposing an extension to the LaRC03 failure criteria, referred to as the LaRC04 failure criteria. Neglecting the assumption of a plane stress condition, the failure criteria were rederived for cases involving triaxial loading and accounting for shear nonlinearity.

2.1.2. PROGRESSIVE DAMAGE MODELING TECHNIQUES

On some scale, the presence of damage in a material will affect either its mechanical response [2.16] or its propensity for additional damage to form. In fiber-reinforced polymers, the gradual accumulation of microscale matrix cracking can have a measureable effect on the global response of the material, while, in the case of compressive loading in the fiber directions, also increasing the likelihood of local fiber kinking [2.13] and other failure modes. In the context of progressive damage modeling, careful consideration of the method and resolution with which damage is represented is key to accurately modeling its initiation, progression, and eventual instability.

The conceptually simplest case to consider for modeling damage propagation is a single, dominant crack progressing through a homogenous, isotropic material. For brittle materials, the complete removal of elements from the mesh when the failure criterion is satisfied can accurately represent the crack propagation through the mesh. However, the singularity at the crack tip will not be accurately represented due to the (at least) one-element thickness of the damage, and the sudden failure of each element will cause bursts of strain energy to be released [2.19]. Hahn and Tsai [2.20] observed that a gradual failure model, rather than a complete failure model, better

represented the off-axis failure processes of cross-ply carbon and glass fiber-reinforced epoxy laminates. This observation holds true for modeling damage progression through most brittle resin materials.

In cases in which the direction of crack propagation is known a priori and the mesh has been designed to accommodate the crack growth, the nodal release [2.17] and nodal splitting [2.18] techniques can be applied. If the direction of crack propagation is not known a priori, the crack path will likely bisect elements of the original mesh as it progresses. Re-meshing algorithms have been successfully implemented in several cases to accommodate for meandering crack fronts; however, error is introduced when linking the internal variables of old and new meshes [2.19], and the model becomes less computationally efficient if re-meshing is frequently required.

Beissel et al. [2.21] proposed the Element-Failure Method (EFM) to account for the gradual failure of the elements along a meandering crack propagation path. Using EFM, an element through which the crack tip passes is failed (i.e., retains the ability to sustain compressive stresses only). To avoid the release of bursts of strain energy associated with the sudden failure of an element, a set of nodal forces are applied to the failed element containing the crack tip. These applied nodal forces are initially equal to the internal forces of the element. As the crack tip progresses through the element (i.e., the damage becomes more severe), the nodal forces are gradually reduced to zero. A similar approach was previously proposed by Bakuckas et al. [2.18] to smooth crack growth as modeled using the nodal splitting technique.

Tay et al. [2.19] expanded the EFM of Beissel to model the progressive failure of composite materials. For a fully intact element, there exists a set of internal nodal forces which are in equilibrium with the nodal forces of the adjacent elements. As damage develops in an element, the ability for that element to transfer force is decreased by some amount, depending on the mode and severity of the damage. External nodal forces are applied to failing elements in equal magnitude and opposite direction to the net internal nodal forces of the adjacent elements.

This process is performed iteratively until the net internal nodal forces of the adjacent elements reach the desired fraction of their undamaged values. No changes are made to either the original mesh or the elemental stiffness matrices, reducing the computational cost of the model. The elemental stiffness matrix and the nodal forces are related through:

$$C_{ij}\,u_j = f_i, \tag{2.21}$$

where C_{ij} is the elemental stiffness tensor, and u_j and f_i represent the nodal displacements and forces, respectively. For any desired effective change in the stiffness properties of an element, a set of corresponding external nodal forces can be determined [2.1].

Rather than *effectively* modifying the components of the elemental stiffness matrix, the gradual onset and progression of damage in composite materials has been modeled by several authors by *directly* modifying the material properties of damaged elements. This technique is broadly referred to as the Material Properties Degradation Method (MPDM). Significant flexibility exists in this approach regarding how specific damage modes are represented and what material properties they affect. However, care must be taken to ensure the thermodynamic validity of any proposed stiffness tensor which incorporates damage.

Tan [2.22] proposed that the effective stiffness properties of a damaged lamina could be written in terms of the undamaged stiffness properties and scalar damage state variables as:

$$\begin{aligned} E_1 &= (1-d_1)E_1^0 \\ E_2 &= (1-d_2)E_2^0 \\ G_{12} &= (1-d_6)G_{12}^0, \end{aligned} \tag{2.22}$$

where E_1^0, E_2^0, and G_{12}^0 are the undamaged stiffness terms, d_1, d_2, and d_6 are damage state variables which vary from zero (undamaged) to one (fully damaged), and E_1, E_2, and G_{12} are damaged stiffness terms. Nuismer and Tan [2.23] developed a closed-form elasticity solution for unidirectional laminae of particular matrix crack spacing to solve for these damage state variables, but found the resultant stiffness terms to be laminate-dependent.

Matzenmiller et al. [2.24] proposed a diagonal fourth-order damage tensor M to represent the relationship between the effective ($\hat{\sigma}$) and nominal (σ) stresses of a damaged element through:

$$\hat{\sigma}_i = M_{ij}\,\sigma_j, \tag{2.23}$$

The tensor product of the undamaged compliance tensor H^0 and the damage tensor can be used to relate the nominal stress and strain ε:

$$\varepsilon_k = H^0_{ki}\,\hat{\sigma}_i \tag{2.24}$$

$$\varepsilon_k = H^0_{ki} M_{ij}\,\sigma_j \tag{2.25}$$

The damaged compliance tensor H can then be represented as:

$$H = \begin{bmatrix} \dfrac{1}{(1-d_1)E_1} & -\dfrac{\nu_{21}(\boldsymbol{d})}{(1-d_2)E_2} & 0 \\ -\dfrac{\nu_{12}(\boldsymbol{d})}{(1-d_1)E_1} & \dfrac{1}{(1-d_2)E_2} & 0 \\ 0 & 0 & \dfrac{1}{(1-d_6)G_{12}} \end{bmatrix}, \tag{2.26}$$

where Matzenmiller assumed the Poisson's ratios to be functions of the state-of-damage. Significant experimental work on the damage processes of unidirectional lamina indicate that the Poisson effect does not vary with increased matrix crack density; the required symmetry of the damaged stiffness tensor requires both off-diagonal terms to be independent of damage. As such, the damaged compliance tensor can be simplified to:

$$\mathrm{H} = \begin{bmatrix} \dfrac{1}{(1-\mathrm{d}_1)\mathrm{E}_1} & -\dfrac{\nu_{21}}{\mathrm{E}_2} & 0 \\ -\dfrac{\nu_{12}}{\mathrm{E}_1} & \dfrac{1}{(1-\mathrm{d}_2)\mathrm{E}_2} & 0 \\ 0 & 0 & \dfrac{1}{(1-\mathrm{d}_6)\mathrm{G}_{12}} \end{bmatrix} \tag{2.27}$$

The resulting damaged stiffness tensor is:

$$\mathrm{C} = \frac{1}{\mathrm{D}}\begin{bmatrix} (1-\mathrm{d}_1)\mathrm{E}_1 & (1-\mathrm{d}_1)(1-\mathrm{d}_2)\nu_{21}\mathrm{E}_2 & 0 \\ (1-\mathrm{d}_1)(1-\mathrm{d}_2)\nu_{12}\mathrm{E}_1 & (1-\mathrm{d}_2)\mathrm{E}_2 & 0 \\ 0 & 0 & \mathrm{D}(1-\mathrm{d}_6)\mathrm{G}_{12} \end{bmatrix} \tag{2.28}$$

where

$$D = 1 - (1 - d_1)(1 - d_2)\nu_{21}\nu_{12} \tag{2.29}$$

Lapczyk and Hurtado [2.25] further simplified the damaged stiffness tensor of Matzenmiller, assuming that the presence of cracks oriented in either the local 1- or 2-directions reduce the ability of the lamina to reduce shear deformation.

Maimí et al. [2.26] derived a similar result for the damaged compliance tensor; however, the assumption of a thermodynamically irreversible damage process was their starting point. If a complementary free energy density G can be formulated in terms of the internal stresses, stiffness properties, and the state-of-damage, the corresponding compliance tensor can be calculated through:

$$H = \frac{\partial^2 G}{\partial \sigma^2} \tag{2.30}$$

For example, the authors postulated the complementary free energy density of a damaged orthotropic lamina to be:

$$G = \frac{\sigma_{11}^2}{2(1-d_1)E_1} + \frac{\sigma_{22}^2}{2(1-d_2)E_2} - \frac{\nu_{12}}{E_1}\sigma_{11}\sigma_{22} + \frac{\sigma_{12}^2}{2(1-d_4)G_{12}}, \tag{2.31}$$

neglecting all temperature and moisture effects. Solving for the compliance tensor associated with this assumed complementary free energy density equation yields the compliance tensor formulated by Matzenmiller.

2.1.3. DAMAGE EVOLUTION

Whether through the manipulation of elemental material properties or through the application of nodal forces, the ability for an element to carry load and resist deformation can be diminished upon satisfying certain failure criteria. Both EFM and MPDM are capable of representing multiple, simultaneous, and coincident modes of damage. Several methods have been proposed regarding how to model particular damage modes and how to evolve the size and severity of damage upon continued loading after damage initiation.

Lee [2.27] developed a three-dimensional FE program capable of representing the initiation and progression of fiber fracture, matrix cracking, and delaminations in a biaxially-loaded, unidirectional fiber-reinforced laminate with a center hole. The maximum normal and maximum shearing stress failure criteria were used for each failure mode. At failure, certain terms of the elemental stiffness matrix were set equal to zero, depending on the mode of failure. For example, satisfaction of either fiber failure criterion resulted in the complete failure of the element (i.e., all stiffness terms set equal to zero). However, satisfaction of either matrix failure criterion caused only the stiffness terms associated with the local 2-direction to be set equal to zero:

$$C_{\mathrm{m}} = \begin{bmatrix} C_{11} & 0 & C_{13} & 0 & 0 & 0 \\ 0 & 0 & 0 & 0 & 0 & 0 \\ C_{13} & 0 & C_{33} & 0 & 0 & 0 \\ 0 & 0 & 0 & 0 & 0 & 0 \\ 0 & 0 & 0 & 0 & C_{55} & 0 \\ 0 & 0 & 0 & 0 & 0 & 0 \end{bmatrix} \tag{2.32}$$

Likewise, satisfaction of either delamination failure criterion resulted in the zeroing of the stiffness terms associated with the local 3-direction:

$$C_{\mathrm{d}} = \begin{bmatrix} C_{11} & C_{12} & 0 & 0 & 0 & 0 \\ C_{12} & C_{22} & 0 & 0 & 0 & 0 \\ 0 & 0 & 0 & 0 & 0 & 0 \\ 0 & 0 & 0 & 0 & 0 & 0 \\ 0 & 0 & 0 & 0 & 0 & 0 \\ 0 & 0 & 0 & 0 & 0 & C_{66} \end{bmatrix} \tag{2.33}$$

While simple to implement, the sudden, complete failure of the elements does not compare well with experimental observations [2.20]; the load bearing capacity of composite materials is rarely completely lost after an initial failure. The use of nonzero MPDM damage state variables (or through the partial failure of elements via EFM) would better represent the expected behavior. Additionally, convergence errors are known to occur when stiffness terms are set to zero without removing the failed element from subsequent calculations [2.1].

Tan [2.22] determined the damage state variable associated with the residual stiffness of a lamina containing one transverse matrix crack per element to be 0.20 using the elasticity solution

of cracked lamina developed by Nuismer and Tan [2.23]. Due to a lack of sufficient experimental data, Tan [2.22] and Tan and Perez [2.28] proposed parametric FE studies to determine the appropriate static damage state variables associated with tensile fiber fracture, matrix cracking due to compression and shear loading, and compressive fiber failure. Camanho and Matthews [2.29] developed a three-dimensional FE progressive damage model of a mechanically fastened joint of a composite laminate utilizing the results of such parametric studies; the damage state variables for tensile fiber fracture, matrix cracking due to compression and shear loading, and compressive fiber failure were found to be 0.07, 0.40, and 0.14, respectively. The stiffness terms of an element were degraded according to these internal damage state variables upon satisfying the corresponding Hashin [2.8] failure criterion. Comparing micrograph data in the regions where damage initiation was predicted and the computational results achieved using the proposed failure model, a satisfactory correlation between the two data sets was established.

Motivated by the small size of most failures with respect to elements, Reddy et al. [2.30] proposed to gradually degrade the stiffness properties of failing elements rather than reducing them to a static characteristic level. Reducing the stiffness of an element only to the level just under the exceeded failure criterion better represents the failure processes associated with quasi-static loading. Also, by using larger damage state variables (e.g., near unity) and allowing repeated failures of individual elements, the accumulation of damage can be represented. However, Reddy notes that modifying individual elemental stiffness matrices very often is computationally burdensome and suggests using damage state variables between 0.4 and 0.6 for each successive failure.

The semi-empirical nature of the aforementioned methods of progressive damage modeling has led to the development of more physically-based approaches for determining the severity of the internal damage state variables and advancing the state-of-damage. Through the principles of continuum mechanics, fracture mechanics, and experimental observations regarding the damage processes of composite materials, several authors have worked toward either reducing

the requisite number of or entirely eliminating the need for semi-empirical inputs in their proposed damage evolution laws.

Matzenmiller et al. [2.24] proposed a set of thermodynamic requirements for any equations representing damage growth, chief of which is the requirement for nonnegative energy dissipation:

$$D = \sum_{i=1} \frac{\partial G}{\partial d_i} \dot{d}_i \geq 0, \tag{2.34}$$

where D is the rate of energy dissipation, G is the complementary free energy density, and d_i is the damage state variable associated with the i^{th} failure mode. For the case of uniaxial tensile loading oriented in the fiber direction, the damage state variables are assumed to evolve according to the assumed exponential function:

$$d_i = 1 - \exp\left[\frac{1}{m_i}(1 - {\varphi_i}^{m_i})\right], \tag{2.35}$$

where φ_i is a failure criterion indicative of damage when greater than or equal to unity, and m_i is a constant semi-empirical softening term. As the failure criterion is increasingly exceeded, damage becomes more severe. The softening term is the only input which differentiates the post-failure behavior of different materials. Gama et al. [2.31] performed a parametric study on the effect of the softening term on the post-failure behavior of a single element for various loading and boundary conditions. Material behaviors ranging from elastic-brittle fracture to strain-hardening were represented with the appropriate selection of m. However, different failure modes will affect the overall material response differently, requiring individual softening terms. As such, new materials require mechanical testing designed to isolate each failure mode to study its effect on the post-failure behavior prior to selecting a set of softening terms.

Maimí et al. [2.26] assumed a more general exponential function to determine the damage state variables associated with each failure criterion:

$$d_i = 1 - \frac{1}{\mathrm{F}(\varphi_i)} \exp\left[A_i\left(1 - \mathrm{F}(\varphi_i)\right)\right] \mathrm{F}\left(\varphi_j\right), \tag{2.36}$$

where $\mathrm{F}(\varphi_i)$ is a function of the failure criterion, A_i is damage law parameter, and $\mathrm{F}\left(\varphi_j\right)$ is a coupling factor between other damage state variables and failure criteria. However, unlike the Matzenmiller equation, the damage law parameters A_i are explicitly solved in terms of physically meaningful values. By integrating the energy dissipation equation and equating the result with the Bažant [2.32] crack band model, the damage law parameters can be determined by evaluating:

$$\int_0^\infty \frac{\partial G}{\partial d_i} \dot{d}_i dt = \int_1^\infty \frac{\partial G}{\partial d_i} \frac{\partial d_i}{\partial \varphi_i} d\varphi_i = \frac{G_i}{L_c}, \tag{2.37}$$

where G_i is the fracture toughness associated with the i^{th} failure mode and L_c is the characteristic length of the element. For the case of fiber fracture, the damage state variable can be determined to be:

$$d_1 = 1 - \frac{1}{\varphi_1} \exp\left[\frac{2X_T^2 L_c}{2E_1 G_i - L_c X_T^2}(1 - \varphi_1)\right] \tag{2.38}$$

As it is widely accepted the fiber fracture is independent of other failure modes, the coupling term $\mathrm{F}\left(\varphi_j\right)$ can be neglected. For cases involving interactive failure modes (e.g., fiber kinking, matrix cracking, etc.), however, iterative methods are required to solve for the damage law parameters.

2.2. MONITORING & INSPECTION METHODS

The increased use of composite laminates in general aviation and commuter aircraft serves as an impetus to identify the nondestructive inspection (NDI) method most appropriate for various damage scenarios and the corresponding nondestructive test (NDT) methodology necessary to determine the extent of existing damage and the formation of new failures. The use of composites is particularly challenging for NDI and NDT because of the different modes of failure encountered in composite structures and their complexity and multiplicity.

The concern regarding NDI in composite structures is focused on two separate problems: (i) the detection and inspection of existing damage that is embedded in the structure, caused by foreign objects (e.g., runway stones, bird strikes [2.1], etc.), induced during handling (e.g., dropped tools, runway accidents, etc.), present due to manufacturing anomalies (e.g., resin-poor regions, inadequate bonding, etc.), or occurred during prior service load [2.34]; and (ii) the detection and inspection of newly formed damage, or failures, that occur during service, in real-time. Existing damage and new failures often link and interact. Existing damage often serves as a source for the onset of new failures and their subsequent growth and accumulation, ultimately triggering a catastrophic fracture.

The presence of damage in sandwich composites is more complex than that experienced with conventional metallic structures: (i) damage consists of multiple modes, including fiber fracture, fiber/matrix interfacial failure, matrix cracking, matrix splitting, matrix crazing, delamination, skin-to-core disbonding, intra-cell dimpling, face wrinkling, core crushing, core shear, and local core indentation [2.35]; (ii) the number of individual cracks related to most damage modes could be extremely large; (iii) numerous modes of damage occur at the same site, often interacting [2.36] and obscuring each other from the penetrating eye of the NDI technique used, making it difficult to identify and discern individual modes; and (iv) the criticality of the damage, or its propensity to grow, are rarely obvious. The complexity of the actual state-of-damage in composites renders a reliable, accurate, and timely prediction of damage criticality highly difficult.

Furthermore, the site where damage is most anticipated to occur is often not obvious in composite aircraft structures, particularly when nonvisual damage is of concern. When composites are used in aircraft structures, they oftentimes span very large regions in a uniform manner. Thus, many of the commonly used NDI techniques, such as ultrasound, radiography, and eddy current are not practical in terms of evaluating damage criticality in an affordable and

timely manner. These NDI techniques are mostly focused on inspecting suspected sites and, when present, on mapping internal nonvisual damage.

Despite these difficulties, several means of measuring deformation and monitoring the formation and progression of damage through composite aircraft structures have been developed and successfully implemented. Brief reviews of several such methods are discussed here.

2.2.1. DIGITAL IMAGE CORRELATION

Electrical resistance strain gages have been widely used to characterize structures' mechanical response to load since the 1940s [2.37]. Their installation ahead of cracks in metallic structures provides valuable information for calculating the stress concentration factors for fracture mechanics-based analyses and damage tolerance studies. However, their application to the characterization of structures composed of advanced composite materials is often fraught with difficulties. The increased sensitivities to gage misalignment due to orthotropic material properties [2.38] and gage sizing and location due to the architecture of woven composites [2.39] complicate the experimental setup and data reduction. Further, damage processes in advanced composite structures are often more complicated, affecting larger regions than in conventional metallic structures. As a result, the selection of strain gage locations becomes both more important and difficult because the sites of strain concentrations at various stages of damage progression are less clear a priori. The digital image correlation (DIC) method addresses these issues while also greatly increasing the amount of recorded data for a given test.

The DIC method is a non-contact, optical means of measuring the full-field deformation of the surface of a test specimen. A series of digital images of a test specimen is taken while unloaded and at multiple load intervals. A field of points on the surface of the specimen, distributed according to a user-defined planar density (as explained below), can be tracked through the series of images by recognition of the gray-scale intensity distribution in the vicinity

of each tracked point. Through the use of fundamental mechanics of materials and continuum mechanics principles, the in-plane strains can be calculated from the recorded displacement data.

Test specimens are usually prepared by applying a stochastic, high-contrast pattern to the measured surface so as to create easily differentiable unit areas to assist in their tracking during deformation. When the surface texture of the test specimen is sufficiently rough and the resolution of the digital images is sufficiently high with respect to the surface details of the specimen, it may not be necessary to apply any additional artificial pattern [2.40]. The DIC method has been successfully coupled with several advanced microscopic measurement techniques in this manner, as described thoroughly in the review by Pan et al. [2.41].

Several commercial and open-source software packages utilizing the DIC method are available. In this investigation, the instrumentation developed by GOM mbH (Mittelweg 7-8, 38106 Germany) was used. While the terminology used throughout the following discussion is that adopted by GOM regarding their ARAMIS DIC system [2.42], the basic principles discussed are fundamental to all DIC-based methods.

Through a series of recorded digital images taken while a specimen is under various load levels, the displacements of a field of points can be tracked by comparing the gray-scale intensity distributions in the immediate vicinity of each point. Each tracked point is the center of a *facet*, with the spacing between facets referred to as the *facet step*, Figure 2.1. Each facet represents the region in which the gray-scale intensity distribution is quantified. Facets can vary in size and shape and are not bounded by the facet step, allowing overlap in the regions used to track each point, Figure 2.2. The facet step and *facet size* are both defined in terms of pixels.

Facets are identified throughout a series of images by first quantifying the gray-scale intensity distribution of the facets in the baseline image, then using either a cross-correlation or least squares criterion to search the subsequent images for each facet. The center of each facet in the subsequent images will be located where the value of the cross-correlation coefficient field is

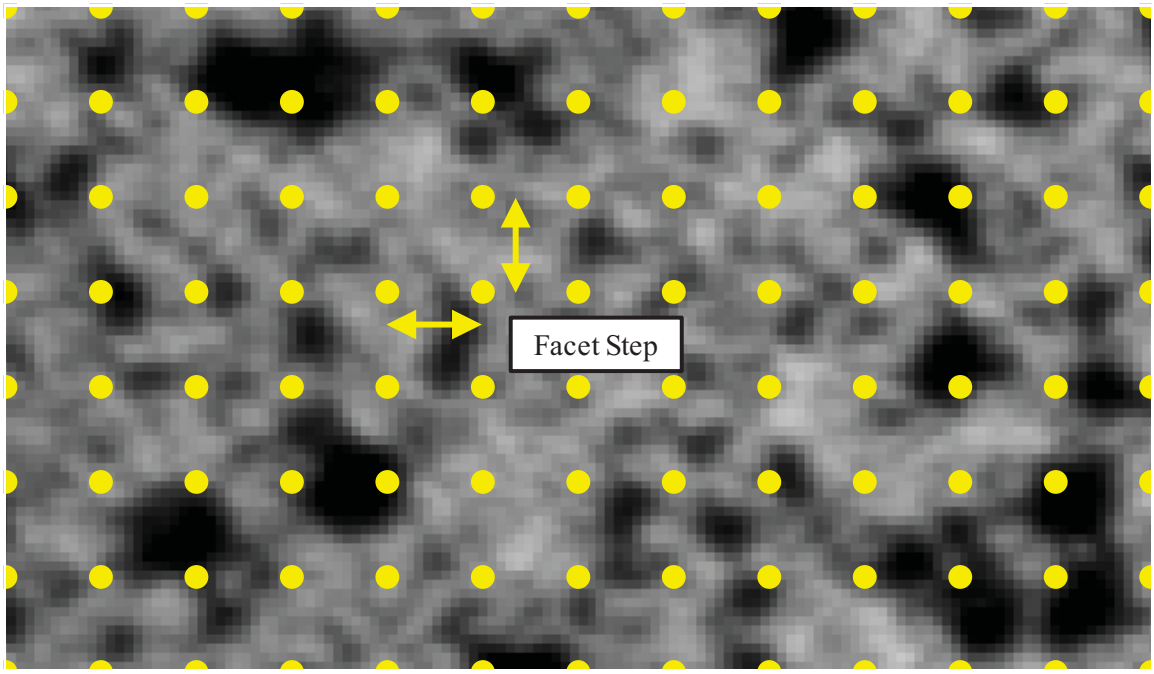

Figure 2.1. Stochastic, black and white pattern with grid of points at which displacement is to be measured. The spacing between the points is referred to as the facet step.

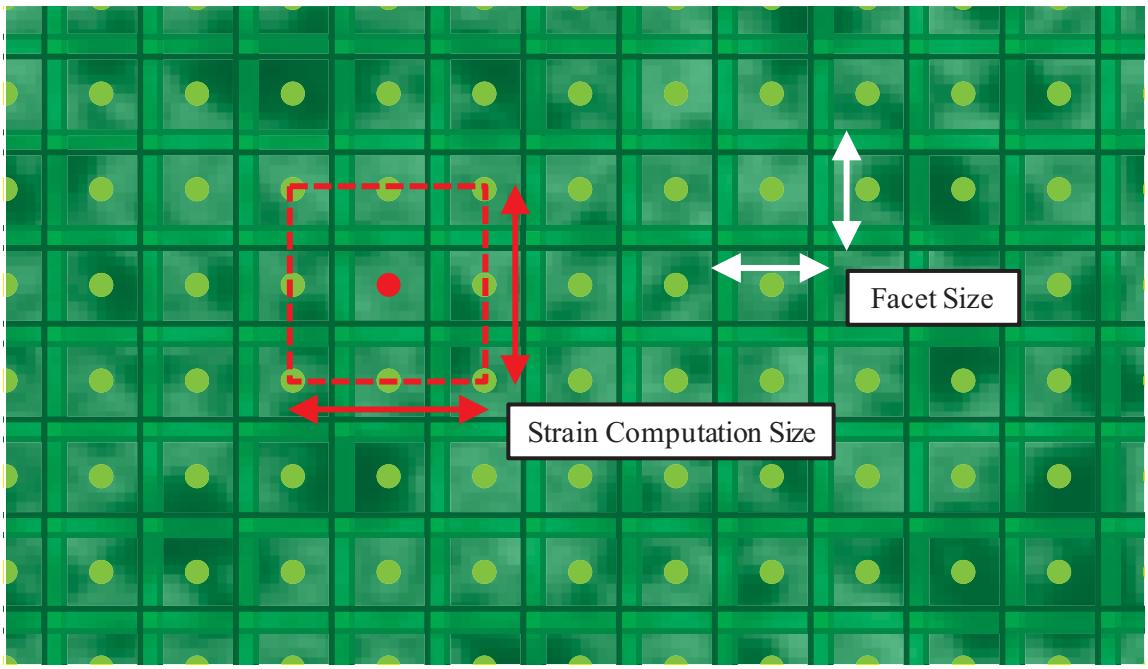

Figure 2.2. Facet size and a 3x3 strain computation size illustrated with respect to the facet field shown in Figure 2.1.

maximum (or where the value of the least squares coefficient field is minimum) when calculated with respect to its location in the baseline image. The two criteria are expressed as follows:

$$C_{\mathrm{CC}} = \sum_{i=-N}^{+N} \sum_{j=-M}^{+M} f(x_i, y_j) g(x_i', y_j') \tag{2.39}$$

$$C_{\mathrm{LS}} = \sum_{i=-N}^{+N} \sum_{j=-M}^{+M} \left[f(x_i, y_j) - g(x_i', y_j') \right]^2, \tag{2.40}$$

where C_{CC} and C_{LS} are the coefficients related to the cross-correlation and least squares criteria, respectively, and $f(x_i, y_j)$ and $g(x_i', y_j')$ are the gray-scale values at pixel (i, j) in an N by M pixel facet in the baseline and deformed images, respectively. Several additional variations of these two criteria are described by Pan et al. [2.41]. For a series of high-resolution images, searching the entire image for each facet is computationally costly [2.43]. Also, large rigid body translations and rotations of the test specimen with respect to the camera can cause erroneous determinations of facet locations in the subsequent images [2.41]. An accurate initial guess of the location and orientation of a facet through the series of images eases the computational burden of the process by localizing the region in which to maximize (or minimize) the correlation coefficient. Specifying a starting point (i.e., the location and orientation of a single facet through the series of images) in each image of the data set also solves issues related to rigid body translations and rotations [2.42].

Knowing the locations of each facet throughout the series of images, determining the displacements and strains requires only the application of fundamental mechanics of materials [2.44] and continuum mechanics [2.45] theories. Designating the locations of a field of points in a baseline image and in a deformed image as $d\mathrm{X}$ and $d\mathrm{x}$, respectively, the two fields are related through

$$d\mathrm{x} = \mathbf{F} \cdot d\mathrm{X}, \tag{2.41}$$

where **F** is the deformation gradient tensor. The deformation gradient tensor takes into account all rigid body translations, rotations, and deformations of the field of points with respect to the baseline image. Further, **F** can be decomposed into the tensor **R**, which accounts for rigid body rotation, and the right stretch tensor **U**, which accounts for deformation, as follows:

$$\mathbf{F} = \mathbf{R} \cdot \mathbf{U} \tag{2.42}$$

The engineering strain ε can be easily extracted from the stretch λ through their relation:

$$\varepsilon = \lambda - 1. \tag{2.43}$$

Knowing the planar location history of a field of points, the extraction of the planar strains is conceptually straightforward. However, to assign a single value to the strain at a particular facet requires further consideration.

While displacements, strains, and their derivatives are continuous in a physical material, the DIC measurements do not naturally adhere to this requirement. Because the strains measured via DIC are not continuous, strains calculated with respect to different neighboring facets would yield multiple results for individual facets.

The strains at each facet must be calculated over an area of at least 3 by 3 facets, as shown in Figure 2.2. Assuming a first-order shape function for strain, a system of two equations with four unknowns is generated for each facet involved in the strain computation

$$\begin{aligned} x_i^{'} &= x_i + u + \frac{\partial u}{\partial x}(x_i - x_0) + \frac{\partial u}{\partial y}(y_j - y_0) \\ y_j^{'} &= y_j + v + \frac{\partial v}{\partial x}(x_i - x_0) + \frac{\partial v}{\partial y}(y_j - y_0), \end{aligned} \tag{2.44}$$

where x_0 and y_0 are the coordinates of the central facet, x_i, y_j, $x_i^{'}$, and $y_j^{'}$ are the baseline and deformed coordinates of the facet at location (i, j), and u and v are the displacements of the central facet along the x and y directions. With only two neighboring facets considered, the four unknowns can be solved, from which the strains are easily reduced using the strain-displacement relations:

$$\varepsilon_x = \frac{\partial u}{\partial x}$$

$$\varepsilon_y = \frac{\partial v}{\partial y} \tag{2.45}$$

$$\varepsilon_{xy} = \frac{1}{2}\left(\frac{\partial u}{\partial y} + \frac{\partial v}{\partial x}\right)$$

While it is possible to determine the strain at a particular facet by considering the displacement of only two neighboring facets, it is beneficial to use all available neighboring facets. This approach can offer significant data redundancy, eliminating much noise from the recorded DIC data. The redundancy in data is resolved via least squares error minimization.

2.2.2. ACOUSTIC EMISSION

The acoustic emission (AE) technique is an NDT method that is used to detect the onset of failure and monitor its progression during loading, in real-time. The detection of failure is based on the energy released as a result of the formation of new fracture surfaces (i.e., cracks, delaminations, etc.) during loading. The resulting elastic stress wave propagates through the material and the corresponding AE signal, as measured by the receiving sensor, is recorded. This signal is analyzed using a variety of well-established methods (e.g., [2.46]–[2.49]). The available literature on the theory and applications of AE is vast [2.50], with several published historical reviews of the field (e.g., [2.51], [2.52]). Accordingly, the articles cited throughout this section are oftentimes individual examples of many similar case studies.

The conventional wisdom of using AE is that it could serve multiple purposes, namely: (i) detecting the initiation and progression of failure and determining when it occurs in terms of load and/or number of fatigue cycles, (ii) locating sites of failure and tracking its progression, and (iii) determining the dominant failure modes. These three objectives should be accomplished simultaneously, in real-time, during loading, with the ultimate goal of evaluating damage criticality.

The first objective, detecting the onset of failure, has been successfully implemented under a wide variety of testing conditions. Early studies in the application of AE to damage processes in fiber-reinforced materials involved monitoring the number of counts (i.e., threshold crossings of a recorded waveform) and the rate of their accumulation with a single sensor as either load (e.g., [2.53]) or cycle count (e.g., [2.54]) were increased. Fuwa et al. [2.53] compared the stress-strain response of fiber-reinforced polymers and the cumulative counts generated during a uniaxial tensile test. Initial count accumulation was noted to begin prior to stress-strain nonlinearity, indicating the early stages of the damage process had only a nominal effect of the global material response.

Monitoring the rate of damage accumulation is accomplished by studying the accumulation of AE signals and the characteristics of their waveforms with applied load. Once failure occurs at a given load level, AE activity increases rapidly with applied load, nearly exponentially when the load reaches its ultimate. Fracture is normally anticipated when the rate of accumulation of events is so rapid that it continues at that rate under a constant load. Bussiba et al. [2.55] studied damage processes in carbon/carbon unnotched and notched three- and four-point bending tests. Three distinct stages of AE count accumulation were observed: no activity during linear-elastic portion, a linear increase in activity after the material strength was reached, and a significant jump and exponential progression at fiber failure.

As a passive NDT method, AE cannot quantitatively determine the extent of existing damage in terms of damage size and shape. Only a single opportunity exists to detect the stress wave resultant of a failure: when it forms. Existing dormant damage that is not affected by the applied load will not generate an AE signal. Thus, dormant damage will not be detected by monitoring AE. Under certain circumstances, however, such existing dormant damage may become a source of emission generated by fretting of the fracture surfaces [2.56]. Although such fretting-generated emission is normally considered as noise, it is important to realize that it could often serve as an indicator of existing damage and provide reliable information as to the

approximate site of that damage. In many cases, especially during fatigue loading, the amount of fretting emission exceeds the emission generated by new failures. Further, it has been shown that under controlled laboratory conditions, at low-frequency cyclic loading (e.g., 1.0 Hz), when having a single dominant mode of damage (e.g., matrix splitting and transverse matrix cracks), the source of the repeated fretting-generated emission could be located, and the progression of the cracks could be tracked (e.g., [2.57]–[2.60]).

The second objective, determining the source location of new failures, is obtained by reducing the recorded arrival time and sensor location data of several AE hits via triangulation. Note that an AE signal recorded by a single sensor is defined as a *hit*, while a set of signals that generates a locatable physical change in the structure is defined as an *event*. While the basic method of determining the source location is straightforward, several possible sources of error and uncertainty exist and must be taken into account.

For a homogeneous, isotropic, non-dispersive material, the source location of a stress wave in n spatial dimensions can be determined with arrival time data from at least $n + 1$ sensors (e.g., for linear location one needs at least two sensors, and for planar location one needs at least three sensors). In such a material, the material wave speed c can be assumed to be constant, independent of both propagation direction and distance. The source location and arrival time can be related via the square of the distance traveled by the stress wave:

$$(x_S - x_i)^2 + (y_S - y_i)^2 = (ct_i)^2, \tag{2.46}$$

where x_S and y_S are the planar coordinates of the source location, x_i and y_i are the planar coordinates of the i^{th} sensor, and t_i is the time elapsed between the stress wave initiation and its detection by the i^{th} sensor. However, for the vast majority of cases, t_i is not explicitly known a priori. To address this, the arrival time data are rearranged with respect to the first recorded stress wave:

$$t_i = t_0 + \Delta t_i \tag{2.47}$$

where t_0 is the time elapsed between the stress wave initiation and its detection by the nearest sensor, and Δt_i is the difference in arrival times between the sensor closest to the source and the i^{th} sensor. This makes the unknowns include the n spatial dimensions and one temporal dimension. To solve for the source location in a planar system, data from at least three sensors must be available, generating three equation of the following form:

$$\begin{aligned} 2(x_j - x_i)x_S + 2(y_j - y_i)y_S + 2c^2(\Delta t_j - \Delta t_i)t_0 \\ = x_j^2 + y_j^2 - x_i^2 - y_i^2 + c^2(\Delta t_i^2 - \Delta t_j^2) \end{aligned} \tag{2.48}$$

If arrival time data are available for more than the minimum number of required sensors, the system of equations becomes redundant. Redundancy in arrival time data reduces the negative effects of any variations in sensor sensitivity, quality of sensor coupling, and any other hardware- or setup-related discrepancies. The method of least squares can be used to determine the source location for redundant systems [2.61].

To accurately locate new failures in real-time, the proper selection of the AE sensors (i.e., in terms of sensitivity, frequency range, size, etc.), the selection of the preamplifier parameters (i.e., frequency band, noise filtering, etc.), and the measurement of the wave speeds for the subject material/structure must be performed. Additionally, the accuracy and relevancy of the results depend on the manner in which the sensors are placed on the structure, e.g., their placement relative to potential failure sites and to sites of extraneous emission, their location relative to each other, the use of the proper coupling with the tested structure, and others. One of the more important difficulties in locating failure in composite structures is that with increasing load the number of cracks formed throughout the structure increases markedly. That is, the state-of-material is changing continuously, affecting the speed and dispersion characteristics of stress waves in the material, possibly resulting in a distorted location of the actual site of failures.

In anisotropic materials, the wave speed cannot be assumed to be constant in all directions. Like the stiffness and strengths of fiber-reinforced composite materials, wave speed is

a function of orientation relative to the fiber directions. Kundu et al. [2.62] re-derived the triangulation equations assuming that the wave speed is a known function of θ, the angle between the local material coordinate system the wave path through an anisotropic material.

$$(x_S - x_i)^2 + (y_S - y_i)^2 = (c(\theta)t_i)^2 \tag{2.49}$$

Experiments were carried out by dropping plastic and steel balls at known locations on a graphite/epoxy plate and comparing the original and modified triangulation methods' abilities to accurately identify the source location [2.63]. Significant improvement in source location was observed when the variation of wave speed with material orientation was considered.

The definition of the arrival time of a stress wave is critical to accurately identifying the source location. The arrival time of a stress wave is most commonly defined as the initial crossing of a user-defined amplitude threshold value. This approach is computationally efficient, simple to apply, and reasonably accurate for homogenous, non-dispersive materials. However, stress waves most oftentimes consist of multiple wave modes (e.g., extensional and flexural) and are traveling through dispersive (i.e., wave velocity depends on frequency) media [2.64]. Modal acoustic emission (MAE) takes these facts into consideration. Gorman [2.65] and Gorman and Prosser [2.66] stated that accurate AE source location must take into consideration the multiple modes of a stress wave. While extensional modes have a constant wave velocity, the flexural mode components are dispersive, with their velocities varying with the square root of their frequency. Using MAE, Surgeon and Wevers [2.67] demonstrated the effect of using the arrival time of specific frequency components on linear source location using two AE sensors on a carbon fiber-reinforced sample under three-point bending. The number of required sensors was later shown to be reduced by using the arrival times of multiple frequency components at individual sensors [2.68].

The third objective, identifying the major modes of failure, is accomplished via signal analysis of AE waveforms. In laboratory tests, a great deal of effort over the past three decades was directed toward identifying the various failure mechanisms that occur in composites during

loading via reduction of AE waveform data. Conventional analyses involve studying the distributions of typical waveform characteristics (e.g., amplitude, duration, counts, energy, etc.). Becht et al. [2.69] studied damage propagation in glass-reinforced polymer laminates, attempting to distinguish different failure modes via AE waveform characteristics. *Fiber* and *inter-fiber* (i.e., matrix cracking, delamination, etc.) failures were distinguished by fitting their respective amplitude distributions to an assumed exponential function:

$$I = I_0 D^{-n} \tag{2.50}$$

where I is the count rate, D is the discriminator threshold level, and I_0 and n are constants. The authors found that the dominant failure mode (i.e., either fiber or inter-fiber failure) corresponded to different values of n. Barré and Benzeggah [2.70] studied damage mechanisms in short glass fiber-reinforced polymers using AE and scanning electron microscopy. A correlation was found between damage mechanisms (i.e., matrix cracking, interface failure, fiber pull-out, and fiber fracture) and AE amplitude ranges for the specific material and experimental setup: matrix cracking ranged from 40 to 55 dB, interfacial failure from 60 to 65 dB, fiber pull-out from 65 to 85 dB, and fiber fracture from 85 to 95 dB. Siron et al. [2.71] reported similar results, observing that low duration and amplitude waveforms are evident of matrix microcracking, medium duration and amplitude waveforms are evident of delamination initiation and growth, and medium duration and high amplitude waveforms are evident of fiber fracture.

It should be emphasized that AE signals are generated by numerous modes of failure in filamentary composites, on both the micro- and macroscales. The multiple modes of failure and their interactions often make it difficult to isolate and separate them to identify a direct correspondence between a specific mode of failure and distinct corresponding AE signal intensities [2.72].

Furthermore, when loading approaches fracture, stress waves are generated at rapid rates, increasing the likelihood of simultaneously stimulating nearby AE sensors. Thus, these bursts of stress waves are recorded and considered by the AE instrumentation as a single waveform of

increased intensities. Additionally, the AE sensors can also be hit by stress waves reflected from either the boundaries of the structure or from internal free surfaces formed by newly created cracks or from those present within existing damage. These reflected stress waves may become superimposed with legitimate AE signals that are generated by new failures. Because of these interactions and the simultaneous occurrence of multiple stress waves, the separation, identification, and classification of AE signals is a formidable task.

The difficulties discussed throughout this section are greatly increased when AE is monitored in large, complex composite structures that are subjected to combined loading. Unwanted emission generated by the test fixtures and loading apparatus could interfere with and obscure the emission generated from within the test section [2.67]. Further, anticipating catastrophic fracture by monitoring the rate of AE events generated is often not accurate: bursts of stress waves recorded as single AE hits underestimate the actual number of hits generated by failures, while the emission generated by fretting overestimate the emission generated by actual damage. For certain composite materials, the audible level of emission is the best real-time predictor of ultimate fracture. It is the friction-generated emission that is most probably responsible for the typical exponential rise of AE activity with increasing load.

Nevertheless, despite the difficulties enumerated on the accuracy of the AE technique, and the complications which arise when transferring laboratory-based results to practical applications, the passive nature of the AE method provides an attractive technique for real-time damage monitoring regarding important aspects of testing of composite structures. The AE technique, when applied by a trained professional, is an important NDT tool that could provide valuable information on several of the key objectives enumerated above.

2.2.3. FREQUENCY RESPONSE

The frequency response (FR) technique is an active NDT method that consists of monitoring the waveforms propagated through a structure as a result of an induced mechanical

pulse. The technique applied in this study is based on the introduction of constant-amplitude sinusoidal waves of continuously varying frequencies through a wideband piezoelectric actuator (pulser) and measuring the frequency response of the material through a similar wideband receiver (e.g., AE sensor) located a distance away, similar to the acousto-ultrasonic method of Vary [2.73].

The FR method implemented in this study used the hardware and waveform analysis techniques of the AE method, thus its simplicity and ease of application. The FR system consists of at least one pair of sensors, one to act as a pulser and the other as a receiver, and AE-based data acquisition hardware and software. Using a waveform generator board, the pulser excites the structure at the desired frequency range (e.g., 20 to 1000 kHz). The optimal frequency range depends on the structure and material being tested. The receiver records the signals propagating in the pulser-receiver path. The acquired waveforms are processed to determine the transmitted signal properties, such as peak amplitudes, peak frequencies, shifts in frequency components, area under the power spectrum curve, etc.

The pulser and receiver are stationary throughout the FR testing. As a result, any change in the signature of the transmitted waveform with respect to baseline measurements indicates a change in the material characteristics along the pulser-receiver path. The transfer function relating the input and output waveforms can be represented as:

$$O(t) = I(t) \otimes P(t) \otimes M(t) \otimes R(t). \tag{2.51}$$

An input signal, $I(t)$, is sent to the pulser; the pulser converts the electrical signal into an acoustic (mechanical) signal via $P(t)$; the acoustic signal is modified by the transfer function of the medium, $M(t)$; a receiving sensor converts the acoustic signal into an electrical signal with its transfer function, $R(t)$. In the FR test, as $I(t)$, $P(t)$, and $R(t)$ are constant, any change in the output signal, $O(t)$, is related to a change in the transfer function of medium, $M(t)$.

In the case of composite materials, the changes in the transfer function of the medium, $M(t)$, can be caused by any of several failure modes, including matrix cracking, fiber fracture, delamination, etc. The resulting frequency response and its correspondence with the mode, extent, and severity of the internal damage depends on a variety of test and material variables such as the intensity of the input pulse, frequency range used, pulser-receiver distance, structural and material configuration, degree of anisotropy, and directionality of the fibers. The extraction of the actual material transfer function via deconvolution would be mathematically taxing for even a very simple laboratory test [2.67]. Consequently, only the changes in the time- and frequency-domain characteristics of the recorded signal are analyzed.

The required number of pulsers and receivers and their separation depend on the monitored structure, and the desired coverage area and data resolution, Figure 2.3. The more densely the sensors are clustered, the higher the detection resolution. The FR method can monitor long distances depending on the attenuation of acoustic waves in the material. The Composite Damage Detection System developed by Acellent Technologies, Inc. (835 Stewart Drive, Sunnyvale, CA, USA) uses this principle and a grid of thin piezoelectric sensors to monitor large composite structures.

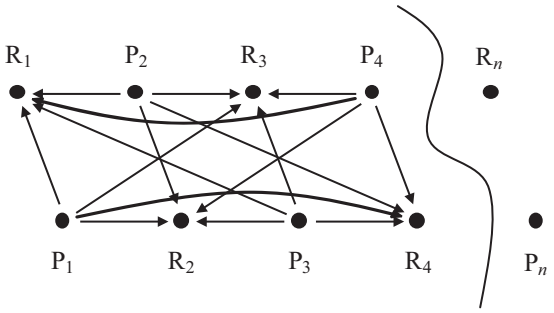

Figure 2.3. Example of a possible experimental setup for FR testing, showing the multiple wave paths which can be monitored with an array of pulsers and receivers. (R: Receiver, P: Pulser).

2.2.4. ULTRASOUND

The large regions of composite aircraft fuselage structures that have a propensity to contain nonvisual subsurface damage necessitate a means of performing active, accurate, and time-efficient inspections during the regularly scheduled inspections of aircraft. Ultrasound is well-established as such an NDI technique for the inspections of both metallic and composite structures, with several books published on the subject (e.g., [2.74], [2.75]). Thus, it is not the intent of this section to review progress in ultrasonics, but merely to provide the basic principles and a brief review as the technique pertains to the limited ultrasonic inspection work conducted during the course of this investigation.

Ultrasound is an active NDT method based on the concept of introducing high-frequency (e.g., 0.5 to 25 MHz) acoustic waves into a structure via piezoelectric transducers and monitoring either the resultant reflections (i.e., pulse-echo mode) or the transmitted signal (i.e., through-transmission mode) for variations in either the time-of-flight or the amplitude at different locations. Homogeneous, solid materials will allow various modes of sound waves (e.g., extensional, flexural, Rayleigh, Lamb, etc.) to propagate at a constant wave speed. If this wave speed is known for the particular material being tested, the thickness of an undamaged sample can be measured by transmitting a signal perpendicular to the sample and measuring the time-of-flight (i.e., the time between transmitting the wave and detecting its reflection) via:

$$s = \frac{ct}{2}, \tag{2.52}$$

where s is the depth, c is the wave speed, and t is the time-of-flight. The free surfaces of any internal discontinuities will also reflect any input sound waves, resulting in shorter recorded time-of-flight values. As result, the presence and depth of internal discontinuities can be detected by monitoring the time-of-flight values over the surface area of a part.

Using normal-beam transducers, nonvisual, subsurface damage parallel to the part surface (e.g., delaminations and face sheet-to-core disbonds) can be detected. In a pulse-echo

configuration, a discontinuity in the path of the ultrasonic wave results in a shorter recorded time-of-flight, indicating the possible presence of damage at a calculable depth. Angle-beam transducers can similarly be used to scan for discontinuities perpendicular to the part surface; these discontinuities would not be detected using normal-beam transducers because no appreciable portion of their wave path is obstructed. For low-density core sandwich configurations, through-transmission ultrasound (rather than pulse-echo) is most oftentimes required to inspect the full thickness of the sandwich due to the extremely low density of the core materials. Alternatively, pulse-echo ultrasound can be performed from both sides of the sandwich to inspect both face sheets individually, if possible.

In a comparative NDT study, Balageas [2.76] used through-transmission ultrasonics, shearography, and active infrared thermography to measure the extent of Barely Visible Impact Damage (BVID) in a sandwich structure composed of glass fiber-reinforced face sheets and a foam core. In terms of affected surface area, Balageas found that through-transmission ultrasonics detected the largest area affected by damage when compared with the other NDI methods. However, Růžek et al. [2.77] observed that for cases involving BVID, ultrasonic inspection results oftentimes underestimate the *actual* damage region of sandwich composites. While high-energy impacts cause fiber fracture and delaminations in the face sheets, damage associated with BVID includes mostly surface deformation and honeycomb core distortion without introducing any additional discontinuities in the wave path.

To inspect very large structures, automated systems, such as the Mobile Automated Scanner (MAUS) and the Automated Ultrasonic Scanning System (AUSS) by Boeing are necessary to perform inspections in a reasonable amount of time. However, alternate inspection methods capable of inspecting larger regions in single scans (e.g., thermography and shearography) may be preferable for certain applications and/or industries.

2.2.5. THERMOGRAPHY

Thermography, generally speaking, is the measurement of infrared radiation emitted from a test specimen and calculating its surface temperature. With regards to NDT, thermography is a noncontact, optical inspection method capable of inspecting large areas for nonvisual, subsurface damage parallel to the surface of the test specimen. Several industries, including aerospace, automotive, manufacturing, and others, have adopted thermography as a regular inspection tool, with several variations of the basic method (e.g., both passive and active NDT) having developed for certain specialized applications.

Passive thermography involves monitoring the ambient surface temperature of a test specimen. This approach is usually utilized for specimens that exist and/or operate at high temperatures relative to their environment. For example, Howell et al. [2.78] successfully inspected the space shuttle wing leading edge and several artificially damaged samples mounted in the shuttle cargo bay while in orbit using passive thermography. Also, Kroll et al. [2.79] have proposed a thermographic pressure vessel leak detection system which detects the lower surface temperature of damaged pressure vessels in the vicinity of a leak resultant of the expansion of gas through the damage.

Active thermography requires the artificial heating of test specimens. Within active thermography, several additional variations exist, encompassing different application methods (e.g., thermal irradiation and electromagnetic induction), frequency (e.g., one-time and periodic), durations, and amplitudes of the applied heat [2.80]. The parameters and variables of active thermography selected for a specific test specimen depend on the thermal properties and thickness of the specimen. Thin specimens composed of a material with a higher thermal conductivity (e.g., metals) require less input energy than thicker specimens composed of a material with a lower thermal conductivity (e.g., laminated composites) [2.81].

In flash thermography, a brief, one-time pulse of light energy from a flash lamp is used to heat the surface of the test specimen while an infrared camera records the radiation emitted from

the surface over time, producing a set of digital images of the surface temperature. Each pixel in this data set can be treated as a one-dimensional temperature time history. For a homogenous, pristine specimen, its surface temperature can be described by:

$$T_{\text{surf}}(t) - T_{\text{surf}}(0) = \frac{Q}{\sqrt{\kappa\rho c\pi t}}, \tag{2.53}$$

where Q is the input thermal energy per surface area, κ is the thermal conductivity, ρ is the material density, c is the specific heat of the specimen material, and t is the transient time [2.82].

For an undamaged, uniform test specimen, the surface temperature falls predictably as heat from the surface diffuses into the material. The surface cooling rate is affected by the presence of any embedded inhomogeneities in the material. Internal flaws, such as disbonds, voids, and inclusions, obstruct the flow of heat into the specimen, causing detectable variations in the surface temperature [2.83].

Raw thermographic data are often noisy due to temperature fluctuations of the testing environment and the testing hardware. However, the rate of temperature change is much less sensitive to these sources of error. The first and second derivatives of equation (2.53) with respect to the natural logarithm of time are –0.5 and zero, respectively:

$$\frac{\partial}{\partial\big(\ln(t)\big)}\ln\big(T_{\text{surf}}(t) - T_{\text{surf}}(0)\big) = -\frac{1}{2} \tag{2.54}$$

Variations from these two constant values in the contour plots of the first and second derivatives are indicative of inhomogeneities in the specimen, oftentimes acting as a clearer indicator than the raw temperature data.

2.2.6. COMPUTER-AIDED TAP TEST

The “coin tap” method is a well-established, qualitative inspection method for detecting defects in composite materials in aerospace applications. With this technique, a stiff object, such as a coin or screw driver handle, is used to tap along the surface of a composite structure. When

tapped, regions of undamaged material sound clean and crisp while damaged regions sound dull and deadened. This method is an inexpensive and simple approach for inspecting composites for subsurface damage; however, it is highly user-dependent and inconsistent [2.84]. The Computer-Aided Tap Tester (CATT), developed by Iowa State University (ISU), is able to generate quantitative stiffness data using the same principles which govern the standard coin tap test. The system consists of a brass-tipped accelerometer (impactor), electronic circuitry for conditioning the signal and measuring the impact duration, and a laptop computer that contains data acquisition and processing software [2.85].

During a typical, audible coin tap inspection, it is the frequency of the sound wave resultant of the tap which indicates the presence of internal damage. The semispherical tip of the impactor used in the CATT system outputs a voltage pulse, representative of the load-time history of the tap. The duration of the voltage pulse is analogous to the audible frequencies of the coin tap method, with low impact durations indicating good material and long impact durations indicating damage. The impact duration of a semispherical tapper on a flat surface can be modeled as

$$\tau = 2.94\left(\frac{5}{4Mn\sqrt{v}}\right)^{\frac{2}{5}} \tag{2.55}$$

$$M = \frac{1}{m_T} + \frac{1}{m_S} \tag{2.56}$$

$$n = \frac{4\sqrt{R_T}}{3\pi(k_T + k_S)}, \tag{2.57}$$

where τ is the impact duration, v is the velocity at impact, m_T and R_T are the mass and radius of the tapper, and m_S and k_S are the mass and stiffness of the sample [2.86]. Researchers at ISU found that for a wide variety of composite aircraft components, a simple grounded spring model may be used to describe the response to a tap [2.87]. From the spring model, the local stiffness may be deduced by knowing only the measured impact duration and the mass of the impactor.

$$k_S = \left(\frac{\pi}{\tau}\right)^2 m_T \tag{2.58}$$

The impact duration, as well as the calculated local stiffness, can then be used for producing contour plots of the tested region. These contour plots reveal not only the defects and damage in a part, but also the internal structure, such as, for sandwich composites, core splices and ply overlays.

CHAPTER 3: EXPERIMENTAL PROCEDURES

3.1. INTRODUCTION

Residual strength tests were performed for six full-scale honeycomb sandwich composite aircraft fuselage panels. The panels were quasi-statically subjected to combinations of internal pressurization, hoop, and longitudinal loading up to failure. The deformation and failure processes of the panels were monitored using multiple methods during the tests. Voluminous nondestructive inspection (NDI) data were also collected, pre- and posttest, to characterize any change in the state-of-damage. A detailed description of the test fixture, the panels, and the monitoring and inspection methods are presented in this chapter.

3.2. TEST FACILITY

The testing of the composite fuselage panels was conducted at the Full-Scale Aircraft Structural Test Evaluation and Research (FASTER) facility, located at the Federal Aviation Administration (FAA) William J. Hughes Technical Center, Atlantic City International Airport, NJ. The FASTER fixture is capable of subjecting full-scale curved fuselage panels to loadings representative of those experienced by a narrow-body aircraft under actual operating conditions for either long-term fatigue or quasi-static residual strength loading conditions. A general view of the FASTER fixture can be seen in Figure 3.1.

The FASTER fixture features a unique adaptation of mechanical, fluid, and electronic components and is capable of applying internal pressurization, hoop, longitudinal, and shear loads to a fuselage panel. The panel is set on top of a D-shaped pressure box and bonded with an elastomeric seal. The system is capable of using either air or water as the pressurizing medium, although water was used in each of the composite panel tests. Hoop- and longitudinal-edge loads are applied to the panel by 14 hoop and 8 longitudinal computer-controlled loader arms. Each loader arm consists of a water actuator, a lever arm, a fulcrum, a load cell, and a whiffle tree,

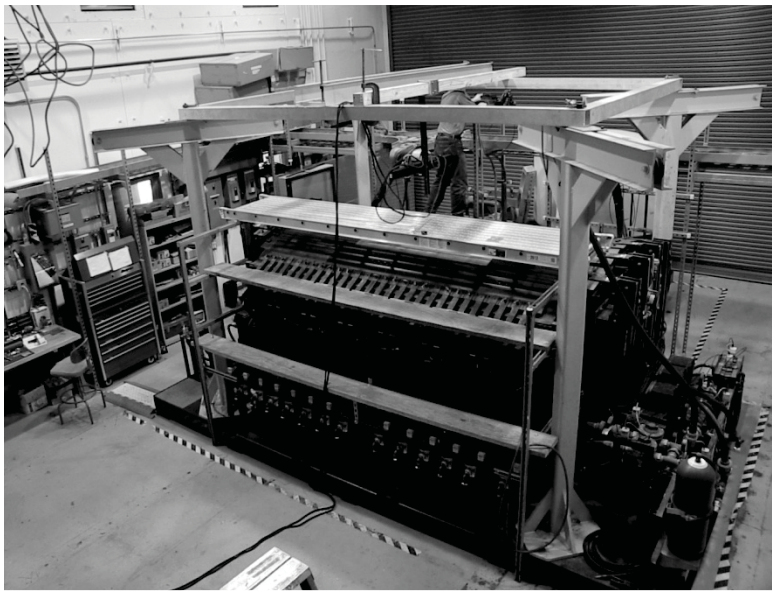

Figure 3.1. General view of FASTER fixture.

Figure 3.2. The lever arm is connected to the actuator at its base, to the load cell at its top (point 'A' in Figure 3.2), and rotates about the fulcrum (point 'C' in Figure 3.2). In-plane tensile loads are applied to the panel edges (point 'B' in Figure 3.2) via inflation of the water actuator. As the water actuator inflates, the bottom of the lever arm is displaced inward and rotates about the fulcrum, displacing the top of the lever arm outward. The loads applied by each lever arm are monitored by the load cell installed in-line with the whiffle tree, which transfers the loads to the panel equally via four pin holes along the panel edges. Each hoop loader whiffle tree distributes the load over 16 inches of the panel edge and each longitudinal loader whiffle tree distributes the load over 14 inches of the panel edge. In total, loads are applied to the panels via 28 0.5-inch-diameter holes along each hoop edge and via 16 such holes along each longitudinal edge.

The maximum applicable force for each FASTER loader arm is 25 kips. However, for especially compliant panels, such as the sandwich composite panels used in this study, the loader arms of the FASTER fixture may be stroke-limited rather than load-limited, effectively reducing the maximum applicable load. To maximize the available stroke of each loader arm, additional

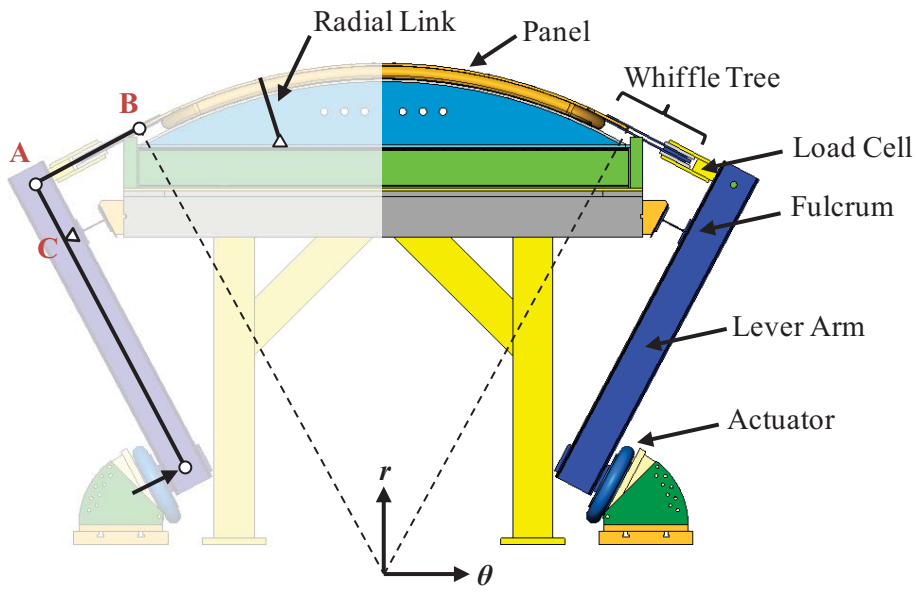

Figure 3.2. FASTER loader arm schematic.

thin metal sheets were installed as necessary behind the loader fulcrums to ensure the water actuators were fully closed prior to each residual strength test.

As mentioned, the FASTER fixture is capable of applying shear loads to curved fuselage panels. This is accomplished by bonding two longitudinal skis to the exterior surface of the panels and displacing them in opposite directions. However, no shear loads were applied during the testing of the composite panels.

Prior to this study, only conventional aluminum alloy fuselage panels had been loaded using the FASTER fixture. These conventional fuselage panels, in addition to their aluminum alloy skin, are composed of several substructural components, including frames, stringers, etc.; composite fuselage panels have no such substructural components. The applied hoop loads for conventional fuselage panels are distributed between the aluminum alloy skin and the frames, with the load attachment points on the frames acting as an additional source of radial displacement constraint in the FASTER fixture. This additional constraint protects against the excessive radial displacement and/or bending of the panels which could result from nonequivalent

internal pressurization and hoop loading. Ten radial link assemblies were designed, fabricated, and installed to provide this additional constraint during the loading of the composite panels.

Each radial link assembly consisted of three separate links: one central, tensile link to limit outward radial displacement and two compressive links to limit inward radial displacement, Figure 3.3. The radial link assemblies attached to 6″x6″x¾″ curved aluminum plates bonded to the interior surface of each panel. Each curved aluminum plate contained a threaded center hole that served as a connection point for the tensile link and two shallow holes that served as guides for the compressive links. The opposite end of each link assembly was securely fastened to the base of the pressure box. To avoid unnecessary application of any bending to the panels, the tensile links contained two hinges and a double universal joint, providing sufficient additional degrees of freedom. To further minimize any unnecessary loading, the tensile links were installed with slack roughly equal to the expected radial displacement of the loaded panels. The compressive links were not installed with any slack since no inward radial displacement was expected. Load cells were installed in-line with the tensile links to monitor radial reactions during loading.

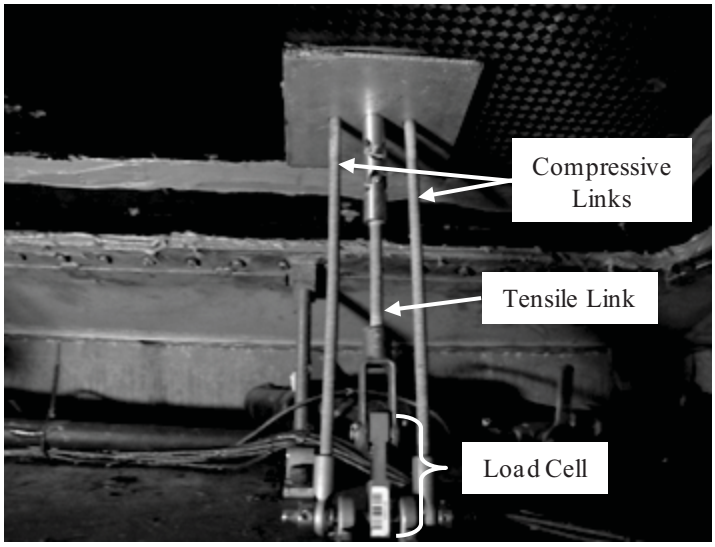

Figure 3.3. Radial link assembly, as installed.

The application of the loads to the panels is controlled by a full proportional integral derivative (PID), closed-loop feedback error control process. The control and data acquisition systems of the FASTER fixture operate at a maximum frequency of 150 Hz. However, due to the expected long durations of the composite panel tests, in order to minimize the file sizes of the archived data, data were saved at a much lower frequency of approximately 1.4 Hz. Data acquisition from all strain, load, and pressure transducers were monitored in real time and archived for posttest analyses. During testing, particular attention was paid to the real-time load and pressure transducer data to ensure uniform behavior amongst the loader arms and proper functioning of the system as a whole.

Additional information on the FASTER facility can be found in references [3.1, 3.2].

3.3. PANEL DESCRIPTION

The fuselage panels used in this study were constructed of a honeycomb sandwich composite material representative of those currently used in certain general aviation class aircraft (e.g., Adam A500). However, the geometry of the panels is representative of a narrow-body aircraft (e.g., Boeing 737) in order to be compatible with the current tooling of the FASTER fixture, Figure 3.4. The fabrication of the test panels was performed by Adam Aircraft Industries, Inc., Englewood, CO. By design, sandwich composites, such as those used in this study, distribute their tensile and compressive in-plane loads to the stiffer face sheets, while any transverse loads are taken on by the thick core material.

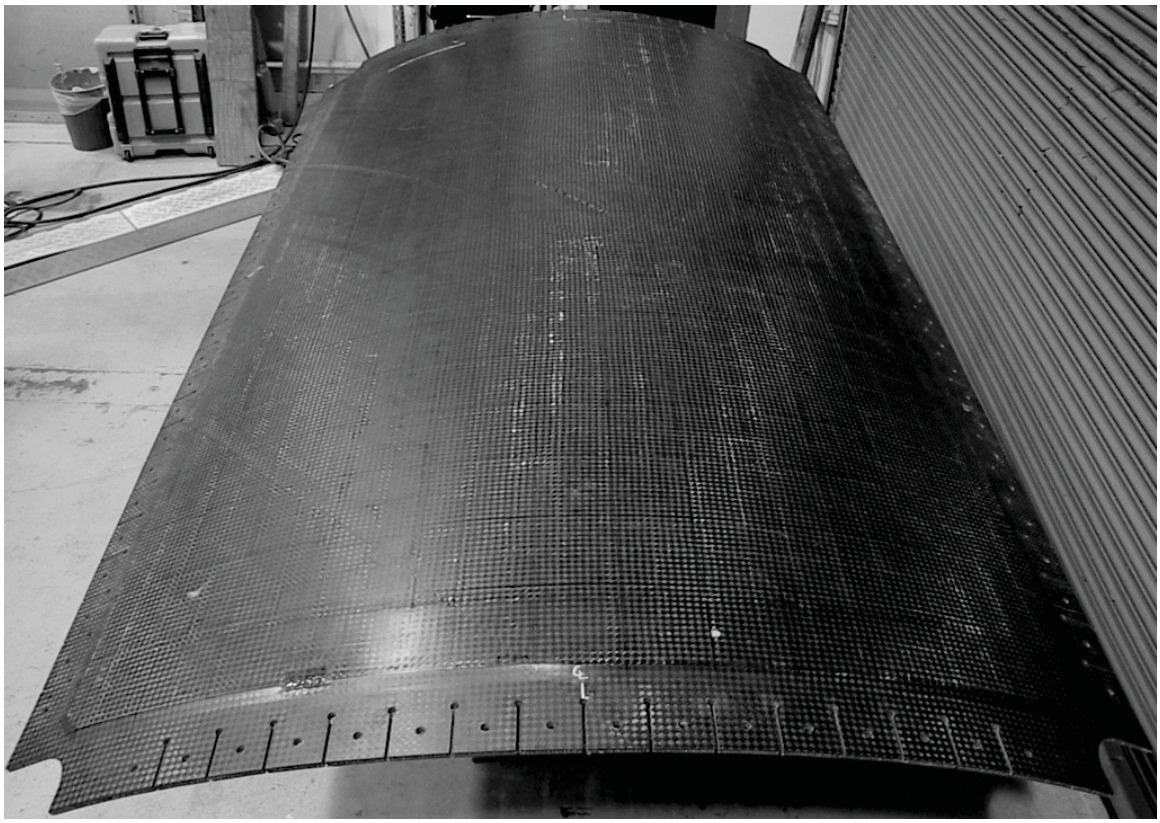

Figure 3.4. General view of a sandwich composite aircraft fuselage panel tested in this investigation

The panels were fabricated using a 0.0085-inch thick Toray Composites T700SC-12K-50C/#2510 plain-weave carbon/epoxy fabric prepreg for the face sheets and a DuPont™ Nomex® Hexcel Composites HRH-10/OX-3/16-3.0 honeycomb core with over-expanded cells. The face sheets and core were bonded using Hysol® EA9696 film adhesive (0.060 psf). The approximate unit cell size of the plain-weave laminae was 0.625 inch. Manufacturer-supplied material properties for the constituent materials are listed in Table 3.1. Note that the material properties listed for the prepreg material are for a woven lamina, not a unidirectional fiber-reinforced lamina. Accordingly, the in-plane properties in the 1- and 2-directions are nearly equivalent.

Table 3.1. Manufacturer-Supplied Material Properties.

Toray T700SC-12K-50C/#2510 Plain Weave Prepreg			
E_1^T	8,286,000 psi	F_1^T	116,427 psi
E_1^C	7,943,000 psi	F_1^C	108,373 psi
E_2^T	8,173,000 psi	F_2^T	104,249 psi
E_2^C	7,066,000 psi	F_2^C	107,986 psi
G_{12}	623,000 psi	F_{12}^S	22,465 psi
ν_{12}	0.085		
Hexcel HRH-10/OX-3/16-3.0 Nomex Honeycomb			
E_3	17,000 psi	F_3^C	350 psi
G_{13}	6,000 psi	F_{13}^S	135 psi
G_{23}	3,000 psi	F_{23}^S	115 psi

Each curved panel was 125 inches long, 78 inches along its curvature, and had an internal radius of 74 inches, Figure 3.5. The central test section of the panels, where it was assumed that any edge effects would be minimal and that the applied loads would be distributed as intended, was 48 inches in the longitudinal direction and 24 inches in the hoop direction. The quasi-isotropic composite lay-up within the test section of the panels was $[45/0/45/\ Core_{½}]_S$, with the honeycomb core having a thickness of 0.75 inch, Figure 3.6d. The region of the panel fabricated with this lay-up extended over a larger area, covering 104 inches in the longitudinal direction and 59 inches in the hoop direction.

The load application region, extending 3.5 inches away from each hoop edge and 4.5 inches away from each longitudinal edge of the panels (Figure 3.5), was reinforced with additional prepreg plies to avoid local failures at the load application points prior to any damage developing in the central test section. The honeycomb core in the load application region was potted using Hysol® EA9394 epoxy paste adhesive and had a reduced thickness of 0.25 inch. The composite lay-up within the load application region of the panel was $[45_2/0/45/0/45/0/45/0/45/0/45_2/Core_{½}]_S$, Figure 3.6a. To avoid having the applied in-plane loads attracted to the reinforced panel edges, notches with blunted edges were introduced between each load application point, through the entire reinforced section of the laminate.

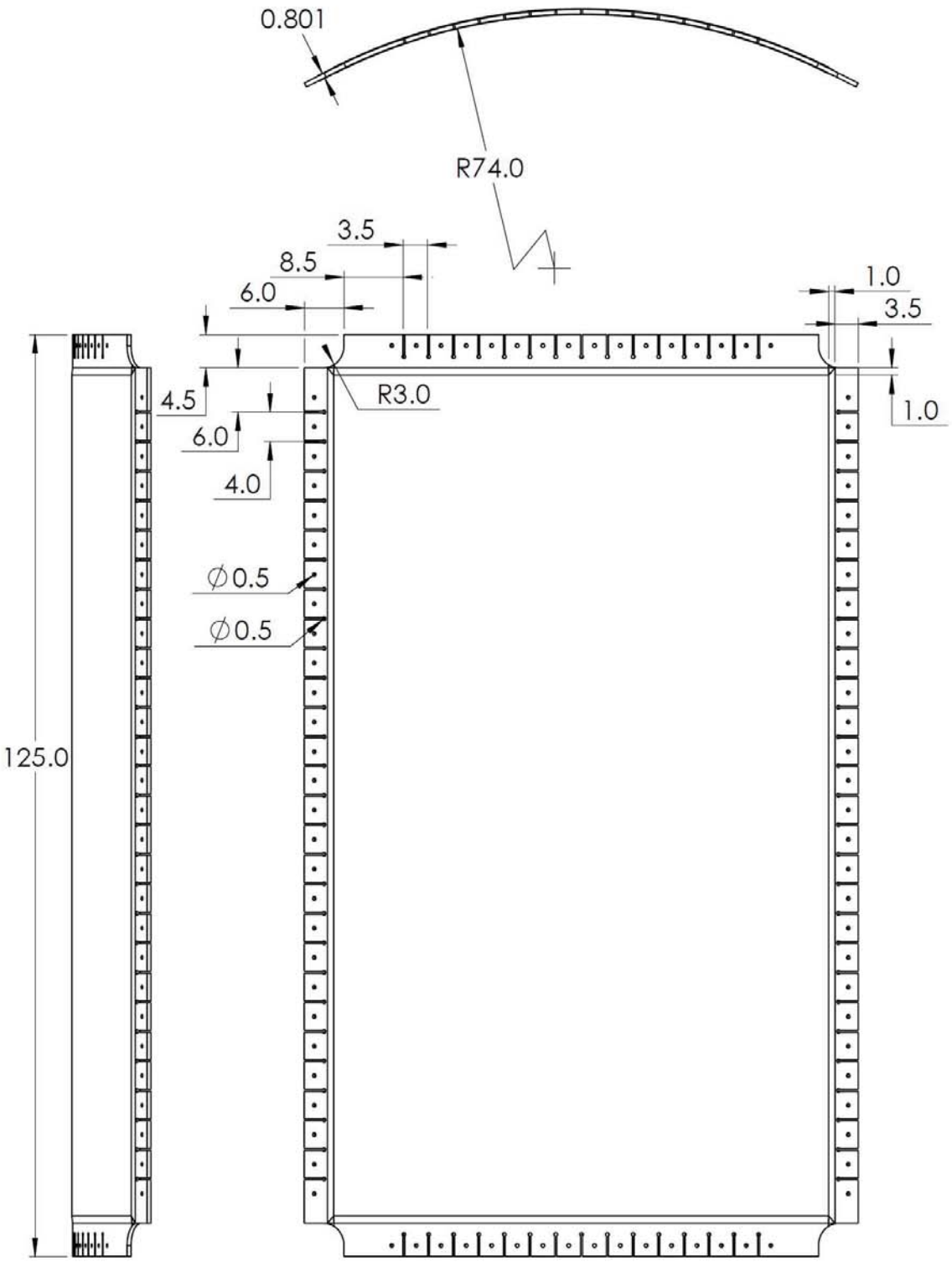

Figure 3.5. General dimensions of the sandwich composite aircraft fuselage panels.

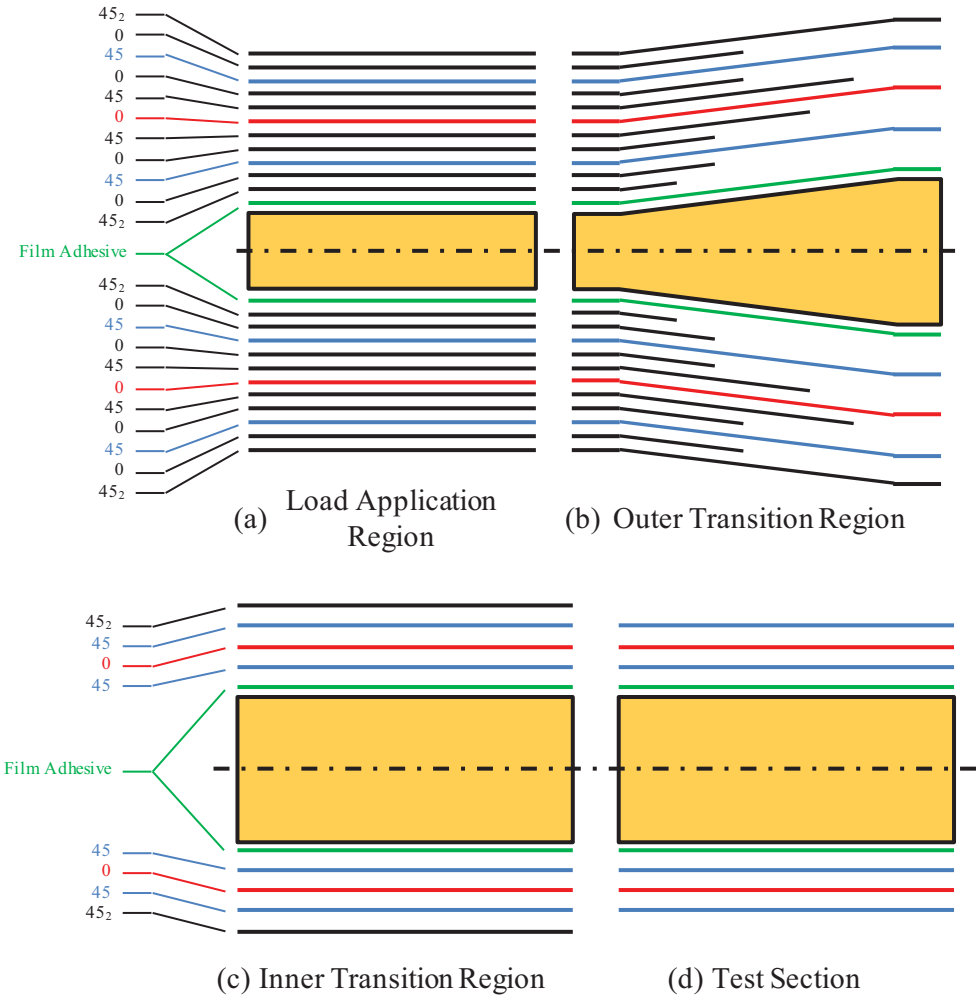

Figure 3.6. Composite lay-ups for (a) the load application region, (b) the outer transition region, (c) the inner transition region, and (d) the test section.

Two transition regions were located between the load application region and the test section. The outer transition region, Figure 3.6b, which extended one inch inward from the hoop and longitudinal edges, linearly increased the core thickness from 0.25 inch to 0.75 inch and reduced the composite lay-up to $[45_3/0/45/Core_{½}]_S$. The inner transition region, Figure 3.6c, which extended an additional 5 inches inward from the hoop and longitudinal edges, had a constant core thickness of 0.75 inch and a composite lay-up of $[45_3/0/45/Core_{½}]_S$. The locations of the four composite lay-up regions are shown schematically in Figure 3.7.

Upon delivery, the overall quality of the panels was visually assessed. Upon inspection, a large discrepancy was observed regarding the distribution of epoxy resin. The exterior face sheets tended to be resin-poor and the interior face sheets tended to be resin-rich. This discrepancy was observed in each of the six panels. Examples of each case are shown in Figure 3.8. In addition, a large elliptical disbond was discovered in panel CP5, discussed further in Section 3.4. Also, panels CP4, CP5, and CP6 did not have potted cores in the load application region.

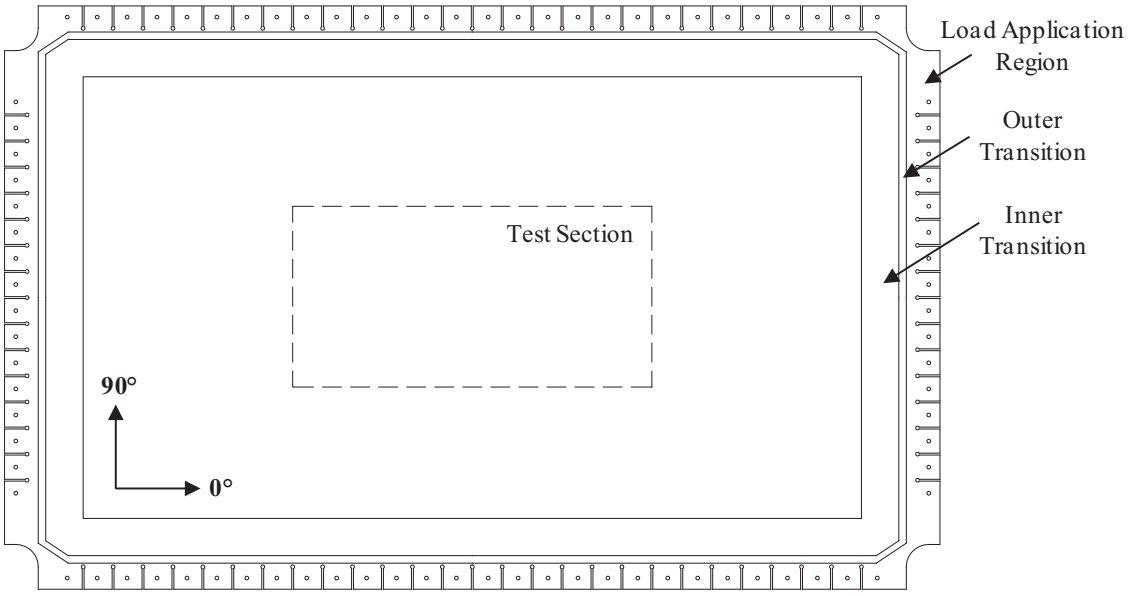

Figure 3.7. Schematic of composite panel showing different composite lay-up regions.

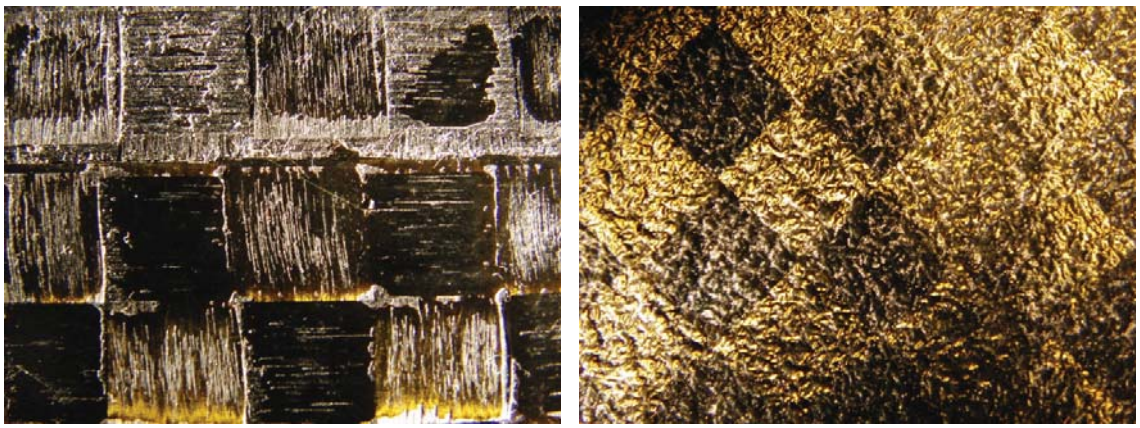

(a) (b)

Figure 3.8. Examples of (a) resin-poor and (b) resin-rich sections of the composite panels.

3.4. DAMAGE CONFIGURATIONS

Six panels (designated CP1 through CP6) were tested throughout the course of this study. Panel CP1 contained no artificial damage and was used to collect baseline data for use in the calibrations of various inspection methods and computer models. After the required baseline data were collected, artificial damage was introduced in the form of a 3-inch by 3-inch crossed slit through the exterior face sheet. This configuration of the original panel was designated CP1A and was representative of damage resultant of a tool drop. A more severe artificial state-of-damage was later introduced to panel CP1 in the form of a 10-inch long by 1/16-inch wide longitudinal notch through the full thickness of the panel, Figure 3.9a. This configuration of the original panel was designated CP1B.

Panel CP2 contained a 10-inch diameter hole through the exterior face sheet, representing a debonded repair patch, Figure 3.9b. Panels CP3 and CP4 contained 10-inch long, 0.5-inch wide, circumferential, through-thickness notches. Panel CP5 contained a 10-inch long, 0.5-inch wide, longitudinal, through-thickness notch, Figure 3.9c. Panel CP6 contained a 10-inch long, 0.5-inch wide, through-thickness notch, oriented 45º from the longitudinal direction of the panel, Figure 3.9d. Damage scenarios in panels CP3 through CP6 were intended to represent sites of

high-energy discrete source damage, such as that resultant of a blade separation. The artificial damage in panels CP2 through CP6 was machined by Adam Aircraft Industries, Inc. shortly after panel curing. Each of the machined notches contained semicircular (i.e., 0.25-inch radius) notch tips at either end.

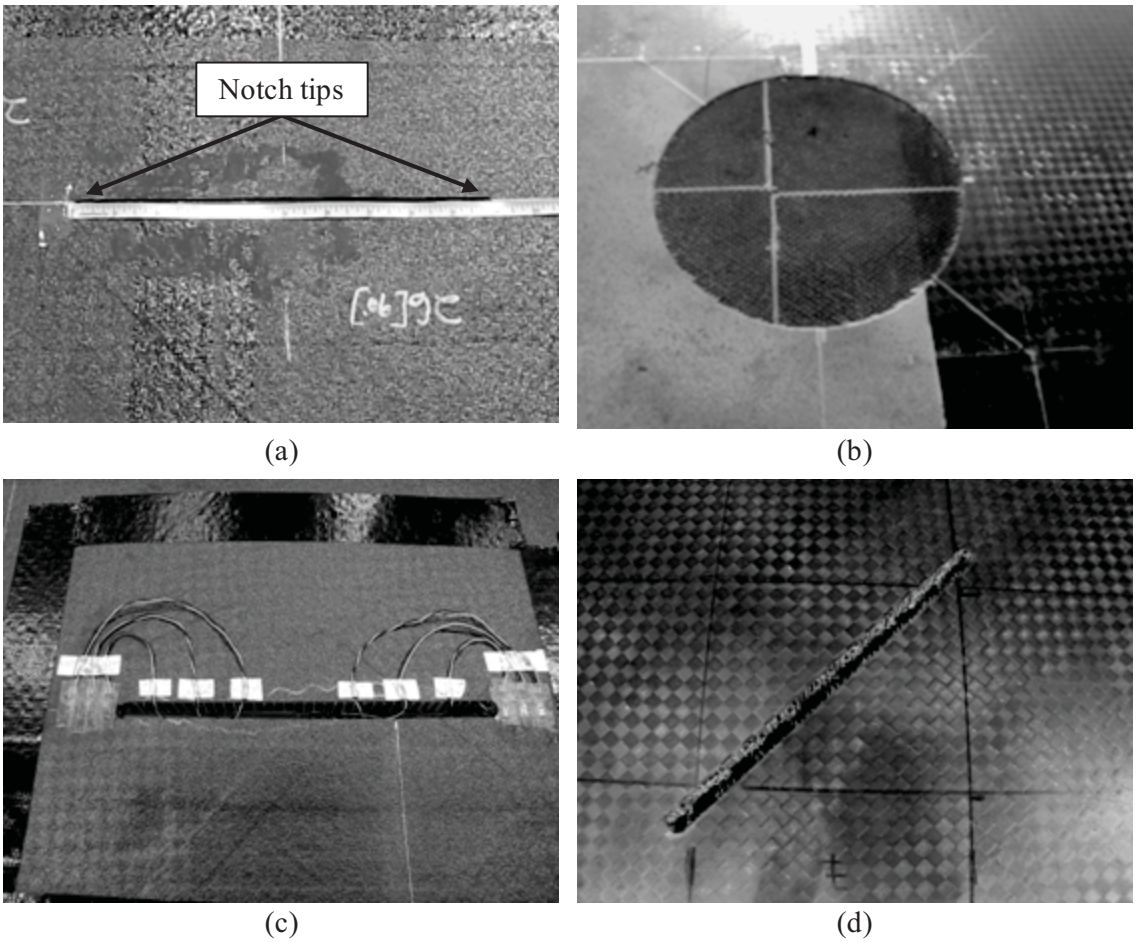

Figure 3.9. (a) The panel CP1B 10-inch long, 1/16-inch wide, longitudinal notch, as seen from the panel interior; (b) the panel CP2 10-inch diameter hole through the exterior face sheet; (c) the panel CP5 10-inch long, 0.5-inch wide, longitudinal notch, as seen from the panel interior, and (d) the panel CP6 10-inch long, 0.5-inch wide, inclined notch, as seen from the panel exterior.

All of the artificial damage modes were inserted at the center of their respective panels' test section, with the exception of panel CP5. The longitudinal notch in panel CP5 was shifted 10 inches along the longitudinal axis of the panel. This was due to a 9-inch by 14-inch elliptical skin-to-core disbond, which was too close to the intended location for the CP5 notch. It was determined that at its installed location, no interaction would occur between the notch and the disbond. The elliptical disbond was henceforth considered an additional damage configuration to be independently monitored and studied.

3.5. PANEL PREPARATION

The panels were connected to the FASTER fixture pressure box via an elastomeric seal installed along the outer edge of the test section. The seal was bonded to the panel using PR-1422 Class B aircraft fuel tank sealant over an area approximately 4 inches wide along the outer perimeter of the test section, as shown in Figure 3.10a. The pressure box seals were connected to the pressure box by tightening a series of equally spaced bolts over a layer of room-temperature vulcanization (RTV) silicone sealant.

The ten radial link assemblies were bonded to the interior surface of the panels via the curved aluminum plates (Figure 3.10b) using PR-1422 Class B aircraft fuel tank sealant. The plates were installed with a 20-inch center-to-center spacing along the longitudinal direction of the panels, 23.5 inches in the hoop direction from the midline of the panels, Figure 3.11.

Panels that contained through-thickness damage required that a seal be installed on the interior face sheet to contain the pressurizing medium during the tests involving the application of internal pressurization and hoop loads. While any severe through-thickness damage in the fuselage of an aircraft would depressurize the cabin, the evaluation of the through-thickness damage while still under pressure represents the state-of-loading immediately after the formation of the through-thickness damage.

It was important minimize the load attracted to the seal, so as to not diminish the severity of the damage being evaluated. A thin, hard, plastic sheet was bonded directly to the panel using PR-1422 Class B aircraft fuel tank sealant, Figure 3.10c. The width of the bonded area between the hard plastic sheet and the panel was approximately 2 inches. The hard plastic layer served to stop the seal from bulging through the through-thickness damage openings. The next layer of the patch was a thin rubber sheet, approximately 20″ by 10″, bonded to the panel and the hard plastic sheet by PR-1422 Class B aircraft fuel tank sealant. RTV silicone sealant was applied along the edges of each rubber seal to prevent water ingression under the patch, Figure 3.10d.

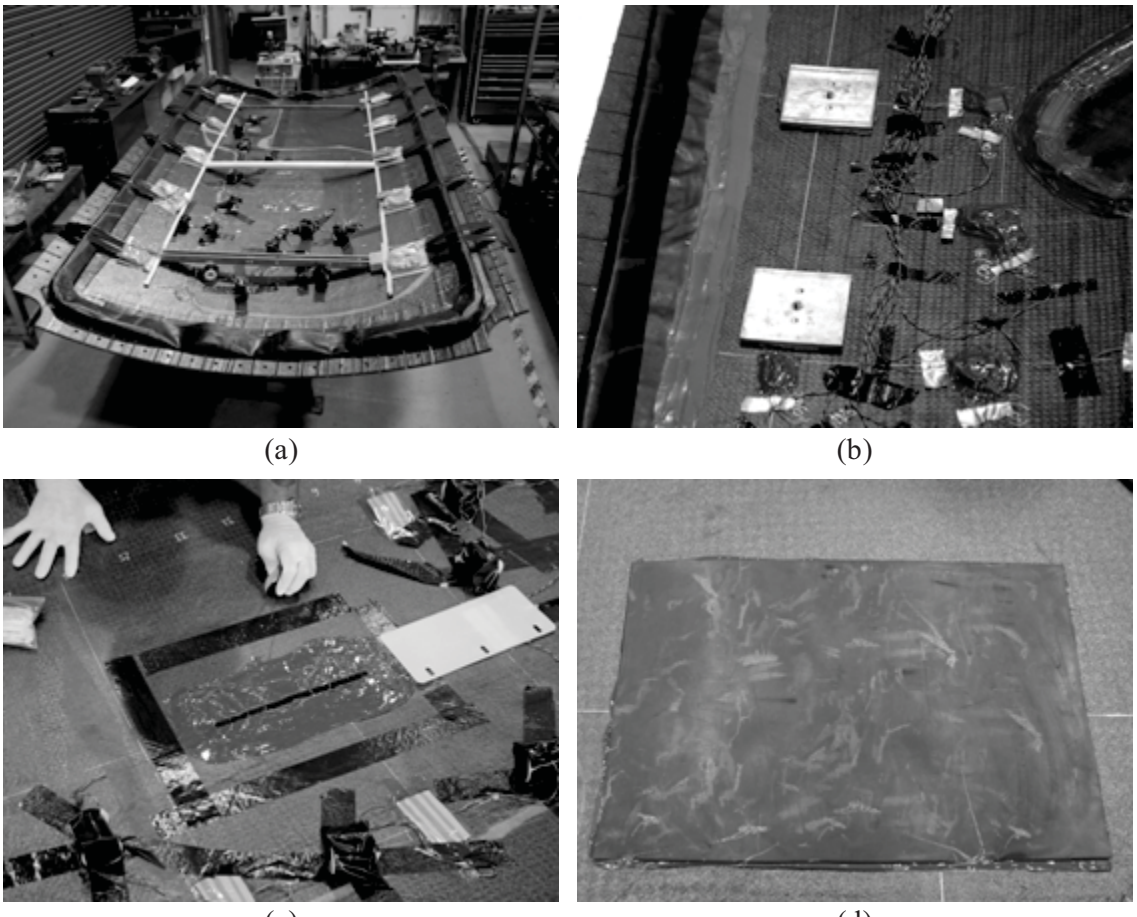

(a) (b)

(c) (d)

Figure 3.10. (a) Bonded pressure box seal during cure time, (b) radial link plates, (c) application of hard plastic through-thickness seal, and (d) rubber through-thickness seal.

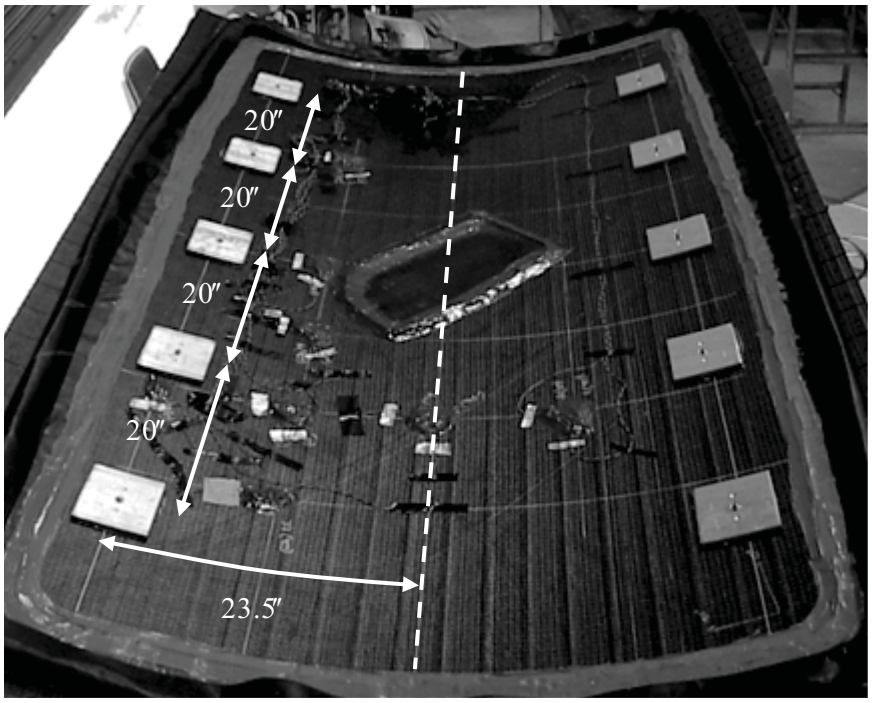

Figure 3.11. Radial link assembly connection points.

3.6. APPLIED LOADS

The loads for the residual strength test of each panel were applied in a configuration for which failure was deemed most likely, given the particular initial state-of-damage. To gather strain distribution data for multiple loading configurations for each state-of-damage, low-load strain surveys were conducted for each panel, prior to its residual strength test. The strain surveys also served to ensure that the applied loads were properly balanced and that the desired symmetry was maintained. The magnitudes of the applied loads of the strain surveys were typically between 10% and 30% of the maximum applied loads of the residual strength tests (Table 3.2), with the intention being that no additional damage would be generated as a result of the strain surveys.

Three loading configurations were applied during the strain surveys for each panel: (i) combined hoop loading, longitudinal loading, and pressurization; (ii) hoop loading and

pressurization; and (iii) longitudinal loading. During each strain survey, both strain gage and digital image correlation (DIC) data were collected at equal load steps up to the maximum load, Table 3.3. Loads were applied at either 10% or 20% increments depending on the magnitude of the maximum planned load; strain surveys conducted at low maximum loads were typically conducted with 20% increments. Loads were increased between steps over a period of thirty seconds, pausing at each load step for approximately one minute to allow all loaders to reach their respective end points prior to taking any measurements. The same general loading and measurement procedure was followed in the residual strength tests.

For the residual strength tests, loads were quasi-statically applied in equal loads steps up to the estimated failure loads, Table 3.2. A test would end when either the panel failed catastrophically or the maximum capacity of the FASTER fixture was met. In the latter cases the panels were either completely intact or suffered minor, localized failures. A localized failure is characterized by either visual surface damage, such as matrix cracking and fiber breakage, or nonvisual subsurface damage, as indicated by any of the monitoring or inspection methods.

Table 3.2. Maximum planned residual strength test loads. [3.3]

Panel	Loading Condition	Long [lbf/in]	Hoop [lbf/in]	Pressure [psi]
CP1	Longitudinal	1500	0	0.00
CP1A	Longitudinal	1500	0	0.00
CP1B	Hoop and Pressure	0	1750	23.63
CP2	Combined	1750	1750	23.63
	Hoop and Pressure	0	1750	23.63
	Longitudinal	1500	0	0.00
CP3	Combined	1400	592	8.00
CP4	Longitudinal	1400	74	1.00
CP5	Hoop and Pressure	100	1110	15.00
CP6	Combined	1500	1500	20.3

Table 3.3. Strain survey loads. [3.3]

Panel	Loading Condition	Long [lbf/in]	Hoop [lbf/in]	Pressure [psi]
CP1	Combined	1000	1000	13.50
	Hoop and Pressure	0	500	6.75
	Longitudinal	500	0	0.00
CP1B	Combined	438	438	5.90
	Hoop and Pressure	0	438	5.90
	Longitudinal	438	0	0.00
CP2	Combined	500	500	6.75
	Pressure and Hoop	0	500	6.75
	Longitudinal	500	0	000
CP3	Combined	300	252	3.40
	Hoop and Pressure	0	252	3.40
	Longitudinal	300	0	0.00
CP4	Combined	300	252	3.40
	Hoop and Pressure	0	252	3.40
	Longitudinal	300	0	0.00
CP5	Combined	300	252	3.40
	Hoop and Pressure	0	252	3.40
	Longitudinal	300	0	0.00
CP6	Combined	150	150	2.03
	Hoop and Pressure	0	200	2.70
	Longitudinal	200	0	0.00

A problem arises if a set of loaders on one side of the panel outperforms the loaders on the opposite side of the panel. This potential disparity in loader performance can result in a rigid body displacement of the panel toward the outperforming loaders. This rigid body displacement causes the closed water actuators of the underperforming loading fixtures to act as a source for reactive, rather than applied, forces. As such, the in-plane loads will remain balanced, but this behavior reduces the available stroke of the system by up to 50%. The application of low off-axis loads during an otherwise unidirectional test works to fix the panel in place, avoiding large rigid body displacements in the major direction of loading. This is the rationale behind the low off-axis loads applied during the loading of panels CP4 and CP5, Table 3.2.

During the residual strength tests of panels CP4 and CP5, the loading function was modified to isolate acoustic emission (AE) resultant of the fretting of existing fracture surfaces

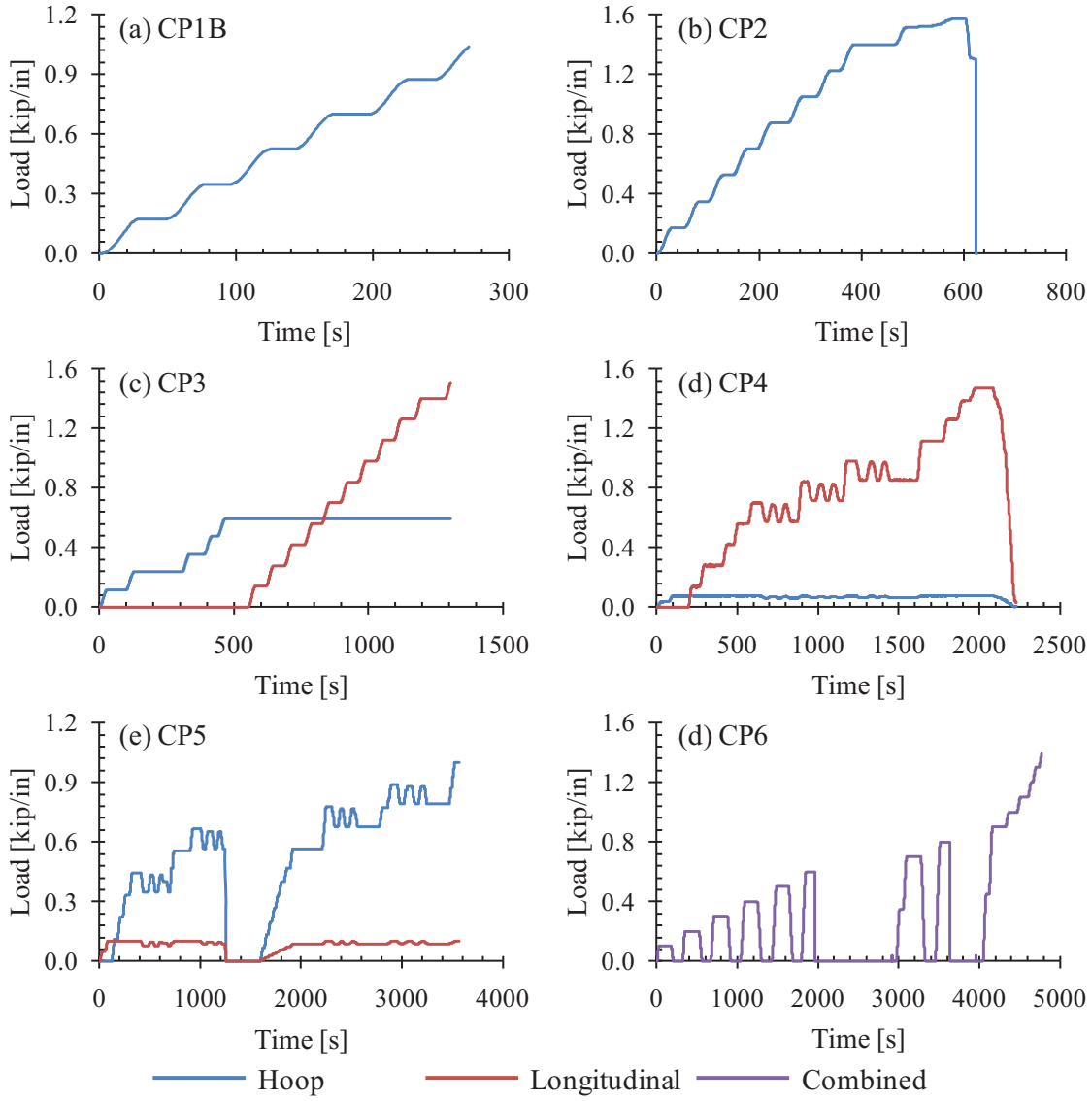

Figure 3.12. Applied loading functions.

from the AE resultant of new damage formation. Loads were oscillated between 10% and 90% of the range between the current and previous load steps to generate this pure friction emission data. During the residual strength tests of panel CP6, the application of the loads was again modified. After each load step, the panel was brought down to zero load before proceeding to the next load step. This was done to allow for frequency response (FR) measurements to be taken under load

and under zero load, and also to generate pure friction-based emission from existing fracture surfaces. The AE and FR test setups are discussed in detail in Sections 3.8.1 and 3.8.2.

The applied loading function for the residual strength test of each panel is shown in Figure 3.12. Note, for panels CP1 and CP2, several attempts were made to fail the panels, with only the final attempts for each plotted in Figures 3.12a and 3.12b, respectively. The entire loading history of each panel is discussed in detail in Chapter 4.

3.7. DEFORMATION MEASUREMENTS

Deformation and strain measurements were taken by two means: strain gages and DIC. Strain results were available during the tests while DIC data were available only after processing the recorded data. Details on the implementation of each method are discussed in this section.

3.7.1. STRAIN GAGES

Strain gages were installed on each of the composite panels to ensure symmetry of load application, for real-time monitoring of the panel strains, and for validation of the full-field deformation and strain DIC data. The strain gage maps for each panel can be seen in Figures 3.14 through 3.21. Strain readings were recorded during load holds occurring at equal load intervals up to the maximum applied loads. Strain and load data were also continuously recorded to a buffer file at a frequency of approximately 1.4 Hz.

Both uniaxial and rosette-style Vishay Micro-Measurements strain gages were used in this investigation, all of which were 350 Ohm resistors and were bonded to the panel surfaces using MBond-200 adhesive. The specific strain gage models and their general locations are specified in Table 3.4. A three-conductor vinyl-coated twisted cable was used to connect strain gages installed on the exterior surface of the panel. Strain gages installed on the interior panel surface were connected using Teflon-coated cables and were sealed with PR-1422 Class B aircraft fuel tank sealant.

The test section of each panel was instrumented with pairs of uniaxial strain gages oriented to measure strain in the longitudinal and hoop directions. Back-to-back pairs were installed on both the interior and exterior surfaces of the panels. Each panel was instrumented with these groups of strain gages spaced 12 inches apart along half of the test section perimeter, with an additional group at an adjacent corner, Figure 3.14. The symmetry of loads and strains across the panel could be evaluated by comparing the measured results from the three gaged corners of the panels. Strain gage results obtained from panel CP1, discussed in Chapter 4, indicated that the strains across the test section of the panel were not perfectly uniform. As such, additional gages were installed in the load application and transition regions of the panel to better characterize the distribution of strains across the panels and to identify any load attraction to the stiffer composite lay-up of the load application region.

Additional strain gages were installed on the interior and exterior face sheets in the vicinity of the sites of expected strain concentrations (i.e., near the artificial damage sites). It should be noted that no strain gages were installed on the exterior face sheet in the area monitored by the DIC system, discussed in Section 3.7.2. For panel CP1A, three uniaxial strain gages

Table 3.4. Strain gage types and general locations.

Panel	Strain Gage Model	Location
CP1	CEA-06-250UN-350	Throughout
CP1A	CEA-06-250UN-350	Exterior face sheet
	CEA-13-062UW-350	Interior face sheet and ahead of damage
CP1B	CEA-06-250UN-350	Exterior face sheet
	CEA-13-062UW-350	Interior face sheet and along notch axis
	CEA-13-062UR-350	0.125 inch ahead of notch tips
CP2	CEA-06-250UN-350	Throughout
CP3	CEA-06-250UN-350	Throughout
CP4	CEA-06-250UN-350	Throughout
CP5	CEA-06-250UN-350	Throughout
CP6	CEA-13-250UR-350	Exterior face sheet
	CEA-06-250UN-350	Interior face sheet
	CEA-06-062UN-350	Along notch axis

oriented to monitor longitudinal strain were installed ahead of the 3-inch long, hoop-oriented slit. The three gages were located 0.125, 1.125, and 2.125 inches ahead of the tip of the hoop-oriented slit, Figure 3.15. For panel CP1B, strain gage rosettes were installed 0.125 inch ahead of each notch tip. Three additional uniaxial strain gages, oriented to monitor hoop strain, were spaced at one-inch intervals away from rosette gages along the longitudinal direction, Figure 3.16. For panel CP2, pairs of uniaxial strain gages were oriented tangent to the edge of the hole at 0°, 45°, and 90°, 0.25 and 0.75 inch radially away from the edge of the hole, Figure 3.17. Additionally, a pair of uniaxial strain gages was installed under the center of the hole, on the interior surface. For the panels CP3 through CP5, uniaxial strain gages oriented perpendicular to the axes of the notches were installed 0.25, 0.75 and 1.25 inches ahead of the notch tips on the interior and exterior face sheets (e.g., Figure 3.13). For panel CP6, strain gage rosettes were installed 0.25, 0.75 and 1.25 inches on the interior and exterior face sheets ahead of one notch tip, while uniaxial gages oriented normal to the notch were installed on the interior panel surface ahead of the other notch tip, Figure 3.21.

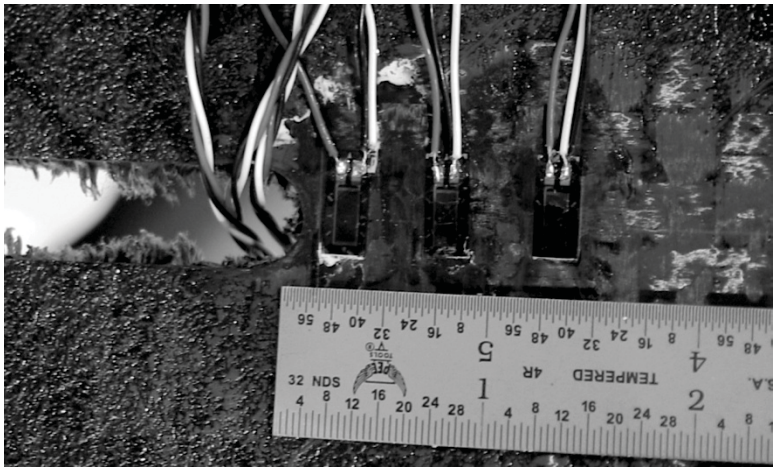

Figure 3.13. Strain gages installed ahead of the panel CP5 notch tip on the interior panel surface.

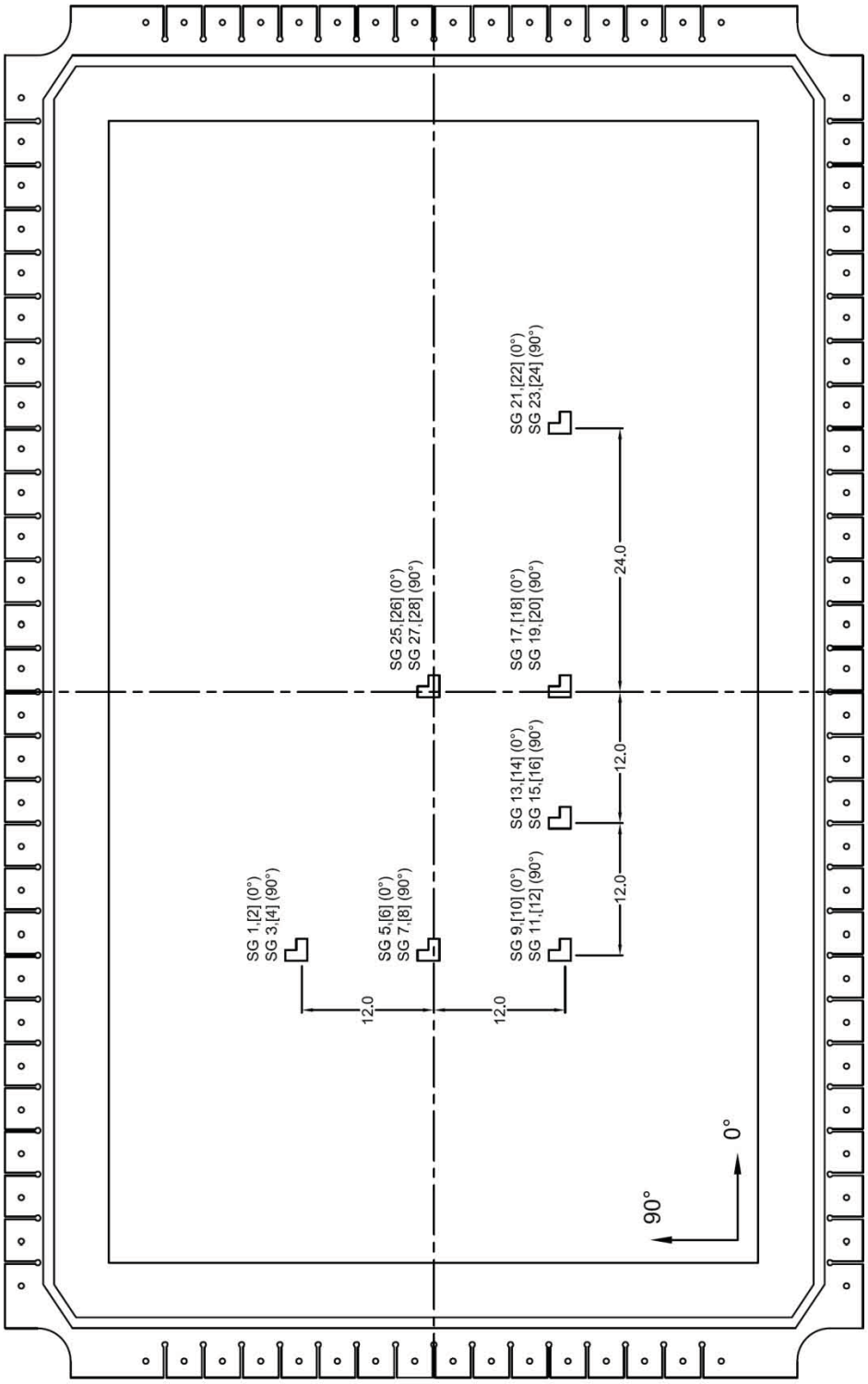

Figure 3.14. Strain gage map for panel CP1. All measurements are as measured on the exterior panel surface. Strain gage numbers in brackets are installed on the interior panel surface.

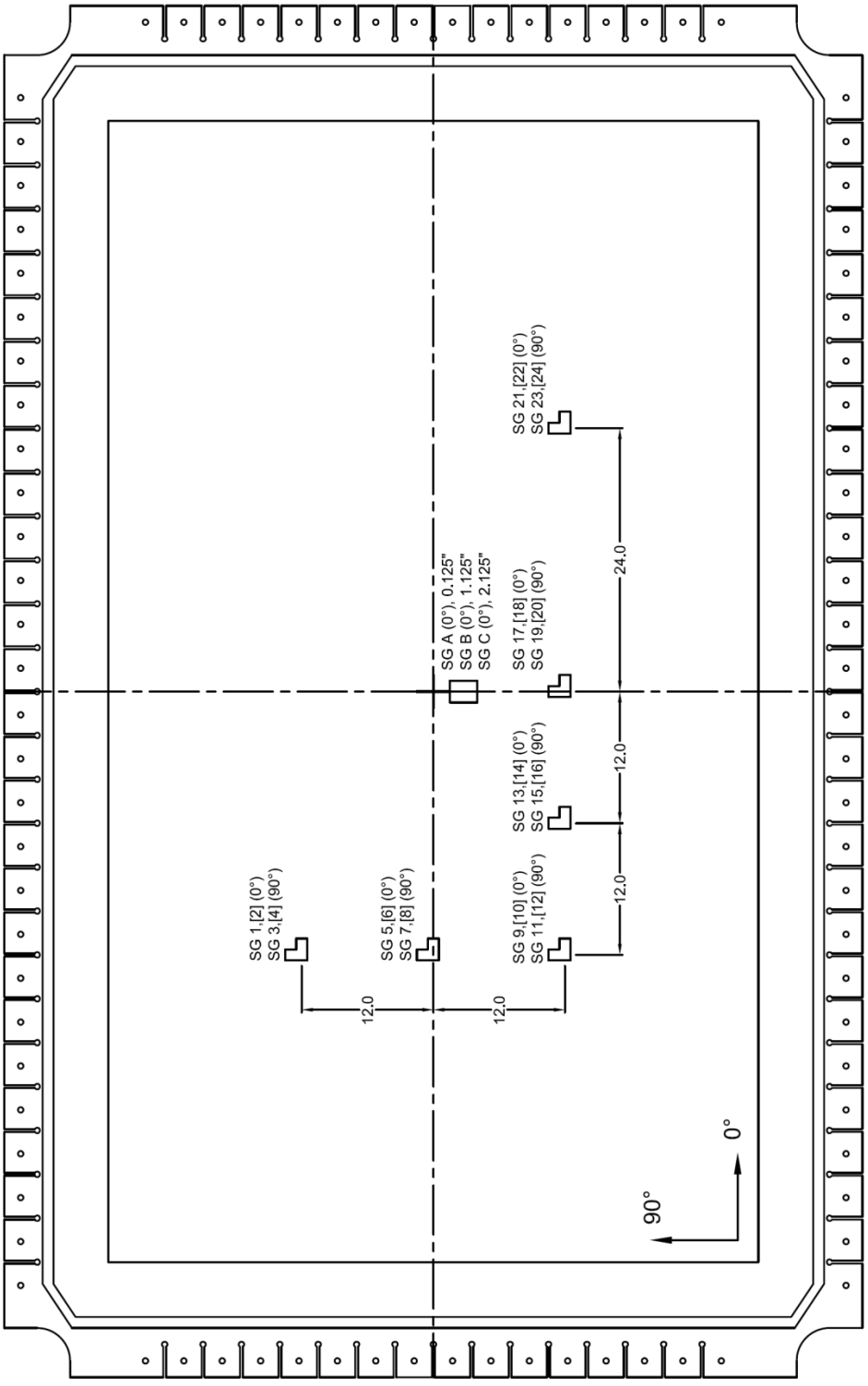

Figure 3.15. Strain gage map for panel CP1A. The distances listed for the strain gages installed in the vicinity of the damage indicate their distance from the damage. All measurements are as measured on the exterior panel surface. Strain gage numbers in brackets are installed on the interior panel surface.

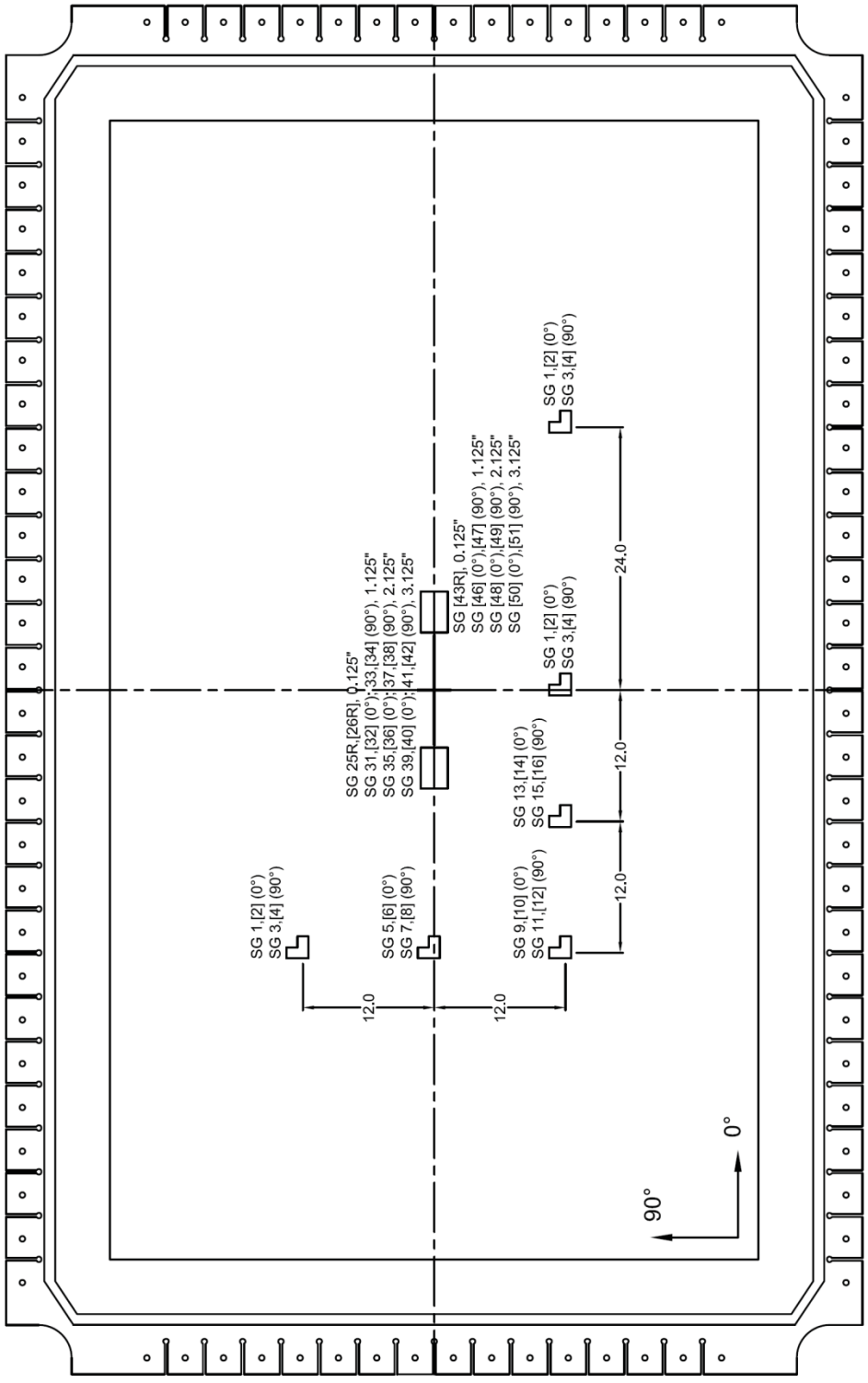

Figure 3.16. Strain gage map for panel CP1B. The distances listed for the strain gages installed ahead of the notch tips indicate their distance ahead of the notch tip. All measurements are as measured on the exterior panel surface. Strain gage numbers in brackets are installed on the interior panel surface.

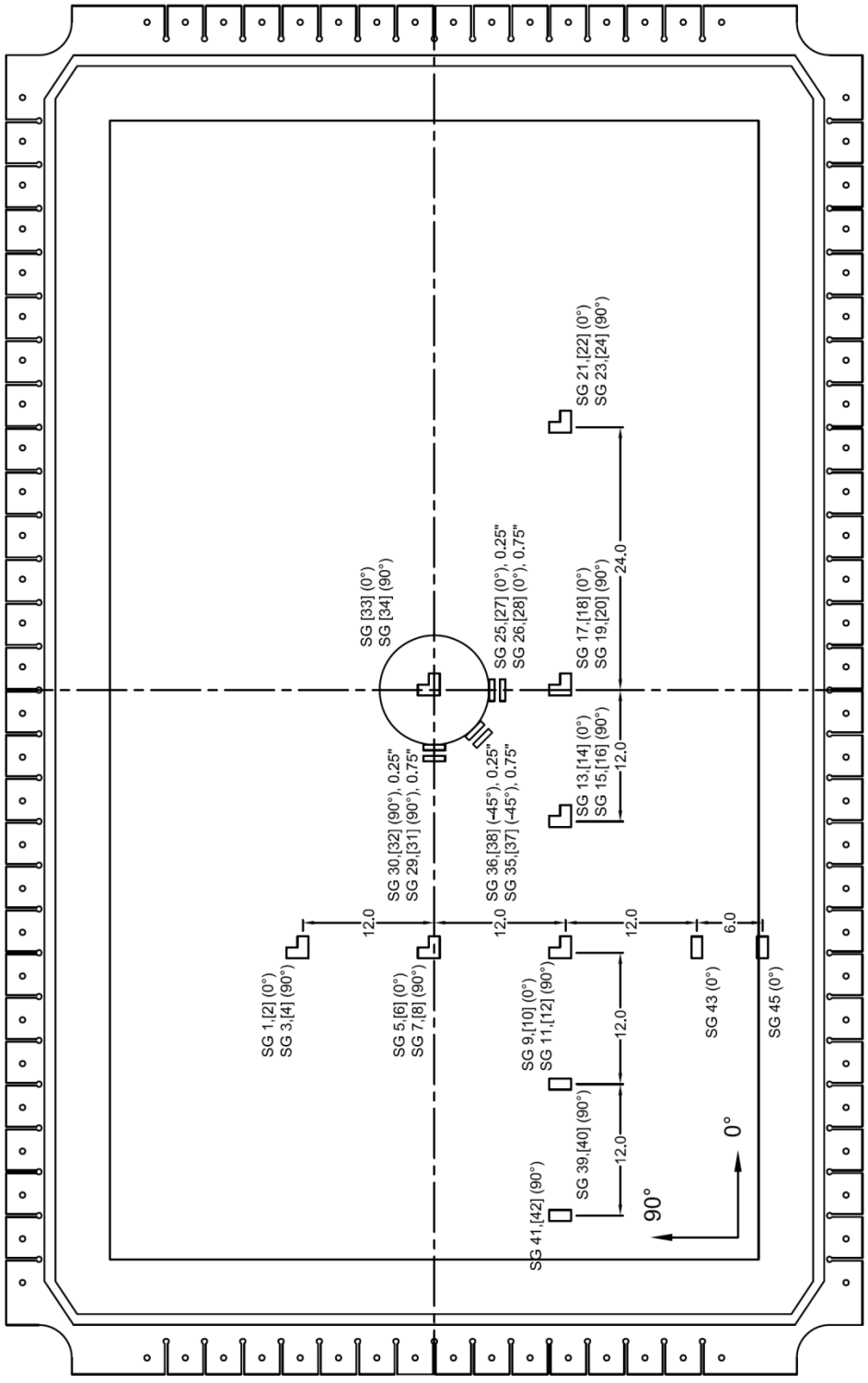

Figure 3.17. Strain gage map for panel CP2. The distances listed for the strain gages along the edge of the hole indicate their distance away from the edge of the hole. All measurements are as measured on the exterior panel surface. Strain gage numbers in brackets are installed on the interior panel surface.

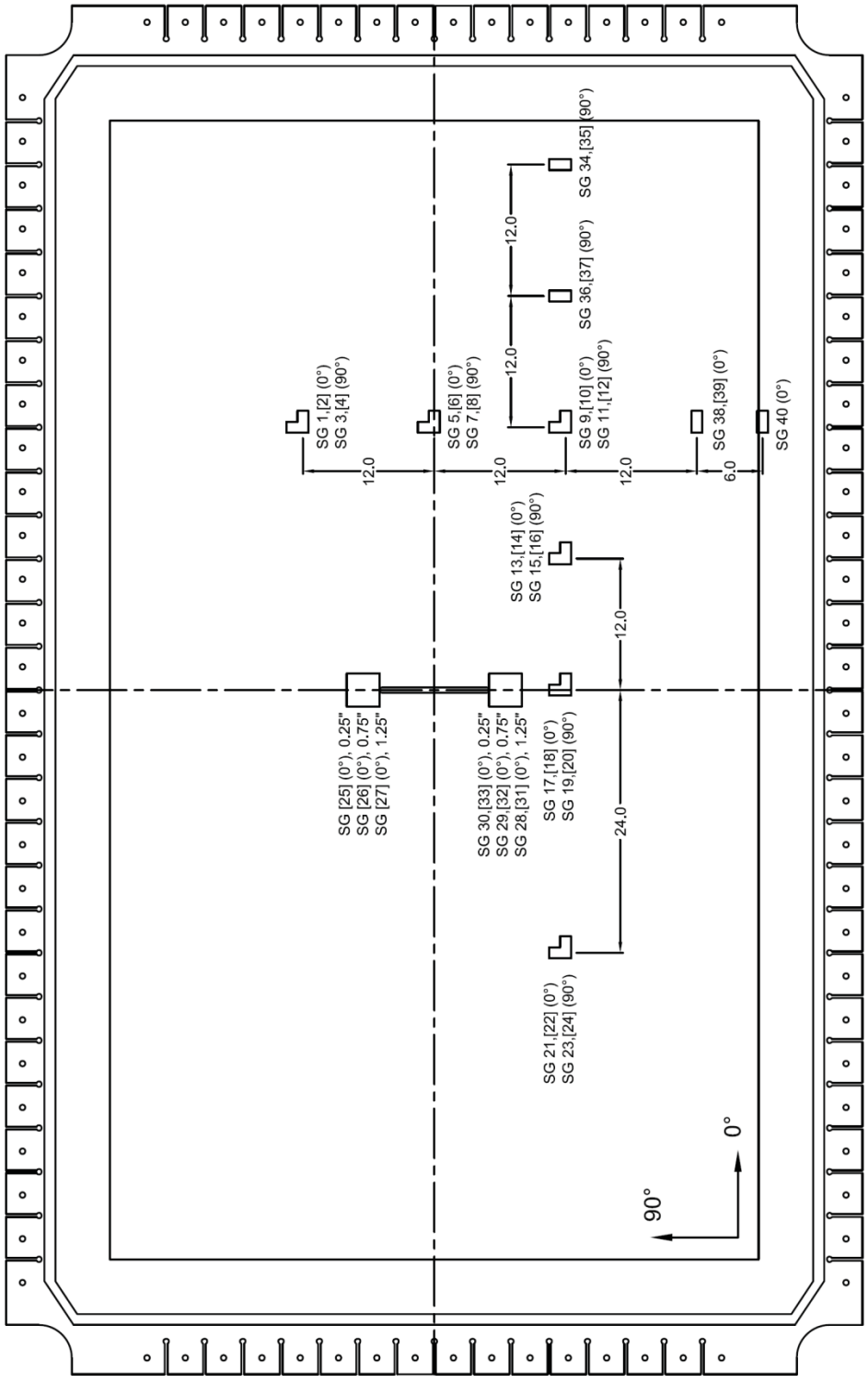

Figure 3.18. Strain gage map for panel CP3. The distances listed for the strain gages installed ahead of the notch tips indicate their distance ahead of the notch tip. All measurements are as measured on the exterior panel surface. Strain gage numbers in brackets are installed on the interior panel surface.

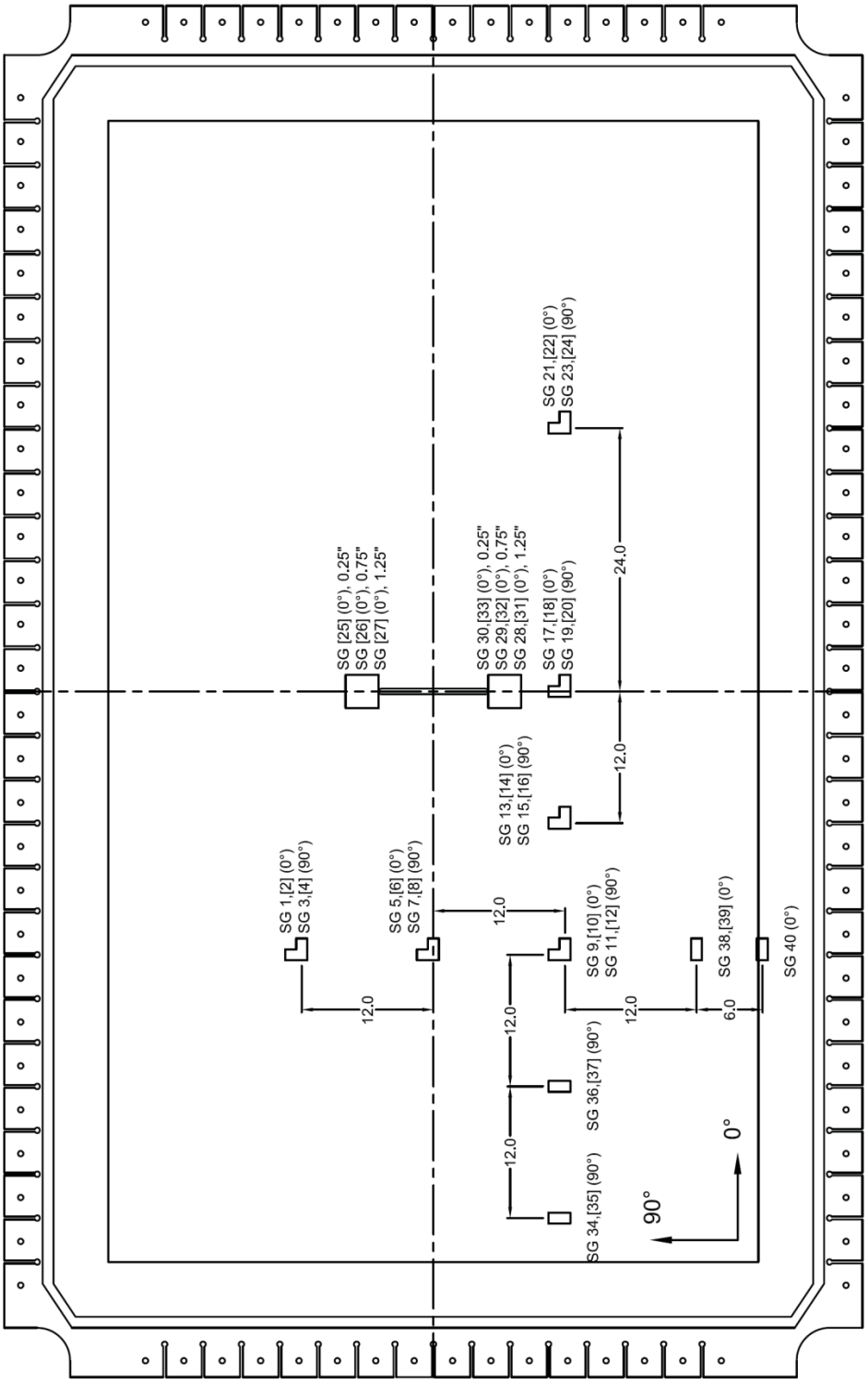

Figure 3.19. Strain gage map for panel CP4. The distances listed for the strain gages installed ahead of the notch tips indicate their distance ahead of the notch tip. All measurements are as measured on the exterior panel surface. Strain gage numbers in brackets are installed on the interior panel surface.

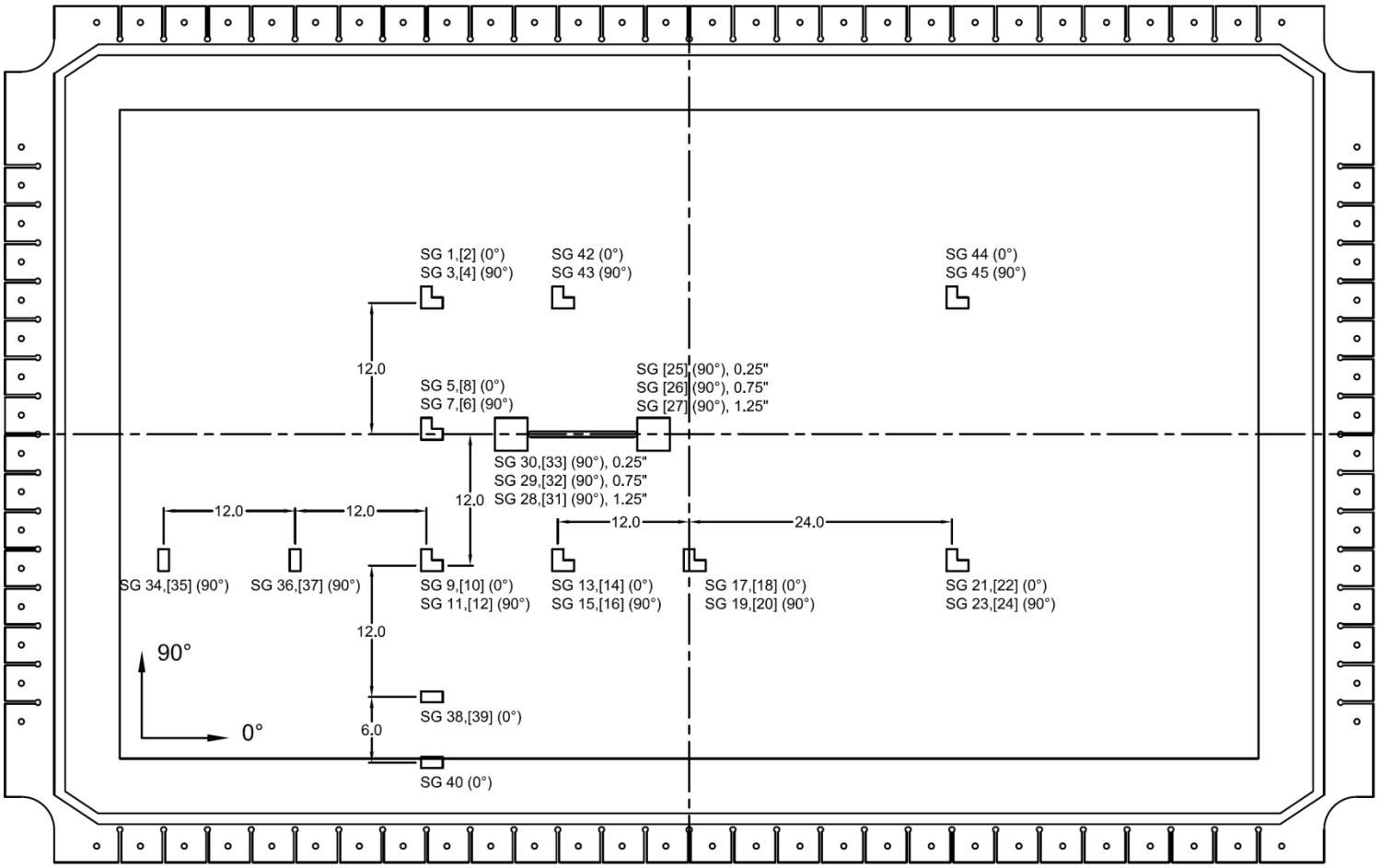

Figure 3.20. Strain gage map for panel CP5. The distances listed for the strain gages installed ahead of the notch tips indicate their distance ahead of the notch tip. All measurements are as measured on the exterior panel surface. Strain gage numbers in brackets are installed on the interior panel surface.

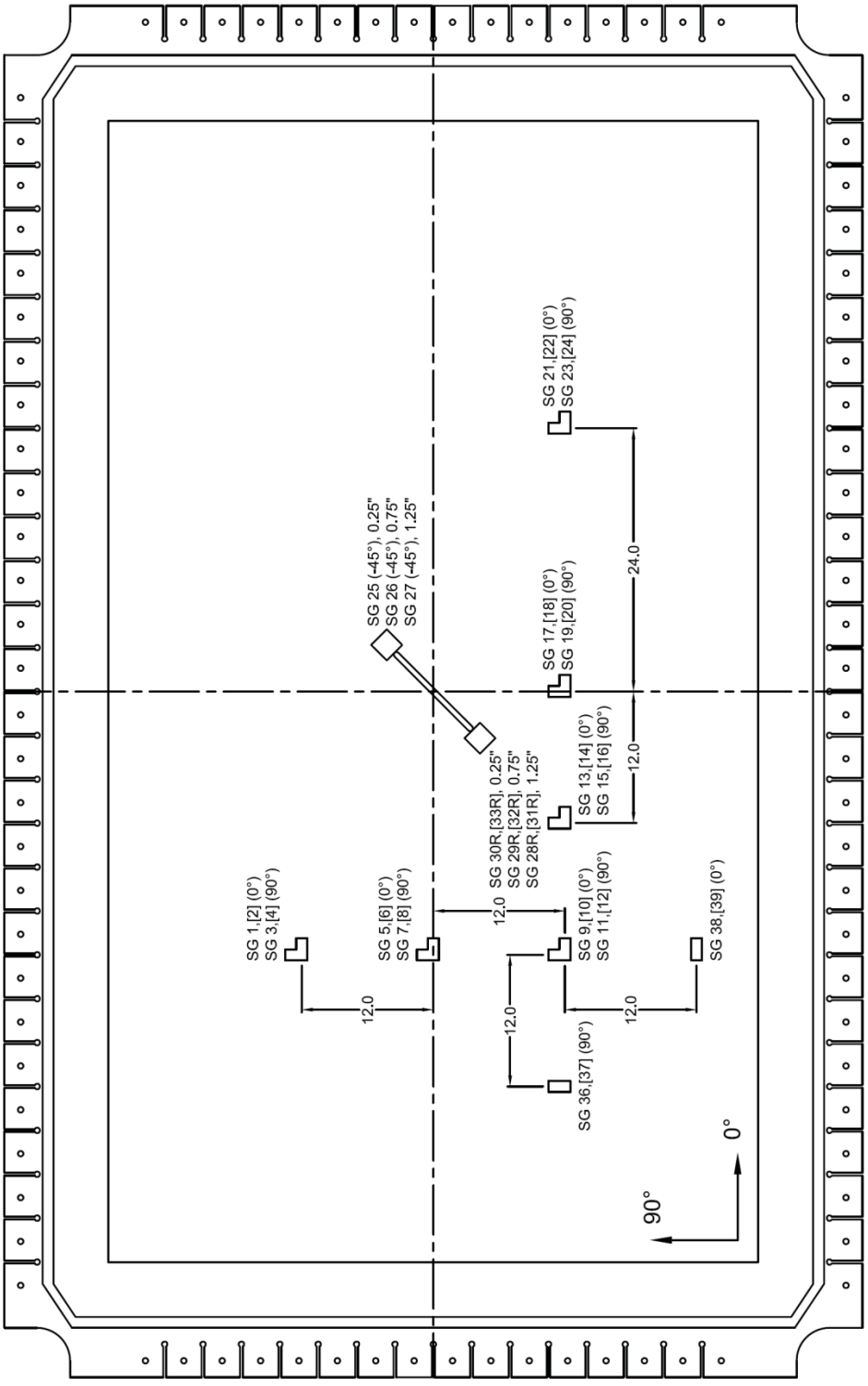

Figure 3.21. Strain gage map for panel CP6. The distances listed for the strain gages installed ahead of the notch tips indicate their distance ahead of the notch tip. All measurements are as measured on the exterior panel surface. Strain gage numbers in brackets are installed on the interior panel surface.

3.7.2. DIGITAL IMAGE CORRELATION METHOD

Full-field deformation and strain data were recorded during the loading of the test panels using the ARAMIS 4M three-dimensional deformation and strain DIC system. The system, using two 4-megapixel cameras. The camera focal lengths, working distances, and the approximate dimensions of the monitored areas for each panel are listed in Table 3.5. An angle of 25° between the two cameras was maintained for each test setup. The DIC system setup for panel CP5 is shown in Figure 3.22a.

Prior to testing, the regions of the panels to be monitored by the DIC system were coated with a high-contrast stochastic speckle pattern. Flat black spray paint was used to create a random pattern over a flat white base layer. The coarseness of the pattern directly affects the resolution of the measured deformation field, and must be appropriately applied. The nozzle of the black spray paint can was bored out with a drill bit to increase the output droplet size and to increase the likelihood of larger spurts of paint to create an appropriately random and textured pattern. An example of the desired pattern is shown in Figure 3.22b.

Baseline images were taken while the panels were unloaded to establish the initial unstrained configuration. Additional images were recorded at each load step, after the loaders had reached their end points, and after any visible change in the state-of-damage ahead of the monitored notch tip occurred.

Table 3.5. DIC system setup parameters.

Panel	Focal Length [mm]	Working Distance [in]	Measured Area [in^2]
CP1A	50	20	5 x 5
CP1B	28	25	12 x 12
CP2	20	38	24 x 24
CP3	28	25	18 x 18
CP4	28	25	18 x 18
CP5	28	18	6 x 6
CP6	28	18	6 x 6

(a) (b)

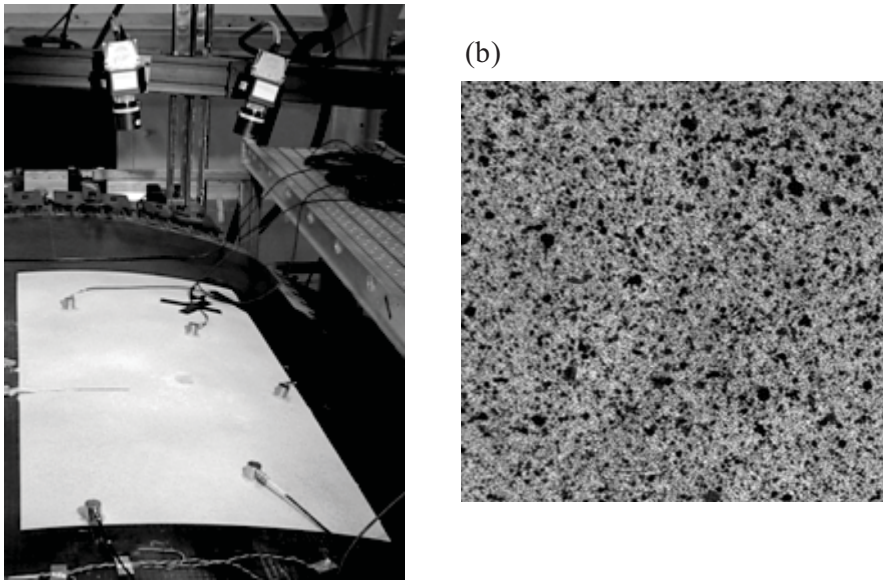

Figure 3.22. (a) DIC system setup for panel CP3, and (b) an approximately 2 inch by 2 inch sample of the high-contrast, stochastic DIC pattern applied to each panel.

Deformation and strain measurements using this DIC system were validated by comparing calculated full-field strain results to strain gage data (Section 4.3.2), and were later used to validate finite element results. Prior to performing any such comparisons, the calculated strain data required post-processing to remove the significant amount of noise which is inherent in DIC measurements, described in detail in Section 4.3.1. The strain gages installed in close proximity to the artificial damage modes of each panel were used to validate the DIC measurements. Since no strain gages were located in the areas monitored by the DIC system, symmetry was assumed across the major axes of the panels and the strain gage data collected from the opposite side of the damage was while validating the data. Comparison of the strain gage and DIC data sets was performed using data prior to the formation of any additional damage.

3.8. DAMAGE MONITORING & INSPECTION METHODS

Several nondestructive inspection (NDI) methods were employed during this study, including thermography, computer-aided tap testing, ultrasound, and x-radiography, to measure the extent of damage in the composite panels. Each of these methods has been used to successfully assess the states-of-damage in structures constructed of composite materials. However, to detect the initiation of damage it is also necessary to implement damage monitoring methods capable of detecting damage during testing. Such methods include the acoustic emission and frequency response techniques, both implemented in this study.

3.8.1. ACOUSTIC EMISSION

Acoustic emission (AE) data were recorded during the residual strength test of each panel, with the sole exception being during the last load step of the residual strength test of panel CP3 due to a system malfunction. The AE test instrumentation, developed by Physical Acoustics Corporation (PAC), used in this study consisted of data acquisition boards, software, and sensors. The AE data acquisition boards (PCI/DSP-4) and AEWin software controlled the AE sensors and acquired the data together with parametric information. The data acquisition boards had a 16-bit A/D conversion capability and a 132 MB/s transfer rate. AE data acquisition was conducted using a hit-based approach with a 40-dB threshold and time-based approach for root-mean-square (RMS) voltage, average signal level (ASL), and absolute energy. Analog filter ranges varied, depending on the sensor type. The general system configuration is shown in Figure 3.23. Emission characteristics and waveform data were collected at a maximum rate of 5 MHz, with a Hit Definition Time (HDT) of 0.8 ms and a Hit Lock-out Time (HLT) of 1 ms.

The HDT and HLT are user-selected, pretest parameters. The HDT represents the time that must elapse after the last threshold crossing of an AE waveform for it to be defined as a complete waveform. If an additional threshold crossing occurs after the last threshold crossing of the previous waveform, but before the HDT has ended, a new HDT must pass before the

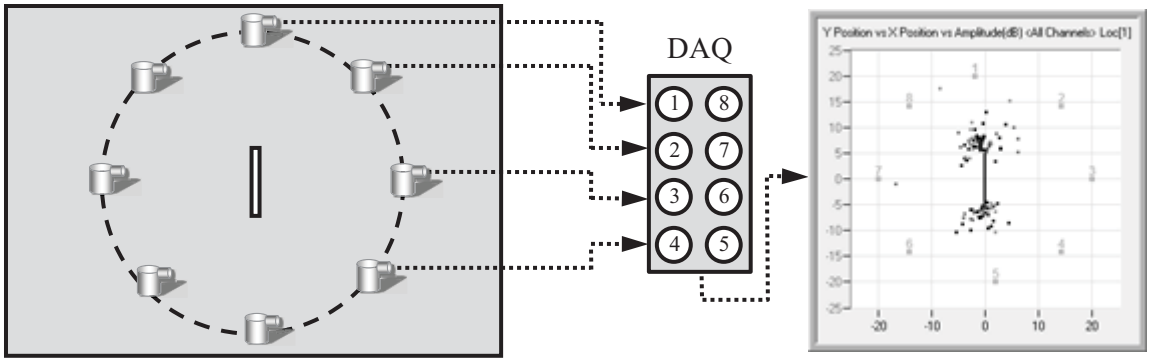

Figure 3.23. Acoustic emission system and general sensor layout.

waveform is determined to have ended. This process repeats itself until no new threshold crossing occurs within the most recently triggered HDT. The HLT is the period of time that immediately follows the end of a full HDT during which the AE channel is temporarily deactivated and no new information can be received.

Tests were conducted with four different PAC sensor models: R15, R15I, R6I, and WDI. The first two panels, CP1 and CP2, were instrumented with PAC model R15 resonant sensors, operating in the frequency range of 50–200 kHz with a resonant frequency of 150 kHz. AE signals were amplified by PAC Model 1220 preamplifiers, having a 40-dB gain with a 20-kHz high-pass filter and a 400-kHz low-pass filter. Panels CP4 and CP5 were instead instrumented with PAC model R15I sensors, which have integrated 40-dB preamplifiers. Panels CP5 and CP6 were instrumented with PAC model R6I resonant sensors, which operate in the frequency range of 35–100 kHz with a resonant frequency of 55 kHz, and have integrated 40-dB preamplifiers with a 30-kHz high-pass filter and a 165-kHz low-pass filter. Panels CP3 and CP4 were instrumented with PAC model WDI wideband sensors, which operate in the frequency range of 50–300 kHz, and have integrated 40-dB preamplifiers with a 32-kHz high-pass filter and a 1.1-MHz low-pass filter. The above frequency ranges are based on the ASTM E1106 calibration standard, per PAC's specification sheets. The frequency response of each sensor type is shown in

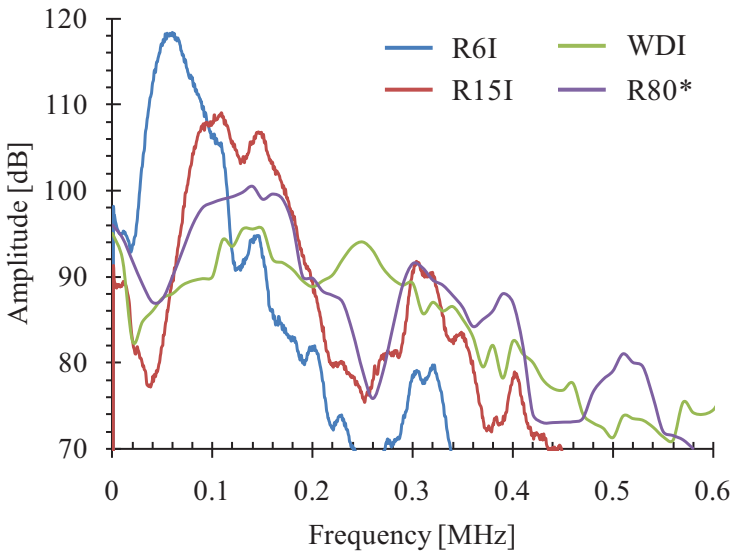

Figure 3.24. Frequency response of the PAC R6I, R15I, WDI, and R80 AE sensors, based on ASTM E1106. The response of the R80 sensors is that of a signal being run through a 40-dB preamplifier.

Figure 3.24. Due to its higher sensitivity, the R6I could provide an earlier detection and better location of damage initiation; however, it was also more sensitive to extraneous noise from throughout the panels and loaders. The wideband sensors were used to understand the frequency content of the AE signals generated by the dominant failure modes in the composite panels and to reduce the large amount of low-intensity hits generated by extraneous emission.

Panels CP1 and CP2 were used largely to develop a testing procedure for the monitoring of AE in the full-scale composite fuselage panels. As a result, little reportable data was recorded. For panel CP1A, six R15 sensors were placed along the perimeter of a 36-inch diameter circle with the damage at its center, Figure 3.25a. Five sensors were installed at 45° intervals along half of the perimeter (covering the arc between the two circumferential notch tips), with an additional sensor located ahead of the opposite longitudinal notch tip. For panel CP1B, seven R15 sensors were placed along the perimeter of a 30-inch diameter circle with the longitudinal notch at its center, Figure 3.25b. No sensors were installed in the quarter of the panel designated for DIC measurements. For panel CP2, seven sensors were placed at 45° intervals along

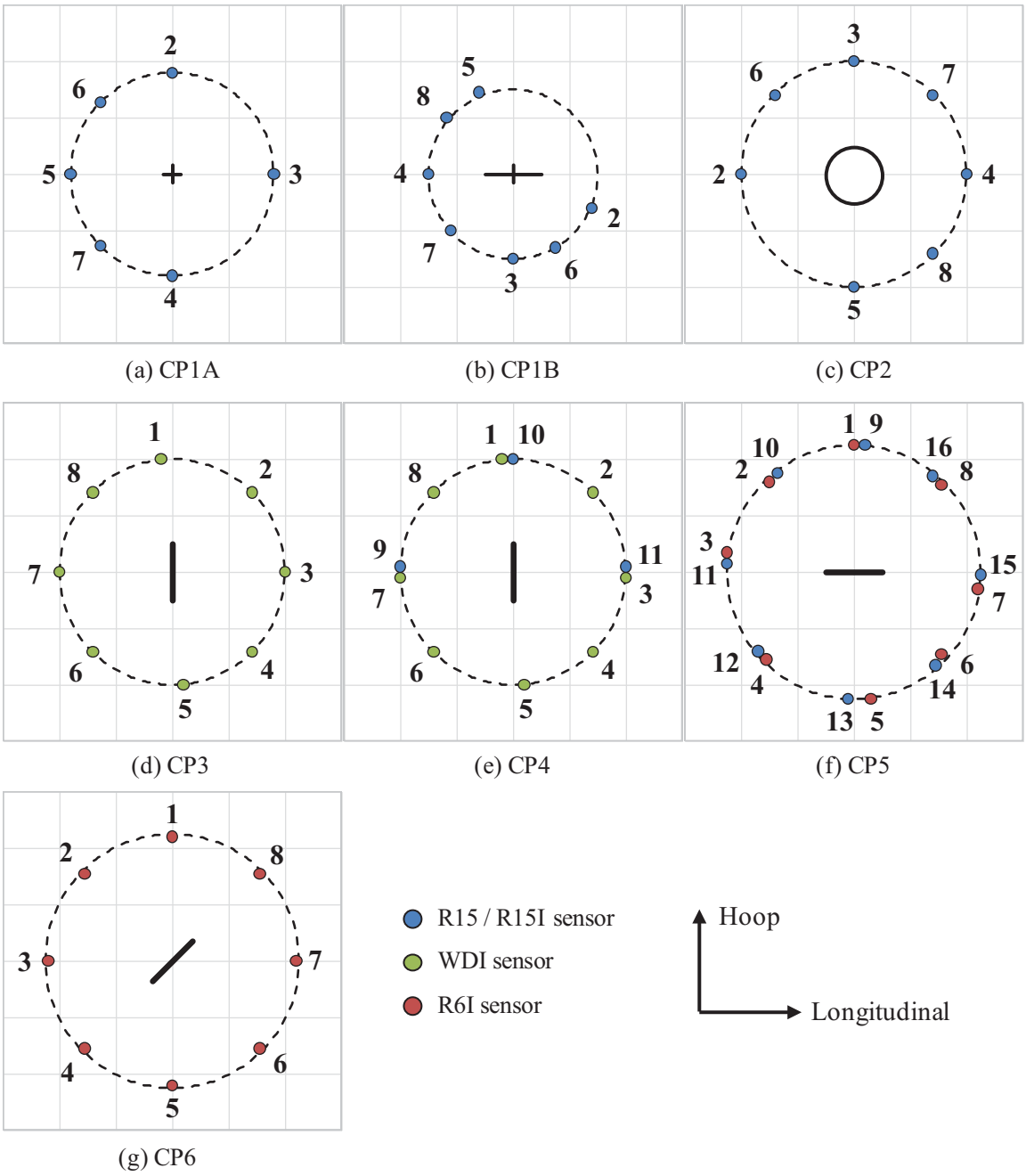

Figure 3.25. AE sensor locations, numbering, and models for each monitored panel. The dashed line represents the AE gage section for each sensor configuration. The grid spacing is ten inches for each panel.

the perimeter of a 40-inch diameter circle with the 10-inch diameter hole at its center (Figure 3.25c); again no sensors were installed in the quarter of the panel designated for DIC measurements.

The sensor placements for panels CP3 through CP6 were more uniform. Sensors were placed at 45° intervals around the center of the artificial damage for each of the remaining panels. For panels CP3 and CP4, eight WDI sensors were placed along the perimeters of 40-inch diameter circles with the circumferential notches at their centers. For comparative purposes, three additional R15I sensors were placed next to three WDI sensors on panel CP4. For panels CP5 and CP6, eight R6I sensors were placed along the perimeters of 45-inch diameter circles with the notches at their centers. Also for comparative purposes, panel CP5 was instrumented with an additional set of eight R15I sensors alongside the R6I sensors. The location, numbering, and model of each sensor is shown schematically in Figure 3.25.

Wave speed in the laminate was measured as functions of both distance and angle relative to the composite lay-up. This was done using two sensors, a pulser and a receiver, to measure the wave speed of an induced signal over various distances and angles. A PAC model R80 sensor was used as the pulser and a WD sensor was used as the receiver. To assess the dependence on angular variation with respect to the lay-up, the sensor pair was placed at 22.5° increments along a 10-inch radius arc. The highest wave speed, approximately 188,000 in/s, occurred along the ±45° directions and the lowest, approximately 170,000 in/s, occurred along the 0°/90° directions, Figure 3.26a. Multiple measurements were conducted at various distances (Figure 3.26b), yielding similar results (within ±5,000 in/s), irrespective of pulser-receiver distance. Noting that the angles between the notch tip and the nearest three sensors are ~0° and ~55° the AE data analyses discussed herein were all performed using the average wave speed of 180,000 in/s.

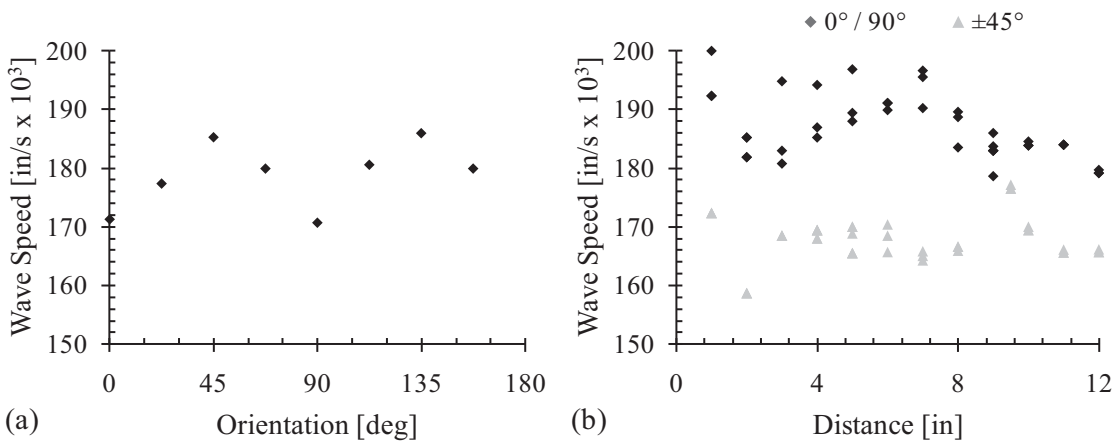

Figure 3.26. (a) Wave speed variation with angle, at a fixed distance of 10 inches, and (b) wave speed variation with distance, along the 0°/90° and ±45° directions.

3.8.2. FREQUENCY RESPONSE

The frequency response (FR) technique applied in this study is based on the introduction of constant-amplitude sinusoidal waves of continuously varying frequencies through a wideband piezoelectric transmitter and measuring the frequency response of a segment of the panel through a similar receiver located a distance away. Preliminary testing indicated that the material did not transmit frequencies above 400 kHz. Accordingly, a 100–400 kHz input pulse was used with 0.1 ms duration.

The FR testing instrumentation consisted of a waveform generator, data acquisition boards, an actuator, and a receiver. The waveform generator (ARB-1410 board) and the data acquisition boards (PCI/DSP-4) were both manufactured by PAC. The ARB-1410 board is a PCI-bus-based, highly precise (14-bit), high-speed (100 MSample/s), arbitrary waveform generator card. The data acquisition boards were synchronized with the waveform generator so that the data acquisition started acquiring waveforms via the receiving sensor when the actuator induced a pulse signal into the material. The arrival time of received waveforms indicated the time of flight of the pulse signal from pulser location to receiver location.

PAC model R80 and WD sensors were used for the actuators and receivers, respectively. The R80 sensor operates in the frequency range of 50–400 kHz and the WD sensor has a wideband response in the range of 50–300 kHz, based on the ASTM E1106 calibration standard, Figure 3.24. All received signals were amplified by a 40-dB preamplifier ahead of the data acquisition board. A schematic of the general system setup is shown in Figure 3.27.

FR studies were conducted during the residual strength tests of panels CP5 and CP6. For panel CP5, two pulser-receiver pairs were located ahead of the notch tip, 2.0 inches apart, with the first pair, P1-R1, just ahead of the notch tip, Figure 3.28a. The pulser-receiver separation distance was 10.0 inches. For panel CP6, four pulser-receiver pairs were used: three pairs ahead of the notch tip monitored by the DIC system, located 0.0, 2.0, and 4.0 inches ahead of the notch tip, and one pair 2.0 inches ahead of the other notch tip, Figure 3.28b. The pulser-receiver separation distance for panel CP6 was increased to 14.0 inches. All sensors were coupled to the panels using hot glue.

The pulser-receiver distance for each case was selected to obtain an acceptable signal-to-noise ratio while minimizing any interference with DIC measurements. Prior tests showed that the elevated notch tip strain field typically did not extend beyond a radius of approximately 5 inches from the notch tip prior to a catastrophic fracture. A detailed calibration study, presented

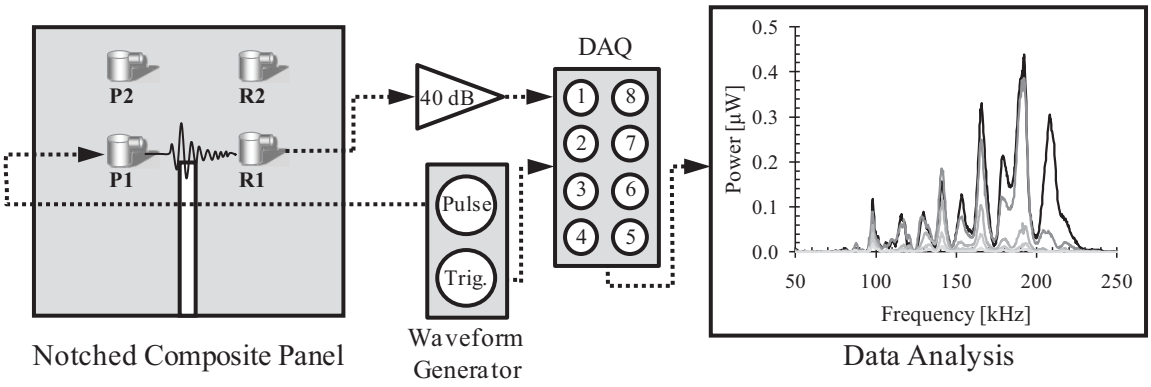

Figure 3.27. FR test setup schematic.

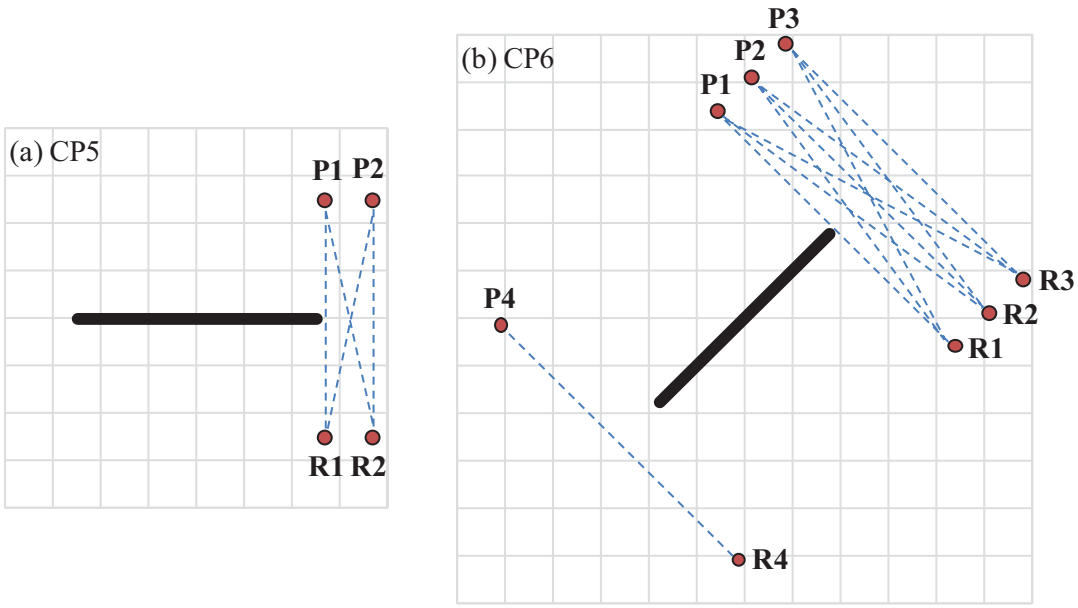

Figure 3.28. FR sensor layout for panels (a) CP5 and (b) CP6. The grid spacing is two inches for each panel. The dashed lines are indicative of the wave paths evaluated by the pulser-receiver pairs.

in Chapter 7, indicated that FR results greatly depend on both the pulser-receiver separation distance and the orientation of the composite lay-up relative to their position. Knowing this, both the pulsing and receiving sensors were kept stationary throughout each test.

3.8.3. THERMOGRAPHY

The EchoTherm® flash thermography system, developed by Thermal Wave Imaging, Inc., was used to inspect the panels for nonvisual defects and damage. The FAA Airworthiness Assurance NDI Validation Center at Sandia National Laboratories provided the system and established the inspection procedure using a sample of the sandwich composite panels. Data were recorded at 60 frames per second and captured over an 11-second period of time. The raw data and first and second derivatives of temperature with respect to time were used to scan the panels. The system provided an image of approximately 6 inch by 5 inch and was capable of either taking single images or multiple images established in a grid pattern to be combined into a

larger file. Thermographic inspections of the entire test section from both the interior and exterior surfaces were conducted for each panel before and after loading.

3.8.4. COMPUTER-AIDED TAP TESTING

Tap testing was conducted as another method to detect nonvisual damage. The tests were performed using the Computer-Aided Tap Tester (CATT) developed by Iowa State University. The CATT is a portable inspection device based on the "coin tap" method, but with capabilities that allow it to produce quantitative images from what has traditionally been only a qualitative, audible test. The CATT consists of a brass-tipped accelerometer (impactor), electronic circuitry for conditioning the signal and measuring the impact duration, and a laptop computer that contains data acquisition and processing software, Figure 3.29.

Before and after each residual strength test, tap test data were collected in the immediate vicinity of the artificial damage, in areas suspected of additional pretest damage (e.g., the panel CP5 skin-to-core disbond), and from areas in which more wide-field NDI techniques (e.g., thermography) gave indications of damage. Inspections were performed by taping down a 0.25-inch square grid to the panel surface and using the automatic tapper. The automatic tapper was

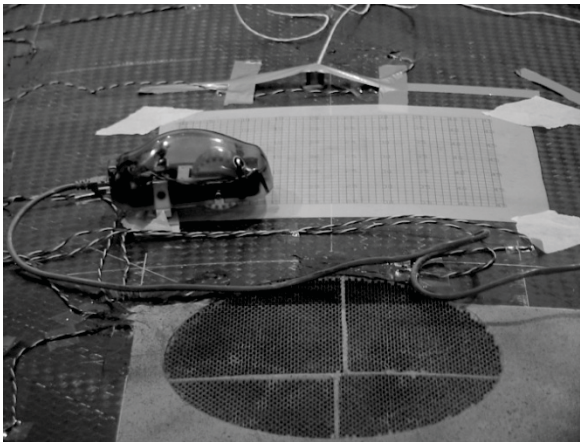

Figure 3.29. Automatic CATT tapper and the 0.25-inch grid applied to the exterior surface of panel CP2.

rolled along each row of the grid one column at a time. A manual tapper was then used to rescan any anomalously high or low readings.

3.8.5. ULTRASOUND AND COMPUTED TOMOGRAPHY

Ultrasonic pulse-echo inspections and x-radiographic computed tomography (CT) scans of certain panel sections of interest were carried out posttest. These inspections were performed at the Airworthiness Assurance NDI Validation Center at Sandia National Laboratories.

Three specimens were inspected: (i) a section of panel CP2 containing one hoop and one longitudinal tangent of the original exterior face sheet hole, measuring approximately 20 inches by 18 inches; (ii) a section of panel CP4 containing one 10-inch by 0.5-inch circumferential notch tip, measuring approximately 18 inches by 18 inches; and (iii) a section of panel CP5 containing the large elliptical face sheet-to-core disbond discovered pretest, measuring approximately 30 inches by 16 inches. Each of these specimens were manually removed from the panels using a reciprocating saw prior to performing the ultrasonic inspections and x-radiographic CT scans.

The ultrasonic pulse-echo inspections were performed using a Boeing MAUS V system, using water as a couplant. Prior to the inspections, the edges of the specimens and any through-thickness damage were sealed with tape to avoid wetting the honeycomb core. The thickness of the panels and the emptiness of the core material prohibited the performing of through-transmission inspections. Data were recorded with a resolution 0.030 inch at a sample frequency of 25 MHz. GE sensors were used to scan the specimens using frequencies of 10 and 15 MHz (the maximum for the available sensors) with a 0.75-inch delay line. C-scans were generated for each specimen from both the interior and exterior surfaces. The geometry of the scanned sections varied for each panel section.

X-radiographic CT scans were performed for each of the three panel sections. The panels were mounted on a rotating stage and a series of radiographic images were recorded at small-angle increments. The section of panel CP2 can be seen mounted on the rotating stage in

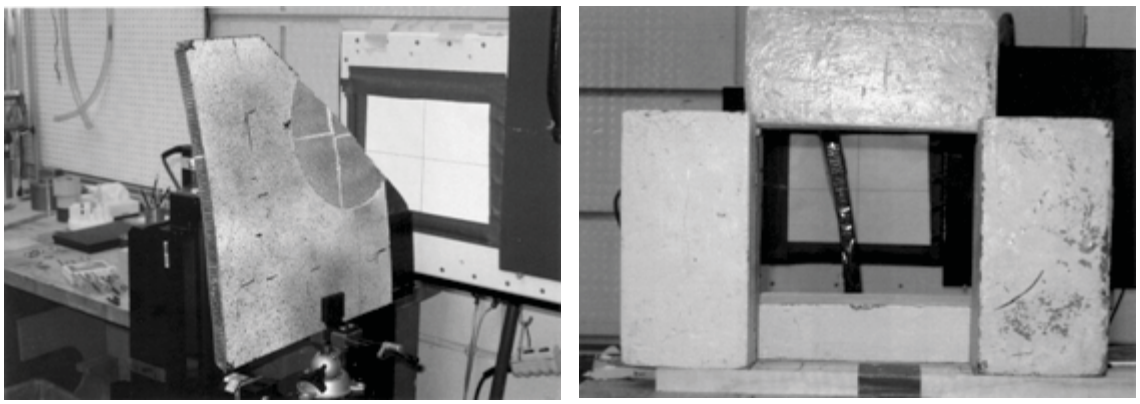

(a) (b)

Figure 3.30. Experimental setup for x-radiographic scan of a section of panel CP2: (a) angle view and (b) camera view.

Figure 3.30. The set of radiographic images was then assembled into three-dimensional image of the panel sections using MATLAB.

3.8.6. SCANNING ELECTRON MICROSCOPY

A fractographic analysis was performed via scanning electron microscopy (SEM) for samples taken from the notch tip region of panel CP5. The SEM inspections were performed with an FEI XL30 Environmental SEM at the Drexel University College of Engineering Centralized Research Facilities.

To fit inside the vacuum chamber of the microscope, each sample was limited to a width of 0.625 inch. The two face sheets of the sandwich composite were separated and inspected individually. This was accomplished by manually cutting through the core material. In most cases, however, the core in the immediate vicinity of the fracture surface was already severely damaged, so minimal, if any, alterations were required. Each sample was coated with carbon prior to inspection to facilitate the SEM imaging. The carbon coating was performed before each SEM session. Samples were mounted using a small vice with set screws. The vice was secured to the carbon/epoxy face sheets at the base of the specimens, opposite the fracture surface.

CHAPTER 4: PANEL STRAIN AND DEFORMATION FIELDS

4.1. INTRODUCTION

Series of strain surveys and residual strength tests were conducted for each of the full-scale honeycomb sandwich composite aircraft fuselage panels. The panels were quasi-statically subjected to combinations of internal pressurization, hoop, and longitudinal loading up to either panel fracture or the maximum capacity of the FASTER fixture, as described in Section 3.6. During these tests, the deformation and strain response of the panels were measured using two systems: (i) sets of strain gages were installed in the vicinity of the inserted artificial damage and throughout the remaining test section and load application regions (Section 3.7.1), and (ii) the digital image correlation (DIC) method was used to monitor the full-field strain in the vicinity of the inserted artificial damage (Section 3.7.2).

Strain gage and loader data collected from the FASTER data acquisition system provided a thorough history of the deformation of the panels in terms of the in-plane strains and out-of-plane bending. The performance of the loaders must be taken into consideration when analyzing any unexpected panel deformations. The severity of the inserted artificial damage in each panel was characterized by sets of strain gages installed in the most critical regions. In this chapter, the strain gage and loader data for all six panels are presented and discussed in detail.

The DIC method performed detailed measurements of the panel deformation during loading, offering the ability to perform analyses otherwise impossible utilizing only the point-wise strain gage data. The full-field DIC data allow for the identification of the most critical strain components in the vicinity of the damage and the characterization of the elevated strain fields ahead of the damage (e.g., in terms of maximum recorded strains, strain concentration factors, the shape of the elevated strain field, etc.). While the notched panels generally exhibited few stages of visible damage extension prior to catastrophic fracture, the driving forces behind damage propagation can be identified through analysis of the DIC-recorded strain fields

preceding individual localized failures. In this chapter, only the DIC data from panel CP5 are presented and discussed in detail. The DIC strain contour plots from all other panels are presented in Appendix A.

4.2. STRAIN GAGE AND LOADER DATA

Voluminous strain gage and loader data were collected from the FASTER fixture data acquisition system during the strain surveys and residual strength tests of the panels. Load cell data from each of the hoop and longitudinal loaders were recorded, as well as the applied internal pressure. Any tensile loads that developed within the radial link assemblies were also recorded. However, an insufficient number of functioning load cells was available to monitor each of the radial link assemblies. As a result, the complete state-of-loading for the panels is not available.

During the thirty-second load steps, certain loaders were observed to lag behind their targets, causing slight imbalances in the applied loads. To minimize this effect on the measured strain distributions across the panels, the target loads were held after the thirty-second load steps to allow the loaders to reach their targets and ensure equilibrium. The point-wise strain measurements reported throughout this chapter are the measurements taken after equilibrium was achieved at each load step. Strain gage data are also reported as a function of time for gages installed in the immediate vicinity of any artificial damage to better characterize damage progression. The strain gages were installed on the interior and exterior face sheets of the panels as indicated in the strain gage maps presented in Section 3.7.1.

All of the strain gages were zeroed prior to the installation of the pins which connected the panel edges to the loader whiffle trees described in Section 3.2. Any preloading of the panels resultant of their attachment to the loaders and fastening the pins could then be quantified. Free play in the loaders could cause both an artificial shift in the strain response to applied load and nonlinearity through the first two to three load steps. To compensate for this unwanted behavior and to isolate the strain response of the panels due to the applied loading, a curve fit can be

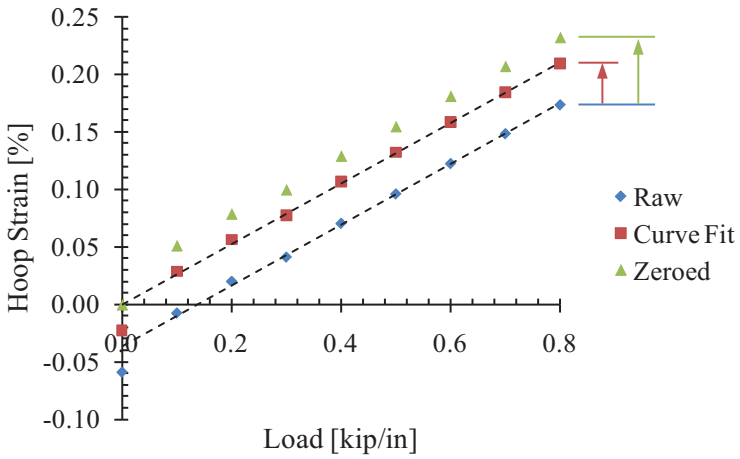

Figure 4.1. Comparison of raw strain gage data, strain gage data shifted due to curve fitting, and strain gage data zeroed prior to the start of the test, applied to strain gage SG27 of panel CP1 while under combined loading.

performed for the latter strain measurement points, through which linearity is expected, and the data shifted to pass through the origin, Figure 4.1. However, this strain gage data reduction procedure could not be adopted herein because of the complexity of some of the loading functions applied in this investigation (e.g., the low off-axis loads in panels CP4 and CP5). Insufficient load steps exist for any nonlinearity of the strains due to the initial off-axis loads to be identified, offering no clear point to which the strain due to the major direction of loading should be shifted. Accordingly, all strain gage data presented in this chapter were simply zeroed to the point immediately before any nonzero load commands were set. The curve fitting method is later applied to select data for the purposes of finite element model validation in Chapter 8.

4.2.1. PANEL CP1

As mentioned in Section 3.4, panel CP1 initially contained no damage and served as the baseline case for which the structural response of the panels was characterized and the strain and damage monitoring systems (e.g., DIC, acoustic emission, thermography, etc.) were calibrated. Panel CP1 also served to determine the ability of the FASTER fixture to load a full-scale

composite fuselage panel and to accordingly adjust the fixture setup (e.g., in terms of controller gains, loader alignments, available stroke, etc.). As a result, the full load history of panel CP1 (Table 4.1) contains a large number of strain surveys and residual strength tests during which their target loads (Tables 3.3 and 3.2, respectively) were not met. The loads listed in Table 4.1 are the maximum applied loads in each loading attempt.

Strain surveys were conducted in each of the three loading configurations: (i) combined hoop loading, longitudinal loading, and pressurization; (ii) hoop loading and pressurization; and (iii) longitudinal loading. While several tests were conducted for each loading configuration, only those which reached their target loads are discussed in detail. All such panel tests are assigned a unique designation to indicate test type and loading number (e.g., CP1-SS-C1 can be interpreted as "Panel CP1, Strain Survey, Combined Loading, Loading No. 1"). Nineteen strain survey tests were conducted for panel CP1, ten of which reached their target loads: four under combined loading up to 1000 lbf/in, three under 500 lbf/in hoop loading and 6.75 psi internal pressure, and three under 500 lbf/in longitudinal loading.

Under the combined loading conditions for panel CP1, equal loads per length along the four sides of the test section were applied. The hoop loaders effectively covered 112 inches of the panel edge in the longitudinal direction and the longitudinal loaders effectively covered 56 inches along the panel curvature, accounting for most of the test section and inner transition lay-up regions (Section 3.3); the hoop and longitudinal *loads per length* are defined with respect to these dimensions. Because these dimensions are relatively large compared to those of the central test section, it was initially assumed that these sections of the panel that were not directly in-line with either the hoop or longitudinal loaders would have minimal influence on the load distribution throughout the central test section.

The balanced plain-weave fabric used in the face sheets resulted in approximately equal stiffness (i.e., less than 3% difference) in the hoop and longitudinal directions. As a result, the measured hoop and longitudinal strains were expected to be approximately equal with equal

Table 4.1. Load History of Panel CP1.

Loading	Designation	Maximum Applied Loads		
		Long [lbf/in]	Hoop [lbf/in]	Pressure [psi]
Combined	-	600	600	8.10
Combined	-	200	200	2.70
Combined	-	600	600	8.10
Combined	-	600	600	8.10
Combined	-	600	600	8.10
Combined	CP1-SS-C1	1000	1000	13.50
Combined	-	600	600	8.10
Combined	-	900	900	12.15
Combined	CP1-SS-C2	1000	1000	13.50
Combined	-	800	800	10.80
Combined	-	400	400	5.40
Combined	CP1-SS-C3	1000	1000	13.50
Combined	CP1-SS-C4	1000	1000	13.50
Hoop	CP1-SS-H1	0	500	6.75
Hoop	CP1-SS-H2	0	500	6.75
Hoop	CP1-SS-H3	0	500	6.75
Longitudinal	CP1-SS-L1	500	0	0.00
Longitudinal	CP1-SS-L2	500	0	0.00
Longitudinal	CP1-SS-L3	500	0	0.00
Longitudinal	CP1-RST-1	1200	0	0.00
Longitudinal	CP1-RST-2	1200	0	0.00
Longitudinal	-	300	0	0.00
Longitudinal	CP1-RST-3	1200	0	0.00

loading in the two directions for this loading configuration (i.e., tests CP1-SS-C1,2,3,4). An example of the actual response for one such test is shown in Figure 4.2, showing the strain recorded by strain gages oriented in the hoop and longitudinal directions on the exterior surface of the panel. (No interior strain gage data were available due to improper sealing of the strain gages from the water in the FASTER fixture pressure box.) The results show a large difference between the hoop and longitudinal strains. Additionally, there is a much wider spread in the longitudinal strains than in the hoop strains.

Significant load attraction to the panel edges was found to be the primary cause of the disparity in hoop and longitudinal strains although loaded equally in both directions. Early in the test program the greater stiffness of the load application region lay-up was identified as likely to cause load attraction. As mentioned in Section 3.3, several blunted slits were inserted between

each load application point, through the stiffer lay-up, decreasing its ability to carry additional load. However, the additional stiffness of the transition regions and the application of the longitudinal loads to only the central 56 inches of the panel curvature led to the attraction of the applied longitudinal loads to the panel edges. Therefore, it was assumed that some nonuniform distribution of load existed across the panels.

Examination of the strain gage data from the combined loading strain surveys of panel CP1 showed that the hoop and longitudinal strains varied little along the hoop and longitudinal directions, respectively. However, the distributions of longitudinal strain with hoop position and hoop strain with longitudinal position proved to be an excellent measure of panel edge load attraction and of the nonuniformity of the strains throughout the central test section (excluding the effects of any artificial damage), Figure 4.3. Plots of these longitudinal and hoop strain distributions for each panel CP1 strain survey are shown in Figure 4.4. Similar plots are presented throughout this chapter to represent the far-field strain response of each panel. In each such plot, a coordinate system is established where the origin is located at the center of the panel, and the longitudinal and hoop directions represent the *x*- and *y*-directions, respectively.

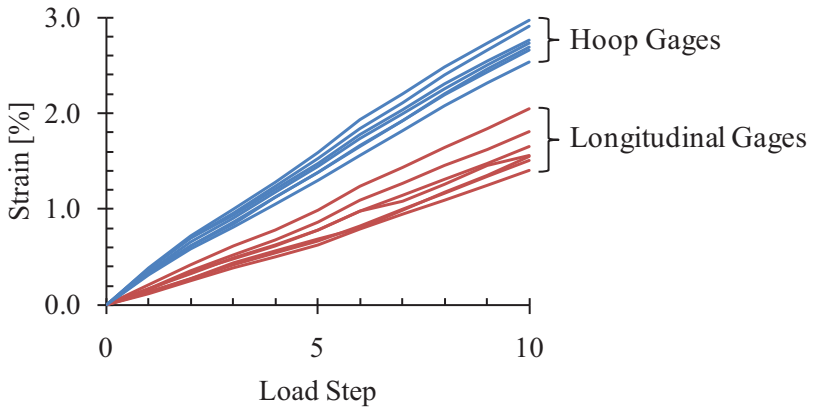

Figure 4.2. Comparison of all exterior strain gage data for panel CP1, test CP1-SS-C4, showing the notable difference between the hoop and longitudinal strains despite equal loading in the two directions.

As mentioned earlier, the results of the combined loading strain surveys of panel CP1 indicated a significant disparity in the hoop and longitudinal strains, as well as a significant spread amongst the recorded longitudinal strains, Figure 4.4a. The maximum longitudinal strains were recorded along the crown (i.e., center) of the panel, decreasing with increased proximity to the panel edges. Panel CP1 had strain gages installed at only three different hoop positions and four different longitudinal positions. As seen in the figure, no significant variation in the hoop strains with longitudinal position was observed under combined loading, Figure 4.4b. Data from tests CP1-SS-C1 and CP1-SS-C2 are not presented due to relatively high radial link assembly loads (i.e., between 400 and 700 lbf at the final load step) when compared to tests CP1-SS-C3 and CP1-SS-C4.

Similar results were recorded under hoop loading and pressurization. The maximum longitudinal strains were located along the center of the panel, decreasing with increased proximity to the panel edges, Figure 4.4c. No clear trend is apparent regarding the distribution of hoop strain with longitudinal position, though strain gage SG23, located at +24 inches longitudinally from the panel center, was the only gage to output readings close to the expected values amongst those plotted in Figure 4.4d. All hoop loaders performed well during the hoop loading strains surveys, though the radial link assemblies can affect the measured strains as well by introducing unintended bending loads to the panels. Radial link assemblies #3 and #4, located -20 and 0 inches longitudinally from the center of the panel, respectively, could have caused the anomalously low strain gages; however, no significant loads were measured in either link. The longitudinal loading strain survey results again yielded similar results: the maximum longitudinal strains were located at the panel center (Figure 4.4e) and the hoop strain distribution offered no clear trends (Figure 4.4f).

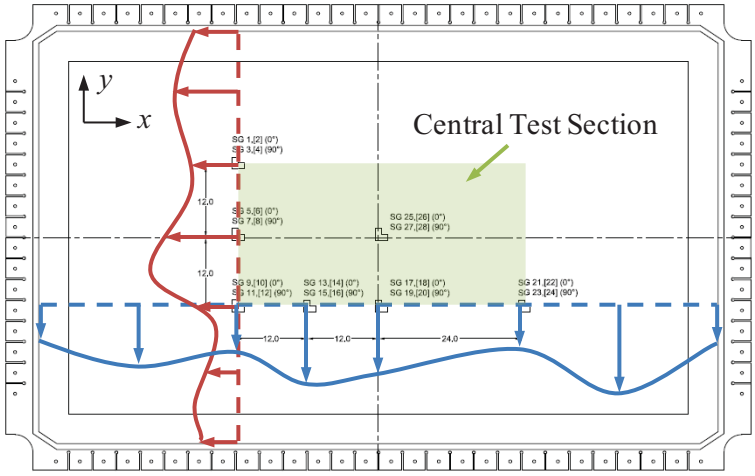

Figure 4.3. Schematic showing the distribution of longitudinal strain with hoop position (red) and hoop strain with longitudinal position (blue).

Comparing the results of the combined loading strain surveys and the separate hoop and longitudinal strain surveys, the effect of applying combined loads of comparable magnitudes is apparent, though its influence differs between the hoop and longitudinal directions. While the applied longitudinal loads were twice as high during the combined loading strain surveys than during the longitudinal loading strain surveys, the measured longitudinal strains varied by less than 5% due to the high hoop strains of the combined loading case. The hoop strains, on the other hand, were almost 50% higher for the combined loading case than the hoop loading case, despite the high longitudinal loads of the combined loading case. Clearly, the attraction of the applied longitudinal loads results in both lower longitudinal strains and a decreased Poisson effect in the hoop direction. As a result, the combined loading of panels CP3 and CP6 had a significant effect on the overall magnitudes and the distributions of strain throughout the panels, discussed in Sections 4.2.3 and 4.2.6, respectively.

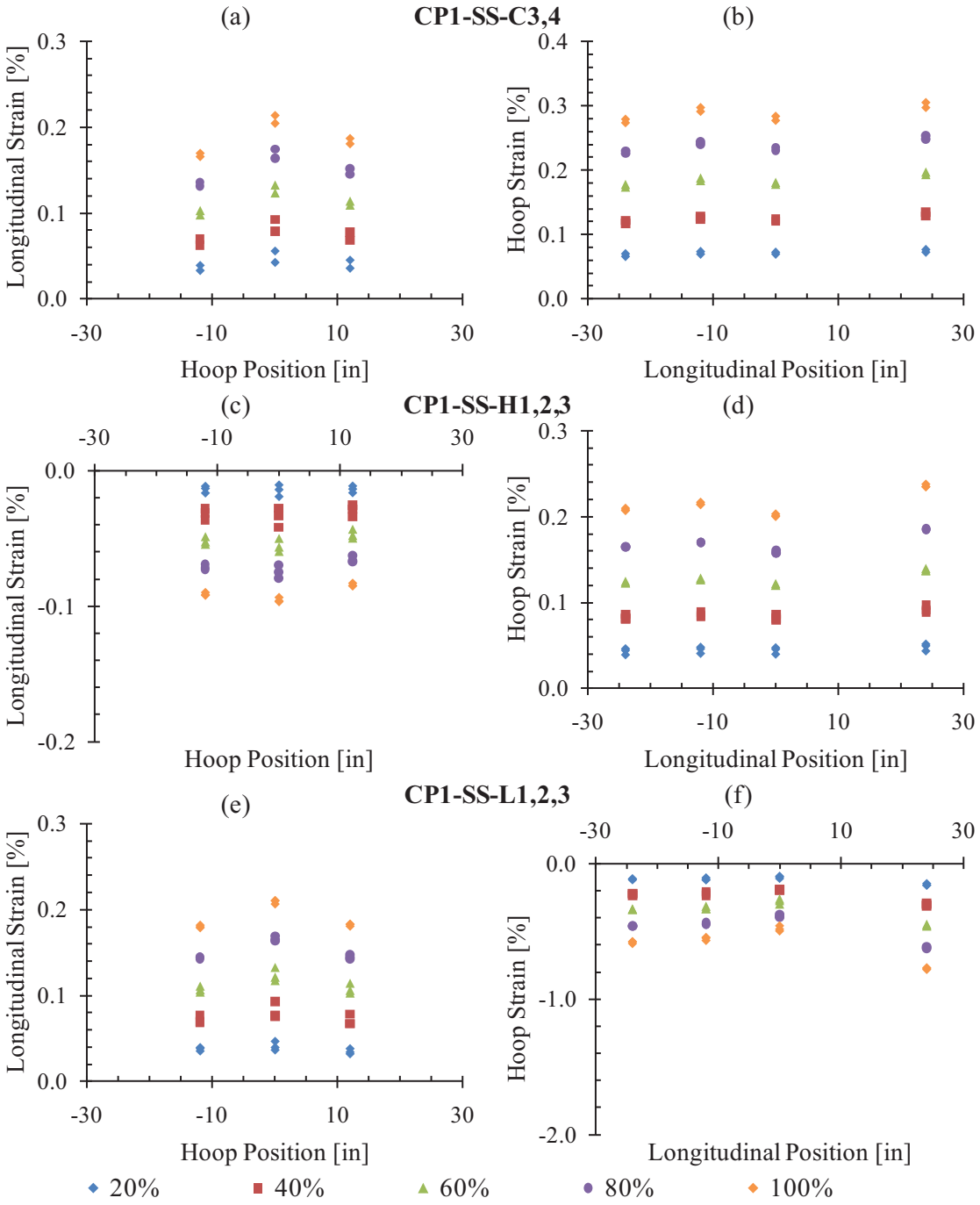

Figure 4.4. Strain distributions measured on the exterior surface of panel CP1 during the strain surveys. The percentages in the legend are with respect to the maximum applied loads listed in Table 4.1 for the tests indicated in bold.

Upon completing the strain surveys of panel CP1 and gathering sufficient baseline data for the various nondestructive inspection (NDI) methods used during this investigation, four attempts were made to load the panel up to capacity (i.e., loading the panel to catastrophic fracture). The target loads for each attempt were 1500 lbf/in longitudinal load, Table 3.2. However, due to the stroke limits of the FASTER fixture, only three attempts reached a load higher than was previously applied during the strain surveys, 1200 lbf/in in the longitudinal direction. No visible signs of damage were observed nor were any indications of nonvisual damage detected.

To maximize the usefulness of the baseline panel, progressively more severe artificial states-of-damage were introduced to the panel until it could be loaded to fracture. As mentioned in Section 3.4, two perpendicular 3-inch slits were introduced into the exterior face sheet at the panel center, forming a cross. This damage was representative of damage resultant of a tool drop or a similar low-energy impact event. The available stroke of the FASTER fixture longitudinal loaders was adjusted and two attempts were made to load the panel to fracture using the same target load of 1500 lbf/in in the longitudinal direction; the target load was only reached during second attempt, Table 4.2.

Figure 4.5 shows the performance of the hoop and longitudinal loaders, as well as the loads detected in the radial link assemblies during test CP1A-RST-2. All longitudinal loaders performed well through the first seven load steps, after which longitudinal loader #1 was consistently 4% short of the target load; longitudinal loader #6 was also 8% below the target load at the final load step, Figure 4.5b. All hoop loaders performed well (i.e., staying near zero load) throughout the duration of the test, with the exception of hoop loader #4, which steadily increased to approximately 1.2 kips between the fifth and tenth load steps, Figure 4.5a. This behavior was due to the water actuator for that loader becoming completely closed and reactively loading the panel. Radial link loads were typically less than 400 lbf, with the exceptions of links #2 and #8 approaching 600 lbf at the last load step Figure 4.5c.

Table 4.2. Load History of Panel CP1A.

Loading	Designation	Maximum Applied Loads		
		Long [lbf/in]	Hoop [lbf/in]	Pressure [psi]
Longitudinal	CP1A-RST-1	1350	0	0.00
Longitudinal	CP1A-RST-2	1500	0	0.00

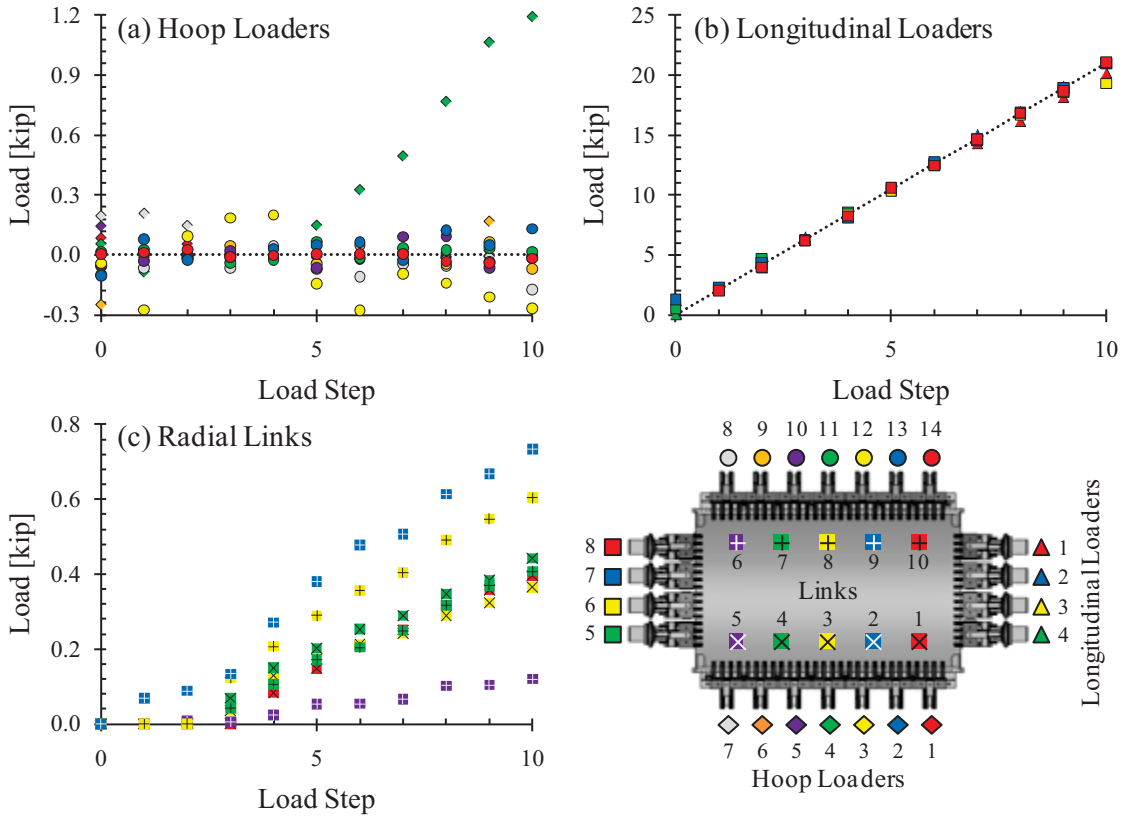

Figure 4.5. Loader performance charts for panel CP1A, test CP1A-RST-2. Loader and radial link numbers are indicated in the accompanying schematic.

Throughout the testing of the six composite panels, it was often observed that some loaders would fall short of their target loads during the final two to three load steps of a residual strength test. While noting that a specific loader was short of its target load may explain an anomalous strain gage reading, determining the effect of unexpected loader performance on the internal forces of the panel is not a trivial problem. The actual applied longitudinal and hoop

loads per unit length are estimated as the average of all the loaders divided over the loaded length of the panel edge:

$$\text{Hoop Load/Length} = \frac{1}{16}\left(\frac{1}{14}\right)\sum_{i=1}^{14}\left(P_{\text{hoop}}\right)_i \tag{4.1}$$

$$\text{Long. Load/Length} = \frac{1}{14}\left(\frac{1}{8}\right)\sum_{j=1}^{8}\left(P_{\text{long}}\right)_j , \tag{4.2}$$

where $\left(P_{\text{hoop}}\right)_i$ and $\left(P_{\text{long}}\right)_j$ are the load cell readings from the i^{th} hoop and the j^{th} longitudinal loaders, respectively. As mentioned in Section 3.2, the hoop and longitudinal loaders were spaced 16 and 14 inches, center-to-center, respectively. Plotting strains versus this average applied load per length removes any nonlinearity which may be observed while plotting strain versus the intended loads.

The far-field strain response of panel CP1A is shown in Figure 4.6. Results are similar to those recorded for the panel CP1 strain surveys, showing no major effect of introducing the 3-inch crossed slit. Figure 4.6b indicates that all gages except strain gage SG23 recorded lower-than-expected strain readings. In this case, however, appreciable tensile loads developed in several radial links during the test, Figure 4.5. Furthermore, the unintended reactive hoop load

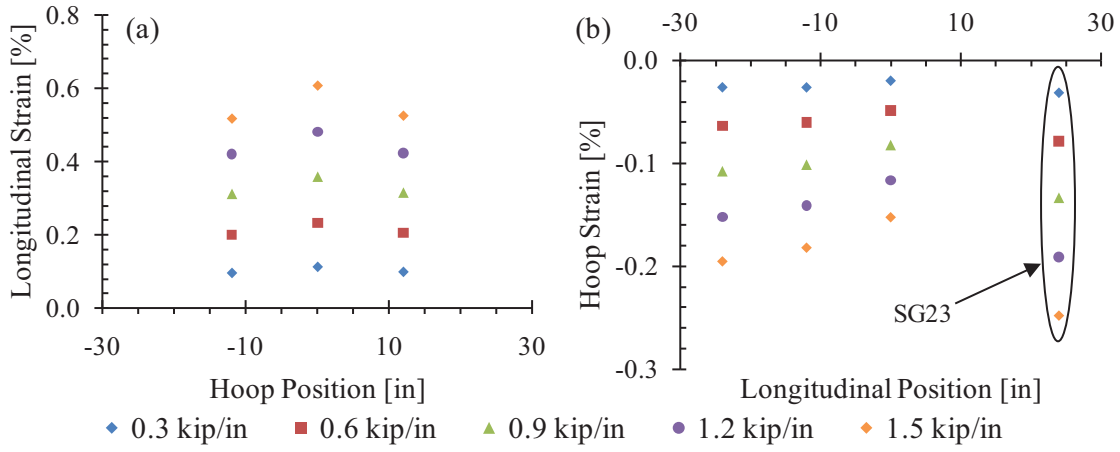

Figure 4.6. Distribution of (a) longitudinal strain with hoop position and (b) hoop strain with longitudinal position for panel CP1A, test CP1A-RST-2.

may have caused accidental bending of the panel. No functioning strain gages were installed on the interior surface of the panel to confirm panel bending.

Three strain gages were installed ahead of the slit oriented in the hoop direction to capture the severity of the longitudinal strain concentration due to the addition of the artificial damage. The gages, designated SG A, SG B, and SG C, were installed 0.125, 1.125, and 2.125 inches ahead of the slit, respectively, Figure 3.15. The longitudinal strain response to load in the region ahead of the slit is shown in Figure 4.7a. Also included in the plot is the far-field strain response of the panel, as represented by SG17, which is located 10.5 inches ahead of the slit, along its axis. The data are replotted in Figure 4.7b as a function of distance ahead of the slit. Clearly, the artificial damage of panel CP1A did not cause a significant rise in the state-of-strain. The average strain concentration factor throughout loading was only 1.37, resulting in a maximum measured longitudinal strain of 0.65% ahead of the slit. The strain response to load was linear throughout loading, indicating no significant development of any nonvisual damage. Consequently, more severe artificial damage was introduced to panel CP1A, and it was redesignated as panel CP1B.

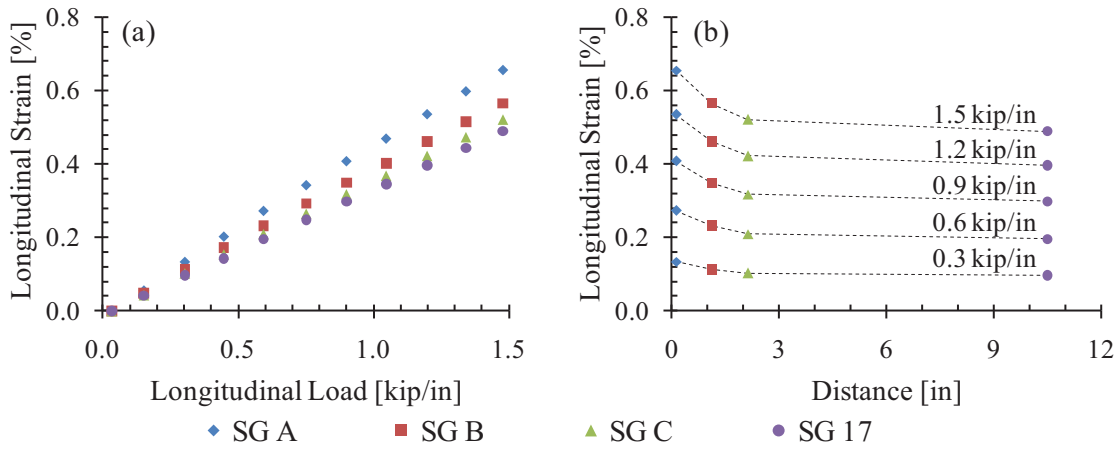

Figure 4.7. Notch tip strains as functions of (a) load and (b) distance from the notch tip for panel CP1A, test CP1A-RST-2.

Panel CP1B contained a through-thickness, 10-inch long, 1/16-inch wide notch, oriented in the longitudinal direction and located at the center of the panel. Several strain surveys were conducted (all at load levels as compared with those applied to panels CP1 and CP1A) after introducing the 10-inch long notch to the panel, Table 4.3. The results did not differ significantly from those recorded for panel CP1, and, therefore, are not reported here. The target loads for the residual strength test of panel CP1B were 23.625 psi pressure and 1750 lbf/in hoop load, Table 3.2. Equal load steps of 2.3625 psi and 175 lbf/in hoop load were applied. The panel fractured while loading from the fifth to the sixth load steps at 14.03 psi internal pressure and 1040 lbf/in hoop load. Throughout the range of the applied loads, the hoop and longitudinal loaders behaved perfectly and no radial link loads were recorded above 200 lbf, Figure 4.8.

The strain response to increasing loads and the distributions of strain along the hoop and longitudinal directions of panel CP1B are shown in Figure 4.9 and Figure 4.10, respectively. Nonlinearity was observed in the low-load hoop strain response of the panel, likely due to free

Table 4.3. Load History of Panel CP1B.

Loading	Designation	Maximum Applied Loads		
		Long [lbf/in]	Hoop [lbf/in]	Pressure [psi]
Combined	-	438	438	5.90
Combined	-	438	438	5.90
Combined	-	438	438	5.90
Hoop	-	0	438	5.90
Hoop	-	0	438	5.90
Hoop	-	0	438	5.90
Longitudinal	CP1B-SS-L1	438	0	0.00
Longitudinal	CP1B-SS-L2	438	0	0.00
Longitudinal	CP1B-SS-L3	438	0	0.00
Combined	CP1B-SS-C1	438	438	5.90
Combined	CP1B-SS-C2	438	438	5.90
Combined	CP1B-SS-C3	438	438	5.90
Hoop	CP1B-SS-H1	0	438	5.90
Hoop	CP1B-SS-H2	0	438	5.90
Hoop	CP1B-SS-H3	0	438	5.90
Longitudinal	-	44	0	0.00
Hoop	CP1B-RST-1	0	1040	14.03

play in the hoop loaders; a generally linear response was observed afterwards. The presence of the notch caused a notable decrease in the longitudinal strains along the crown of the panel, reducing the variation in longitudinal with hoop position (Figure 4.10a), as compared with panel CP1 (Figure 4.4c). Comparing the hoop strain results with those obtained from panel CP1 (Figure 4.4d), lower hoop strains were detected at the panel center due to the internal force redistribution around the notch (Figure 4.10b).

Strain redistribution before the ultimate fracture of panel CP1B is apparent when examining the strain gage data in proximity to the notch tips, Figure 4.11. Three sets of strain gages were installed in the vicinity of the notch tips; one exterior and two interior. As mentioned in Section 3.7.1, no strain gages were installed on the exterior surface ahead of one notch tip to

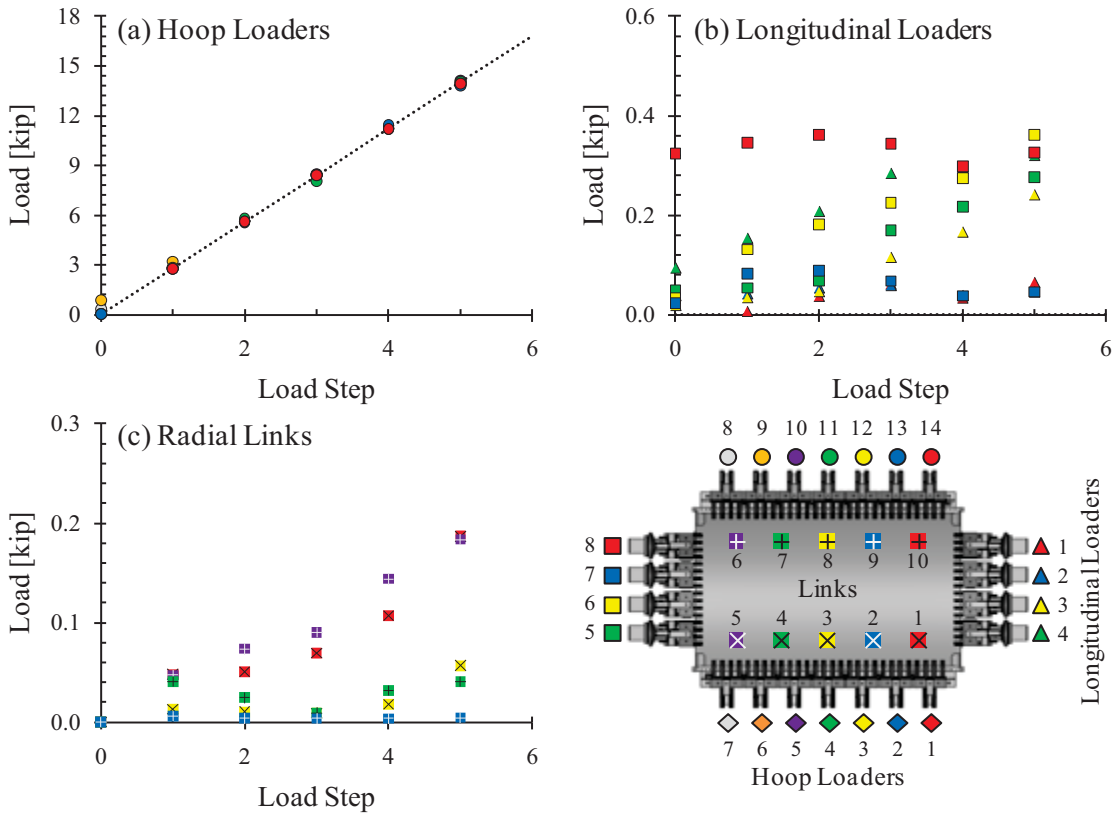

Figure 4.8. Loader performance charts for panel CP1B, test CP1B-RST-1. Loader and radial link numbers are indicated in the accompanying schematic.

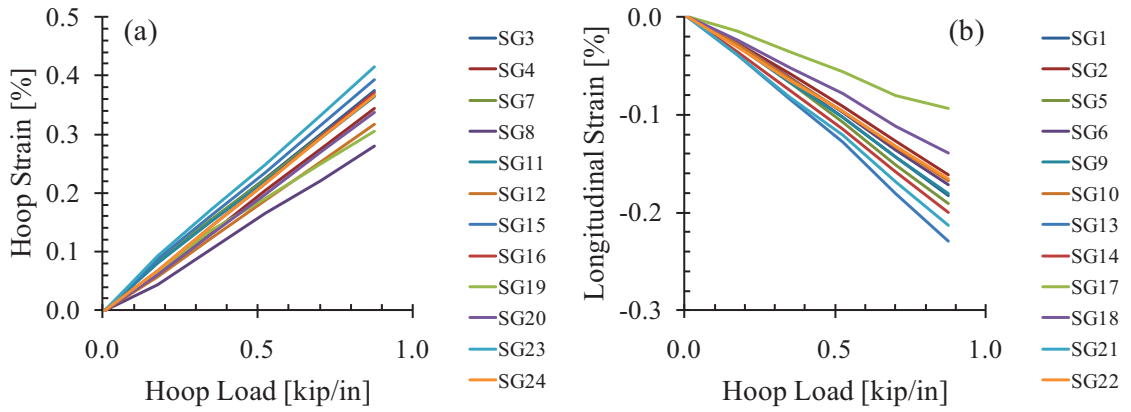

Figure 4.9. Far-field (a) hoop and (b) longitudinal strain response to hoop loading in the test section of panel CP1B, test CP1B-RST-1. The strain gage map for this panel is presented in Section 3.7.1.

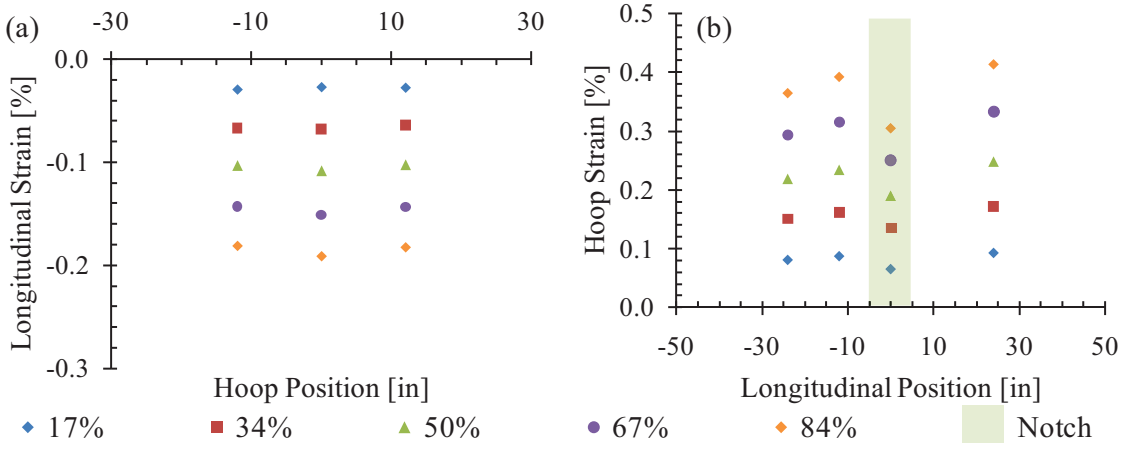

Figure 4.10. Distribution of (a) longitudinal strain with hoop position and (b) hoop strain with longitudinal position for panel CP1B, test CP1B-RST-1.

allow for unimpeded measurements by the DIC system. Strain gage rosettes were installed 0.125 inch ahead of the gaged longitudinal notch tips, with three additional uniaxial gages installed at one-inch intervals along the axis of the notch away from the rosettes. All three rosette gages failed shortly after loading beyond 56% of the panel fracture load; however, no visible damage was observed at the notch tip monitored by the DIC system (i.e., notch tip 2), Figure 4.12a. Prior to failure, the maximum measured hoop strain by SG25H was 1.62% in the exterior face sheet,

though nonlinearity was first observed upon exceeding 1.03% hoop strain, Figure 4.11a. The strain concentration factor at the notch tip was 4.52, as calculated using strain gages SG25H and SG7 prior to the detection of local failures in the immediate vicinity of either gage. This represents a notably more severe situation than panel CP1A, which exhibited an average strain concentration factor of 1.37 throughout loading. Strain gages SG[26H] and SG[43H] showed strains of 1.03% and 1.02%, respectively, in the interior face sheet prior to localized failures occurring in the vicinity of the gages. Despite these localized failures disrupting the measurements of the gages installed closest to the notch tips, no significant nonlinearity was observed in the neighboring gages (i.e., SG33, SG[34], SG[47]). That is, the elevated strain field extended less than one inch ahead of the damage front at this load level. Upon loading beyond the fourth load step, strain redistribution occurred again, as expected. Strain gages SG33 and SG[34], located 1.125 inches ahead of notch tip 1, exhibited sudden increases in hoop strain, indicating increased proximity to the damage front (i.e., damage propagation) prior to the ultimate fracture of the panel.

The first instance of visible damage at notch tip 2 occurred at 84% of the panel fracture load, Figure 4.12b. The failure of the black and white paint coating used for the DIC measurements greatly enhanced the detection of visible damage on the large composite panel. The damage ahead of the notch tip appeared to be comprised of localized matrix cracking and fiber breakage, extending approximately 0.52 inch ahead of the original notch tip. As mentioned, upon further loading, the panel suddenly failed in a catastrophic manner, nearly breaking in half along the crown of the panel, Figure 4.12c. The dynamic fracture of the panel masked any and all intermediate stages of damage progression, making any confirmation of the evolution of damage initiation and growth at the notch tip via posttest inspections impossible.

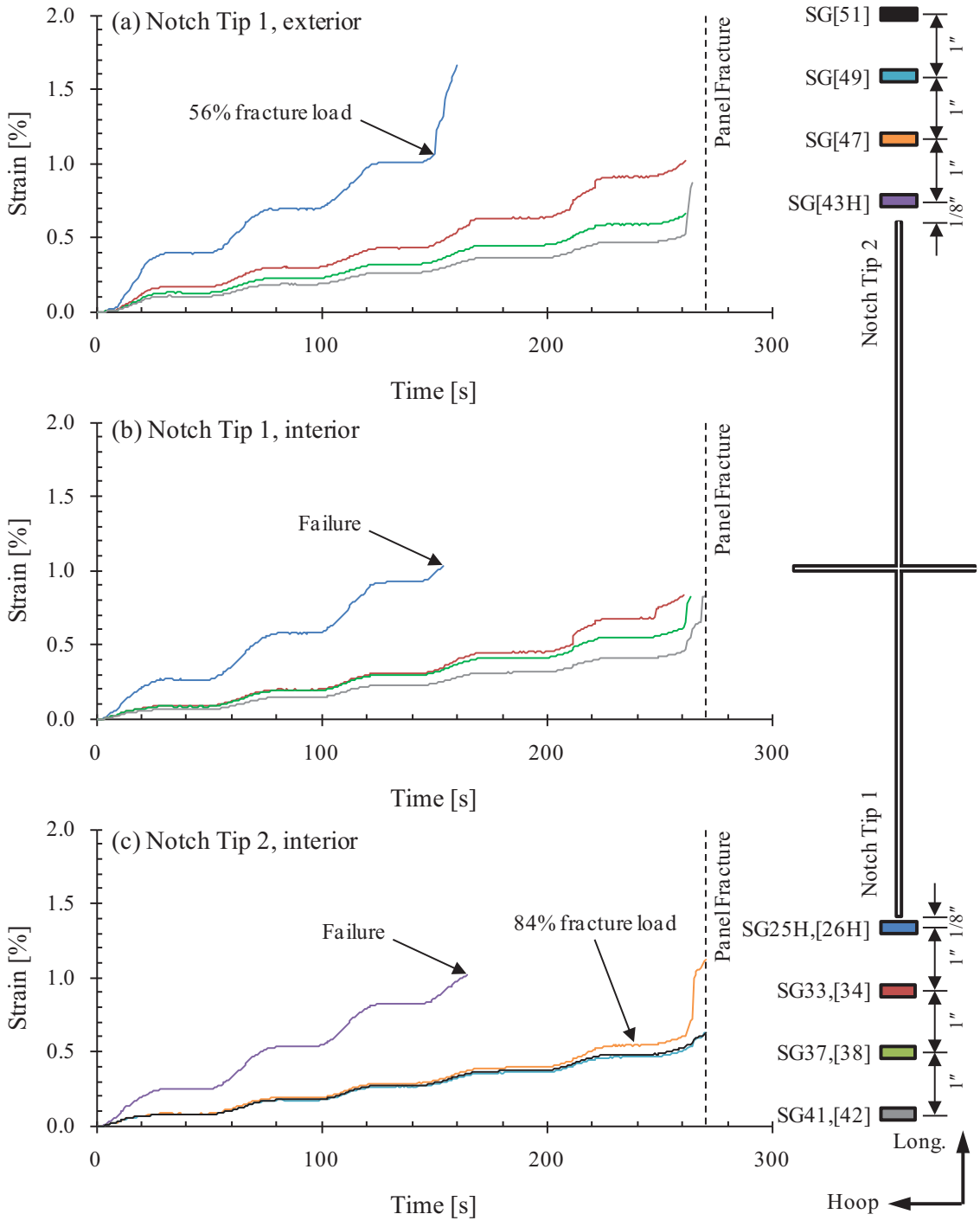

Figure 4.11. Notch tip strain history for panel CP1B, test CP1B-RST-1. The locations of the strain gages are indicated in the schematic on the right. Strain gage numbers in brackets indicate being installed on the interior surface of the panel.

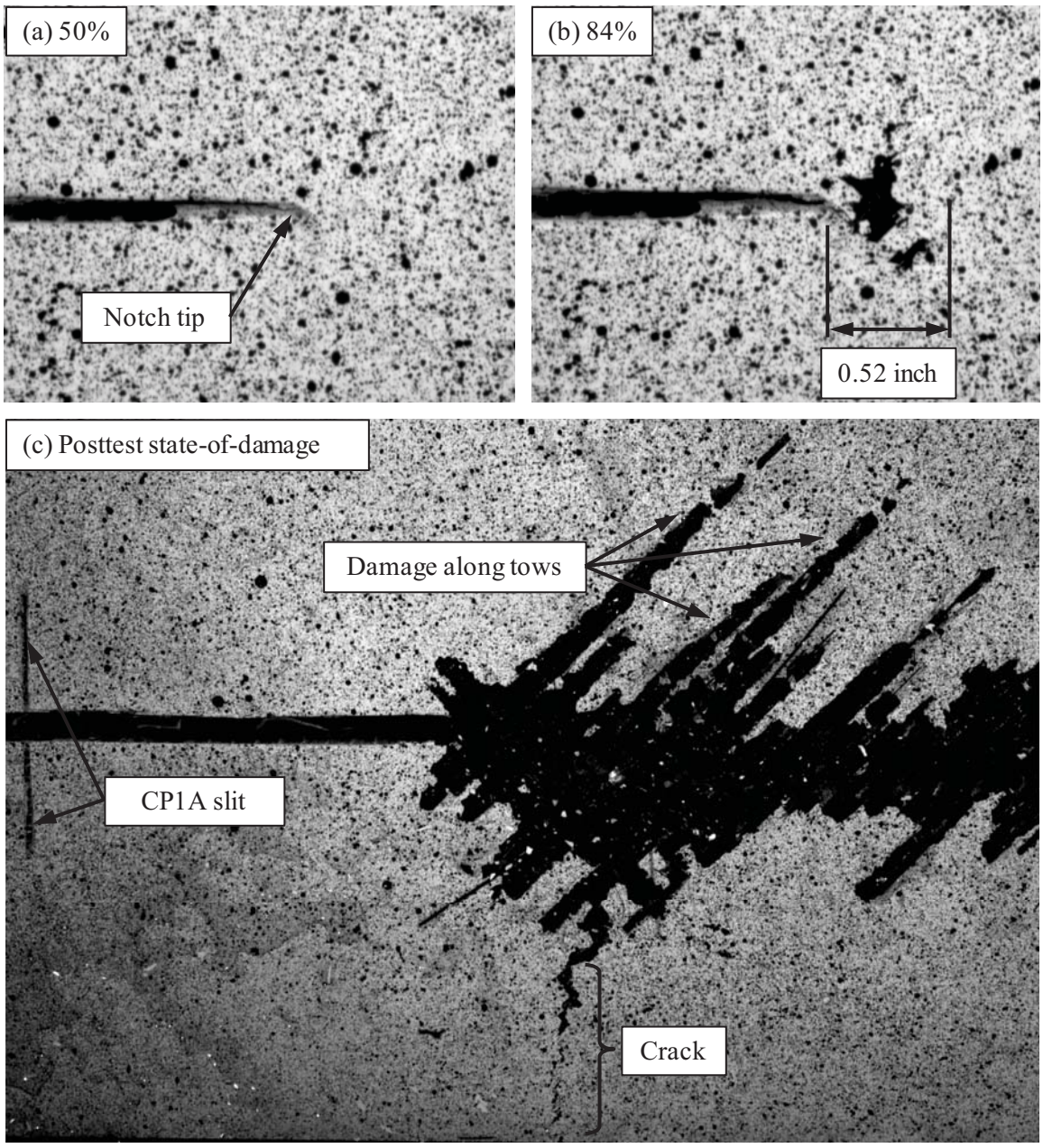

Figure 4.12. Progression of visual damage in panel CP1B, test CP1B-RST-1. (1) Notch tip at 50% of the panel fracture load, (b) state-of-damage after being loaded up to 84% of the panel fracture load, and (c) posttest state-of-damage, showing the extensive damage along the +45° fiber tows, the brittle hoop-oriented through-thickness crack, and the CP1A hoop slit.

The final state-of-damage of panel CP1B not only extended to over 100 inches in length along the longitudinal axis of the panel, but also affected regions over five inches away from the major fracture. In the immediate vicinity of the notch tip, a through-thickness crack is visible in the hoop direction as well as widespread matrix cracking due to the high-energy fiber fractures along the ±45° fiber tows of the plain-weave exterior ply.

4.2.2. PANEL CP2

Panel CP2 contained a 10-inch diameter hole through the exterior face sheet located at the center of the panel. Strain surveys were conducted under all three loading conditions to maximum loads of 500 lbf/in, Table 4.4. Due to the symmetry of the artificial damage, each of the loading conditions were essentially equivalent in terms of propensity to produce damage. As a result, residual strength tests were conducted under all three loading conditions. As mentioned in Section 3.6, the maximum planned loads for the residual strength tests of panel CP2 were 1500 lbf/in for the longitudinal loading condition, 1750 lbf/in in both the longitudinal and hoop directions for the combined loading conditions, and 1750 lbf/in for the hoop loading condition, Table 3.2. Several attempts were made for the residual strength tests under each loading condition, none of which fully reached the target loads due to limitations of the loading fixture. However, three cases still reached significant loads for the longitudinal loading condition (97, 98, and 99% of the target load), as did four cases for the combined loading condition (77, 80, 93, and 89%), and three for the hoop loading condition (79, 79, and 87%), Table 4.4.

The results obtained from the strain surveys of panel CP2 offered more complete data on the strain distributions across the panel, Figure 4.13. As mentioned in Section 3.7.1, additional strain gages were installed near the transition regions of all panels after CP1B to better characterize the distributions of longitudinal strain with hoop position and hoop strain with longitudinal position, especially near the load application points. Generally, the strain survey

Table 4.4. Load History of Panel CP2.

Loading	Designation	Maximum Applied Loads		
		Long [lbf/in]	Hoop [lbf/in]	Pressure [psi]
Combined	CP2-SS-C1	500	500	6.75
Hoop	-	0	100	1.35
Hoop	CP2-SS-H1	0	500	6.75
Longitudinal	CP2-SS-L1	500	0	0.00
Longitudinal	CP2-RST-L1	1448	0	0.00
Longitudinal	CP2-RST-L2	1472	0	0.00
Longitudinal	CP2-RST-L3	1486	0	0.00
Combined	CP2-RST-C1	1350	1337	18.41
Combined	CP2-RST-C2	1400	1393	18.85
Combined	CP2-RST-C3	1650	1600	22.64
Combined	CP2-RST-C4	1560	1555	21.23
Hoop	-	0	350	4.73
Hoop	-	0	350	4.73
Hoop	-	0	525	7.09
Hoop	-	0	700	9.45
Hoop	CP2-RST-H1	0	1379	18.92
Hoop	CP2-RST-H2	0	1388	18.92
Hoop	CP2-RST-H3	0	1550	21.26

results from the central test section of panel CP2 were comparable to those obtained from panel CP1. The maximum longitudinal strains were found to be in the center of the panel under all three loading conditions, decreasing with increased proximity to the panel edges. The additional strain gages outside the central test section revealed a roughly parabolic distribution of longitudinal strains with hoop position. Hoop strains were found to be nearly uniform along the length of the test section, decreasing slightly near the panel transition and load application regions, primarily as a result of the increased stiffness of the panel edges. Hoop strains in the center of the panel were also consistently lower due to the presence of the hole in the exterior face sheet. The maximum far-field strains were again significantly lower under combined loading conditions compared to the separate hoop or longitudinal loading conditions; the peak longitudinal strains were 60% lower under combined loading than under longitudinal loading, and the peak hoop strains were 35% lower under combined loading than under hoop loading.

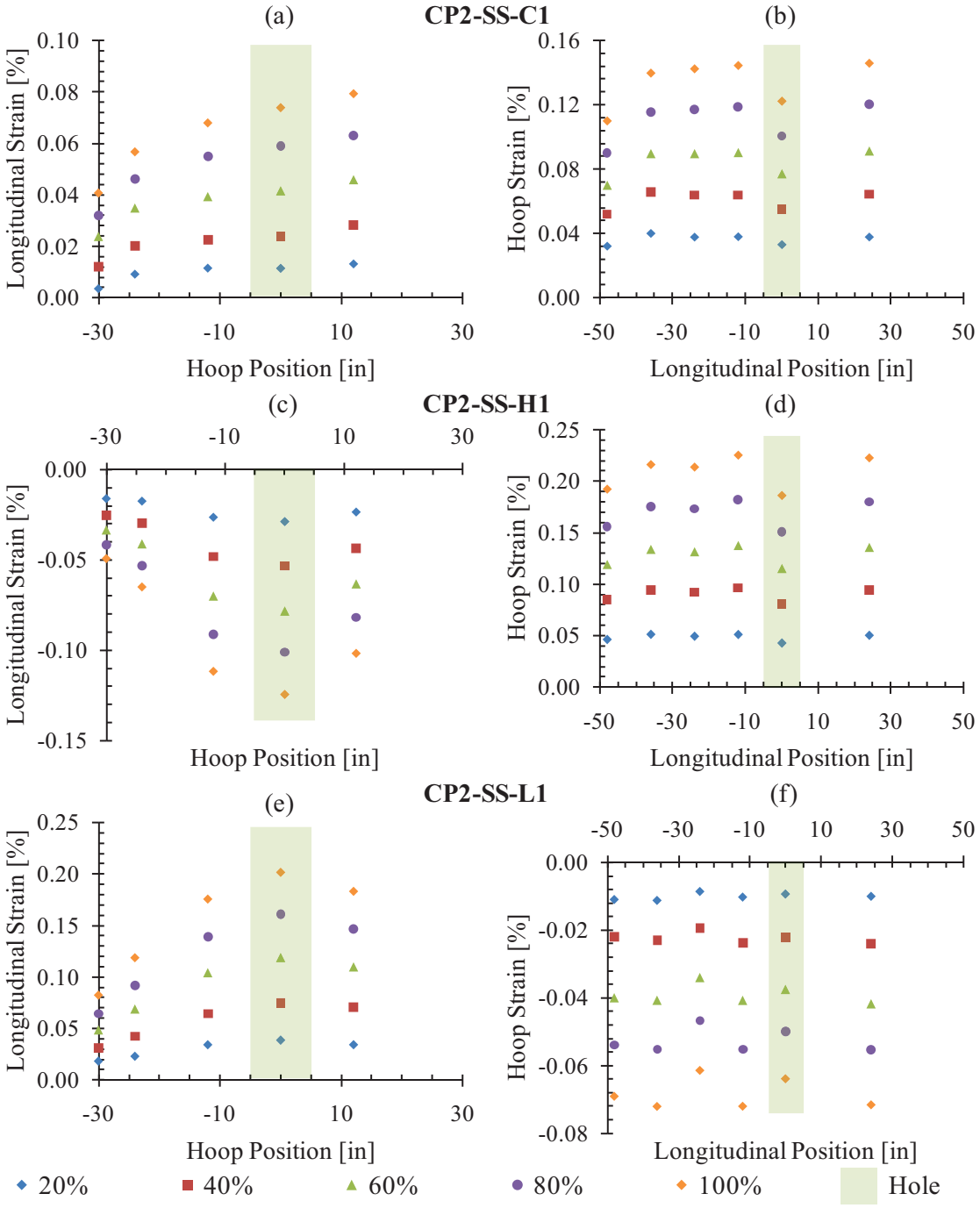

Figure 4.13. Strain distributions measured on the exterior surface of panel CP2 during the strain surveys. The percentages in the legend are with respect to the maximum applied loads listed in Table 4.4 for the tests indicated in bold.

The strain survey results displayed in Figure 4.13 indicate that, for the loading range evaluated, the highest far-field strains occurred in the hoop direction under the hoop loading condition. Assuming that the hoop and longitudinal loaders of the FASTER fixture had approximately equal limits in terms of both maximum load and available stroke, this suggested that the most severe state-of-strain would develop along the edge of the hole as a result of loading in the hoop direction. However, due to both the slightly unbalanced nature of the plain-weave prepreg and the curvature of the panel, the strain concentration factors along the periphery of the hole should not be assumed to be uniform. As a result, the strain concentration factors and maximum strain values along the edge of the hole were investigated, as discussed below.

Strain data from the gages installed along the edge of the hole for the residual strength tests under the longitudinal and hoop loading conditions are shown in Figure 4.14. Linear responses of strain with increased load were observed for both loading conditions, and the strain concentration factors for both loading conditions were approximately 2.0 with respect to the far-field strains. The maximum strains measured along the edge of the hole were 1.46% at 1.55 kip/in hoop loading (Figure 4.14d) and 1.06% at 1.49 kip/in longitudinal load (Figure 4.14b). While the strain concentration factors along the edge of the hole were relatively constant, the load attraction to the panel edges, which has been observed to decrease the longitudinal strains across the panel, caused the hoop loading condition to be the more critical loading configuration.

The residual strength tests of panel CP2 under combined loading conditions (Figure 4.15) reached hoop and longitudinal loads comparable to the individual hoop and longitudinal loading condition tests, Table 4.4. However, the strains recorded along both the hoop and longitudinal tangents to the edge of the hole were significantly lower under combined loading than the individual hoop and longitudinal loading conditions.

Strain gages SG36 and SG35 were installed between the hoop and longitudinal tangents, 0.25 and 0.75 inch away from the hole edge, respectively, oriented in the -45° direction (Figure 3.17). These gages detected strains between 0.6% and 0.8% under 1.4 kip/in combined loading

(tests CP2-RST-C2,3,4), lower than the maximum strains recorded under the separate hoop and longitudinal loading conditions. That is, no failure could have been expected under the combined loading conditions at any location along the edge of the hole. As a result, within the load and stroke capacity of the FASTER fixture, the most critical loading condition was the internal pressurization and hoop loading condition. Accordingly, the final residual strength test, CP2-RST-H3, was the only one to result in the formation of visible damage, as discussed below.

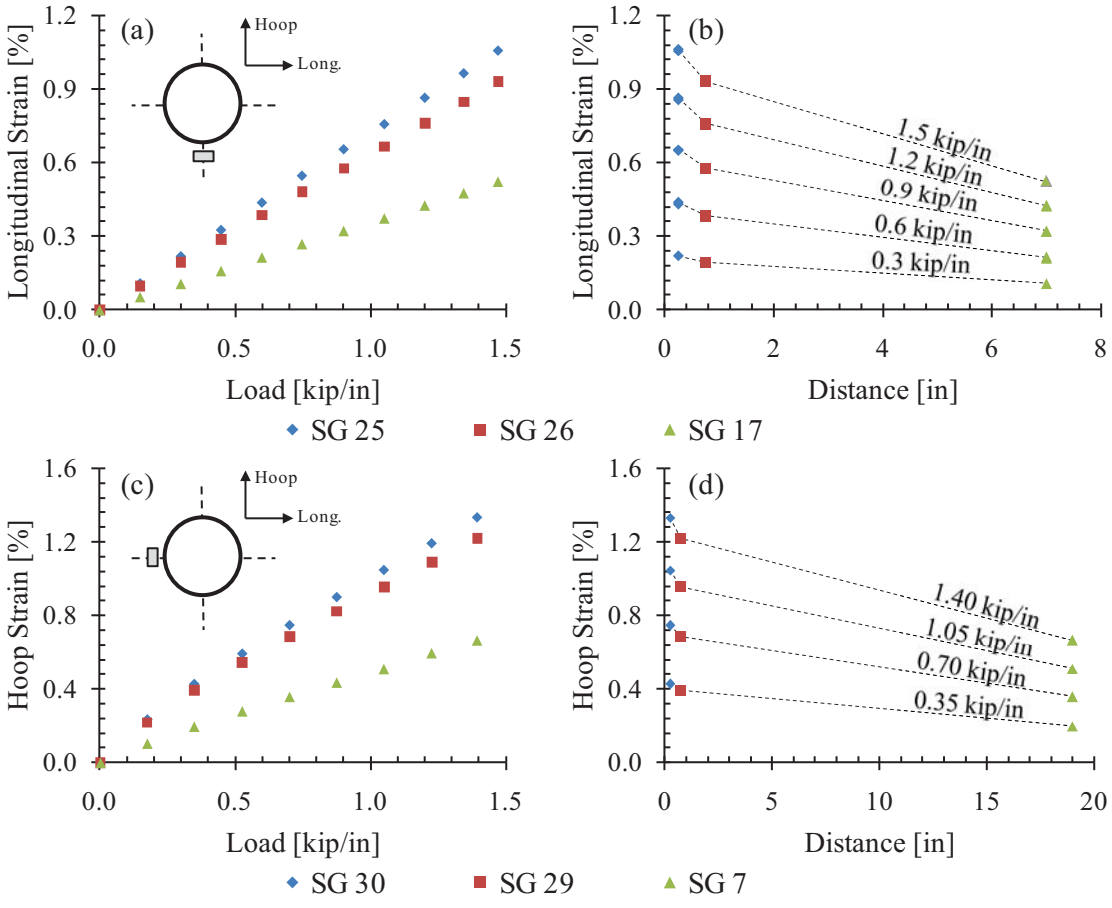

Figure 4.14. Longitudinal strain as functions of (a) load and (b) distance from the hole edge in the hoop direction for tests CP2-RST-L2 and CP2-RST-L3; and hoop strains as functions of (c) load and (d) distance from the hole edge along the crown of the panel for test CP2-RST-H3.

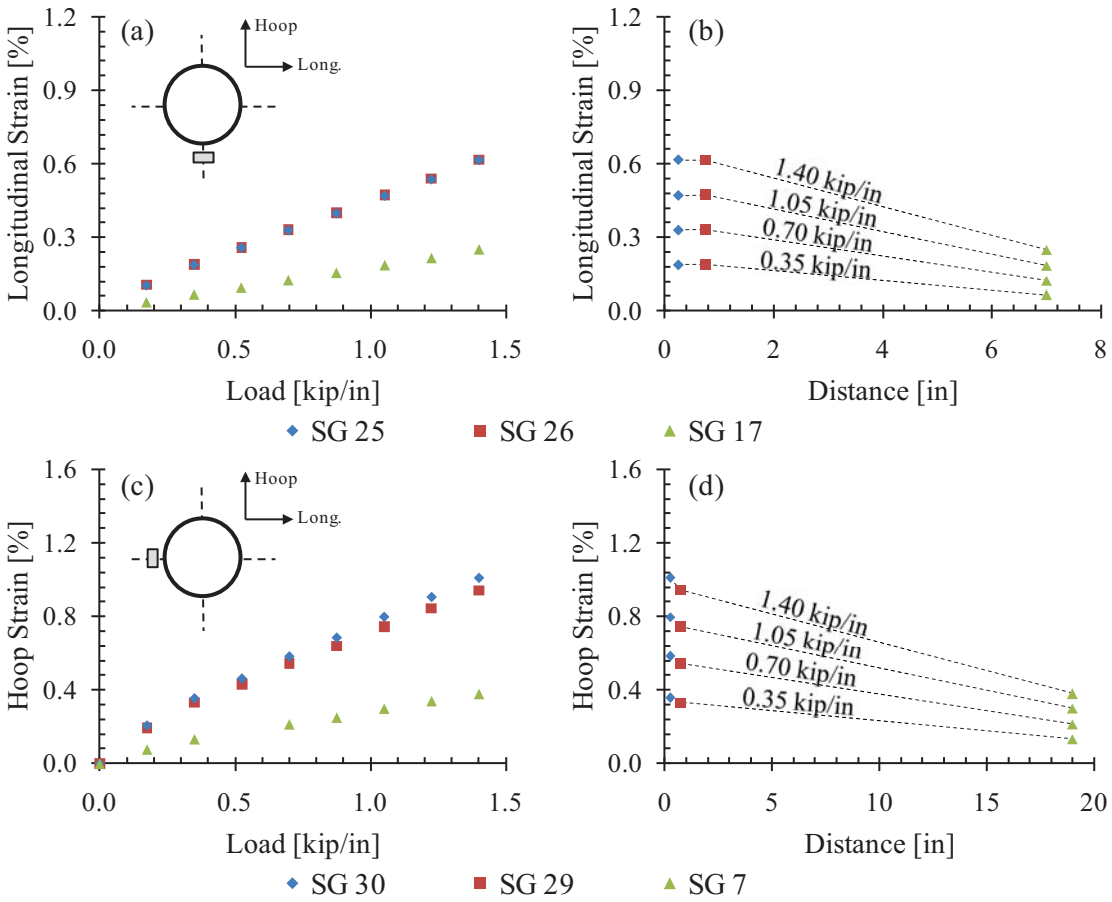

Figure 4.15. Longitudinal strain as functions of (a) load and (b) distance from the hole edge in the hoop direction, and hoop strain as functions of (c) load and (d) distance from the hole edge along the crown of the panel. Data taken from panel CP2, test CP2-RST-C2.

The loader performance charts for test CP2-RST-H3 are presented in Figure 4.16. Several hoop loaders failed to reach their target loads during the eighth and ninth load steps, Figure 4.16a. Longitudinal loaders #5 and #6 applied loads between 0.8 and 0.9 kip during the final two load steps due to their water actuators becoming fully closed, reactively loading the panel. In addition, loads in radial links #1 and #6 gradually increased to 400 and 600 lbf, respectively, between load steps four and nine.

The strain-time history of the strain gages oriented to measure the hoop strain tangent to the edge of the hole is shown in Figure 4.17. The strain gages installed on the exterior surface of

the panel, Figure 4.17a, are compared with a far-field strain gage (SG7), and the interior gages, Figure 4.17b, are compared to a gage installed underneath the center of the hole (SG[34]). Neither set of gages offered indications of localized failures or damage progression, and a linear strain response to increasing load was observed as well. The unsteady strain response of the last load step shown in Figure 4.17 is the result of the loaders nearing their capacity, and was not resultant of any damage processes.

The recorded hoop strains along the edge of the hole on the exterior and interior surfaces of the panel were 1.46% and 1.28%, respectively. No indications of damage were recorded despite exceeding the manufacturer-supplied lamina failure strain (1.41% and 1.28% in the

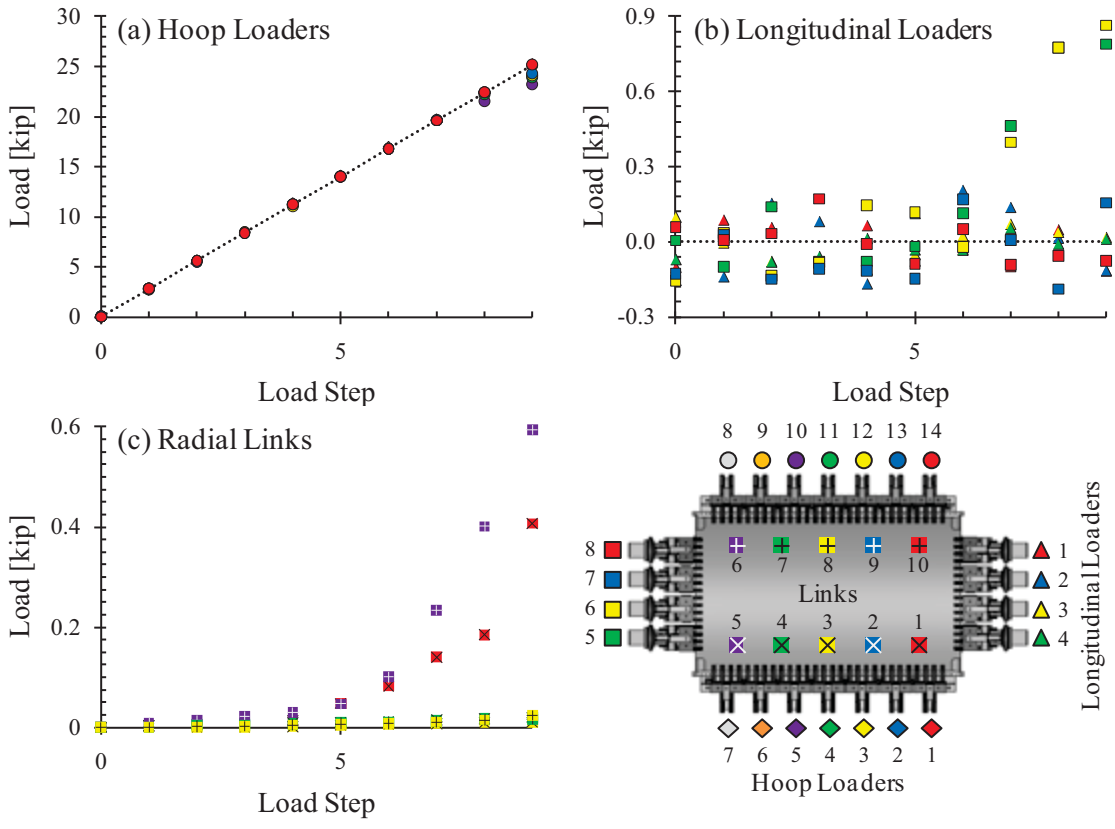

Figure 4.16. Loader performance charts for panel CP2, test CP2-RST-H3. Loader and radial link numbers are indicated in the accompanying schematic.

material 0° and 90° directions, respectively) on the exterior panel surface. However, the exterior plies contain fibers along the ±45° directions, along which no critical strains were detected.

The disparity in the exterior and interior strains is indicative of localized panel bending in the vicinity of the hole. Assuming that bending strains varied linearly through the sandwich thickness, surface strain measurements are valid throughout their corresponding face sheet due to the great disparity between the thicknesses of the individual face sheets and the full sandwich composite. Therefore, the 1.46% hoop strain measured on the exterior panel surface is also representative of the hoop strain of the exterior face sheet mid-ply, indicating failure in the 90°-oriented fibers.

While no visible damage was observed posttest in the gaged regions around the hole, visible damage was observed along the edge of the hole monitored by the DIC system. A small spall was observed along the crown of the panel upon reaching the maximum applied loads in test CP2-RST-H3, Figure 4.18. The damage consisted of both fiber breakage and matrix cracking. The plain-weave structure of the exterior lamina is visible throughout the image, though these tow separations of the weave were visible pretest due to the resin-poor nature of the exterior face sheets, as discussed in Section 3.3, and not a result of panel loading. The presence of nonvisual, subsurface damage for panel CP2 is further discussed in Sections 5.2.3, 5.4, and 5.5.

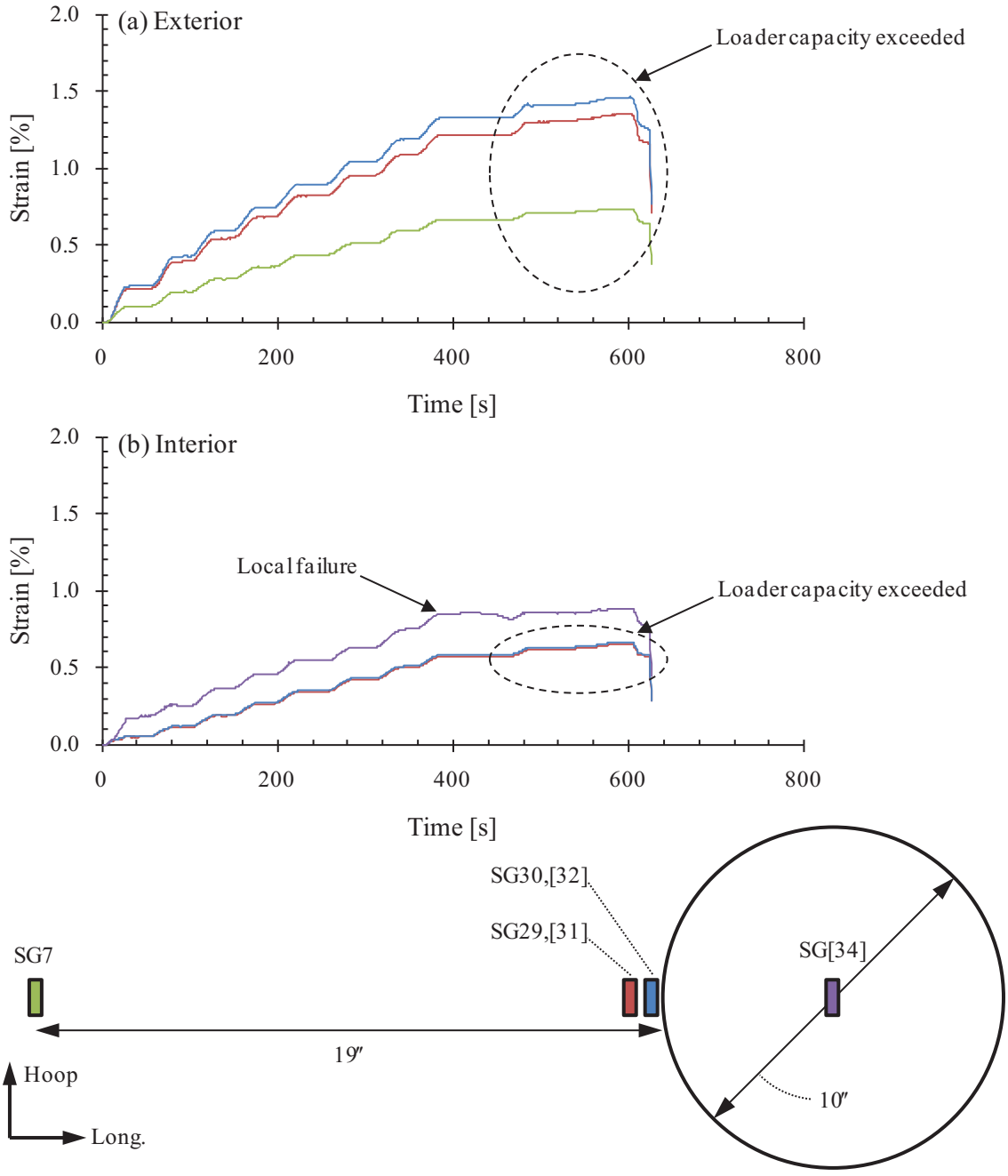

Figure 4.17. Hole edge strain history for panel CP2, test CP2-RST-H3. Strain gage numbers in brackets indicate interior surface gages.

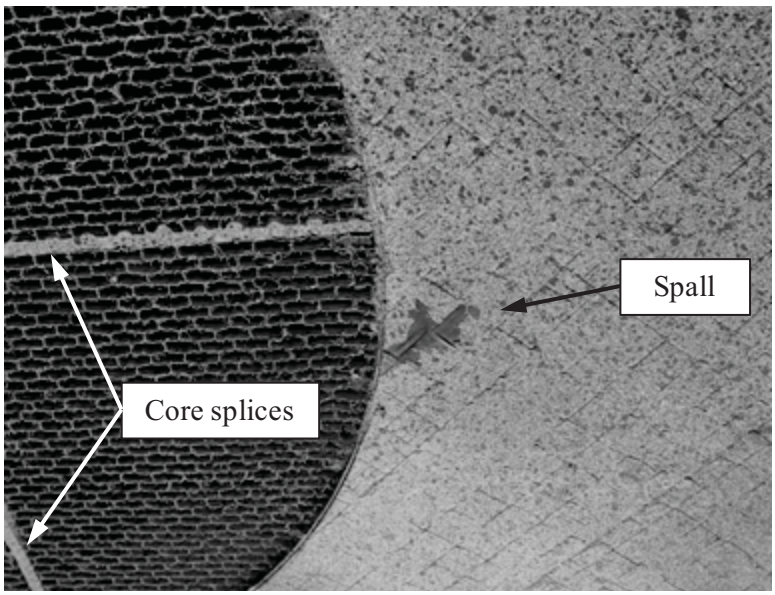

Figure 4.18. Posttest state-of-damage for panel CP2.

4.2.3. PANEL CP3

Panel CP3 contained a through-thickness, 10-inch long, 0.5-inch, wide circumferential notch, located in the center of the panel. Six strain survey tests were conducted: two under combined loading up to 300 lbf/in longitudinal load, 252 lbf/in hoop load, and 3.40 psi internal pressure; two up to 252 lbf/in hoop loading and 3.40 psi internal pressure; and two up to 300 lbf/in longitudinal loading, Table 4.5. The combined loading condition no longer had equal nominal *loads per length* in the hoop and longitudinal directions due to the previously observed load attraction to the portions of the panels outside the regions effectively covered by the longitudinal loaders (i.e., outside the central 56 inches along the panel curvature). To generate equivalent strains in the hoop and longitudinal directions, Raju and Tomblin [4.1] suggested using longitudinal loads per length defined with respect to the full width of the panel test section and inner transition region (approximately 67.5 inches) rather than to the central 56 inches along the panel curvature. Using this method, approximately equal peak strain values were recorded in the hoop and longitudinal directions during the combined loading strain surveys. For the sake of

consistency within this investigation and with respect to tests conducted using the FASTER fixture in previous investigations, the hoop and longitudinal loads per length were still defined using equations (4.1) and (4.2). As a result, the combined loading conditions ceased to have nominally equal loads (Table 4.5), though approximately equal strains were recorded in both the hoop and longitudinal directions.

The maximum planned loads for the residual strength test of panel CP3 were 8.0 psi internal pressure, 592 lbf/in hoop load, and 1400 lbf/in longitudinal load, Table 3.2. Five equal load steps of 2.0 psi and 118.4 lbf/in hoop load were applied and held for the duration of the residual strength test. Equal load steps of 140 lbf/in longitudinal load were subsequently applied, Figure 3.12c. The panel failed catastrophically at a maximum load of 8.0 psi internal pressure, 592 lbf/in hoop load, and 1507 lbf/in longitudinal load, Table 4.5.

The strain survey results for each of the six tests performed for panel CP3 are presented in Figure 4.19. The nearly parabolic distribution of longitudinal strain with hoop position, first observed in the strain survey results of panel CP2, is again apparent under all three loading conditions. Strain gage SG40, located at -30 inches hoop position, exhibited anomalously high longitudinal strains during both combined loading strain survey tests (Figure 4.19a). All available hoop, longitudinal, and radial link load data were as expected, though radial link #2, the closest loader to SG40, had no functioning load cell installed at the time. The presence of the

Table 4.5. Load History of Panel CP3.

Loading	Designation	Maximum Applied Loads		
		Long [lbf/in]	Hoop [lbf/in]	Pressure [psi]
Combined	CP3-SS-C1	300	252	3.40
Hoop	CP3-SS-H1	0	252	3.40
Longitudinal	CP3-SS-L1	300	0	0.00
Combined	CP3-SS-C2	300	252	3.40
Hoop	CP3-SS-H2	0	252	3.40
Longitudinal	CP3-SS-L2	300	0	0.00
Hoop, then Longitudinal	-	300	252	3.40
Hoop, then Longitudinal	-	300	252	3.40
RST	CP3-RST-1	1507	592	8.00

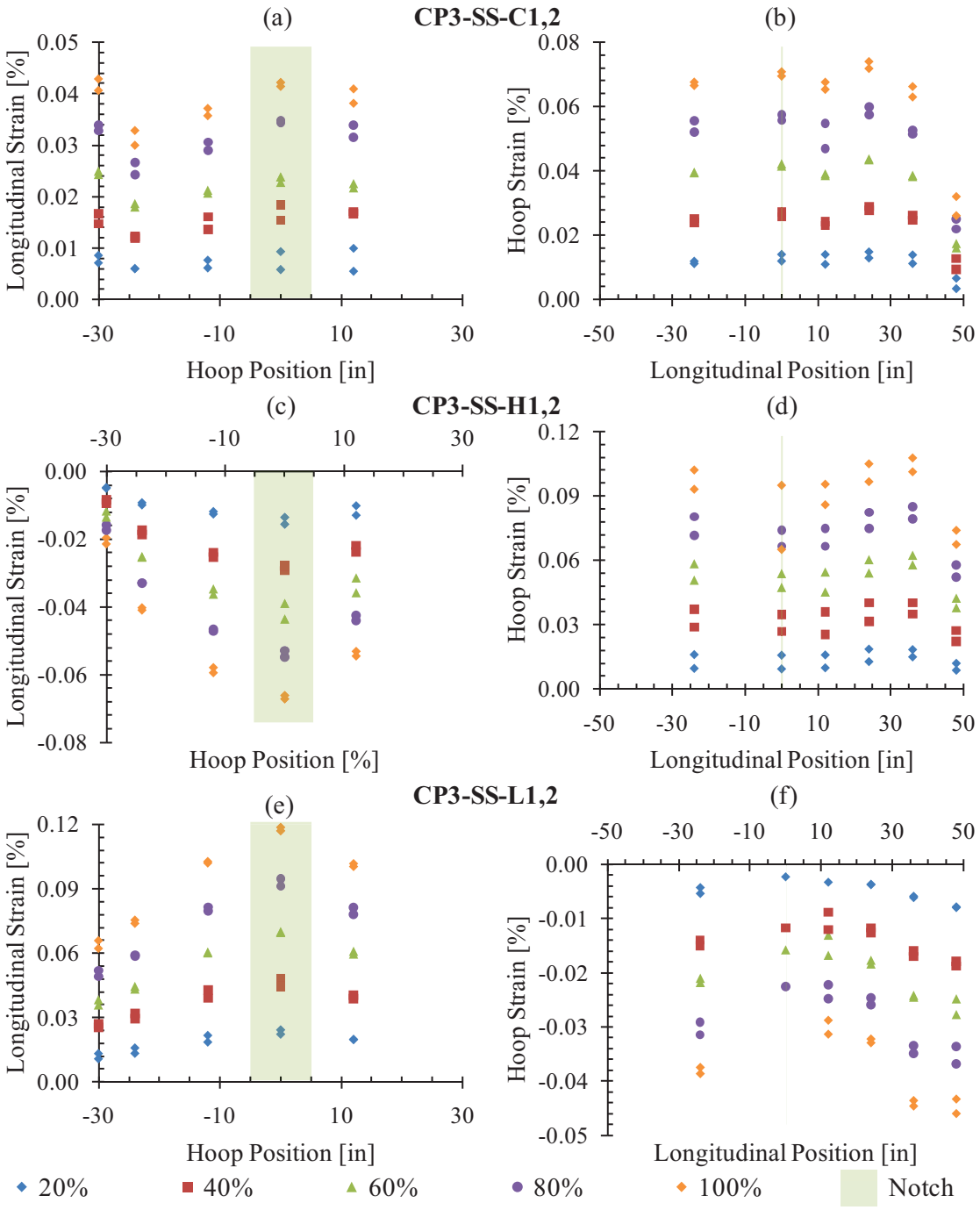

Figure 4.19. Strain distributions measured on the exterior surface of panel CP3 during the strain surveys. The percentages in the legend are with respect to the maximum applied loads listed in Table 4.5 for the tests indicated in bold.

circumferential notch did not have any significant effect on the longitudinal strain distribution when compared to the baseline results of panel CP1, indicating that the far-field regions of the test section (e.g., 24 inches longitudinally away from the notch axis) offered a good basis for determining the strain concentration factors associated with the notch tips. The distributions of hoop strain with longitudinal position were as expected, remaining nearly constant throughout the test section, substantially decreasing only 24 inches beyond the central test section.

Exceptional loader performance was observed during the sole residual strength test of panel CP3 (i.e., test CP3-RST-1), Figure 4.20. The recorded hoop and longitudinal loader data were in good agreement with the target loads. No radial link load readings exceeded 200 lbf, Figure 4.20c. However, the load cell installed in-line with radial link #7 did output low compressive loads (i.e., 40–60 lbf) between the second and ninth load steps. The construction of the radial link assemblies does not allow for any compressive loads on the central gaged link. It seems, therefore, that the load cell was either initially in tension or not functioning properly during the test.

The far-field strain response to longitudinal load in the test section during the residual strength test of panel CP3 is shown in Figure 4.21; unlike previous such plots, both the interior and exterior strain gages are displayed. Longitudinal loading was identified as the critical loading condition for this panel, and, therefore, the strain response to the initial hoop loading is not shown here. The longitudinal strain response, Figure 4.21b, is very uniform across the test section throughout loading, with the maximum strains occurring along the crown of the panel. This is expected given the previous findings regarding the nearly parabolic distribution of longitudinal strain with hoop position. The hoop strain response to longitudinal loading, Figure 4.21a, was notably less uniform. Linearity of the hoop strain response was observed up to 74% of the fracture load. Linearity was observed throughout the longitudinal strain response.

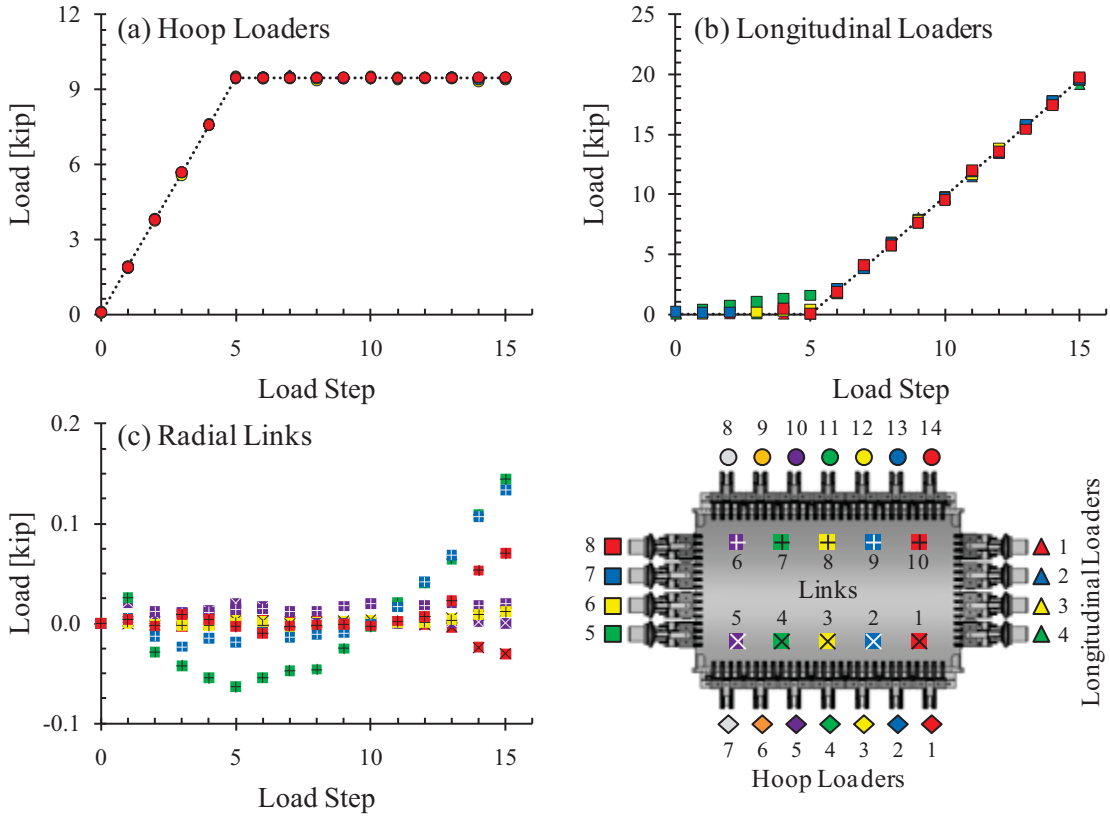

Figure 4.20. Loader performance charts for panel CP3, test CP3-RST-1. Loader and radial link numbers are indicated in the accompanying schematic.

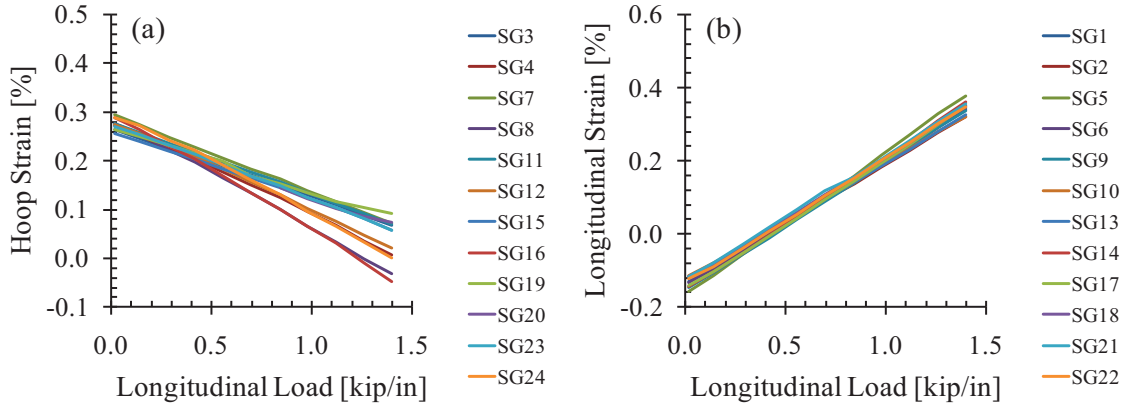

Figure 4.21. Far-field (a) hoop and (b) longitudinal strain response to longitudinal loading in the test section of panel CP3, test CP3-RST-1.

As mentioned briefly regarding the strains around the periphery of the hole in panel CP2 in Section 4.2.2, the surface strain measurements are representative of the strains throughout the thickness of their respective face sheet. While bending is expected in the immediate vicinity of the artificial damage in each of the panels, bending in the far-field regions of the panel should be minimal. Given point-wise strain data from the exterior and interior surfaces, the deformation of a plate could be determined for a homogenous isotropic material. However, the analysis for the composite sandwich configuration under investigation is more complicated.

Figure 4.22 compares the longitudinal and hoop strain distributions in the exterior and interior face sheets during the residual strength test of panel CP3, allowing for basic observations

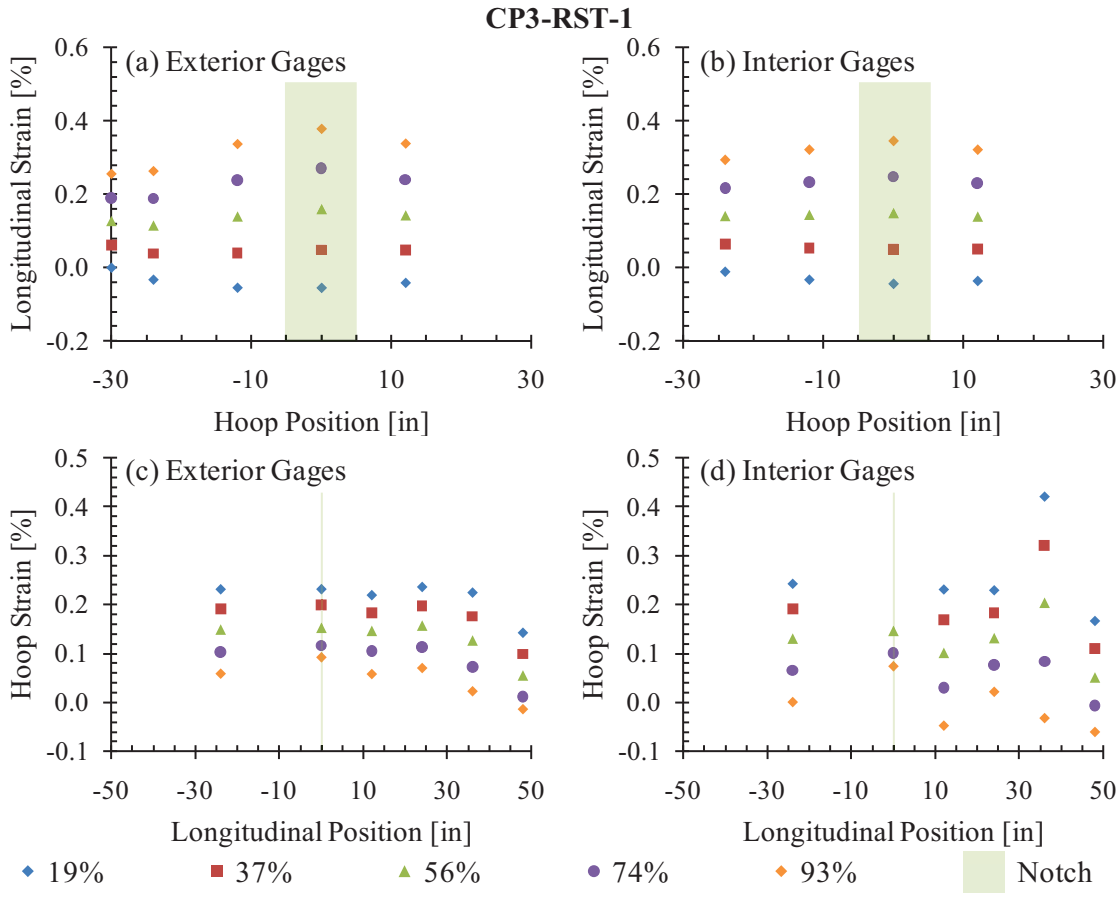

Figure 4.22. Longitudinal and hoop strain distributions across panel CP3 at various longitudinal loads during test CP3-RST-1.

regarding panel bending (e.g., in terms of degree of bending, direction, uniformity, etc.). For the purposes of discussing panel bending, the cylindrical coordinate system of the curved panels is used, in which the panel thickness is parallel to the *r*-direction, the hoop direction is parallel to the θ-direction, and the longitudinal direction is parallel to the *z*-direction. The exterior and interior longitudinal strains were very similar, indicating minimal bending about the θ-axis throughout loading. The hoop strains, however, showed that bending occurred about the *z*-axis, increasing in severity with increasing loads. This is unexpected considering that the applied hoop loads and internal pressure were in equilibrium throughout loading and no considerable radial link loads were recorded. However, compressive loading may have occurred within the radial link assemblies, contributing to this panel deformation behavior. Further discussion on panel bending is presented in Section 4.2.4 in regards to panel CP4. This unexpected strain gage behavior may also be attributed to the natural scatter of the data due to the various potential sources of error discussed in Section 2.2.1 (e.g., gage misalignment, gage mislocation, poor gage application, etc.).

The 10-inch long, 0.5-inch wide, circumferential notch of panel CP3 produced a strain concentration factor at the notch tip of 4.40, as calculated using strain gages SG30 and SG17 prior to the detection of local failures in the immediate vicinity of either gage. This represents only a slightly less severe initial state-of-damage in terms of strain concentration factor than the 1/16-inch wide notch of panel CP1B, with a strain concentration factor of 4.52 for its particular loading condition.

The first indication of damage progression in panel CP3 occurred at the notch tip monitored by the DIC system (i.e., notch tip 2). A slight failure was observed in the DIC coating 0.139 inch ahead of the notch tip at 65% of the panel fracture load, likely as a result of matrix cracking underneath the DIC coating, Figure 4.24a. Upon loading to 68% of the fracture load, the strain readings of SG[25], on the interior surface of the panel, abruptly increased from 0.87% to 1.24%, indicative of damage propagation, Figure 4.23c. No obvious redistribution of strain to the

next nearest gage 0.50 inch away was observed, which indicates that the damage was highly localized. Local failures were observed at each of the three strain gages ahead of the notch tips during the next load increase: SG30 failed upon reaching 78% of the fracture load with a maximum longitudinal strain of 1.12%, causing the reading of SG29 to jump from 0.54% to 1.29%, and soon after fail at 1.41% longitudinal strain (Figure 4.23a); SG[33], on the interior surface, failed at the same load level (Figure 4.23b); and SG[25] underwent a second sudden increase in measured strain, quickly exceeding 2.0% (Figure 4.23c). The visible damage ahead of notch tip 2 advanced to 0.566 inch ahead of the notch tip upon reaching the next load step, 84% of the panel fracture load, Figure 4.24b.

Upon loading up to the penultimate load step, several additional failures were observed. The visible damage ahead of notch tip 2 advanced to 0.611 inch ahead of the notch tip at 91% of the panel fracture load, Figure 4.24c. At the same load level, strain gage SG28, located 1.25 inches ahead of the notch tip, increased from 0.80% to 1.32%, Figure 4.23a. Strain gages SG[32] and SG[31] each experienced sudden increases in their measured interior surface strains, increasing from 0.72% to 1.06% and from 0.44% to 0.50%, respectively, Figure 4.23b. Similar sudden increases in the interior surface strains measured by SG[26] and SG[27] were observed upon reaching 92% of the panel fracture load, Figure 4.23c. The visible damage ahead of notch tip 2 advanced to 1.139 inches ahead of the notch tip upon reaching 93% of the panel fracture load, Figure 4.24d. The visible notch tip damage propagated in a self-similar manner, extending through approximately two plain-weave unit cells. Significant matrix cracking was visible along the notch tip extension, zigzagging through the checkerboard pattern of the plain-weave fabric. No additional damage advancement was observed via the DIC system images or the array of strain gages ahead of the notch tips prior to the ultimate fracture of the panel at 1507 lbf/in longitudinal load, 8.0 psi internal pressure, and 592 lbf/in hoop load.

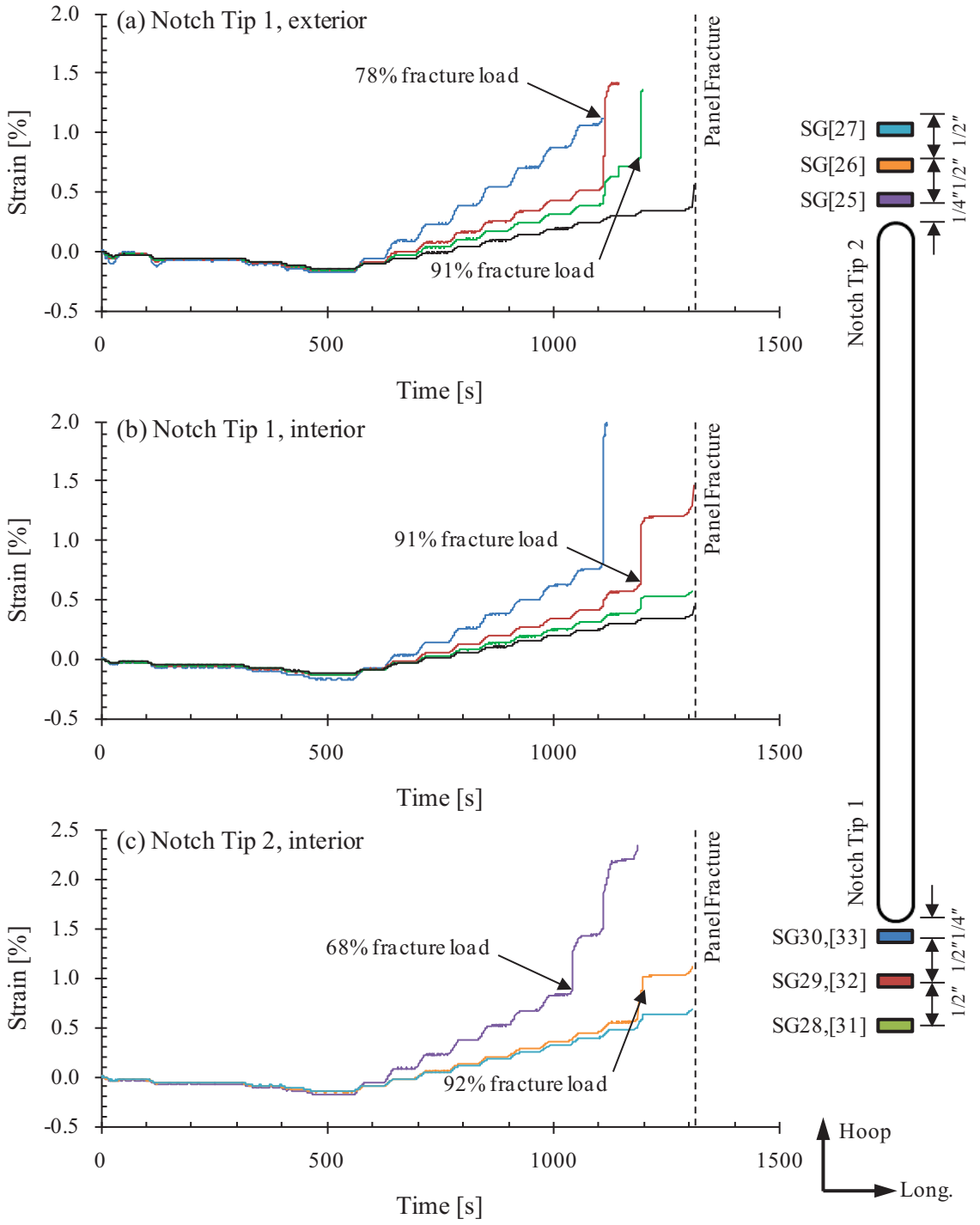

Figure 4.23. Notch tip strain history for panel CP3, test CP3-RST-1. The locations of the strain gages are indicated in the schematic on the right. Strain gage numbers in brackets indicate being installed on the interior surface of the panel. The black curves are representative of strain gages SG17 and SG[18], measuring the far-field response along the axis of the notch.

The final fracture of panel CP3 broke the panel into two halves, similar to the final fracture of panel CP1B. The major fracture was antisymmetric about the plane of the original notch, propagating at an angle inclined by roughly 20° with respect to the hoop direction, Figure 4.24e. Significant damage is visible several inches away from the major fracture, Figure 4.24f. The distant failures are along tows of the weave which experienced high-energy fiber fractures

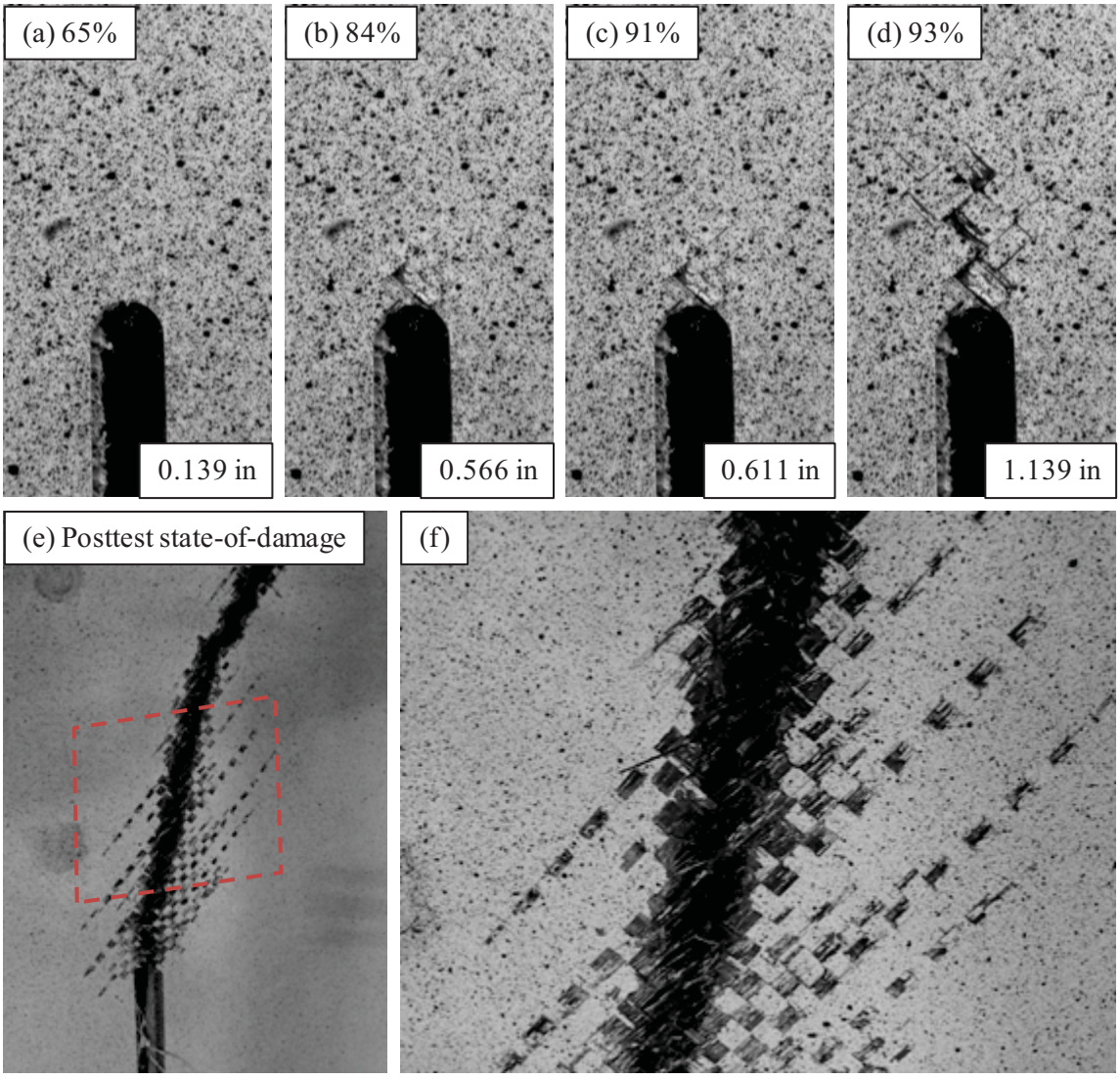

Figure 4.24. Development of visible notch tip damage for panel CP3, test CP3-RST-1. The percentages in the figure are with respect to the loads listed in Table 4.5. The measurements in the figure are the distance from the notch tip to the farthest visible damage, measured along the axis of the notch.

during the sudden fracture of the panel, resulting in far-reaching matrix cracking and damage to the plain-weave structure.

4.2.4. PANEL CP4

Panel CP4 contained a through-thickness, 10-inch long, 0.5-inch wide, circumferential notch, identical to that machined into panel CP3, located in the center of the panel. Nine strain survey tests were conducted: three under combined loading up to 300 lbf/in longitudinal load, 252 lbf/in hoop load, and 3.40 psi internal pressure; three up to 252 lbf/in hoop loading and 3.40 psi internal pressure; and three up to 300 lbf/in longitudinal loading, Table 4.6.

The maximum planned loads for the residual strength test of panel CP4 were 1400 lbf/in longitudinal load, 1.0 psi pressure, and 74 lbf/in hoop load, Table 3.2. The low pressure and hoop loads were applied to merely avoid rigid body translation in the fixture in the hoop direction, as discussed in Section 3.6. Two equal load steps of 0.5 psi and 37 lbf/in hoop load were applied and held for the duration of the residual strength test. Equal load steps of 140 lbf/in longitudinal load were subsequently applied, Figure 3.12d. The test was terminated when the maximum applicable longitudinal loads of the FASTER fixture were reached. For the setup of the test

Table 4.6. Load History of Panel CP4.

Loading	Designation	Maximum Applied Loads		
		Long [lbf/in]	Hoop [lbf/in]	Pressure [psi]
Combined	CP4-SS-C1	300	252	3.40
Longitudinal	CP4-SS-L1	300	0	0.00
Hoop	CP4-SS-H1	0	252	3.40
Hoop, then Longitudinal	-	300	74	1.00
Combined	CP4-SS-C2	300	252	3.40
Longitudinal	CP4-SS-L2	300	0	0.00
Hoop	CP4-SS-H2	0	252	3.40
Combined	CP4-SS-C3	300	252	3.40
Longitudinal	CP4-SS-L3	300	0	0.00
Hoop	CP4-SS-H3	0	252	3.40
Hoop, then Longitudinal, with cyclic	-	300	74	1.00
RST	CP4-RST-1	1470	74	1.00

fixture during this test, this corresponded to 1470 lbf/in longitudinal load, 1.0 psi pressure, and 74 lbf/in hoop load.

The strain survey results for each of the nine tests performed for panel CP4 are presented in Figure 4.25. Since panels CP3 and CP4 had the same artificial notches and the same loads for the strain surveys, the strain results were very similar in both panels. The nearly parabolic distribution of longitudinal strain with hoop position was again apparent under all three loading conditions. The distributions of hoop strain with longitudinal position were as expected, uniform throughout the test section. The strains recorded under combined loading were again notably lower than those recorded when the hoop and longitudinal loads were applied separately; this effect leads to an important difference between panels CP3 and CP4, as follows.

Having only nominal internal pressure and hoop loads applied to panel CP4 decreased the influence of the Poisson effect compared to panel CP3. This, in turn, allowed for higher longitudinal strains to be reached throughout the test section and at the critical regions ahead of the two notch tips at lower applied longitudinal loads. Re-examining Figure 4.23, the far-field longitudinal strains in panel CP3 did not become positive until 30% of the panel fracture load had been reached; though, as expected, the notch tip strains increased more quickly, becoming positive after reaching 14% of the panel fracture load. Regardless of magnitude, not applying any considerable hoop loads leads to a more severe state-of-strain to be expected ahead of the notch tips in panel CP4. However, panel CP4 did not undergo a catastrophic fracture despite its ostensibly more severe loading condition compared to panel CP3. The details of the residual strength test of panel CP4 (i.e., test CP4-RST-1) are discussed below.

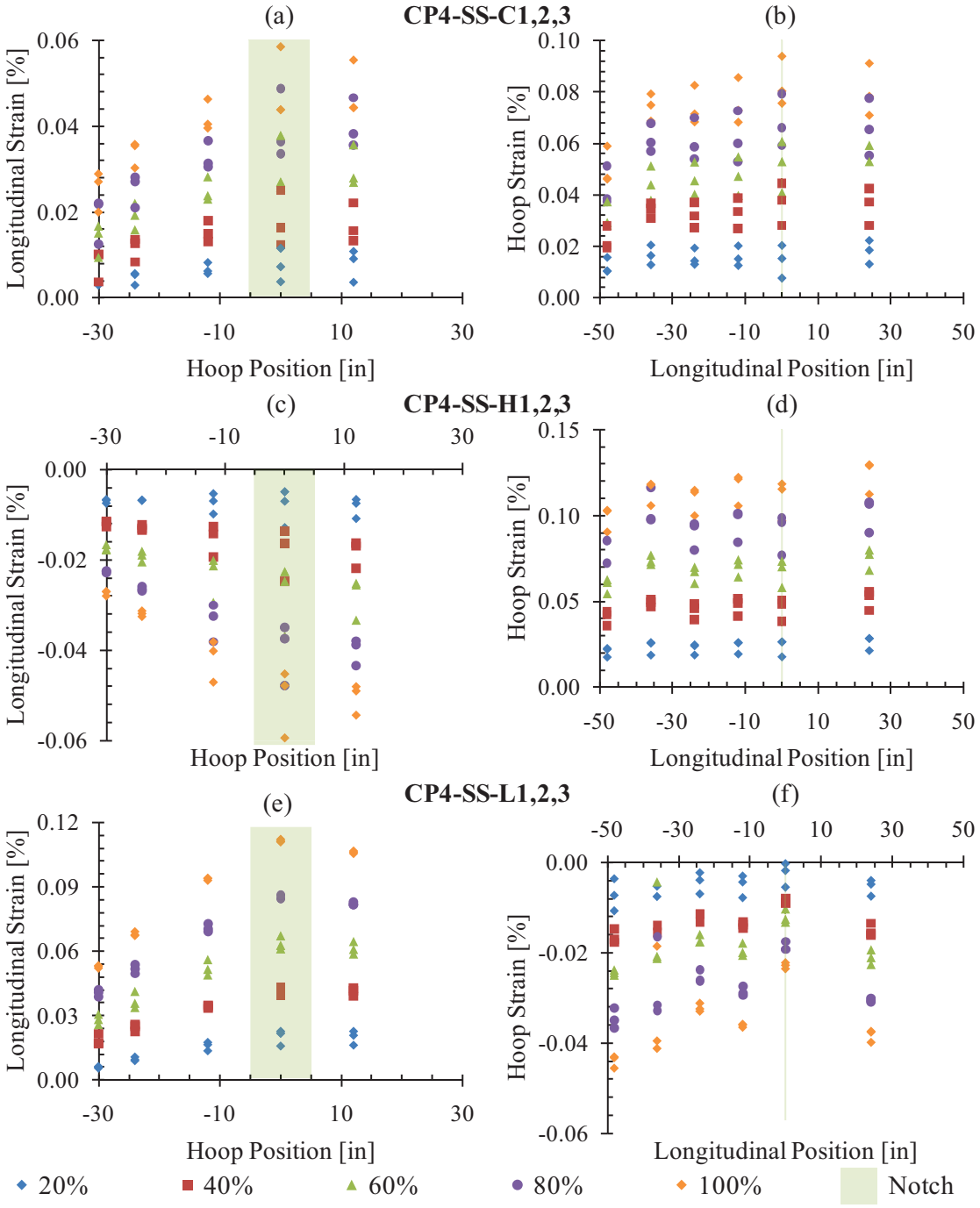

Figure 4.25. Strain distributions measured on the exterior surface of panel CP4 during the strain surveys. The percentages in the legend are with respect to the maximum applied loads listed in Table 4.6 for the tests indicated in bold.

Hoop and longitudinal loader performance during the residual strength test of panel CP4 followed their targets well through the ninth load step. At the tenth and eleventh load steps, longitudinal loader #3 was at 97% and 87% of its target load and loader #7 was at 93% and 82% of its target load, respectively, decreasing the effective applied longitudinal load of the final load step from 1540 lbf/in to 1470 lbf/in (Figure 4.26b). The water actuator of hoop loader #4 became fully closed during the final two load steps, resulting in additional reactive loads to develop (Figure 4.26a). Additionally, three radial links had tensile loads in excess of 400 lbf, and another two exceeding 200 lbf (Figure 4.26c). Unlike previous residual strength tests, each monitored radial link exhibited nonzero tensile loads throughout the majority of the test. The radial links were likely installed nearly taut, not having sufficient slack to allow for the expected radial

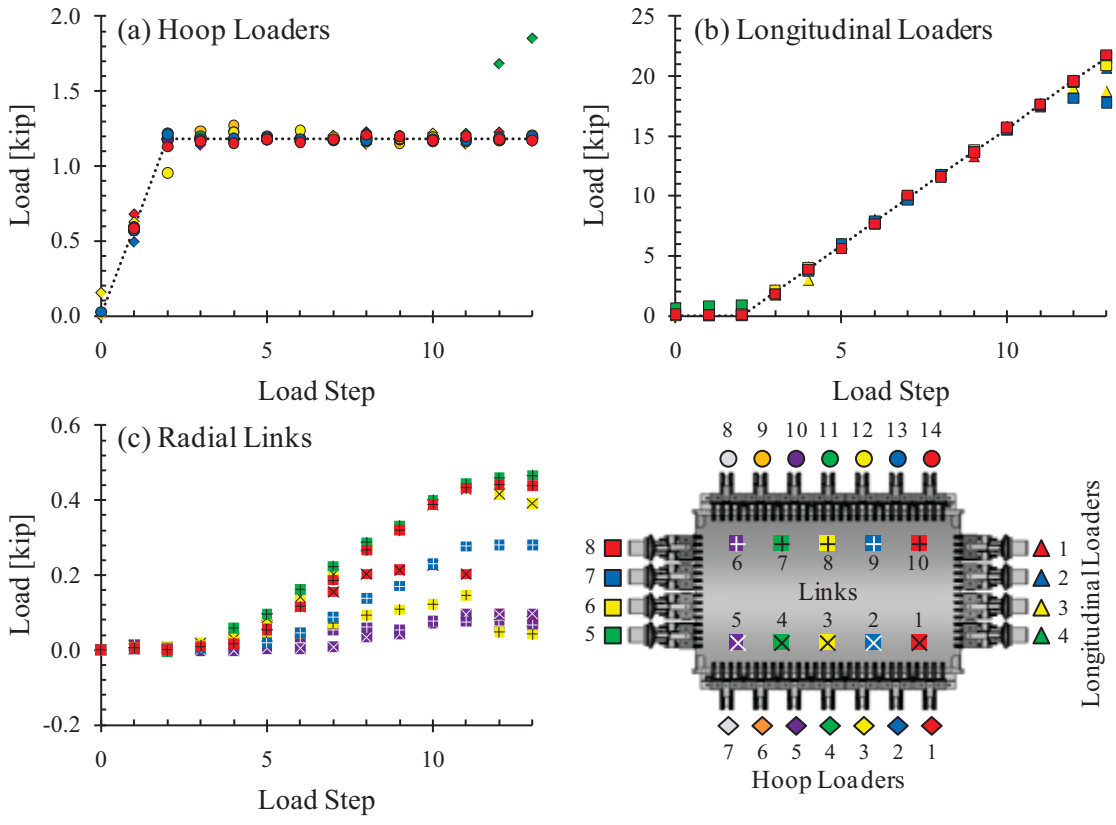

Figure 4.26. Loader performance charts for panel CP4, test CP4-RST-1. Loader and radial link numbers are indicated in the accompanying schematic.

displacement of the panel. The radial link loads recorded in panel CP4 merited their inclusion in the global finite element (FE) models, as discussed in Chapter 8.

The far-field strain response to longitudinal load in the test section during the residual strength test of panel CP4 is shown in Figure 4.27. The hoop and longitudinal strains under longitudinal loading was similar to that exhibited by panel CP3, with the exception that lower initial strains (i.e., strains at zero applied longitudinal load) were present due to the lower internal pressure and hoop loading of panel CP4. The longitudinal strain response, Figure 4.27b, was very uniform across the test section throughout loading, with the maximum strains occurring along the crown of the panel, as expected. The hoop strain response to longitudinal loading, Figure 4.27a, was less uniform, as was observed for panel CP3. Nonlinearity in both the hoop and longitudinal strain response was first observed beyond 76% of the maximum applied longitudinal loads (i.e., the same applied longitudinal load at which nonlinearity was first observed in the hoop strain response of panel CP3). While nonlinearity was observed in both panels at the same load level, the average far-field test section strains of the two panels varied greatly (0.25% in panel CP3 and 0.36% in panel CP4) at these loads, indicating that failure may be better estimated via stress-based criteria rather than strain-based criteria for the particular

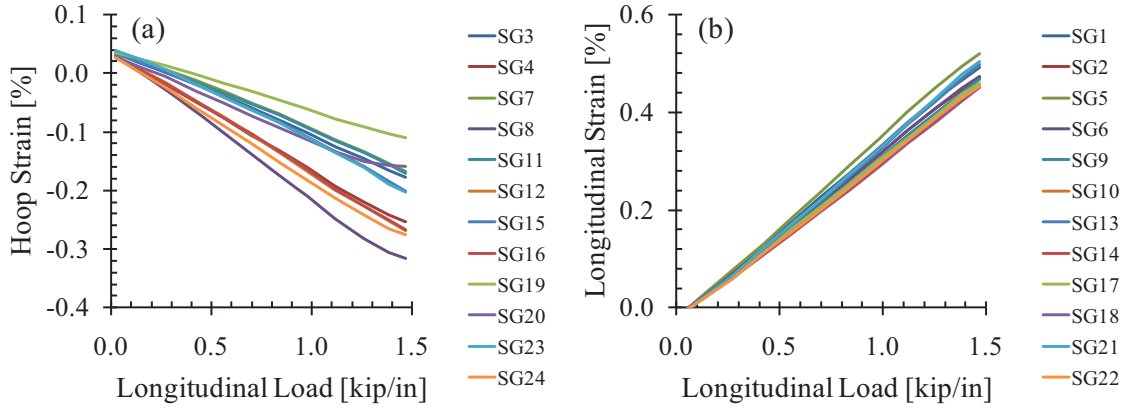

Figure 4.27. Far-field (a) hoop and (b) longitudinal strain response to longitudinal loading in the test section of panel CP4, test CP4-RST-1.

material, geometry, and loadings used throughout this investigation. This is discussed with regards to the notch tip strains in Section 4.3 and to the FE models in Chapter 8.

Figure 4.28 compares the longitudinal and hoop strain distributions on the exterior and interior surfaces during the residual strength test of panel CP4. The difference between the exterior (Figure 4.28a) and interior (Figure 4.28b) longitudinal strains increased linearly from zero to approximately 0.045% with longitudinal loading. Assuming that strains due to bending vary linearly through the thickness of the sandwich composite, the percent of the measured strains due to bending can be calculated through:

$$\% \text{ Bending} = \frac{\varepsilon_{\text{ext}} - \varepsilon_{\text{int}}}{\varepsilon_{\text{ext}} + \varepsilon_{\text{int}}} \tag{4.3}$$

The measured strains due to bending did not exceed 10% of the sandwich mid-plane strain, indicating minimal bending about the θ-axis (with respect to the panel coordinate system established in Section 4.2.3). Raju and Tomblin [4.1] used Eq. (4.3) to characterize the severity of panel bending as a function of applied loads. While Eq. (4.3) does represent the severity of the panel bending with respect to the strains due to in-plane loading, it should be noted that a constant percent bending with increasing load represents increasingly severe panel curvature while a constant difference between the exterior and interior strains represents a constant panel curvature. The measured hoop strains in the residual strength test of panel CP4 indicated that positive bending of the panel about the z-axis occurred as a result of the initial internal pressure and hoop loading, but decreased to near-zero levels with the application of the high longitudinal loads. The development of negative panel bending about the z-axis in the central test section of a panel is expected when tensile loads occur in the radial links while internal pressure is applied to the panel. Considering a cross section of a panel in the r-θ plane under such loading conditions, the panel can be simplified to a beam with the radial links acting as pin supports and the internal pressurization acting as a uniform distributed load, Figure 4.29. The internal pressure causes localized positive panel bending in the immediate vicinity of the radial link attachment points

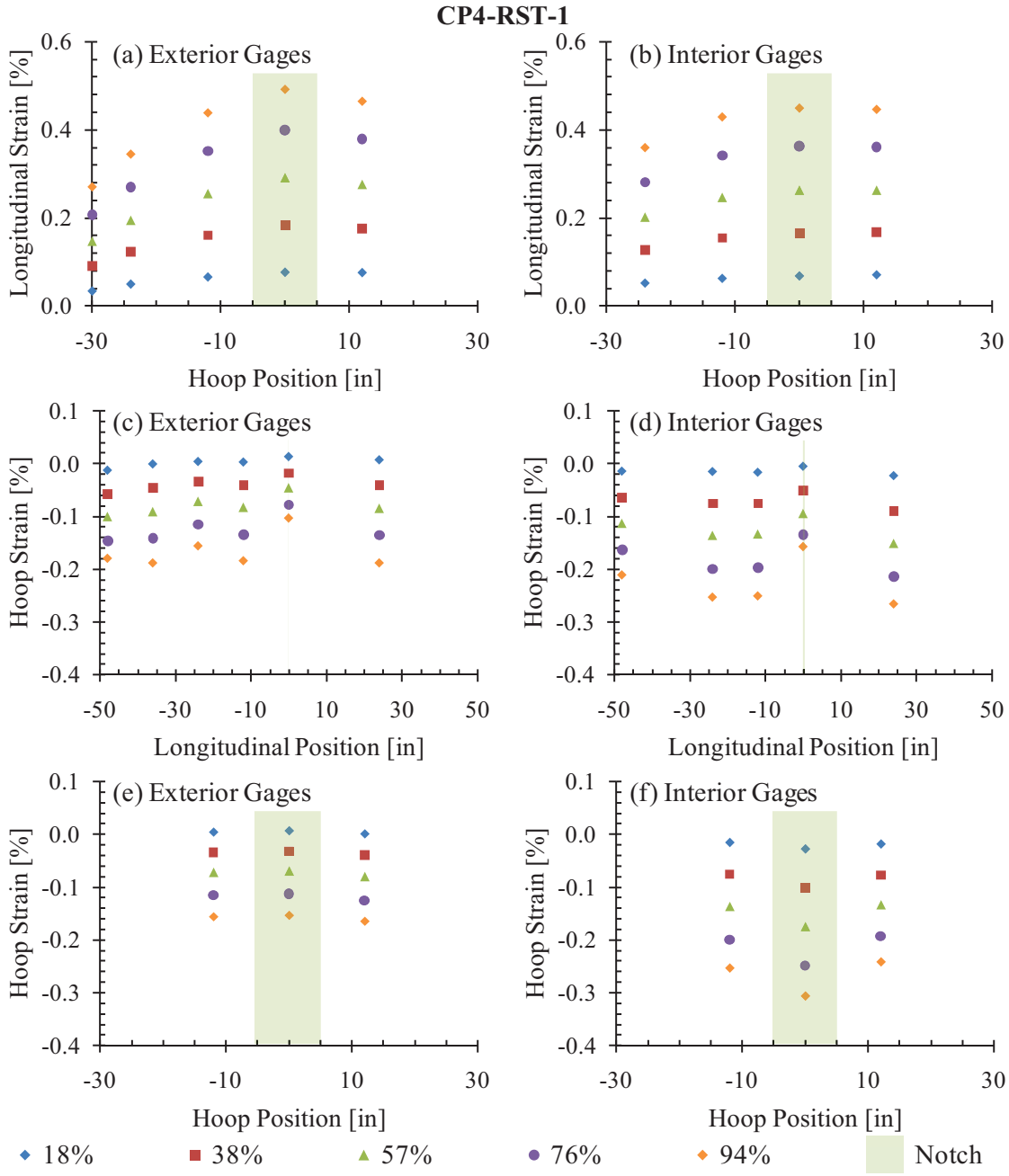

Figure 4.28. Longitudinal and hoop strain distributions across panel CP4 at various longitudinal loads during test CP4-RST-1.

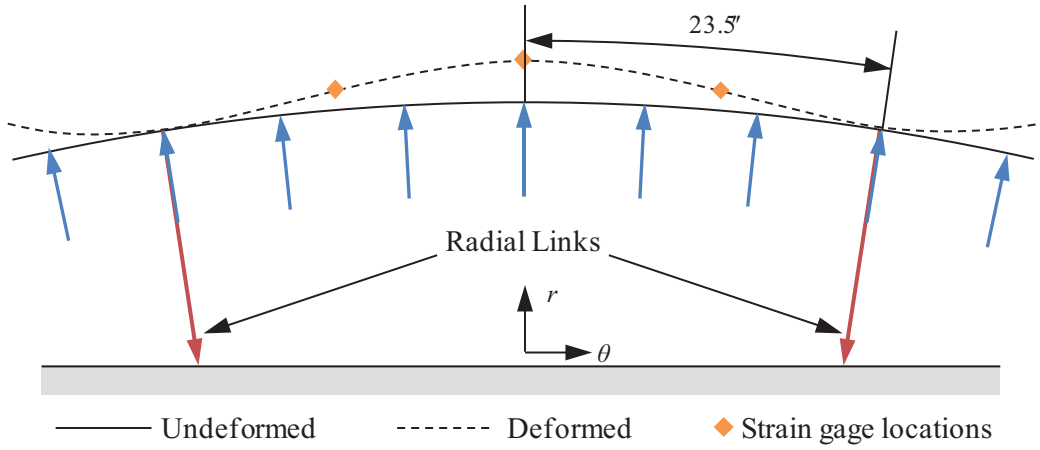

Figure 4.29. Illustration of panel bending about the z-axis during test CP4-RST-1.

(located 23.5 inches from the crown of the panel) and negative panel bending throughout the central test section, Figure 4.29. The measured hoop strains across the test section agree with the expected behavior, showing a maximum exterior/interior hoop strain differential along the crown of the panel, Figure 4.28e and Figure 4.28f.

Examining the notch tip strain data from the residual strength test of panel CP4, the severity of the notch tip in terms of strain concentration factor was lower than that observed during the residual strength test of panel CP3, 4.09 versus 4.40, respectively, as calculated using strain gages SG30 and SG17 at 76% of the maximum applied loads prior to the detection of local failures in the immediate vicinity of either gage. The difference was somewhat more pronounced when comparing the interior notch tip strain gages, 2.85 versus 3.26. While bending of the panels is expected in the immediate vicinity of the notches, the increased far-field bending exhibited by panel CP4 may have been caused by the higher radial link loads. Further, differences in the thickness of the applied sealant on the interior surface of the panels (Section 3.5) could have attracted loads differently, causing differences in the apparent severity of the notch tips in the two panels, most notably with regards to the interior face sheet strains.

The first indication of damage progression in panel CP4 occurred at notch tip 1 on the exterior panel surface. Upon loading to 64% of the maximum applied longitudinal load, a localized failure occurred in the vicinity of strain gage SG30 after surpassing 1.15% longitudinal strain; no obvious redistribution of strain to the next nearest gage was observed, Figure 4.30a. Upon reaching the seventh load step (67% of the maximum load), matrix cracking was observed in the DIC coating 0.099 inch ahead of the notch tip, Figure 4.31a. The interior face sheet near notch tip 1 also provided indications of damage progression at this load as the strain reading of SG[33] abruptly increased from 0.83% to 1.05%, Figure 4.30b. While loading up to the eighth load step, evidence of increased damage progression was observed in the exterior and interior face sheets of both notch tips. Strain gage SG29, located 0.75 inch ahead of notch tip 1, began to exhibit a nonlinear response to increased load upon reaching 70% of the maximum load. Strain gage SG[25], located 0.25 inch ahead of notch tip 2, also exhibited nonlinear behavior at this load, jumping from 0.84% to 1.25%, Figure 4.30c. Upon reaching 74% of the maximum load, SG[33] experienced a second sudden jump in its strain reading, increasing from 1.29% to 1.47%. The visible damage ahead of notch tip 2 advanced from 0.099 inch to 0.413 inch upon reaching the eighth load step, 76% of the maximum load, Figure 4.31b. Continued loading up to the ninth load step (86% of the maximum load) caused SG[33] and SG[25] to fail and additional visible damage ahead of notch tip 2, Figure 4.31c. The visible notch tip damage advanced along the +45° fiber tow upon reaching 92% of the maximum load, extending the damage to 0.615 inch, as measured along the axis of the notch, Figure 4.31d. The new damage consisted of fiber breakage along the intersections of the tows in the plain-weave structure of the prepreg lamina; this was the final state-of-damage observed ahead of notch tip 2 in panel CP4. Strain gage SG29 failed at a strain of 1.13% upon reaching 96% of the maximum applied load (Figure 4.30a), indicating a damage extension beyond 0.75 inch from notch tip 1, Figure 4.31e. The final extent of the notch tip damage is more clearly visible in the DIC strain fields presented later in this chapter and in the NDI data presented throughout Chapter 5.

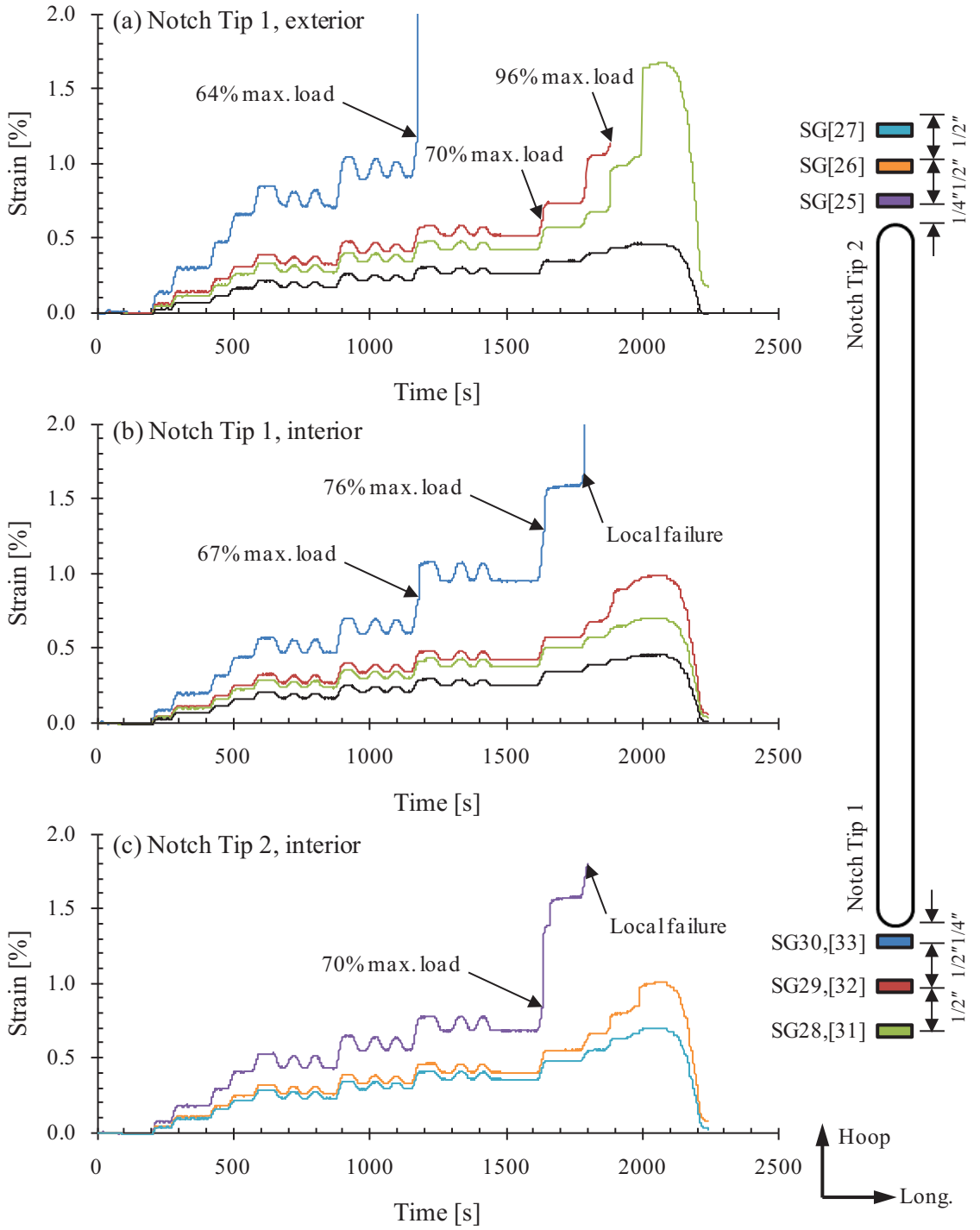

Figure 4.30. Notch tip strain history for panel CP4, test CP4-RST-1. The locations of the strain gages are indicated in the schematic on the right. Strain gage numbers in brackets indicate being installed on the interior surface of the panel. The black curves are representative of strain gages SG17 and SG[18], measuring the far-field response along the axis of the notch.

No additional damage advancement was observed via the DIC system images or the array of strain gages ahead of the notch tips prior to reaching the maximum applied longitudinal load of 1470 lbf/in. During the last applied load step, several longitudinal loaders approached their capacity, allowing no higher longitudinal loads to be applied in a uniform manner with the current setup of the fixture. The test was terminated with the non-catastrophic state-of-damage shown in Figure 4.31.

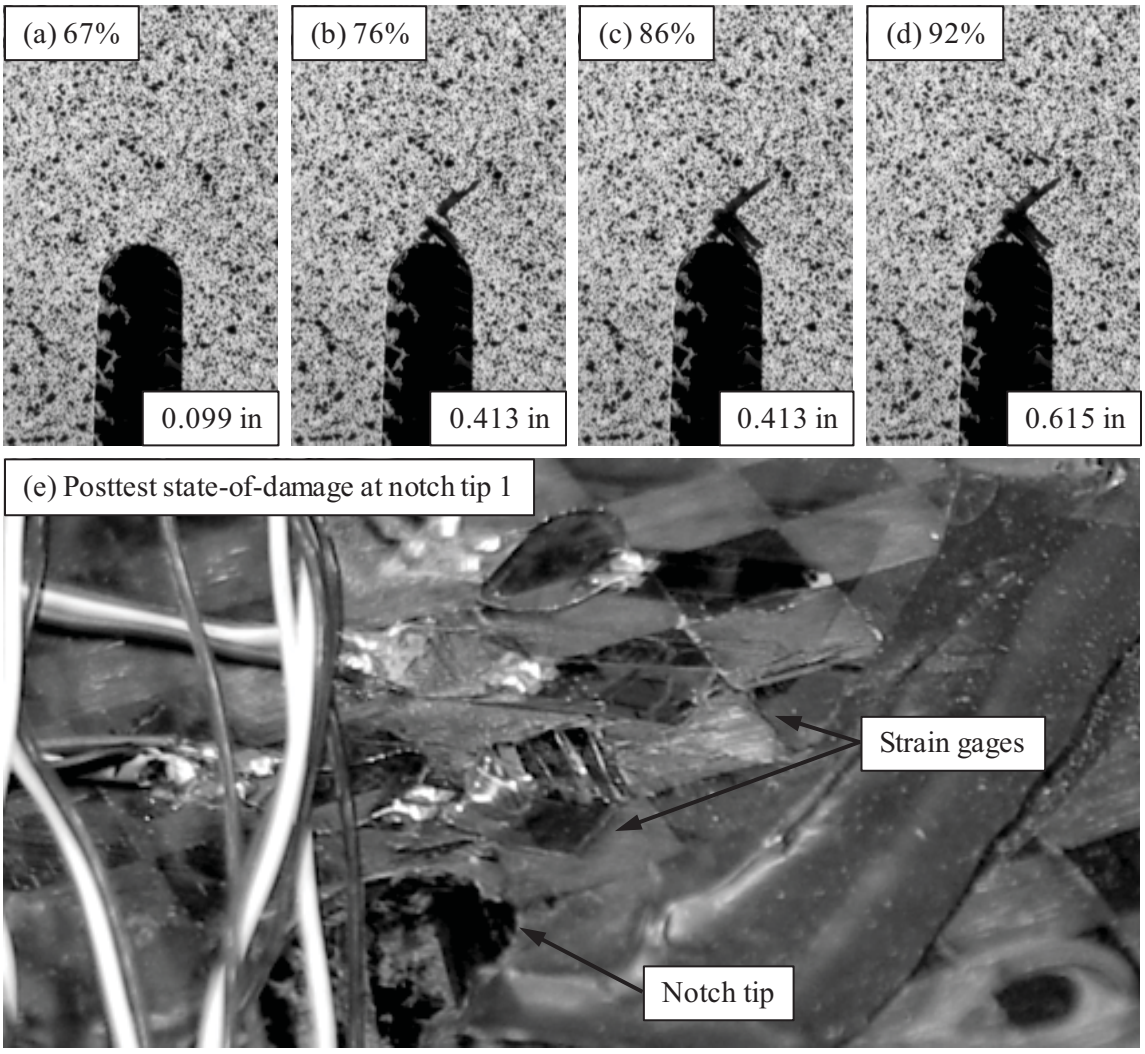

Figure 4.31. Development of visible notch tip damage for panel CP4, test CP4-RST-1. The percentages in the figure are with respect to the loads listed in Table 4.6. The measurements in the figure are the distance from the notch tip to the farthest visible damage, measured along the axis of the notch.

4.2.5. PANEL CP5

Panel CP5 contained a through-thickness, 10-inch long, 0.5-inch wide, longitudinal notch, located along the crown of the panel. As mentioned in Section 3.4, the notch was shifted along the crown of the panel by 10 inches toward strain gage SG7 because of the large elliptical skin-to-core disbond located too close to its original planned location at the center of the panel, Figure 3.20. Eight strain survey tests were conducted for panel CP5: four under combined loading up to 300 lbf/in longitudinal load, 252 lbf/in hoop load, and 3.40 psi internal pressure; two up to 252 lbf/in hoop loading and 3.40 psi internal pressure; and two up to 300 lbf/in longitudinal loading, Table 4.7.

The maximum planned loads for the residual strength test of panel CP5 were 15.0 psi internal pressure, 1110 lbf/in hoop load, and 100 lbf/in longitudinal load, Table 3.2. The low longitudinal loads were applied to avoid rigid body translation of the panel in the fixture in the hoop direction, as discussed in Section 3.6. Two equal load steps of 50 lbf/in longitudinal load were applied and held for the duration of the residual strength test. Equal load steps of 1.5 psi pressure and 111 lbf/in hoop load were subsequently applied. The panel failed catastrophically

Table 4.7 Load History of Panel CP5.

Loading	Designation	Maximum Applied Loads		
		Long [lbf/in]	Hoop [lbf/in]	Pressure [psi]
Combined	CP5-SS-C1	300	252	3.40
Combined	CP5-SS-C2	300	252	3.40
Combined	CP5-SS-C3	300	252	3.40
Longitudinal	CP5-SS-L1	300	0	0.00
Hoop	CP5-SS-H1	0	252	3.40
Combined	CP5-SS-C4	300	252	3.40
Longitudinal	CP5-SS-L2	300	0	0.00
Hoop	CP5-SS-H2	0	252	3.40
Longitudinal, then Hoop	-	100	252	3.40
Longitudinal, then Hoop	-	100	202	2.72
Longitudinal, then Hoop	-	100	202	2.72
Longitudinal, then Hoop	-	100	252	3.40
RST	CP5-RST-1	100	960	13.50

while holding at the ninth load step (i.e., 13.5 psi internal pressure, 960 lbf/in hoop load, and 100 lbf/in longitudinal load).

Representative strain survey results from each of the three evaluated loading conditions for panel CP5 are presented in Figure 4.32. It should be noted here that the far-field strain survey results of the previous panels were generally not affected by the presence of the slits, holes, and notches. The results of each panel maintained close similarity to the strain distributions found in the baseline panel throughout the test section. The shifted position of the longitudinal notch in panel CP5, however, affected the majority of the far-field test section strain gages (Figure 3.20). For instance, the nearly parabolic distribution of longitudinal strain with hoop position was generally apparent under the hoop (Figure 4.32c) and longitudinal loading (Figure 4.32e) conditions, though each showed significantly decreased longitudinal strains along the crown of the panel due to the close proximity of the notch. The strain gages used to characterize the distribution of longitudinal strain with hoop position were located only 7 inches longitudinally ahead of the notch tip. As a result, the three central strain gages (SG1, SG5, SG9) were affected by the kidney-shaped strain field centered about the notch tip, as discussed in Section 4.3.

The distributions of hoop strain with longitudinal position were also influenced by the presence of the notch, especially for the gages located at -12 and 0 inches longitudinal position, strain gages SG15 and SG19, respectively. Note that the notch was located between -15 and -5 inches longitudinal position (Figure 3.20). Strain gage SG19 was located within the elevated strain field ahead of the notch tips under the combined and hoop loading conditions, resulting in the consistently higher hoop strain readings (Figure 4.32b and d). At the location of strain gage SG15, within the longitudinal span of the notch, the internal forces of the panel were partially redirected around the notch tips, resulting in lower hoop strains. The longitudinal loading condition results were similar to those of the baseline panel due to no significant elevated strain fields developing ahead of the notch tips.

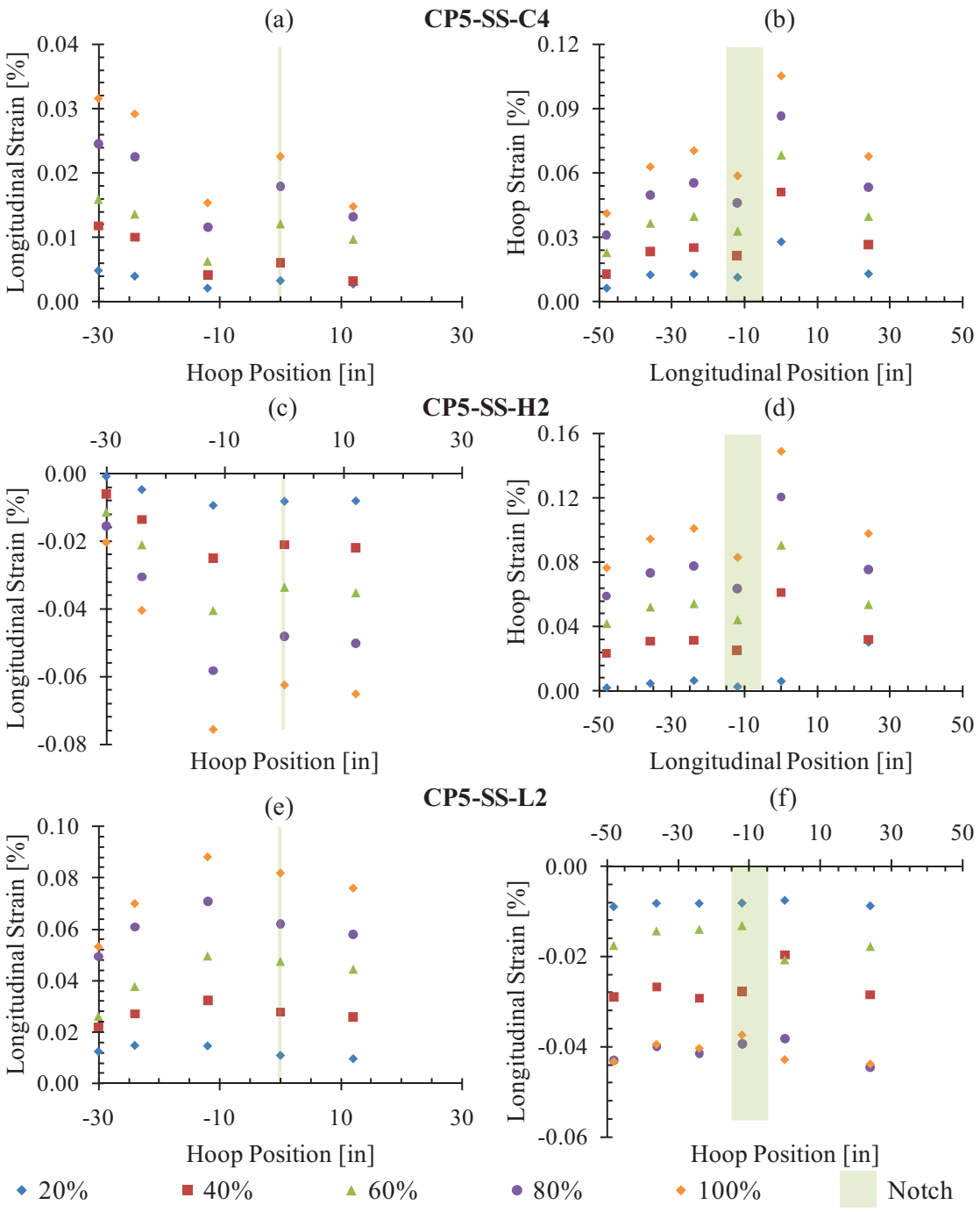

Figure 4.32. Strain distributions measured on the exterior surface of panel CP5 during the strain surveys. The percentages in the legend are with respect to the maximum applied loads listed in Table 4.7 for the tests indicated in bold.

While the strain survey results for panel CP5 varied significantly from those recorded in the baseline and the other notched panels, each discrepancy was accounted for using basic observations regarding the loading and damage configuration. Considering the effects of the off-center notch and the skin-to-core disbond, similar behavior in terms of in-plane strains, panel bending, and damage progression, were expected during the residual strength test of panel CP5.

During the residual strength test of panel CP5, four hoop loaders reached, on average, 89% of their target loads during the last five load steps, yielding an average applied hoop load of 960 lbf/in at the ninth load step, Figure 4.33a. The four poorly performing loaders were loaders #9 through #12, all located on the same side of the panel. As a result, the equilibrium of the panel could not be satisfied by accounting for only the hoop loaders, longitudinal loaders, and radial

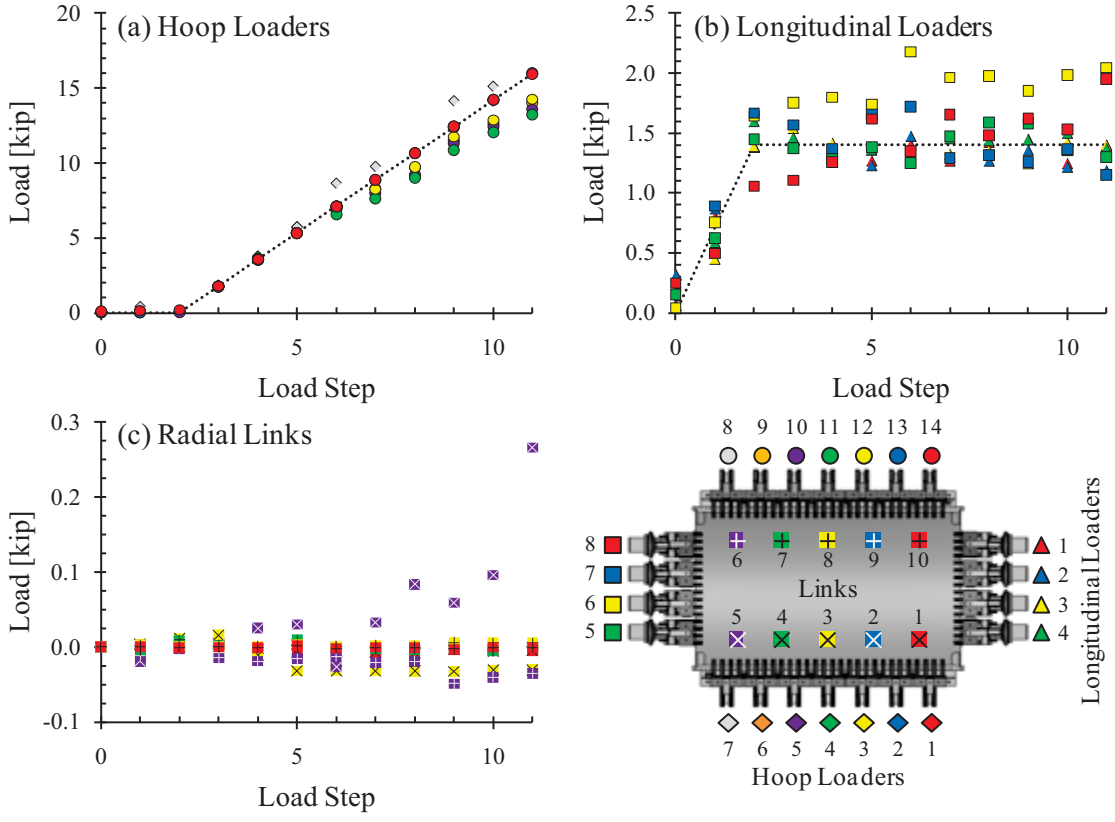

Figure 4.33. Loader performance charts for panel CP5, test CP5-RST-1. Loader and radial link numbers are indicated in the accompanying schematic.

link load cell data. As constructed, the load cells installed in-line with the longitudinal loaders only measured loads in the longitudinal direction and not along the axes of the load attachment points to the panel. Therefore, it is assumed that the unaccounted for hoop load was distributed amongst the longitudinal loaders, in order to maintain panel equilibrium Several longitudinal loaders exhibited erratic performance during the test, though this was found to be caused by their water actuators being fully closed and applying additional reactive loads, Figure 4.33b.

The far-field strain response to hoop load in the test section during the residual strength test is shown in Figure 4.34. The hoop and longitudinal strain response to hoop loading was similar to that exhibited by panel CP1B, with the exception of the slight initial offset due to the low longitudinal loads applied to panel CP5. The hoop strain response, Figure 4.34a, was generally uniform throughout loading, with strain gages SG19 and SG20 showing above average strains due to their position ahead of one of the notch tips. Strain gages SG3, SG7, and SG15 exhibited nonlinearity with increased load between the second and fourth load steps. The longitudinal strain response, Figure 4.34b, was generally linear throughout loading, with the often observed nearly parabolic strain distribution with hoop position causing the expected spread within the data. Nonlinearity in the hoop strain response was first observed for the strain gages along the axis of the notch beyond 80% of the panel fracture load, and became apparent throughout the panel beyond 90% of the fracture load. Nonlinearity was apparent in the longitudinal strain response during the first few load steps due to free play in the loaders and during the final load step, at which point the damage ahead of the notch tips had a significant effect on the performance of the panel.

The interior and exterior longitudinal strain results indicated that increased hoop loading and pressurization caused progressively more pronounced bending of the panel about the θ-axis, Figures 4.35a and 4.35b. No significant panel bending was observed about the panel z-axis, Figures 4.35c and 4.35d. As discussed in Section 4.2.4, significant bending of the panel about the

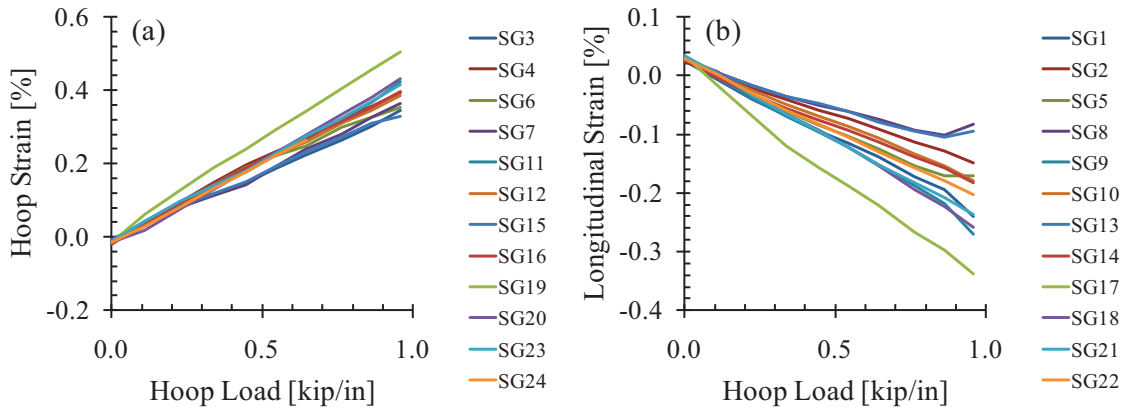

Figure 4.34. Far-field (a) hoop and (b) longitudinal strain response to hoop loading in the test section of panel CP5, test CP5-RST-1.

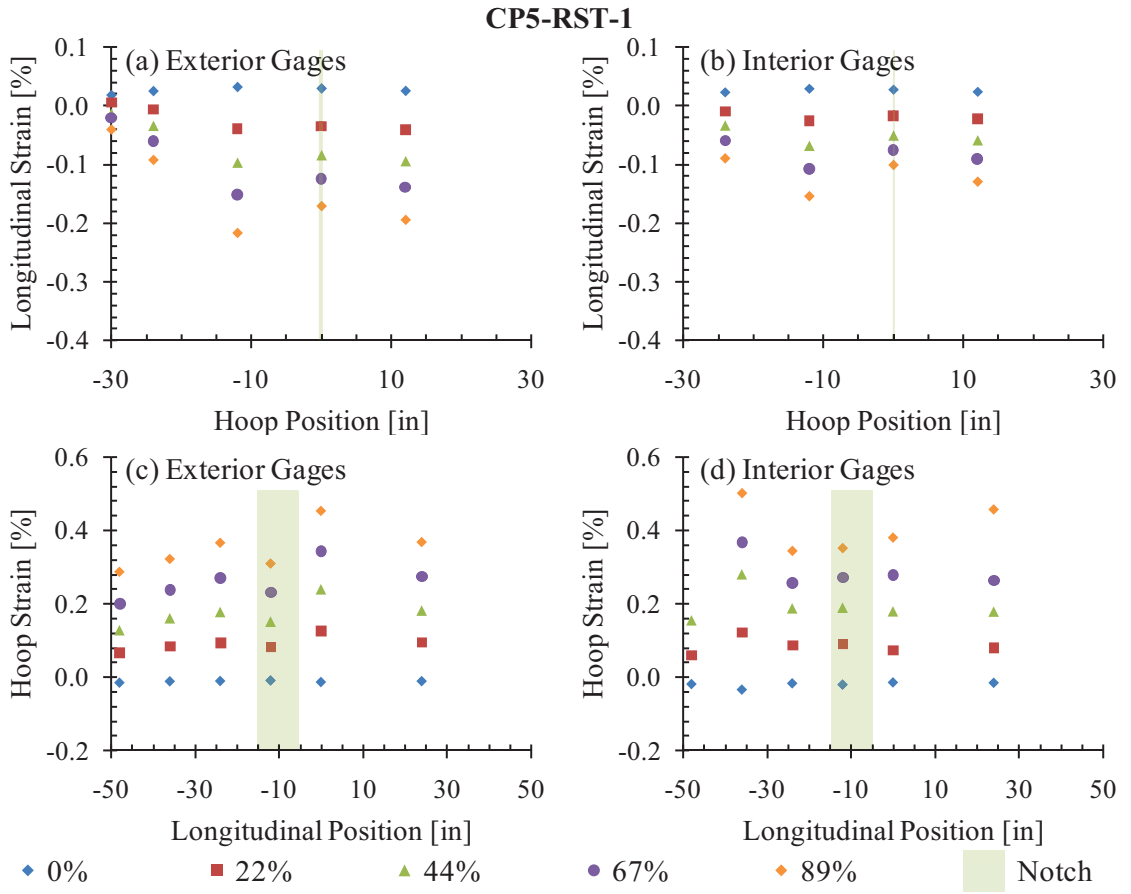

Figure 4.35. Longitudinal and hoop strain distributions across panel CP5 at various hoop loads during test CP5-RST-1.

z-axis requires tensile loads in the majority of the radial links; this was not the case during the residual strength test of panel CP5.

The elevated hoop strain fields ahead of panel CP5 notch tips were characterized by a strain concentration factor of 3.83. This was calculated using strain gages SG30 and SG7, installed on the exterior panel surface, 0.25 and 9 inches ahead of notch tip 1 (Figure 3.20), at the sixth load step. The first indication of damage progression occurred at notch tip 2 in the interior face sheet. Upon loading to 67% of the panel fracture load, the strain readings of SG[25], located 0.25 inch ahead of the notch tip, jumped abruptly from 0.84% to 1.95%, Figure 4.36c. Since this strain value is far above the lamina failure strain, it is assumed that damage propagated through the region monitored by the strain gage. Each of the strain gages installed 0.25 inch ahead of their respective notch tips failed while loading to the next load step: SG[33] failed at 1.31% at 70% of the fracture load, SG[25] failed at 2.23% at 73% of the fracture load, and SG30 failed at 1.33% at 77% of the fracture load.

The first instance in which damage was detected at the notch tip monitored by the DIC system occurred at 82% of the panel fracture load, Figure 4.37a. Localized damage was observed 0.304 inch ahead of the notch tip in the -45° fiber tow through which the notch tip was machined. Failure was also indicated by the sudden redistribution of strain in the interior face sheet near the same notch tip. The readings of SG[26], located 0.50 inch ahead of the notch tip, jumped from 0.68% to 1.15% and SG[27], located 1.25 inches ahead of the notch tip, jumped from 0.56% to 0.65%. Upon reaching 92% of the fracture load, the visible damage extended to 0.352 inch ahead of notch tip 2, Figure 4.37b. Another simultaneous indication of damage by the strain gages installed on the interior panel surface was detected, as well. Strain gage SG[26] failed at a strain level of 1.69%, and the corresponding redistribution of strain caused the strain readings of SG[27] to jump from 0.77% to 1.08%. With continued loading to 93% of the fracture load, the visible damage ahead of notch tip 2 advanced to 1.237 inches, Figure 4.37c. The damage progressed

along the axis of the original notch, alternating between failing the +45° and -45° tows of the plain-weave prepreg.

At 99% of the panel fracture load, damage propagated through the locations of the remaining strain gages ahead of the notch tips. Ahead of notch tip 1 on the exterior panel surface, SG29 and SG28 failed abruptly, Figure 4.36a. The corresponding strain gages on the interior surface of the panel, SG[32] and SG[31], failed at 1.16% and 0.84% hoop strain, respectively, Figure 4.36b. Strain gage SG[27], 1.25 inches ahead of notch tip 2, failed at 1.56% hoop strain, Figure 4.36c. Therefore, the damage within the exterior and interior face sheets ahead of each notch tip had extended at least 1.25 inches prior to the ultimate fracture of the panel. After reaching a load of 13.5 psi internal pressure, 960 lbf/in hoop load, and 100 lbf/in longitudinal load, the load was held for the recording of additional photogrammetric data. After holding the load at this level for 43 seconds, the panel fractured abruptly. A final image of the state-of-damage ahead of notch tip 2 showed only a slight advancement to 1.322 inches prior to fracture, Figure 4.37d. That is, approximately 1.3 inches of damage extension (1.0% of the overall panel length) was sufficient to cause catastrophic fracture.

The final state-of-damage of panel CP5 extended to the lay-up transition regions on either end of the panel, Figure 4.37e. While the far-reaching matrix cracking and damage to the woven fabric again occurred, much of the damage did not extend an inch beyond the major fracture of the panel.

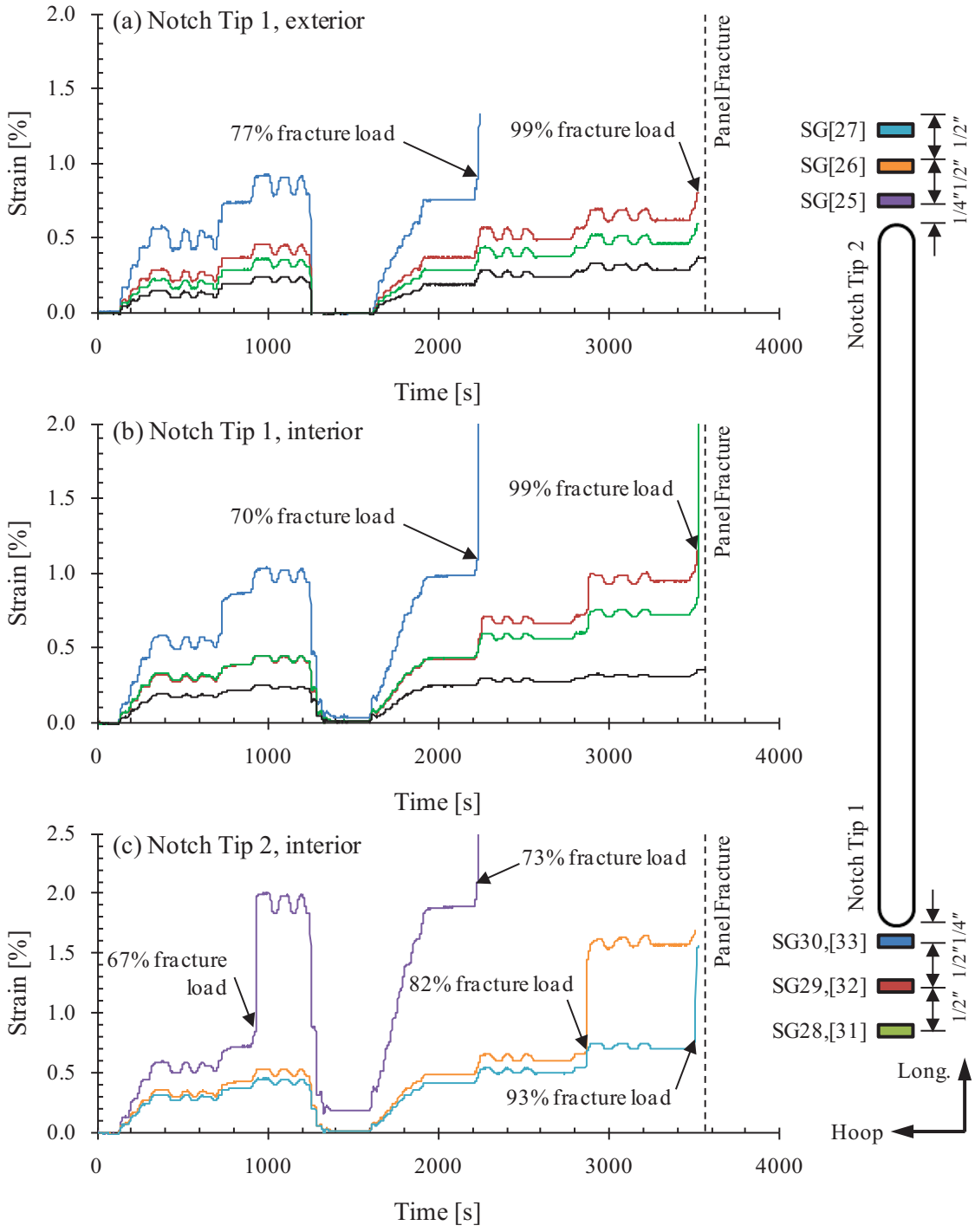

Figure 4.36. Notch tip strain history for panel CP5, test CP5-RST-1. The locations of the strain gages are indicated in the schematic on the right. Strain gage numbers in brackets indicate being installed on the interior surface of the panel. The black curves are representative of strain gages SG[6] and SG7, measuring the far-field response along the axis of the notch.

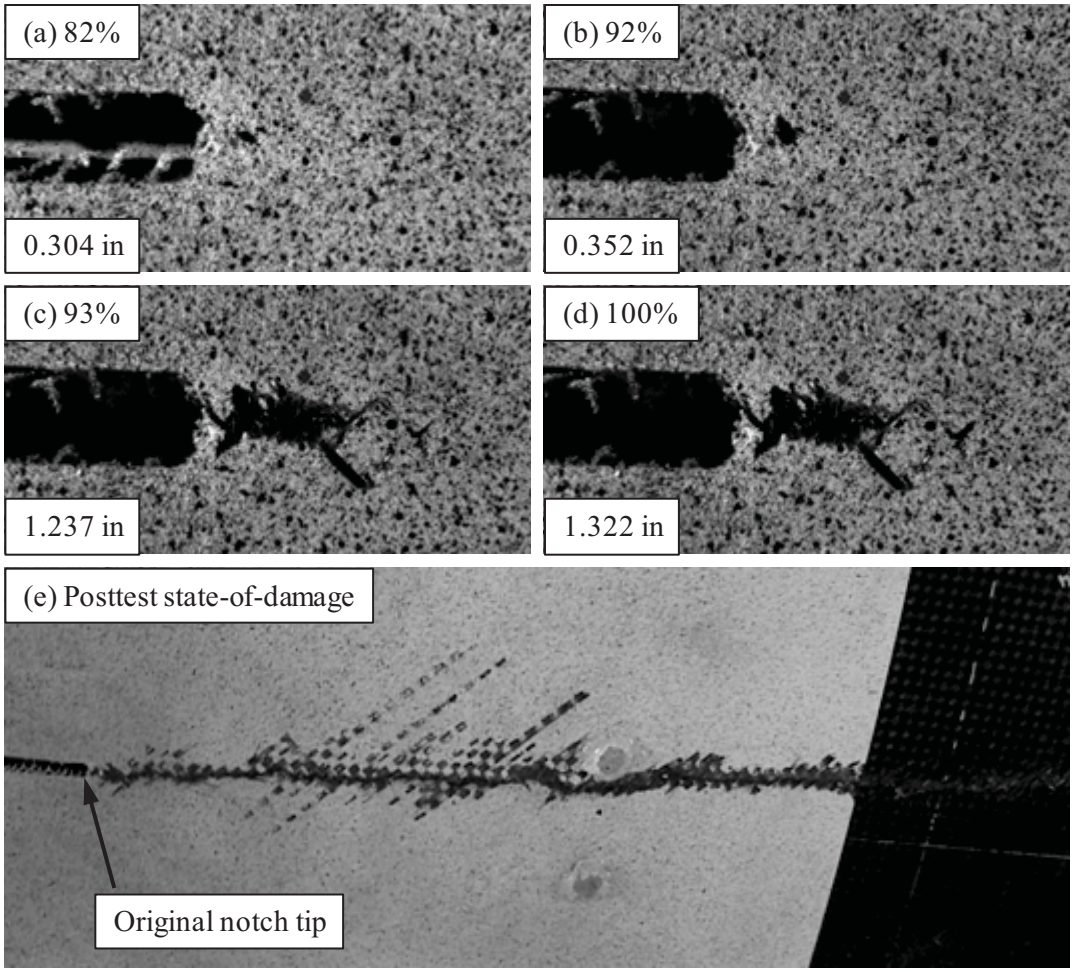

Figure 4.37. Development of visible notch tip damage for panel CP5, test CP5-RST-1. The percentages in the figure are with respect to the loads listed in Table 4.7. The measurements in the figure are the distance from the notch tip to the farthest visible damage, measured along the axis of the notch.

4.2.6. PANEL CP6

Panel CP6 contained a through-thickness, 10-inch long, 0.5-inch wide notch inclined at 45°, located at the center of the panel. Seven strain survey tests were conducted for panel CP6: four under combined loading up to 150 lbf/in longitudinal load, 150 lbf/in hoop load, and 2.03 psi internal pressure; two up to 200 lbf/in hoop loading and 2.70 psi internal pressure; and one up to 200 lbf/in longitudinal loading, Table 4.8. Due to the orientation of the notch, the combined loading condition was expected to cause the most severe state-of-strain ahead of the notch tips.

As a result, the combined loading strain surveys were limited to especially low load levels to avoid producing any damage prior to the residual strength test.

The maximum planned loads for the residual strength test of panel CP6 were 20.27 psi internal pressure, 1500 lbf/in hoop load, and 1500 lbf/in longitudinal load, Table 3.2. Equal load steps of 1.35 psi pressure, 100 lbf/in hoop load, and 100 lbf/in longitudinal load were applied. The panel failed catastrophically while loading from the thirteenth to the fourteenth loads steps.

It should be noted that the combined loading conditions for panel CP6, for both the strain surveys and the residual strength test, have nominally equal applied loads per length in both the hoop and longitudinal directions, unlike the combined loading cases for panels CP3, CP4, and CP5. As mentioned in Section 4.2.3, the attraction of the applied longitudinal load to the unloaded portion of the test section and transition region near the hoop loaders causes lower longitudinal strains throughout the test section when compared to the hoop strains due to the same applied hoop loads per length. While the combined loading condition remained more critical than either the hoop or longitudinal loading conditions, the inclined notch in panel CP6 had a bias toward failing along its hoop tangent due to the higher hoop strains throughout the test section.

Table 4.8. Load History of Panel CP6.

Loading	Designation	Maximum Applied Loads		
		Long [lbf/in]	Hoop [lbf/in]	Pressure [psi]
Combined	-	60	60	0.81
Combined	CP6-SS-C1	150	150	2.03
Hoop	CP6-SS-H1	0	200	2.70
Longitudinal	-	40	0	0.00
Combined	CP6-SS-C2	150	150	2.03
Hoop	CP6-SS-H2	0	200	2.70
Longitudinal	CP6-SS-L1	200	0	0.00
Combined	-	30	30	0.41
Combined	CP6-SS-C3	150	150	2.03
Combined	CP6-SS-C4	150	150	2.03
RST	CP6-RST-1	1388	1375	18.78

The strain survey results from each of the three loading conditions for panel CP6 are presented in Figure 4.38. The nearly parabolic distribution of longitudinal strain with hoop position was again apparent while under all three loading conditions with the exception of the gage installed at +12 inches along the hoop axis (i.e., SG1, Figure 3.21). Strain gage SG1 output anomalously high longitudinal strain readings during each strain survey and residual strength test. No unusual loader or radial link load activity was observed in the vicinity of that strain gage. Furthermore, the interior strain gage readings from the same location did not show any unexpectedly high strains, indicating that the unexpected behavior was due to either localized damage in the exterior face sheet or due to poor gage application. The distributions of hoop strain with longitudinal position were generally uniform throughout the test section. Similar to panel CP5, the strain gage installed within the longitudinal span of the notch (i.e., the highlighted region in Figure 4.38) recorded lower strains than the adjacent strain gages, while the far-field strain gages located along the axis of the notch (i.e., at coordinates -12, -12) recorded higher strains. While none of the strain gages installed at this location were perpendicular to the notch, the inclined orientation of the notch with respect to the hoop and longitudinal directions caused high strain fields to develop under all three loading conditions.

The hoop and longitudinal loaders performed well throughout the duration of the residual strength test of panel CP6. Hoop loader #9 was the only exception, failing to reach its target load at the thirteenth and fourteenth load steps, Figure 4.39a. The radial link loads were generally below 200 lbf, with only the load cell installed in-line with radial link #3 detecting loads above 250 lbf at the final load step, Figure 4.39c. However, a drop in the measured loads of each of the radial links was detected between the third and fourth load steps. This drop corresponded to a rigid body translation of the panel in the hoop direction, observed via the recorded images used in the DIC analysis. Because the radial link load cells cannot be loaded in compression, they were apparently installed without sufficient slack and became tightened during the strain surveys. It

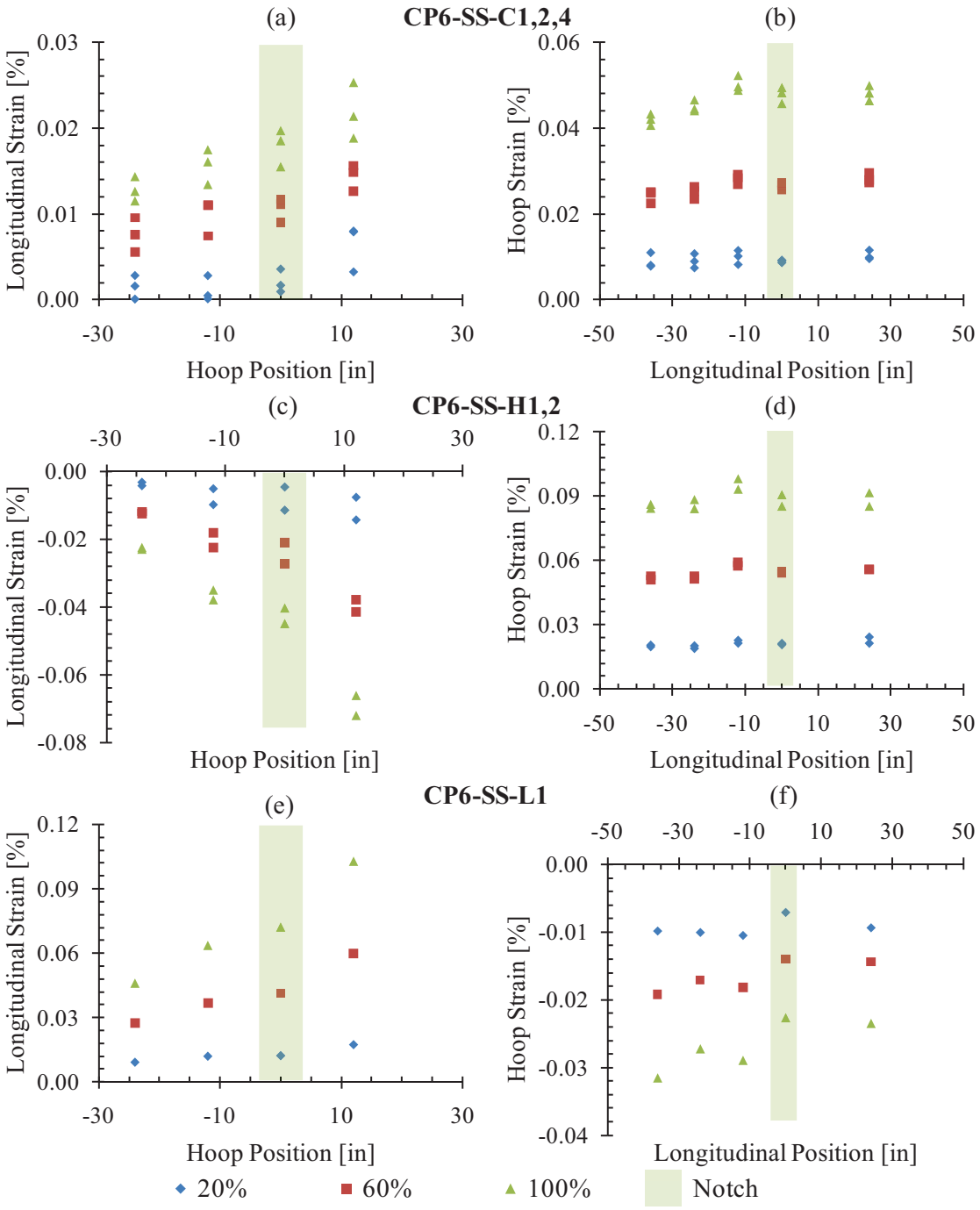

Figure 4.38. Strain distributions measured on the exterior surface of panel CP6 during the strain surveys. The percentages in the legend are with respect to the maximum applied loads listed in Table 4.8 for the tests indicated in bold.

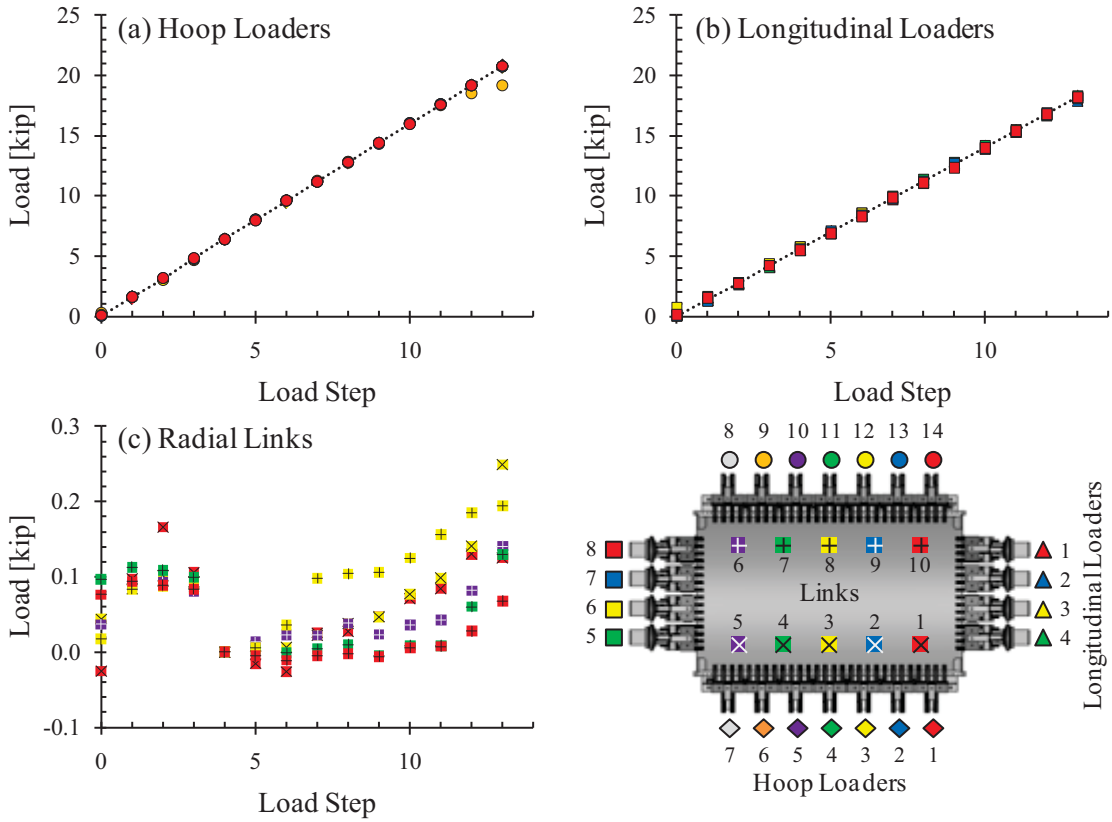

Figure 4.39. Loader performance charts for panel CP6, test CP6-RST-1. Loader and radial link numbers are indicated in the accompanying schematic.

seems that the loading and unloading of the panel during the residual strength test loosened the links resulting in the load drop recorded after the fourth load step.

The far-field strain in the test section during the residual strength test is shown in Figure 4.40. The hoop strain response to combined loading was very uniform throughout the majority of the loading range, Figure 4.40a. The longitudinal strain response, Figure 4.40b, contained the scatter expected of the nearly parabolic longitudinal strain distribution with hoop position. The maximum longitudinal strains occurred along the crown of the panel, decreasing with increased proximity to the hoop loaders. The rigid body translation of the panel between the third and fourth load steps, mentioned earlier, caused a notable shift in the hoop and longitudinal strain response of the panel, though linearity was maintained before the third and after the fourth load

steps. Nonlinearity due to the formation of damage in the panel was first observed after reaching 65% of the panel fracture load, notably earlier than in the previous panels. Due to the nominally equal hoop and longitudinal loads applied, the average far-field hoop strain response in the test section was higher than that recorded for the longitudinal strains, as expected.

Similar distributions of the far-field test section hoop and longitudinal strains were observed during the residual strength test as were observed in the combined loading strain surveys, Figure 4.41. Because of the nearly equal exterior and interior longitudinal surface strains, no clear indication of bending about the panel θ-axis is present, Figure 4.41a and b. The exterior hoop strain gages were consistently higher than their interior counterparts throughout loading, indicating negative panel bending about its z-axis, Figure 4.41c and d; however, the average difference between the exterior and interior strains steadily decreased with increased loading, becoming almost negligible during the notch tip failure processes. As a result, minimal panel-wide bending was present during the latter stages of damage propagation and any observed bending was a result of the original notch and any additional damage.

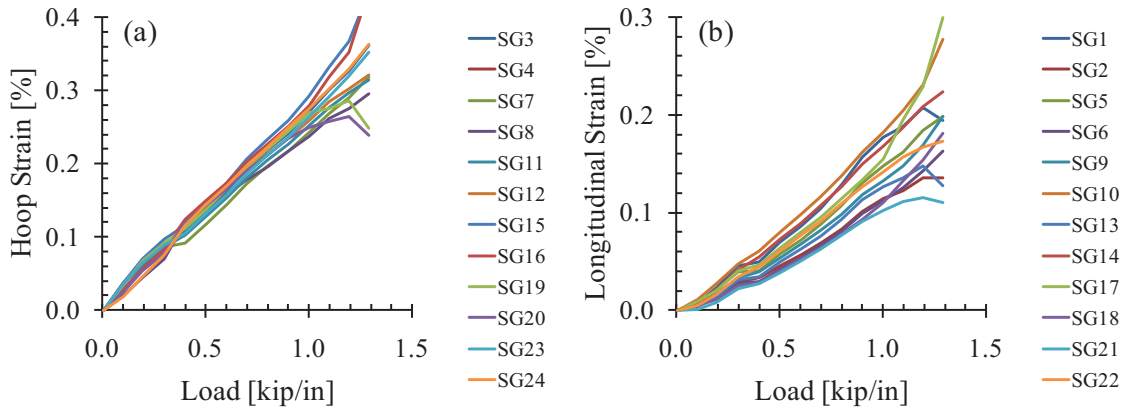

Figure 4.40. Far-field (a) hoop and (b) longitudinal strain response to combined loading in the test section of panel CP6, test CP6-RST-1.

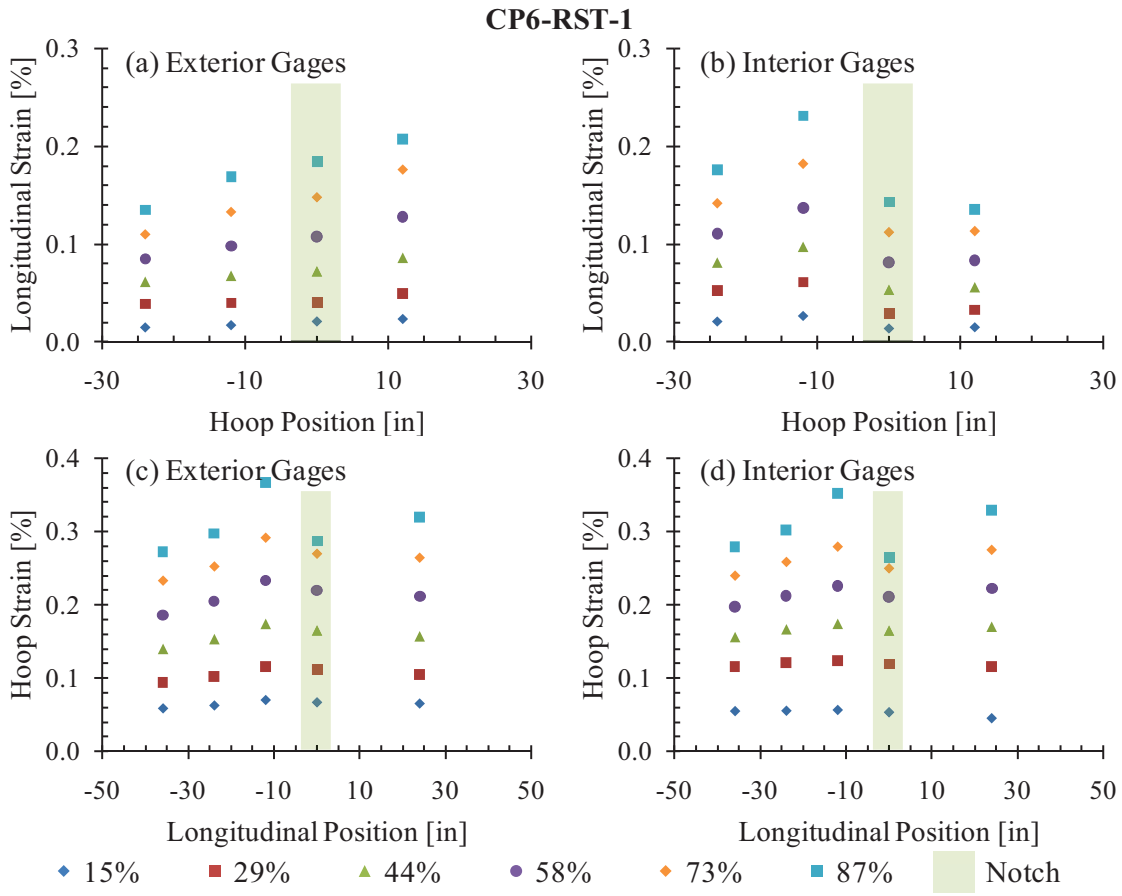

Figure 4.41. Longitudinal and hoop strain distributions across panel CP6 at various loads during test CP6-RST-1.

The first indication of damage progression in panel CP6 occurred at notch tip 1 in the exterior face sheet, Figure 4.42. Upon loading to 58% of the panel fracture load, the strain readings of SG30N, located 0.25 inch ahead of the notch tip, suddenly dropped from 1.02% to 0.95%; no obvious redistribution of strain to the next nearest gage was observed, Figure 4.42a. Damage propagated through the region monitored by strain gage SG30N while loading up to the next load step. At 65% of the fracture load, damage was observed at notch tip 2 via the DIC images (Figure 4.43a), with small cracks visible along the hoop tangent of the monitored notch tip. Upon reaching the 73% of the fracture load, material in the vicinity of strain gages SG[25] and SG[26], installed 0.25 and 0.75 inch ahead of notch tip 2 on the interior panel surface, failed

after reaching strains of 1.43% and 0.57%, respectively. As had been observed in the previous panel tests, the propagation of damage occurred in sudden, discrete bursts. The strain readings of SG[26] were well below the lamina failure strain (1.28% in the direction perpendicular to the notch in the exterior ply), indicating that the notch tip damage propagated past both strain gages in a single burst. At this same load, material in the vicinity of strain gage SG[33N] failed after reaching 0.72% notch-normal strain; strain redistribution was observed in strain gages SG[32N] and SG[31N], installed 0.75 and 1.25 inches ahead of the notch, respectively.

Upon reaching 77% of the panel fracture load, material in the vicinity of strain gages SG29N and SG[32N], installed 0.75 inch ahead of notch tip 1 on the exterior and interior surfaces, respectively, failed. Additional matrix damage was also visible approximately 0.3 inch ahead of notch tip 2, Figure 4.43b. Fiber fracture and more extensive matrix cracking occurred within the tow through which the notch tip was machined at 78% of the fracture load, extending approximately one inch perpendicular to the notch axis, Figure 4.43c.

The two remaining strain gages at notch tip 1 (SG28N and SG[31N]), each installed 1.25 inches ahead of the notch tip, abruptly failed at 80% of the panel fracture load, followed by strain gage SG[27], installed ahead of notch tip 2, at 84% of the fracture load. At this load, damage continued to propagate perpendicular to the notch and advanced to the next three fiber tows ahead of the notch tip, Figure 4.43d. Similar progression of the damage was observed through 94% of the fracture load, at which point the state-of-damage extended approximately 3.1 inches perpendicular to the notch axis, Figure 4.43f.

The panel ultimately failed at 18.78 psi internal pressure, 1375 lbf/in hoop load, and 1388 lbf/in longitudinal load. The final fracture followed a meandering path, extending to the corners of the panel, Figure 4.43g. Damage extended through the plain-weave architecture of the face sheets several inches away from the major fracture of the panel.

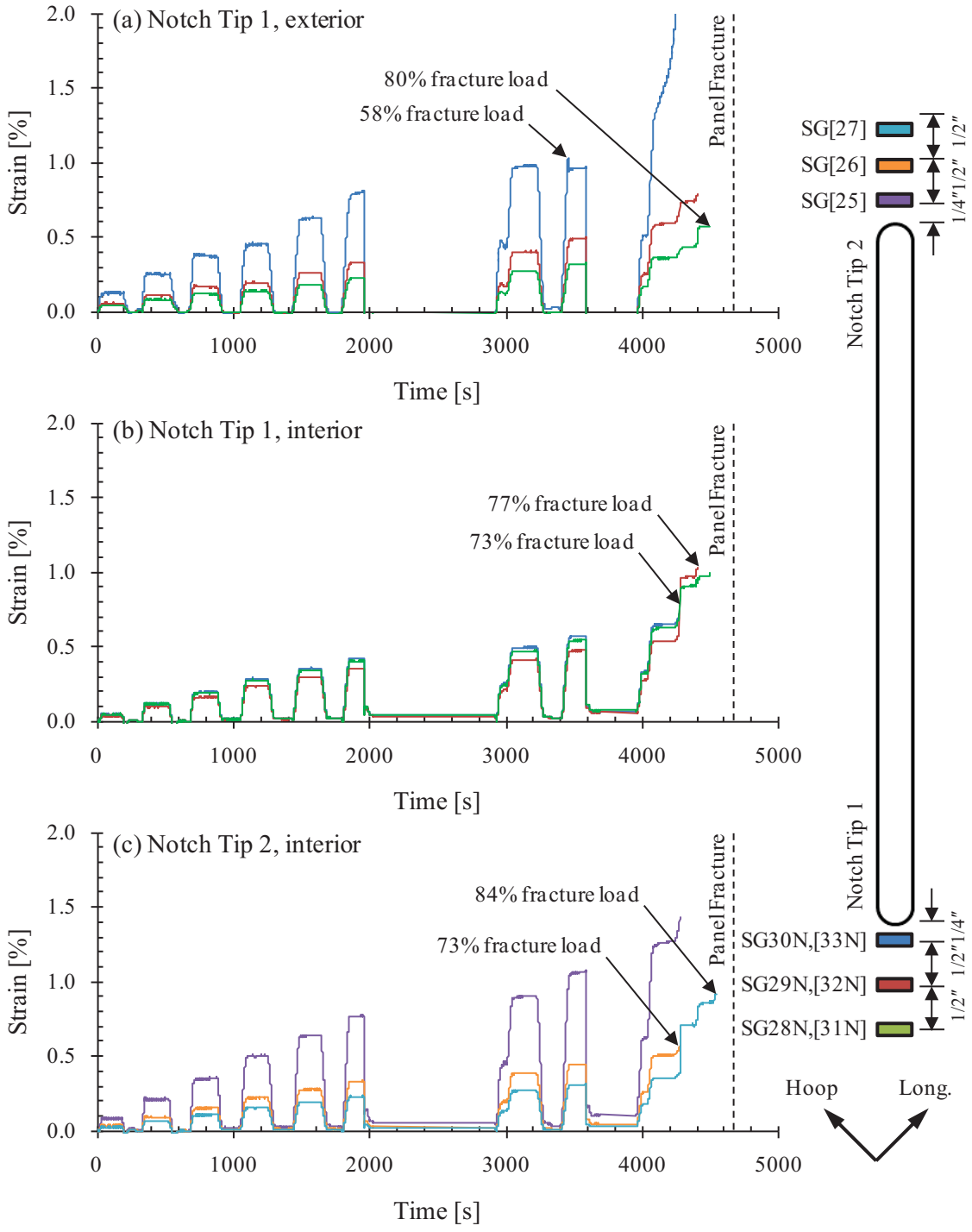

Figure 4.42. Notch tip strain history for panel CP6, test CP6-RST-1. The locations of the strain gages are indicated in the schematic on the right. Strain gage numbers in brackets indicate being installed on the interior surface of the panel.

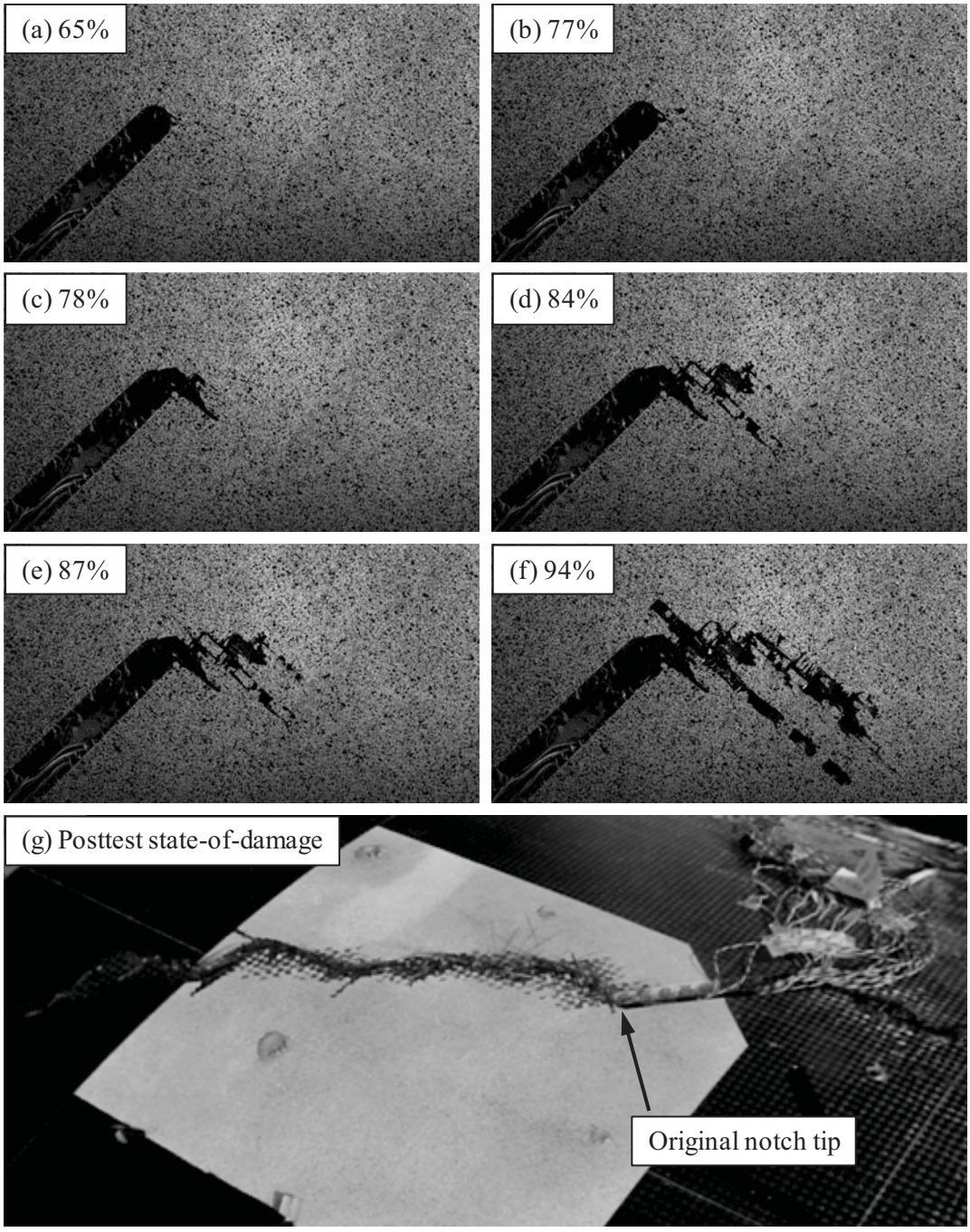

Figure 4.43. Development of visible notch tip damage for panel CP6, test CP6-RST-1. The percentages in the figure are with respect to the loads listed in Table 4.8.

4.2.7. RESIDUAL STRENGTH TEST SUMMARY

The fracture loads of all six panels are listed in Table 4.9. For panels which did not undergo catastrophic fracture, the listed load is the maximum applied load. Despite the severity of the artificial damage introduced to the panels, every panel was able to withstand loads far in excess of realistic in-flight operating conditions. The damage processes observed in the notched panels all involved high-energy, bursts of damage formation and propagation prior to fracture. For each panel which underwent catastrophic fracture, one to three inches of damage propagation was observed prior to abruptly extending the full span of the panel. However, while relatively few stages of damage development preceded panel fracture, several opportunities existed to detect the damage prior to instability. Indications of damage, either via strain gage measurements or visual inspection, occurred for each panel between 56% and 68% of the panel fracture loads.

While the collected strain gage and loader data characterized very well the severity of the artificial damage introduced to each of the panels through the early stages of damage development, changes in the state-of-damage ahead of the original notch tip often reduced their effectiveness. Localized failures in the immediate vicinity of strain gages are easily detected, as they often cause large, sudden discontinuities in the recorded strain response. However, such indications often also diminish the gage's ability to characterize the structural response. In the case of panel CP6, all gages installed ahead of the notch tips failed before reaching 84% of the

Table 4.9. Residual Strength Test Results Summary.

Panel	Maximum Loads			1st indication of damage
	Long [lbf/in]	Hoop [lbf/in]	Pressure [psi]	
CP1A	1500	0	0.00	N/A
CP1B	0	1040	14.08	0.56
CP2	0	1550	21.26	N/A
CP3	1507	592	8.00	0.65
CP4	1470	74	1.00	0.64
CP5	100	960	13.50	0.67
CP6	1388	1375	18.78	0.58

panel fracture load, having no means to characterize the panel deformation during the most critical stages of damage propagation. Furthermore, if the development of damage does not proceed along the originally suspected path, such as was the case for panel CP6, the collected strain gage data will likely fail to accurately represent the critical state-of-strain which is driving the propagation of damage through the material. The DIC method was used to record the full-field displacement and strain fields ahead of the artificial damage in each panel, complementing the recorded strain gage data. The results obtained using the DIC method are presented here.

4.3. DIGITAL IMAGE CORRELATION DATA

Photogrammetric measurements of the full-field deformation and strain in the vicinity of the inserted damage were recorded in all panels at each load step during the strain surveys and residual strength tests. Additionally, photogrammetric measurements were performed following any observed change in the visual state-of-damage. Contour plots of the components of strain along each principal material direction (i.e., 0, 90, +45, and -45 degrees), as well as the principal and Tresca strains, were generated. Panel CP5 exhibited several distinct stages of self-similar damage development and extension along its original axis. Therefore, this panel represented the best case for comparing the results obtained with the DIC system and the strain gage data ahead of the notch tip. Accordingly, the results obtained from panel CP5 are presented and discussed in detail in this chapter. Results from the remaining panels are cited throughout the present discussion, though the complete set of their strain contour plots is presented in Appendix A.

As mentioned in Section 4.1, the data captured using the DIC method offers the opportunity to perform analyses of the notch tip failure processes that are more comprehensive compared to when utilizing point-wise strain gage data. Furthermore, the DIC images provide full-field displacement and strain data sets to be used in validating the FE models developed in this work (Chapter 8), as well as a thorough characterization of the strain fields and the driving forces of damage propagation. A thorough comparison of the recorded strain gage data and the

DIC results is presented ensuring that a proper DIC experimental setup and appropriate post-processing parameters were utilized and selected, Section 4.3.2. The various strain components ahead of the artificial damage fronts are examined and the forces driving (or limiting) damage progression are discussed, Section 4.3.3. While the strain gage data and visual inspections provided useful data on the geometry of any observed damage extensions, the effective notch extension (i.e., the locus of the elevated strain field) does not necessarily correspond to the farthest visible damage. Therefore, the relationship between the extent of visible damage and the loci of the strain fields is discussed in Section 4.3.4.

4.3.1. POST-PROCESSING AND DATA FILTERING

As was discussed in Section 2.2.1, the strain contours reduced from DIC measurements do not exhibit the expected continuity of continuum mechanics or FE solutions. The calculated strain values are simply derivatives of the measured displacement fields, which are, in turn, based off tracking a field of points through a series of digital images. Errors in the measured displacement fields are often small with respect to the measured values. Yet, any discontinuities in the displacement field are magnified in the computed strain fields, producing high levels of noise with a propensity to mask the actual deformation of the material. To overcome this difficulty, the appropriate filtering of the strain data is necessary to obtain reasonably smooth strain contours for use in either quantitative or qualitative assessments of the overall panel deformation. While filtering is necessary, caution should be exercised to not filter too excessively while smoothing the strain contours. For cases in which a pronounced stress riser is being characterized, over-filtering the data can mask the actual intensity of the strain field. This is analogous to the proper selection of a strain gage model based on gage section: smaller gage sections yield higher resolution, but may be more susceptible to localized anomalies in the inspected material offsetting the accuracy of the measurement. Accordingly, consideration of a virtual gage length is useful when selecting appropriate filtering parameters.

The virtual gage length chosen for each panel was 0.1 inch, which is the average characteristic element size in the vicinity of the notch tips in the global FE models of the panels (Section 8.2) and similar to the gage sections of the strain gages used throughout this investigation (which ranged from 0.062 inch to 0.250 inch), Section 3.7.1. The virtual gage length is a function of the facet step and the strain length. The strain length can be defined as the odd value *n* for an *n* by *n* grid of facets whose displacements are used to calculate the strain values of the central facet. The virtual gage length, in units of length, can be calculated through:

$$\text{VGL} = (\text{facet step})(n-1)(\text{linear pixel density}), \tag{4.4}$$

where the facet step is in pixels, *n* is strain length, and the linear pixel density has units of length per pixel [4.2]. A facet size of 11 by 11 pixels and a strain length of three facets were used for each panel. The facet step was then chosen to obtain a virtual gage length as close to 0.1 inch as possible, given the linear pixel density associated with the experimental setup of each panel. While the calculation of strain takes into consideration the displacements of several adjacent facets, noise still exists and additional filtering of the data is required. Five runs of a median filtering scheme were applied over a 3 by 3 facet area to sufficiently smooth the data. Because the DIC data of each panel had the same planar facet density (as a result of selecting the facet step to produce equivalent virtual gage lengths), the same filtering scheme was used for all panels.

4.3.2. NOTCH TIP STRAINS

The hoop strain field ahead of the notch tip in panel CP5 at 67% of the panel fracture load is shown in Figure 4.44. The three dashed lines represent both the global panel coordinate system and line segments along which strains were examined while characterizing the strain field and reconstructing the notch tip failure processes. A kidney-shaped strain field, characteristic of the stress field ahead of a crack that is subjected to Mode I loading in an isotropic material, is centered about the notch tip. This type of strain distribution is expected considering the fact that the face sheets were made using a quasi-isotropic composite layup. The elevated strain field

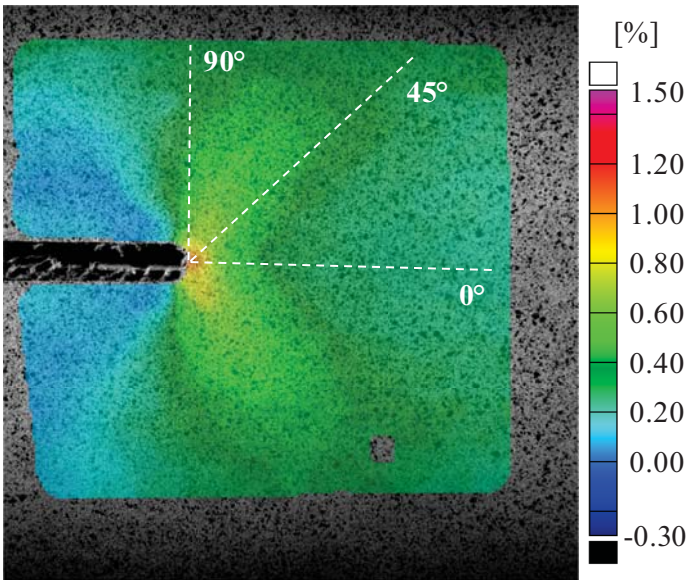

Figure 4.44. DIC hoop strain data for panel CP5 at 67% of the panel fracture load, showing the cross sections along which the quantitative DIC strain data are compared with strain gage data.

extended less than two inches along the axis of the notch, and nearly the full six-inch height of the area monitored by the DIC system at this load level. As expected, the regions immediately above and below the notch exhibited very low hoop strains due to the free edges of the notch perpendicular to the hoop direction.

As mentioned in Section 3.7.2, point-wise strain was recorded via a group of strain gages installed along the axis of the notch while the full-field strain was recorded via photogrammetry ahead of the opposite notch tip. Any comparisons between the strain gage data and the photogrammetric measurements are relevant only if it is assumed that the strain fields ahead of each notch tip are the same. The strain gage data discussed throughout Section 4.2 indicate that this symmetry assumption is appropriate. This assumption was made for the results obtained up to the first indications of damage. Therefore, the direct comparison of the notch tip strain gage data and the DIC strain data is appropriate up to 67% of the fracture load of panel CP5.

The symmetry of strains ahead of the two notch tips led to generally similar states-of-damage ahead of the two notch tips, as was observed in the strain gage results. However, the

precise loads at which damage extended from the two notch tips were rarely equal. Accordingly, any correlations made after the initiation of damage should be considered qualitative only. Direct comparison of the strain data from the opposite notch tips will often disagree at specific load levels after the initiation of damage, but trends may be apparent in regards to the overall progression.

Good correlation was observed in panel CP5 between the strain gage and DIC results up to the initial indications of damage (i.e., the propagation of damage through the location of strain gage SG[25] on the interior panel surface), Figure 4.45. Furthermore, during the load hold preceding the catastrophic fracture of the panel, each of the three strain gages installed on the exterior surface of notch tip 1 had failed, Figure 4.36, and the visible state-of-damage at notch tip 2 had extended 1.322 inches ahead of the notch tip (Figure 4.37d), indicating similar states-of-damage.

Strain gage SG30, installed 0.25 inch ahead of notch tip 1 (Figure 4.36), recorded strains that were consistently 20% higher than those determined by the DIC data ahead of notch tip 2. This difference between the two data sets may be due to the particular location of the strain gage with respect to the plain-weave unit cells, differences in the quality of the two notch tips (as machined), lack of local symmetry between the two notch tips, etc. However, the DIC data filtering diminishing the magnitudes of the notch tip strains is the most likely cause. Accurate determination of the singularity located at the notch tip is quite difficult with any measurement technique. Therefore, the *true* strain concentration factor (i.e., the strain concentration factor as calculated using the actual notch tip strains, unlike that calculated using the strain gages installed either 0.125 or 0.25 inch ahead of the damage) could not be determined experimentally in this investigation. However, results 0.50 inch beyond the notch tip correlated closely, indicating that the region affected by the filtering is less than 0.50 inch in radius.

The progression of damage in panel CP5, as shown in Figure 4.37, is apparent in the DIC notch tip hoop strain history, Figure 4.45. Localized failures and damage extensions were

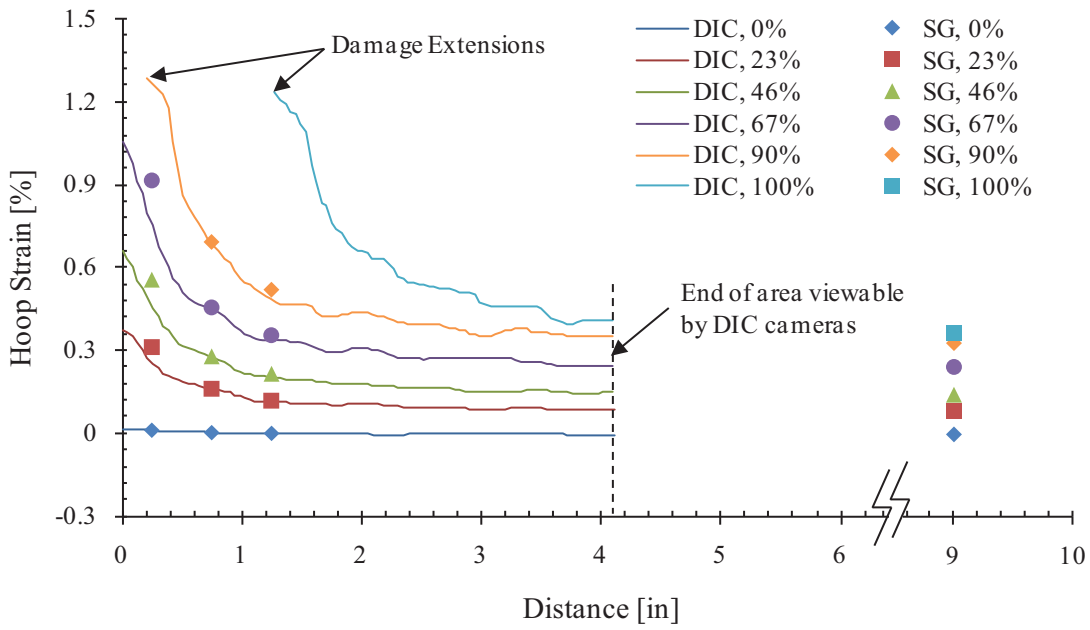

Figure 4.45. Comparison of notch tip hoop strains as measured via the DIC system and the set of strain gages along the axis of the notch in panel CP5, test CP5-RST-1. The DIC strain data were taken from the contour plots in Figure 4.51.

observed upon reaching hoop strains of 1.2–1.4%, correlating very well with the lamina failure strain of 1.28% in the hoop direction of the face sheet mid-ply. The sharp strain gradient within two inches of the notch tip is well characterized by the three installed strain gages. The close proximity of the strain gages allows for small notch tip damage extensions to affect multiple gages (i.e., the failure of one gage will result in the redistribution of strain to the neighboring gage, ensuring that no intermediate damage extensions go unrecorded). As a result, estimates of the damages extension are possible via examination of the strain gage locations and the magnitudes of any sudden relative increases in strain. Similar comparisons were made using the DIC and notch tip strain gage data from the other panels.

The notch tip strain gages of panel CP1B measured hoop strains ahead of notch tip 1 (Figure 4.11), which were consistently greater than those measured via the DIC system, Figure 4.46. Strain gage SG25H, 0.25 inch ahead of notch tip 1, failed prior to reaching 67% of the panel fracture load, at which point the material ahead of notch tip 2 was still fully intact, clearly

exhibiting different rates of damage progression. This difference indicates that the state-of-strain ahead of notch tip 1 was indeed more severe than that ahead of notch tip 2. Notch tip damage extensions occurred for hoop strains in excess of 1.2%, as measured by both strain gages and DIC, correlating well with the lamina failure strain of the mid-ply. The effect of the DIC data filtering is apparent within 0.2 inch of the notch tip; the sharp decrease in the slope of the strain contour is artificial.

The 1/16-inch wide longitudinal notch introduced to panel CP1B was manually machined using a Dremel rotary tool and may have not produced two notch tips of similar severity (i.e., in terms of sharpness, radius, uniformity through the panel thickness, etc.). This may have contributed to the difference in the strains ahead of the two notch tips.

While the hoop strains along the edge of the hole in panel CP2 exceeded 1.5% during its final load step (Figure A.8f), the visible damage (Figure 4.18) along the edge of the hole was not observed until after test CP2-RST-H3 was completed. The strain gage and DIC data sets show only typical increases in the magnitude of the strain field, and no indications of damage extensions (i.e., nonlinearity in the strain response, abrupt failures of gages, etc.), Figure 4.47. However, the strains themselves measured by the DIC system are indicative of subsurface damage along the edge of the hole. The face sheet mid-ply contained fibers oriented in the hoop direction, parallel to the high strains. As a result, subsurface damage can be assumed to have occurred in this region. The presence of such subsurface damage is confirmed via thermography in Section 5.2.3.

The large region monitored by the DIC system during the residual strength test of panel CP2 allowed for certain important observations. The two dark bands seen in the strain contour plots of Figure A.8 are regions in which the rolls of prepreg overlay, oriented in the longitudinal and +45° directions. This overlay increases the thickness the exterior face sheet by an additional 0.0085 inch, decreasing the measured surface strains by redistributing the loads throughout all available plies. The region of the hoop strain field affected by the diagonal overlay is indicated in

Figure 4.47, with an apparent decrease in hoop strain visible 2.6 inches ahead of the hole. Additional oscillations are also perceptible in both Figure 4.47 and the strain contour plots in Figures A.8 through A.12. These additional oscillations in the DIC strain data are approximately equal in wavelength to the unit cell of the plain-weave prepreg face sheet material. Each unit cell contains alternatingly visible woven fiber tows, each of which has its own localized strain distribution. The combined effect of calculating strain components aligned with only one (or neither) of the visible fiber tows and the filtering of the data masks the influence of the weave. It is important, therefore, to not intentionally filter out the influence of the weave on the DIC strain field. Otherwise, the measured severity of any stress risers would be further diminished.

As mentioned in Section 4.2.4, panels CP3 and CP4 were essentially identical tests, with the only key difference being the realistic in-flight internal pressure and hoop load applied to panel CP3 (Table 4.5) and the nominal pressure and hoop load applied to panel CP4 (Table 4.6). Due to its higher applied hoop loads, panel CP3 was expected to exhibit lower longitudinal strains and fail at a higher longitudinal load than panel CP4. Notch tip strains of 1.2% were measured via DIC ahead of notch tip 2 in panel CP3 at 74% of the panel fracture load (Figure 4.48), producing a 0.566-inch notch tip damage extension, Figure 4.24b. These results are similar to those obtained with panels CP1B and CP5, though the nominal lamina strain in the face sheet mid-ply was 1.41% in the longitudinal direction. Upon loading to 84% of the panel fracture load, longitudinal strains ahead of the damage front in excess of 1.85% were detected prior to the further propagation of damage to 1.139 inches ahead of the notch tip. Excellent correlation between the strain gage and DIC data was maintained for the entire loading range, indicating nearly equal rates of damage propagation from the two notch tips.

Panel CP4 exhibited consistently higher notch tip and far-field longitudinal strains than panel CP3 (Figure 4.49), though visible damage propagated to only 0.615 inch ahead of notch tip 2, Figure 4.31d; note that panel CP3 failed at a higher longitudinal load than that applied to panel CP4 (1507 lbf/in versus 1470 lbf/in, respectively). Similar to the early stages of damage

development in panel CP3, longitudinal strains of 1.2% occurred at 67% of the maximum load, preceding the observed 0.413-inch damage extension, Figure 4.31b. However, at 92% of the maximum load, strains in excess of 1.9% were measured, driving the formation of the 0.615-inch damage extension; longitudinal strains over 2.1% occurred while under the maximum applied load without any additional observed damage propagation.

The notch tip strain gages of panel CP6 were oriented to record the notch-normal strains ahead of notch tip 1 (Figure 4.42), which recorded strains consistently greater than those measured ahead of notch tip 2 using the DIC system, Figure 4.50. Throughout loading, however, good correlation was observed between the two data sets at distances greater than one inch ahead of the notch tips. Indications of failure ahead of notch tip 1 were observed in the strain gage data as early as 58% of the panel fracture load. No such indications (e.g., nonlinearity of strain response, failure of strain gage, etc.) were observed for the material ahead of notch tip 2 at this load level. The higher strains ahead of notch tip 1 and the earlier indications of damage indicate a more severe state-of-strain (due to the combined effect of variations in load, quality of the machined notch tips, location of the notch tips with respect to the weave, etc.) than that ahead of notch tip 2.

Visible notch tip damage was observed ahead of notch tip 2 at 65% of the panel fracture load, Figure 4.43a. However, as mentioned, no indications of any change in the state-of-damage ahead of notch tip 2 were recorded via the strains along the axis of the notch. The non-self-similar damage progression prevented the detection of the damage in Figure 4.50, illustrating the importance of full-field measurements and inspections.

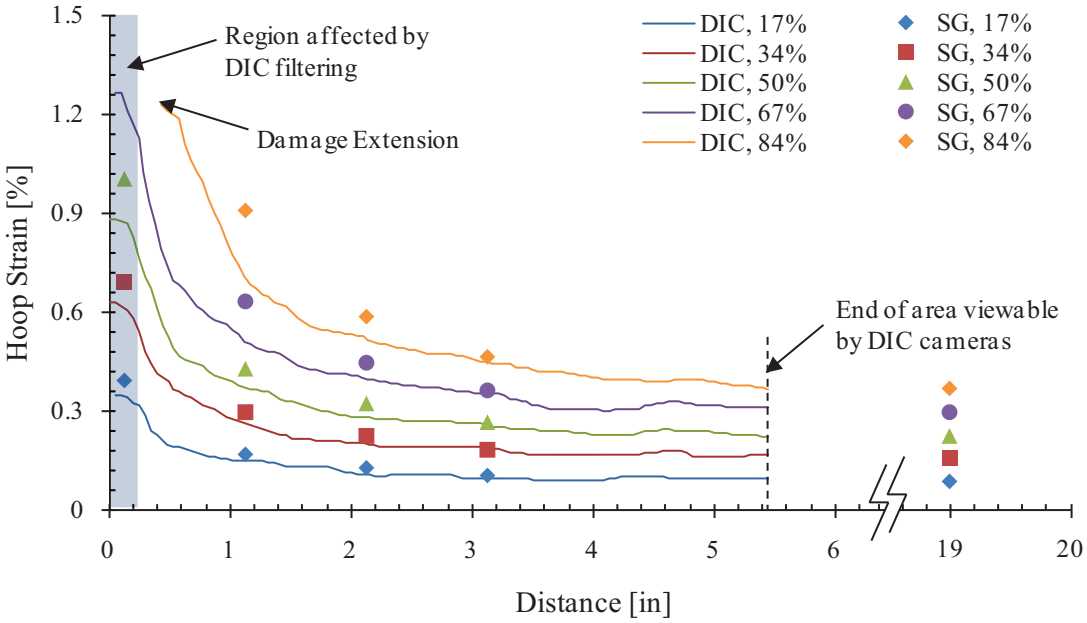

Figure 4.46. Comparison of notch tip hoop strains as measured via the DIC system and the set of strain gages in panel CP1B, test CP1B-RST-1. The DIC strain data were taken from the set of contour plots represented in Figure A.2.

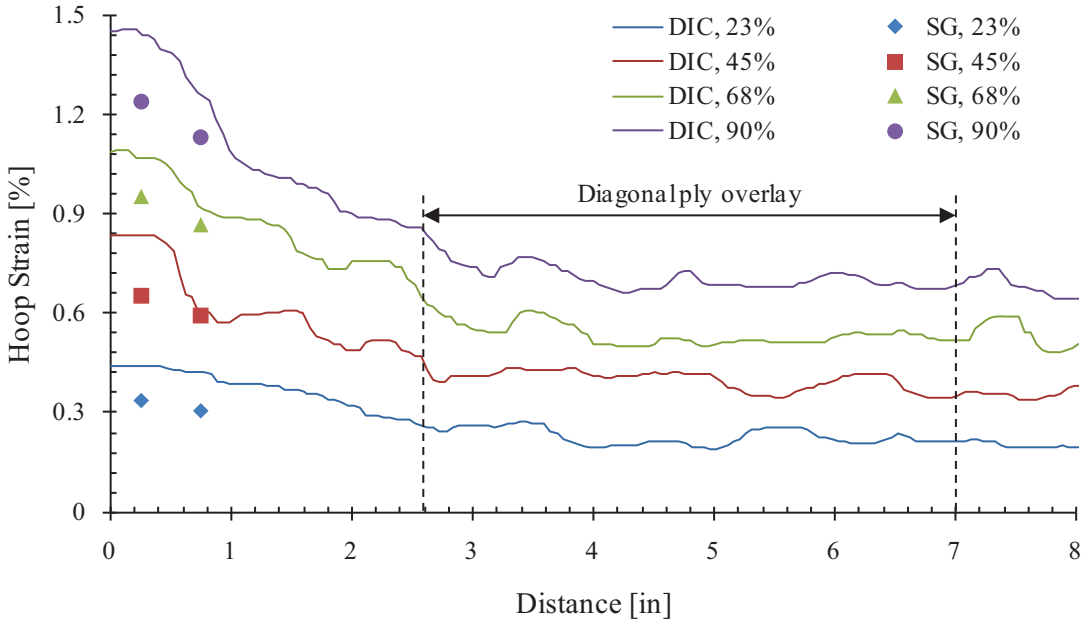

Figure 4.47. Comparison of hoop strains along the crown of the panel, as measured via the DIC system and the set of strain gages in panel CP2, test CP2-RST-H3. The DIC strain data were taken from the set of contour plots represented in Figure A.8.

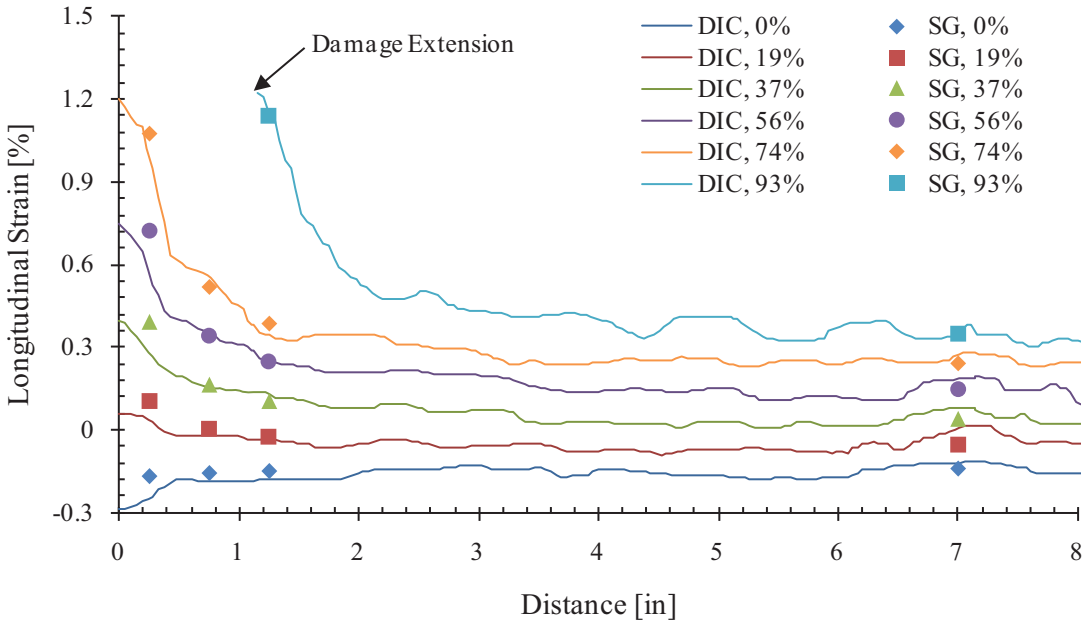

Figure 4.48. Comparison of notch tip longitudinal strains as measured via the DIC system and the set of strain gages in panel CP3, test CP3-RST-1. The DIC strain data were taken from the set of contour plots represented in Figure A.13.

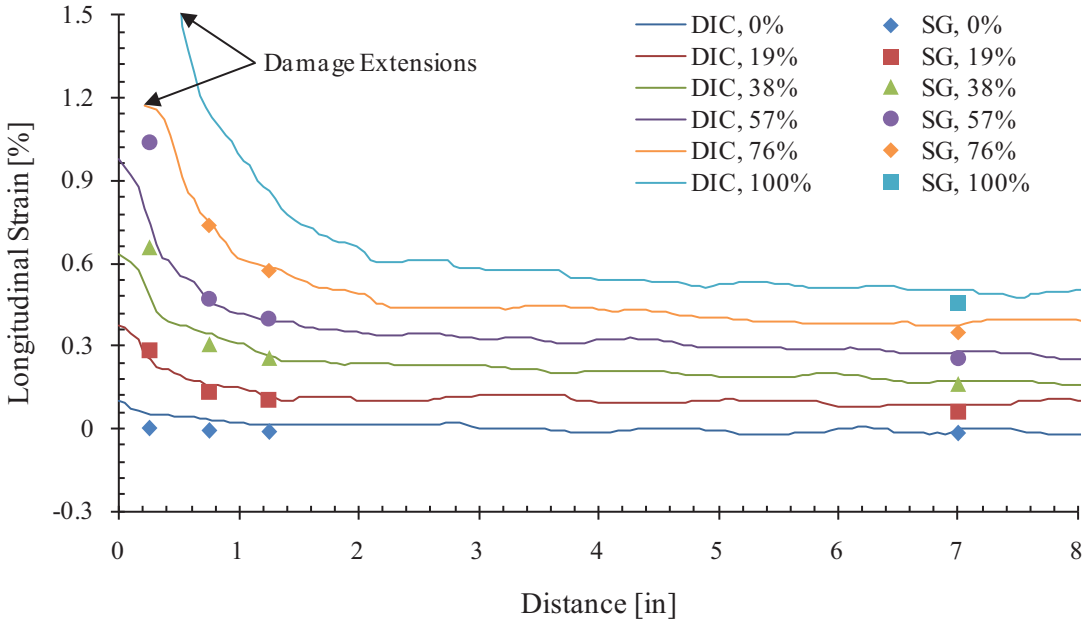

Figure 4.49. Comparison of notch tip longitudinal strains as measured via the DIC system and the set of strain gages in panel CP4, test CP4-RST-1. The DIC strain data were taken from the set of contour plots represented in Figure A.19.

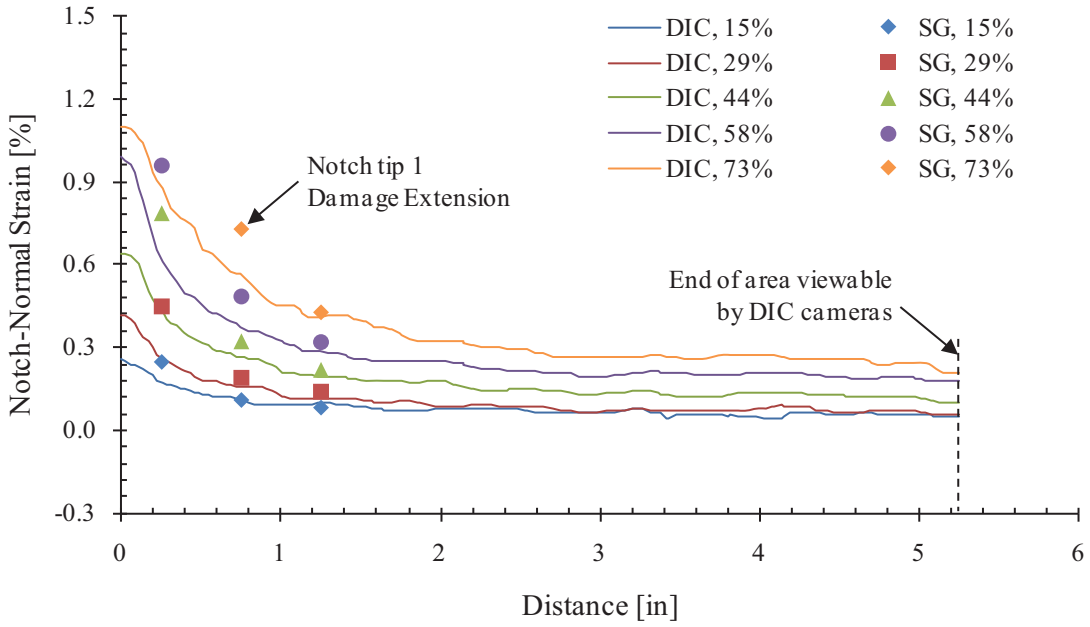

Figure 4.50. Comparison of notch tip notch-normal strains as measured via the DIC system and the set of strain gages in panel CP6, test CP6-RST-1. The DIC strain data were taken from the set of contour plots represented in Figure A.31.

The plain-weave unit cells containing the machined notch tips in panels CP3 and CP4 failed at strains lower than the nominal lamina failure strain, while the continued propagation of damage occurred at significantly higher strains. Amongst all the panels, scatter was observed in the initial notch tip failure strains. This variability was associated with the machining of the notch tip with respect to the plain-weave prepreg.

The notch tip, as machined, acted as a defect on the unit cell scale, decreasing the load bearing capacity of the damaged tow. This is a key reason for the scatter in the notch tip failure strain among the various panels. Note that the initial damage extensions were less than the unit cell size of 0.625 inch. This depends, of course, on what portion of the unit cells ahead of the notch were machined. Furthermore, due to the low frequency at which DIC measurements were taken, the magnitudes of the strain driving damage progression are only approximate, likely underestimating the actual material strain immediately preceding failure.

The damage extensions from each notch tip did not precisely follow the axis of the original notch. The paths of damage propagation depended not only on the actual state-of-stress at the notch tip, but also on the plain-weave geometry of the prepreg material. As a result, the locations of the strain gages were not necessarily ahead of or perpendicular to the site of each subsequent failure. Consideration must be paid to the full-field strain results, in which the strain components driving further damage progression and their exact locations within the material can be identified and tracked. This is of particular importance for panels CP4 and CP6, where the path of damage propagation deviated from the notch axis.

4.3.3. IDENTIFICATION OF FAILURE PROCESSES

While the strain gage data and the progression of damage in the notched panels correlated reasonably well, the majority of the notch tip strain gages measured only those strains oriented perpendicular to the original notch tip. These components of strain were assumed to be those which would drive the damage processes due to the applied loading conditions for each notched panel residual strength test. However, because failure may occur in each ply independently, careful consideration of the components of strain in the principal material directions of each ply is essential.

As discussed in detail in Section 4.2.5, panel CP5 exhibited five stages of damage development, including the final catastrophic fracture of the panel, Figure 4.37. Hoop strain contour plots of the panel CP5 notch tip region are presented in Figure 4.51, including DIC data recorded at the load levels that preceded the visible notch tip damage extensions. At 67% of the panel fracture load, prior to the formation of any notch tip damage, the hoop strains formed the typical kidney-shaped strain field, Figure 4.51a. While no visible damage was observed ahead of the notch tip at 80% of the fracture load, hoop strains up to 1.4% were recorded (Figure 4.51b), preceding the formation of the visible damage at 82% of the fracture load, shown in Figure 4.37a. The notch tip damage progression seen in Figure 4.51c is evident by the locus of the strain field

shifting approximately 0.3 inch to the right. The visibility of the damage suggests that the damage occurred in the exterior ±45° ply. However, while damage is present in the exterior ply, failure did not necessarily independently occur there. Sudden high-energy failures in any of the face sheet plies caused collateral damage in the adjacent plies due to the thinness of the face sheets (0.0255 inch). As a result, a failure in the 0°/90° mid-ply would result in visible damage to the exterior ±45° ply. Comparison of the strains in the hoop direction (Figure 4.51b), in the +45° degree direction (Figure 4.52b), and in the -45° direction (Figure 4.53b) indicates that failure likely occurred in the face sheet mid-ply, since the strains along the ±45° fiber directions in the exterior ply did not exceed 0.80% at this load level, which is well below the lamina failure strains. The damage progression in panel CP5 followed this same trend up to its penultimate state-of-damage: the maximum strains were oriented perpendicular to the notch, driving failure in the mid-ply. The mid-ply failures quickly redistributed the stresses to the remaining outer ±45° plies, causing significant shear within the weave, resulting in fiber breakage and matrix cracking along the affected tows, Figure 4.37c.

During the load hold preceding the catastrophic fracture of the panel, the DIC strain contour plots revealed three distinct strain concentrations ahead of the notch tip damage extension, along tows oriented in the -45°, 0° and +45° directions, Figure 4.52f. These strain concentrations are most apparent in the principal (Figure A.29f) and Tresca (Figure A.30f) strain contour plots. The strain concentrations in the ±45° tows appear approximately 0.3–0.4 inch diagonally away from the visible damage front. The subsequent damage extension resulted in the catastrophic fracture of the panel. Such branching of the strain concentrations from the original notch tip illustrate the advantages of performing full-field strain measurements in composite structures. While the final state-of-damage clearly progressed along the axis of the crown of the panel, visible damage also occurred at the location of the strain concentration located along the +45° tow, Figure 4.37e. Matrix cracking along the damaged fiber tows is evident at the location of the strain concentration and within the next unit cell. The DIC notch tip strain fields place the

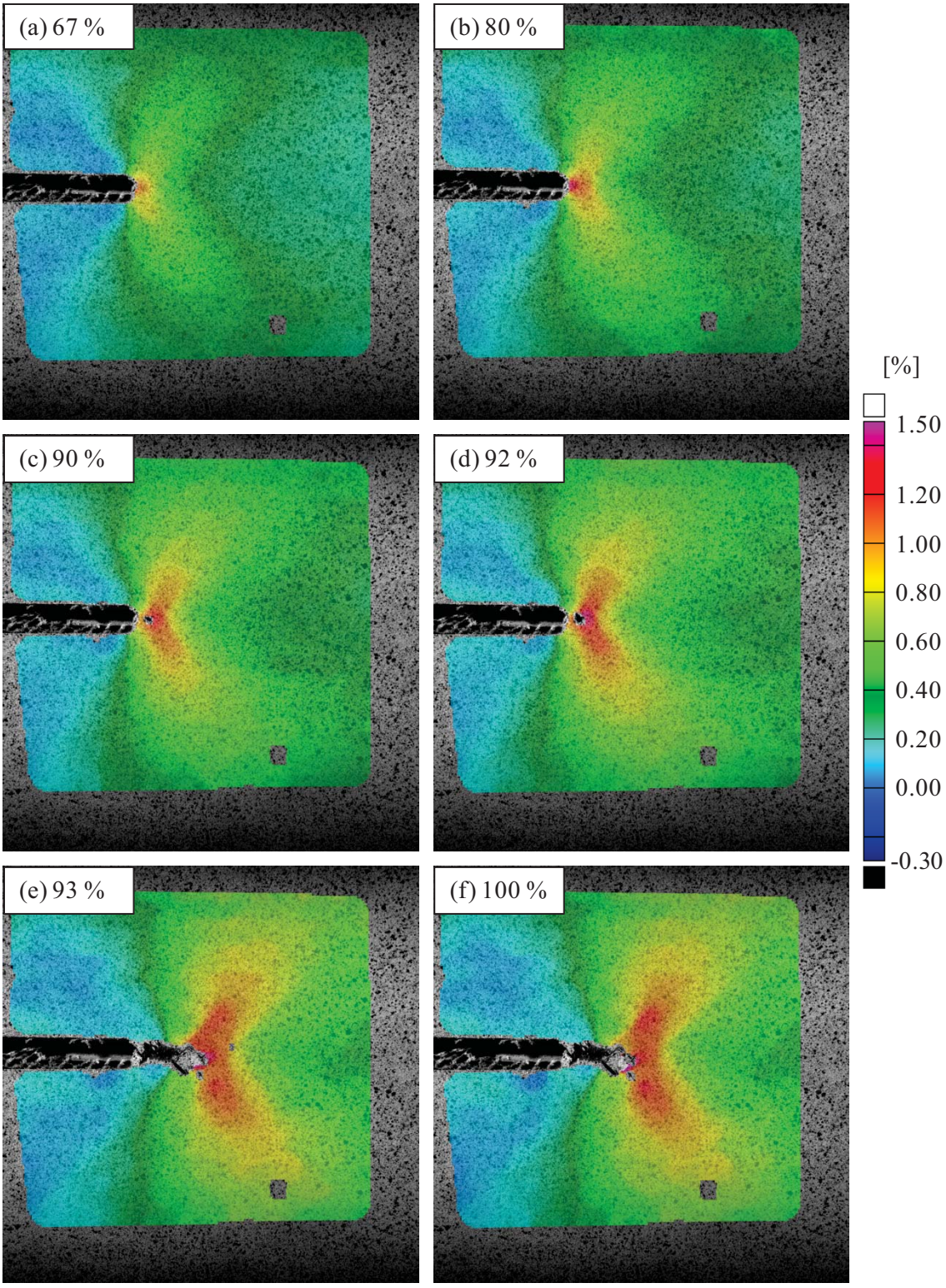

Figure 4.51. Hoop strain contour plot for panel CP5, test CP5-RST-1. The maximum applied load was 13.5 psi internal pressure, 960 lbf/in hoop load, and 100 lbf/in longitudinal load.

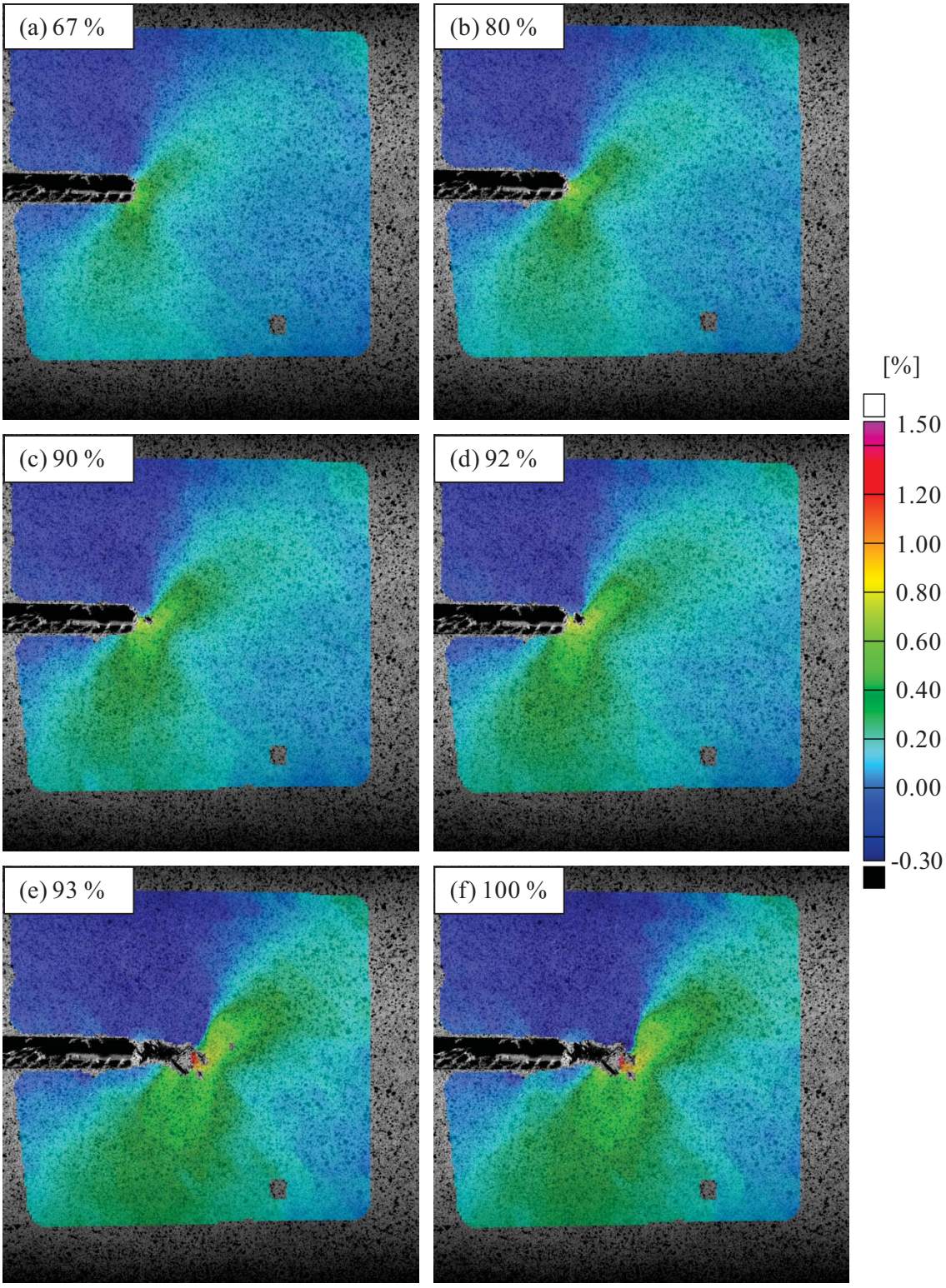

Figure 4.52. Contour plot of the strain in the +45° direction for panel CP5, test CP5-RST-1. The maximum applied load was 13.5 psi internal pressure, 960 lbf/in hoop load, and 100 lbf/in longitudinal load.

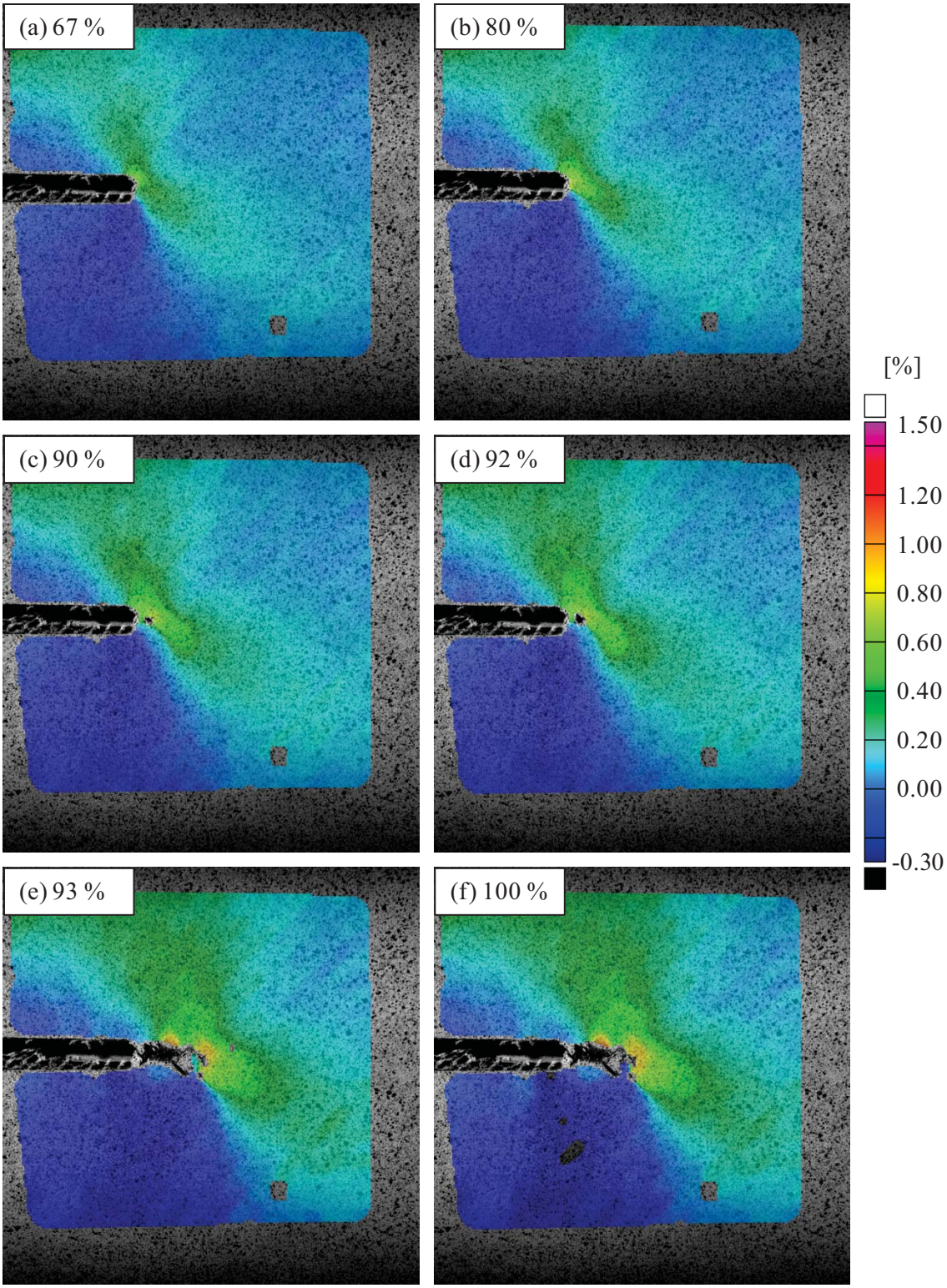

Figure 4.53. Contour plot of the strain in the -45° direction for panel CP5, test CP5-RST-1. The maximum applied load was 13.5 psi internal pressure, 960 lbf/in hoop load, and 100 lbf/in longitudinal load.

visible failure processes in a far richer context, offering insight about which plies failed due to which components of strain, allowing the brief history of the propagation of damage to be better understood.

Similar strain analyses were performed for all other panels tested during this investigation. The strain contours for the remaining panels appear in Appendix A. The appendix includes contour plots of strain oriented in the 0°, 90°, +45°, and -45° panel directions, as well as contour plots of the principal and Tresca strains.

The strain contour plots of the regions ahead of the notches in panels CP1B, CP3, and CP4 revealed generally similar damage processes to those observed in panel CP5. The notches installed in each panel were oriented perpendicular to fiber tows in the 0°/90° mid-ply. In each case, the strains normal to the notch (i.e., those most critical in the mid-ply) were significantly higher than those in the ±45° directions, causing damage to initiate and propagate through the mid-ply. The initial visible damage extended through only the unit cell of the weave which contained the machined notch tip, with the strain concentration at the tip of the initial damage extension remaining close to the original notch axis. Panels CP1B and CP4 offered few stages of visible damage development, making an assessment of the driving forces behind damage progression difficult. Panel CP3, however, exhibited several stages of damage development. Hence, a comparison of the driving forces behind damage progression in panels CP3 and CP5 was conducted.

Prior to panel fracture, the notch tip damage of panel CP3 extended 1.139 inches (Figure 4.24d) and developed an asymmetric elevated strain field with respect to the notch axis, Figure A.13f. The strain contours ahead of the notch tip indicated that the particular geometry of the damage and applied loading configuration caused critical loading of fibers oriented in both the +45° direction in the exterior ply (Figure A.15f) and the 0° fibers of the mid-ply (Figure A.13f). The strain concentrations in the two plies were nearly coincident. As a result, the final fracture of the panel was driven by the joint failure of the two exterior-most plies. This correlates well with

the final state-of-damage, in which widespread matrix cracking was visible along the +45° tows of the exterior ply and the major fracture propagated in the hoop direction, Figure 4.24e. In contrast, the ultimate fracture of panel CP5 exhibited minimal damage at distances away from the major fracture for the first several inches of damage progression (Figure 4.37e), indicating that the failure process was primarily driven by the failure of the inner 90° fibers.

This widespread visible damage did not occur in panels whose failure process was dominated by the failure of the 0°/90° mid-ply. In these cases, the two outer ±45° plies did not fail due to excessively high stresses or strains ahead of the notch, but rather absorbed much of the released fracture energy. As observed, however, the exterior ±45° plies often experienced collateral damage as a result of high-energy failure of the adjacent ply, though this secondary failure process resulted in a far smaller damaged region of the panel surface.

While panel CP4 did not exhibit any signs of failure in the exterior ply, the state-of-strain ahead of the notch tip was more severe than that indicated by the strain data along the notch axis. Under maximum load, principal strains exceeded 1.5% throughout the material within a 0.50 inch radius of the locus of the elevated strain field, Figure A.23f. Significant strains were detected in the 0°, +45°, and -45° directions by the DIC system. The contour plots of the strain normal to the notch axis lost symmetry, with a strong bias along the +45° direction after the notch tip damage extended to 0.615 inch, Figure 4.31d. The final state-of-damage included a small crack oriented in the -45° direction about which an elevated strain field of the strain component in the +45° direction was centered, Figure A.21. The NDI data presented in Sections 5.2.4, 5.4, and 5.5 indicate that subsurface damage extended 1.75 inches away from the notch tip along a +45° tow. Since similar damage propagation was observed in panels CP3 and CP5, it could be assumed that panel CP4 was very close to further damage progression and/or catastrophic fracture just prior to terminating the test.

The residual strength tests of panels CP4 and CP5 each ended just prior to developing more complex states-of-damage, including multiple independent crack paths and relying on

separate components of stress and strain to drive further damage progression. As a result, the majority of the recorded damage progression data characterized only self-similar notch tip damage extensions, driven by a single failure process. The residual strength test of panel CP6, however, exhibited several stages of complex notch tip damage development, offering further insight into the response of the investigated material to realistic flight loading conditions.

As discussed in Section 4.2.6, the nominally equal combined loading of panel CP6 was biased toward generating higher strains in the hoop direction. Regardless, a generally symmetric strain field developed ahead of the notch tip prior to the formation of any damage, Figure A.31a. Visible damage was first observed along the hoop tangent of the notch upon loading to 77% of the panel fracture load, with further visible fiber breakage developing by 82% of the panel fracture load. The major fracture of the panel proceeded along the longitudinal axis of the panel, producing widespread damage along several diagonal tows. The progression of damage through the tows oriented perpendicular to the notch axis and the failures along these tows were driven by separate strain components.

Like all previous panels, the initial failure in panel CP6 was limited to the unit cell through which the notch was machined, Figure 4.43a. Examination of the contour plots of the various components of strain indicated that the highest strains were oriented in the hoop direction, causing the occurrence of the initial failure (Figure A.33a). The locus of the elevated hoop strain field was located approximately 34° away from the notch axis along the semicircular notch tip, corresponding with the location of the initial visible damage. This initial failure occurred in a tow oriented in the -45° direction ahead of the notch. Elevated hoop strains continued to drive further damage progression along the -45° tow through which the original notch tip was machined up to 82% of the panel fracture load, Figure A.33c. For the remainder of the panel CP6 residual strength test, the two mentioned failure processes (i.e., extending the damage front in the longitudinal direction and generating damage along the diagonal fiber tows) were clearly distinguishable. The notch-normal strain field was consistently centered at the location through

which damage progressed to the next fiber tow perpendicular to the notch (e.g., Figure A.31d), while the hoop strain fields were consistently centered near the end of the visibly damaged -45° tows (e.g., Figure A.33d).

While the development of damage involved failure processes located in separate plies, the interactions of the failures seemed to delay the ultimate fracture of the panel, rather than creating a more severe state-of-damage. In panel CP3, the joint occurrence of failures in the exterior and middle plies led to self-similar notch tip damage extensions and led to the catastrophic fracture of the panel; though, in that case, the failures were occurring at the same location, amplifying their combined effect. Here, as the failures driven by the notch-normal strains extended the notch through the weave, failures driven by elevated hoop strains continually blunted the notch tip, as is evident in Figure A.31f. The initial path taken by the damage during the catastrophic fracture (Figure 4.43g) indicates that the hoop strains were the dominant driving force of the final panel fracture, overcoming the blunting caused by the notch-normal strains.

4.3.4. CHARACTERIZATION OF EFFECTIVE DAMAGE EXTENSIONS

The visible extent-of-damage (i.e., the greatest distance between the original notch tip and any visible damage, as measured along the notch axis) as a function of load was presented and discussed for panels CP3, CP4, and CP5 throughout Section 4.2, and is summarized in Figure 4.54. Panels CP1B and CP2 only one stage of visible damage progression was recorded, and the circuitous path of the major fracture through panel CP6 cannot be so simply represented; therefore, data from these three panels are not reported here.

While the extent of visible damage offers insight into regions which have been affected by the propagation of damage, the presence of damage does not translate into the inability of the material to effectively carry load, especially in composites materials. Visible damage may be indicative of only localized matrix cracking while load-bearing fibers may be fully intact. Accordingly, the effective notch tip damage extension is oftentimes smaller than the extent of the

visible damage. Conversely, subsurface fiber fractures could occur ahead of visual damage, or even prior to the first instance of visible damage, effectively advancing the notch tip without offering any visible indication. As a result, the elevated strain fields ahead of the notches which underwent generally self-similar crack growth were examined. Measurements were made from the original notch tips to the locus of the elevated strain field; these results are shown in Figure 4.54.

Throughout the results obtained from each of the three panels, the extent of visible damage typically overestimated the effective notch tip damage extensions, as measured via DIC, throughout loading. This trend was most prominent in panels CP3 and CP5. While the progression of the extent of visible damage with load was stepwise due to the sudden bursts of visible damage extension in these two panels, the strain field locus measurements showed a smoother, exponential-type increase in effective notch extension, Figure 4.54a and c. The results from panel CP4 showed a linear progression of both the visible damage and the strain field locus up to its final state-of-damage, Figure 4.54b. The early stages of damage progression in panel CP4 were quite similar to those exhibited by panel CP3, apparently just short of an additional major damage extension.

The measurements of the damage ahead of the notch tip discussed in this chapter will play an important role in the development and validation of the local FE models discussed in Chapter 8. The extent of visible damage serves only as an indication of a failure of unknown severity or criticality at some distance ahead of the notch tip. Measurement of the strain field locus indicates the effective notch tip damage extension and can be compared with the results of FE models, assessing the full three-dimensional state-of-damage ahead of the notch tip and determining how far the center of the elevated strain field was displaced.

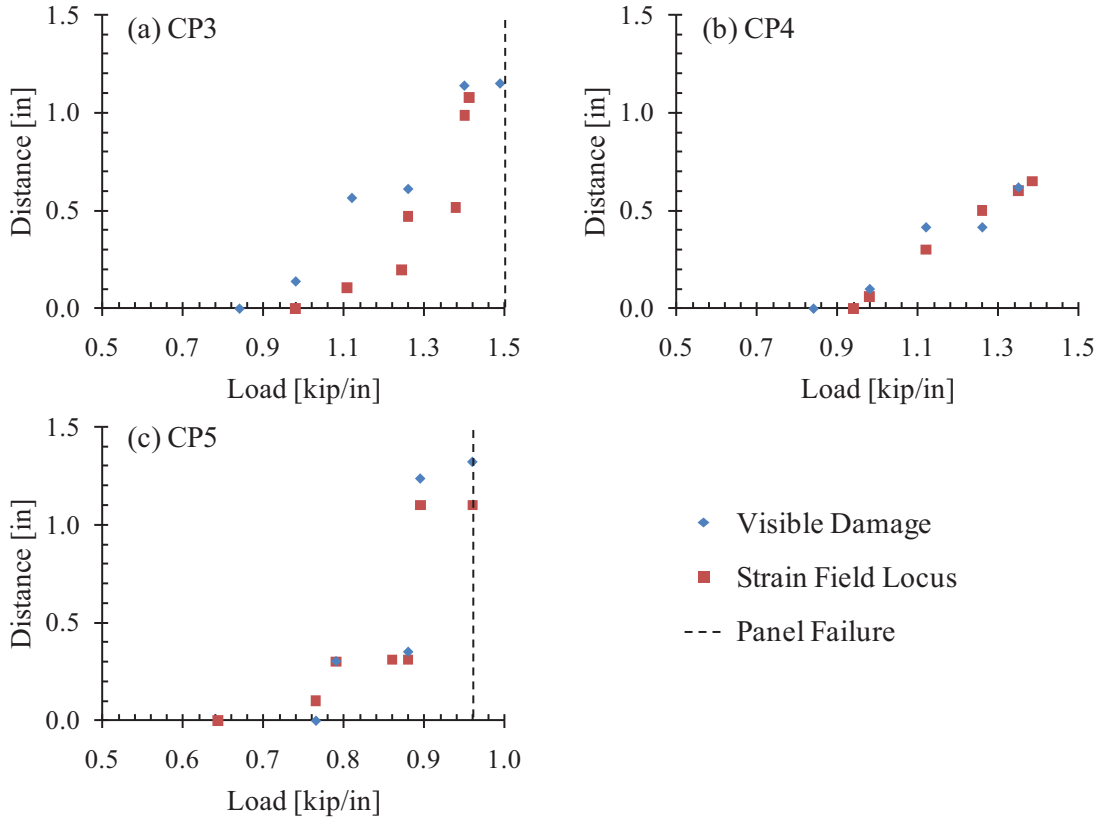

Figure 4.54. Comparison of visible notch tip damage extensions, as measured along the axis of the original notch, and the locus of the strain field ahead of the notch tip, as measured via DIC.

4.4. CONCLUSIONS

A series of strain surveys and residual strength tests were conducted for each of the full-scale honeycomb sandwich composite aircraft fuselage panels. During these tests, the deformation and strain response of the panels were measured using sets of strain gages and the digital image correlation (DIC) method. The loading fixture performed well throughout the testing of each panel. However, some loaders exceeded their capacity and failed to reach their target loads during the final load steps of particularly high-load tests. All such deviations and the actual applied loads were documented. Slight bending of the panels was detected through comparisons of the exterior and interior strain gages, though such bending was low in the areas of interest and were masked by the significant bending due to the artificial damage. Despite the

severity of the inserted artificial damage modes, each of the panels withstood loads far exceeding realistic flight loading conditions.

The strain increased linearly up to the initiation of damage at the notch tips. The notch tip strain gage histories depicted the progression of the damage from the notch tips, showing sudden bursts of damage progression, tending to abruptly extend through whole fiber tows. The carbon/epoxy laminae failed upon reaching the nominal failure strains, though the severity of the failures depended on the ply location within the laminate (i.e., failures in the mid-plies were constrained by the exterior plies, while failures in the exterior plies tended to affect distant portions of the failed tows). Photographic records of the damage initiation and propagation were recorded. As a result, the strain gage behavior was associated with the physical damage processes. The data recorded with the strain gages and the DIC system correlated very well in the regions ahead of the artificial damage in each panel.

The DIC data offered the ability to determine the distribution of the various components of strain necessary to evaluate the notch tip failure processes. By identifying the strain components that were responsible for damage formation and progression, the specific plies undergoing failure were identified. While most of the notched panels exhibited primarily self-similar notch tip damage extensions, panel CP6 exhibited clearly separate failure modes driven by separate strain components. The photographic records of the notch tip damage provided information regarding the locations of failures, though the distance from the original notch tips to the loci of the elevated notch tip strain fields proved to be a more useful measure of effective notch tip damage extension.

The data presented in this chapter are complemented by the extensive nondestructive inspection (NDI) data collected before, during, and after the residual strength tests. This NDI data are presented in Chapters 5 through 7. Together, a rich knowledge base exists concerning the development of the deformation and strain fields of the panels as a result of critical loading

and the damage which formed as a result. These data are used extensively in the development and validation of the FE models presented in Chapter 8.

CHAPTER 5: NONDESTRUCTIVE INSPECTIONS

5.1. INTRODUCTION

Several methods were used to qualitatively and quantitatively characterize the state-of-damage in the sandwich composite fuselage panels that were tested in this investigation. This chapter describes the internal damage as recorded via several nondestructive inspection (NDI) techniques, including thermography, computer-aided tap test (CATT), ultrasound, and x-radiographic computed tomography (CT). Additionally, the fracture surface morphology was examined via scanning electron microscopy (SEM).

5.2. THERMOGRAPHY

As mentioned in Section 3.8.3, thermography data were recorded before and after the loading of each panel. Panel CP1B was the first panel to exhibit any measureable damage growth and will be the first case discussed here. For the case of panel CP1B, only the region in the immediate vicinity of the notch was inspected prior to loading; damage formation and propagation was assumed to be localized to this region. However, as discussed in Section 4.2.1, the final state-of-damage was much more severe, extending the entire length of the panel. Posttest thermographic inspections were performed throughout the region affected by the panel fracture, although baseline data did not exist for this entire region.

Because of the widespread fracture exhibited by panel CP1B, the entire test section of all remaining panels was scanned prior to the residual strength tests. However, the baseline thermography data of all later panels revealed only details of the internal structure of the sandwich composite panels, detecting no additional unknown initial damage sources. Therefore, a full discussion on the pre- and posttest results of panel CP1B is presented here, involving the structural components of the sandwich composite, the effect of the major fracture on performing thermographic measurements, and the final state-of-damage of the panel. Additionally, posttest

results obtained from the exterior face sheet hole in panel CP2, the circumferential notch in panel CP4, and a large skin-to-core disbond discovered in panel CP5 are presented and discussed.

As discussed in Section 2.2.5, the dissipation of energy into a sample can be explicitly modeled if the thermal properties (such as thermal conductivity and specific heat) of the examined material are well known. However, due to the different properties of the constituent materials and the sandwich composite configuration of the panel, a quantitative assessment of the thermographic data becomes very difficult. Therefore, the focus here is on the qualitative assessment of the internal damage, noting the relative differences in the surface temperature and its first and second time derivatives. Accordingly, the physical meaning is detached from the color scales for the collected data; the color scales in the following figures were simply selected to optimize the clarity of each image.

5.2.1. PRETEST RESULTS OF PANEL CP1B

A thermographic image of a section of panel CP1B, prior to loading, is shown in Figure 5.1. The figure shows a composite image of nine thermographic measurements. The first derivative of the surface temperature with respect to time is displayed to highlight the differences in the rate of heat dissipation. Several of the structural elements of the composite are visible, including hoop and longitudinal core splices, several internal ply overlays, the plain-weave pattern of the prepreg face sheet material, and the 10-inch long by 1/16-inch wide notch.

No preexisting damage was identified in the immediate vicinity of the notch via the inspection of the raw thermographic data or its derivatives. However, several nonvisual damaged areas were identified post-fracture, in addition to the visual damage resultant of the panel fracture.

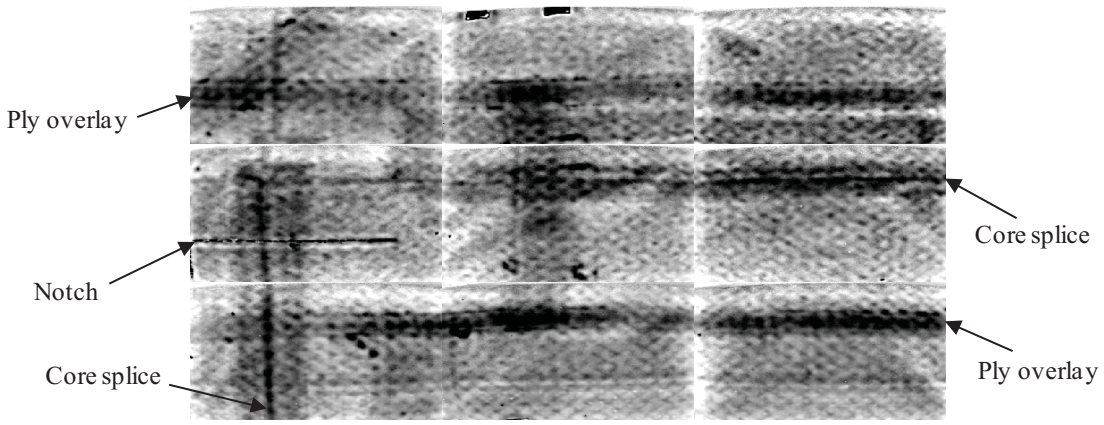

Figure 5.1. First derivative of temperature with respect to time of panel CP1B in the immediate vicinity of the notch, prior to loading the panel to fracture.

5.2.2. POSTTEST RESULTS OF PANEL CP1B

Figure 5.2 is a composite thermographic image of the raw surface temperature data of the damage propagated from the notch. This is the notch tip monitored by the DIC system (Section 4.2.1, and Figures A.2 through A.7). A grid of 7 images in the longitudinal direction by 3 images in the hoop direction was used to construct the figure, with the notch tip located on the left. Ply overlays are visible in the exterior ±45° layer, as well as in the mid-ply (i.e., in the hoop and longitudinal directions).

Outside the major fracture, matrix cracking and damage to the plain-weave structure of the face sheet fabric material is very apparent (the dark regions in Figure 5.2). The exterior face sheet ply contained ±45° fiber tows which had been pulled out of the weave, resulting in matrix cracking extending several inches away from the major fracture. This failure of the weave caused separations between tows within individual plies and between the adjacent plies.

The presence of the severe surface damage made thermographic inspections in the immediate vicinity of the fracture largely ineffective; the majority of the heat tended to dissipate into the fracture rather than through the remaining intact material. However, thermographic measurements taken from regions which did not include the major surface damage did reveal

subsurface damage. Figure 5.3 shows the first derivative of temperature with respect to time of the highlighted region in Figure 5.2. Darker regions in plots of the first derivative of temperature with respect to time represent lower cooling rates, which are often indicative of subsurface gaps, voids, or inclusions which impede the flow of heat into the material. Two such indications of subsurface flaws are visible in Figure 5.3.

Similar results were obtained from examination of the thermographic data obtained from the damaged region ahead of the opposite notch tip, Figure 5.4. The structural components of the composite (e.g., ply overlays) are clearly visible, however, the severity of the major fracture of the panel made inspections in the vicinity of the through-thickness damage immaterial. As a result, the derivatives of the highlighted region in Figure 5.4 were examined for any indications of possible subsurface damage, Figure 5.5. Lower cooling rates were observed in one region,

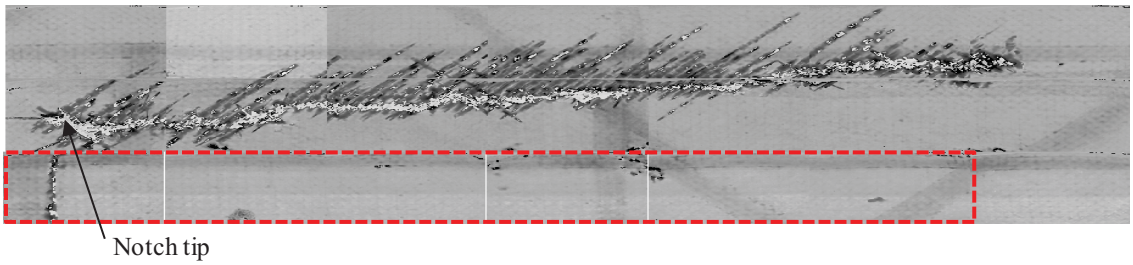

Figure 5.2. Surface temperature data taken from the external surface of panel CP1B, showing the damage propagating from the notch tip monitored by the DIC system. The notch tip is on the left side of the figure.

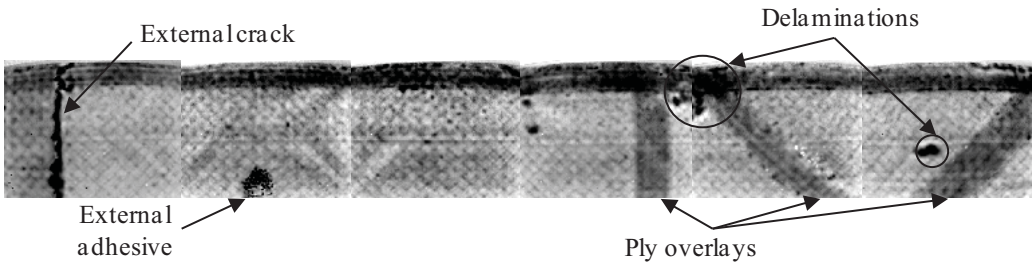

Figure 5.3. First derivative of temperature with respect to time of the highlighted region in Figure 5.2. CATT data from this same region is displayed in Figure 5.11.

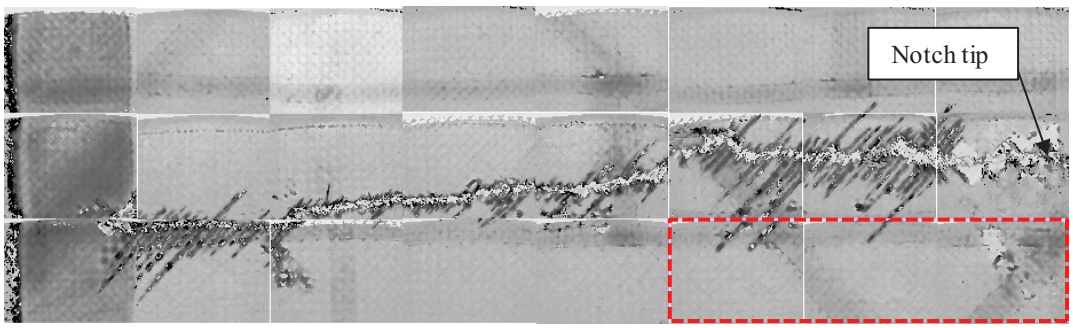

Figure 5.4. Surface temperature data taken from the external surface of panel CP1B, showing the damage propagating from the notch tip not monitored by the DIC system. The notch tip is on the left side of the figure.

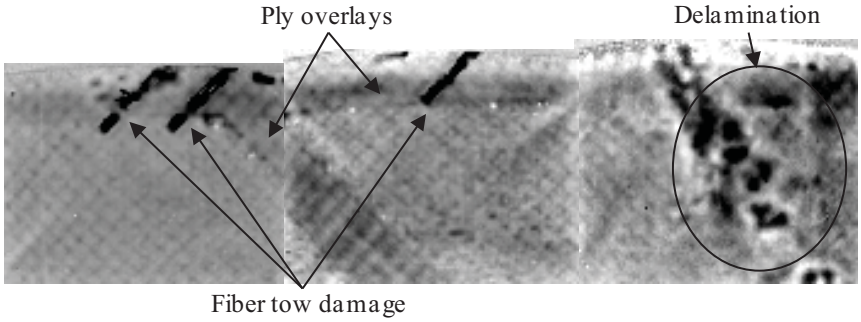

Figure 5.5. First derivative of temperature with respect to time of the highlighted region in Figure 5.4. CATT data from this same region is displayed in Figure 5.12.

indicative of a possible delamination. Comparisons of these thermographic images with CATT results (Section 5.3) of the same regions confirmed the presence of delaminations.

5.2.3. POSTTEST RESULTS OF PANEL CP2

As explained in Section 4.2.2, several attempts were made to load panel CP2 to failure under various loading configurations (i.e., internal pressurization and hoop loading; longitudinal loading; and combined internal pressurization, hoop loading, and longitudinal loading). Visual damage was observed after the last attempt (Figure 4.18), though the damage was highly localized. As discussed in Section 4.3.2, the hoop strains recorded along the edge of the hole

were indicative of subsurface failures occurring over a larger area in the exterior face sheet mid-ply.

Figure 5.6 shows the second derivative of temperature with respect to time in the region of panel CP2 where visual damage was observed. The dark region along the edge of the hole in the thermographic image corresponds to the observed visual damage, which indicates the likely presence of a delamination at this site. Matrix cracking and damage to the woven fiber tows in the mid-ply, similar to those observed in the latter stages of damage development for panels CP3 (Figure 4.24), CP5 (Figure 4.37), and CP6 (Figure 4.43), would cause interlaminar separations to form between the adjacent plies. Therefore, the presence of subsurface damage at this location would correlate well with expectations.

5.2.4. POSTTEST RESULTS OF PANEL CP4

Panel CP4 was the only notched panel to not fail catastrophically. However, the final load applied was very near the apparent fracture load. Therefore, it offers a unique opportunity to study the state of nonvisual damage at a stage of damage progression quite near catastrophic fracture. It should be noted that the development of notch tip damage in those panels that failed

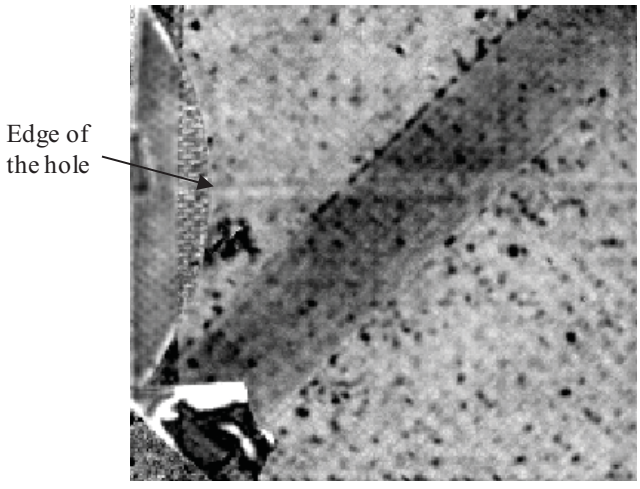

Figure 5.6. Second derivative of temperature with respect to time after 9.009 seconds for a region containing the hoop tangent to the hole of panel CP2.

catastrophically is largely obscured by their sudden, explosive fracture. Figure 5.7 shows the first derivative of temperature with respect to time at three different times after the surface was heated. The notch tip damage is clearly visible in all three frames, extending approximately 1.75 inches diagonally from the notch tip; this is considerably more severe than the observed visual state-of-damage at the maximum applied load, which extended only approximately 0.50 inch diagonally, Figure 4.31d.

As time progresses after a surface is initially heated, the thermographic data corresponds to states-of-damage deeper in the material. In addition to the notch and notch tip damage, Figure 5.7a clearly shows the plain-weave pattern of the face sheets, a diagonal ply overlay, and an area where the DIC coating had been damaged to the right of the notch. The internal details of the sandwich composite become visible at later cooling times, Figure 5.7b.

In Figure 5.7c, an arc segment is visible ahead of the notch, with a square grid with similar thermal behavior outside this arc. These guide fibers, placed between the honeycomb core and face sheets, were used during the construction of the face sheets to aid in properly laying

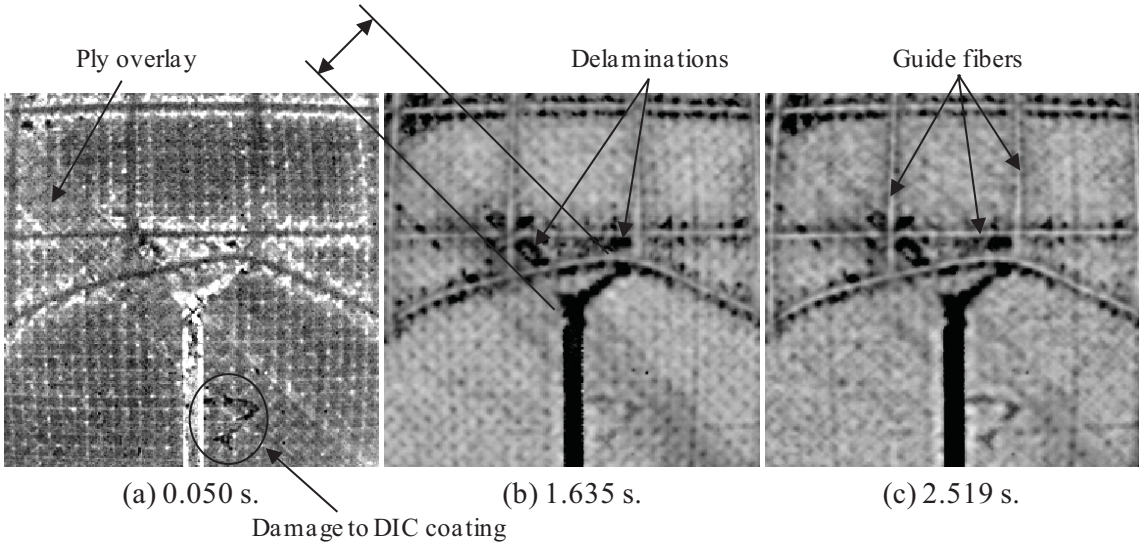

Figure 5.7. First derivative of temperature with respect to time after (a) 0.050, (b) 1.635, and (c) 2.519 seconds for panel CP4.

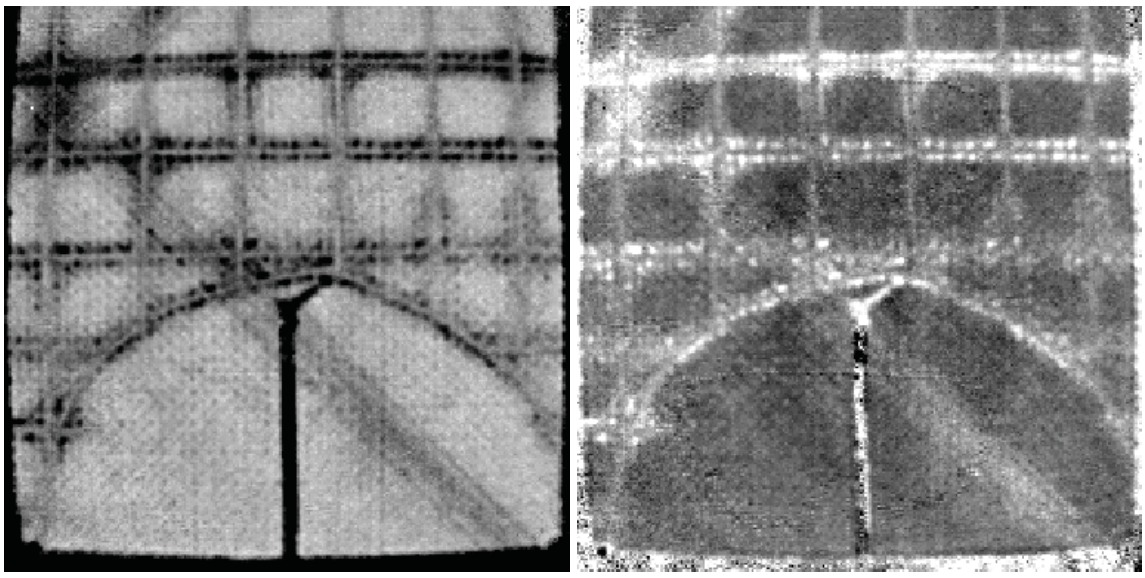

(a) (b)

Figure 5.8. (a) First derivative of temperature with respect to time after 1.251 seconds, and (b) second derivative of temperature with respect to time after 3.237 seconds for the notch tip of panel CP4 monitored by the DIC system.

up the plies and machining the notch. Thermographic scans over a larger region were performed to show these details more clearly, Figure 5.8. The exact location of the guide fibers through the thickness of the sandwich composite will be more clearly presented in an x-radiographic CT scan, discussed later.

Along the grid of guide fibers, regions of decreased cooling rates are seen in Figure 5.8a. This is indicative of possible delaminations occurring due to the presence of the guide fibers. However, no correlating indications were found using the other inspection methods.

5.2.5. DETECTION OF DISBOND IN PANEL CP5

A large, elliptical, skin-to-core disbond was discovered in panel CP5 while installing strain gages on the exterior surface. While nonvisual, the panel deformed freely in the out-of-plane direction upon manually applying any load to the exterior face sheet in the disbonded region, and the fretting between the honeycomb core on the face sheet was clearly audible. The

dimensions of the disbond were estimated to be approximately 14 inches along its major axis, parallel to the longitudinal direction of the panel, and 9 inches along its minor axis, along the hoop direction.

Thermographic measurements were taken from the exterior face sheet to confirm the estimated disbond dimensions, Figure 5.9a. However, no variations in the surface temperature or its derivatives were observed. This was initially attributed to the effective thermal properties of the honeycomb core, which are generally similar to those of a void caused by a disbond.

Honeycomb cores have a very low density, and, in terms of percent volume, consist mostly of empty space. As a result, most of heat is dissipated into the empty core space rather than into the core material itself. Furthermore, the bonded area between a honeycomb core and the face sheets is relatively small in proportion to the total face sheet surface area, offering few paths along which heat could travel. Therefore, the effective thermal properties of a good bond, a poor bond, and no bond at all vary very little, making the assessment of the bond quality via thermography very difficult. All this suggests that disbonds are difficult to detect in honeycomb sandwich composites and that inspections ought to be performed from both the interior and exterior surfaces of such composites. Consequently, a set of thermographic images were taken of the interior surface of the sandwich composite.

The thermographic measurements from the interior face sheet revealed that the elliptical disbond was indeed between the interior face sheet and the honeycomb core, and confirmed the estimated dimensions, Figure 5.9b. Several features, such as ply overlays, an aluminum connection plate for a radial link assembly, and a repair patch, can be seen in Figure 5.9b. Figure 5.10 shows the first and second derivatives of temperature with respect to time at times selected to enhance the clarity of the repair patch and the surrounding material. The location of the skin-to-core disbond underneath a repair patch suggests that either the repair was an effort to treat the disbond, or the disbond was a result of the repair patch installation.

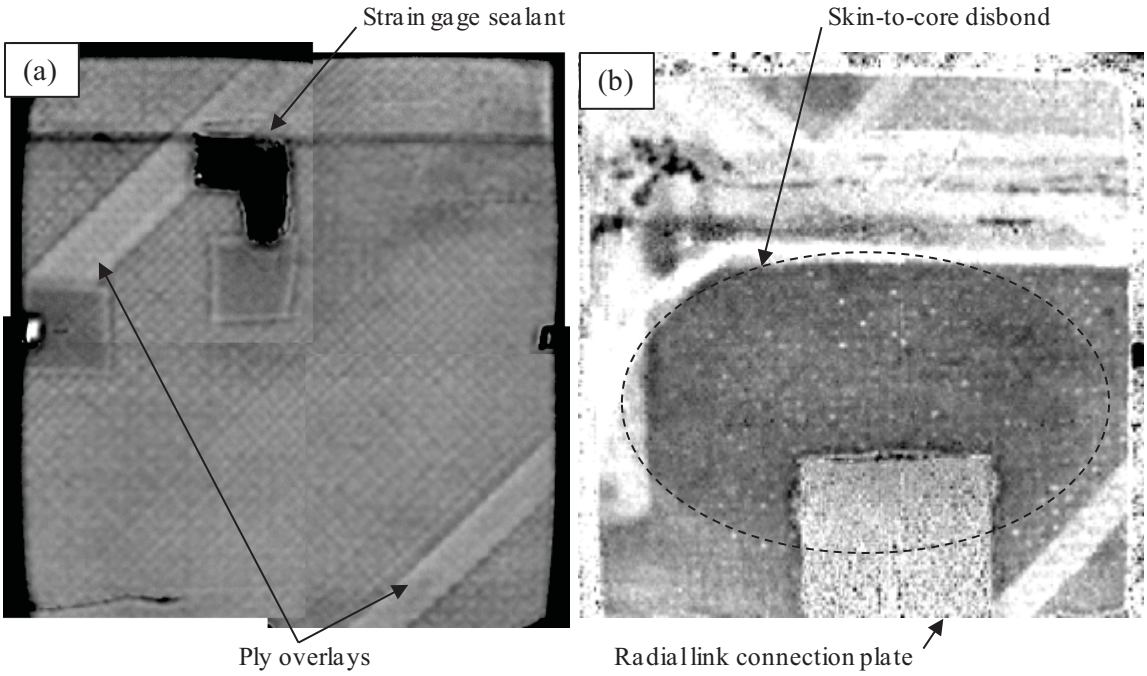

Figure 5.9. (a) First derivative of temperature with respect to time after 4.138 seconds from the exterior, and (b) the second derivative of temperature with respect to time after 2.519 seconds, taken from the interior of panel CP5.

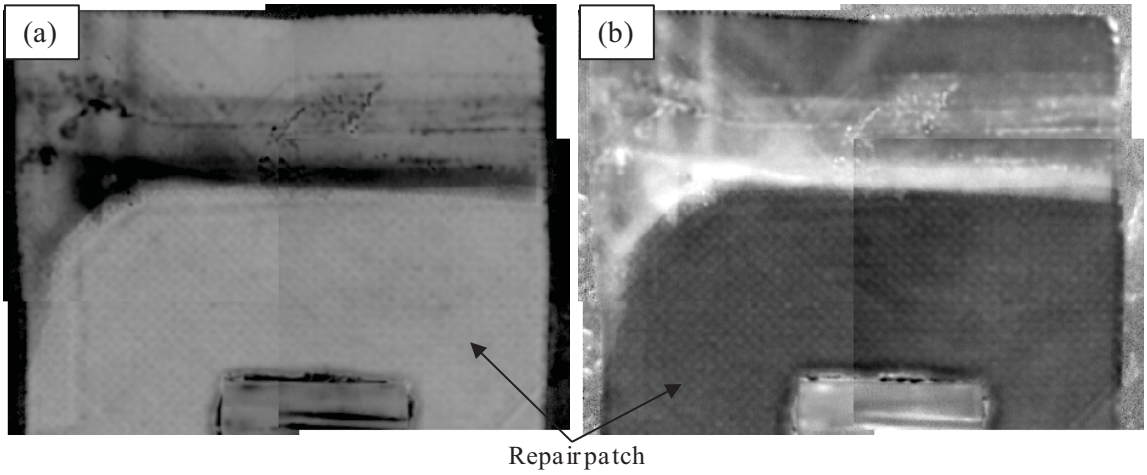

Figure 5.10. (a) First derivative of temperature with respect to time after 3.971 seconds from the exterior, and (b) the second derivative of temperature with respect to time after 7.324 seconds, taken from the interior of panel CP5.

5.3. COMPUTER-AIDED TAP TEST

Computer-aided tap test (CATT) inspections were initially planned to be performed before and after each panel test in the immediate vicinity of the suspected failure sites. However, CATT inspections are very time-intensive; one manual tap inspects a 0.0625 square inch area, requiring 480 individual taps to inspect an area equivalent to the area inspected by a single thermography scan. Therefore, posttest inspections were limited to regions suspected of containing nonvisual damage, as per the results of other wide-field inspection methods (i.e., thermography). Pretest thermography scans indicated that no significant nonvisual damage was present in the panels with few exceptions, such as the large disbond in panel CP5.

Comparison between the thermography results and the stiffness contour plots generated from the impact duration data of the CATT system offered greater confidence in both the accuracy and the interpretations of the results of both systems. Selected regions of panel CP1B that were inspected via thermography were examined using the CATT system. Figure 5.11 shows a stiffness contour plot corresponding to the thermography inspection of the region of panel CP1B shown in Figure 5.3. Overall, the two measurements compare very well with each other. The area suspected to be delaminated (due to its reduced cooling rate as measured via thermography) had a lower stiffness than the surrounding material, further supporting the finding of the delaminated area. The hoop-oriented external crack and ply overlays are also visible. Figure 5.12 is analogous to Figure 5.5, providing a similar validation of the identification of a delamination.

Pretest and posttest inspections were performed in the region of panel CP5 containing the large skin-to-core disbond, Figure 5.13. The CATT inspections were performed from the exterior face sheet. Unlike the thermography inspections from the exterior (Figure 5.9a), CATT successfully detected and characterized the disbond. Comparison of the pre- and posttest results indicate some disbond growth, though the increased tap duration (and corresponding reduced stiffness) of the region within the disbond suggests a more complete separation between the core

and the face sheet. It should be noted, however, that the posttest inspections were performed long after the test, and after the region containing the disbond was cut out of panel CP5 with a reciprocating saw.

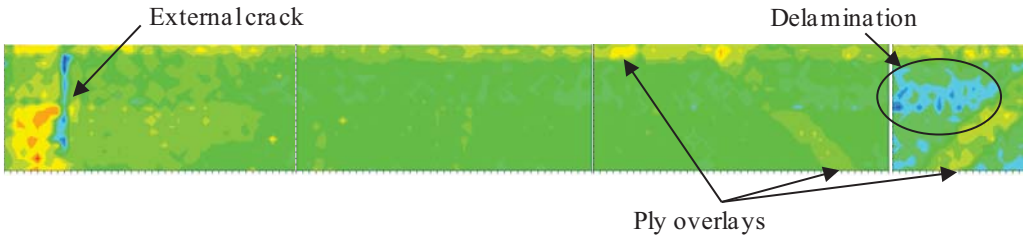

Figure 5.11. Stiffness contour plot of the region of panel CP1B shown in Figure 5.3.

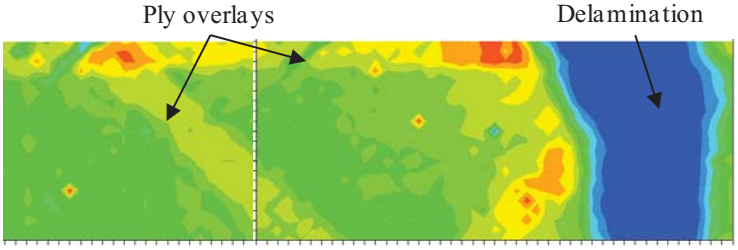

Figure 5.12. Stiffness contour plot of the region of panel CP1B shown in Figure 5.5.

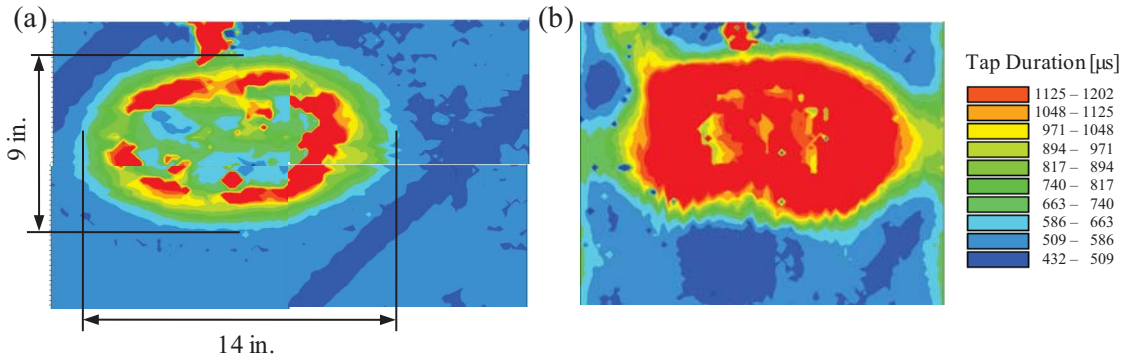

Figure 5.13. Tap duration contour plot of the skin-to-core disbond in panel CP5 taken from the exterior face sheet, (a) pretest and (b) posttest, showing extension of the disbond.

5.4. ULTRASOUNIC INSPECTIONS

As discussed in Section 3.8.5, posttest ultrasonic inspections were performed for three samples, taken from panels CP2, CP4, and CP5. Panel CP2 was inspected along the hoop and longitudinal tangents to the exterior face sheet hole, the notch tip region of panel CP4 was inspected, and the large disbond in panel CP5 (detected via thermography and CATT) was inspected, as well.

Time-of-flight and amplitude results from the ultrasonic pulse-echo inspections of panel CP2 are shown in Figure 5.14, with a schematic of the hole showing the relative locations and dimensions of the inspected regions. The time-of-flight data clearly revealed the structural components of the face sheet, such as the longitudinally oriented core splice, the diagonal ply overlay, and the plain-weave structure of the exterior ply, Figure 5.14a. This image correlates well with the thermographic image shown in Figure 5.6. Also visible in the time-of-flight plots are several doughnut-shaped discolorations scattered throughout the inspected regions. These are the imprints of the base supports of the thermographic inspection equipment. The slight surface indentations were made while resting the equipment on the panels during earlier inspections.

Regarding the color scale of the time-of-flight data, black and orange are representative of short time-of-flight values (indicative of discontinuities close to the inspected surface) while dark blue color represents long time-of-flight values, tuned to the maximum thickness of the specimen. However, the skin-to-core interface tends to reflect the transmitted ultrasonic signals, whether pulse-echo or through-transmission. Therefore, the effective maximum thickness of the specimens is that of the face sheets, not of the full sandwich composite.

The black and orange regions along the edges of the time-of-flight plots correspond to tape on the surface used to seal the specimen edges from the water couplant used during the inspections. This is clearly seen along the edge of the hole at the bottom of Figure 5.14a and the left side of Figure 5.14c. The light green region protruding diagonally away from the hole edge in Figure 5.14c corresponds to the location of the visual damage (Figure 4.18), and is indicative

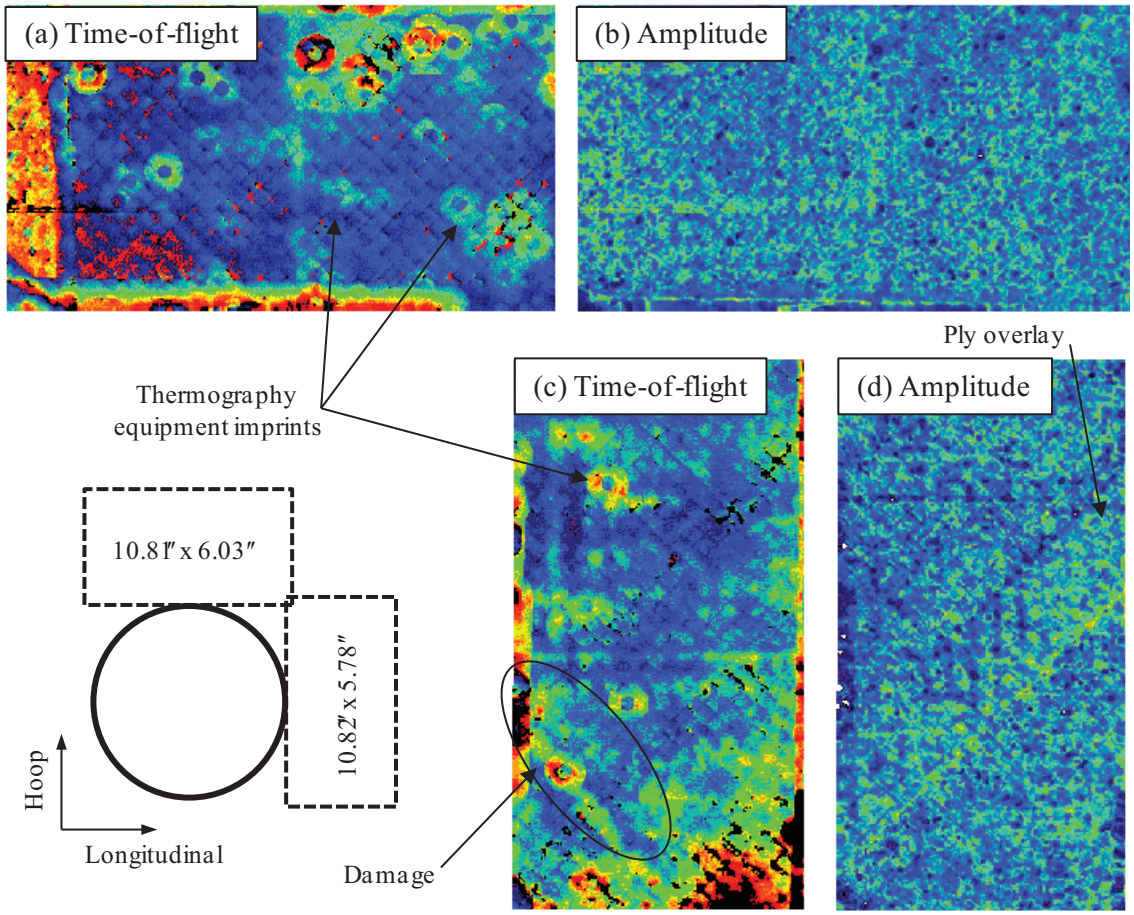

Figure 5.14. Ultrasound scans of panel CP2 at 15 MHz, showing (a) time-of-flight and (b) amplitude plots of the longitudinal tangent of the hole, and (c) time-of-flight and (d) amplitude plots of the hoop tangent of the hole.

of a discontinuity between the plies of the face sheet. This corresponds well with the thermographic images discussed in Section 5.2.3.

The structural components of the composite are visible in the amplitude plots, but with less clarity than the time-of-flight data. Also, no clear indication of damage was observed in the region that contained visual damage in the amplitude plots.

Ultrasonic inspections of the notch tip of panel CP4 were performed at 10 and 15 MHz, Figure 5.15. Similar results were recorded using the two frequencies. However, it is clear for this case that the higher frequency inspection offered better through-thickness resolution. The minor surface indentations resultant of the thermography inspection equipment are clearer in the

15 MHz (Figure 5.15c) than in the 10 MHz (Figure 5.15a) time-of-flight plots. Likewise, the grid of guide fibers located between the honeycomb core and the exterior face sheet are more apparent in the 15 MHz (Figure 5.15d) than in the 10 MHz (Figure 5.15b) amplitude plots.

The extent-of-damage in the vicinity of the notch tip is indicated by the light green area protruding diagonally away from the notch tip in the time-of-flight image (Figure 5.15c) and the corresponding blue area in the amplitude image (Figure 5.15d). The ultrasonic damage

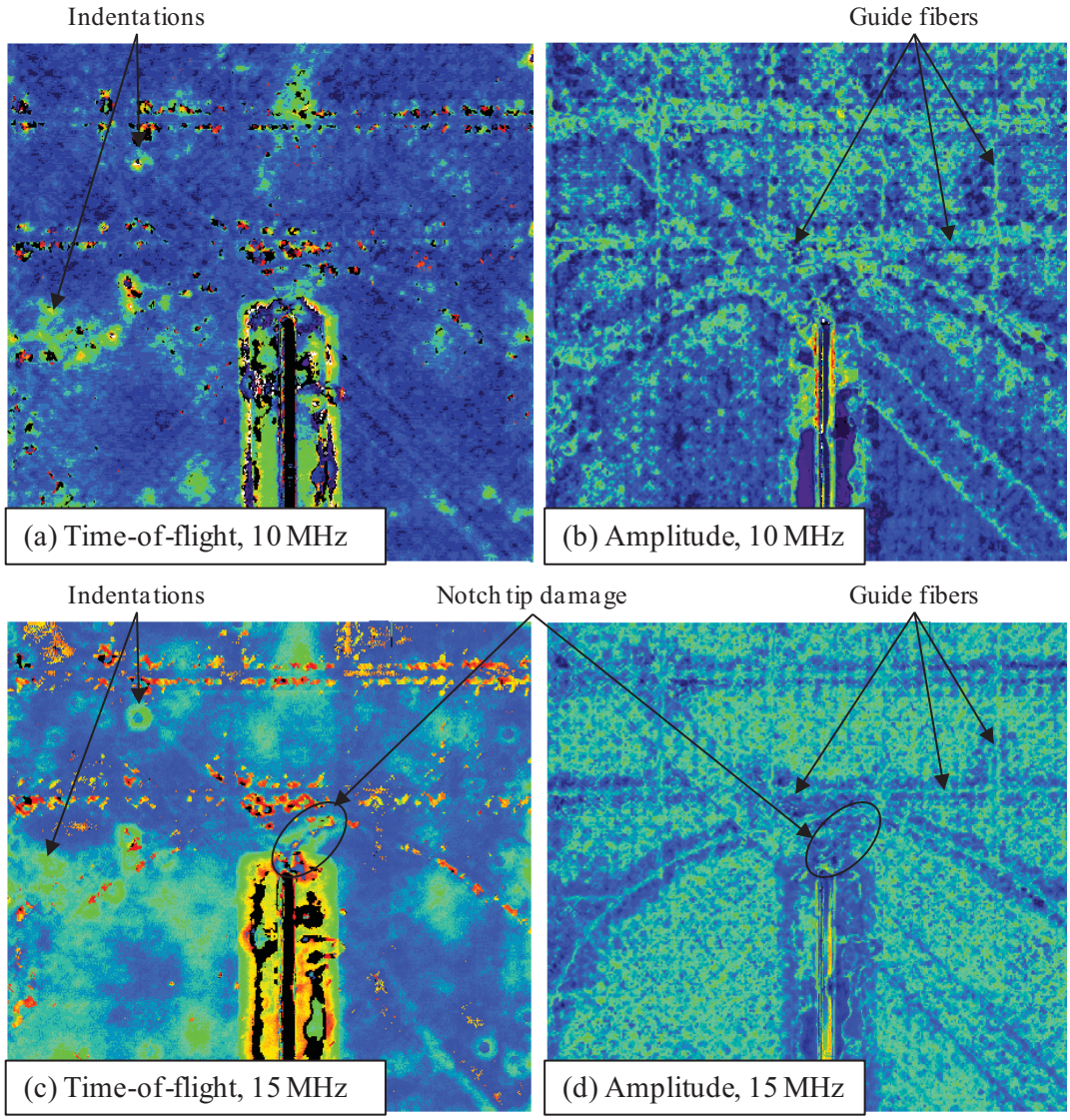

Figure 5.15. Ultrasound scans of notch tip of panel CP4.

indications, like the thermography results presented in Figure 5.7, show that subsurface damage extended further away from the notch tip than was visually observed, Figure 4.31d.

Ultrasonic inspections were performed for the disbonded region of panel CP5 at both 10 and 15 MHz. However, no indications of the disbond were apparent in either the time-of-flight or amplitude plots. Considering that no damage to the face sheets was observed in this region, and ultrasonic signals reflect off the interior surface of the face sheets, these results were expected.

5.5. X-RADIOGRAPHIC COMPUTED TOMOGRAPHY

Similar to all inspection methods which store and process data digitally, x-radiographic computed tomography (CT) scans have a finite resolution. Typical samples for such inspections are on the coupon-scale (i.e., approximately one inch in size), allowing for the characterization of small features and micro-scale failures. The relatively large-scale specimens inspected in this investigation (Section 3.8.5) prohibited the high-resolution characterization of individual failures. However, useful information regarding the structure of the composites and the general location of damage could still be extracted. Accordingly, samples of panels CP2, CP4, and CP5 were inspected after their residual strength tests.

X-radiographic CT scans of panel CP2 successfully identified the visual surface damage, Figure 5.16a, but could not detect the additional subsurface damage that was detected via thermography, Figure 5.6. The ply overlay and core splice were detected, however, and are highlighted in the deeper radiographic slice of panel CP2 shown in Figure 5.16b. A clear view of the over-expanded cells of the honeycomb core is also available. No damage or significant deformation of the core is apparent.

Delaminations may exist within the exterior face sheet, but the low resolution of the scans prohibited their detection; each face sheet had only 4 to 6 pixels representing its full thickness. As a result, the identification of delaminations was very difficult with the size of the inspected specimens.

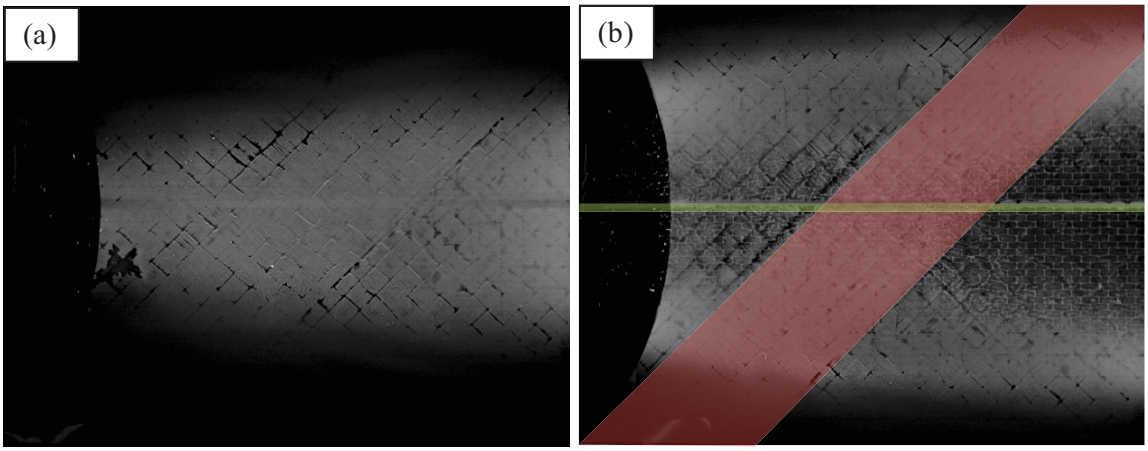

Figure 5.16. X-radiographic CT scans of panel CP2 (a) surface and (b) through the exterior face sheet. A core splice and ply overlay are highlighted in green and red, respectively.

The CT scans of the CP4 notch tip region correlate very well with the results obtained from the thermographic (Figure 5.7) and ultrasonic inspections (Figure 5.15). Matrix cracking along the plain-weave fiber tows of the fabric is present at distances away from the notch tip greater than what was visually observed, Figure 5.17a. Details of the guide fibers used during the construction of the face sheets are also clearly visible and in good agreement with the thermographic and ultrasonic results, Figure 5.17b. The location of the guide fibers through the thickness of the sandwich, between the external face sheet and the honeycomb core, can be seen in Figure 5.17c. The guide fibers cause a slight distortion of the honeycomb core walls where they are bonded to the face sheets. However, no further damage or distortion of the honeycomb core was observed.

The exact size and shape of the skin-to-core disbond in panel CP5 could not be seen via the CT examination due to the tendency of the disbond to remain closed and the low spatial resolution of the recorded images. However, its presence could be determined at select locations between the interior face sheet and the honeycomb core. Cross-sectional views of panel CP5 allow for a general inspection of the skin-to-core bond integrity, Figure 5.18. The resin used to adhere the face sheets and core can be seen in the CT scans as bright white material at the top and

bottom of the honeycomb core. The figure shows that the resin material was missing at several locations between the interior face sheet and the core within the disbonded region.

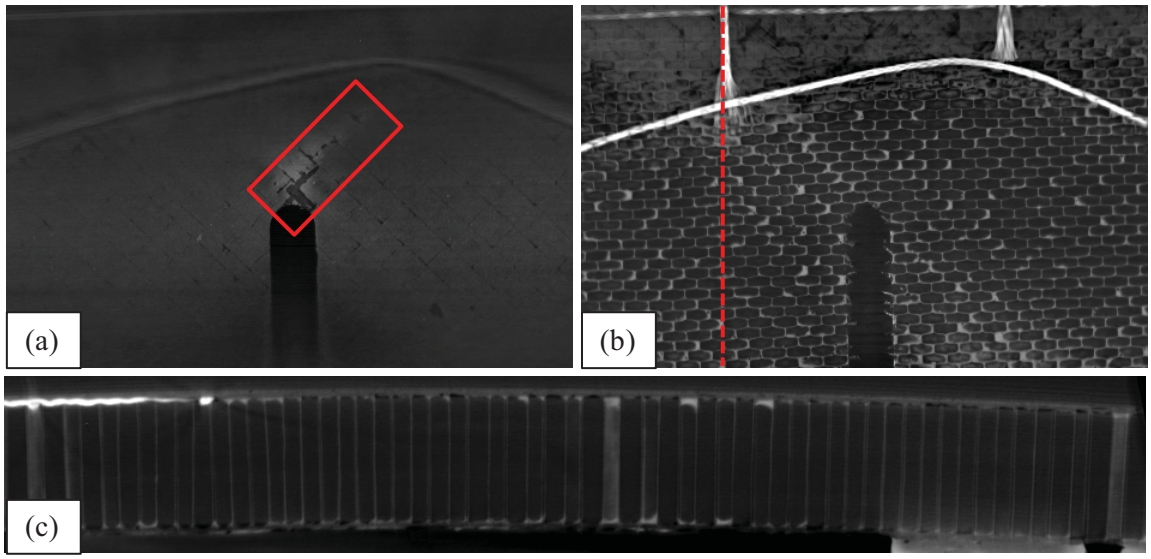

Figure 5.17. X-radiographic CT scans of panel CP4 in the (a) θ-z plane through the exterior face sheet, (b) θ-z plane between the exterior face sheet and the core, and (c) r-θ plane through the dashed line in Figure 5.17b.

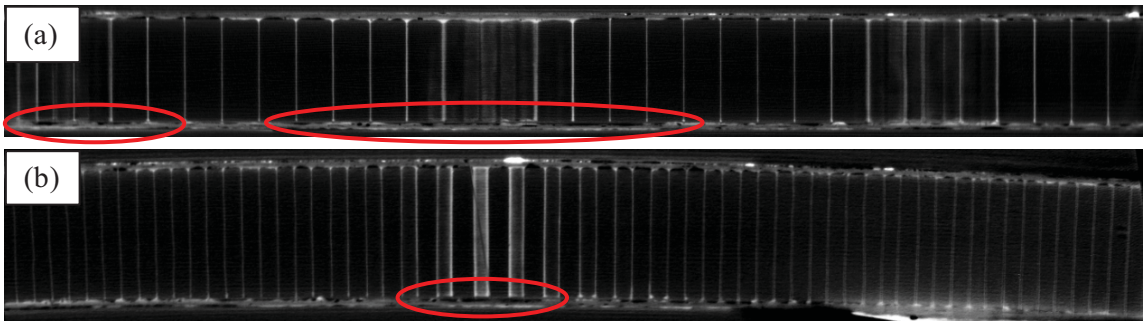

Figure 5.18. X-radiographic CT scans of the large disbond in panel CP5 in the (a) r-z and (b) r-θ planes. The skin-to-core disbonds are highlighted in red.

5.6. SCANNING ELECTRON MICROSCOPY

Examinations of the notch tip region of panel CP5 were conducted via scanning electron microscopy (SEM). The purpose of these examinations was to identify the major modes of failure and to assess the severity of the final fracture in the immediate vicinity of a notch tip.

The sample was approximately 0.625 inch in the longitudinal direction and 0.625 inch in the hoop direction, and included the interior face sheet and the honeycomb core. The exterior face sheet was not examined due to excessive damage. Figure 5.19 shows the posttest exterior face sheet notch tip damage. Figure 5.20 and Figure 5.21 show the SEM specimen before and after being cut down to size, respectively. Clearly, some fibers are missing in Figure 5.21 that were present in Figure 5.20; these fibers were loose and were removed so as not to damage the microscope during the examination. Fiber imprints on the sample will later reveal where these fibers were located. Much of the material at the fracture surface was either lost during the sudden, dynamic fracture of the panel or connected to the opposite fracture surface

For the purposes of discussion, the examined fracture was subdivided into three regions: region A, region B, and the transition area, as shown in Figure 5.21. Region A begins at the machined notch tip and extends through the region parallel to the 0° direction. Region B spans the region of the fracture surface parallel to the -45° direction. The transition area is located at the juncture between regions A and B.

The coordinate system shown in Figure 5.21 is the panel's global coordinate system as it relates to ply orientation. The 0° and 90° directions are the longitudinal and hoop directions of the panel, respectively. Defining an *r*-axis as being parallel to the sandwich thickness, mutually orthogonal to the in-plane 0° and 90° directions, the SEM imaging plane is the 0°-*r* plane. The edge noted in Figure 5.21 was examined by arranging the sample in the microscope such that the images were taken looking downward at the sample. With this direction and orientation of examination, 0° fibers appear within the examined surface, 90° fibers are orthogonal to the examined surface, and ±45° fibers appear at an oblique direction.

Figure 5.19. The exterior view of the notch tip of panel CP5 that was monitored by the DIC system, showing the notch and the fracture emanating from the notch tip propagating from left to right through the face sheet material.

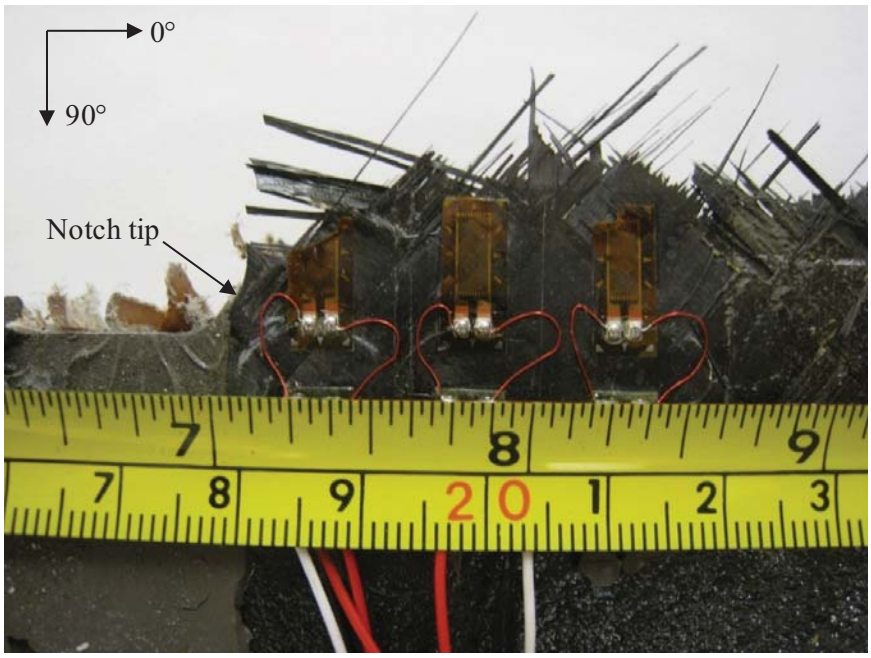

Figure 5.20. The interior view of the panel CP5 notch tip. The upper half has been removed. This image shows the interior of the top half of the section shown in Figure 5.19.

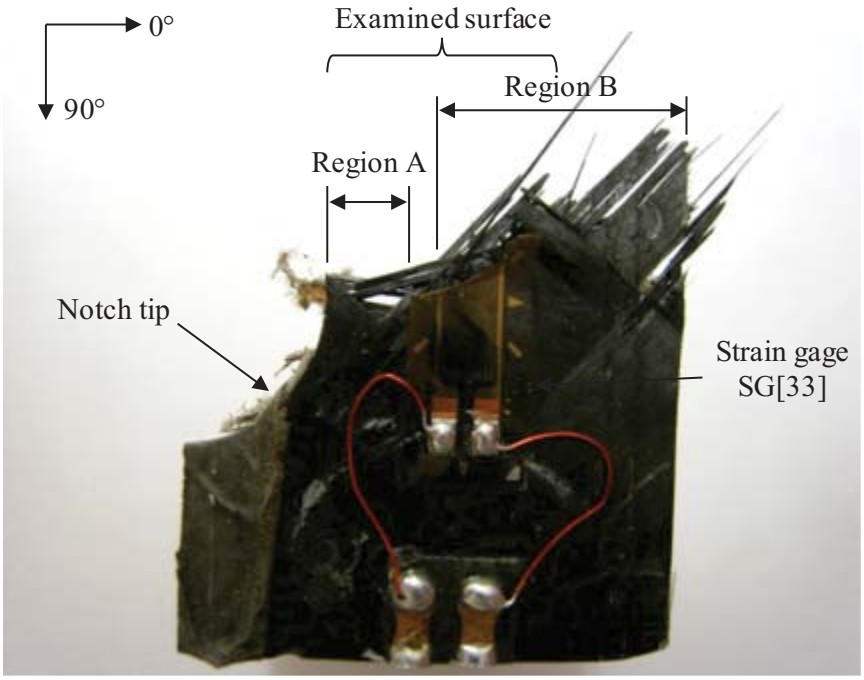

Figure 5.21. SEM sample from CP5 notch tip. One-half of the semicircular notch tip is on the left side of the sample. Strain gage SG[33] (Figure 3.20) measures 0.22 inch in width, and used as a reference in this discussion.

Three distinct features were frequently observed under the SEM: fiber imprints, loose fiber bundles, and the plain-weave fabric. Figure 5.22 clearly shows fiber imprints along the mid-ply 90° fiber tow, indicating the occurrence of fiber/matrix interfacial failure. The fibers which formed the imprints were adjacent to the 0° fiber tow of the woven fabric, some of which are seen on the left side of the figure.

Excessive matrix cracking, parallel to the 0° fiber tows at the machined notch tip, can be seen in Figure 5.23. Several loose 0° fiber bundles with roughly circular cross sections are found throughout this area, measuring between 100 μm and 200 μm in diameter. While the fiber bonding within the bundles seems to be intact, the fiber tows are splintered into many such smaller bundles.

In this specimen, several loose bundles are found in the 0° and ±45° directions, but not in the 90° direction. Due to the notch orientation and loading configuration of panel CP5, the 90°

fibers experienced the most critical loading state. Therefore, the accumulated fiber fractures and the widespread fiber tow pull-outs greatly reduced the likelihood of finding intact 90° fibers along the fracture surface.

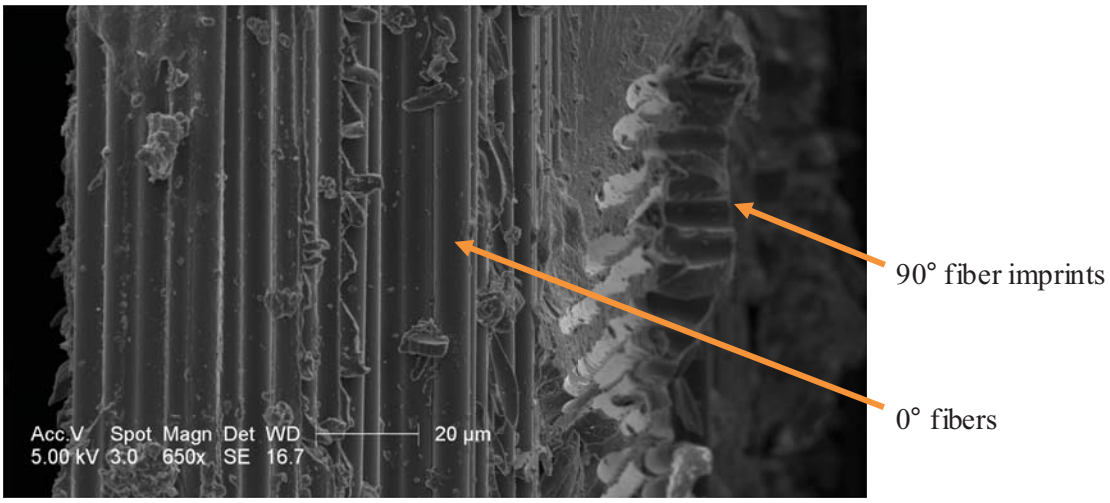

Figure 5.22. Fiber imprints in the 90° fiber tow on the right (perpendicular to the examined surface) and fiber imprints in the perpendicular 0° fiber tow (oriented vertically).

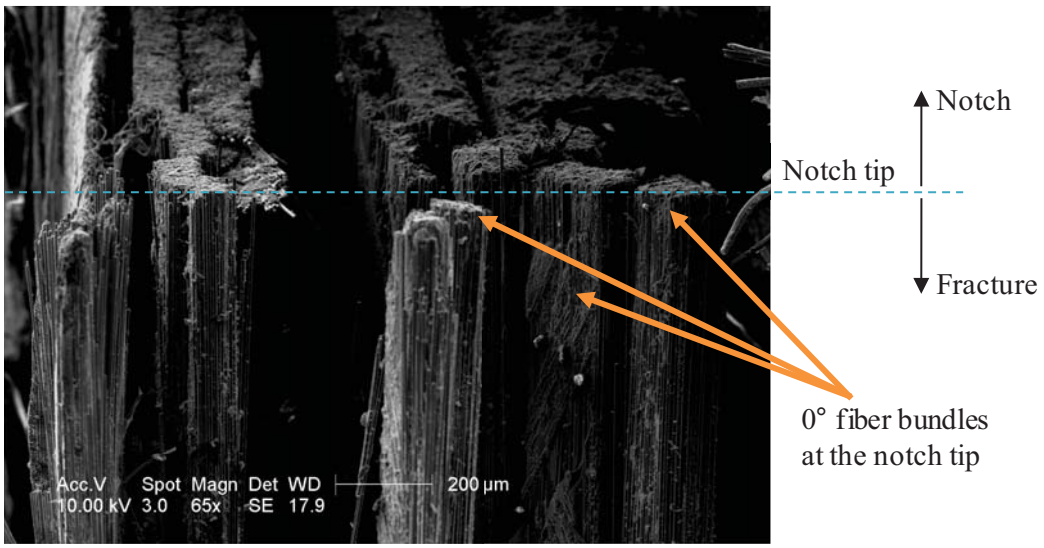

Figure 5.23. SEM image showing extensive matrix cracking and delaminations in the vicinity of the notch tip of panel CP5. Several 0° fiber bundles at the notch tip are visible.

A photo montage of the fracture surface is shown in Figure 5.24, identifying key areas of interest. The notch tip is at the top of the image, the exterior face sheet surface with the strain gage is on the left edge, and the honeycomb core material is on the right side of the face sheet. The montage does not represent the full length of the sample. The montage begins at the notch tip and extends to the right of the strain gage, as shown in Figure 5.21.

The transition area, where the fracture surface transitions from parallel to 0° fibers to parallel to -45° fibers, is identified in Figure 5.24a. Within region A (i.e., the area closest to the notch tip), the fiber bundles which appear oriented in the plane of the page are 0° bundles. Other bundle orientations can be determined using this as a reference. Within region B, the fiber bundles which appear oriented in the plane of the page are -45° bundles.

Figure 5.24b shows the fiber bundle orientations with color highlighting. Fibers far out of focus were left uncolored because their orientation could not be confidently determined. Working from left to right in Figure 5.24b, it was expected to find the exterior ±45° fiber tows, followed by 0° and 90° fiber tows, and the interior ±45° fiber tows. However, certain fiber tows are missing on the core side of the sample. The fractographs show mostly the 0° and 90° bundles on the core side (right side) of the face sheet in the location the ±45° bundles are expected. It is likely that the sudden catastrophic fracture of panel CP5 caused several whole tows to fall off.

Several failure modes were observed on the fracture surface, including matrix cracking, delamination, fiber/matrix interfacial failure, the fracture of both fiber filaments and bundles, and the pull-out of fiber tows and bundles from the weave. Figure 5.24 illustrates the extent and multiplicity of the failure modes present along the fracture surface. The sudden, catastrophic fracture of the panel obscures the development, evolution, and interactions of the various failure modes, but the individual failure modes can still be discerned. For example, Figure 5.23 shows a close-up view of the immediate vicinity of the notch tip, showing matrix cracking and widespread delaminations in this region, leaving only loose fiber bundles.

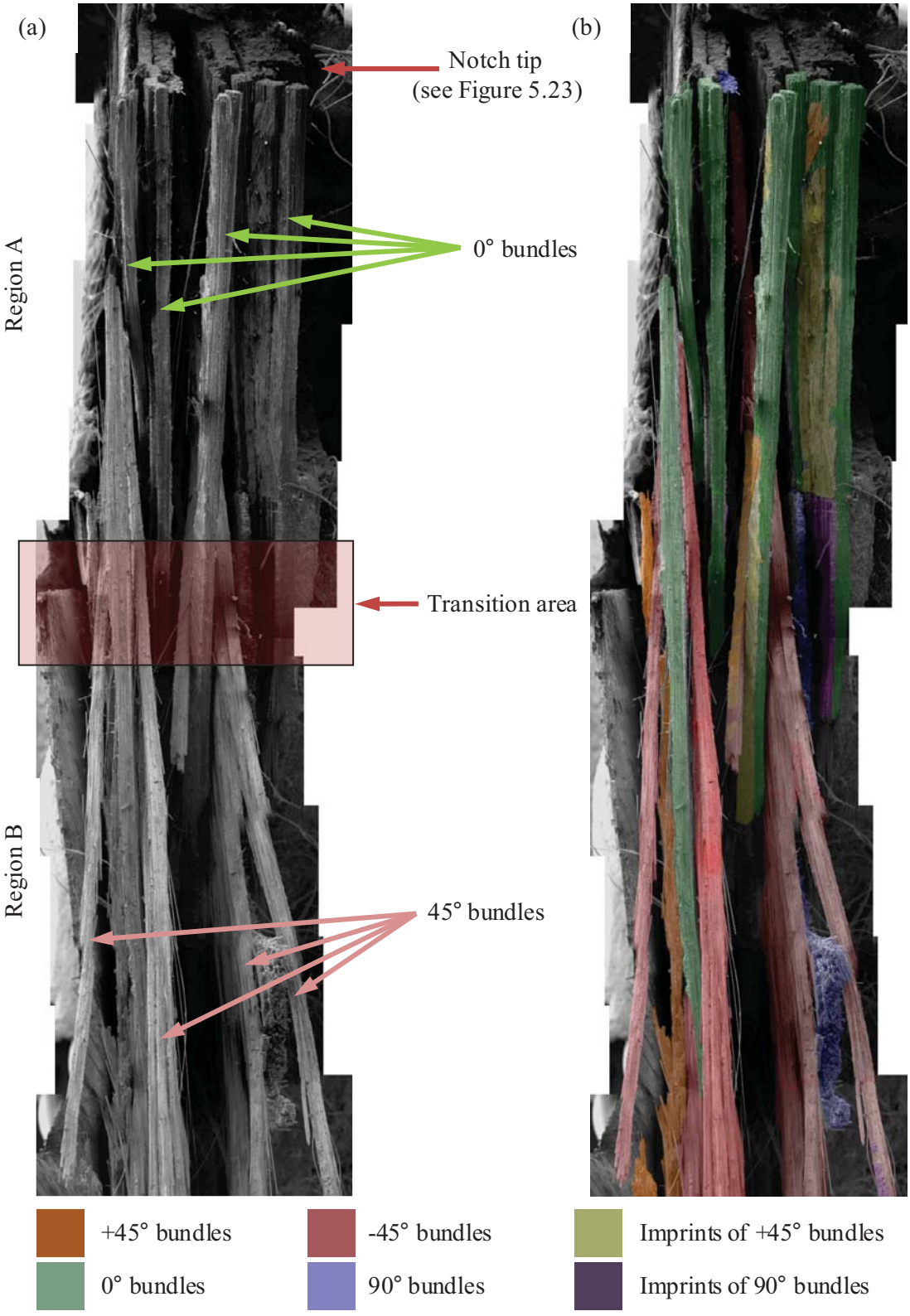

Figure 5.24. (a) SEM photo montage with key characteristics noted. (b) Same image with fibers colored based on orientation.

Delaminations extended well beyond the notch tip region, as apparent by the large separations between the laminae. The plain-weave architecture of the prepreg layers was severely damaged as well, essentially leaving no fiber bundles bound to those of another interwoven tow. Several fiber imprints are seen on the remaining intact matrix material. Detailed examination of Figure 5.24 shows several such regions.

As was observed in the catastrophic fracture of each of the panels, fiber fractures along the major fracture of the panel caused widespread matrix cracking and damage to the plain-weave fabric, extending several inches on either side of the fracture (e.g., Figure 4.37). In the immediate vicinity of the notch tip, the most predominant occurrence of fiber fracture was in the fibers perpendicular to the notch (i.e., the 90° fibers), Figure 5.25. The initial failure of the 90° fiber tows redistributed the load to the ±45° fibers of the neighboring laminae, causing collateral damage to them, as discussed in Section 4.3.3. An example of ±45° fiber fracture is presented in Figure 5.26, with a close-up view in Figure 5.27.

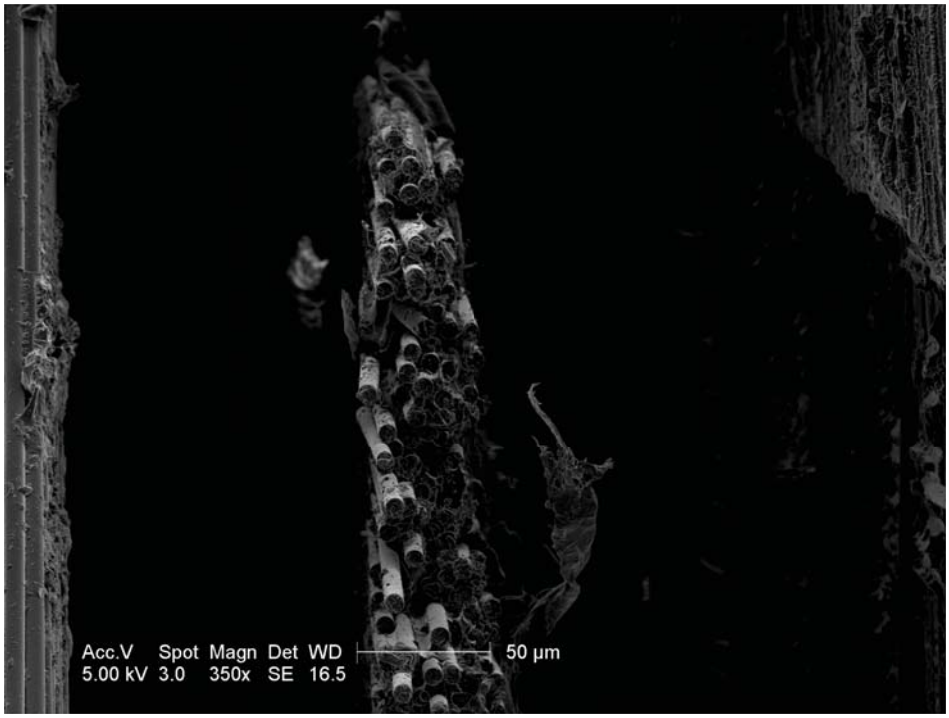

Figure 5.25. SEM image of 90° fiber fractures.

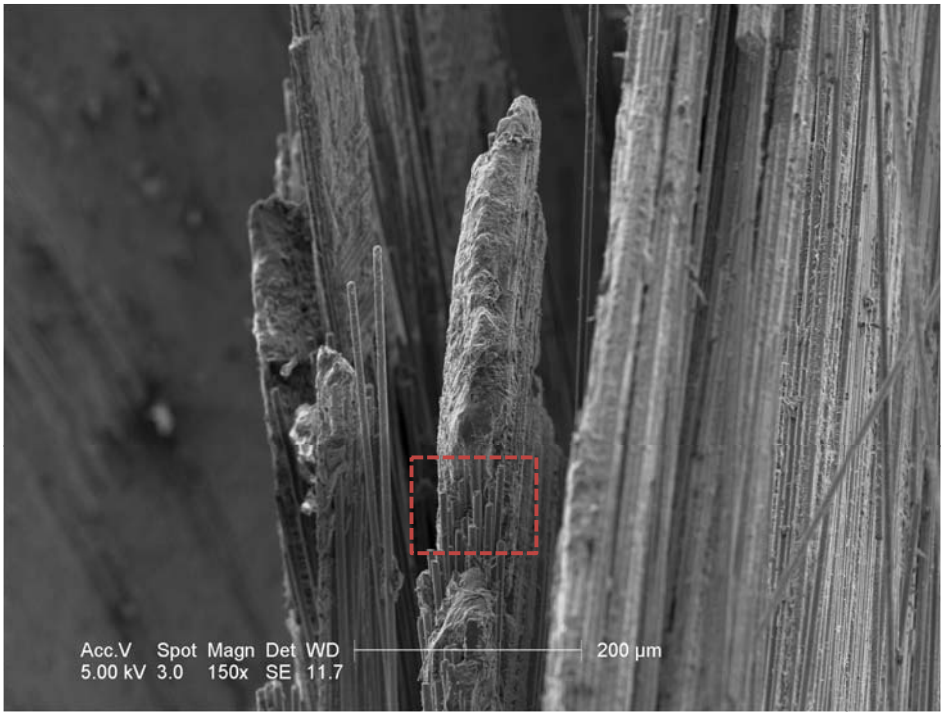

Figure 5.26. SEM image of fiber fractures of 45° fibers.

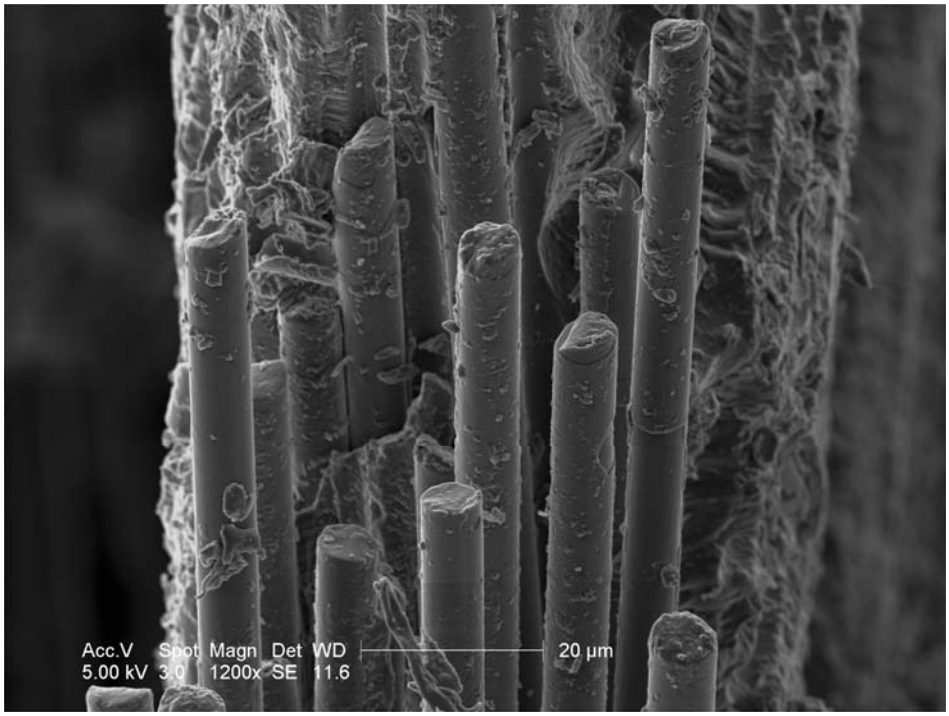

Figure 5.27. SEM image of highlighted region in Figure 5.26, showing 45° fiber fractures.

5.7. CONCLUSIONS

Several methods were used to qualitatively and quantitatively characterize the state-of-damage in the sandwich composite fuselage panels. The ability of several nondestructive inspection techniques (i.e., thermography, computer-aided tap test (CATT), ultrasound, and x-radiographic computed tomography (CT)) to detect nonvisual, subsurface damage in these structures was assessed and compared. Varying degrees of correlation were achieved between each of the applied methods.

Thermography successfully mapped out the internal structure of the composite face sheets and detected nonvisual, subsurface defects parallel to the inspected surface. The inspections were able to be completed over large areas (i.e., 16 sq. ft.) in relatively short periods of time. Thermographic measurements were capable of characterizing the skin-to-core bond integrity, but could not penetrate into the core or through to the opposite face sheet. Therefore, thermography should perform well at detecting delaminations in solid laminates, but access to both the external and internal surfaces of sandwich composites is required to detect delaminations.

The CATT system was effective at detecting and quantifying both the extent and severity of delaminations and disbonds, successfully detecting both near- and far-side disbonds in the investigated sandwich composite material. For the high-resolution scans performed in this investigation, the method proved to be time consuming when compared to the thermographic measurements, even for measuring relatively small areas (e.g., 1 sq. ft.). However, while using the CATT system to scan for unknown delaminations and disbonds in the field, the initial goal is to detect the presence of damage. As a result, lower-resolution scans could be performed, greatly increasing the speed at which the inspections could be completed without any significant decrease in the threshold of detectability.

The results obtained via the ultrasonic inspections were comparable to the thermographic data in terms of ability to map out the internal structure of the face sheets and detect in-plane

defects. Neither the quality of the skin-to-core bond nor the integrity of the honeycomb core itself could be assessed. The frequencies at which the panels were scanned (i.e., 10 and 15 MHz) were too high to characterize the honeycomb core, through which significant high-frequency signal attenuation is typical. Conversely, higher scanning frequencies (e.g., 20–30 MHz) would have led to a better characterization of any delaminations between the plies of the face sheets.

X-radiographic CT scans were performed for select specimens. Several structural components of the sandwich composites were clearly visualized. However, the relatively large size of the specimens (i.e., between 20 and 30 inches in length) made any inspection of the interlaminar states-of-damage difficult to assess due to the resulting low spatial resolution of the data. The fractographic examinations offered supplementary information regarding the specific failure modes, their locations, and their multiplicity. Several failure modes were observed on the fracture surface, including matrix cracking, delamination, fiber/matrix interfacial failure, the fracture of both fiber filaments and bundles, and the pull-out of fiber tows and bundles from the weave.

Both the x-radiographic CT scans and the SEM studies could have been performed at far greater resolutions and for many more samples. However, it is not the goal of this dissertation to study the micromechanical failure processes of sandwich composites, but rather to study and model the global behavior of sandwich composite structures containing damage of progressively increasing severity on larger scales. Therefore, the NDI techniques capable of characterizing the states-of-damage throughout the structures were of more use and were more thoroughly implemented.

CHAPTER 6: EXPERIMENTAL RESULTS – ACOUSTIC EMISSION

6.1. INTRODUCTION

The conventional wisdom of using acoustic emission (AE) as a nondestructive evaluation technique is that it could serve multiple purposes, namely: (i) detecting the initiation and progression of damage, and determining when it occurs in terms of load; (ii) locating sites of failure and tracking its progression; and (iii) determining the dominant failure modes. These three purposes are addressed in this chapter, evaluating their feasibility in the context of monitoring the formation, progression, and eventual instability of damage in full-scale composite aircraft fuselage panels. Further, two key questions of practical importance to be addressed are whether monitoring AE could serve as an early warning of incipient failures in the composite materials and whether it could serve as an early warning of imminent fracture. Discussions on the potential errors related to sensor failure and AE channel saturation are presented. Data recorded from panels CP1B, CP3, CP4, CP5, and CP6 are reported, analyzed, and discussed herein. Insufficient data AE were recorded to perform proper analyses of panels CP1A and CP2.

6.2. MONITORING DAMAGE INITIATION AND PROGRESSION

The accumulation of AE events generated during loading of the five panels is shown in Figure 6.1. These are typical and fundamental plots normally reported in the literature on AE; similar plots are often generated to track the accumulation of counts (e.g., [6.1]), rather than events. (Note: the definition of 'counts', events', and other AE-related nomenclature are given in Section 2.2.2) In all cases, the results show, qualitatively, a nearly exponential increase in the accumulation of events with load. Quantitatively, however, the number of events recorded and the rate of their accumulation is quite different in the six plots, indicating a dependence on the loading functions, the direction of the notch relative to the applied load, the type of sensors used, etc. Not surprisingly, the number of events accumulated and the rate of their accumulation in

panels CP3 and CP4 are lower than in the other panels. The former two panels used wideband sensors and were subjected primarily to longitudinal loading. Panels CP1B, CP5, and CP6 used resonant sensors and were subjected to internal pressure and hoop loads, with either no (CP1B), nominal (CP5), or equal (CP6) longitudinal loads.

Damage accumulated during loading results in an increasing rate of emission, often accompanied with intermittent generation of trains of hits, and/or rapid bursts of emission, that appear most often when the load approaches its ultimate. The varying rates of events accumulated at the higher load levels seen in Figure 6.1, however, resulted primarily from the particular sequence of the loading steps, cyclic loading, and unloading applied to the panels, as described in Section 3.6. Reloading panel CP6, following unloading from elevated loads, generated emission that initiated at load levels lower than the previous maximum load, as expected. This behavior is known in AE literature as the Felicity effect [6.2], a phenomenon which is particular to composites.

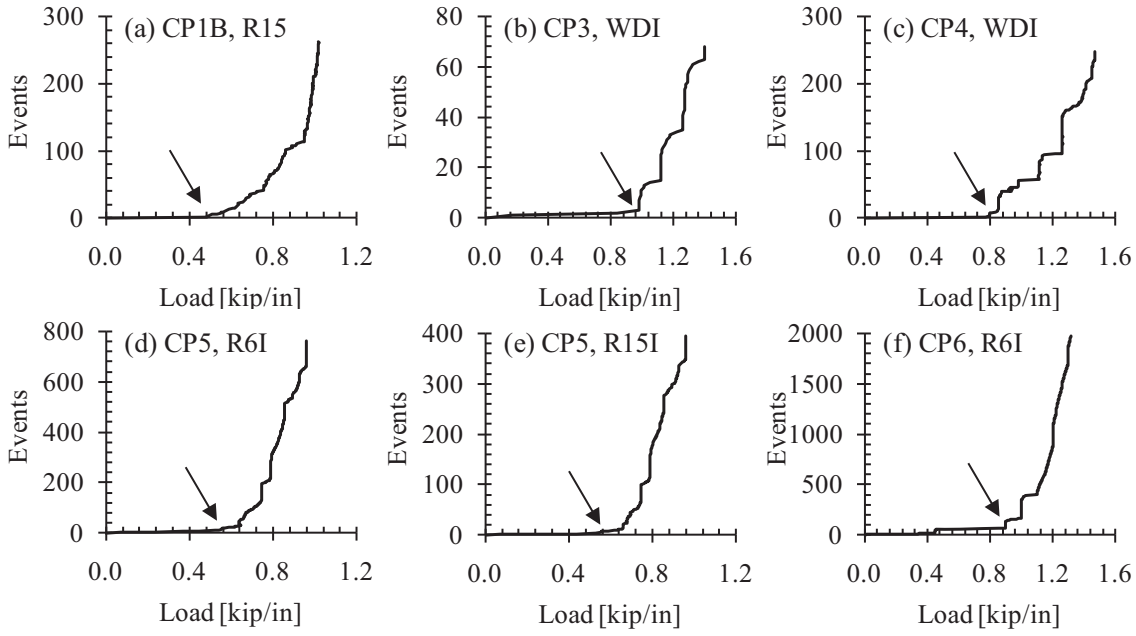

Figure 6.1. Accumulation of locatable events with applied load, showing the load at which damage initiated and the rapidly increasing AE activity as the panels approached fracture.

The results such as those shown in Figure 6.1 are helpful in detecting the load at which the first damage occurred. This information can be typically obtained in real-time. The results indicate that damage was first detected at approximately 45% of the fracture load of panel CP1B, 65% of the fracture load of panel CP3, 55% of the maximum load of panel CP4, 57% of the fracture loads of panels CP5, and 65% of the fracture loads of panels CP6. For panel CP5, the R15I and R6I sensors both detected the first failures at 57% of the fracture load. The rapid rate of event accumulation at the higher load levels is indicative of imminent catastrophic fracture.

The events accumulated during loading are shown in Figure 6.2. Each point in the figure indicates the load at which an event occurred and its amplitude. The AE results shown in Figure 6.2 were recorded with R15 sensors for panel CP1B, WDI sensors for panels CP3 and CP4, and with R6I sensors for panels CP5 and CP6. Panel CP5 was instrumented with a second set of R15I sensors, as well.

The loading of panel CP1B consisted of internal pressure (up to a maximum of 14.0 psi) with a corresponding hoop load; no longitudinal load was applied. The first indication of damage, as recorded by the AE system, occurred at a hoop load of approximately 480 lbf/in (while loading up from the second to third load steps). Five AE events were detected, all with amplitudes less than 80 dB. With each subsequent load step, locatable emissions were detected at increasing rates. While increasing from the fifth to sixth load steps, the notch tip damage rapidly progressed and the panel failed catastrophically. The final failure process was accompanied with increasing amounts of emission, Figure 6.1a. Several high-amplitude events preceded the panel fracture during the last load increase.

Panel CP3 was subjected to increasing longitudinal load (up to a fracture load of 1507 lbf/in) under constant internal pressure (8.0 psi) and corresponding hoop load. AE activity was first detected at a load level of 980 lbf/in (65% of fracture load, at the seventh load step). Essentially all of the emission was of low amplitude, below 60 dB. More significant AE activity occurred when the load reached 1120 lbf/in (71% of the fracture load), mostly of low- and mid-

amplitudes, between 40 dB and 80 dB with a few high-amplitude events above 90 dB. Further increase of the load, to 1260 lbf/in and beyond was associated with increasing emission throughout the amplitude range. The figure does not show any AE activity during the final load step because the AE system malfunctioned.

Panel CP4 contained a circumferential notch identical to that of panel CP3. However, it was subjected to essentially only longitudinal load with a constant nominal internal pressure (1.0 psi) and the corresponding hoop load. The panel was not loaded to fracture; the maximum longitudinal load reached was 1470 lbf/in. A relatively small number of low- and mid-amplitude events were generated when the longitudinal load reached 980 lbf/in (67% of the maximum load, at the seventh load step). The three high-amplitude events may have been generated by critical damage at the notch tip, correlating with the slight visible damage observed in the corresponding digital image correlation (DIC) images, Figure 4.31a. A few low-amplitude events were generated also during the subsequent brief load-hold period, while no events were generated during the three load cycles that followed. The lack of fretting emission suggests that no significant nonvisual fracture surfaces had formed. The subsequent four load steps were accompanied with substantial increases in emission. Most of the emission was in the low- and mid-amplitude range, with only 13% of the events having amplitudes greater than 80 dB.

The loading of panel CP5 consisted of internal pressure (up to a maximum of 13.5 psi) with a corresponding hoop load and a low constant longitudinal load (100 lbf/in). The first indication of damage, as recorded by the AE system, occurred at a hoop load of approximately 444 lbf/in (at the fourth load step). Three AE events with amplitudes between 45 and 67 dB were recorded. Some additional emission occurred when the hoop load was increased to 643 lbf/in. Most AE events generated were below 70 dB (typically associated in the AE literature with matrix cracking, disbonding, or delaminations) with a few events of higher amplitude. Increasing the load to 768 lbf/in generated an abundance of AE activity. While no visible damage was observed ahead of the notch tip monitored by the DIC system, a nonlinear strain response was

observed on the interior panel surface at this load level, Figure 4.36c. Increasing the load to 862 lbf/in was accompanied by significant AE activity which could have resulted from the visible 0.3-inch notch tip damage extension, Figure 4.37a. However, the emission could have been generated from other regions within the AE gage section. Rapid and audible bursts of AE activity occurred during the final load increase to 960 lbf/in hoop load, during which a large extension of notch tip damage, of over 1.3 inches, was observed, Figure 4.37d. The vast majority of the total AE activity occurred during the last three load steps, however, less than 3% of the events had amplitudes greater than 80 dB.

Panel CP6 was subjected to an internal pressure of 18.8 psi with corresponding hoop loads, combined with an equal longitudinal loading (up to fracture load of 1375 lbf/in), and it contained a notch inclined by 45° to the longitudinal direction of the panel. The AE results shown in Figure 6.2f indicate that the damage initiated at a load level of 900 lbf/in (at the ninth load step), 65% of the fracture load. That is, the AE results indicated damage initiation at a load that is similar to that recorded in panel CP5. Successive increases of the load up to 1300 lbf/in generated an increasing amount of AE activity that accompanied extensions of the notch tip damage.

It should be noted, however, that the data presented in Figure 6.1 and Figure 6.2 are for all of the events recorded from throughout the panel, not necessarily only those generated from damage at the notch tips. Abundant extraneous acoustic activity is often generated from the loading fixtures, disbonded regions, wave reflections, and fretting among existing and newly formed fracture surfaces. More precise information regarding notch tip damage initiation and progression can be obtained by analyzing the source locations of the events shown in Figure 6.2 and correlating these results with the progression of notch tip damage as recorded via the DIC system. This issue is discussed in detail in the Sections 6.3 and 6.4. Nevertheless, the pattern of AE generation described above indicates that monitoring AE served as a reliable early-warning device for both the formation of new damage and for anticipating imminent fracture.

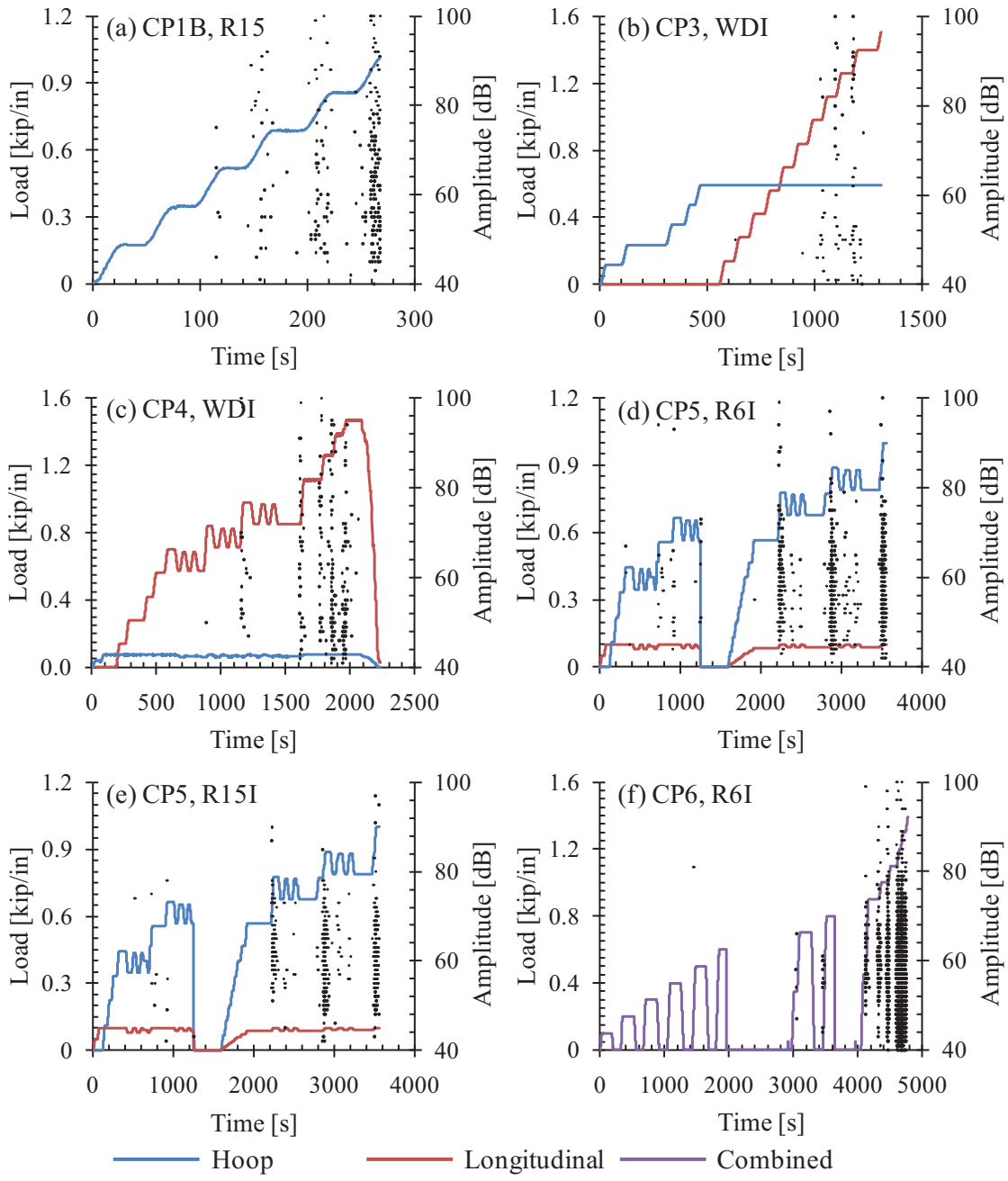

Figure 6.2. Load-time history and accumulation of AE events and their amplitudes generated during the loading of each panel. The solid lines represent the applied loads and each individual point represents a single locatable AE event. The sensor set used in each panel is indicated in the individual plot titles.

6.3. SOURCE LOCATION

Planar source location plots of AE events generated during the loading of the panels are shown in Figure 6.3. The location of each sensor and its numbering is indicated in each plot. Each point in these plots represents the source location of an event. Note that multiple events may have occurred at the same location. The location plots show increased AE activity near the two notch tips. The data, however, also show that there are numerous events that were generated throughout the entire panel, particularly in panels CP5 and CP6. Nevertheless, in all panels, a large number of AE events were generated from outside the notch tip regions, obscuring the emission generated by damage at the notch tips.

Panels CP3 and CP4 generated a smaller number of events when compared with the other panels. It should be noted, however, that these panels were instrumented with the less-sensitive wideband (WDI) sensors. Further, AE data were not recorded during the final load step of panel CP3, and panel CP4 was not loaded to fracture. The AE activity seen in panel CP6 is much greater than in panels CP1B and CP5. This is due to the panels having different loading functions and panel CP6 having a notably higher fracture pressure, 18.8 psi, compared to 14.0 psi in panel CP1B and 13.5 psi in panel CP5. As shown in Figure 6.1, higher loads corresponded with increased emission amongst panels gaged with the same sensor types. Note that twice as many events were recorded in panel CP5 with the R6I sensor set than with the R15I sensor set. Analysis of the frequency spectra of the waveforms recorded using the wideband sensors showed that most of the activity occurred in the 50–60 kHz range. Therefore, the 55-kHz resonant R6I sensors were the most effective sensors available for the purpose of locating damage and anticipating fracture for the composite panels tested in this investigation.

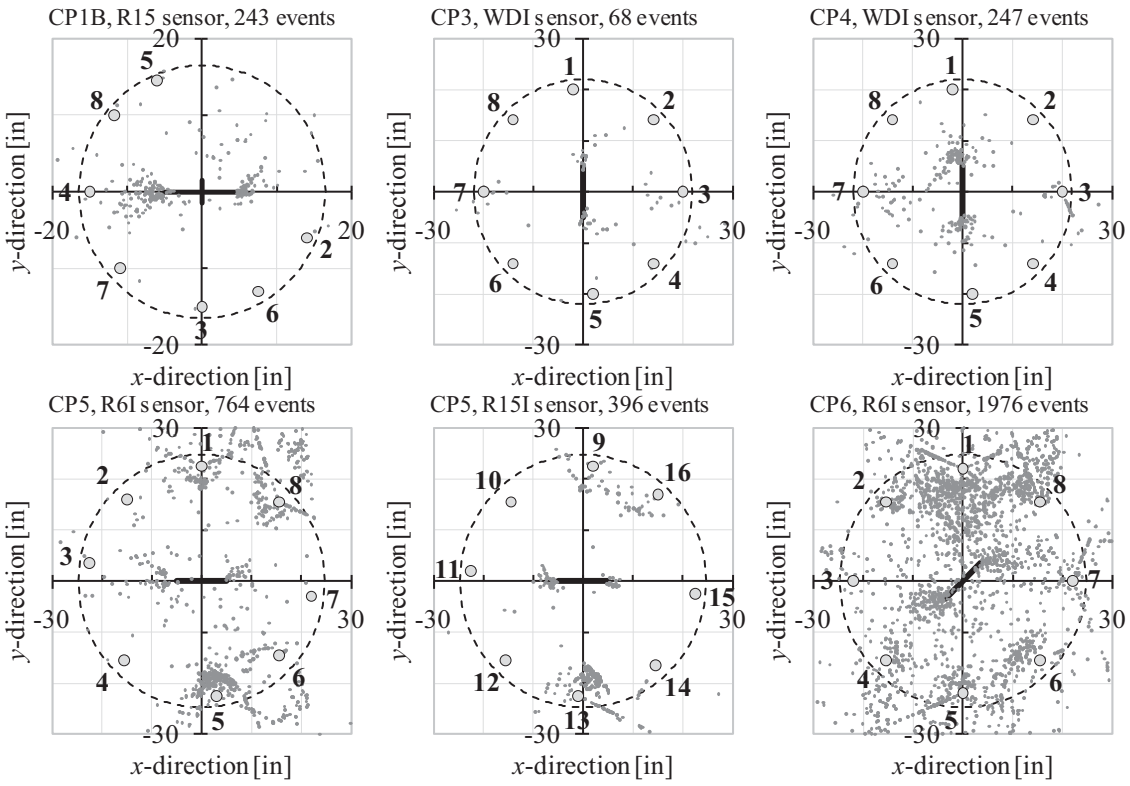

Figure 6.3. Planar source location plots showing the location of the events recorded in each panel. The total number of events recorded in the AE gage section is indicated in the individual plot titles.

Nondestructive pretest inspections of panel CP5 revealed that there was a large skin-to-core disbond between sensors no. 5 and no. 6 (see Sections 3.4, 5.2.5 and 5.3). The plots for panels CP5 and CP6 also show several additional clusters of events located away from the notches (e.g., near sensor no. 1 in panel CP5 and sensor no. 6 in panel CP6). These events are assumed to have been generated by fretting that emanated from existing delaminations and disbonds, and from the connection bonded plates connected to the radial link assemblies. In some cases, clusters of events formed straight lines along the lines drawn through adjacent sensor locations (e.g., near sensor no. 1 in panel CP5 with the R6I sensors; sensor no. 13 in panel CP5 with the R15I sensors; and near sensors no. 1, 5, and 7 in panel CP6). These artifacts are due to the location algorithm not properly locating events generated from outside the polygon formed by

the locating sensors. However, these events were mostly generated from outside the AE gage section, and, therefore, were not considered in the following analysis.

The location of the events generated by new damage at the notch tips could be modified and improved by accounting only for the high-intensity events: those that are presumably caused by the formation of new cracks, thus excluding most of the extraneous emission caused by fretting, loading fixtures, etc. This could be obtained by filtering the AE data set according to the intensities that distinguish the emission generated by new failures from that generated by fretting and other extraneous sources. For example, Figures 6.4 through 6.6 show the AE event source location plots with such a filtering scheme applied for panels CP5 (using both R6I and R15I sensors) and CP6. The AE data were filtered to include only high-intensity events, as indicated in the individual source location plots. The selected AE signal feature (i.e., intensities) ranges of the filtered data were based on a careful review of the events generated from the notch tip regions and comparing them with the intensities of the signals generated from remote regions within the AE gage section. Also taken into consideration were experimental observations cited in the literature (e.g., [6.3] and [6.4]). A thorough discussion on waveform intensities and their correlations with various failure mechanisms and extraneous sources is presented in Section 6.5.

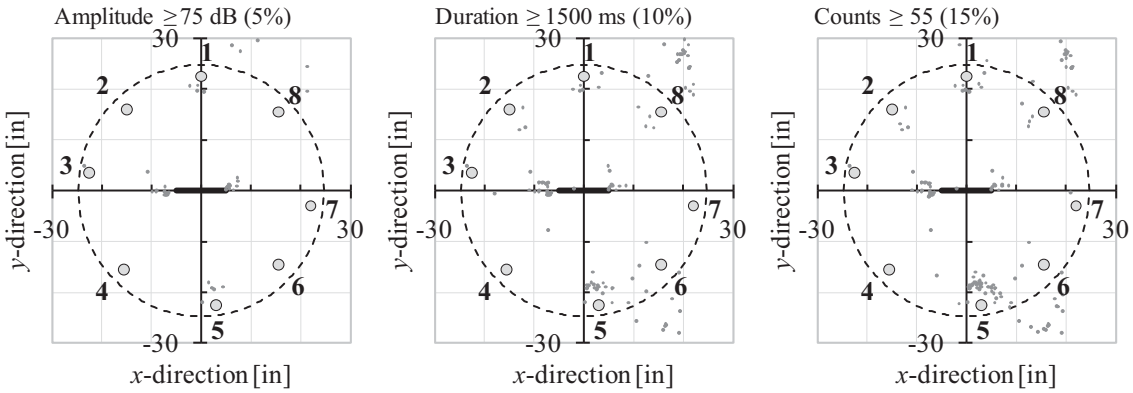

Figure 6.4. Planar source location plots showing the location of events, recorded with R6I sensors throughout loading of panel CP5 that have waveform features above selected values. The listed percentages are of the total number of events generated from within the AE gage section.

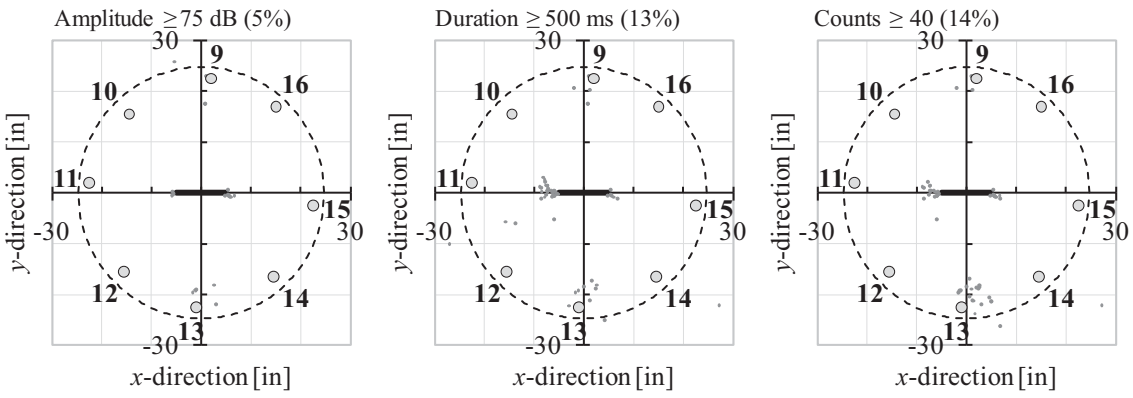

Figure 6.5. Planar source location plots showing the location of events, recorded with R15I sensors throughout loading of panel CP5 that have waveform features above selected values. The listed percentages are of the total number of events generated from within the AE gage section.

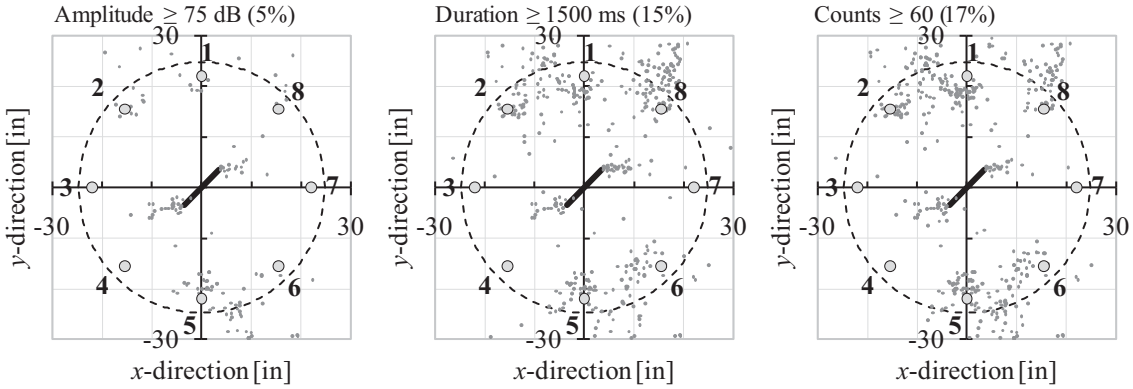

Figure 6.6. Planar source location plots showing the location of events, recorded throughout loading of panel CP6 that have waveform features above selected values. The listed percentages are of the total number of events generated from within the AE gage section.

The filtered source location plots indicate that through appropriate data filtering most of the extraneous emission scattered throughout the panels could be eliminated. Compared with the unfiltered source location plots of Figure 6.3, the filtered data shown in Figures 6.4 through 6.6 more clearly show clusters of events localized in the immediate vicinity of the notch tips of each panel. However, a comparison with the source location plots of the unfiltered data in panels CP1B, CP3, CP4, and CP5 revealed that several events in the immediate vicinity of the notch tips

had been inappropriately filtered out, and that events which appeared to be associated with the notch tip damage were scattered, approximately, over a larger region, ranging 1 inch behind to 5 inches ahead of the notch tips and 5 inches on both sides of the notch centerline (60 in^2 per notch tip). In panel CP6, the events clustered ahead of the notch tips spread, approximately, over a region 10 inches along the longitudinal direction and 6 inches along the hoop direction of the panel (60 in^2 per notch tip). For the purpose of the following discussion, these regions are defined herein as the notch tip regions.

A total of 764 events were recorded from within the circular 24.75-in radius AE gage section of panel CP5 with the R6I sensors, Figure 6.3. Of these, 76 events (10%) were generated from the two notch tip regions, 16 (21%) of which had amplitudes greater than or equal to 75 dB, Figure 6.4. While 20 events were scattered throughout the remaining AE gage section within this amplitude range, no appreciable extraneous event clusters were detected. Similar results were obtained with the R15I sensors (Figure 6.5); of the 396 events, 64 events (16%) were generated from the two notch tip regions. Of these, 12 events (11%) had amplitudes greater than or equal to 75 dB. Nine additional events were scattered throughout the remaining AE gage section, but, again, no appreciable extraneous event clusters were detected.

In the case of panel CP6, of the 1976 events recorded with the R6I sensors from within the circular 24.75-in radius gage section (Figure 6.3), 243 events (12%) were generated from the two notch tip regions. Of these, 38 events (16%) had amplitudes greater than or equal to 75 dB, Figure 6.6. However, an additional 62 events with amplitudes greater than or equal to 75 dB were located throughout the remainder of the AE gage section. That is, for panel CP6, no characteristic amplitude threshold existed for the events generated from the notch tip regions. Similar analyses with filters defined in terms of durations and counts yielded similar results. Further increasing of the filter thresholds removed too many events from the notch tip regions.

The feature-based filtering applied above is fraught with numerous uncertainties. In large composite structures, the event intensities recorded by a given sensor depend not only on the

mode of failure but also on other factors, such as (i) the distance between the source and the sensor (i.e., wave dispersion and attenuation characteristics of the material); (ii) the direction of the signal path relative to the filaments; (iii) the presence of discontinuities (i.e., new failures) that occurred along the path of the AE signal; and (iv) the rate of emission from within the panel and from extraneous sources. The effect of these factors on the event intensities recorded by the AE system could be quite significant, and could be even larger than the differences in intensities of events that are associated with different modes of failure. Further, the selection of filtering limits of the event intensities is quite subjective in terms of selecting the controlling intensity or intensities and their upper/lower limits. Finally, it should be recalled that feature-based filtering is based on the intensities of the first hit recorded by the sensor array. That is, it is based on a single sensor event-feature analysis. As a result, events emanating from an actual damage source whose path to the nearest sensor through the material is affected by any one of the possible sources of error that affect the intensities of the AE signals could be erroneously filtered while employing a feature-based data filtering approach.

Alternatively, the source location plots of *n*-hit events (i.e., hitting at least *n* sensors for source location calculation, where *n* is greater than three, introducing redundant measurement to the planar source location) provide a more reliable, better-defined, simple, and precise location distribution of the AE sources, which is one of the most important goals of using the AE technique in large composite structures. This approach is more aggressive in defining an event because it requires arrival time data from additional sensors, yielding a more precise location of the AE source. Also, the results are less dependent on the quality of the first-hit sensor, integrity of the sensor/surface coupling, etc. For the particular case of this investigation and the specific experimental setup employed, it was determined that five-hit events provided the optimal event filtering. The source location plots of such five-hit events show that most of these high-intensity events were generated from the notch tips region, Figure 6.7. Comparing the number of three-hit events (Figure 6.3) with the number of five-hit events (Figure 6.7) shows that with the resonant

sensors used in panels CP5 and CP6 only 12% to 17% of the three-hit events recorded were five-hit events, while the percentages were 57% and 62% for the wideband sensors used in panels CP3 and CP4, respectively. The higher percentage in the latter is due to their lower sensitivity and thus their lower propensity to be triggered by low-intensity events. For panel CP1B, however, 82% of the three-hit events were five-hit events; this can be attributed to the smaller AE gage section (of 16.5-inch radius) and closer spacing of the sensors, allowing the weaker stress waves to reach a larger number of sensors.

The pattern and extent of the five-hit events clustered near the notch tips (Figure 6.7) are in good agreement with the observed final states-of-damage, Figure 6.8. Panel CP1B fractured in

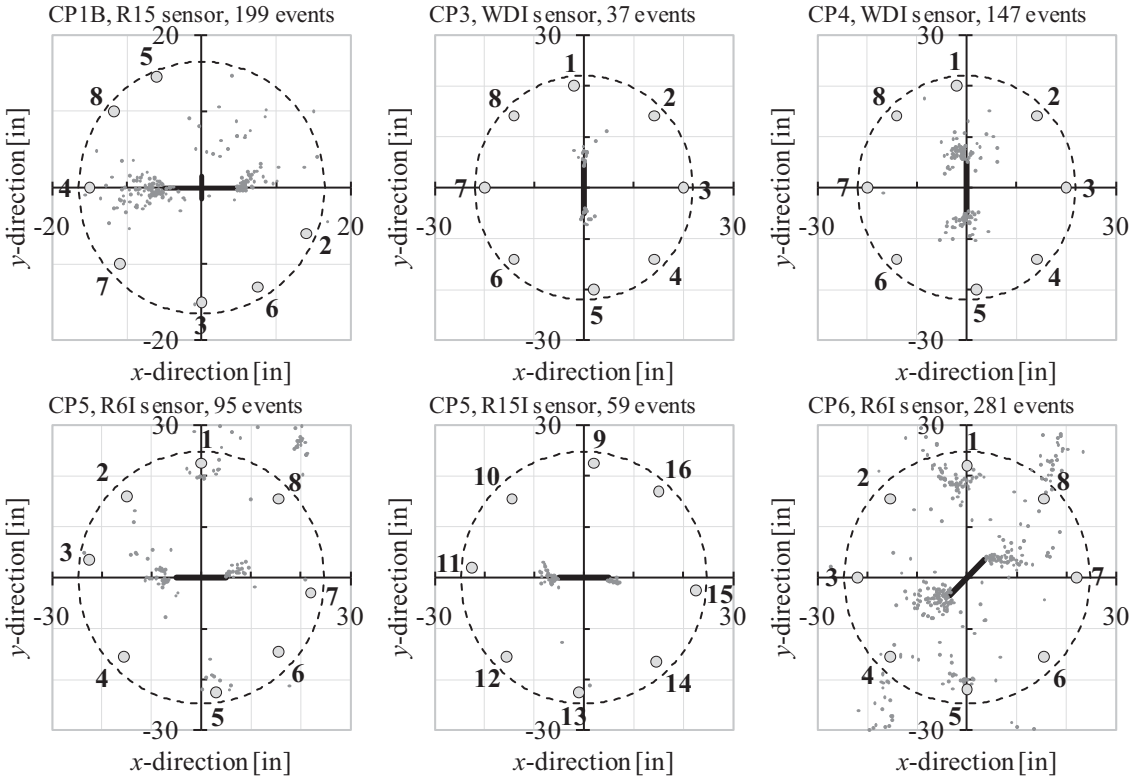

Figure 6.7. Planar source location plots of five-hit events recorded throughout loading. The numbers of events in the figure are those generated from within the circular 16.5-inch-radius gage section for panel CP1B, the 22-inch-radius gage section for panels CP3 and CP4, and the circular 24.75-inch-radius gage section for panels CP5 and CP6.

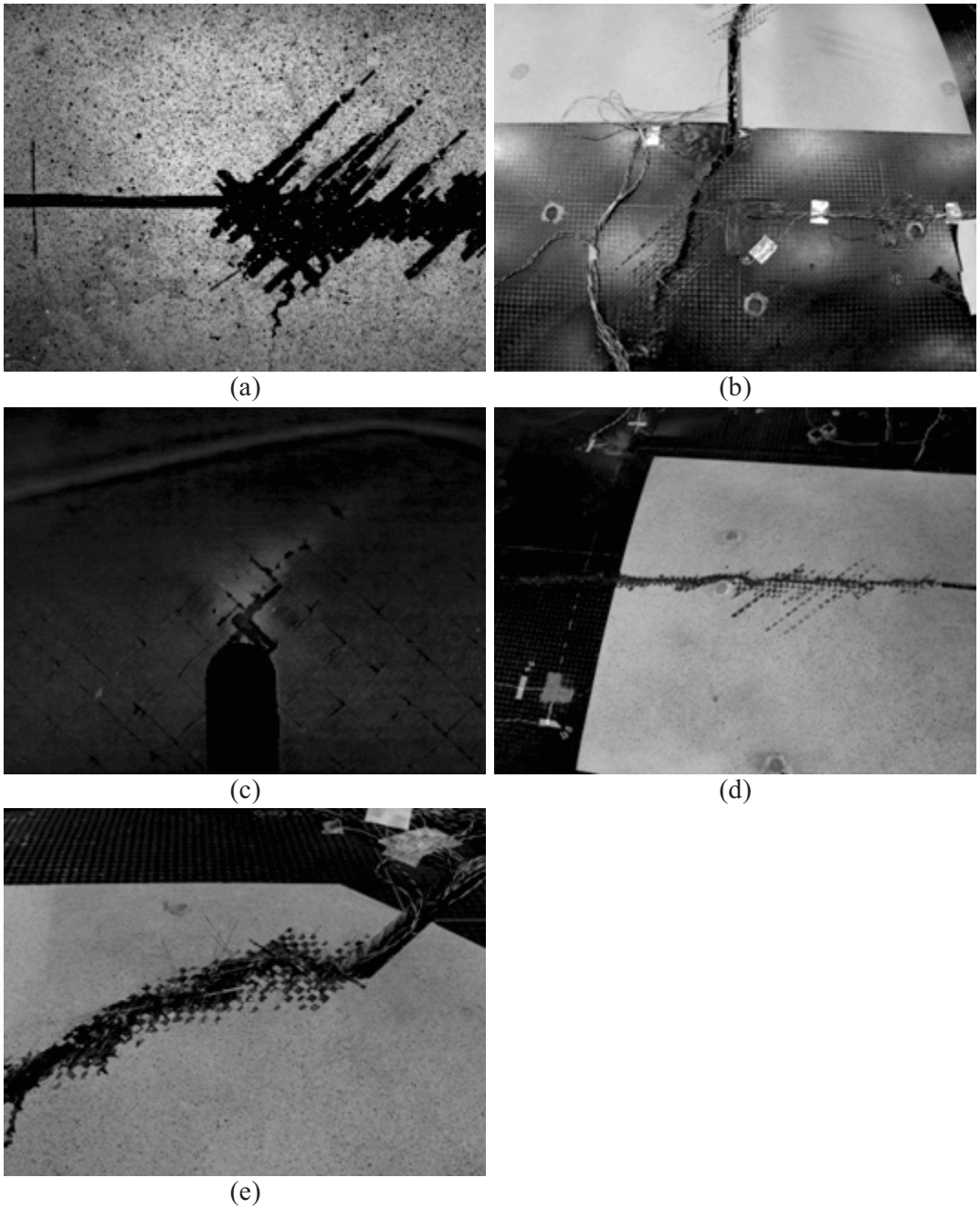

Figure 6.8. Notch tip damage and final fracture for panels (a) CP1B, (b) CP3, (c) CP4, (d) CP5, and (e) CP6.

a self-similar manner, proceeding along the crown of the panel. However, prior to the ultimate fracture of the panel, the damage formation and progression was highly localized to the notch tip regions. The notch tip damage in panels CP3 (Figure 6.8b) and CP4 (Figure 6.8c) progressed in a similar manner; for each, damage was highly localized, with panel CP3 fracturing in an antisymmetric pattern, Figure 6.8b. Once the localized notch tip crack in panel CP5 reached its critical extent, which could be evaluated from the clusters of events near the two notch tips in Figure 6.3, catastrophic fracture of the panel progressed abruptly in a self-similar manner, Figure 6.8d. The notch tip damage in panel CP6 progressed initially along the longitudinal direction of the panel, Figure 6.8e. The extent of the notch tip damage that triggered the final fracture of the panel correlates well with the clusters of five-hit events next to the two notch tips shown in Figure 6.7.

6.4. CORRELATIONS WITH VISUAL NOTCH TIP DAMAGE

The event location plots shown in Figure 6.3 and Figure 6.7 are replotted in a histogram format in Figure 6.9 for three-hit events. The corresponding event-energy location histograms are also shown in the figure. These event and event-energy location histograms show the distribution of the cumulative state of damage at fracture, both in terms of amount of damage and its severity, respectively.

The three-hit event location histograms (Figure 6.9) show that events were generated from throughout the AE gage section of the panels. The number of events recorded with the WDI sensors in panels CP3 and CP4 is much smaller than that recorded by the resonant sensors in panels CP1B, CP5, and CP6. Unlike panels CP5 and CP6, a very small number of three-hit events were located along the edge of the AE gage section in panels CP3 and CP4. This could be attributed to the lower sensitivities of the wideband sensors. Panel CP1B, using the R15 sensors, also did not detect a significant number of events near the panel edges. However, the sensors in panels CP5 and CP6 were located 7.5 inches closer to the hoop loaders and radial link assembly

attachment plates than those in panel CP1B (Section 3.8.1). This holds true for panels CP3 and CP4 as well (where the difference was 2.5 inches with respect to panels CP5 and CP6). Yet, the sensitivity difference in the sensor sets seems to be the dominant factor.

The large clusters of events generated along the longitudinal edges of panel CP5 (Figure 6.3) were most likely caused by extraneous emission generated from the loading fixtures and from the radial link assembly connections. Additionally, clusters of events were also generated from the large, elliptical skin-to-core disbond. Matrix cracking and disbond extension from within and along the boundaries of the disbonded areas may have been the source of emission. The emission generated in panel CP6 is much more widespread, significantly masking the clusters of three-hit events generated by notch tip damage, Figure 6.9f. A large amount of emission was generated from the hoop edges, possibly caused by the high biaxial loads which resulted in significant shear strains within the plain-woven face sheet fabric. The increased acoustic activity in panel CP6 was also attributed to the higher fracture pressure (18.8 psi), 35% higher than the fracture pressure of panel CP5 (13.5 psi).

The event and event-energy location histograms of the three-hit events, Figure 6.9, show that in each panel the majority of the recorded events were generated away from the notch tips. However, these events were of relatively low energy content; the high-energy events were clustered in the immediate vicinity of the notch tips. The event-energy location histograms for panels CP5 and CP6 indicate that the three-hit events generated from the loading fixtures, the radial link assemblies, and the disbonded areas were mostly low-energy events. This suggests that additional, undetected three-hit events may have been generated from throughout panels CP3 and CP4, but could not trigger the less-sensitive WDI sensors.

Similar event and event-energy location histograms are shown for five-hit events in Figure 6.10. With the exception of panel CP6, essentially all five-hit events were generated from the notch tips. For panel CP6, the event and event-energy location histograms indicate that

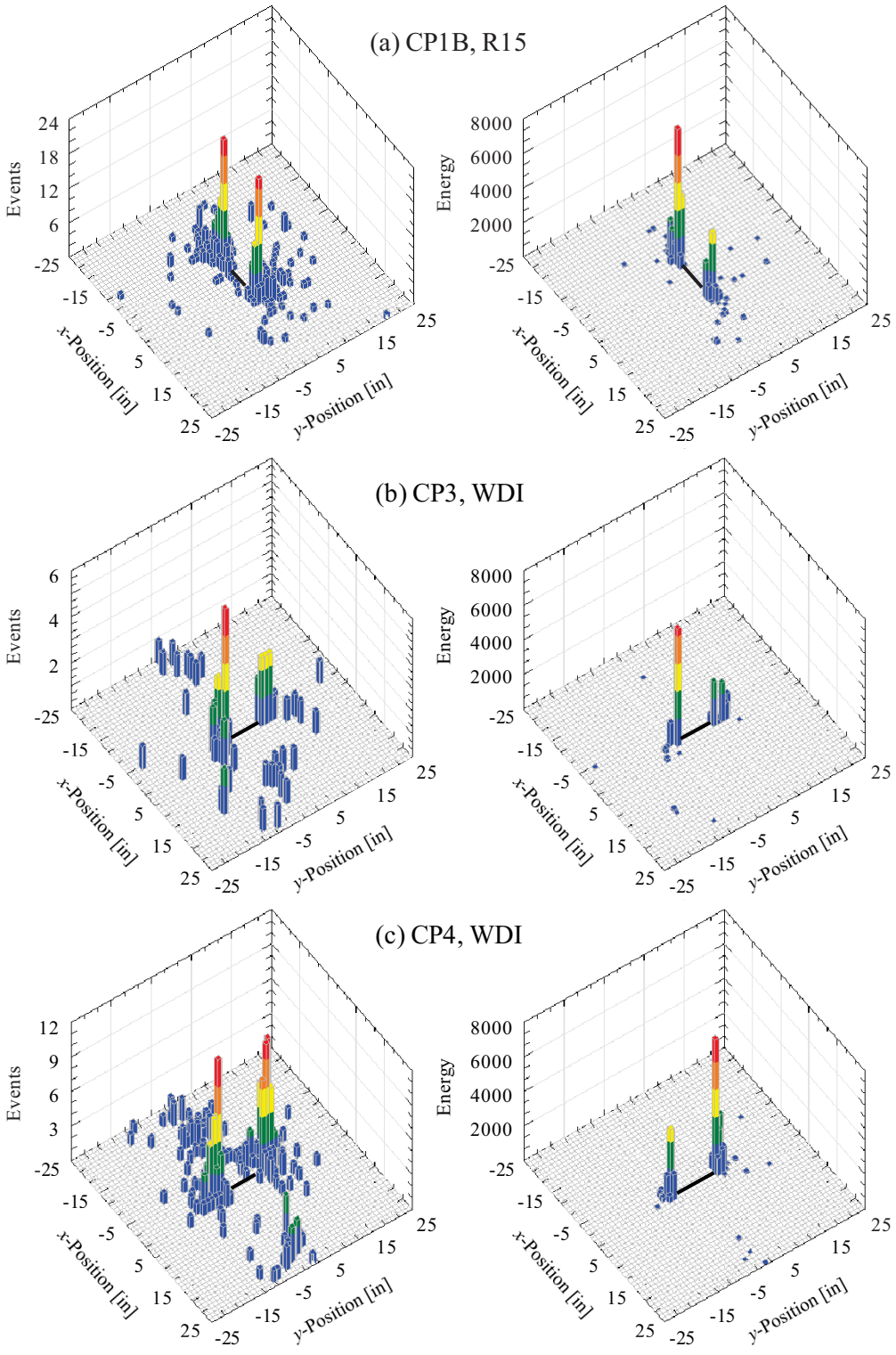

Figure 6.9. Three-dimensional event and event-energy location histograms for three-hit events recorded throughout loading of the four panels. Event-energy histograms clearly indicate the location of damage growth and the extent of damage at the notch tips. (Note the different scales)

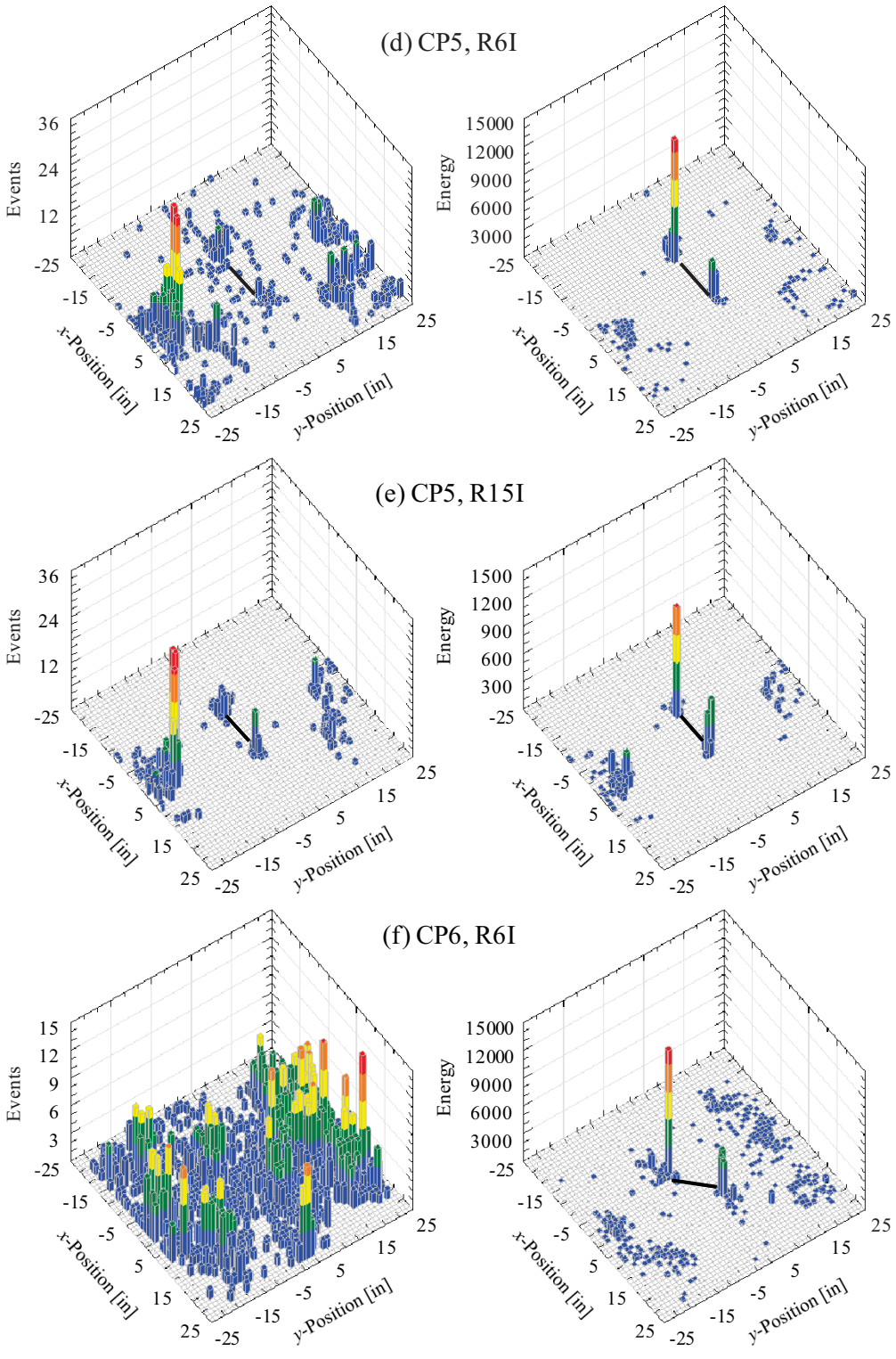

(Figure 6.9 continued)

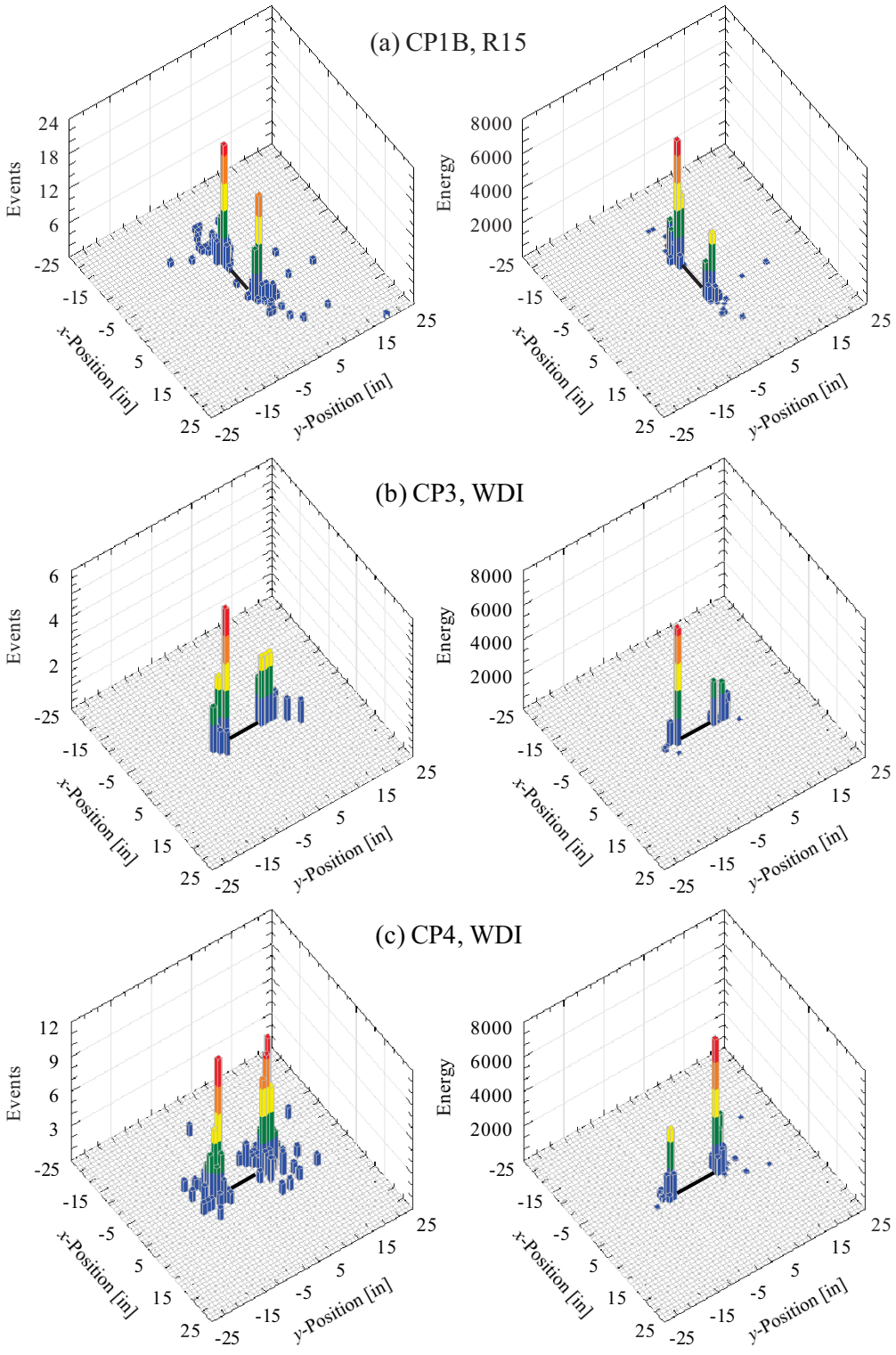

Figure 6.10. Three-dimensional event and event-energy location histograms for five-hit events recorded throughout loading of the four panels. Event-energy histograms clearly indicate the location of damage growth and the extent of damage at the notch tips. (Note the different scales)

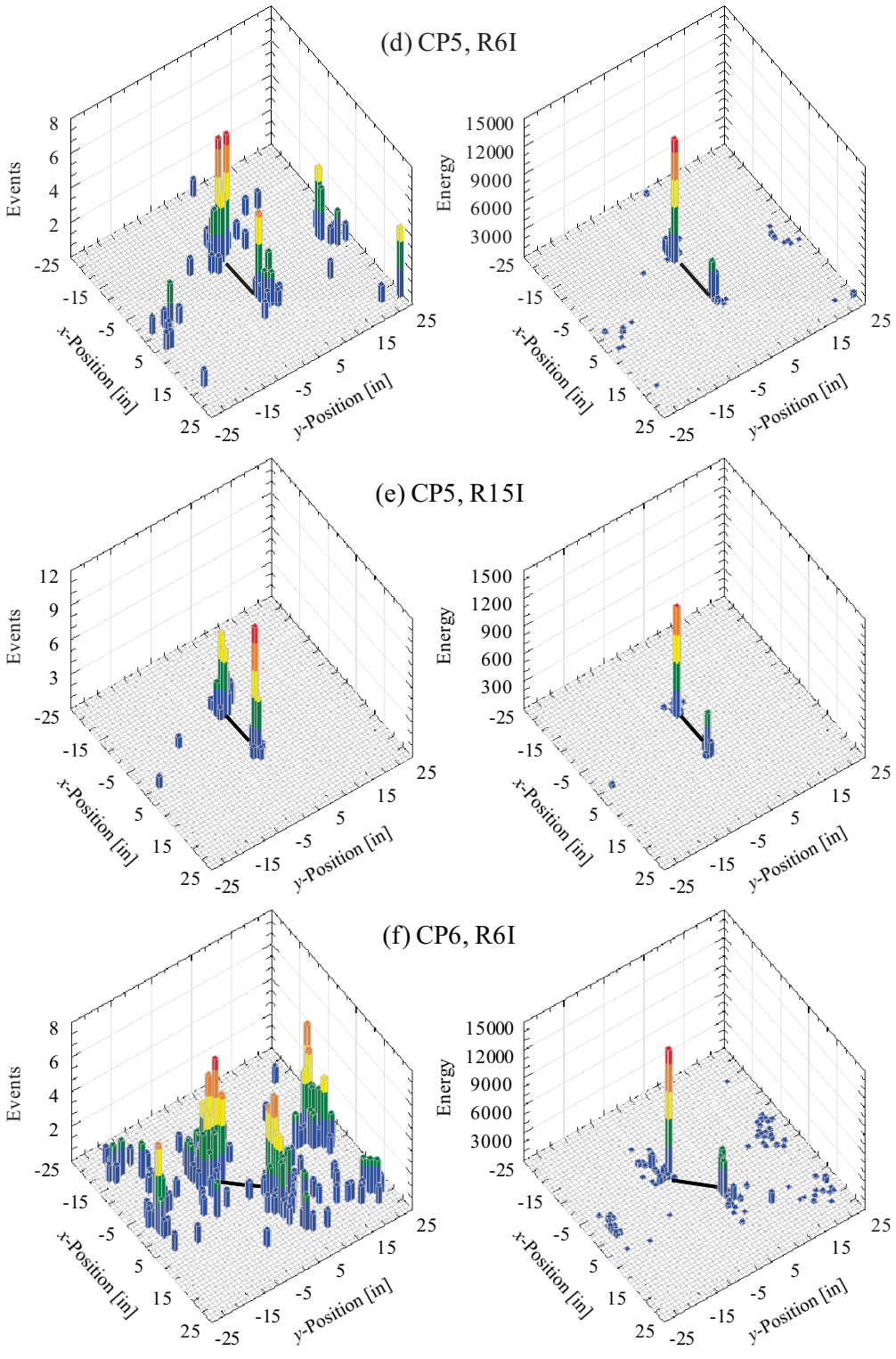

(Figure 6.10 continued)

essentially all the high-energy, five-hit events occurred at the notch tips. In all cases, the largest amount of energy was released at the notch tips, as expected.

The five-hit event and energy location histograms show that a large number of the low-intensity events were eliminated and that the high-energy AE activity occurred primarily in the vicinity of the notch tips. That is, these plots clearly show that by using AE the actual failures and sites of catastrophic fracture could be located in large composite sandwich panels, subjected to complex quasi-static loading, that contain different damage scenarios under various loading functions.

Of great interest is to determine whether the load at which damage initiates, and the progression, extent, and severity of damage could also be identified by monitoring AE. This could be best done by correlating the AE event location histograms with the actual notch tip damage initiation and progression. Such a correlation between the notch tip damage initiation and progression, as recorded by AE and from the DIC strain fields, is shown in Figures 6.11 through 6.15. The event and event-energy location histograms are plotted for three-hit and five-hit events and are compared with their corresponding notch tip strain fields. (The notch tip in the location histograms that corresponds to that shown in the photogrammetric images is noted in figure caption.) The principal strain is used in the correlations shown in Figures 6.11 through 6.15 so as to represent the most severe state-of-strain, in any direction, as measured via the DIC system. Similar correlations could be performed for all other strain components discussed in Chapter 4. For this purpose, the figures shown in Appendix A should be correlated with the event and event energy histograms shown in Figures 6.11 through 6.15. As discussed earlier, the location histograms of the five-hit events and event-energies offer a clearer indication of the state-of-damage at the notch tip as compared with the corresponding histograms of three-hit events. The latter set of histograms, however, is included in order to illustrate the large amount of emission that was generated from regions other than the notch tips and for comparison purposes with the five-hit event and event-energy histograms.

Manufacturer-supplied data on the ply failure strain of the graphite/epoxy woven fabric used in this investigation were: $\varepsilon_{1,ult}$ = 1.41% and $\varepsilon_{2,ult}$ = 1.28%. However, the fact that the panels were curved and subjected to multiaxial loading and the effects of the laminate fabrication process on the effective mechanical properties must be taken into consideration. Absent laminate data, it was assumed for the purpose of the discussion herein, that internal lamina failure processes occur when the strains in the exterior ply (as measured via DIC) reach approximately 1.0%. Since the photogrammetric measurements provide only exterior surface strain fields, surface strain fields of 1.0% are a reliable indicator of higher interlaminar strain fields and possible internal failures caused by matrix cracking, fiber breakage, and delamination. In fact, a detailed finite element stress analysis near the notch tip indicates that 0°/90° mid-plies were subjected to a higher strain field than the exterior ±45° plies. The results of this analysis are discussed in greater detail in Chapter 8.

As mentioned, acoustic activity in panel CP1B was first detected just prior to reaching the third load step, 525 lbf/in hoop load, Figure 6.2a. The few events recorded were located at one of the notch tips, where a maximum principal strain of approximately 0.8% was observed via DIC, though no high-energy events were generated. While the observed surface strains are well below the expected failure strain, the narrow (i.e., 1/16-inch wide) notch increases the likelihood of having a high strain concentration in the 0°/90° mid-ply, increasing the propensity for subsurface, nonvisual damage. Increasing the hoop load to 700 lbf/in, a notable increase in acoustic activity occurred and AE signals of appreciable energy occurred at one of the notch tips. The notch tip strains, as measured via DIC, increased to approximately 1.0% at this load level. This correlated well with the failure of strain gages SG25H and SG[26H] ahead of the same notch tip, Figures 4.11a and 4.11b. A similar progression in acoustic activity in terms of number of events and event-energy content was observed upon further loading up to 875 lbf/in, which was accompanied by a visible notch tip damage extension, effectively extending the notch by 0.52 inch. No increase in terms of the notch tip principal strain was observed. The panel failed while

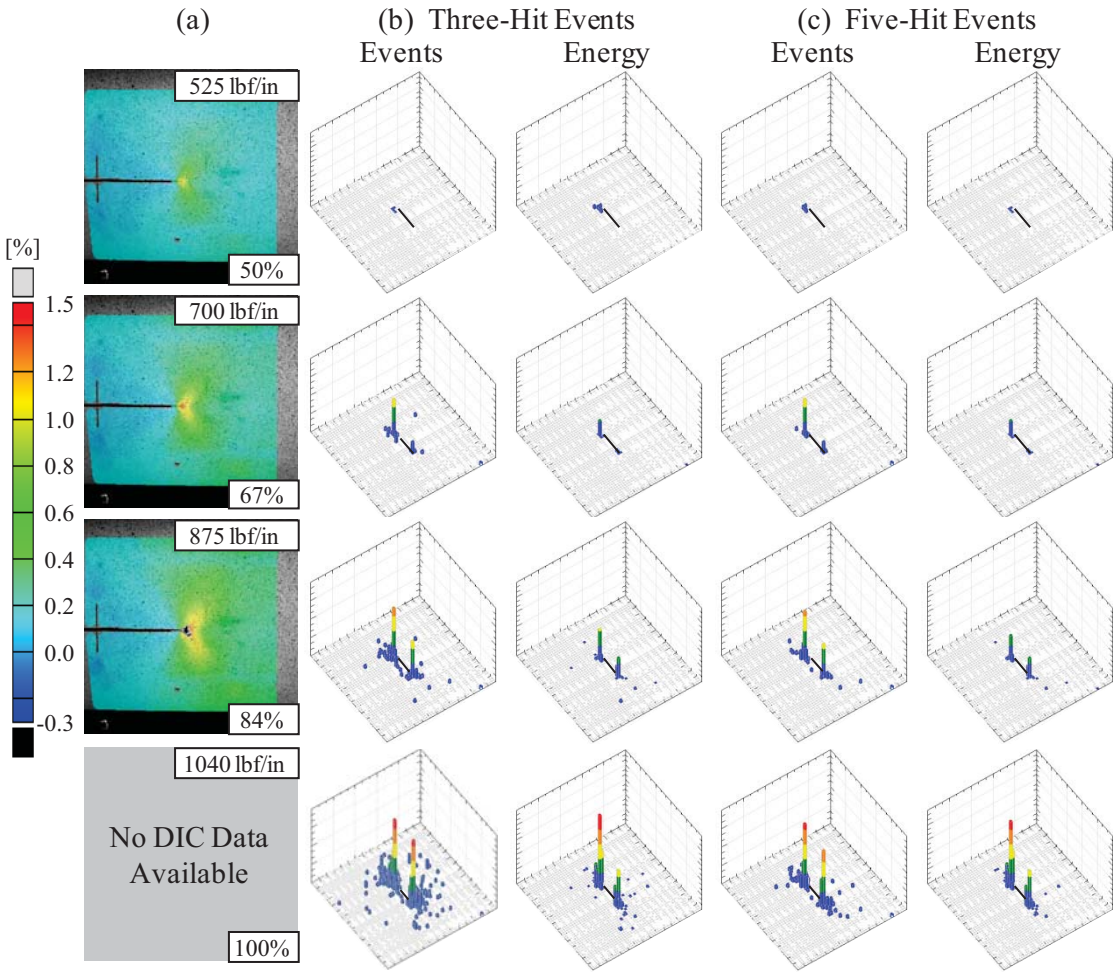

Figure 6.11. Correlation between notch tip damage and AE of panel CP1B at selected loads, showing: (a) the notch tip principal strain field; location histograms of (b) three-hit events and (c) five-hit events, and the corresponding location histograms of event-energy. The notch tip shown in the DIC images is on the lower right side of the location histograms.

loading up to the next load step, at 1040 lbf/in hoop load. The event and event-energy accumulations increased at a higher rate, with almost all of the activity clustered in the immediate vicinity of the two notch tips.

The photogrammetric images of the principal strain field ahead of the notch tip of panel CP3, Figure 6.12, show that the first indication of failure (i.e., strain > 1.0%) occurred when the load reached 1120 lbf/in (74% of the maximum load, at the eighth load step shown in Figure 6.2b). At this load level, the largest principal strain at the notch tip was approximately 1.2%,

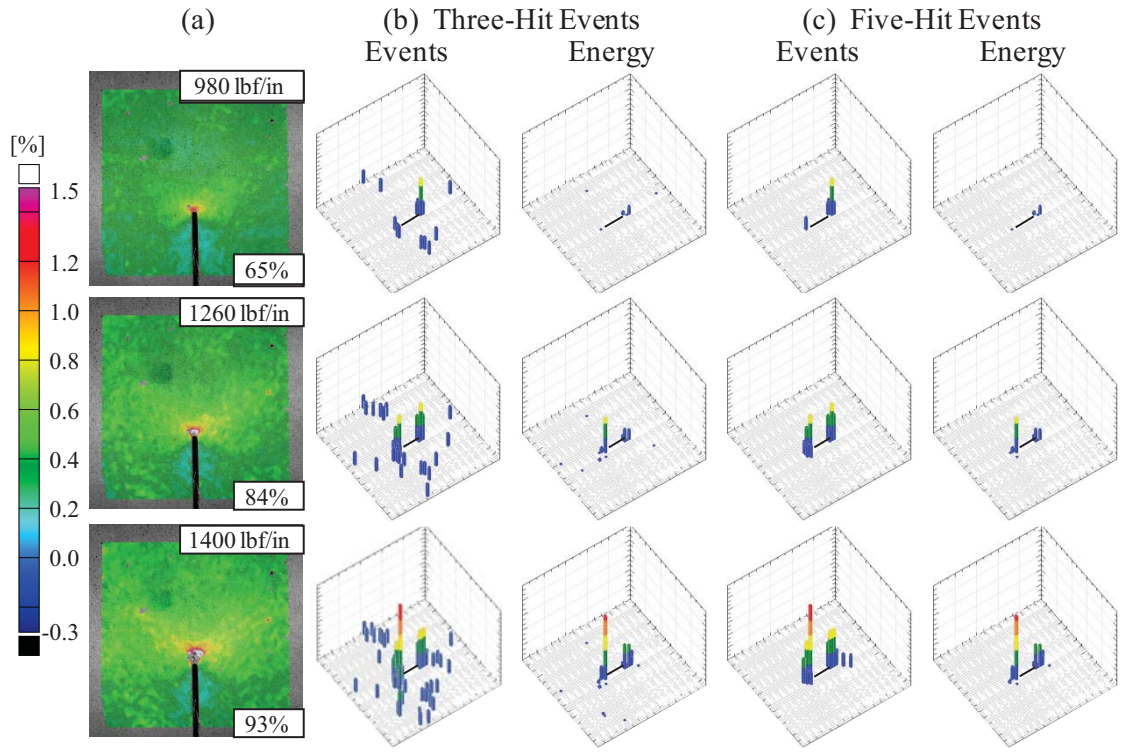

Figure 6.12. Correlation between notch tip damage and AE of panel CP3 at selected loads, showing: (a) the notch tip principal strain field; location histograms of (b) three-hit events and (c) five-hit events, and the corresponding location histograms of event-energy. The notch tip shown in the DIC images is on the upper right side of the location histograms.

extending approximately 0.5 inch ahead of the notch tip. The corresponding AE location histograms also indicate the occurrence of localized notch tip damage. Further increase of the load to 1260 lbf/in and 1400 lbf/in increased the largest principal strains to over 1.5%, extending the damaged area to approximately 0.6 and 1.1 inches ahead of the notch tip, respectively. These results correlate quite well with the notch tip damage as recorded from the corresponding location histograms.

The results for panel CP4, Figure 6.13, are quite similar. The AE location plots show that first occurrence of notch tip damage occurred at 840 lbf/in (i.e., 57% of the maximum applied load), at the eighth load step shown in Figure 6.2c. This load level is significantly lower than in panel CP3, where notch tip emission initiated at 1120 lbf/in. Similarly, the load level

corresponding to the first occurrence of visible notch tip damage via DIC is significantly lower from that observed in panel CP3. This difference in AE results, and the corresponding notch tip strain field, is attributed to the different loading functions applied to the two panels, Figure 3.12. The photogrammetric image at that load level shows that the largest principal strain at the notch tip was approximately 0.8%. Increasing the load to 980 lbf/in yielded a maximum principal strain of 1.0%, extending approximately 0.25 inch ahead of the notch tip. The AE location histograms show a similar extension of the notch tip damage. Matrix cracking became visible at 1120 lbf/in, extending the damage by approximately 0.4 inch, accompanied by a principal strain of 1.0%. The AE results show a corresponding increase in the cumulative event-energy at the notch tip. Notch tip crack opening occurred at 1260 lbf/in and 1350 lbf/in, where the largest principal strains at the notch were over of 1.50%, extended as far as 0.75 and 1.25 inches, respectively. The AE location distribution histograms show similar notch tip damage extension.

The photogrammetric images for panel CP5 show that at 643 lbf/in (9.0 psi, at the fifth load step shown in Figure 6.2) the principal strain reached approximately 1.0% within a localized region of less than 0.25 inch ahead of the notch tip. While emission was generated from other areas of the panel, essentially all five-hit events were generated from the notch tip. The emission generated from throughout the panel and from the loading fixtures increased with increasing load, as expected. However, the majority of the emission generated from the notch tip region was mostly of high-energy. The photogrammetric image recorded at 768 lbf/in shows that the largest principal strain was nearly 1.4%, with the strains over 1% extending 0.5 inch ahead of the notch tip. No visual damage was observed at this load level. This effective, nonvisual notch tip damage extension was accompanied by a simultaneous increase of high-intensity emission, indicating subsurface damage (i.e., in the 0°/90° mid-ply). At the next load level (862 lbf/in), the high strain field was further increased and extended, yielding visible matrix cracking and damage to the plain-weave architecture of the fabric. This damage extended approximately 0.3 inch ahead of the notch tip, effectively constituting a notch tip damage extension. While a significant

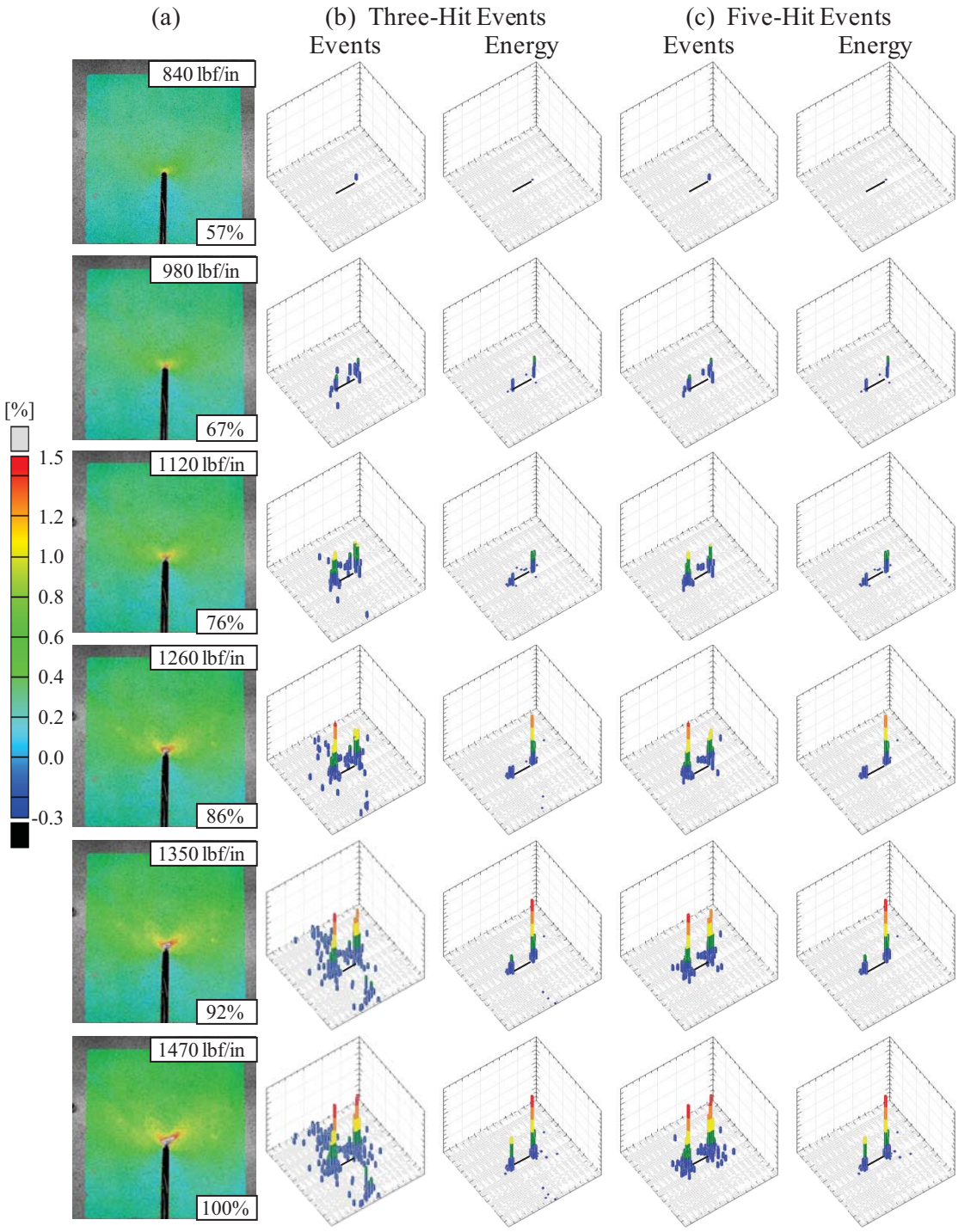

Figure 6.13. Correlation between notch tip damage and AE of panel CP4 at selected loads, showing: (a) the notch tip principal strain field; location histograms of (b) three-hit events and (c) five-hit events, and the corresponding location histograms of event-energy. The notch tip shown in the DIC images is on the upper right side of the location histograms.

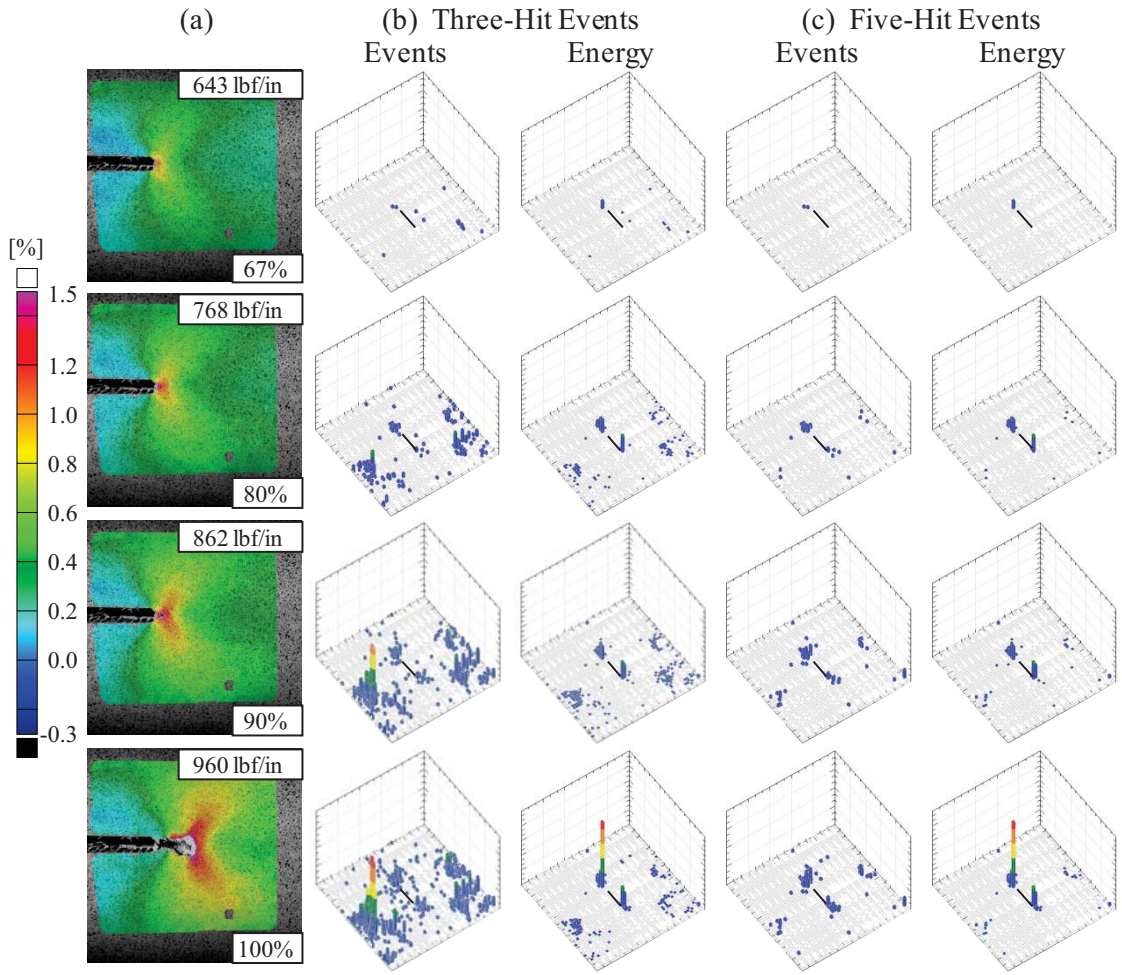

Figure 6.14. Correlation between notch tip damage and AE of panel CP5 at selected loads, showing: (a) the notch tip principal strain field; location histograms of (b) three-hit events and (c) five-hit events, and the corresponding location histograms of event-energy. The notch tip shown in the DIC images is on the lower right side of the location histograms.

amount of emission was generated from throughout the panel, the notch tip damage progression could be clearly identified by the high-intensity five-hit events. At the final load-hold, during which the panel fractured, the notch tip damage extended to over 1.2 inches, which was accompanied with a large amount of high-intensity events.

The case of panel CP6 was quite different compared to the previous panels. The higher loading (18.8 psi internal pressure and equal longitudinal and hoop loading up to fracture load of 1390 lbf/in) and the inclined notch resulted in AE that greatly exceeded that generated in the

other panels. Early indication of AE occurred at a load level of 800 lbf/in (10.8 psi, at the eighth load step, Figure 6.2), 58% of the fracture load. The principal strain at the notch tip was approximately 1.0%, indicating the onset of notch tip damage which is also confirmed by the corresponding location histograms. A small amount of emission was generated along the edges of the panel with only a few AE events generated from the notch tip. All the emission was of low energy. At 900 lbf/in (12.15psi), 65% of the fracture load, the notch tip strain increased to approximately 1.1%, and was accompanied by a localized matrix cracking. Increasing the load further to 1000 lbf/in caused the notch tip strain to increase to nearly 1.2%. A large number of three-hit events spread all over the panel, primarily along its edges, all of low energy. The number of AE events at the notch tip increased, extending along the longitudinal direction. This behavior became more pronounced with increasing the load to 1100 lbf/in. Additional damage occurred at the notch tip, extending the damage approximately 0.75 inch in the longitudinal direction, with the largest principal strain approaching 1.5% at the tip of the visible damage extension.

The event-energy location histograms show a similar pattern. The emission generated from throughout the panel was all of low intensity, caused by various extraneous sources. The notch tip damage increased markedly at a load level of 1200 lbf/in, displaying a step-wise and meandering damage progression in the longitudinal direction. The corresponding AE event location histograms show that emission generated from throughout the panel increased significantly, yet it was all of low intensity. The five-hit event location histograms of the corresponding high-energy events exhibited a remarkably similar pattern to the damage extension recorded via photogrammetry. The last load step, 1300 lbf/in combined loading, caused extensive notch tip damage, approximately 2.0 inches ahead of the notch tip with the high strain field, with a maximum principal strain of over 1.5%, extending to 2.5 inches. A voluminous amount of three-hit events was generated from the entire panel, again all of low energy.

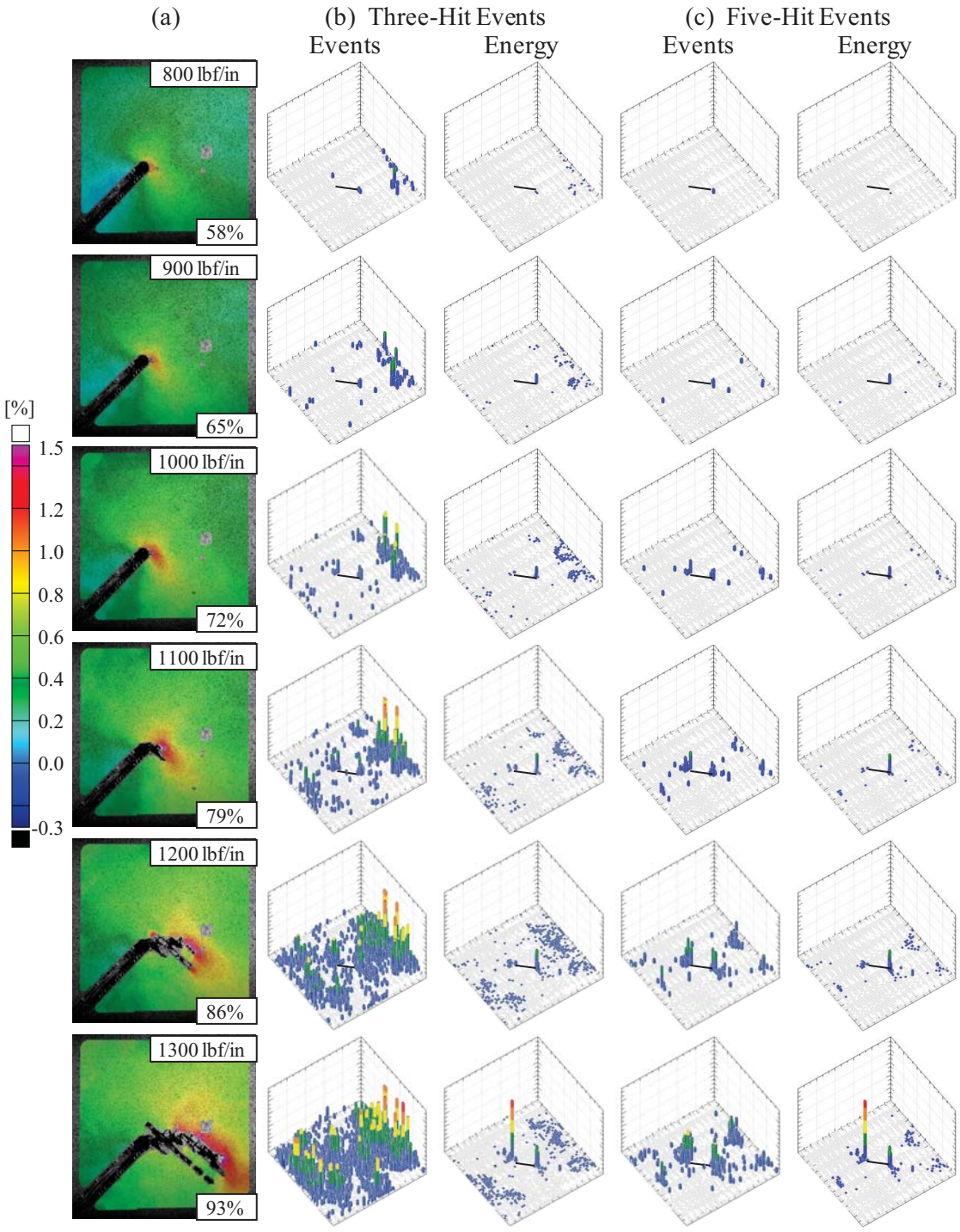

Figure 6.15. Correlation between notch tip damage and AE of panel CP6 at selected loads, showing: (a) the notch tip principal strain field; location histograms of (b) three-hit events and (c) five-hit events, and the corresponding location histograms of event-energy. The notch tip shown in the DIC images is on the right side of the location histograms.

The location histograms of the five-hit events and of the corresponding event-energy clearly show that notch tip damage progression is accompanied by simultaneous increase and extension of high-intensity emission areas. The pattern formed by the events generated at the notch tip and the direction of their progression corresponded very well with the actual failure progression seen in the DIC data. Replaying the accumulation of the AE events shows the progression of the damage ahead of the notch tip with increasing load in a remarkable similarity to that observed via photogrammetry. Further, in all cases AE occurred prior to the occurrence of visible notch tip damage. The results clearly show that when using AE with a proper experimental setup and well-selected pretest settings, AE can be used in large composite structures that are subjected to multiaxial loading to detect the onset of failure, monitor its accumulation, and track failure progression, all in real-time.

6.5. DAMAGE MODE IDENTIFICATION

One of the objectives of monitoring AE is to identify the failure modes that occur during loading. This information could aid in evaluating damage criticality. The failure modes of greatest interest include delamination (for honeycomb sandwich construction face sheet-to-core disbonding is also of great interest), matrix cracking, and fiber breakage. The scanning electron microscopy results discussed in Section 5.6 clearly indicate that all these failures occurred at the notch tip region of panel CP5. A significant amount of pull-out of individual fibers and fiber tows also took place. Radiographs showed that no crushing or any significant deformation or distortion of the honeycomb core was observed, as discussed in Section 5.5.

One of the more conventional approaches to determine whether AE could identify composite failure modes is to analyze the AE events intensities, such as amplitude, duration, counts, and energy. Normally, such an analysis is done qualitatively through examinations and comparisons of the event intensity distribution histograms. Accordingly, the following discussion examines the event intensities of:

(i) All the events generated from within the panel AE gage sections.

(ii) The events generated during the cyclic loading of panel CP5.

(iii) The events generated from the disbonded area and the supporting fixtures of panel CP5.

(iv) The events generated locally from the notch tip regions of each panel.

6.5.1. EVENT INTENSITIES OF ALL EVENTS

The intensity distribution histograms of all the events generated throughout loading for each panel are shown in Figure 6.16. The amplitude distribution histograms show that, generally, the amplitude of most of the events is below 75 dB, averaging between 45 dB and 70 dB, which is normally associated with matrix cracking and delamination. The number of high-amplitude events is very small in all panels, most of which were generated just prior to panel fracture, Figure 6.2.

In each of the panels, most of the events contain less than 50 counts per event; however, a degree of uncertainty surrounds this observation. Unless a distinction can be made between single AE waveforms and trains of AE signals that the AE system considered a single hit of increased counts, the validity of the count distribution histograms, and those of the other waveform characteristics cannot be confidently interpreted. The event duration distribution histograms show that most of the waveforms recorded by the WDI and R15I sensors were less than 0.5 ms in duration, while the R6I sensors recorded events with much longer durations, as long as 2.5 ms, which is expected considering the effect of the extended ring down time on the likelihood of the HDT extending the duration of that hit. The event energy distribution histograms reflect the distribution histograms of the amplitude and duration, and, therefore, do not reveal any new information. The intensity distribution histograms recorded for panel CP6 have a slightly different form as a result of the repeated loading-unloading, Figure 6.2f.

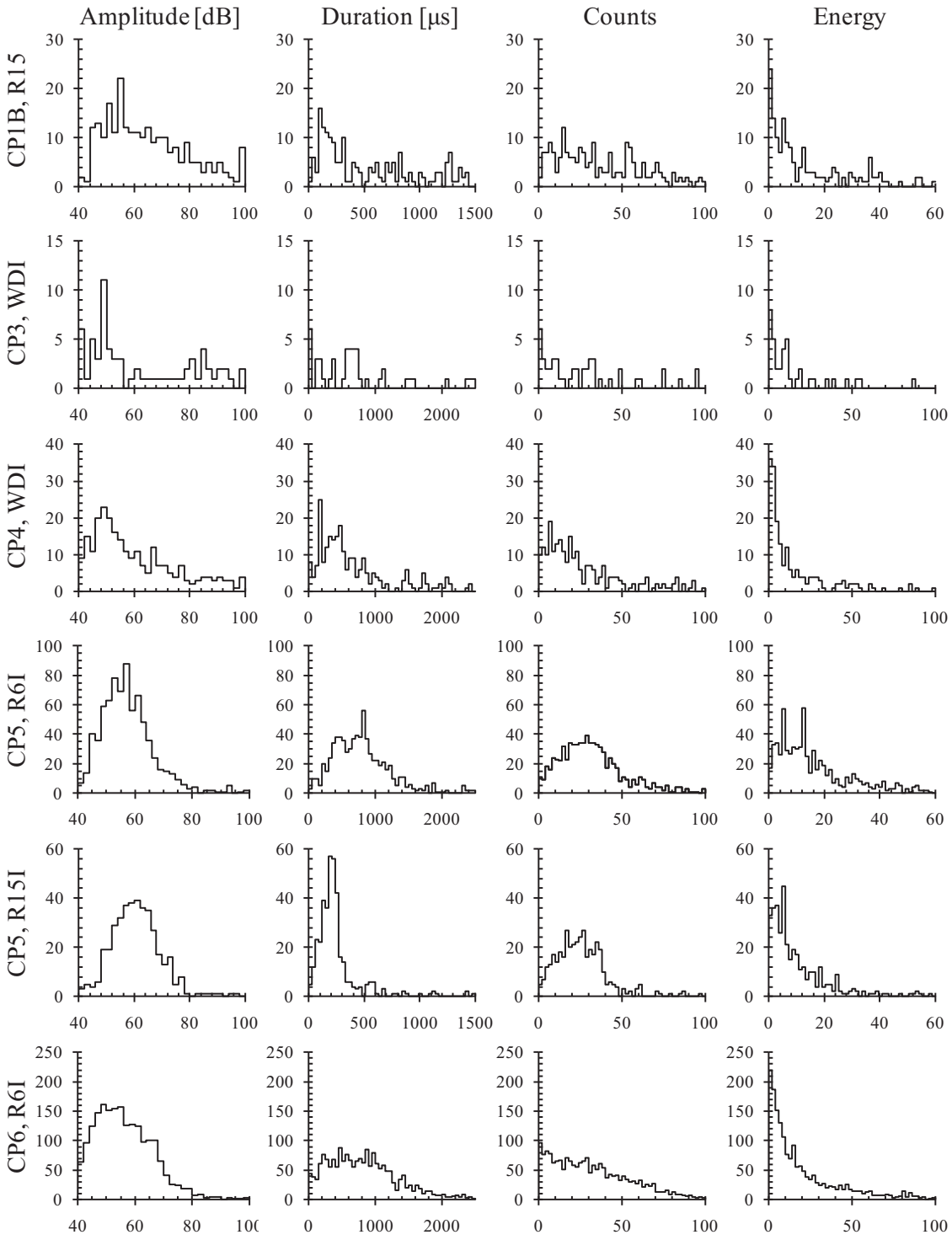

Figure 6.16. Amplitude, duration, counts, and energy distribution histograms of all three-hit events generated throughout the AE gage sections of the panels. For clarity, the distributions are shown in different scales.

The likelihood of a particular AE signal being either a train of waveforms or resultant of only a single waveform can be easily assessed for tests conducted with resonant sensors. A resonant sensor tends to record waveforms at the resonant frequency of the sensor (e.g., 55 kHz for R6I sensors and 150 kHz for R15 and R15I sensors). An AE signal recorded with a resonant sensor should oscillate at the resonant frequency of the sensor. Accordingly, the recorded counts and duration can be used to calculate the average frequency of the waveform through:

$$f_{\text{avg}} = \frac{\text{counts}}{\text{duration}} \tag{6.1}$$

For any AE signal, the calculated average frequency will be approximately equal to the resonant frequency of the sensor. If, however, the HDT is triggered several times by newly arrived AE signals, portions of the duration of the recorded AE signal will not be populated by threshold crossings, thus decreasing the average frequency. These lower average frequencies are indicative of trains of AE signals. Plots of counts versus duration, such as that shown in Figure 6.17 for panel CP5, can be used to illustrate the occurrence of trains of AE signals: while the majority of

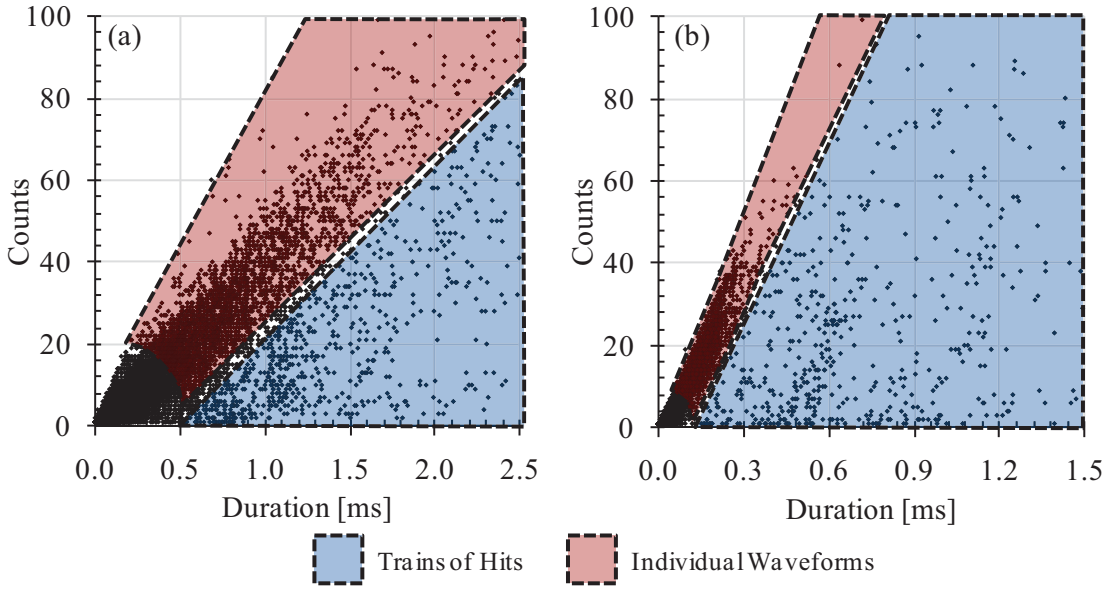

Figure 6.17. Counts versus duration for AE hits from panel CP5 using (a) R6I and (b) R15I sensors. The shaded regions indicate the propensity for trains of hits to exist.

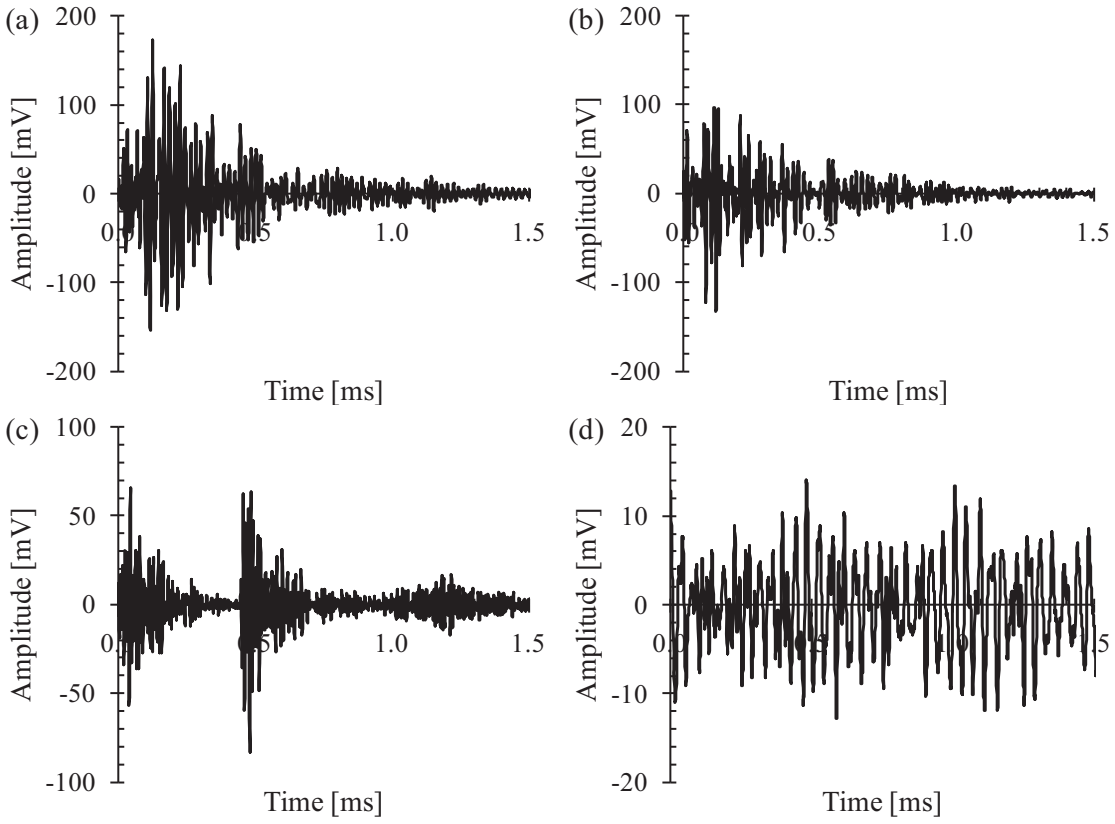

Figure 6.18. Comparison of recorded AE signals from single and multiple stress waves. (a) Single stress wave, 62 counts, 1.344 ms duration; (b) single stress wave, 47 counts, 0.964 ms duration; (c) noise, 58 counts, 2.155 ms duration; (d) multiple stress waves, 10 counts, 1.796 ms duration.

the AE signals are clustered along a line with a slope approximately equal to the resonant sensor frequency, any recorded train of hits will have lower average frequencies, being located in the highlighted region of the figure. Examples of AE signals corresponding to single stress waves (highlighted red region of Figure 6.17a) and trains of hits (highlighted blue region of Figure 6.17a) are shown in Figure 6.18. The recorded AE signal in Figure 6.18c is clearly resultant of separate stress waves reaching the sensor with the HDT. Figure 6.18d shows near-threshold (i.e., 10 mV) oscillations, regularly resetting the HDT, extending the duration of the recorded AE signal.

6.5.2. FRETTING EMISSION GENERATED DURING CYCLIC LOADING

As mentioned earlier, a significant amount of emission could also be generated by fretting, either among existing fracture (or disbonded) surfaces or from extraneous sources, such as the loading fixtures. As discussed, new damage generates emission only once, however, the subsequent fretting among the newly formed fracture surfaces, could continue throughout loading. As a result, the amount of fretting-generated emission could exceed the amount of emission generated by the formation of new cracks. Therefore, to distinguish emission generated by new failures, the characteristics of the fretting-generated waveforms must be identified.

For panel CP5, fretting emission was generated from the radial links and from the large disbond. Most likely, emission generated from the loading fixtures may have also hit the nearby sensors. These AE signals, however, were generated from outside the AE gage section, and, therefore, they should not have been recorded as legitimate events. Nevertheless, these extraneous waves may have hit the sensors within the HDT of legitimate hits that were generated from within the circular AE gage section, possibly distorting some of the AE source location results.

To characterize the intensities of AE events that could have been caused by friction, panel CP5 was subjected to cyclic loading segments, Figure 6.2d. The event intensity histograms of the events generated during the third and fourth segments of cyclic loading for the R6I and R15I sensor sets are shown in Figure 6.19. The histograms show that most of AE signal features have low intensities: amplitude below 70 dB, counts below 40, duration below 1.0 ms for R6I and below 0.5 ms for R15I, and energy below 20. These intensities are similar to the range of intensities of all the events that were generated throughout loading for panel CP5, Figure 6.16. Further, these intensities are similar to those that were characterized in [6.5–6.8] for coupon-type graphite/epoxy specimens as being generated by fretting. Therefore, no waveform features clearly distinguish the AE signals generated via fretting from those generated throughout the panels from those generated by actual damage.

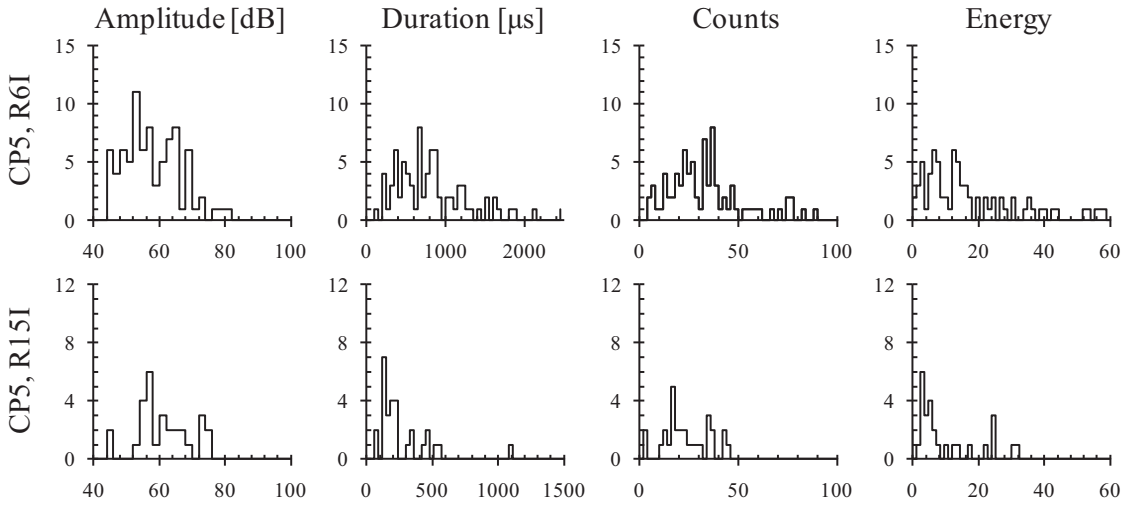

Figure 6.19. Amplitude, duration, counts, and energy distribution histograms of three-hit events generated from the AE gage section of panel CP5 during the third and fourth cyclic load segments. 82 and 29 events were recorded by the R6I and R15I sensor sets, respectively.

6.5.3. EMISSION FROM EXISTING DAMAGE AND LOADING FIXTURES

The source location results of panel CP5 revealed that a significant amount of emission was generated from the region of the large skin-to-core disbond. However, the disbonded area partially overlapped with the site where one of the radial link assemblies attached to the interior surface of the panel. Therefore, no location-based separation of the events generated from these two sources was possible. The locations of the three-hit events generated from these two sources are shown in Figure 6.20 and were analyzed in terms of AE event intensities. The corresponding histograms of the event intensities, Figure 6.21, indicate that most of the intensities of the associated AE signals are low. In fact, the range of the intensities is essentially identical to that recorded for the emission generated during the cyclic loading for both the R6I and R15I sensors, Figure 6.19. This comparison further confirms that the emission clustered in the region of the disbond and the radial link is a result of fretting. The higher range of event intensities shown in these histograms could have been generated by additional matrix cracking within the disbonded region or due to its extension during loading. Finally, Figure 6.3 and Figure 6.9d show event

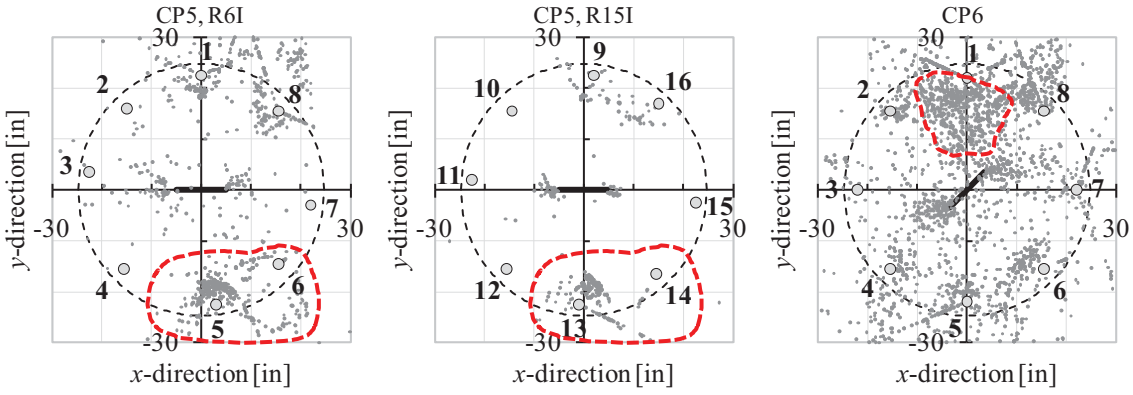

Figure 6.20. Events assumed to be associated with fretting emission from the large skin-to-core disbond and the radial link assembly attachment plate in panel CP5, and a radial link assembly attachment plate in panel CP6.

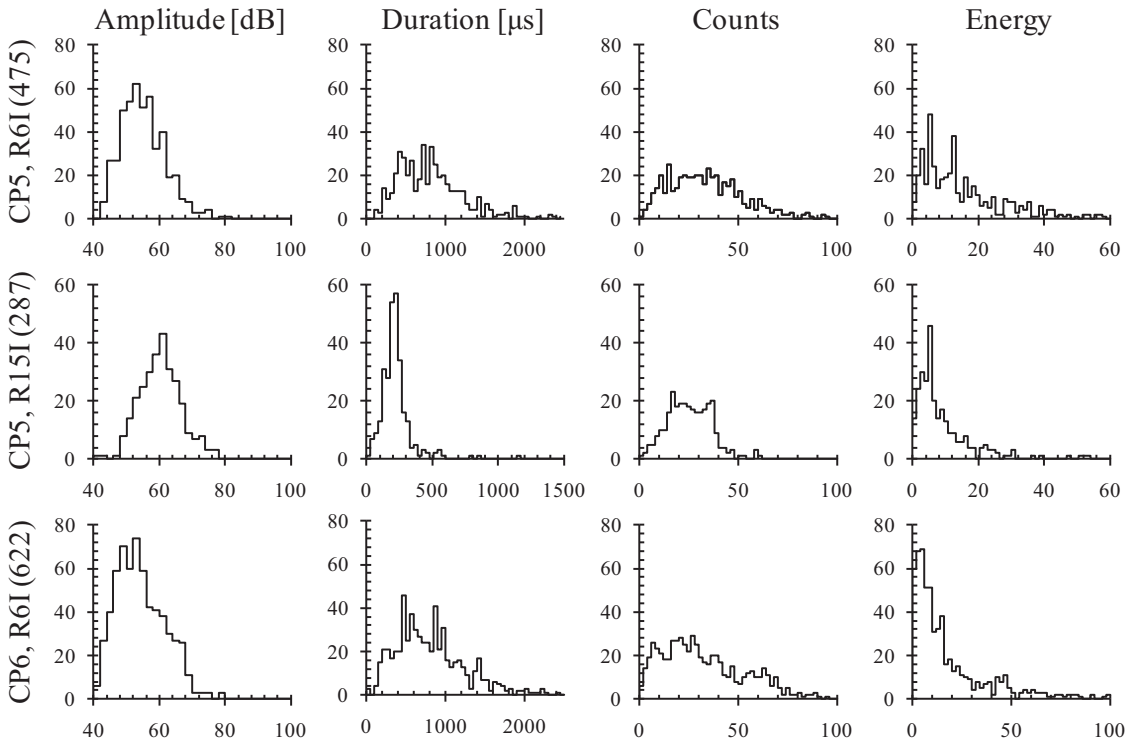

Figure 6.21. Amplitude, duration, counts, and energy distribution histograms of three-hit events generated from the regions of panels CP5 and CP6 highlighted in Figure 6.20. The number of events detected in these regions is denoted in parentheses.

clusters opposite the disbond, confirming that most of the events were generated by fretting and should be considered as extraneous emission. The intensity histograms of these three-hit events are also very similar to those shown in Figure 6.16 and Figure 6.19.

6.5.4. EMISSION GENERATED FROM NOTCH TIP REGIONS

The event intensities of the three-hit events generated from the notch tip regions of the panels are shown in Figure 6.22. The notch tip regions referred to here are the same 60-in^2 regions described in Section 6.3. In panels CP3 and CP4, approximately 60% of the events were generated from within the notch tip regions. Note, however, that the last load step of panel CP3 was not recorded, and panel CP4 was not loaded to fracture. Comparing the amplitude distribution histograms of all events (Figure 6.16) with those that were generated by fretting (Figure 6.19 and Figure 6.21) shows that the events generated from within the notch tip regions of panels CP3 and CP4 contained a much larger percentage of events of a higher amplitude range. These high-amplitude events resulted, primarily, from new failures. However, the distribution histograms of all four intensities show a significant percentage of low-intensity events which were generated either from fretting or from matrix failures. The latter may confirm the examination of the radiograph of CP4 (Figure 6.8c), which indicates that there were also localized matrix cracking and damage to the plain-weave architecture distributed in the vicinity of the notch.

The percentage of three-hit events generated from within the notch regions of panels CP5 and CP6 was much smaller: 10% for sensor R6I and 16% for sensor R15I in panel CP5, and 16% for sensor R6I in panel CP6. Note, however, that the R6I and R15I sensors used in panels CP5 and CP6 are more sensitive than the WDI sensors used in panels CP3 and CP4. Further, the latter two panels were loaded to higher loads, generating a larger number of events from throughout the panels, primarily from the loading fixtures and the disbonded areas. Yet, the event

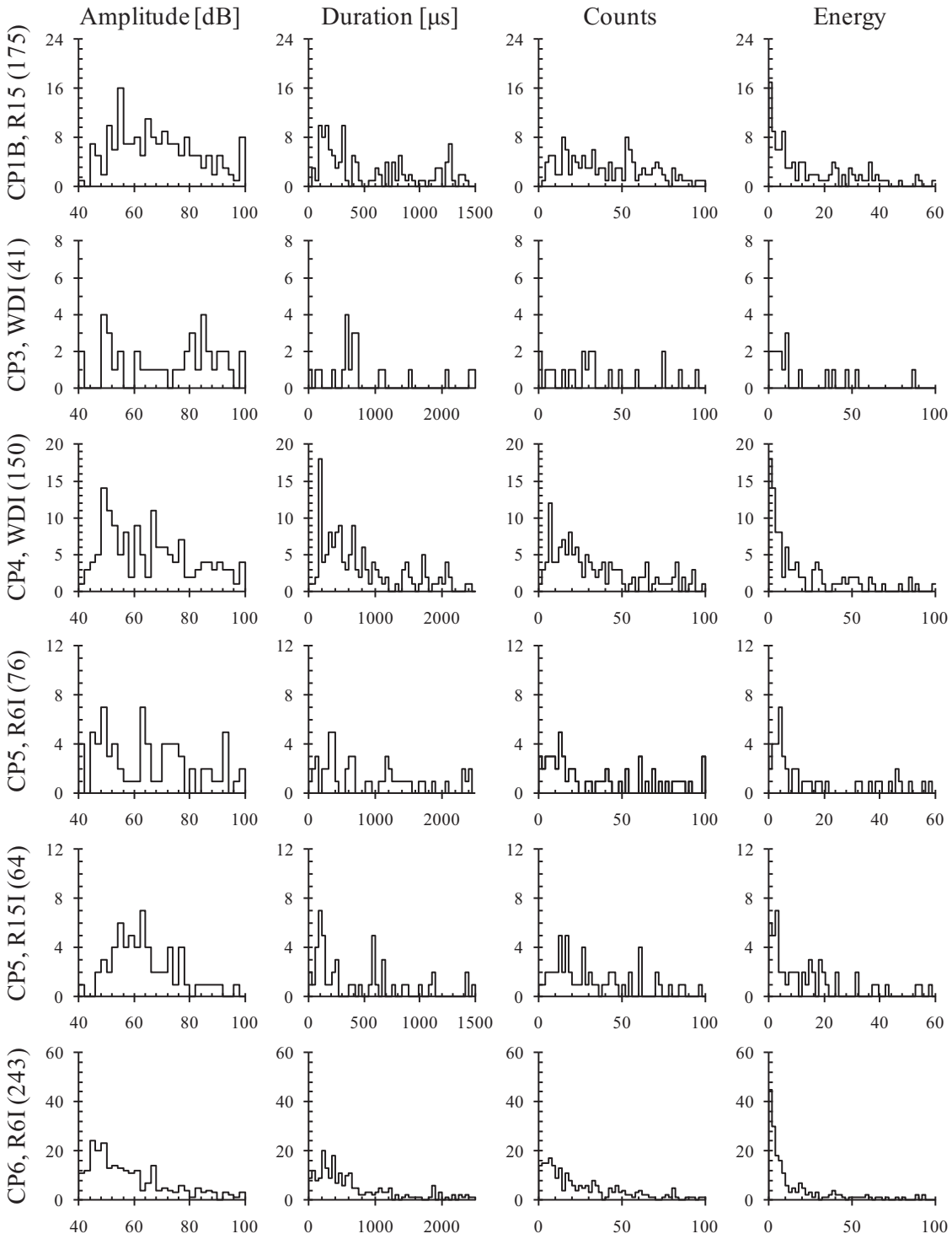

Figure 6.22. Amplitude, duration, event counts, and energy counts distribution histograms of three-hit events generated from the two notch tip regions of the panels. The number of events detected in the notch regions is denoted in parentheses.

intensity distribution histograms of the three-hit events generated from within the notch tip regions of panels CP5 and CP6 are qualitatively very similar to the histograms of three-hit events generated from throughout the panels, Figure 6.16. In other words, no direct correspondence could be made between the emission generated by new failures and that generated by the variety of other extraneous sources of emission. However, when the data are filtered for the high-intensity events (or a higher number of hits are used to define a locatable event), the corresponding location plots indicate quite well where new failures occurred (Figure 6.7), even though a large number of high-intensity events were generated from other regions as a result of trains of friction-generated AE signals being recorded as single high-intensity events.

6.6. TYPICAL WAVEFORMS RECORDED DURING LOADING

Examination of the recorded waveforms could help in interpreting the AE results. Of primary interest is to determine the best sensor type to be used in a particular application, to evaluate whether a particular waveform actually represents a stress wave that was generated by a new failure or whether it is merely a result of extraneous emission, or to determine the extent to which trains of hits were recorded by the AE sensor as a single hit of increased intensity. More recently, efforts were made in establishing a correspondence between the types of failure and the frequency content of the generated waveform (e.g., [6.9] and [6.10]).

The waveforms and power spectra of two typical AE signals recorded by the R6I and R15I sensor sets in panel CP5 are shown in Figure 6.23. The two AE sources were generated at the same load level, 520 lbf/in (54% of the panel fracture load). All eight sensors of both sets of sensors were hit, and located the sources at approximately the same location, immediately ahead of one of the notch tips. The AE signal triggered the first R6I sensor 30 μs after the first R15I sensor was triggered. In the R6I sensor set, the second and third hits were recorded 1.0 μs and 5.3 μs after the first hit, respectively; for the R15I sensor set, both the second and third hits

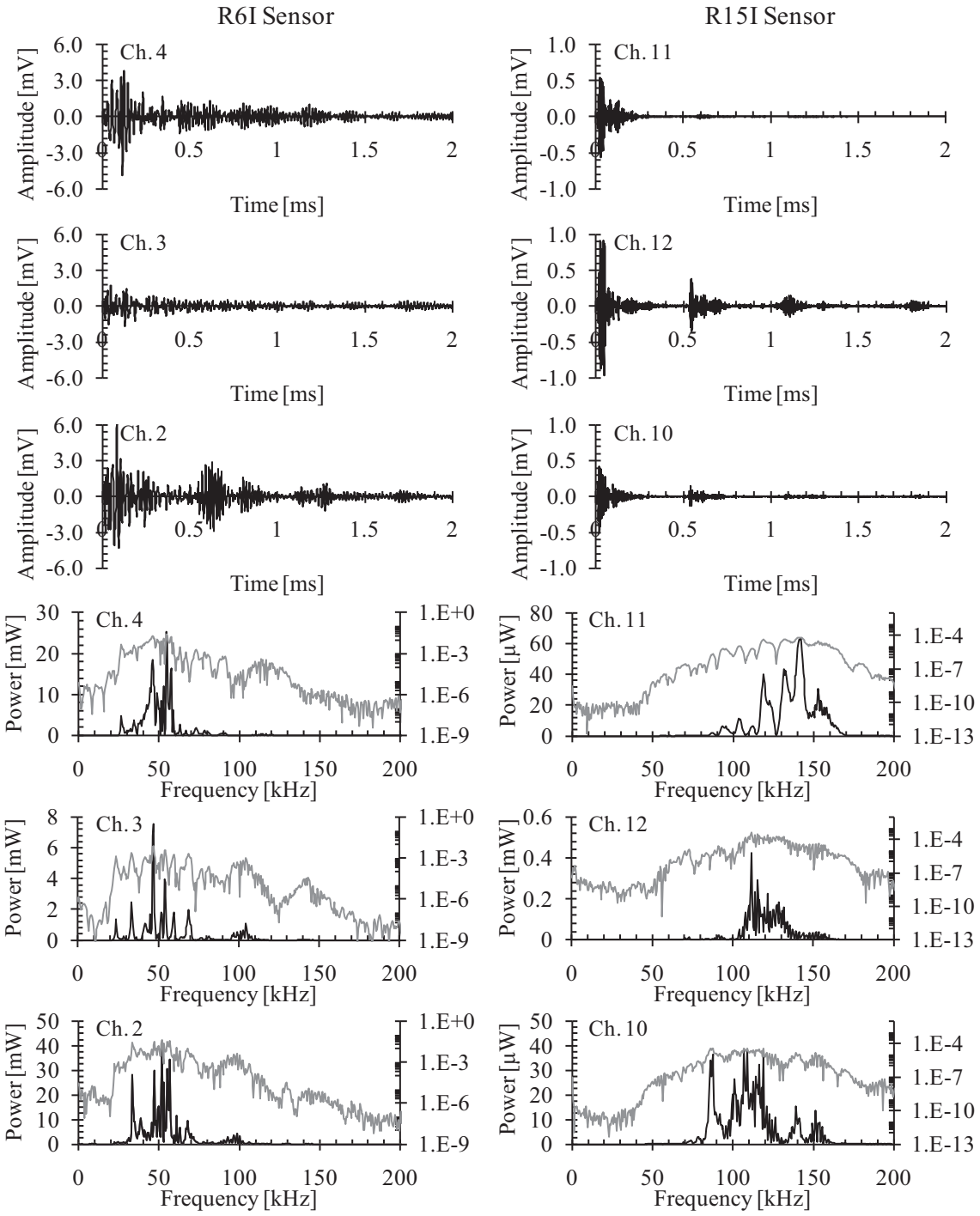

Figure 6.23. Waveforms and power spectra (in linear and logarithmic scales) of the first three signals recorded for two high-amplitude events recorded by the R6I and R15I sensors in panel CP5. The two AE signals were recorded at the same load level and located at the same location by the two sensor sets (i.e., the two waveforms could have been generated by the same failure).

Table 6.1. Intensities of the first three hits of an eight-hit event, recorded by the R6I and R15I sensor sets in panel CP5.

	R6I sensor			R15I sensor		
	Ch. 4	Ch. 3	Ch. 2	Ch. 11	Ch. 12	Ch. 10
Amplitude [dB]	94	85	96	75	80	73
Duration [μs]	9879	7872	11385	669	4700	2481
Counts	402	359	457	48	347	117
Energy	1626	806	2041	39	157	53
Δt [ms]	0	1.0	5.3	0	5.0	5.0

occurred 5.0 μs after the first hit, Table 6.1. It is likely that the two AE signals were generated by the same failure. The location of each AE sensor is indicated in Figure 6.3.

The plots of the three waveforms that hit the first three R6I sensors indicate that several waveforms were superimposed. Some of the secondary waveforms could be reflections from the edges of the panel and/or generated by other extraneous emission. The long duration of the waveforms, approximately 10 ms (Table 6.1), is also an indication of several superimposed waveforms that were recorded by the AE channel as a single waveform: it is much longer than a typical AE signal and longer than an expected stress wave generated by a rapid matrix cracking and/or by fiber fracture. The corresponding power spectra of the waveforms show that the peak frequency is approximately 50 kHz, as expected for the R6I sensor.

The corresponding waveform plots recorded for the first three hits by the R15I sensors are quite different. The main waveform could be easily identified, having a duration which is approximately 0.25 ms. The first hit does not include any secondary waves, thus, its intensities of duration, counts, and energy would seem to be correct as indicated in Table 6.1. The second and third hits, however, include secondary waveforms that occurred well within the HDT, thus, they were superimposed into a single hit of increased intensity. Note, however, that the analysis of the intensities of a locatable event is normally based on the intensities of the first hit only. Thus, the event intensities recorded by the R15I sensor set shown in the figure will be those of the first waveform, which intensities are considerably lower than those of the second hit (e.g., the

durations of the first and seconds hits were 0.7 and 4.7 ms, respectively). The corresponding power spectra for the three hits show that the peak frequency range is between 80 and 150 kHz, as expected when using the R15I sensor.

Examples of low- and medium-amplitude AE signals, generated from the two notch tips of panel CP5, are shown in Figure 6.24. The data of the first three hits of the four AE signals are listed in Table 6.2 together with the time intervals between the first and the subsequent two hits of each of the locatable events. The waveforms of the two AE signals generated from the left-hand side of the notch show trailing waves of low intensities. Accordingly, the durations recorded for these two waveforms were increased, each above 1 ms, although the leading waveform, as seen in Figure 6.24, is much shorter. Recalling that the notch was shifted 10 inches along the crown of the panel toward one side of the panel (Figure 3.20), it could be concluded, based on the characteristic wave speed of the panel face sheet material, that these trailing waves most probably resulted from reflections off the panel edges. No such reflections were recorded from the other notch tip, which was farther away from the nearest panel edge. Similar wave reflections are seen also in Figure 6.23.

Waveforms recorded by WDI sensors in panel CP4 are shown in Figure 6.25 and Figure 6.26, for a low-amplitude (i.e., 42 dB) three-hit event and a high-amplitude eight-hit event, respectively. The two events were generated from the same notch tip. The figures show the waveforms and the corresponding frequency spectra of the first three hits of each event. For clarity, the frequency spectra are displayed in both logarithmic and linear scales. The intensities of the first three-hit events and the time interval between the first and the subsequent hits are listed in Table 6.3 and Table 6.4, respectively. The frequency spectra shown in the figures indicate that the dominant frequency recorded with the WDI sensors was approximately 50 kHz for both the low- and high-amplitude events. The relative power of the higher frequencies, all below 100 kHz, is marginal. It was for these results that panels CP5 and CP6 were tested with the R6I resonant sensors, which yield a more precise location of new damage.

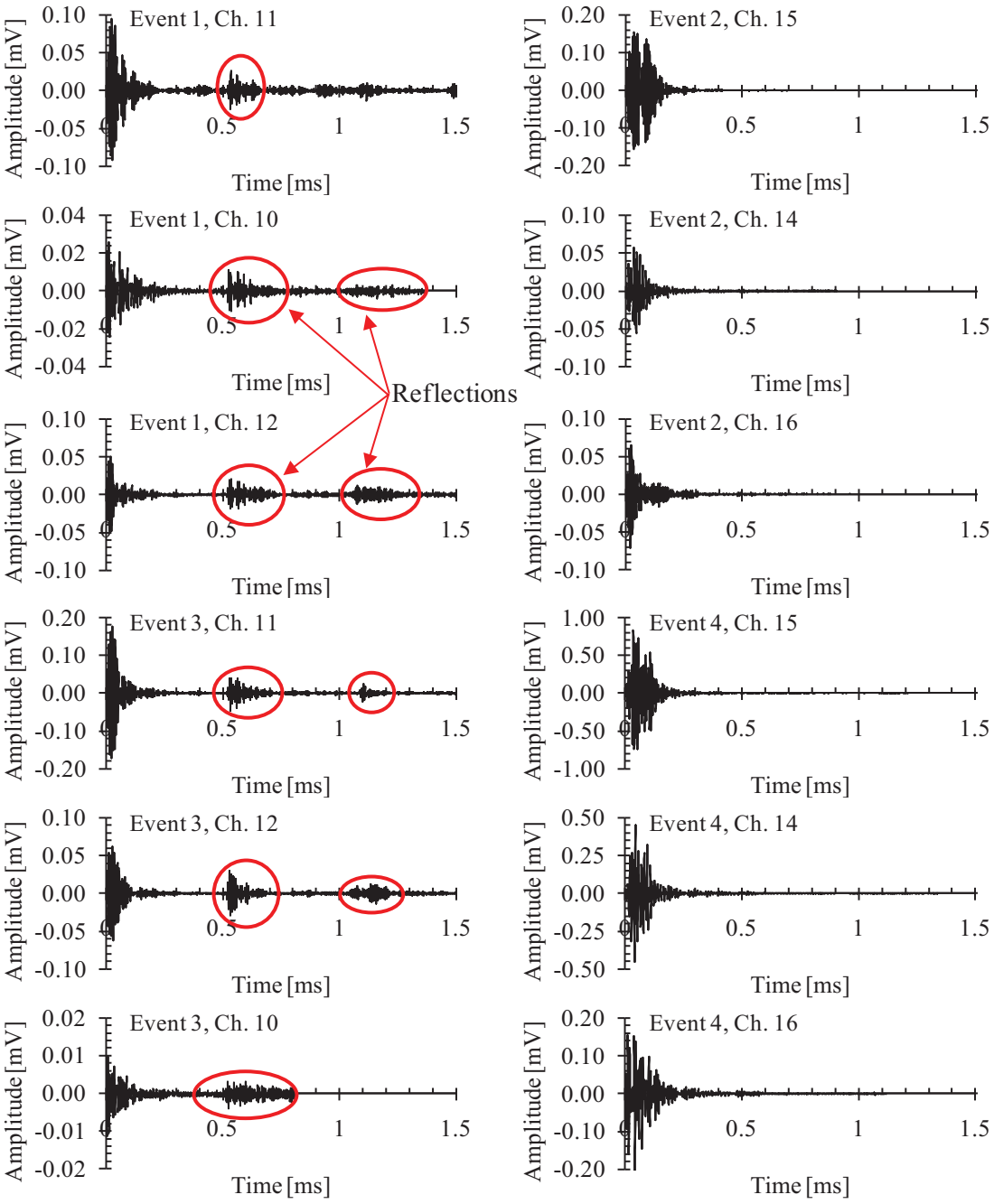

Figure 6.24. Waveforms of low- and medium-amplitude AE signals recorded by the R15I sensors in panel CP5. The waveforms of the AE signals generated from the left notch tip include also the reflections from the edge of the panel. Data of the twelve waveforms are listed in Table 6.2.

Table 6.2. Intensities of the first three hits of four locatable events generated from the notch tips of panel CP5, recorded by R15I sensors.

	Location 1 Three-hit			Location 2 Five-hit			Location 3 Three-hit			Location 4 Five-hit		
Channel	11	12	10	15	14	16	11	12	10	15	14	16
Amplitude [dB]	60	48	54	77	75	76	65	56	41	78	73	66
Duration [μs]	1491	566	1170	877	987	968	1703	1161	9	415	545	315
Counts	29	10	19	87	74	77	46	27	1	44	39	33
Energy	10	2	5	86	48	44	16	7	0	64	30	13
Δt [ms]	0	9.3	18.8	0	11.6	20.0	0	17.7	27.5	0	8.7	20.2

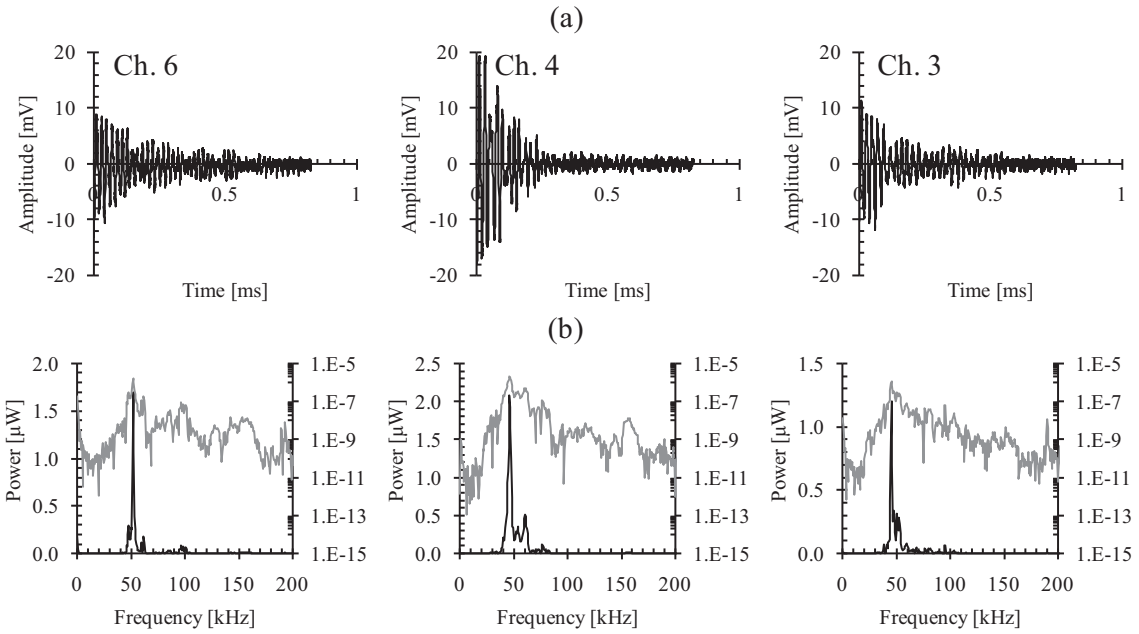

Figure 6.25. Waveforms and power spectra of a low-amplitude three-hit event generated near the notch tip of panel CP4 at 1050 lbf/in (71% of the maximum load) showing: (a) the three waveforms that hit the three neighboring sensors, and (b) the corresponding frequency spectra in linear and logarithmic scales.

Table 6.3. Intensities of the first three hits of a three-hit event, using WDI sensors in panel CP4.

	Ch. 4	Ch. 3	Ch. 2
Amplitude [dB]	42	46	41
Duration [μs]	42	91	62
Counts	1	4	2
Energy	0	1	0
Δt [ms]	0	3.8	33.5

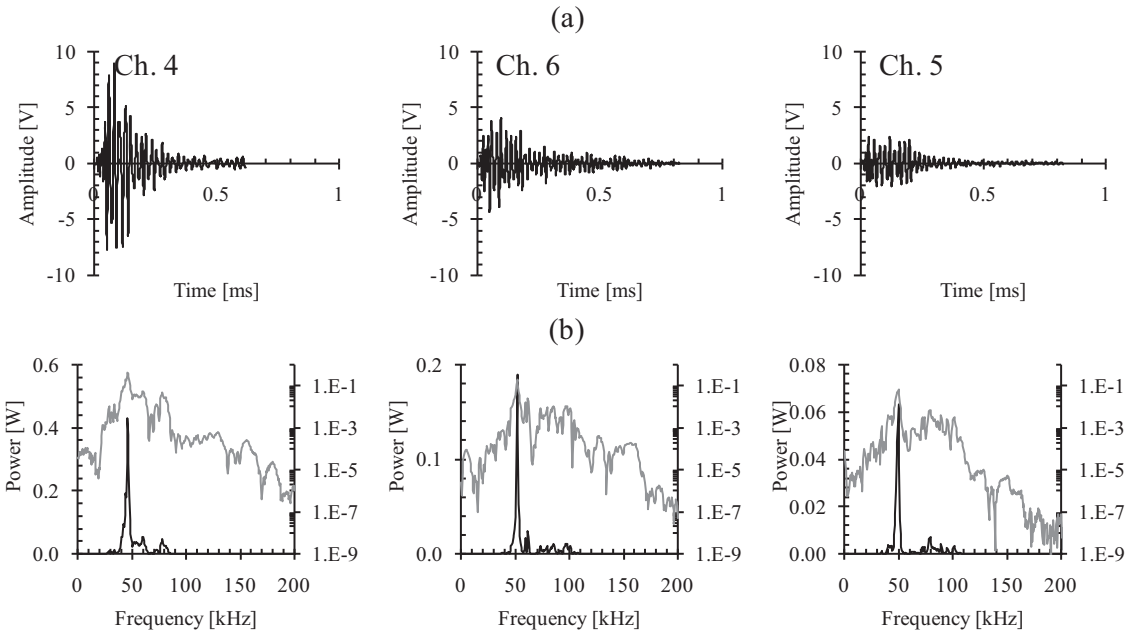

Figure 6.26. Waveforms and power spectra of a high-amplitude eight-hit event generated near the notch tip of panel CP4 at 980 lbf/in (67% of the maximum load), showing: (a) the first three waveforms that hit the three neighboring sensors, and (b) the corresponding frequency spectra in linear and logarithmic scales.

Table 6.4. Intensities of the first three hits of an eight-hit event, using WDI sensors in panel CP4.

	Ch. 4	Ch. 6	Ch. 5
Amplitude [dB]	99	93	88
Duration [μs]	5230	4533	2078
Counts	155	189	86
Energy	1465	957	510
Δt [ms]	0	0	4.2

Similar plots and the details of the AE signal features are shown in Figure 6.27 and Table 6.5 for a low-amplitude (i.e., 44 dB) four-hit event that was generated at a significant distance (i.e., 6 inches) away from the notch tip of panel CP4. Photogrammetric images taken at that load level (76% of the maximum load) did not reveal any high strain levels at that distance that indicate that any damage may have occurred, Figure 6.13. Thus, this event might have been caused by matrix micro-cracking, fretting, or other extraneous emission. Comparing the

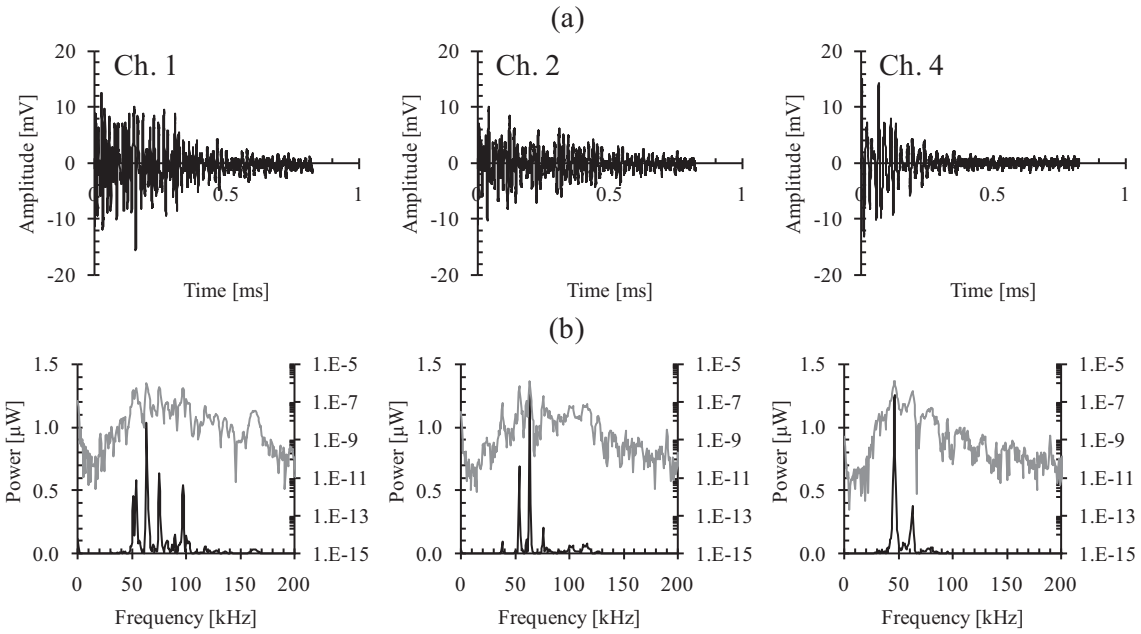

Figure 6.27. Waveforms and power spectra of a mid-amplitude, four-hit event generated away from the panel CP4 notch at 1113 lbf/in (76% of the maximum load), showing: (a) the first three waveforms that hit the three neighboring sensors, and (b) the corresponding frequency spectra in linear and logarithmic scales.

Table 6.5. Intensities of the first three hits of an event generated away from the panel CP4 notch.

	Ch. 1	Ch. 2	Ch. 4
Amplitude [dB]	44	41	44
Duration [µs]	159	42	69
Counts	2	1	1
Energy	1	0	0
Δt [ms]	0	33.6	63.6

frequency spectra of that event with the spectra of the low- and high-amplitude events generated from the notch tip, Figure 6.25 and Figure 6.26, respectively, indicates that the power, in the 50–100 kHz frequency range, of the two events generated from the notch tip is more pronounced, by approximately five orders of magnitude, than that of the remote, low-amplitude event.

Figure 6.28 and the corresponding data listed in Table 6.6 show a similar set of plots and data obtained for a four-hit mid-amplitude event recorded by the WDI sensors in panel CP4 from

the edge of the AE gage section, near sensor no. 7. The power spectra of the three waveforms are quite similar in logarithmic scale; however, in the linear scale format, it could be more readily seen that the AE signal contained a relatively large percentage of lower frequencies (i.e., below 50 kHz), suggesting that this event was generated by fretting or other extraneous noise. These results show that extraneous emission may be distinguishable from emission caused by failure based on the power of the frequency content of the signal, more so than based solely on the waveform features.

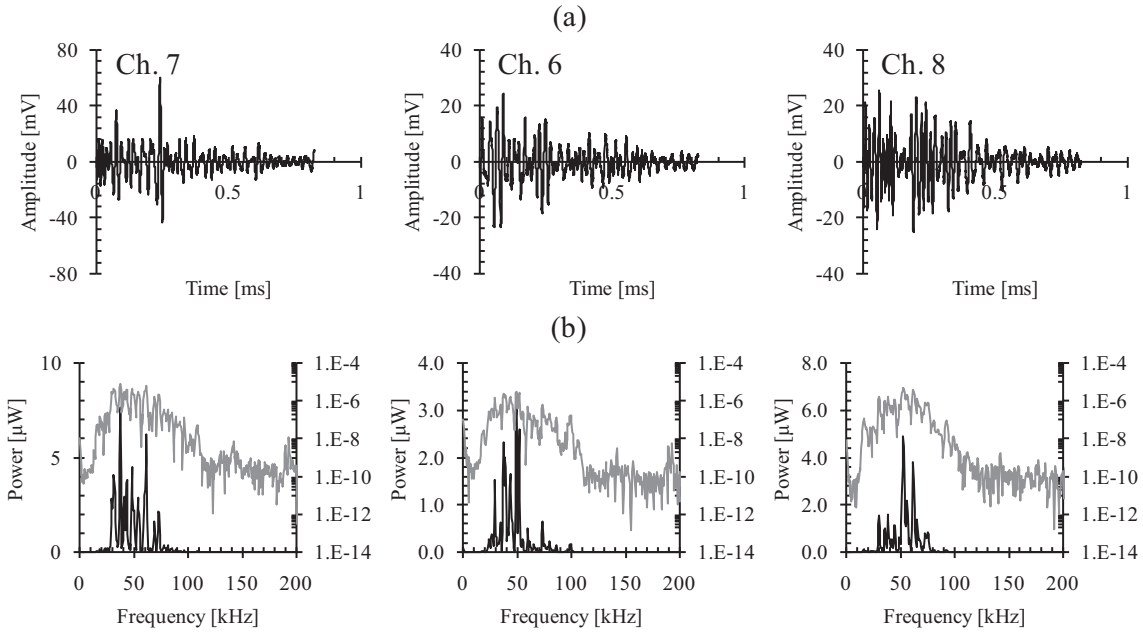

Figure 6.28. Waveforms and power spectra of a mid-amplitude four-hit event generated near sensor no. 7 of panel CP4 at 1385 lbf/in (94% of the maximum load), showing: (a) the three waveforms that hit the three neighboring sensors, and (b) the corresponding frequency spectra in linear and logarithmic scales.

Table 6.6. Intensities of the first three hits of an event generated near sensor no. 7 in panel CP4.

	Ch. 7	Ch. 6	Ch. 8
Amplitude [dB]	56	48	48
Duration [µs]	616	413	525
Counts	20	8	19
Energy	7	3	5
Δt [ms]	0	50.7	52.7

Finally, Figure 6.29 and the corresponding data listed in Table 6.7 show a similar set of plots and data obtained for a mid-amplitude, eight-hit event, generated from the notch tip region of panel CP3, as recorded by WDI sensors. Here, the shape of the waveforms of the first three hits does not seem to be generated simply by an AE signal that was emitted as a result of the formation of a new crack. Rather, it seems that this AE signal was generated by some complex combination of extraneous noise, wave reflection, fretting emission, and possibly even by the

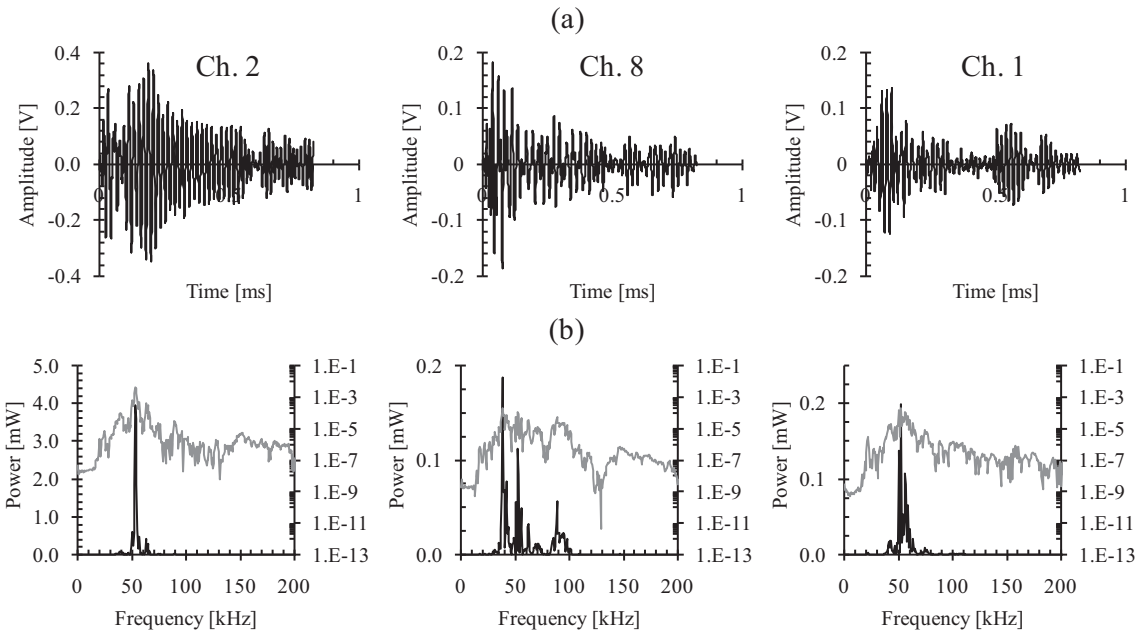

Figure 6.29. Waveforms and the corresponding frequency plots of a mid-amplitude eight-hit event generated near the notch tip of panel CP3 at 1177 lbf/in (78% of the maximum load), showing: (a) the three waveforms that hit the three neighboring sensors, and (b) the corresponding frequency spectra in linear and logarithmic scales.

Table 6.7. Intensities of the first three hits of an eight-hit event, using WDI sensors in panel CP3.

	Ch. 2	Ch. 8	Ch. 1
Amplitude [dB]	71	65	63
Duration [μs]	2626	1503	1372
Counts	138	66	62
Energy	179	44	38
Δt [ms]	0	2.6	2.8

formation of a new crack. The power spectra of the three signals are quite similar in logarithmic scale; however, in the linear scale format it could be more readily concluded that the recorded AE signal is a result of multiple sources.

These preliminary results do not indicate that the frequency spectra of the waveforms recorded with the wideband sensors could be helpful in separating and identifying the formation of the various modes of damage in large honeycomb sandwich composite structures. Neither is it possible to confidently distinguish the emission generated by fretting, reflections, or other extraneous sources. However, they do contribute to a somewhat clearer distinction between AE signals that were generated by new cracks from those that were caused by extraneous emission.

6.7. EVENT MISLOCATION

As mentioned in Section 3.8.1, three R15 sensors were used in addition to the set of eight WDI sensors to monitor the emission from a notch tip in panel CP4. These sensors were installed to compare the source locations and waveform characteristics of the results obtained with two different sensor sets: one resonant and one wideband. The results were as expected; similar source location results were recorded, with a cluster of events around the monitored notch tip.

Significant source location errors were observed from the “unmonitored” notch tip (i.e., the notch tip not located within the triangle formed by the three R15I sensors). Source location triangulation algorithms are known to exhibit increased error for events originating from outside the triangle formed by the monitoring sensors. However, the degree of the observed errors prompted further investigation. For panel CP4, the notch tip was mislocated by approximately 5 inches using the R15I sensor set (Figure 6.30a), and scattered over large regions using the WDI sensor set (Figure 6.30b and c).

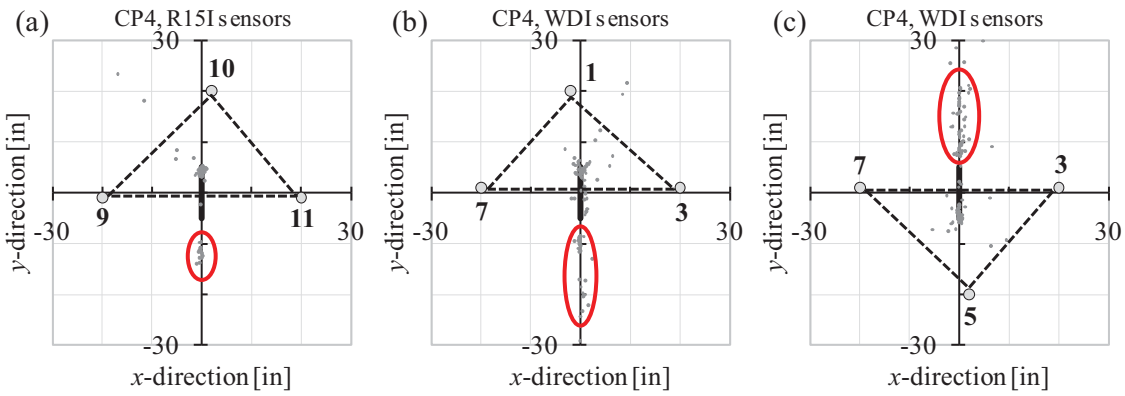

Figure 6.30. Source location plots of events hit by the three sensors indicated in the plots, showing the effect of existing damage and the relative location of the source of emission on the source location plots.

Concerns arose regarding the potential for severe event source location errors to occur during a test if, for some reason, the ability of one or more sensors to accurately detect and record AE signals was impeded (e.g., due to poor coupling, decoupling, etc.). Accordingly, a study was conducted using the data collected from panel CP5 using the R6I sensors. Each of the AE sensors was individually deactivated, and, with only seven out of the eight sensors active, the event source locations were recalculated from the corresponding AE hit data. The results of this study are shown in Figure 6.31.

The most prominent effect of removing a sensor from consideration is the absence of events located in the immediate vicinity of the removed sensor. This is tantamount to identifying the low-intensity three-hit events. Simply, once a sensor is removed, the nearby AE signals need to reach another, farther sensor to be recorded as a locatable event. Weak signals such as those caused by fretting may not reach the farther sensor due to the large attenuation and dispersion which is characteristic of wave propagation in composites. Throughout the panel, the effects of sensor removal on event detection and source location accuracy were observed to be directly related to the distance from the removed sensors. At greater distances from the removed sensor, the effect of removing the sensor was greatly reduced; a distant removed sensor is not considered

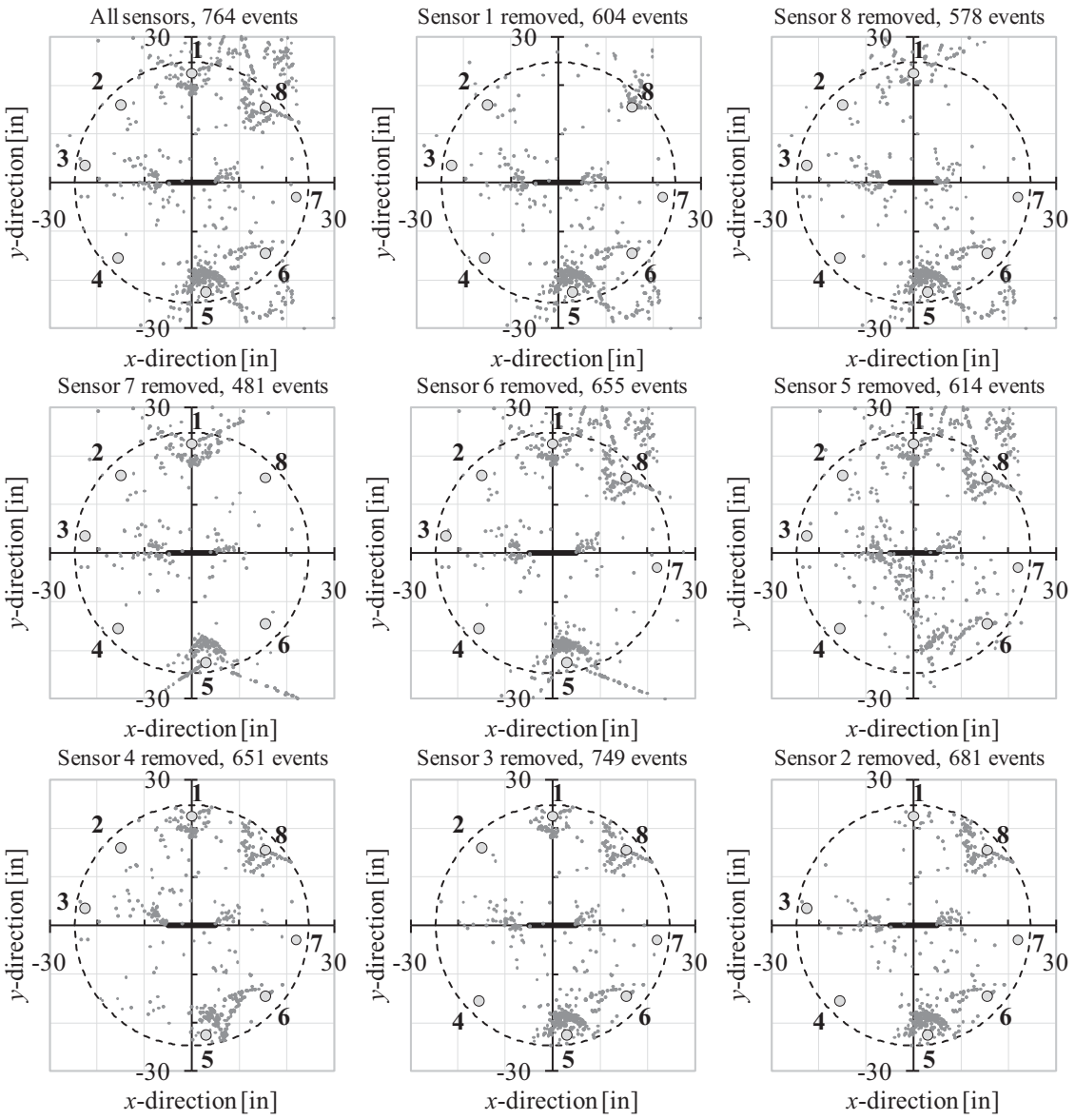

Figure 6.31. The effect of individual sensor malfunction on the source location of the AE data recorded in panel CP5 using the R6I sensor set. Each sensor around the notch was deactivated and the source locations recalculated.

while locating a local, low-intensity event, and high-intensity events hit a large number of sensors, reducing the influence of each individual sensor.

The events located in the vicinity of the notch tips were largely unaffected by the removal of individual sensors; the typical source location distortion was on the order of less than one inch. However, the detection and location of the far-field, low-intensity events was strongly influenced

by the removal of a nearby sensor. If a sensor is deactivated in a particularly acoustically active region of a panel, such as the region of the skin-to-core disbond of panel CP5, the total event count can be notably affected as well. As few as 63% of the total three-hit events were detected in the AE gage section with the removal of sensor no 7.

While this study is of a particularly severe case in which a sensor is effectively removed for the duration of a test, it does demonstrate the potential effects of 'losing' a sensor, either temporarily or permanently. The possible scenarios that this study could represent include situations of poor sensor coupling and severe material failures in the immediate vicinity of a sensor which either damages the sensor or the material to which it is coupled. Furthermore, during particularly acoustically active portions of a test, an AE channel may become saturated, unable to record and analyze newly arriving waveform data, affecting the source location results. This latter issue is discussed in the following section.

6.8. BUSYNESS

The rate at which AE signals are recorded increases with load as a result of the accumulation of the many different failures that occur in large composite structures under high loads. When the load approaches its ultimate, AE activity increases nearly exponentially, Figure 6.1, and the likelihood of stress waves being generated from different sources nearly simultaneously is increased. As a result, AE sensors are often affected by more than one of these stress waves at once. The AE system considers such trains and bursts as a single AE signal of increased counts, duration, and energy. Bursts of AE signals could even be recorded by the AE system as a single hit with superimposed amplitudes.

Not all AE signals are locatable: a relatively large number of hits might be of very low (i.e., near threshold) amplitudes; they may have been generated by extraneous emission from within or outside the AE gage section, hitting only one or two sensors. Nevertheless, once a sensor is hit, the associated channel is busy obtaining a newly defined AE signal, whether it is

generated by new damage (i.e., a legitimate AE signal) or caused by extraneous emission. That channel is busy for a period of time equal to the sum of the duration of the AE signal, the hit definition time (HDT), and the hit lock-out time (HLT), as described in Section 3.8.1. These three durations are illustrated in Figure 6.32a. When trains of AE signals occur, the recorded duration can be quite long, resulting from the repeated triggering of the HDT counter. The degree to which a channel is busy affects the results in terms of the number of recorded hits and their event intensities, and, under certain circumstances, also in determining the source location. Therefore, the discussion below attempts to quantify the degree of *busyness* of a given channel.

Busyness is defined herein as the fraction of time during which a given AE channel is occupied, or busy. A channel being occupied is defined as whenever it is either recording data or deactivated. The busyness of an AE channel can be represented by:

$$\beta = \frac{1}{\tau}\sum_{i=1}^{N_\tau}(D_i + \text{HDT}+\text{HLT}) \tag{6.2}$$

where β is the busyness, D_i is the duration of the i^{th} AE signal, τ is the time interval over which β is evaluated, and N_τ is the number of hits occurring within the time interval τ.

The time interval τ is a post-processing parameter selected while establishing the busyness of an AE channel. In general, selecting longer time intervals for τ (e.g., on the order of the time required to perform a single load step, in the range of minutes) could be used to study the general performance of the experimental setup. Shorter time intervals (e.g., on the order of the longest recorded durations, in the range of milliseconds) could be used to study the busyness during the formation of critical damage. The effect of varying τ is discussed later in this section.

Further interpreting the busyness of an AE channel requires the consideration of all possible scenarios involving the interference of multiple AE waveforms. Figure 6.32 displays five typical scenarios. Figure 6.32b shows two consecutive waveforms which do not interfere with one another; the second waveform's initial threshold crossing occurs after the HLT triggered

by the first waveform has ended. In that case, the AE system will record two independent waveforms, each having its own distinct features.

Figure 6.32c shows the result of a waveform occurring during the HLT of a previous waveform. If the initial threshold crossing of the second waveform occurs during the HLT, the portion of the waveform occurring prior to the end of the HLT will not be recorded, and the second waveform will be truncated, affecting all of the relevant features (e.g., amplitude, duration, counts, energy, rise time, etc.) of that waveform. As shown in the figure, only the portion of the second waveform occurring outside the faded region would be recorded.

Figure 6.32d shows a case where a waveform is fully obscured by the HLT of a previous waveform. In this case, the AE system would record the first AE signal in its entirety while missing the second AE signal altogether. Figure 6.32e shows a case where the second waveform occurs within the HDT of the previous waveform. This would result in the two waveforms being recorded as a single waveform with increased duration, counts, and energy. The amplitude of this extended, two-waveform train would be that of the stronger waveform. The calculated rise time would depend on the stronger signal, as well. A variation on this situation would be when the second waveform occurred within the duration of the first waveform (i.e., the occurrence of a burst of AE signals), Figure 6.32f; this would result in the distortion of all waveform characteristics.

The propensity of these scenarios to occur in composites depends on the rate of damage accumulation. Scenario (b), which is the ideal case, normally exists during the initial phases of damage accumulation, during which period each sensor records each AE signal separately. At higher load levels and during high-rate cyclic loading, scenarios (c), (d), and (e) occur more frequently as a result of the increasing rate of damage accumulation. Prior to fracture, the bursts of AE signals are recorded as single hits with superimposed intensities. The probability that scenario (d) will occur is lower than the other four scenarios, and is dependent on the duration of the HLT relative to the average waveform duration.

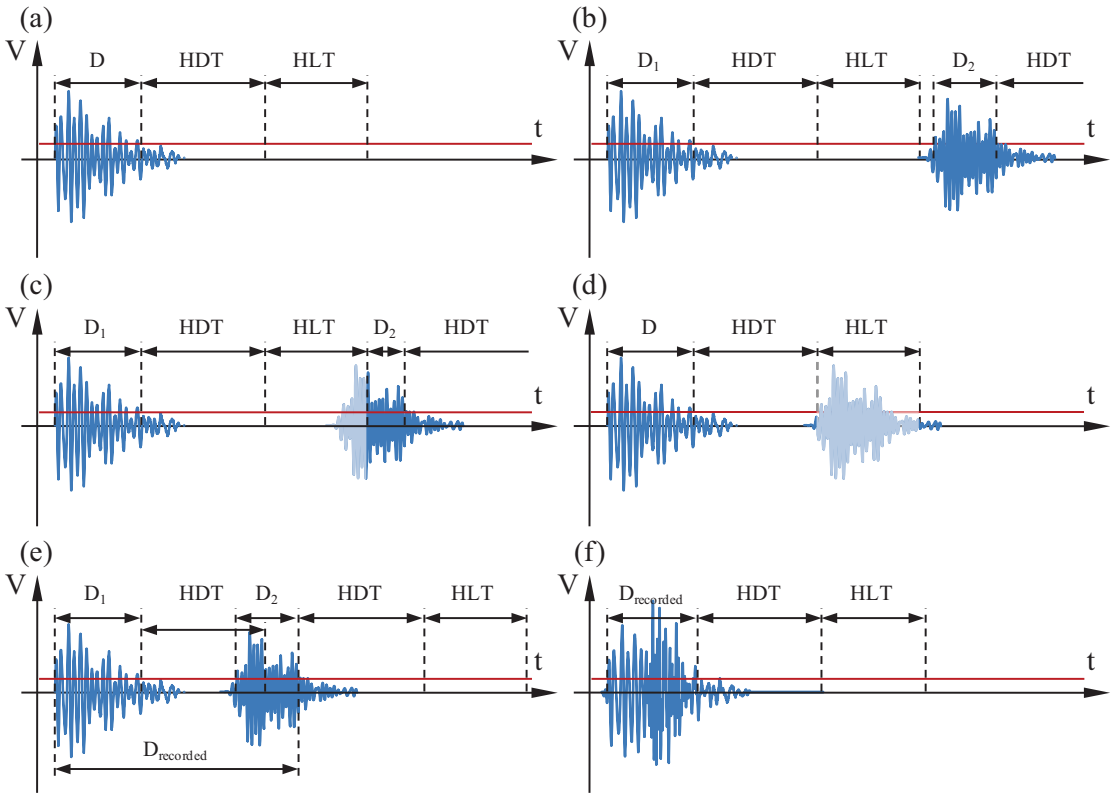

Figure 6.32. Schematics showing the possible interactions of AE waveforms: (a) a single waveform; (b) two non-interfering waveforms; (c) waveform truncated by HLT of previous waveform; (d) waveform fully obscured by HLT of previous waveform; (e) two waveforms considered as a single waveform; and (f) two superimposed waveforms, recorded as a single waveform of distorted characteristics.

The scenarios shown in Figure 6.32 illustrate the case of two stress waves that hit a given sensor within a short time period of less than D_i + HDT+HLT. There are many other possible, more complicated, scenarios. For example, let us consider two similar stress waves that originate from two different locations and that are strong enough to trigger three or more sensors (i.e., both are locatable events). The sequence of the sensors that are hit by the two AE signals and the time interval between the hits of each sensor could affect the recorded data quite significantly. The likelihood of such situations occurring is increased during periods of rapid damage accumulation. Therefore, when the load approaches its ultimate, the rate of emission is so high that an AE channel could be busy for long periods, thus, identifying and recording a fewer number of hits. In

that case, a slower rate of hit accumulation will be recorded by the system, contrary to the expected behavior. Furthermore, the location and intensity data will be all in error.

It seems convenient to separate β into its separate components, so as to represent the specific behavior of the AE channel over time, as follows:

$$\beta = \beta_{\mathrm{D}} + \beta_{\mathrm{HDT}} + \beta_{\mathrm{HLT}} = \frac{1}{\tau}\sum_{i=1}^{N_\tau} D_i + \frac{N_\tau \cdot \mathrm{HDT}}{\tau} + \frac{N_\tau \cdot \mathrm{HLT}}{\tau} \tag{6.3}$$

where β_{D}, β_{HDT}, and β_{HLT} represent the components of β due to D_i, HDT, and HLT, respectively. The component β_{D} represents the channel's busyness due only to the duration of the AE signal, that is, when the time interval between any two successive threshold crossings is less than the HDT (e.g., $\mathrm{D}_{\mathrm{recorded}}$ in Figure 6.32e). Together, β_{D} and β_{HDT} represent the fraction of time during which an AE channel is recording data and waiting for data to append to an existing waveform, while β_{HLT} is the fraction of time during which a channel is deactivated.

To illustrate the issue of AE channel busyness, sensors from the two most acoustically active panels were selected to study busyness: sensor no. 7 from panel CP5 and sensor no. 8 from CP6, both of which were located ahead of the notch tips. Figure 6.33 shows the plots of β and its three components, evaluated during the residual strength tests of panels CP5 and CP6, where appreciable acoustic activity was observed. These two busyness plots correspond to the time interval τ being set to 30 seconds, which was selected to coincide with the period of time over which loads were increased (Section 3.6). As expected, the higher the load, the busier the AE channel. This corresponds with the expected larger rate of damage accumulation. During the initial load steps, the low-frequency cyclic loading, and the load-hold periods, the degree of busyness is negligible (i.e., did not exceed 0.010). This is expected as relatively few AE signals were generated during these periods, Figure 6.2. However, significant spikes appear in the β plots at higher loads. Panel CP5 exhibited peak values of 0.014, 0.022, and 0.036 while loading up to the seventh, eighth, and ninth load steps. Panel CP6 showed higher peaks of 0.027, 0.020, 0.066, and 0.153 while loading from the ninth to twelfth load steps.

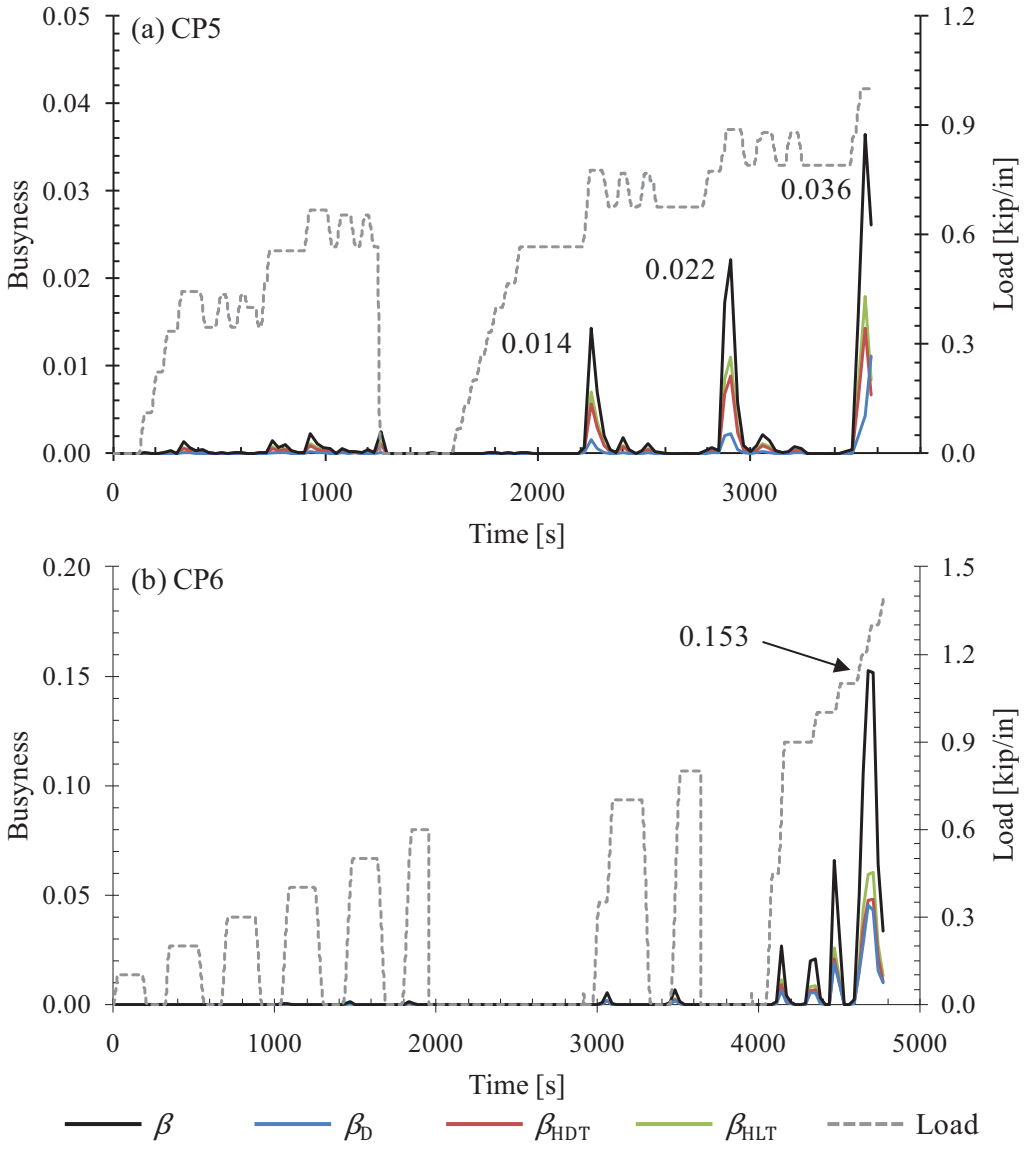

Figure 6.33. Plots of β and its three components, β_D, β_{HDT}, and β_{HLT}, versus time, throughout loading, for sensors located ahead of the notch tips in panels (a) CP5 and (b) CP6, using R6I sensors. τ = 30 sec.

It is important to realize that the peak β values and the time interval τ are closely related; interpreting one without considering the other will often lead to misrepresentation of the channel busyness data. For instance, considering the peak β value of 0.153 corresponding to the load increase from the eleventh to the twelfth load steps of the panel CP6 residual strength test (Figure 6.33b), this indicates that if one additional stress wave were to have hit the sensor during that 30-

second period, there would be an approximately 15% chance that either some overlap would occur with another AE signal or some portion of the signal would not be recorded.

Proper selection of τ often requires only the context in which one intends on discussing the busyness of a particular channel. If the acceptable threshold of error is very low at any point during a test, peak β values should be evaluated using smaller values of τ. If a larger number of AE signals is generated and only an approximate evaluation of the overall potential error is sought, larger τ values can be used (e.g., Figure 6.33). Figure 6.34 shows the dependence of β on τ for the AE hit data collected from sensor no. 8 in panel CP6 during the final three load steps of the residual strength test. Clearly, shorter τ durations yield higher resolution in the busyness data. When τ is decreased to a one-second period, the peak β value of the panel CP6 residual strength test increased to 0.354. This indicates that within that one-second period, there is an approximately 35% chance that some interference amongst AE signals may have occurred in that particular channel. Applications of such high-resolution busyness analysis may include estimating errors in AE source locations and intensity distribution data during periods of critical notch tip damage progression, such as the sudden bursts of damage progression which were observed in this investigation and reported throughout Chapter 4.

As is evident in Figure 6.1, the R6I sensor set detected many more events (764) than the R15I sensor set (396) during the residual strength test of panel CP5, though most of the events were located in the far-field regions of the AE gage section, Figure 6.3d. As mentioned in Section 6.3, the resonant frequency of the R6I sensors coincided with the resonant frequencies of the panels. As a result, the R6I sensors proved to be the most sensitive of the available sensors; the large difference in the cumulative event counts of the two sensor sets was attributed to this disparity in sensitivity. While having increased sensor sensitivity is generally beneficial, if most of the additional recorded data does not enrich the analysis (i.e., are not AE signals emanating

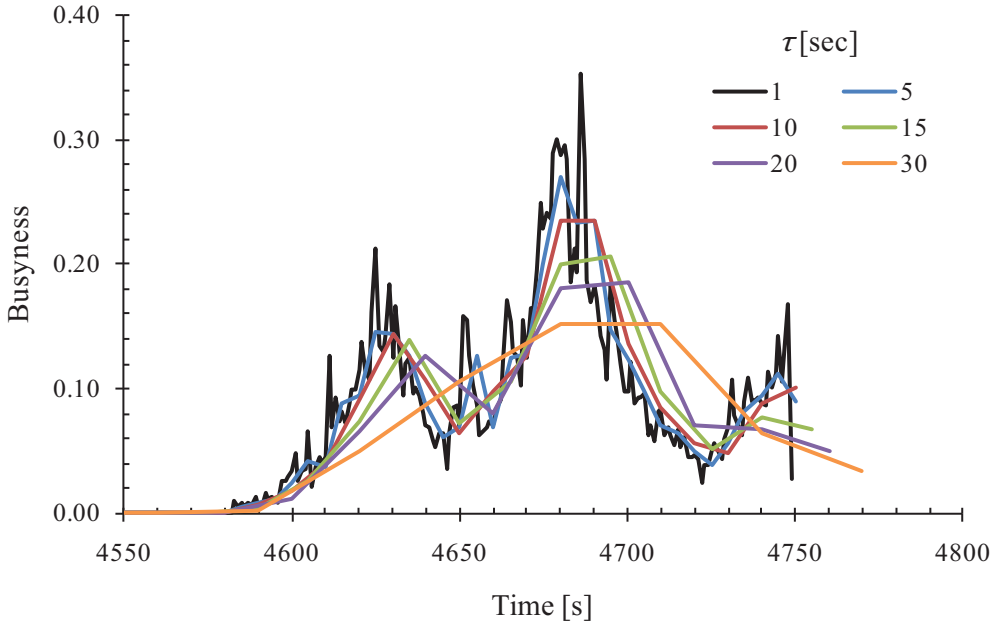

Figure 6.34. Effect of τ on β on the hits recorded during the final three load steps of panel CP6. The busyness is evaluated with τ values of ranging from 1 to 30 seconds. The β curve evaluated with τ equal to 30 seconds is the same as that presented in Figure 6.33b.

from the notch tip failure processes), the increased sensitivity may result in undesirably high β levels without providing any more useful information.

To assess what effect the large number of AE signals from the far-field regions of panel CP5 had on the busyness of R6I sensor no. 7, plots of β were generated and compared to the busyness of R15I sensor no. 15, installed at the same location, Figure 6.35. Comparisons were made at multiple resolutions, employing time increments of 1, 5, and 30 seconds. For clarity, only the final two load steps of the panel CP5 residual strength test are shown.

Throughout loading, the R6I sensor set in panel CP5 recorded almost twice as many three-hit events as the R15I sensor set. A more pronounced effect was observed regarding the peak β values during the last two load increases. Regardless of the time interval over which busyness was calculated, R6I sensor no. 7 was four to six times busier than R15I sensor no. 15, Figure 6.35. That is, the likelihood of AE signal interference was four to six times higher in the

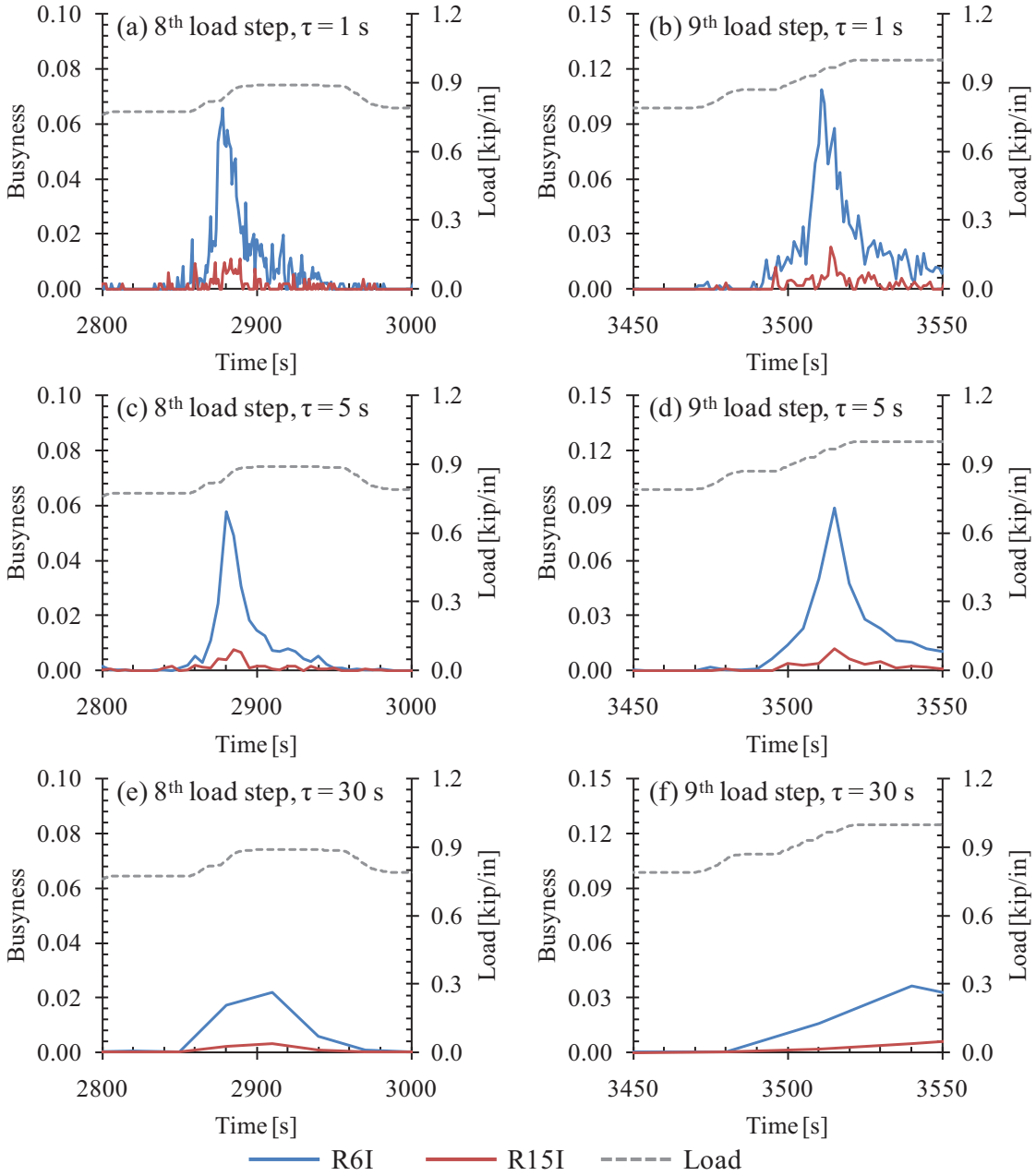

Figure 6.35. Comparison of busyness as determined using R6I and R15I sensors installed at the same location ahead of the notch during the residual strength test of panel CP5. The busyness was evaluated using τ values of 1, 5, and 30 seconds. The R6I sensor β curves evaluated with τ equal to 30 seconds are the same as those presented in Figure 6.33a.

R6I sensor set, despite recording only twice as many events. This is expected since many of the recorded AE signals are not associated with locatable events.

As mentioned in Section 6.3, however, only 76 of the total 764 three-hit events detected by the R6I sensor set were within the notch tip regions; the R15I sensor set detected 64 events in this region. Considering this, the increased sensitivity of the R6I sensor set served primarily to improve the detectability of three-hit events in the far-field regions of the AE gage section. Twelve additional notch tip region three-hit events were detected, increasing the potential for error (in terms of source location, AE signal features, etc.) by four to six times in the process. In general, this observation suggests that the threshold for recording AE signals was set too low for the R6I sensor set, allowing a significant amount of extraneous emission from far-field sources to influence the data recorded from the notch tip regions.

An evaluation of the number of trains of hits occurring during the various loading segments can be estimated by reviewing the data files of the AE signals. Figure 6.36 and Figure 6.37 show the percentile of hit duration recorded during three loading segments and three load-hold periods in panel CP5 by R6I sensor no. 7 and R15I sensor no. 15, respectively. The three loading segments (556–768 lbf/in, 643–862 lbf/in, and 768–960 lbf/in) partially overlap each other because of the sequence of unloading-reloading of the panel, Figure 6.2.

These plots indicate that a relatively large number of hits were of duration longer than expected of a typical AE signal generated in composites by the formation of new damage, as recorded by R6I resonant sensors. For example, Figure 6.36a shows that over 28% of the hits of the R6I sensors were of duration longer than 0.25 ms, 10% of the hits were longer than 0.5 ms, and 2% of the hits having duration over 1.0 ms for the hits generated between 768 and 960 lbf/in hoop load. Clearly, many of these long-duration hits indicate the occurrence of trains of hits. Interestingly, the same trend occurred in all three loading segments, even though the β values of the earlier load steps were relatively low.

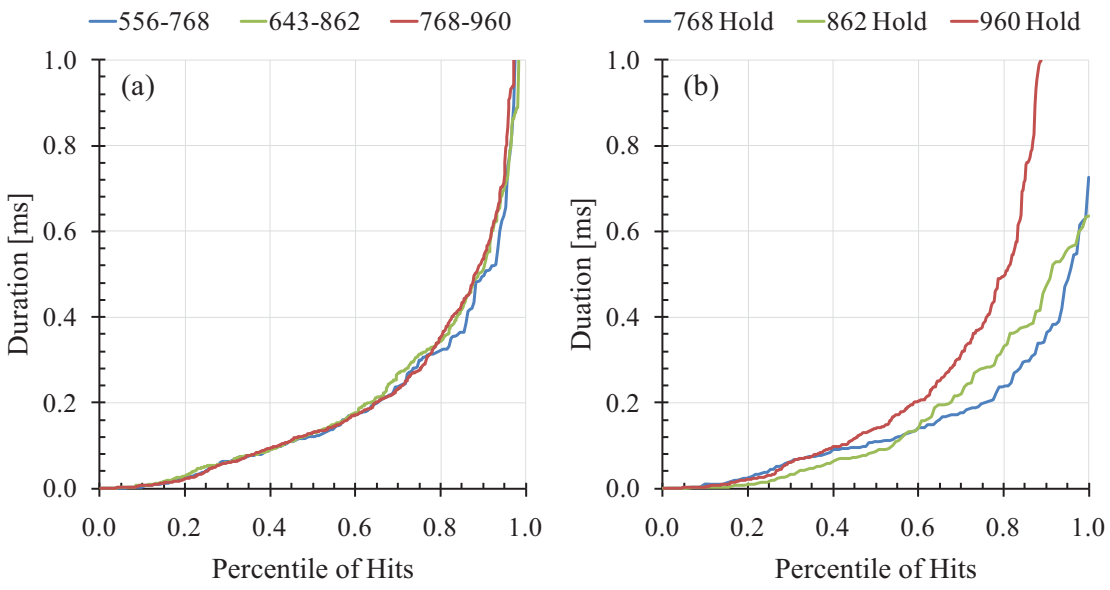

Figure 6.36. Duration plots of AE signals generated in panel CP5, R6I sensor no. 7, during: (a) three loading segments of: 556 to 768 lbf/in (212 hits), 643 to 862 lbf/in (564 hits), and 768 to 960 lbf/in (616 hits) and (b) three load-hold periods of approximately 30 seconds at: 768 lbf/in (72 hits), 862 lbf/in (130 hits), and 960 lbf/in hold (406 hits).

During the load-hold periods, the percentage of AE signals having long durations is smaller, with the exception of the last load-hold period, during which the panel fractured. During the final load-hold, approximately 20% of the hits were longer the 0.5 ms and 12% of the hits were over 1.0 ms. With the exception of the last loading segment and last load-hold period, the hit durations recorded with R15I sensor no. 15 was quite small compared with R6I sensor no. 7, Figure 6.37.

Similar data are shown in Figure 6.38 for the AE signals recorded by R6I sensor no. 8 in panel CP6, installed ahead of notch tip, during four loading segments. Also here the duration plots are nearly the same for all loading segments. The percentage of long duration AE signals is quite large, however: approximately 50% above 0.25 ms, 35% above 0.5 ms, and 12% to 20% over 1.0 ms. The results are irrespective of the number of hits recorded.

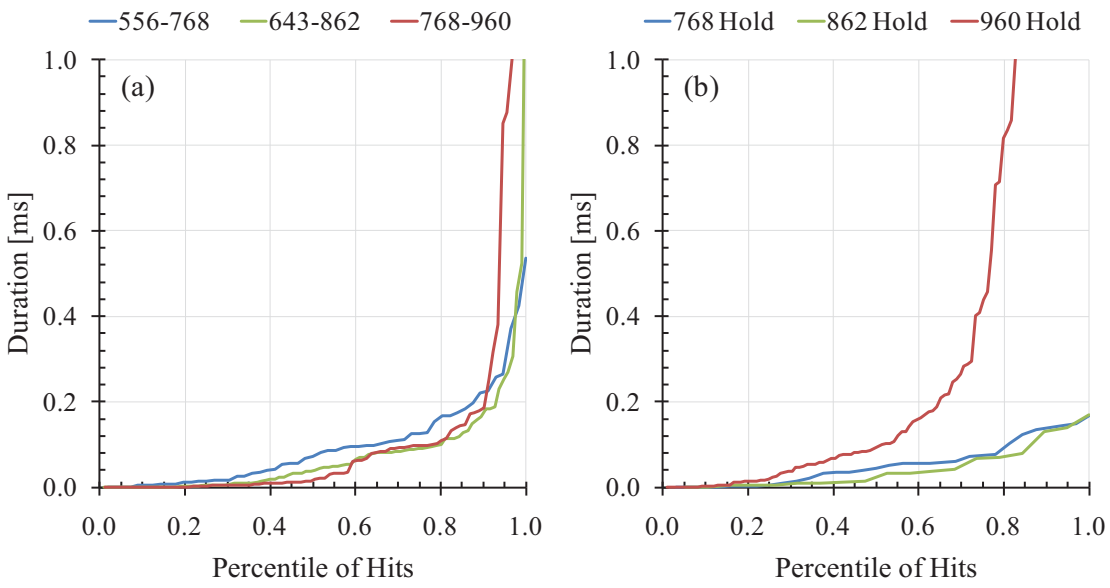

Figure 6.37. Duration plots of AE signals generated in panel CP5, R15I sensor no. 15, during: (a) three loading segments of: 556 to 768 lbf/in (56 hits), 643 to 862 lbf/in (95 hits), and 768 to 960 lbf/in (91 hits) and (b) three load-hold periods of approximately 30 seconds at: 768 lbf/in (32 hits), 862 lbf/in (19 hits), and 960 lbf/in hold (109 hits).

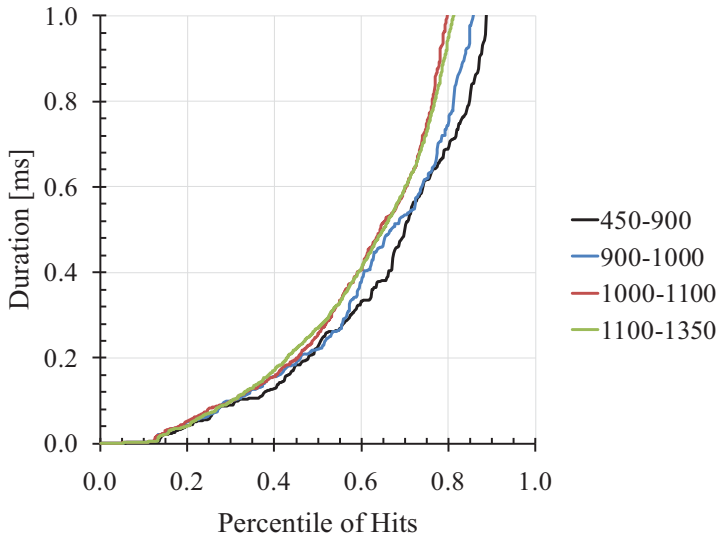

Figure 6.38. Duration plots of AE signals generated in panel CP6, R6I sensor no. 8, during four loading segments of: 450 to 900 lbf/in (421 hits), 900 lbf/in to 1000 lbf/in (546 hits), 1000 to 1100 lbf/in, (1163 hits), 1100 lbf/in to 1350 lbf/in, (6711 hits).

6.9. CONCLUSIONS

The application of the acoustic emission (AE) method in this investigation served multiple purposes and resulted in several enriching observations regarding both the failure processes of the full-scale composite fuselage panels and the AE method itself. The primary goals of the application of the AE method in this investigation included (i) detecting the initiation and progression of damage, and determining when it occurs in terms of load; (ii) locating sites of failure and tracking its progression; and (iii) determining the dominant failure modes. Each of these purposes was addressed, evaluating their feasibility and the measure of their success in monitoring the formation, progression, and eventual instability of damage. Further, the AE method served as an early warning of incipient failures and of imminent fracture, consistently indicating the development of damage prior to becoming visible.

Regarding the first objective, monitoring AE in large composite structures successfully provided early indication for both incipient damage development and ultimate panel fracture in each of the tested panels. AE activity was first detected from the notch tip regions between 45% and 65% of the panel fracture loads while using either resonant or wideband sensors. Warning of the catastrophic failure of the panels was provided via the exponential increase in the rate of AE event accumulation immediately preceding the final fracture. The emissions contributing to the rapid increase in AE event accumulation were not all from the formation of new fracture surfaces. In fact, the majority of the emission was found to originate in the far-field regions of the AE gage section as a result of fretting amongst existing fracture surfaces, the load and support fixtures, far-field disbonds, etc.

Regarding the second objective, the AE source locations associated with new failures coincided with the notch tip regions of each panel. However, the extraneous panel-wide emissions often obscured the notch tip regions. Hit-based filtering (rather than feature-based filtering) was adopted to remove the AE signals associated with extraneous emission. This decreased the dependence of the filtering scheme on the features of the first-recorded hits of

locatable events. It was found that 5-hit event filtering (i.e., considering only events in which AE signals were recorded by at least 5 sensors) performed best in isolating the notch tip emissions.

Significant difficulty was encountered regarding the completion of the third objective, determining the dominant failure modes. It was found that, for all practical purposes, the complexity of the large composite panels prohibited the identification of specific failure modes through reduction of the collected AE data. Comparisons between emissions generated from several known sources, including the notch tips, the fretting of existing fracture surfaces, and the test fixture supports, were made, revealing similar distributions of waveform features (i.e., amplitude, duration, counts, energy, etc.), whether recorded by resonant or wideband sensors. Individual waveforms emanating from various regions of the AE gage sections were evaluated, as well. While no trends were identified in the frequency content of the waveforms suspected of emanating from different sources, the composite material used in this study strongly attenuated the high-frequency content (i.e., greater than 400 kHz) of any propagating stress waves, even over short distances. Frequency content capable of discerning the sources of the AE signals may have been lost due to the particular experimental setup employed in this investigation.

As mentioned, when the load approaches its ultimate, the rate at which AE signals are recorded increases exponentially. As a result, the propensity for multiple stress waves to interfere with another increases as well. Such instances of AE signal interference can affect the accuracy of the determined source locations, the distributions of AE signal intensities, etc. Assessing the likelihood of AE signal interference occurring in the recorded AE data aids in estimating the overall accuracy of the data and the validation of the experimental setup. It was found that considering the percentage of time an AE channel spent recording data, with respect to some characteristic period of the total test time, can be used to estimate the frequency at which such instances of interference may have occurred. Further, while using resonant sensors, the average frequency (i.e., counts per duration) of an AE signal was found to serve as a good indicator as to

whether a recorded signal was caused by either a single stress wave or a train of AE signals originating from different sources.

CHAPTER 7: EXPERIMENTAL RESULTS – FREQUENCY RESPONSE

7.1. INTRODUCTION

The frequency response (FR) method was used to scan for nonvisual, subsurface damage during the loading of two honeycomb sandwich composite fuselage panels: panels CP5 and CP6. Simultaneously, an extensive series of calibration studies were conducted to better understand the dependence of signal attenuation on the length and orientation of the wave path taken through the inspected material. The results of these calibration studies and the results from panels CP5 and CP6 are presented here. The ability of the FR method to detect damage initiation and severity is assessed and compared with the sensitivity of similar inspection and monitoring techniques.

7.2. CALIBRATION STUDIES

An extensive calibration study was performed with a virgin 24 inch by 24 inch panel, with curvature equal to the full-scale panels, made of the same honeycomb sandwich composite material. The goals of this calibration study included recording the waveforms and power spectra of transmitted signals without any influence from the measured material (i.e., a face-to-face, pulser-receiver calibration), developing a better understanding of the dependence of signal attenuation on the length and orientation of the wave path taken through the inspected material, and selecting the sensor couplant which least attenuated the transmitted signal.

As discussed in Section 3.8.2, a constant-amplitude sinusoidal wave of continuously varying frequency was transmitted through the material using wideband piezoelectric transducers. Physical Acoustics Corporation (PAC) model R80 and WD sensors were used as the pulsers and receivers, respectively. A preliminary FR study on panel CP4 indicated that the material tested in this investigation did not transmit frequencies greater than 400 kHz over any considerable distance. Considering this observation and the manufacturer-supplied frequency response profiles of the sensors (Figure 3.24), the input signal frequency was linearly increased from 100

to 400 kHz over a 0.1-ms duration; a nominal 5V amplitude was used during testing. The signal sent to the wave generator is shown in Figure 7.1a, with its corresponding power spectrum shown in Figure 7.1b. Throughout this chapter, the power spectra presented are derived from the recorded time-varying voltage data using a fast Fourier transform (FFT) algorithm and processed via:

$$\mathrm{P}(f) = 2 \cdot \left| \frac{\mathrm{FFT}\big(\mathrm{V}(t)\big)}{n} \right|^2, \tag{7.1}$$

where $\mathrm{P}(f)$ is the power of the recorded waveform in terms of watts with respect to frequency, $\mathrm{V}(t)$ is the amplitude of the recorded waveform in terms of voltage with respect to time, and n is the number of points used in the FFT calculation.

As mentioned in Section 2.2.3, the transfer function associated FR measurements is highly complex. The recorded signals are the convolution of the input signal, the individual frequency response curves of the pulser and the receiver, and the transfer function associated with the stress wave propagating through the material. While the pulser and receiver are both nominally wideband, no such sensors have a perfectly flat frequency response curve, resonating with certain frequencies more than others. Accordingly, it was expected that the power spectrum of the pulse induced by an R80 sensor and measured by a WD sensor would not be flat. A face-to-face calibration was performed with the pulser-receiver pair with an input voltage of 30V. The resulting waveform and power spectrum are shown in Figure 7.1c and Figure 7.1d, respectively. Clearly, a significant portion of the recorded waveform can be attributed to the ring-down of the sensors. Every frequency component of the signal caused the recording sensor to continue vibrating after it had passed, with the final portion of the recorded signal (i.e., after 0.1 ms) appearing to be an amalgamation of all of the recorded frequencies. The power spectrum of the recorded waveform indicates peak frequencies at approximately 151, 219, and 375 kHz, correlating well with the sensitive regions of the frequency response profiles of the pulser and receiver (Figure 3.24). Sensor ring-down can be observed throughout the recorded waveform as

well, where the initial oscillations appear to be purely approximately 100 kHz, but the oscillations later in the waveform (i.e., after 0.05 ms) are clearly a combination of the dominant frequencies.

If the recorded waveforms were unaffected by the frequency response profiles of the pulser and the receiver, and the couplant used between them did not attenuate the signal at all, the recorded signals would appear as shown in Figure 7.1a, and a direct analysis of the waveform may be possible to detect changes in the transfer function of the inspected material (i.e., damage), as discussed in Section 2.2.3. However, with the various peak frequencies apparent from the calibration test (Figure 7.1d) and the ring-down behavior of the sensors (Figure 7.1c), analyzing the power spectra of the waveforms allowed for easier interpretation of the data.

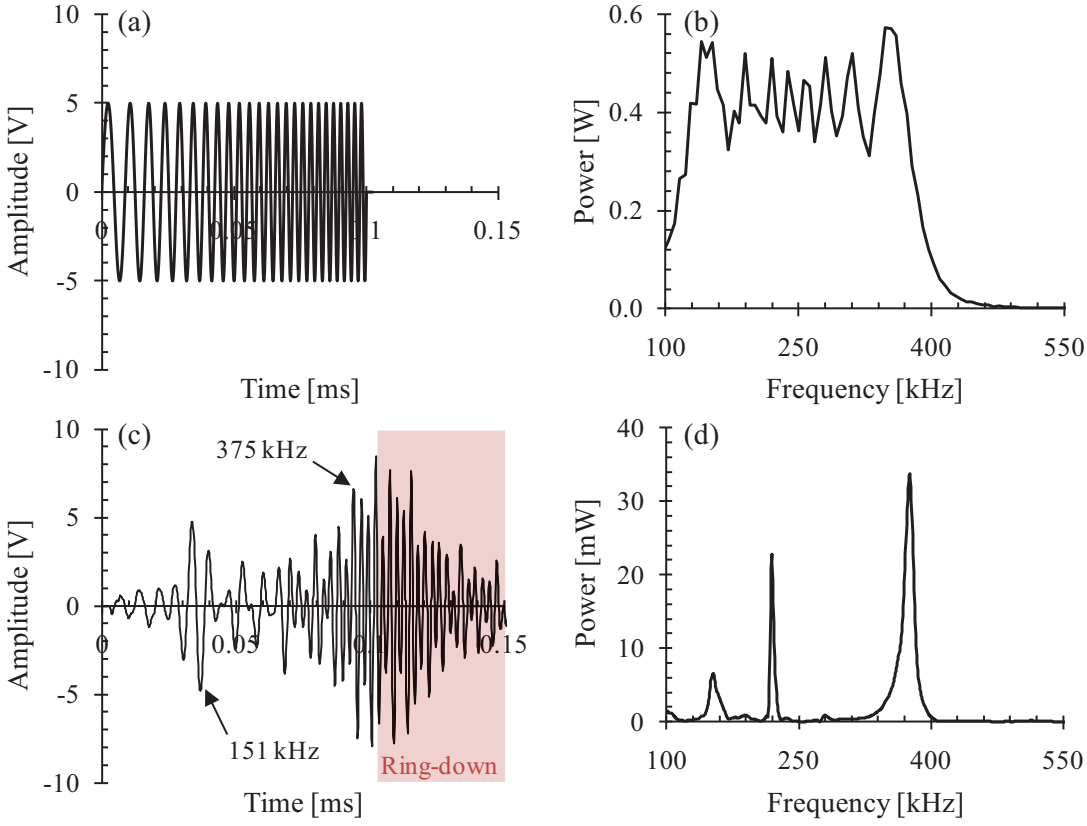

Figure 7.1. (a) FR command signal and (b) corresponding power spectrum, and (c) the face-to-face calibration study waveform and (d) corresponding power spectrum. The command signal was a constant-amplitude sinusoid, with frequencies varying from 100 to 400 kHz, over a 0.1-ms duration.

As was discussed in Section 2.2.2, the stiffness, strength, and wave speed attenuation and dispersion of fiber-reinforced composite materials are functions of fiber directions, laminate configuration, and stacking sequence. Therefore, the effect of orientation and pulser-receiver separation distance on signal attenuation was studied using the 24 inch by 24 inch calibration panel described earlier.

To study the effect of orientation relative to the panel coordinate system on signal attenuation, the actuator (i.e., pulser) was located at a fixed position at the center of the calibration panel while the receiver was moved in 22.5° increments along a 10-inch-radius arc (i.e., along path A-B in Figure 7.2). Figure 7.3 shows the results recorded from these measurements using hot glue as a couplant. The results indicate that notable peaks existed along the ±45° directions, as expected. Two laminae per face sheet contained fibers oriented in the ±45° directions, while only the mid-ply contained fibers oriented in to 0°/90° directions. This lay-up contained more uninterrupted paths for stress waves to travel along in the ±45° directions,

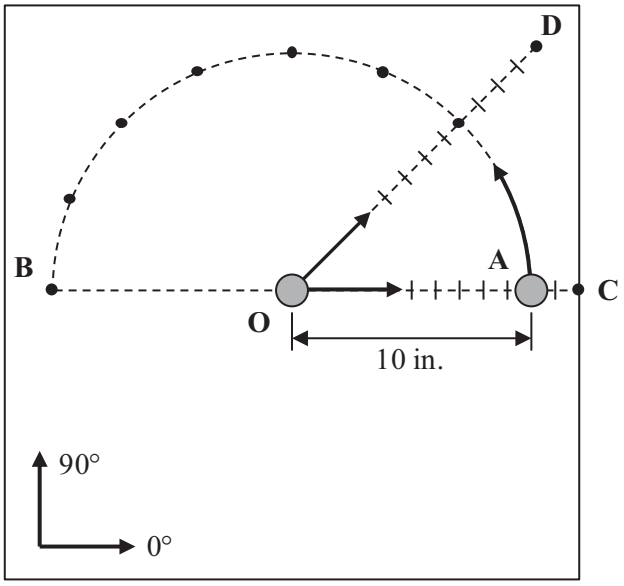

Figure 7.2. Calibration panel schematic, showing the paths along which the attenuation of the transmitted signals was evaluated as functions of orientation relative to the panel coordinate system (path A-B) and pulser-receiver separation distance (paths O-C and O-D).

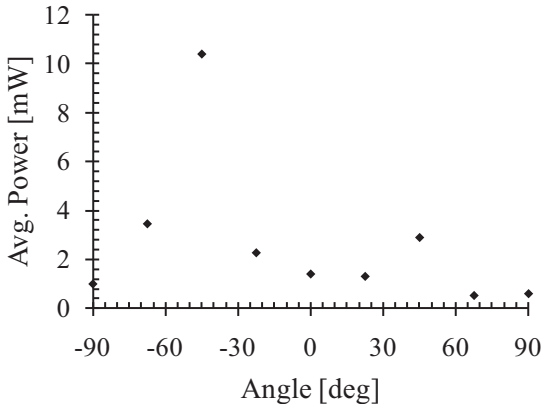

Figure 7.3. Effect of the orientation of signal path through the material on signal attenuation in terms of average power at a fixed pulser-receiver separation distance of 10 inches, using hot glue as a couplant.

decreasing the signal attenuation along these directions. The difference between the peaks in the ±45° directions can be attributed to the particular location of the pulser and receiver with respect to the plain-weave fabric (i.e., application of the pulser directly to a -45° fiber tow resulted in better signal transmission in that direction).

A similar study was conducted to determine the dependence of signal attenuation on pulser-receiver separation distance. The actuator was again located at the center of the calibration panel while the receiving WD sensor was displaced along radial lines in the 0° and 45° directions (i.e., paths O-C and O-D in Figure 7.2). Figure 7.4a shows the results of measurements along the 0° direction. Measurements were taken at one-inch intervals from one to 12 inches in terms of normalized area under the power spectrum, using both vacuum grease and hot glue as couplants. The area under the power spectrum was selected as a measure of overall signal attenuation due to its insensitivity to frequency shifts and the uneven attenuation of individual frequency components.

An exponential trend was observed for the attenuation of signals when propagated up to approximately 8 inches; beyond this distance, the signals attenuated more gradually. The attenuation of sound waves traveling through a material is typically represented through:

$$A = A_0 \exp(-\alpha z), \tag{7.2}$$

where A and A_0 are the attenuated and unattenuated amplitudes, α is the attenuation coefficient, and z is the propagated distance [7.1]. The different rates of signal attenuation are attributed to the different attenuation coefficients of different frequency components (i.e., high-frequency components attenuating more rapidly than low-frequency components). While the same trends were recorded using both vacuum grease and hot glue as couplants, the signals recorded with the hot glue couplant were consistently stronger. Therefore, using hot glue is advantageous as a couplant in acoustic emission (AE) and FR testing.

Figure 7.4b shows the results obtained from several measurements along a radial line oriented in the 45° direction, at one-inch increments between 1 and 14 inches, in terms of normalized area under the power spectrum, using hot glue as the couplant. Results were similar to those obtained along the 0° direction, with signals measured beyond 8 inches exhibiting lower attenuation coefficients. However, the measured signals taken along the 45° line attenuated less with increasing pulser-receiver separation distance than when taken along the 0° line (yielding attenuation coefficients of 0.65 and 0.80, respectively).

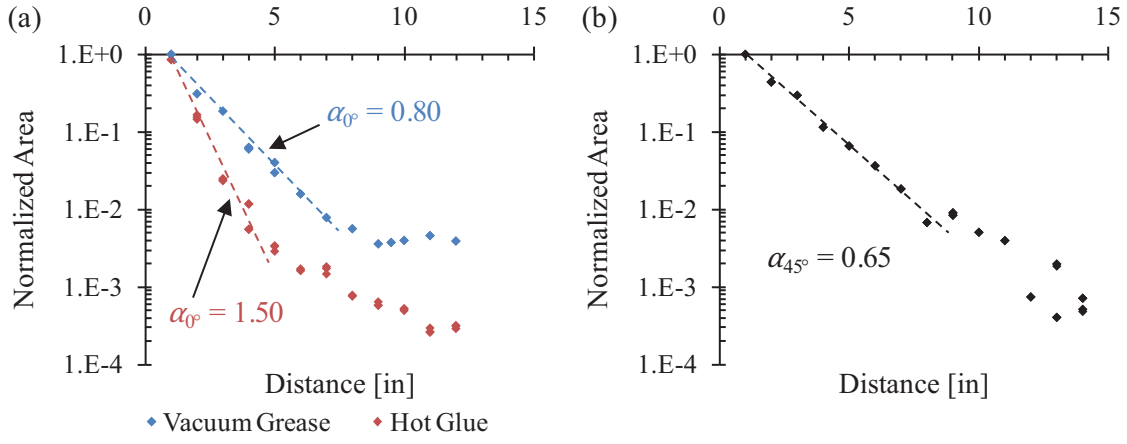

Figure 7.4. (a) Comparison of vacuum grease and hot glue couplants in terms of normalized area under the power spectra while along path O-C in Figure 7.2. (b) Effect of sensor separation distance on signal attenuation along path O-D in Figure 7.2, using hot glue as a couplant.

7.3. PANEL CP5

FR data were recorded from panel CP5 at five different times during the residual strength test, Figure 7.5. Since the FR testing was not a part of the initial test program, the planned loading function did not specifically allot for repeated opportunities to perform FR measurements. As a result, measurements were taken only twice with the panel under no load (i.e., prior to loading, and after an incidental unloading due to a loader fault) and three times under load: after the second, third, and fourth cyclic loading segments. For discussion purposes, these five measurements are designated measurements **A** through **E**, as shown in Figure 7.5. The maximum loads applied prior to each measurement and the loads applied while each measurement was taken are listed in Table 7.1. Measurements were not taken under load earlier in the test because no appreciable indication of nonvisual, subsurface damage was detected. For comparative purposes, Figure 7.5 shows also the three-hit AE events recorded from the panel AE gage section and their respective amplitudes.

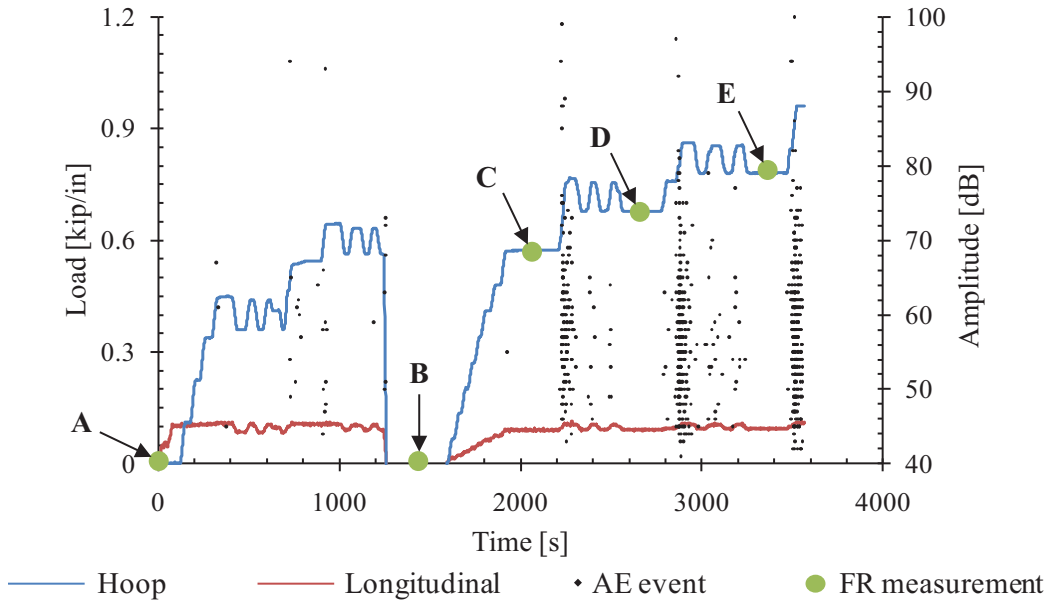

Figure 7.5. FR measurements, with respect to the load-time history and accumulation of AE events from the AE gage section of panel CP5 during loading.

Table 7.1. Applied loads associated with FR measurements.

Measurement		Pressure [psi]	Hoop [lbf/in]	Longitudinal [lbf/in]
A	Max. Applied	0.00	0	0
	During Measurement	0.00	0	0
B	Max. Applied	9.00	643	100
	During Measurement	0.00	0	0
C	Max. Applied	9.00	643	100
	During Measurement	7.65	572	100
D	Max. Applied	10.50	768	100
	During Measurement	9.14	678	100
E	Max. Applied	12.00	862	100
	During Measurement	10.68	780	100

To ensure consistency of the experimental setup and the transfer function of the signal path through the material, 15 pulses were triggered and recorded for each measurement. The 15 recorded waveforms and their corresponding power spectra from each measurement were identical, irrespective of state-of-damage and applied load. The results discussed below are the result of averaging the 15 waveforms recorded during each measurement.

As was discussed in Section 3.8.2, two pulser-receiver pairs were used to monitor the propagation of damage from the notch tip monitored by the digital image correlation (DIC) system. The two pairs monitored the region immediately ahead of the notch tip (i.e., P1-R1) and two inches ahead of the notch tip (i.e., P2-R2), Figure 3.28a. A pulser-receiver separation distance of 10.0 inches was used. Data were collected from the four different wave paths through the material from pulsers no. 1 and 2 to receivers no. 1 and 2. Examples of recorded waveforms from the P2-R2 pair at various load levels are shown in Figure 7.6.

The two waveforms recorded under zero load (i.e., measurements **A** and **B**, Figure 7.5) from the P2-R2 pair are shown in Figure 7.6a and Figure 7.6b, respectively. The two waveforms are very similar; only a slight decrease was observed in the amplitude of the second waveform. However, upon reloading (i.e., measurement **C**), a significant drop in the amplitude of the waveform occurred, Figure 7.6c. These observations are clearly seen in the corresponding

frequency spectra, Figure 7.6d through Figure 7.6f. The decrease in the amplitudes of the peak frequencies was relatively small between measurements **A** and **B** (Figure 7.6e). However, a significant decrease in amplitude occurred upon reloading (Figure 7.6f), particularly in the range of 190 kHz.

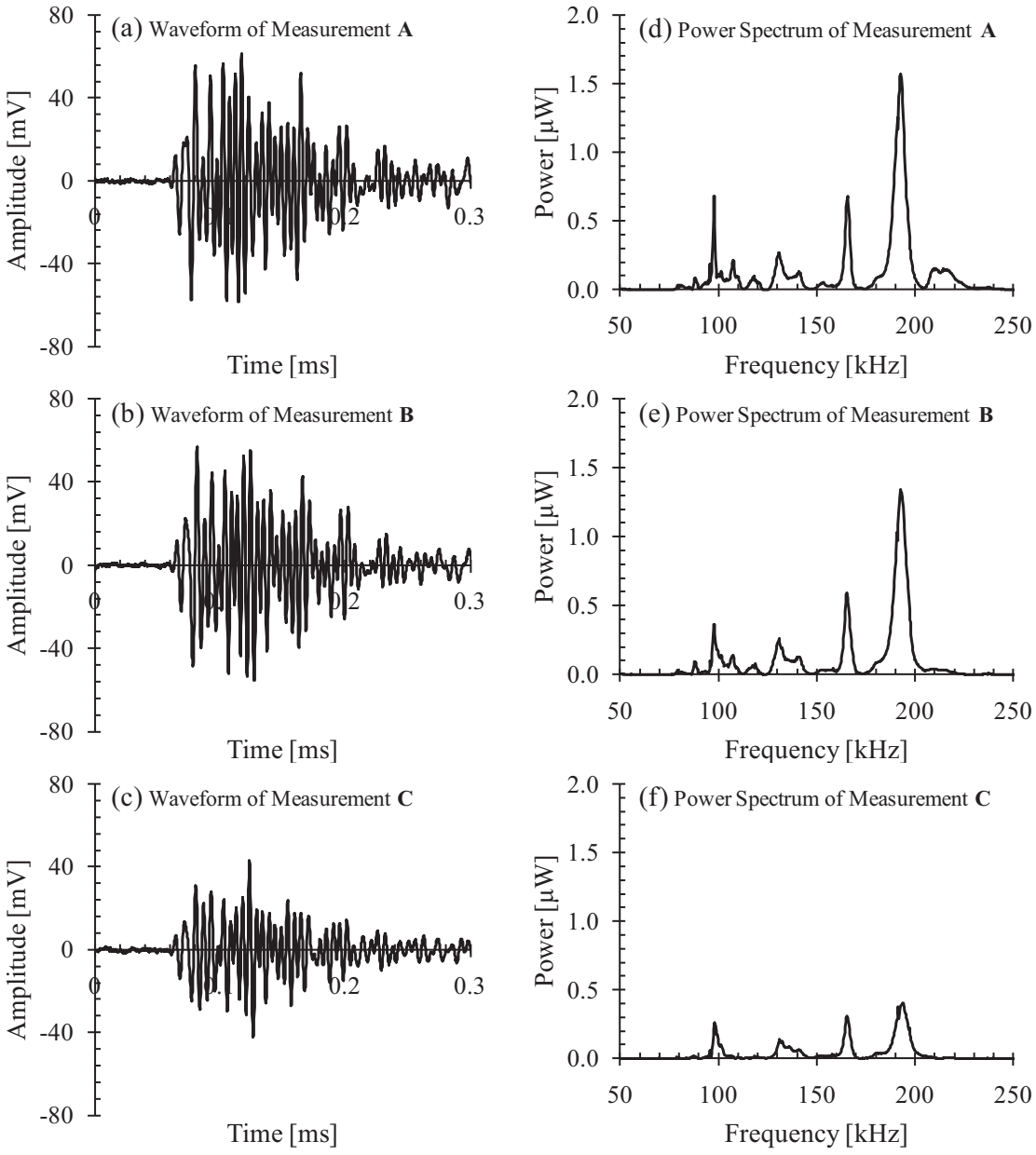

Figure 7.6. Waveforms and their corresponding frequency spectra recorded for measurements **A**, **B**, and **C** (Figure 7.5). These plots are from the pulser-receiver pair P2-R2, located 2.0 inches ahead of the notch tip in panel CP5.

No significant AE activity was detected while reloading the panel, as was expected, indicating no significant change in the state-of-damage, Figure 7.5. The increased signal attenuation upon reloading is attributed to the opening of several nonvisual, subsurface cracks ahead of the notch tip, affecting the characteristics of the stress wave propagating through the material. Further, photogrammetry did not detect any visual damage two inches ahead of the notch tip at this load level, Figure 7.7b. That is, the changes seen in the frequency response in Figure 7.6 occurred although the notch tip damage was nonvisual (as indicated via photogrammetry) and ostensibly not severe (as indicated by the low cumulative AE activity). The limited amount of AE was caused primarily by the fretting of existing internal cracks, not additional damage formation.

The change in waveform peak amplitude with increasing load and increasingly severe damage is similar along all four wave paths, Figure 7.7a. The signals passing closest to the original notch tip (i.e., P1-R1) were notably weaker than that at a distance (e.g., P2-R2). This was expected since, at any given load, more severe damage exists in the immediate vicinity of the notch tip. Relatively little change was observed between the measurements **A** and **B**, while a sharp decrease in peak amplitude was observed after reloading (i.e., measurement **C**), with a signal attenuation steadily increasing with increasing loads (i.e., measurements **D** and **E**). The path through the material monitored by the P1-R2 pair was an exception to this observation; instead, an increase in waveform peak amplitude was observed upon reloading. This increase, however, was relatively slight and within the scatter of the data. Upon further loading, the P1-R2 pair recorded results following the trends established by the other pulser-receiver pairs, showing increased signal attenuation with increasing loads and severity of damage through measurements **D** and **E**, Figure 7.7a. It should be noted that visual damage was not observed ahead of the notch tip until 82% of the panel fracture load (i.e., between measurements **D** and **E**), Figure 7.7d, at which point a significant drop in the FR along each of the wave paths was already apparent.

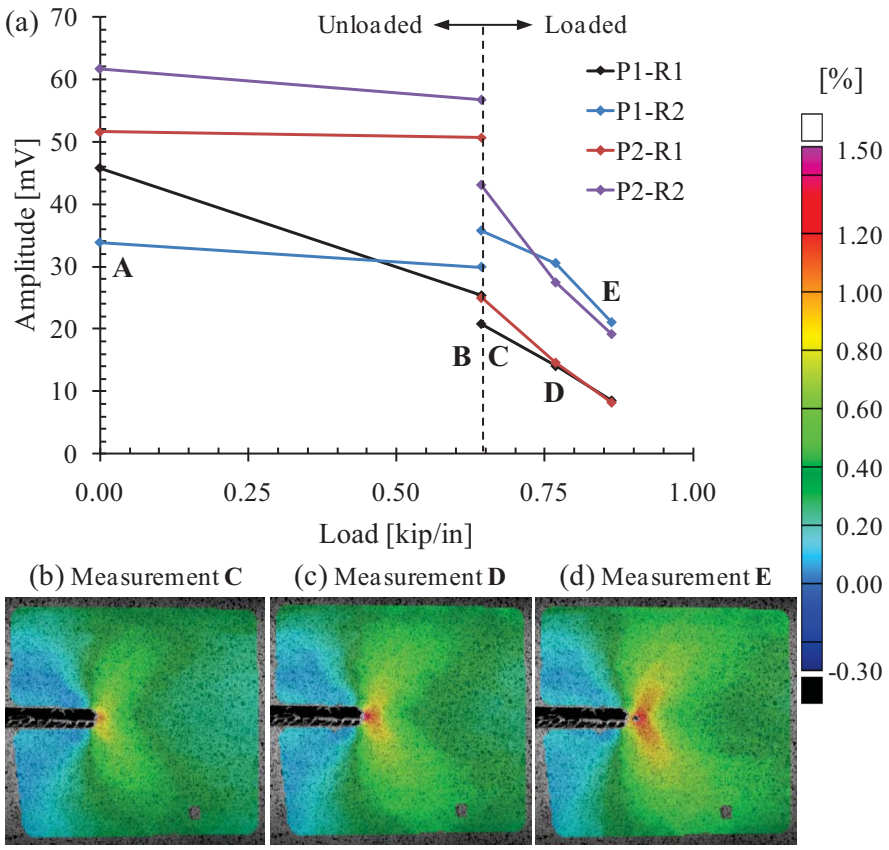

Figure 7.7. (a) Peak amplitudes of the waveforms recorded during the loading of panel CP5, showing the effect of increasing load and more severe states-of-damage. The DIC hoop strain contour plots corresponding to measurements **C**, **D**, and **E** are shown, as well.

Power spectra for all five measurements taken along the four monitored wave paths are shown in Figure 7.8. Note that the scale is different in each of the four plots. Generally, significant signal attenuation was observed with increasing load, with the entire frequency range affected by the changes in the state-of-damage. The area under the power spectrum for each wave path is plotted as a function of applied load in Figure 7.9. These results are similar to those recorded for the waveform peak amplitudes, including the unexpected increase in area under the power spectrum for the P1-R2 pair upon reloading.

Several additional trends are apparent amongst the four pulser-receiver pairs, especially regarding similarities between the power spectra of waveforms from the same pulser (i.e.,

between P1-R1 and P1-R2, and between P2-R1 and P2-R2), Figure 7.8. Data collected from the P1-R1 (Figure 7.8a) and P1-R2 (Figure 7.8c) pairs exhibited significant signal attenuation in the frequency range of 150–230 kHz with each consecutive measurement. A marked difference was even observed between measurements **A** and **B**. As mentioned, this was against expectations as no visual surface damage had been observed and minimal AE activity had been detected up to this point. A second frequency range, between 94 and 124 kHz, showed an increase in the amplitudes of the power spectra between measurements **B** and **C**. This unexpected increase offset much of the observed signal attenuation in the 150–230 kHz range. Data recorded from P2-R1 and P2-R2 pairs exhibited very little signal attenuation between the measurements **A** and

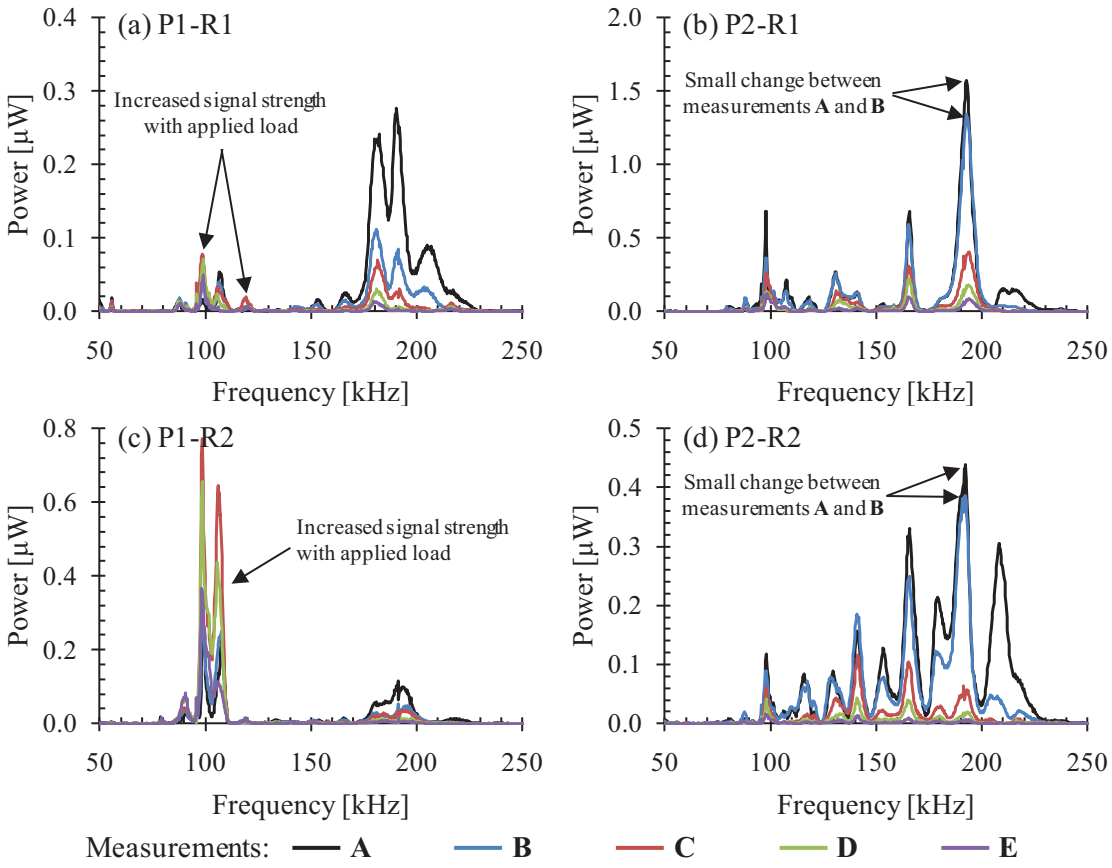

Figure 7.8. Power spectra recorded at several load levels in panel CP5, monitoring four paths through the material: (a) across the notch tip, (b) two inches ahead of the notch tip, (c) along the P1-R2 path, and (d) along the P2-R1 path.

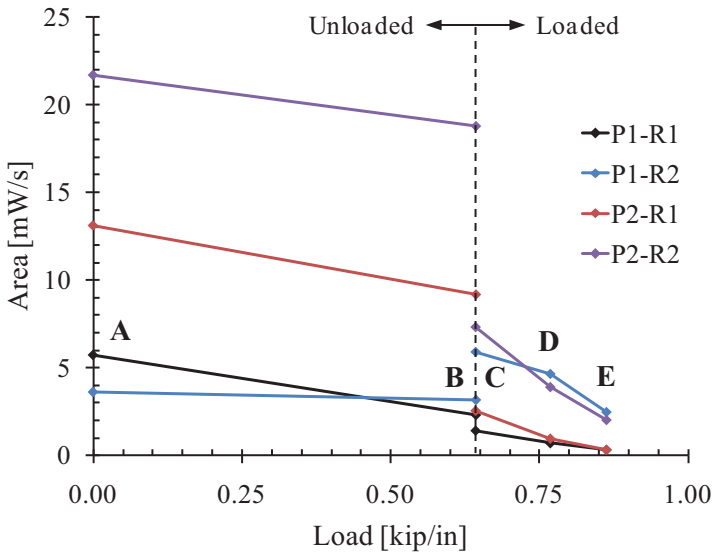

Figure 7.9. The area under the power spectra shown in Figure 7.8. The areas were calculated for the area under the power spectra between 60 and 250 kHz.

B, but attenuated upon further loading, similar to the observed waveform peak amplitude results (Figure 7.7a). No significant shifts in the peak frequencies occurred; shifts, if apparent at all, were less than 2% of the associated baseline peak frequency.

The data recorded from the P1-R1 and P1-R2 pairs in the frequency range of 94–124 kHz are replotted in Figure 7.10a and b, respectively, for clarity. The power spectrum recorded by the P1-R1 pair contained two separate frequency ranges, 94–104 and 114–124 kHz, exhibiting increases in amplitude upon reloading. The power spectrum recorded by P1-R2 pair exhibited similar behavior in the frequency range of 94–112 kHz. Upon further loading, results for both P1-R1 and P1-R2 were as expected, showing increased attenuation at all frequencies with increasing loads and severity of damage, Figure 7.11a.

While these frequency ranges had relatively little significance in the power spectrum of the P1-R1 pair (Figure 7.8a), the P1-R2 pair results were dominated by this frequency range, Figure 7.8c. The areas under the power spectra along the four wave paths are replotted in Figure 7.11b with these frequency ranges removed from consideration. The results conform well to

expectations, consistently decreasing with increased loads. The cause of the redistribution of waveform energy from the high- to low-frequency components merits further consideration and additional investigation.

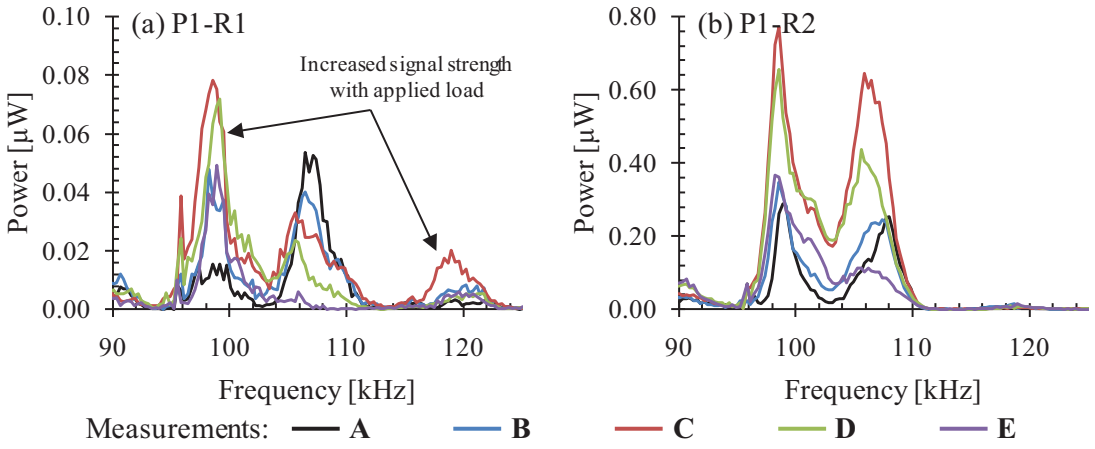

Figure 7.10. Power spectra showing an increase in signal strength from (a) P1-R1, in the frequency ranges of 94–104 and 114–124 kHz; and (b) P1-R2, in the range of 94–112 kHz.

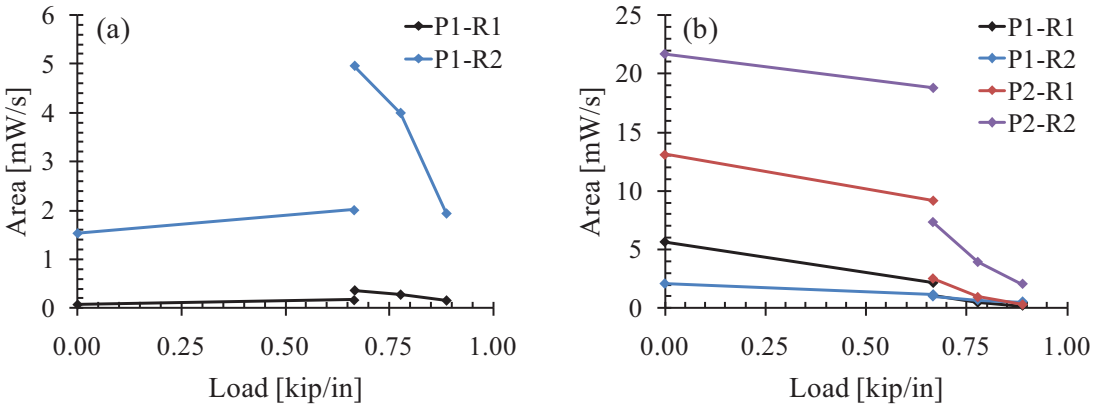

Figure 7.11. The area under the power spectra for (a) the frequency ranges shown in Figure 7.10 and (b) for the whole 60–250 kHz range with the frequency ranges in Figure 7.10 removed.

7.4. PANEL CP6

Based on the results obtained with panel CP5, the same experimental procedure was repeated with panel CP6, however, following a different loading function. As mentioned in Section 3.6, panel CP6 was unloaded after reaching each consecutive load step. After the initial baseline measurements, FR measurements were taken after reaching and unloading from each load step up to the eighth load step, Figure 7.12. Additional FR measurements were taken during the ninth, tenth, and eleventh load steps, but the panel was not unloaded due to the significant AE activity detected, and the desire to keep the loading function similar to the earlier panels while the damage was propagating.

During the test, a hardware error was identified in the waveform generator circuit board. The board did function, but the accuracy and consistency of the transmitted signals in terms of voltage could not be verified, making sound comparisons of the FR measurements taken at different loads during the test impossible. Consequently, no FR results from panel CP6 are reported here.

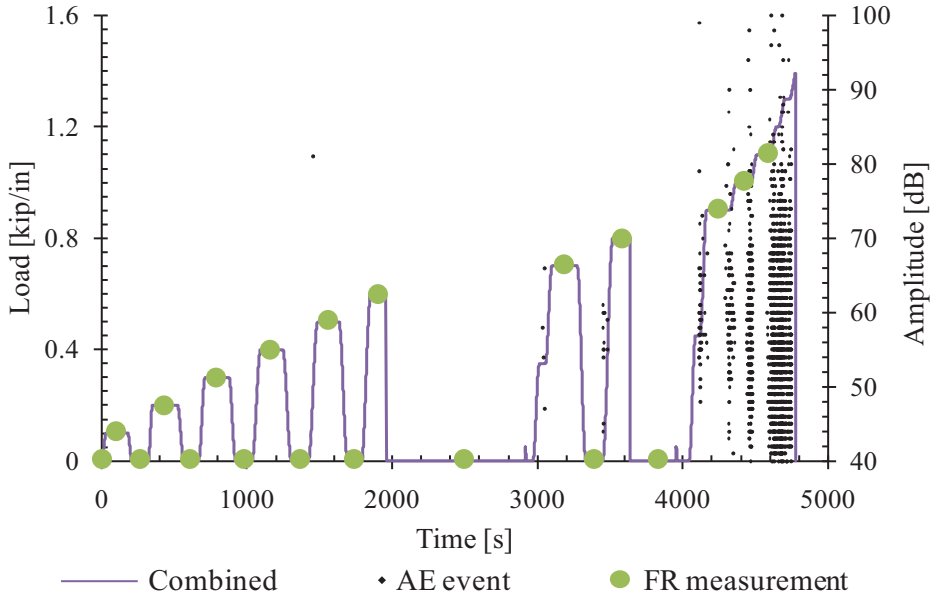

Figure 7.12. FR measurements, indicated with respect to the load-time history and accumulation of AE events from gage section of panel CP6 during loading.

7.5. CONCLUSIONS

It has been shown that the frequency response (FR) technique can be used to qualitatively determine the severity of damage ahead of a notch tip in a full-scale honeycomb sandwich composite fuselage panel during loading. The results indicate that damage initiation and propagation markedly affects the signal attenuation characteristics of the material, relative to baseline measurements taken at the same location and under identical test conditions. Specifically, the transmitted signal is highly sensitive to the presence of internal damage and increased loads, decreasing rapidly with the development of additional damage at the notch tip. No significant frequency shifts of the dominant frequencies were observed.

The presence of damage could be determined in real-time during loading, and results indicated that the FR method is at least as sensitive as the acoustic emission (AE) method. Furthermore, the relative severity of damage could be quantified through either the area under the frequency response curve or the peak amplitudes of either the waveform or the power spectrum at select frequency ranges. That is, application of the FR technique in large-scale composite panels is a simple technique that could provide either real-time assessment or rapid inspection capabilities of the state-of-damage, and act as an early warning of incipient damage. The technique could be applied on-line, that is, it is not necessary to either remove the specimen/structure from the loading fixture or interrupt the loading.

The FR results depend on a variety of material and test variables. However, for a given set of testing conditions and material, good correlation between the state-of-damage and the characteristics of the frequency response was established. The testing procedure could also aid in the optimal selection of AE sensors.

The FR technique as applied in this investigation could not identify the specific mode of failure. The effect of the various modes of failure on the characteristics of the power spectrum could be studied by conducting tests with model composites that exhibit a single mode of failure under loading, such as matrix cracking, delamination, etc. Such studies would provide a more in-

depth understanding of the effect of the various material variables and modes of damage on the characteristics of the frequency response of the subject material.

CHAPTER 8: MODELING AND SIMULATIONS

8.1. INTRODUCTION

The primary objective of this computational study was to accurately and efficiently simulate the formation, progression, and eventual instability of damage in full-scale sandwich composite aircraft fuselage panels originating at severe artificial damage sources through use of the finite element (FE) method. While several advanced computational failure models have been developed for composite materials, most of their derivations and validations have been performed on the coupon-scale in a laboratory environment, neglecting issues related to scalability and real-world application. The modification and application of existing composite material failure concepts to full-scale fuselage structures is necessary for their use in future in-depth aircraft damage tolerance studies and certifications. Computational tools to be used toward this end are proposed and applied in this chapter.

The comprehensive deformation and strain data reported in Chapter 4 and the characterization of subsurface damage via nondestructive inspection (NDI) reported in Chapters 5 through 7 offered means of validating both the general far-field response of the panels and the evolution of damage ahead of the artificial stress risers. In this chapter, FE models of the baseline and notched panels (i.e., panels CP3 through CP6) are developed and their results reported on; models were not developed for panels CP1A, CP1B, and CP2 due to their complex load histories' likelihood to influence their residual strength test performance.

Due both to the large disparity in the characteristic lengths of the panels and the notches, and to the anticipated complex three-dimensional (3-D) state-of-damage ahead of the notch tips, a global/local analysis was performed. Two-dimensional shell elements were used for the global models, representing the entire panels, while 3-D solid elements were used for the local models in the vicinity of the notch tips. The results of the global models were used to drive the boundary conditions of the local models. Custom user subroutines were developed to properly drive the

local models and to allow the formation and propagation of damage through them. The development of both the global and local FE models are described in detail in Sections 8.2 and 8.4, respectively, and their results reported on and compared to the experimental data in Sections 8.3 and 8.5, respectively.

Due to the quasi-static application of loads in the experimental phase of the test program, an implicit FE analysis was performed. Both the global and local models were prepared and solved using ABAQUS 6.8-2. All user subroutines were written in Fortran and are available in Appendix B.

8.2. GLOBAL MODEL DEVELOPMENT

A baseline global FE model representing an undamaged panel was developed and validated using the experimental results of the three strain survey loading conditions, i.e., combined internal pressure, hoop, and longitudinal loading; internal pressure and hoop loading; and longitudinal loading. Several developmental iterations of the global FE models were performed while attempting to accurately represent the distributions of strain across the baseline panel under the three strain survey loading conditions. These models varied in complexity from an initial idealized conceptualization of the panels as portions of a cylindrical pressure vessel to an in-depth representation of the panel geometries, composite lay-ups, and the FASTER fixture loading mechanisms. As the final version of the global FE model encompassed the changes introduced with each successive modeling iteration, only the features of the initial idealized model and the final detailed model are presented here.

8.2.1. INITIAL IDEALIZED MODEL

The FASTER fixture and the composite panels used in this test program were designed in such a way that each panel would be subjected to uniformly distributed hoop and longitudinal loads throughout the test section (except, as expected, in the immediate vicinity of any artificial

or generated damage). The longitudinal loaders were balanced by the two sets of loaders along the opposite edges of the panel while the hoop loads were balanced by the uniformly distributed pressure applied to the interior surface. Therefore, a cylindrical pressure vessel was adopted as the basis for the initial global FE model of the baseline panel.

The full test section of panel CP1 was modeled, spanning 104 inches in the longitudinal direction and 59 inches along the circumference of a 74.4-inch radius cylinder, Figure 8.1. The 74.4-inch radius represented the radial distance to the mid-plane of the test section laminate thickness. The $[45/0/45/Core_{½}]_S$ test section composite lay-up was used throughout the model, using the relevant material properties listed in Table 3.1. Internal pressure was applied to the entire interior surface, with symmetry boundary conditions along the hoop edges producing appropriate uniformly distributed reactive hoop loads tangent to the panel edge. Uniformly distributed edge loads were applied to one longitudinal edge while symmetry boundary conditions were applied to the opposite edge, producing equal uniformly distributed reactive longitudinal loads. The magnitudes of the applied loads were those applied during the strain surveys of panel

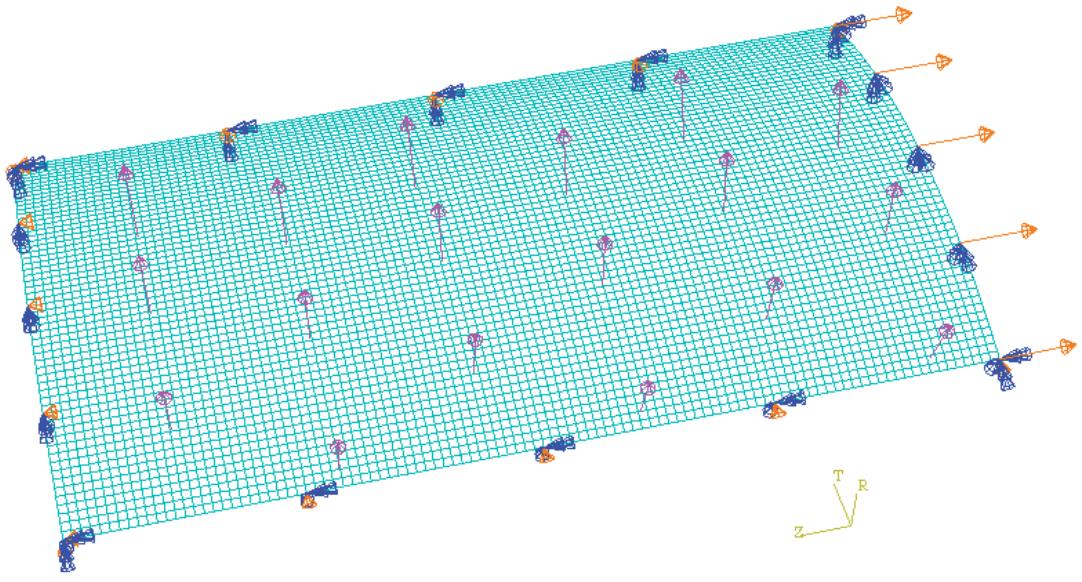

Figure 8.1. The initial idealized baseline panel global FE model, showing the internal pressure and longitudinal loads, symmetry boundary conditions, and 1-inch global element size.

CP1, listed in Table 3.3. The panel was meshed using S4R elements (i.e., 4-node doubly curved general-purpose shell elements with a reduced integration formulation) with a 1-inch global element size.

A validation of the initial baseline global model was performed using the strain survey loading conditions of panel CP1 (Table 3.3). The computational strain distributions on the exterior surface of panel CP1, together with the corresponding strain gage results, are shown in Figure 8.2. The computational results showed a nearly uniform strain distribution throughout the model, varying by less than 2% only in the immediate vicinity of the corners constrained in both the hoop and longitudinal directions. This was expected given the selection of the loading and boundary conditions to emulate the behavior of a cylindrical pressure vessel. Equal hoop and longitudinal strains of approximately 0.22% occurred under the combined loading condition, while strains of 0.20% and -0.09% occurred in the loading and off-axis directions, respectively, for the separate hoop and longitudinal loading conditions. The experimentally observed distributions of strain, both across the panel and within the central test section, were not uniform, however. Rather, nearly parabolic distributions of longitudinal strain with hoop position were identified in each of the panels, and the hoop and longitudinal strain response to equal nominal loads were not equal despite having approximately equal stiffness in the hoop and longitudinal directions. The reasons for such non-uniform strain distributions have been discussed in great detail in Chapter 4.

Free play present in a FASTER loader could cause both an artificial shift in the strain response to applied load, and nonlinearity through the first two to three strain measurements. This nonlinearity could be removed by shifting the strain gage data using the method described in Section 4.2 (i.e., fitting the latter data points to a linear curve and shifting the data so that the curve passes through the origin). In the panel CP1 strain surveys and panel CP6 residual strength test, all loads were ramped up simultaneously, making the identification of nonlinearity in the early load steps and the shifting of the data possible. The multi-step loading functions used for

panels CP3, CP4, and CP5 (e.g., applying two steps of longitudinal loading, followed by nine steps of hoop loading in panel CP5), however, prohibited the application of this post-processing procedure. Therefore, for uniformity, all strain data presented in Chapter 4 were not shifted; rather, they were simply zeroed to the point immediately before any nonzero load commands were set. In this chapter, in order to make a more accurate comparison between the experimental and computational results, the shifting procedure was applied to the experimental strain data of panels CP1 and CP6. Hence, the experimental data of these two panels presented in this chapter are different from that presented in Chapter 4. All data shifts were typically less than 0.02% strain. Furthermore, because the data for remaining notched panels could not be appropriately shifted, the change in the states-of-strain with increased loading served as the better measure for correlation than direct comparison of the experimental and computational results for these panels.

Comparison of the experimental and computational strain data from the CP1 strain surveys revealed the expected discrepancies, Figure 8.2. The longitudinal (Figure 8.2a) and hoop (Figure 8.2b) strain distributions under combined loading showed that the idealized FE model underestimated the longitudinal strains and, correspondingly, overestimated the hoop strains. While the longitudinal strains along the crown of the panel were overestimated by only 10%, the error increased to approximately 20% at the limits of the central test section, and can be assumed to have increased further with increased proximity to the hoop loaders. This is evidenced by the strain gage data from panels CP2 through CP6, which had additional gages installed beyond ±12 inches hoop position. The hoop strains were underestimated by an average of 20% across the test section throughout loading.

The strain responses of the panel to separate hoop and longitudinal loading conditions were similar to the experimental results in terms of average strain through the central test section. The longitudinal strain responses to both hoop (Figure 8.2c) and longitudinal (Figure 8.2e) loading were underestimated along the crown of the panel, but overestimated along the edges of the test section, failing to represent the often observed nearly parabolic distribution of

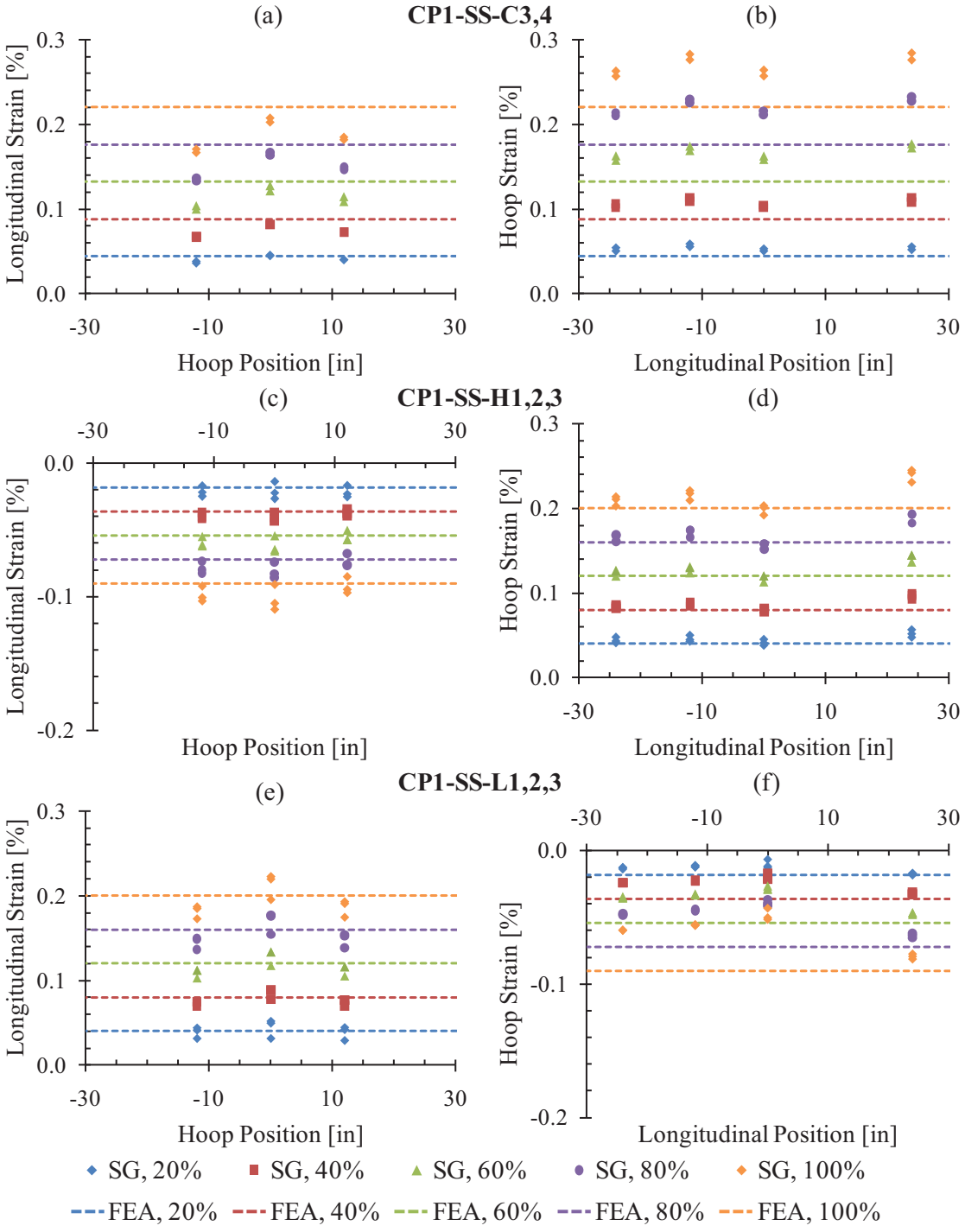

Figure 8.2. Strain distributions on the exterior surface of panel CP1 during the strain surveys as measured via strain gages and as calculated using the initial idealized FE model. The percentages in the legend are with respect to the maximum applied loads for each of the three strain survey loading conditions listed in Table 4.1 for the tests indicated in bold.

longitudinal strain. The hoop strain response to hoop loading (Figure 8.2d) correlated generally well, with the computational results underestimating the experimental results by less than 10%. The lower-than-expected experimental hoop strain response to longitudinal loading discussed in Section 4.2.1 caused for a great disparity with the corresponding computational hoop strain results (Figure 8.2f), though strain gage SG23, located at +24 inches longitudinal position, was within 10% of the predicted values.

As was discussed throughout Section 4.3, failures were observed along multiple material principal directions ahead of the notch tips, and the introduction of error in the strains along any direction could have a significant effect on the prediction of notch tip failures. The accuracy of the predicted state-of-strain throughout the test section and ahead of the notch tips with respect to the experimental data is essential for the development and validation of failure models for use in the local FE models. Regardless of which loading condition is critical for a particular notch geometry, off-axis loads were applied in each case, and have been shown to have an appreciable effect on the state-of-strain throughout the panels. While the initial idealized cylindrical pressure vessel-based global FE model may represent well an actual composite fuselage, it does not address the issues specific to the test panels, such as the details of the panel geometries, composite lay-ups, and the FASTER fixture loading mechanisms and boundary conditions. The following sections detail the thorough investigation conducted on each of these issues and how the global FE models were modified to incorporate them.

8.2.2. GEOMETRY

As mentioned in Section 3.3, the attraction of loads to the reinforced panel edges was understood to be a potential source of error from the beginning of the investigation. The greater stiffness of the composite lay-up used in the load application region was identified as a likely source of load attraction. As a result, blunted slits were inserted between each load application point along the panel edge to decrease the ability of the load application region to carry additional

load, Figure 8.3. However, the additional prepreg plies of the inner and outer transition regions, along with the geometry of the longitudinal load application points, still attracted the applied loads to the panel edges. The FASTER fixture applies longitudinal loads only to the central 56 inches of a panel's curvature; the longitudinally unloaded portions of the panel strongly contributed to the attraction of load away from the central test section. To separate the load paths of the hoop and longitudinal loaders to the test section, the corners of the physical panel in the load application region were removed, leaving a 3-inch radius to reduce the propensity of the panel to fail outside the test section, Figure 3.5. These corner cut-outs were modeled with right angles to maintain an orthogonal mesh and because no failure models were active in the global models, Figure 8.3.

In order to accurately simulate the distribution of strains throughout the central test section, the attraction of the applied loads to the panel edges had to be accurately represented. The geometry and composite lay-up of each section of the panel, as described in detail in Section 3.3, were meticulously modeled. The panel test section had the same geometry, composite lay-up, and material properties as used in the initial idealized cylindrical pressure vessel model. The inner transition region, which extended 5 inches outward from the hoop and longitudinal edges of the test section, had a constant 0.75-inch core thickness and a composite lay-up of $[45_3/0/45/Core_{½}]_S$. The outer transition region, which extended an additional inch outward in the hoop and longitudinal directions, linearly decreased the core thickness from 0.75 inch to 0.25 inch and gradually shifted to the composite lay-up of the load application region, $[45_2/0/45/0/45/0/45/0/45/0/45_2/Core_{½}]_S$. The outer transition region was modeled with an intermediate core thickness (0.375 inch) and a uniform composite lay-up of approximately equal stiffness to the complex lay-up portrayed in Figure 3.6b, $[45_3/0/45/0/45/0/45/Core_{½}]_S$. The load application region was modeled using its actual composite lay-up and 0.25-inch core thickness. The blunted slits were represented by infinitesimally thin slits through the thicker laminate, leaving 1.25 inches intact along the longitudinal edges and 0.50 inch intact along the hoop edges;

the blunted geometry of the slits was not modeled because no failure models were active in the global models and the ability of the panel edges to attract load would be unaffected by the greater detail.

To assess what effects the inclusion of the detailed panel geometry and the various composite lay-ups had on the distributions of hoop and longitudinal strain, two FE models were solved and their results compared, Figure 8.4. The first model contained the detailed panel geometry and the test section composite lay-up throughout, and the second model contained both the detailed panel geometry and the separate composite lay-ups. It was found that the accurate modeling of the panel geometry had a greater effect in regards to causing the nearly parabolic distributions of longitudinal strain with hoop position that were observed experimentally in each of the panels, Figure 8.4a. The inclusion of the various composite lay-ups caused a static decrease in the predicted longitudinal strains. A slight increase in hoop strain within the test section was observed, with a sharp decrease near the panel edges, Figure 8.4b.

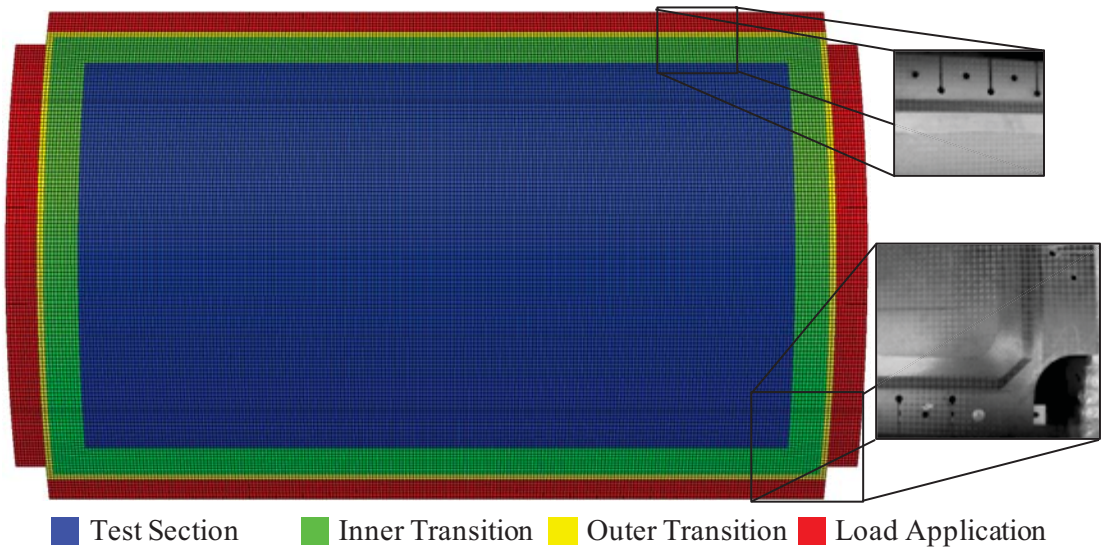

Figure 8.3. Geometry of global FE model for panel CP1, showing details of the panel load application region and corner cut-outs. The locations of the four composite lay-ups are indicated by their color.

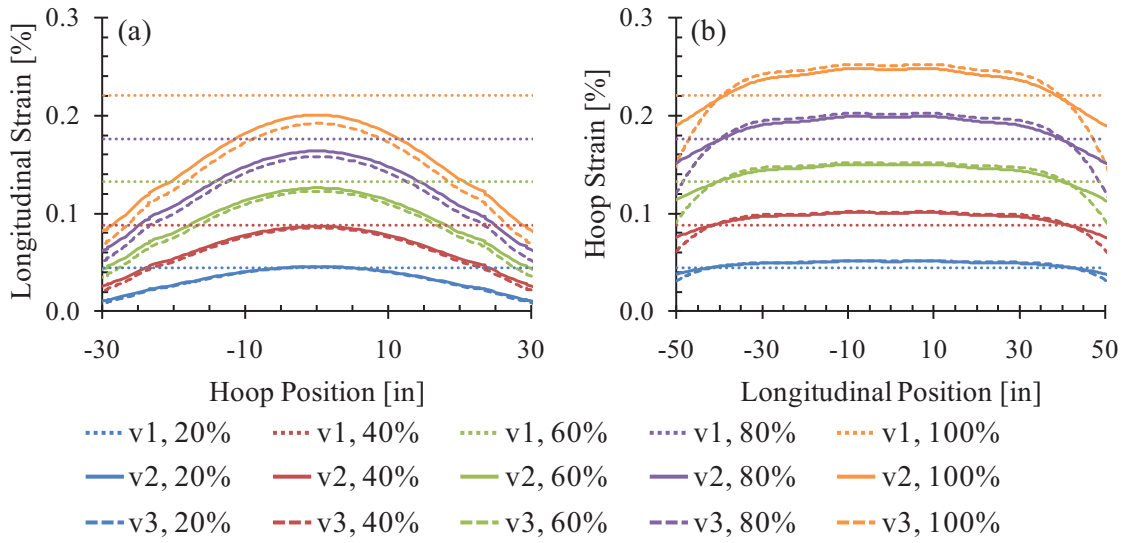

Figure 8.4. Comparison of the effects of global FE model panel geometry and composite lay-ups on the distribution of (a) longitudinal strains with hoop position and (b) hoop strains with longitudinal position for combined loading condition strain surveys for panel CP1. Global FE model v1 represents the cylindrical pressure vessel, model v2 contained the detailed panel geometry with the test section material properties throughout the model, and model v3 contained both the detailed panel geometry and the separate composite lay-up sections.

8.2.3. LOADING AND BOUNDARY CONDITIONS

An initial revision to the modeling of the hoop and longitudinal loads involved applying concentrated forces at each load attachment point, with both the hoop and longitudinal forces defined in the cylindrical coordinate system of the panel, Figure 8.5a. The longitudinal loads were applied in the panel z-direction and the hoop loads were applied in the panel θ-direction. While valid during the initial loading of a panel, increased panel deformation invalidates this system of load application.

A thorough review of the FASTER loading and constraint mechanisms was performed to determine the effects, if any, that panel deformation and displacement had on the orientation of the applied loads with respect to the panel edges. As internal pressure and hoop loads are applied to a panel, the panel stretches in the hoop direction and becomes radially displaced from its original position. Under load, any radial displacement of the joint connecting the top of the lever

arm and the load cell/whiffle tree assembly (point 'A' in Figure 8.5a) is negligible. As a consequence, the load cell must rotate about point 'A', out of its original z-θ plane, to accommodate the radial displacement of the panel. Accordingly, rather than having a purely θ-direction load, the applied loads are then split into hoop and radial components, Figure 8.5b. These radial load components effectively decreased the applied in-plane loads and tended to cause bending of the panels as internal pressure (and therefore radial displacement) increased.

To model this behavior, a simplified representation of the FASTER loaders was developed. Cylindrical coordinate systems were placed at the fulcrum of each lever arm (Point 'C' in Figure 8.5a), with the local r-direction oriented parallel to the lever arm and the z-axis oriented in the longitudinal direction for the hoop loaders portrayed in Figure 8.5. The connection between the lever arm and the load cell was constrained so as to be free only to displace in the local θ-direction and rotate about the local z-axis. The loads were then applied as concentrated forces at the load cell/lever arm connection point parallel to the initial load cell orientation, and allowed to rotate with nodal rotations. Rigid links connected the load cell/lever arm connection point and the load application points along the panel edges, and the links were tied to the nodes of the panel. Similar conditions were applied for the longitudinal loaders, Figure 8.6.

A set of ten radial links, installed to limit excessive radial displacement of the panels in case of misapplication of internal pressurization and hoop loads, acted as an additional source of panel bending. While each link was installed with slack so as to allow for some radial displacement, the amount of slack varied amongst the ten links, causing some to become taut prematurely, applying unequal radial loads to the interior surface of the panels. Due to faulty load cells, an incomplete radial link load data set was recorded during the residual strength tests. Furthermore, all functioning load cells were installed to only record tensile load data, neglecting any compressive loads which may have occurred. While the application of concentrated forces at each radial link attachment point would best represent their effect on the panel deformation, the

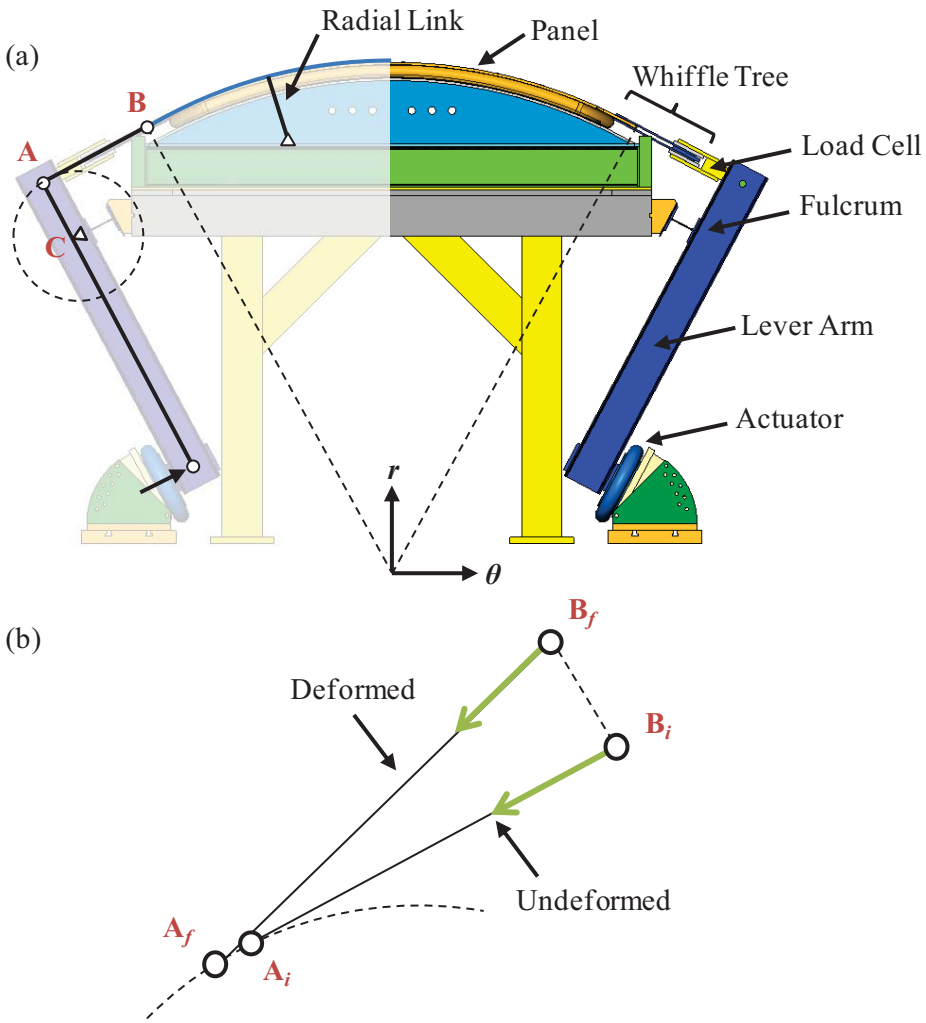

Figure 8.5. (a) General view of the FASTER fixture and hoop loader arms, and (b) a schematic showing the change in the orientation of the hoop loaders with radial displacement of the panel.

incomplete data prohibited this. Therefore, each radial link was modeled as a truss element tied to the interior surface of the panel and pinned to the base of the pressure box. While each radial link assembly consisted of several components (e.g., double universal joints, hinges, threaded rods, etc.), each link was represented by a simple 0.25-inch-radius steel rod.

Internal pressure was applied to the full test section and inner transition composite lay-up regions of the panel. Additional displacement boundary conditions were applied to prohibit rigid body translations of the panels in the hoop and longitudinal directions. These boundary

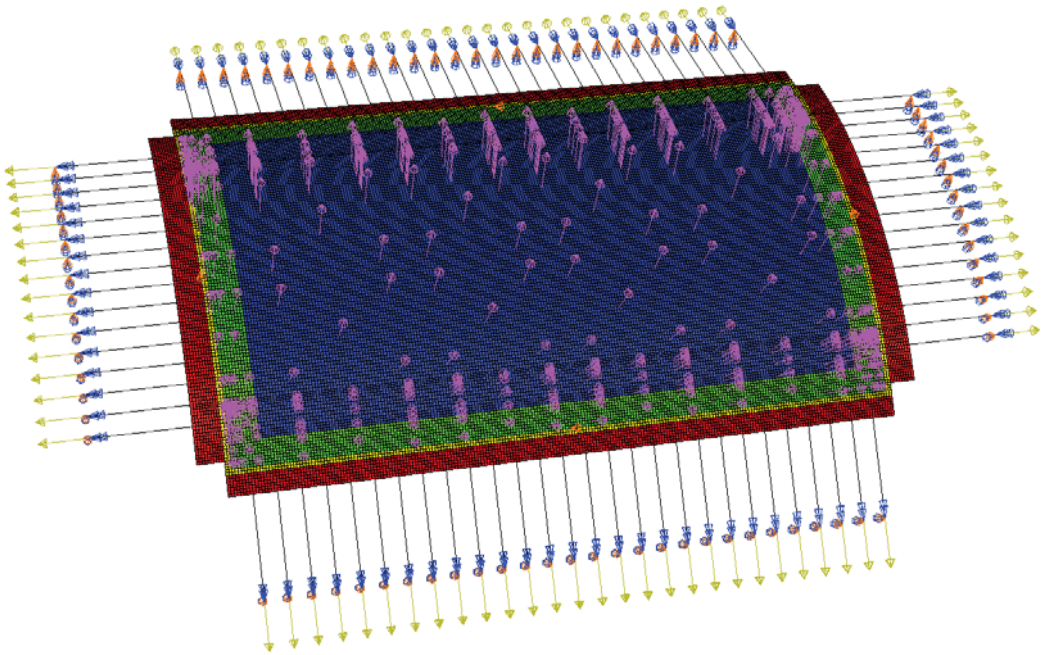

Figure 8.6. Schematic of detailed baseline panel FE model, showing the applied internal pressure, the hoop and longitudinal loader mechanisms, and the rigid body translation boundary conditions between the load application and outer transition composite lay-up regions.

conditions were located between the load application and outer transition composite lay-up regions, along the major axes of symmetry of the panel, Figure 8.6.

8.2.4. ELEMENTS AND MESH

The composite panels were modeled using S4R elements. Element type S4R is a 4-node doubly curved general-purpose shell element with a reduced integration formulation. S4R elements were used throughout the global models for their computational efficiency with respect to the quadratic thick-shell S8R elements. Both the S4R and S8R element types adhere to Mindlin shell theory [8.1], allowing for constant transverse shear strains to develop through the element thickness.

Global models composed of both S4R and S8R elements with equal mesh densities were solved, and their results compared. The two models produced results with less than 1%

difference in terms of both displacement and strain, while the 4-node element model required approximately 5% of the CPU time required for the 8-node element model. The global element size for the panels was 0.5 inches in the far-field regions, while the element size in the vicinity of the notch tips was reduced to approximately 0.1 inches, Figure 8.7. In total, approximately 42,000 elements were used to represent each panel.

The load cell/whiffle tree assemblies of the FASTER loaders were represented by RB3D2 (i.e., 2-node 3-D rigid beam) elements. Each load application point was connected to the top of the loader lever arms by a single RB3D2 element. Each of the ten radial links was modeled with a single T3D2 element. Element type T3D2 is a 2-node linear 3-D truss element. Utilizing the proposed formulation, the loader mechanisms and constraints of the FASTER fixture were realistically represented by including only 98 additional elements.

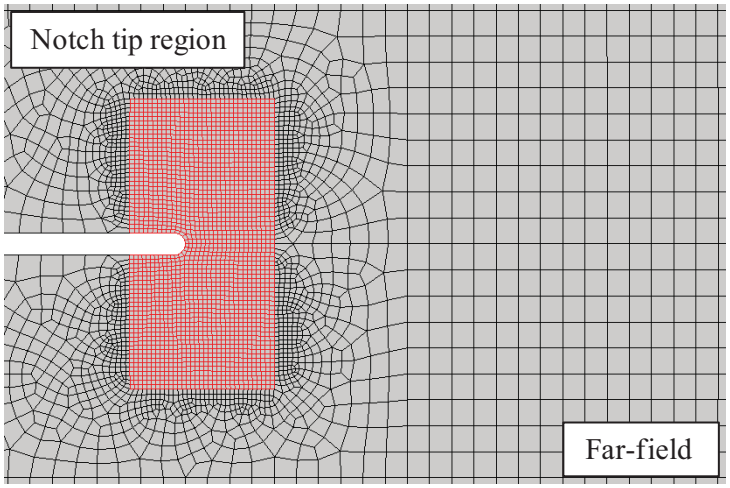

Figure 8.7. Mesh surrounding a notch tip in the global FE model of panel CP5, showing the different mesh densities of the notch tip and far-field regions, and the transition between them.

8.3. GLOBAL MODEL RESULTS

Excellent correlation between the experimental and computational strain results, in terms of both the distribution and magnitudes of the strains, was achieved after incorporating the details of the panel geometries, composite lay-ups, and the FASTER fixture loading mechanisms, Figure 8.8. While loaded under each of the three strain survey loading conditions, the parabolic distribution of longitudinal strain with hoop position was well characterized, reducing the error to less than 10% in each case. The 20% difference in the hoop strain distribution with longitudinal position predicted by the cylindrical pressure vessel-based global FE model was also drastically reduced. The hoop strains resultant of combined loading were underestimated by an average of 9% at the maximum applied load, Figure 8.8b. Likewise, the hoop strains resultant of hoop loading were erred by an average of 6% throughout loading, Figure 8.8d. As mentioned in Sections 4.2.1 and 8.2.1, the three strain gages installed at -24, -12 and 0 inches longitudinal position output unexpectedly low hoop strains while under longitudinal loading, with only strain gage SG23, located at +24 inches longitudinal position, recording hoop strains near the expected values. Figure 8.8f shows that detailed FE model results overestimated the readings of strain gage SG24 by only 5% throughout loading.

The close correlation between the experimental and computational strain results for all three loading conditions for the undamaged panel indicates that the detailed global FE model should accurately represent the load and strain distribution behavior of each of the damaged panels. The global models of panels CP3 through CP6 differ from the detailed CP1 model only in their inclusion of the through-thickness notches, increased mesh density in the vicinity of the notch tips, and the specific loading function applied. Since loading functions of each panel are derivatives of the three baseline panel strain survey loading conditions, a close correlation was expected for each of the subsequent panels in terms of strain distributions. As mentioned in Section 8.2.1, the strain gage results for panels CP3, CP4 and CP5 were not shifted to compensate for any nonlinearity resultant of free play in the FASTER fixture loading mechanisms, and

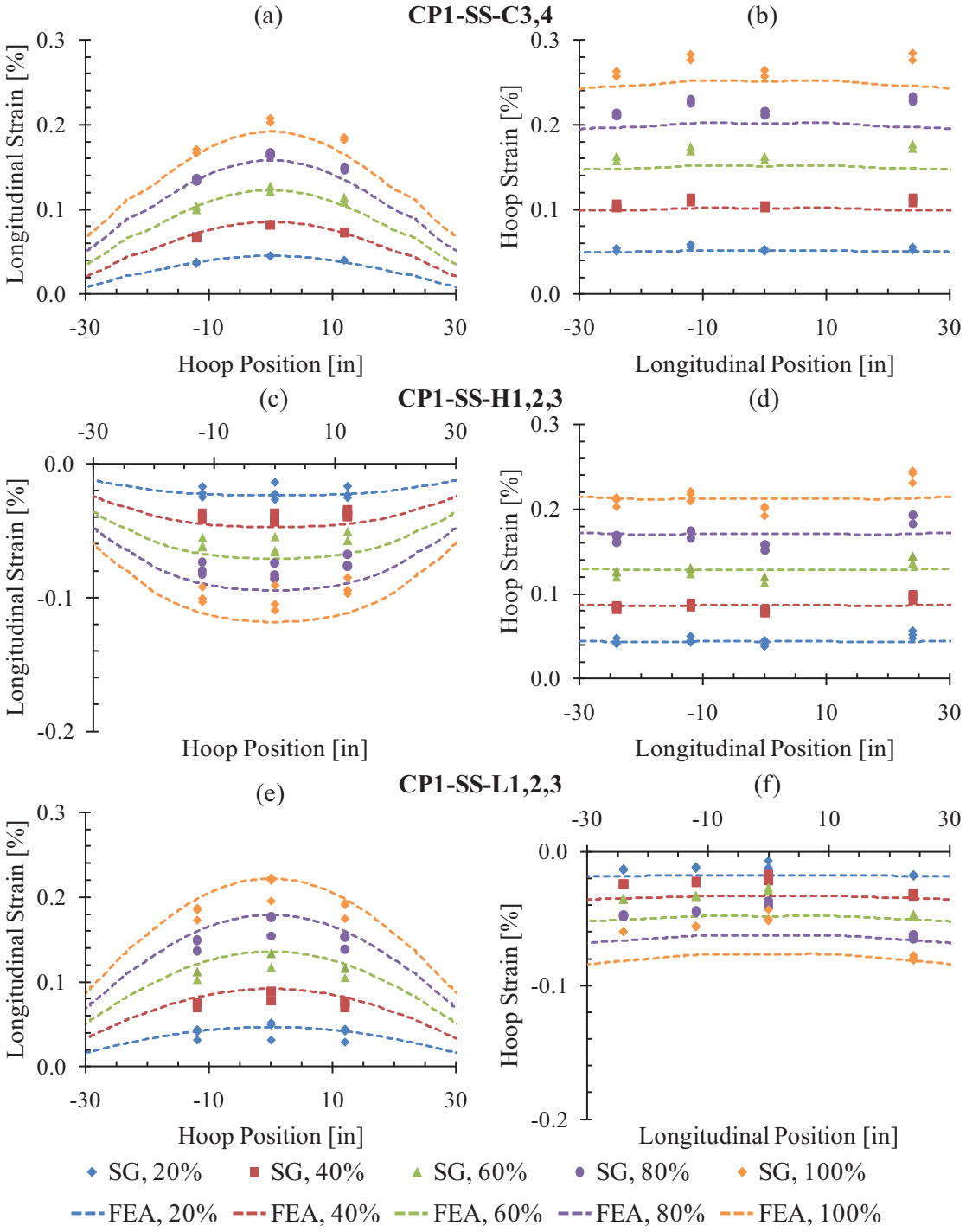

Figure 8.8. Strain distributions on the exterior surface of panel CP1 during the strain surveys as measured via strain gages and as calculated using the final detailed FE model. The percentages in the legend are with respect to the maximum applied loads listed in Table 4.1 for the tests indicated in bold.

emphasis should be placed on the response of strain to increased loading and the overall distribution across the panel rather than its magnitude.

As no failure models were implemented in the global FE models, each model is valid only up to the point of damage initiation. The global FE model longitudinal strain contour plot for the panel CP3 residual strength test at the last load step preceding the observation of visual damage at the notch tip monitored by the digital image correlation (DIC) system is shown in Figure 8.9a. The maximum far-field longitudinal strains are located along the crown of the panel close to the transition between the panel test section and the inner transition region. The longitudinal strains step down sharply moving from the test section to the load application regions due to the increased ply counts; this phenomenon was less pronounced in the vicinity of the hoop loaders due to the need for continuity of the strain field parallel to the transition. Throughout the far-field regions of the test section, the nearly parabolic distribution of longitudinal strain with hoop position is apparent, becoming less pronounced with increased proximity to the notch at the panel center.

The radial links, particularly the six central ones, had an appreciable effect on the global strain contour plot, causing localized regions of decreased strain on the exterior panel surface, indicative of tensile loads in the links. These tensile radial link loads ranged from 364 to 383 lbf in the center of the panel while at 74% of the experimentally observed panel fracture load, decreasing to approximately 115 lbf for those links nearest the longitudinal loaders. This is considerably higher than the experimental data recorded from the gaged links at this load level, none of which exceeded 150 lbf, Figure 4.20c. To assess the influence of radial link loads on the global strain response of the panels, models of the panel CP3 residual strength test were solved both with and without the radial links included. The distribution of longitudinal strain with hoop position was unaffected outside the central 47 inches between the radial link attachment points, and decreased the strains within this region by an average of 8%, Figure 8.10a. Less influence was observed with respect to the distribution of hoop strain with longitudinal position, with the

only affected locations being at ±7 inches longitudinal position, Figure 8.10b; no influence was observed along the axis of the notch. While apparent in its influence in the far-field regions of the panel, the effect of increased radial link loads on the distributions of strain within the central test section and in the vicinity of the notch tips is relatively small, having little influence on the results of the progressive damage studies of the local FE models.

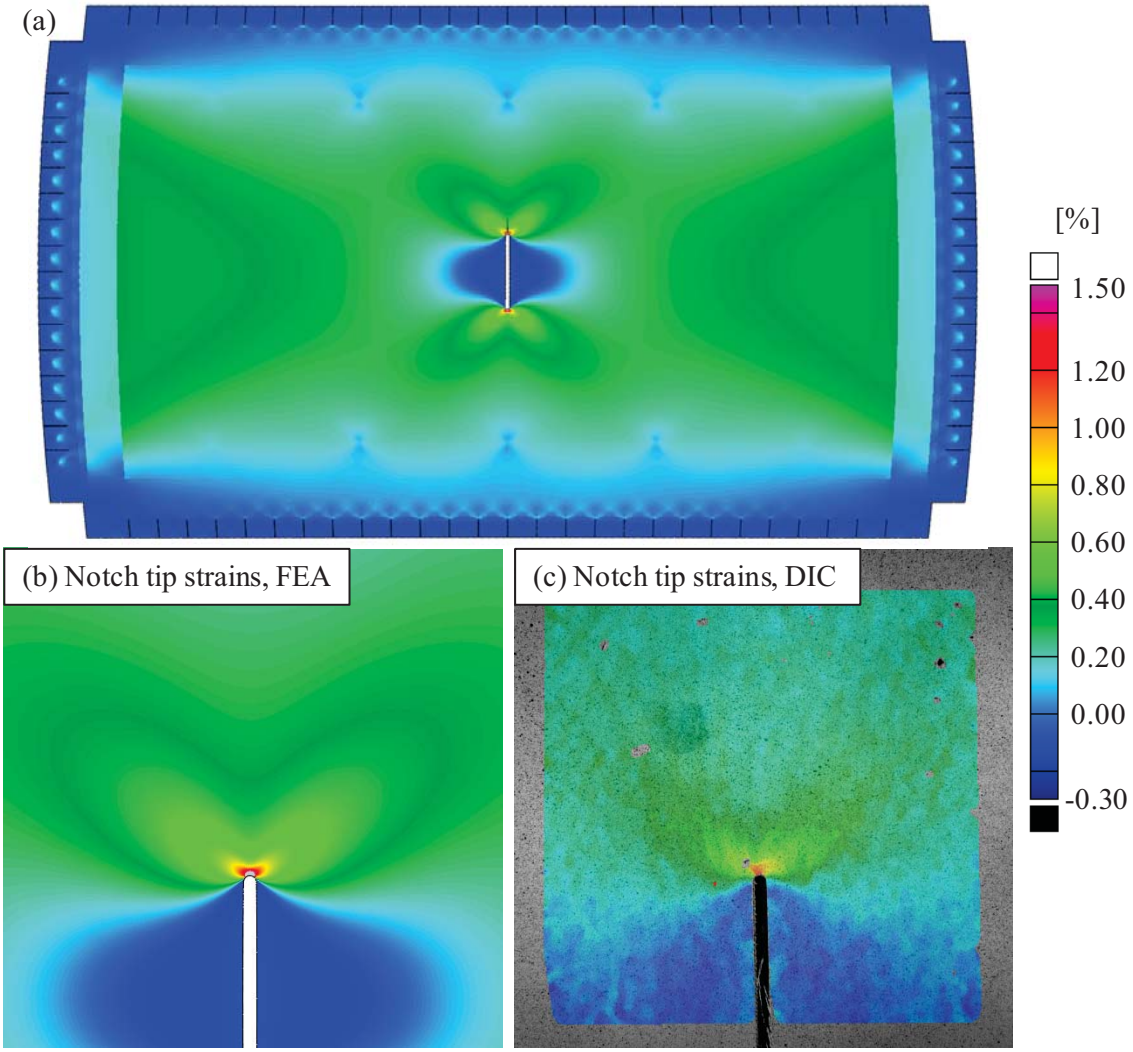

Figure 8.9. Longitudinal strain contours at 74% of the panel CP3 fracture load for (a) the whole panel as calculated via global FEA, (b) the notch tip region as calculated via global FEA, and (c) the notch tip region as measured via DIC.

Excellent correlation was observed between the experimental and computational strain distributions for the panel CP3 residual strength test. The parabolic distribution of longitudinal strain with hoop position was well characterized by the global FE model, Figure 8.11a. The computational results consistently overestimated the strain gage results by a fixed amount, indicating that the structural response was modeled accurately and that free play in the FASTER loaders caused an artificial shift in the strain gage data. Similar results were observed for the distribution of hoop strain with longitudinal position. Excellent correlation was achieved well beyond the test section, capturing the local hoop strain maximum due to the elevated strain field ahead of the notch tip and the sudden decrease in hoop strain with increased proximity to the longitudinal loaders, Figure 8.11b. The differences between the strain gage and global FE model results are constant for each gage, again indicating that free play in the loaders caused an initial offset of the strain gage data.

Typical kidney-shaped elevated strain fields are rooted at the two notch tips (Figure 8.9b), correlating well with the longitudinal strain contour plot recorded via DIC, Figure 8.9c. While the state-of-strain ahead of the notch tip in the global FE model shows higher longitudinal strains than measured via DIC, keep in mind that the DIC strain data within 0.3 inch of the notch tip is artificially reduced due to the filtering scheme applied. The contour corresponding to 0.8% longitudinal strain serves as a good qualitative measure for comparing the full-field notch tip strains in this case; this region extends approximately 0.5 inch ahead of the notch and 0.75 inch perpendicular to the notch in both the FE and DIC data.

Figure 8.12 shows a quantitative assessment of the correlation between the experimental and computational notch tip strain field results. The results are compared in terms of the longitudinal strains along the axis of the notch, similar to the comparison performed to ensure the strain gage and DIC data were in agreement, Figure 4.48. The global FE analysis overestimated the strain gage and DIC data by a fixed amount at each location throughout the panel throughout loading, though the overall distribution of strains and the strain response to increased load agreed

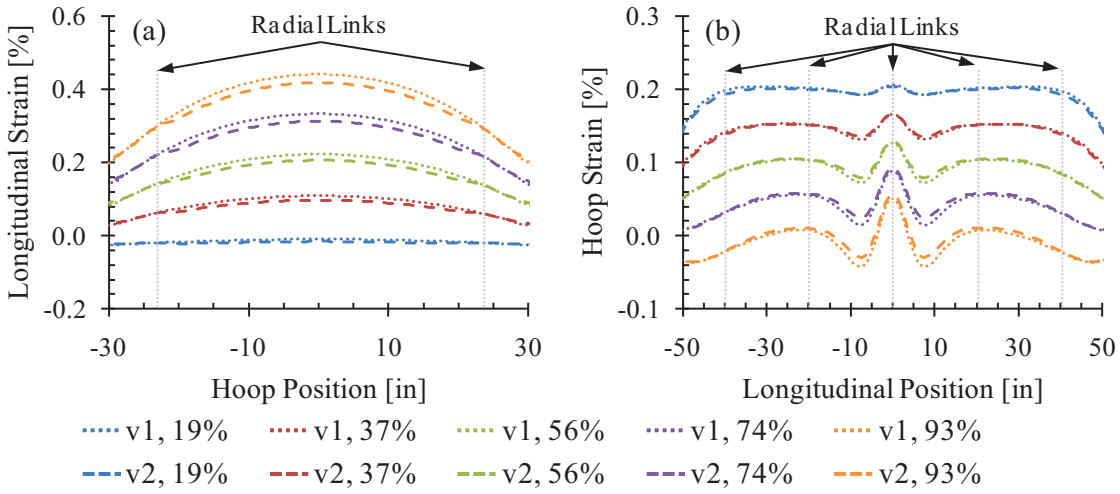

Figure 8.10. Strain distributions on the exterior surface of panel CP3 during the residual strength test as calculated using the detailed global FE model. The percentages in the legend are with respect to the maximum applied loads listed in Table 4.5. Global FE model v1 does not contain radial links, and model v2 does contain radial links.

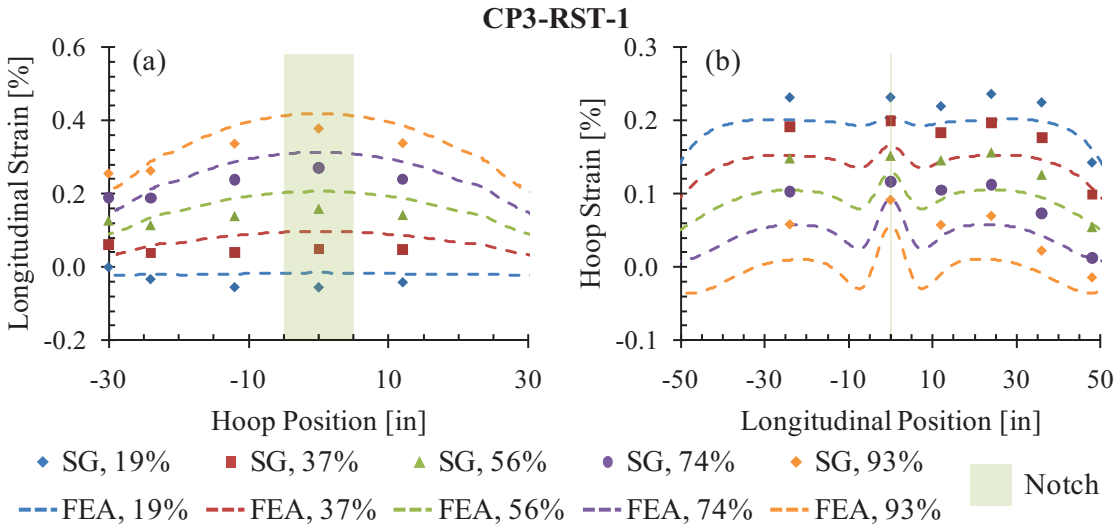

Figure 8.11. Strain distributions on the exterior surface of panel CP3 during the residual strength test as measured via strain gages and as calculated through FEA. The percentages in the legend are with respect to the maximum applied loads listed in Table 4.5.

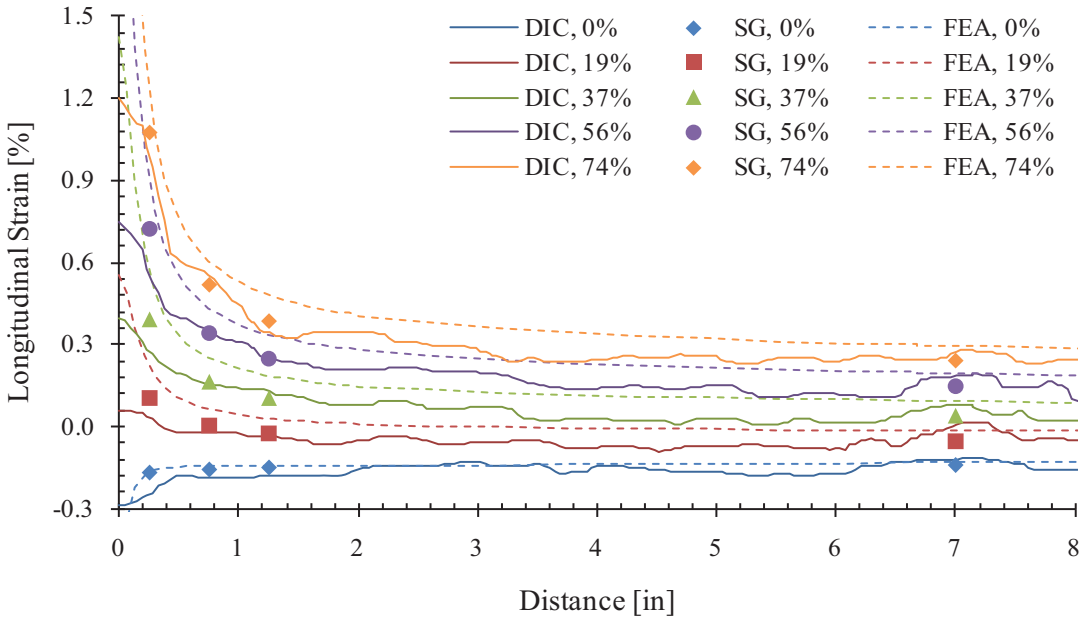

Figure 8.12. Comparison of notch tip strains as measured via the DIC system, the set of strain gages oriented perpendicular to the notch, and the FEA results in panel CP3, run CP3-RST-1.

very well. Within the 0.3-inch radial area around the notch tip, the FE results correlated very well with the strain gage data during the latter load steps as the high strains masked the observed fixed offset. The lower DIC data in this region was due to the applied filtering scheme and should not be used for assessing the accuracy of the models.

Similarly positive results were achieved with the remaining notched panels. The longitudinal strain contour plots of panel CP4 revealed that the maximum longitudinal strains were again located along the crown of the panel at the interface of the test section and inner transition composite lay-up regions, Figure 8.13a. The nearly parabolic distribution of longitudinal strains with hoop position was again apparent, while the distribution of hoop strains with longitudinal position was relatively constant except for the influence of the elevated notch tip strain fields. The global FE far-field longitudinal strain results overestimated the strain gage results by an average of 10% throughout loading, though the overall distribution throughout the test section was in good agreement, Figure 8.14a. The global FE hoop strains were similarly

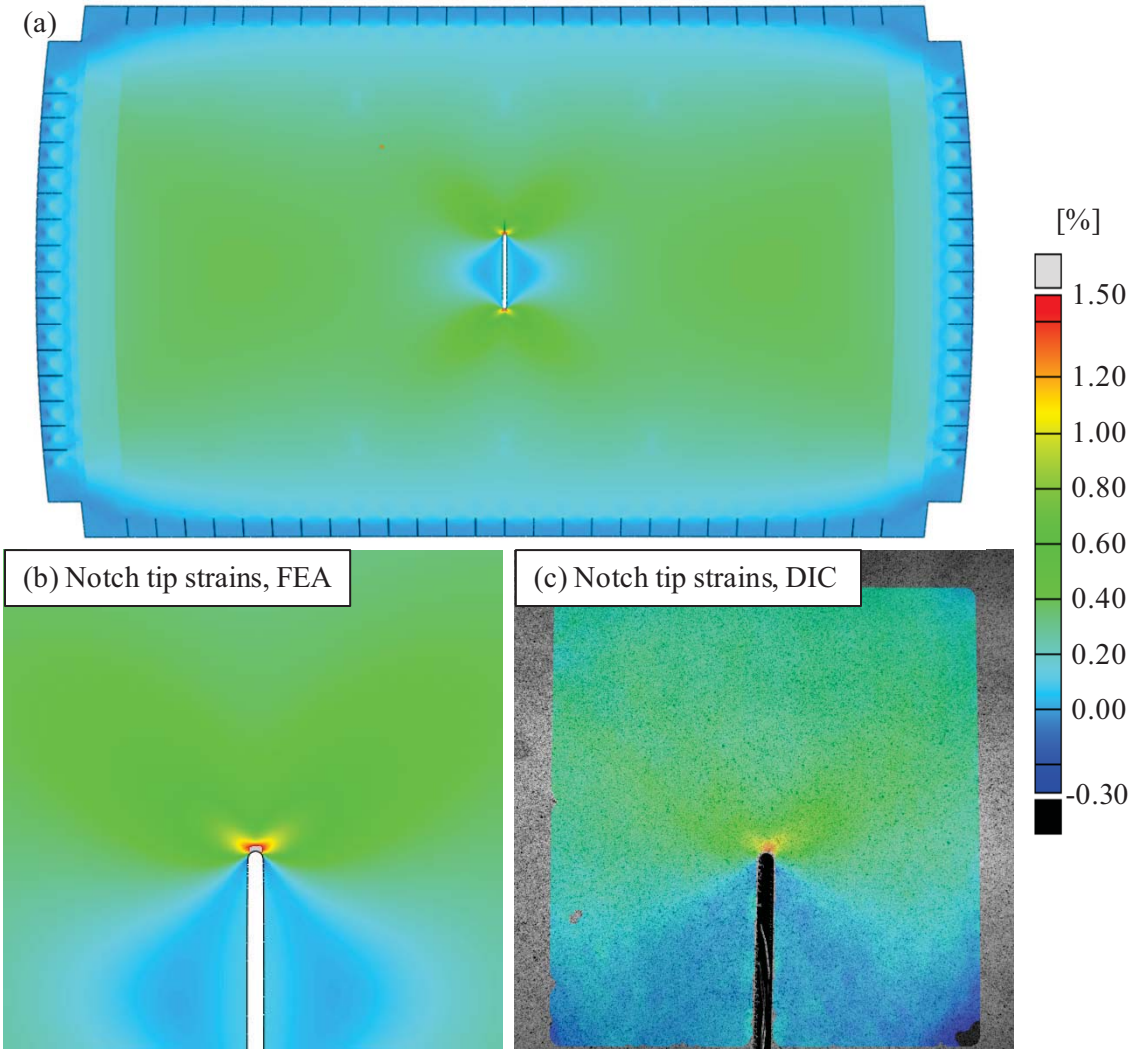

Figure 8.13. Longitudinal strain contours at 67% of the maximum applied load for panel CP4 for (a) the whole panel as calculated via global FEA, (b) the notch tip region as calculated via global FEA, and (c) the notch tip region as measured via DIC.

overestimated, though the effect of the circumferential notch on the far-field hoop strain distribution evident in the strain gage data was well characterized by the model as well, Figure 8.14b.

The predicted notch tip longitudinal strain field (Figure 8.13b) correlated very well with the state-of-strain measured ahead of the notch tip via DIC, Figure 8.13c. While the global FE model predicted strains greater than 1.5% immediately ahead of the notch tip at 67% of the

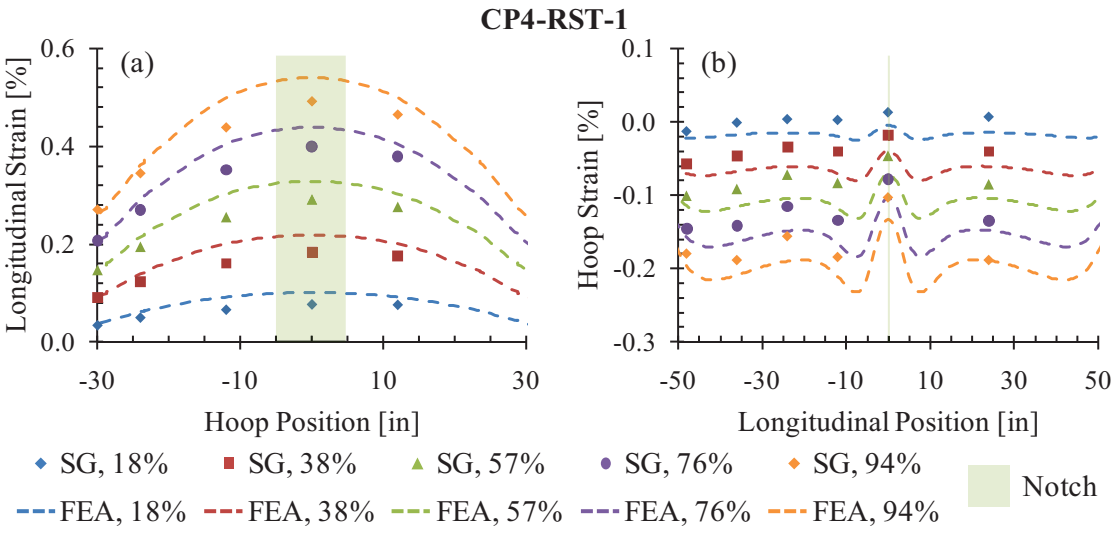

Figure 8.14. Strain distributions on the exterior surface of panel CP4 during the residual strength test as measured via strain gages and as calculated through FEA. The percentages in the legend are with respect to the maximum applied loads listed in Table 4.6.

maximum applied load, both the experimental and computational results show similar contours at strains of approximately 1.1% and 0.7% at this load level, outside the region in which the DIC data is artificially reduced. The longitudinal strains predicted along the axis of the notch agreed very well with the strain gages in the immediate vicinity of the notch tip and with both the strain gage and DIC data at greater distances, Figure 8.15.

The global FE hoop strain contour plot corresponding to 80% of the panel CP5 fracture load exhibited traits similar to those observed in panels CP3 and CP4. The high applied internal pressurization and hoop loads caused defined decreases in the exterior surface hoop strains at the interfaces of the test section, transition regions, and load application region near the hoop loaders, Figure 8.16a; smoother transitions were observed between the composite lay-ups near the longitudinal loaders. The predicted radial link loads were generally lower than the previous panels, reaching approximately 330 lbf at the panel corners and ranging from 80 to 120 lbf amongst the central links. This result correlated well with the near-zero radial link loads measured throughout the residual strength test of panel CP5. Based on the slight influence of the

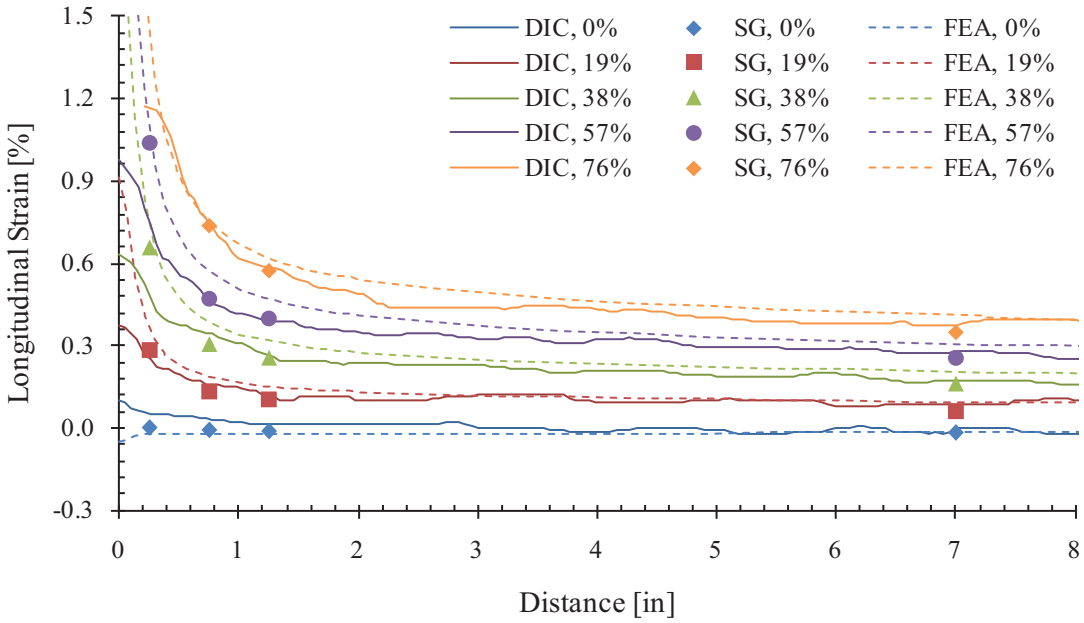

Figure 8.15. Comparison of notch tip strains as measured via the DIC system, the set of strain gages oriented perpendicular to the notch, and the FEA results in panel CP4, run CP4-RST-1.

presence of the radial link loads on the results of panel CP3, the occurrence of the link loads in the panel CP5 global model can be assumed to have negligible influence on the overall global panel deformation.

The increased proximity of the panel CP5 notch to the line along which the distribution of longitudinal strain with hoop position is assessed (Figure 3.20) had a measureable effect on the predicted strain distribution, as was earlier observed via the strain gage measurements in Chapter 4, Figure 8.17a. The longitudinal strains decreased sharply immediately ahead of the notch, with local maxima in the strain distribution occurring at ±8 inches from the crown of the panel. The shifted position of the notch also had a notable effect on the distribution of hoop strain with longitudinal position, Figure 8.17b. The global FE model results indicated an approximate 15% decrease in the hoop strains next to the longitudinal notch, with bordering local maxima resultant of the elevated notch tip strain fields. The hoop strain gage ahead of the right notch tip output strain readings approximately 20% higher than the predicted values, while the remaining hoop

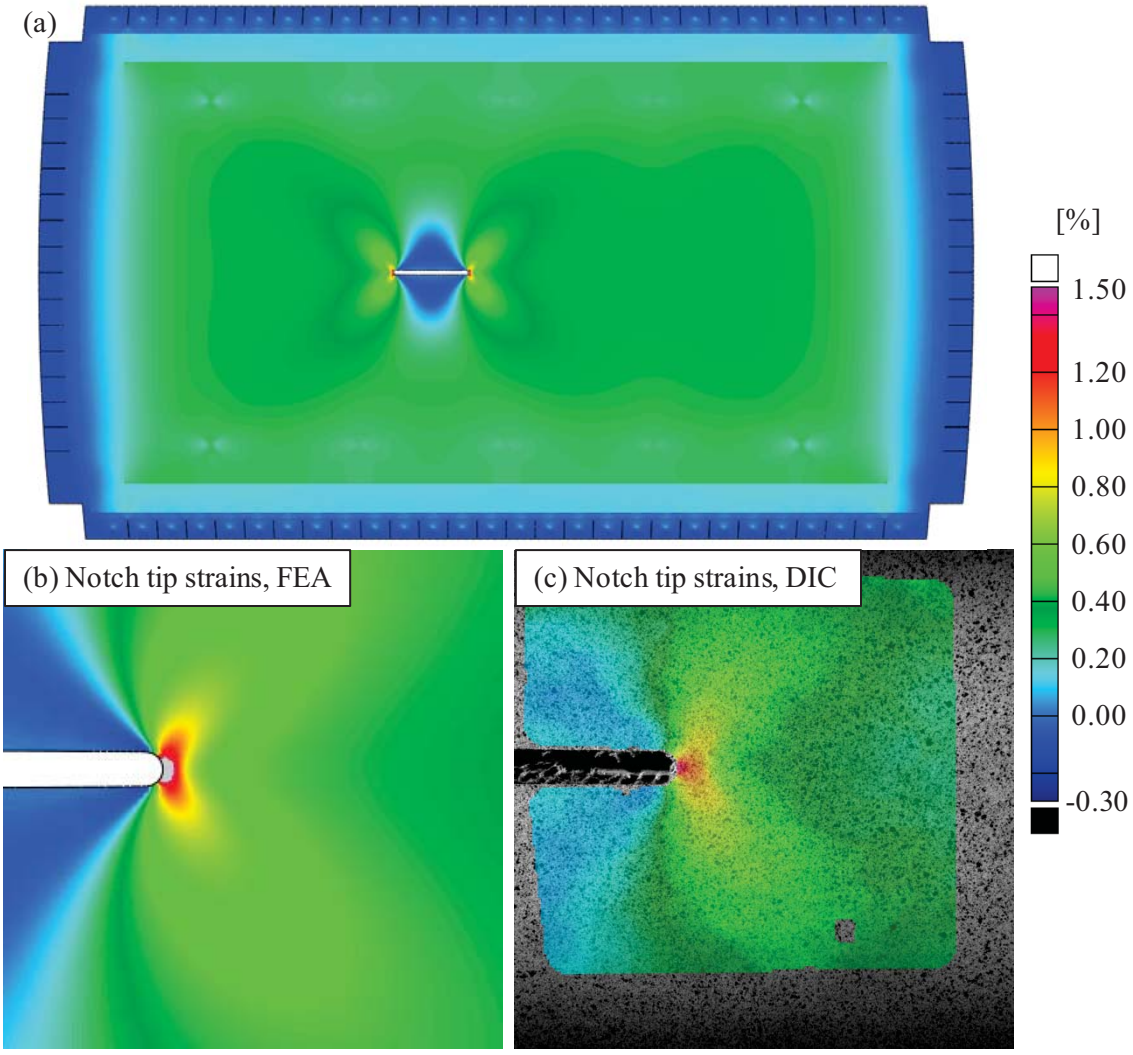

Figure 8.16. Hoop strain contours at 80% of the panel CP5 fracture load for (a) the whole panel as calculated via global FEA, (b) the notch tip region as calculated via global FEA, and (c) the notch tip region as measured via DIC.

strain gage readings were within 5% of the predicted values throughout the loading range. It should be noted that this strain gage (SG19, Figure 3.20) was installed in the region of the large elliptical skin-to-core disbond discussed through Chapter 5, which may be responsible for the otherwise unexpectedly high strain readings.

The predicted notch tip hoop strain field (Figure 8.16b) correlated very well with the state-of-strain measured ahead of the notch tip via DIC, Figure 8.16c. While the global FE model

predicted strains greater than 1.5% immediately ahead of the notch tip at 80% of the panel fracture load, both the experimental and computational results show similar contours at strains of approximately 0.8% and 0.5% at this load level, outside the region in which the DIC data is artificially reduced. The hoop strains predicted along the axis of the notch agreed very well with the strain gages in the immediate vicinity of the notch tip. The global FE results, however, overestimated the experimental data at greater distances at loads greater than 23% of the panel fracture load, Figure 8.17. As mentioned in Section 4.2.5, the hoop strain gages along the crown of the panel exhibited an unexpected nonlinearity with increased load between the second and fourth load steps. The corresponding downward shift in the measured hoop strains is equal to the static amount by which the global FE results seem to overestimate the notch tip strains; the equal spacing of the experimental and computational strain results further suggests that the actual strain response of the notch tip is well represented by the global FE model, Figure 8.18.

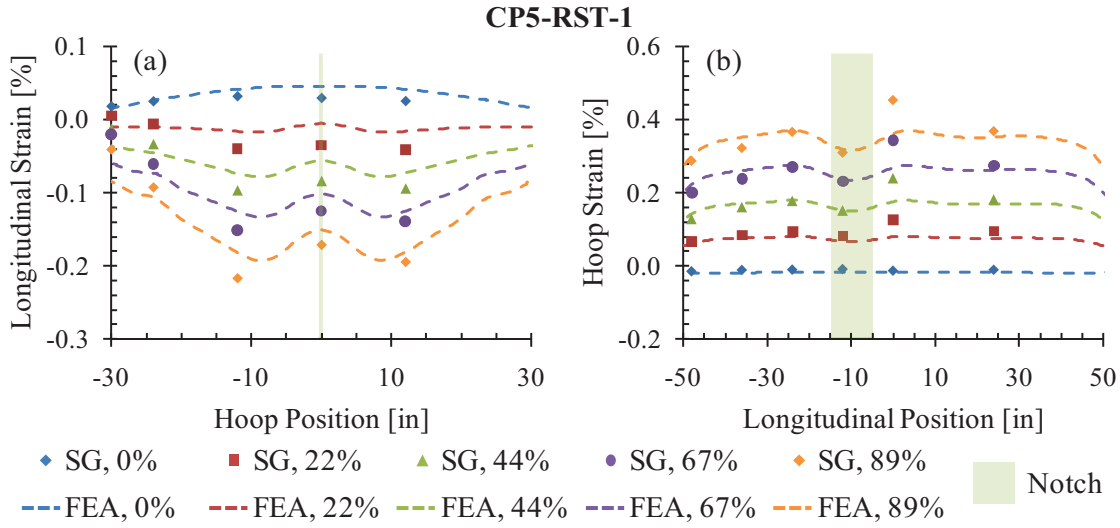

Figure 8.17. Strain distributions on the exterior surface of panel CP5 during the residual strength test as measured via strain gages and as calculated through FEA. The percentages in the legend are with respect to the maximum applied loads listed in Table 4.7.

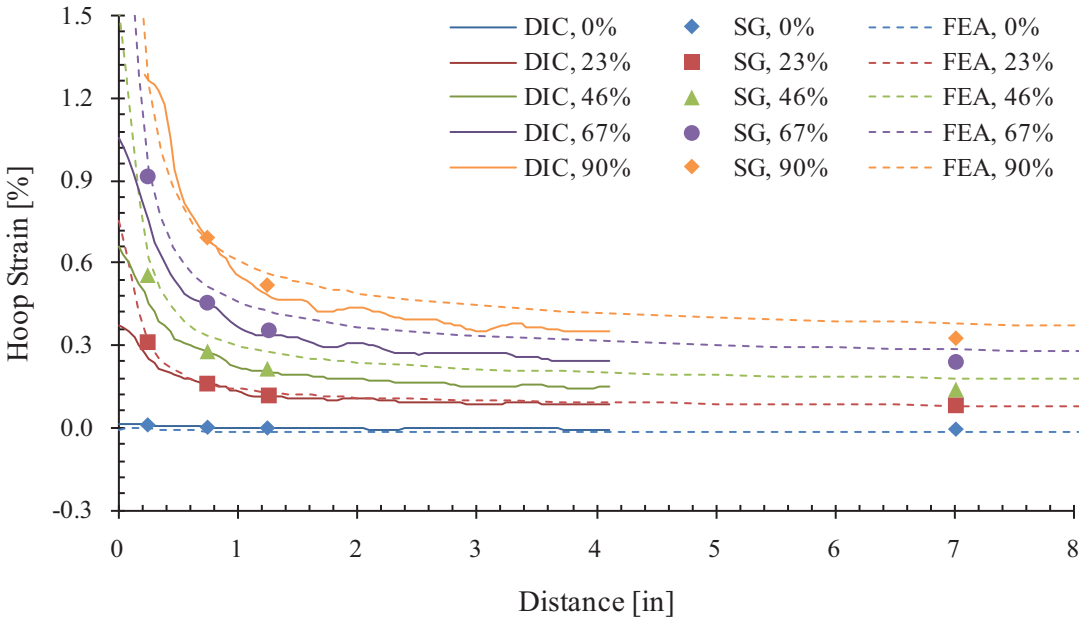

Figure 8.18. Comparison of notch tip strains as measured via the DIC system, the set of strain gages oriented perpendicular to the notch, and the FEA results in panel CP5, run CP5-RST-1.

The notch-normal strain contour plot of panel CP6 at 58% of the panel fracture load exhibits antisymmetry about the crown of the panel, though the elevated strain fields rooted at each notch tip are not symmetric about the notch axis due to the slightly imbalanced combined loading condition discussed in Section 4.2.6, Figure 8.19a. Further inspection of both the predicted (Figure 8.19b) and measured (Figure 8.19c) notch-normal strain fields reveals a slight bias toward the hoop tangent of the notch tip, as expected, given the more significant attraction of load to the hoop edges of the panels than to the longitudinal edges. While the measured strains immediately ahead of the notch tip are almost 33% lower than the notch-normal strains predicted using the global FE model, the contours at strains of 0.80% and 0.50% correlate very well between the experimental and computational data sets, indicating that the low notch tip strains are due to the applied filtering scheme. This is further confirmed by inspection of the notch-normal strains along the axis of the notch, which shows that in the immediate vicinity of the notch tip, good correlation is maintained between the strain gage and global FE data sets despite the low

DIC strain values, Figure 8.20. The global FE strain data tracks within 5% of the measured DIC strains along the axis of the notch beyond 0.50 inch of the notch tip.

The far-field distributions of longitudinal strain with hoop position and hoop strain with longitudinal position from the simulation of panel CP6 is a richer source for model-validating comparisons than the highly symmetric fields generated about the circumferential notches in panels CP3 and CP4. Excellent correlation was observed regarding the distribution of

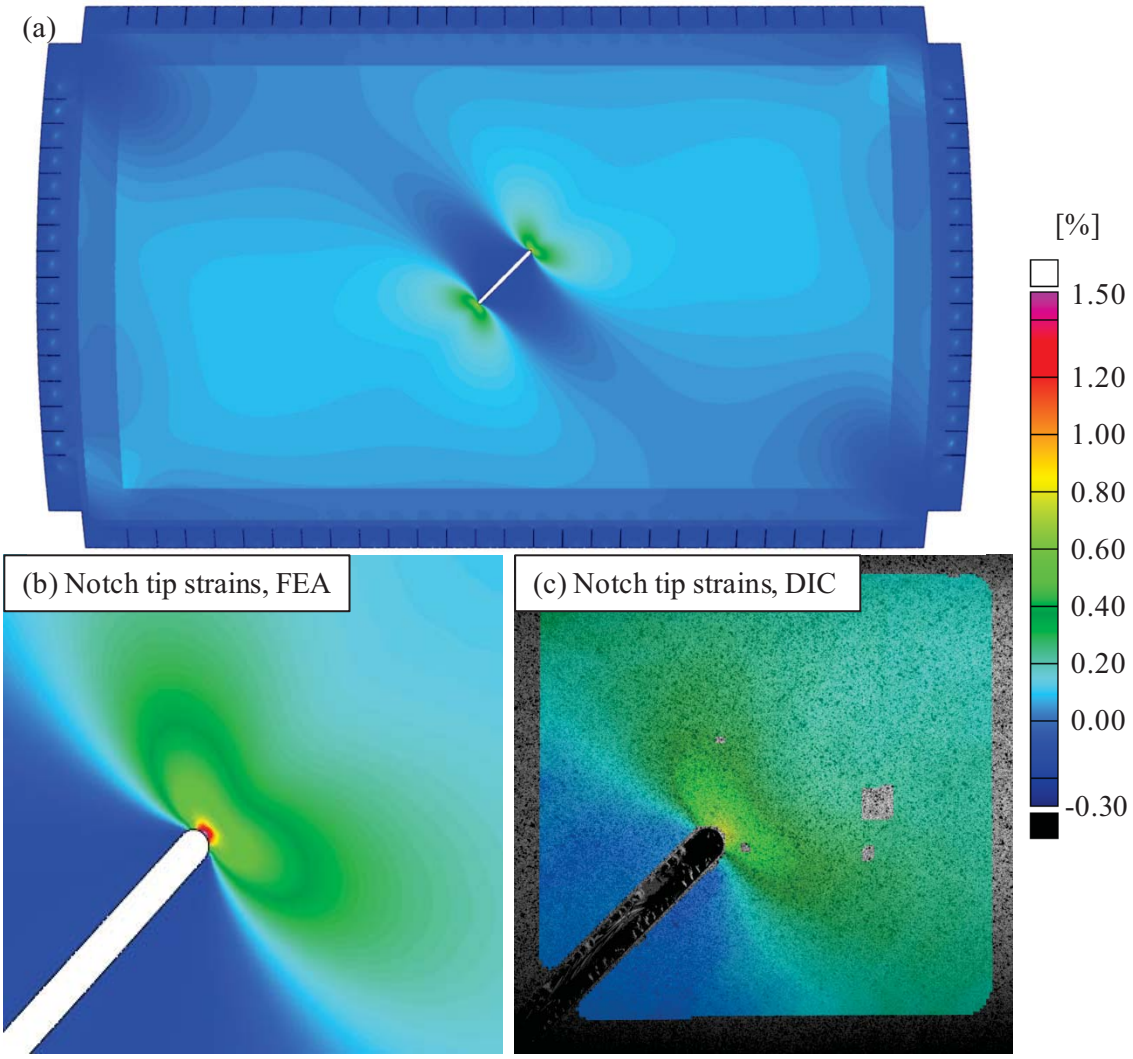

Figure 8.19. Notch-normal strain contours at 58% of the panel CP6 fracture load for (a) the whole panel as calculated via global FEA, (b) the notch tip region as calculated via global FEA, and (c) the notch tip region as measured via DIC.

longitudinal strain with hoop position, characterizing the bias of the field toward -4 inch hoop position due to the increased proximity to the notch tip, Figure 8.21a. Strain gage SG1, located at +12 hoop position and identified as outputting unexpectedly high strain values in Section 4.2.6, failed to correlate with the global FE solution, further suggesting the presence of either a localized material defect or faulty gage application. The distribution of hoop strain with longitudinal position was also well characterized by the global FE results throughout loading, Figure 8.21b. Strain gage SG15, located along the axis of the notch, deviated significantly from the global FE predications during the latter load steps due to the damage extensions from the original notch tip, as is suggested by the notch tip strain gage failures discussed in Chapter 4, and significant acoustic emission activity detected ahead of the notch tips at these load levels, discussed in Chapter 6.

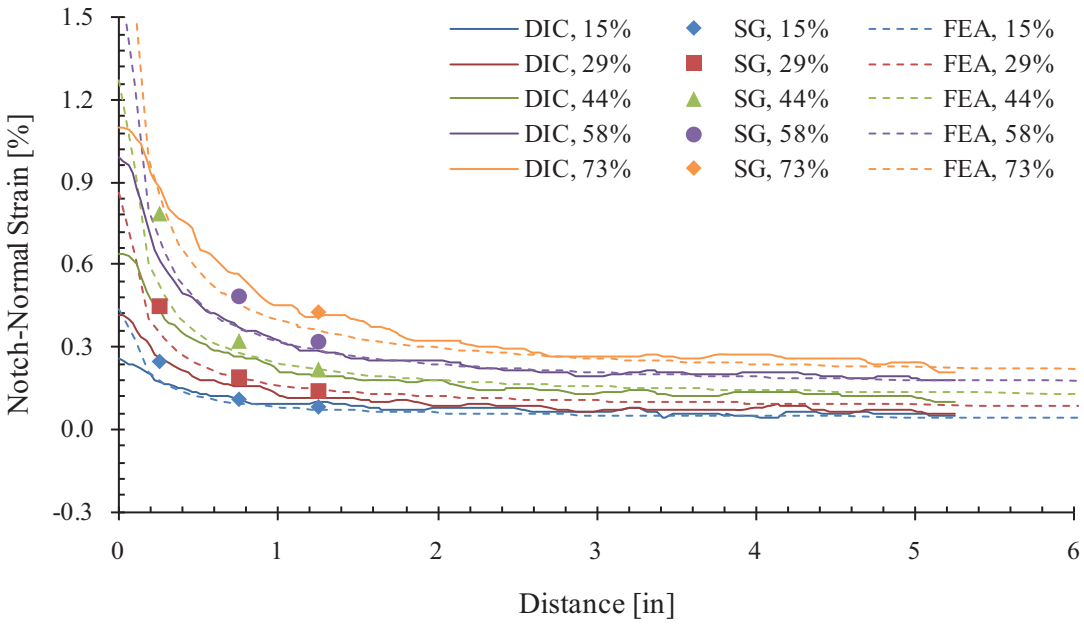

Figure 8.20. Comparison of notch tip strains as measured via the DIC system, the set of strain gages oriented perpendicular to the notch, and the FEA results in panel CP6, run CP6-RST-1.

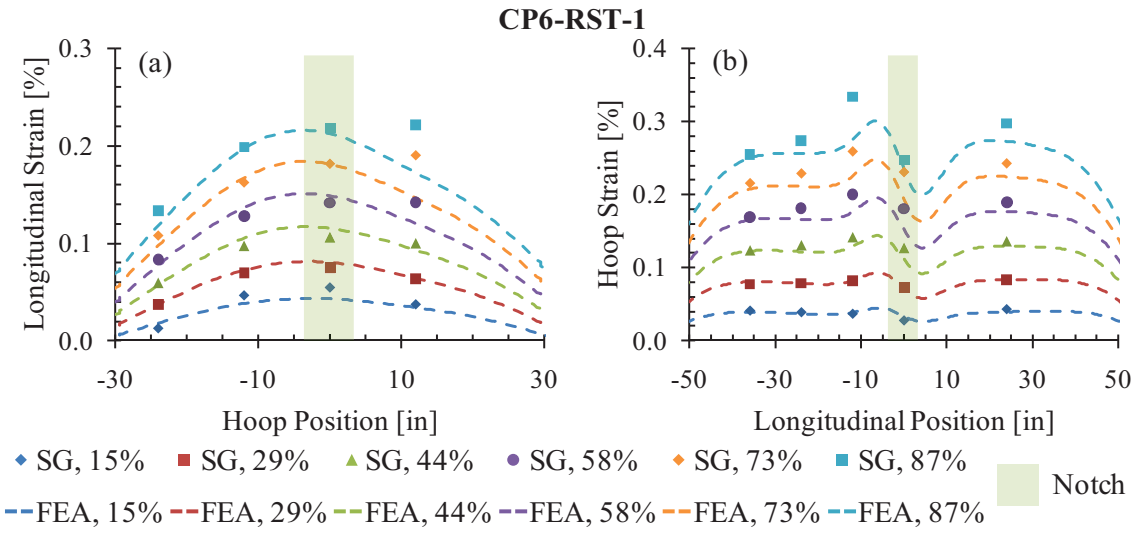

Figure 8.21. Strain distributions on the exterior surface of panel CP6 during the residual strength test as measured via strain gages and as calculated through FEA. The percentages in the legend are with respect to the maximum applied loads listed in Table 4.8.

In general, excellent correlation in terms of both the far-field and notch tip region strain responses to increasing load was obtained between the strain data recorded via the arrays of strain gages and the DIC method, and as predicted by the global FE model solutions for each of the notched panels tested in this investigation. In any cases in which the magnitudes of the two data sets disagreed, correlating trends have been identified amongst the overall distribution of strain and the changes in the states-of-strain with increased load. A thorough and accurate representation of the global deformation of full-scale sandwich composite fuselage panels due to the actual loading mechanisms of the FASTER testing fixture has been achieved, offering a reliable source from which to drive the boundary conditions of the progressive damage local FE models.

8.4. LOCAL MODEL DEVELOPMENT

Having established a set of global FE models capable of accurately representing the deformation and strains of the panels in both the far-field and notch tip regions, the development of the local FE models becomes a relatively simple task. As part of a global/local analysis, the majority of boundary conditions are defined through the results of the global FE models, and the geometry is essentially a 3-D extrusion of a section of the global models. Within this investigation, however, considerable efforts were made regarding the details and scalability of the failure model used to represent the initiation, progression, and eventual instability of damage in full-scale structures. Furthermore, while the boundary condition data was extracted from the global FE model solutions, the means through which it was processed and implemented were modified via custom user subroutines due to the particular deformation behavior observed in the vicinity of the notches. The details of the local FE model development and the contributions of this thesis to the application of progressive damage modeling concepts to full-scale aircraft fuselage structures is presented throughout the following sections.

8.4.1. DESCRIPTION OF THE LOCAL MODELS

Each local FE model contained a single semicircular notch tip ahead of which the state-of-damage was initiated and evolved. The dimensions of the local FE models for panels CP3, CP4 (Figure 8.22), and CP5 (Figure 8.23) were quite similar. For each panel, the mid-plane dimensions of the local model were 3.25 inches parallel to and 6.50 inches perpendicular to the notch axis. The notch tip situated in each model so as to allow two inches of damage progression before reaching the global/local model boundary. The local FE model of panel CP6 measured 6.00 inches in the longitudinal and hoop directions, with the notch oriented at 45° from one corner of the model; the location of the notch tip with respect to the local FE model boundaries is shown in Figure 8.24. The larger geometry of the panel CP6 local FE model was selected due to the extensive damage progression observed prior to the final panel fracture, Figure 4.43f. The

geometry of the local model boundaries and notches was defined with respect to a plane tangent to the crown of the panels, and the cuts were made perpendicular to this plane. Therefore, the length of the notches as measured along the concave panel surface was slightly longer than that as measured along the convex surface.

The thickness of the sandwich composite was modeled as three separate parts: two face sheets and the honeycomb core. Each face sheet was 0.0255 inch thick and was subdivided into three layers through the thickness, one per prepreg ply. The honeycomb core was 0.75 inch thick throughout the local models. Each ply of the face sheets was represented by a single layer of elements in the thickness direction, making the minimum characteristic length of the face sheets 0.0085 inch. With this mesh, each ply of the face sheets was discretely modeled and capable of developing internal damage independent of the adjoining plies. In order to maintain a low element aspect ratio, the global element size in the hoop and longitudinal directions was set to 0.034 inch throughout the face sheets in each of the local FE models. The face sheets and core were modeled as separate parts to be able to be independently meshed and tied together to simulate a perfectly bonded interface, avoiding an unnecessarily fine core mesh. The honeycomb core was meshed with elements roughly equal to the overexpanded honeycomb core cell size: approximately 0.11 inch in the hoop direction and 0.28 inch in the longitudinal direction. The honeycomb core was modeled with two layers of elements through the thickness to maintain a low element aspect ratio.

Element type C3D8R was used throughout each local FE model. C3D8R elements are 8-node 3-D linear brick stress elements, formulated with reduced integration and hourglass control. A total of 109,103 elements were used for the local models of panels CP3 and CP4, 109,042 for panel CP5, and 153,272 for panel CP6.

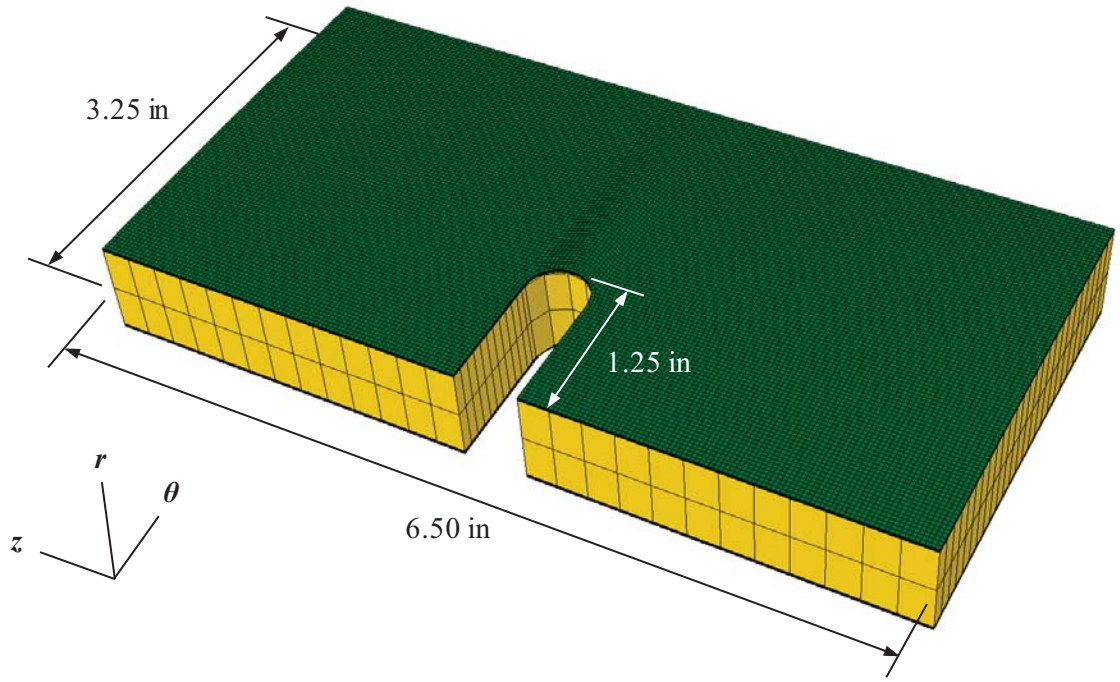

Figure 8.22. Local FE model geometry for panels CP3 and CP4, showing the location of the notch tip relative to the local model boundaries.

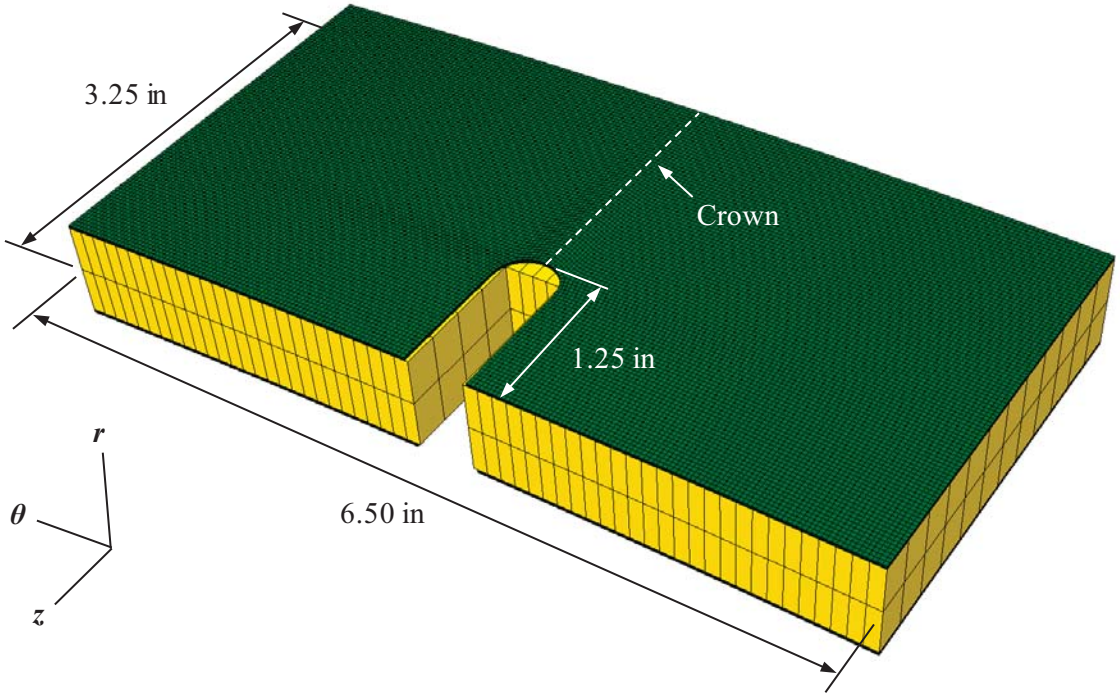

Figure 8.23. Local FE model geometry for panel CP5, showing the location of the notch tip relative to the local model boundaries.

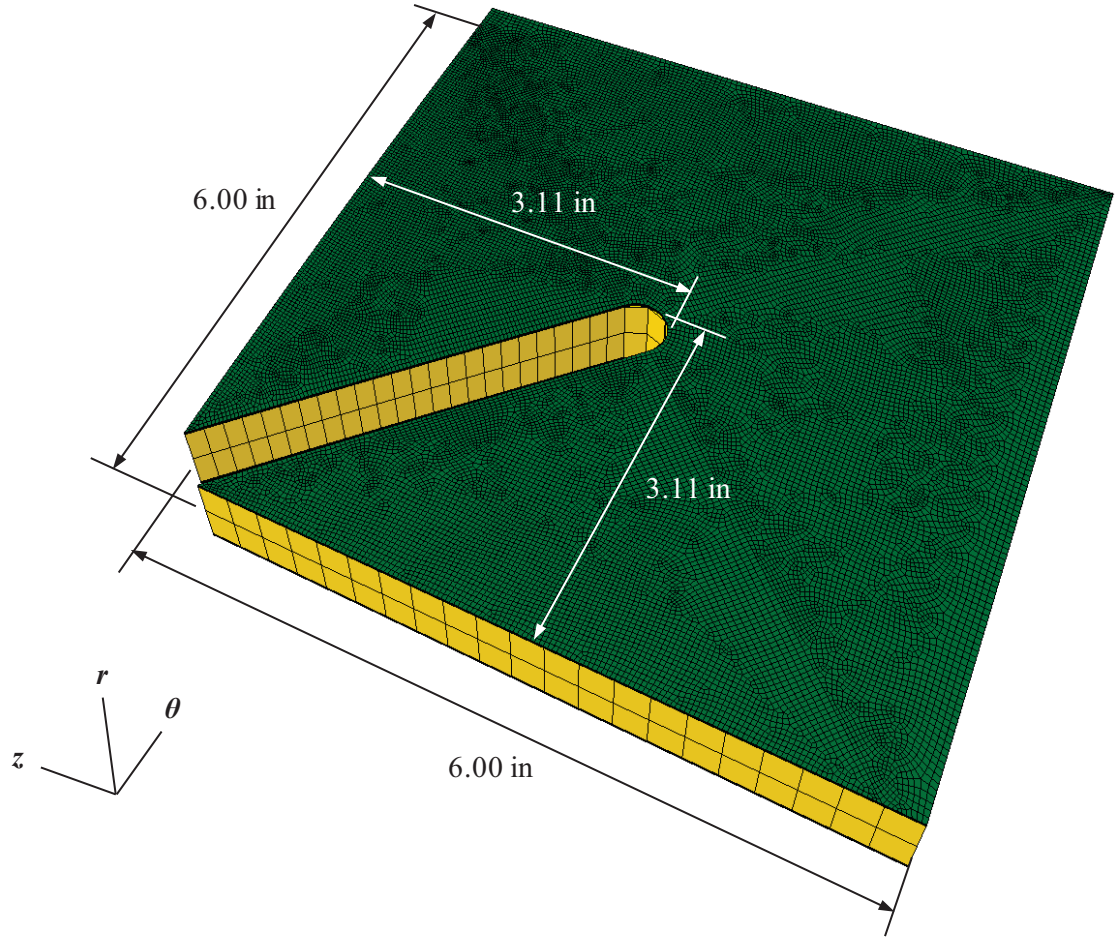

Figure 8.24. Local FE model geometry for panel CP6, showing the location of the notch tip relative to the local model boundaries.

8.4.2. FAILURE MODEL

As mentioned in Section 2.1, accurately predicting the initiation, progression, and eventual instability of damage in large composite structures is a formidable task. First, an appropriate failure criterion must be selected for the material, geometry, and loading configuration under investigation. Once the material is determined to have failed, the effect of the damage on the structural response of the material must be determined. Finally, a method for advancing the state-of-damage with increasing load must be formulated to allow the damage to progress in both size and severity. The failure model presented here for the face sheet material

addresses each of these tasks. No damage modeling of the honeycomb core was conducted as no significant damage to the core material was observed prior to the catastrophic fracture of panels CP1B, CP3, CP5, and CP6 (Section 5.5).

8.4.2a FAILURE CRITERIA

Of the several advanced sets of failure criteria discussed throughout Section 2.1.1, the refinements made in each were primarily focused on improving the ability to predict failure in loading cases involving a combination of compressive and shear loads, whose interactions have been observed to cause notable error in such predictions. Within the tensile-tensile combined loading regime, the failure envelopes associated with most failure criteria overlap [8.2]. In the present study, the loading functions of the residual strength tests of each panel involved only the application of in-plane tensile loads and internal pressure. Therefore, the effect of in-plane compressive loads was not taken into consideration.

Three of the most widely used failure criteria were integrated into the failure model to determine the occurrence of failure for each of the local FE models. They are the maximum strain criterion, the maximum stress criterion, and the Hashin [8.3] failure criterion, given respectively by the following equations:

$$\left|\frac{C_{11}\varepsilon_1}{F_1}\right| \geq 1 \tag{8.1}$$

$$\left|\frac{C_{11}\varepsilon_1 + C_{12}\varepsilon_2 + C_{13}\varepsilon_3}{F_1}\right| \geq 1 \tag{8.2}$$

$$\sqrt{\left(\frac{C_{11}\varepsilon_1 + C_{12}\varepsilon_2 + C_{13}\varepsilon_3}{F_1}\right)^2 + \left(\frac{C_{44}\varepsilon_4}{F_S}\right)^2 + \left(\frac{C_{55}\varepsilon_5}{F_S}\right)^2} \geq 1, \tag{8.3}$$

where C_{ij} is the material stiffness tensor, and ε_i and F_i are the strain and strength in the i^{th} material direction.

8.4.2b MATERIAL DEGRADATION MODEL

A material property degradation model consisting of three damage state variables was used to represent the state-of-damage in each element: d_1 and d_2 represent fiber damage in the local material 1- and 2-directions, and d_3 represents matrix damage in the thickness direction. Each damage state variable decreased any related components of stiffness in the orthotropic material compliance tensor H_{ij}, as demonstrated in Section 2.1.2. The components of the corresponding orthotropic material stiffness C_{ij} are shown below:

$$
\begin{aligned}
C_{11} &= E_1(1-d_1)[1-(1-d_2)(1-d_3)\nu_{32}\nu_{23}]D^{-1} \\
C_{12} &= E_1(1-d_1)(1-d_2)[\nu_{21}+(1-d_3)\nu_{23}\nu_{31}]D^{-1} \\
C_{13} &= E_1(1-d_1)(1-d_3)[\nu_{31}+(1-d_2)\nu_{21}\nu_{32}]D^{-1} \\
C_{22} &= E_2(1-d_2)[1-(1-d_1)(1-d_3)\nu_{31}\nu_{13}]D^{-1} \\
C_{23} &= E_2(1-d_2)(1-d_3)[\nu_{32}+(1-d_1)\nu_{12}\nu_{31}]D^{-1} \\
C_{33} &= E_3(1-d_3)[1-(1-d_2)(1-d_3)\nu_{21}\nu_{12}]D^{-1} \\
C_{44} &= G_{12}(1-d_1)(1-d_2) \\
C_{55} &= G_{13}(1-d_1)(1-d_3) \\
C_{66} &= G_{23}(1-d_2)(1-d_3),
\end{aligned}
\tag{8.4}
$$

where

$$
\begin{aligned}
D = 1 &- (1-d_1)(1-d_2)\nu_{21}\nu_{12} - (1-d_1)(1-d_3)\nu_{31}\nu_{13} \\
&- (1-d_2)(1-d_3)\nu_{32}\nu_{23} \\
&- 2\nu_{12}\nu_{23}\nu_{31}(1-d_1)(1-d_2)(1-d_3)
\end{aligned}
\tag{8.5}
$$

This formulation of the stiffness tensor is a 3-D expansion of that presented in equations (2.28) and (2.29). Each damage state variable can range from zero to one, where zero represents a fully intact element, and one represents an element whose stiffness has been fully degraded. The process of softening components of the stiffness tensor as such was performed by Matzenmiller [8.4], citing numerous experimental results to support the inherent necessary assumptions. Conversely, Maimí [8.5] derived a similar material compliance tensor from an assumed

complementary free energy density equation. For the stiffness tensor formulation used here, the failure of each shear stiffness term is assumed to coincide with the failure of its two corresponding normal directions rather than having an independent damage state variable [8.6].

8.4.2c DAMAGE EVOLUTION LAWS

Having proposed sets of failure criteria to determine the onset of damage and defined the effect of damage on the local material stiffness tensor, a means of assigning a value to the damage state variables must be defined. The evolution of the damage state variables with applied load is related to the amount by which the related failure criterion has been exceeded (i.e., a greater exceedance of a failure criterion results in a more severe state-of-damage). To avoid singularity-related numerical issues, it is important to avoid constructing a local stiffness matrix with any diagonal terms set equal to zero. Exponential relationships between exceeded failure criteria and damage state variables are a common method of gradually reducing stiffness terms to low, nonzero values (e.g., [8.4], [8.5] and [8.7]). As discussed in Section 2.1.3, several such damage evolution laws exist, though many require inputs of various parameters that are empirically determined without any physical bases. The damage evolution law proposed by Maimí [8.5], however, is unique in its sound thermodynamic derivation and usage of common and meaningful physical values:

$$d_i = 1 - \frac{1}{\varphi_i} \exp\left[\frac{2L_c F_i^2}{2E_i G_i - L_c F_i^2}(1 - \varphi_i)\right], \text{ when } \varphi_i \geq 1 \tag{8.6}$$

where φ_i is the exceeded failure criterion associated with the damage state variable d_i; L_c is the characteristic length of the element; and F_i, E_i, and G_i are the strength, Young's modulus, and fracture toughness in the i^{th} material direction. Inclusion of L_c diminishes the mesh size dependence of the solution, causing larger elements to fail more gradually and smaller elements to fail more abruptly. Prior to the onset of damage in an element, φ_i is equal to one. With each successive failure within that same element, φ_i must exceed a value greater than the highest

previously achieved to further change the state-of-damage. Additional damage will occur in the same element only after the new failure threshold is exceeded, and damage is irreversible. No direct interactions between the three damage state variables is modeled; only the indirect influence caused by the redistributions of stress and strain resultant of failure in one direction is present. This formulation of Maimí's damage evolution law was adopted and implemented for failures in each of the three material principal directions.

Throughout the various progressive damage models cited in Chapter 2, each relied on the failure envelope defined by the set of failure criteria adopted during its formulation as an input. While it is widely agreed that most failure criteria correlate in terms of anticipating the onset of failure under uniaxial loading conditions and in the tensile-tensile combined loading regime, investigation into the dependence of damage evolution laws on the selected failure criterion is absent in the literature. The results achieved with each of the three selected sets of failure criteria are compared in Section 8.5.4 in this context.

As mentioned, the coefficient of material parameters found in the exponent of the damage evolution law, equation (8.6), is derived based on the laws of thermodynamics. Further appreciation for its physical significance can be gained upon examining the denominator, which yields the following inequality when rearranged:

$$G_i \geq \frac{L_c F_i^2}{2E_i},$$

in which the right-hand side represents the strain energy within the element. This states that at the onset of damage, this strain energy must be less than or equal to the fracture energy, G_i. If the strain energy is equal to the fracture energy at the onset of damage, then the material would immediately fully fail (perfectly brittle). If G_i is selected to be lower than the strain energy at the onset of failure, then the material should have already failed before the failure criterion was ever satisfied, and the behavior no longer makes physical sense. Other damage evolution formulations which utilize non-physically meaningful values typically accept such unrealistic inputs.

For most laminated composite materials, the material properties needed (i.e., strength, Young's modulus, and fracture toughness) for the selected damage evolution law are all readily available. However, limited data is available on the fracture toughness of woven composites [8.8], of which the face sheets of the structures under investigation are composed. A parametric study on the fracture toughness was conducted using the local FE models of the panel CP5 notch tip and the maximum stress failure criteria. The range of fracture toughness values was from 100 to 500 lbf/in, and the resulting progressions of the extent-of-damage with increased load were compared with the experimental observations reported in Section 4.3.4. Based on this parametric study, a fracture toughness value of 275 lbf/in was obtained and used in all subsequent simulations. These results are reported and discussed further in Section 8.5.2.

8.4.2d VISCOUS REGULARIZATION

Frequently modifying the global stiffness matrix of a FE model, as is necessary with the constantly evolving state-of-damage expected with the proposed failure model, causes convergence issues to emerge, rooted in the resultant material and structural instabilities and their interactions. These convergence issues often lead to the maximum achievable load increments being several orders of magnitude below the target loads, making the representation of gradual failure processes over large load ranges unreasonable in terms of computational cost. A common solution to this dilemma is to incorporate viscous regularization into the calculation of the damage state variables (e.g., [8.5], [8.6], and [8.9]). This procedure artificially toughens the failing material and reduces the rapidity with which the stiffness of an element may change. The definition of an additional input is then required: the viscous regularization term, η. The result of this process is the regularized damage state variable, d_{v}, which is the weighted average of the calculated current damage state variable weighed by the load increment $\Delta \mathrm{t}$ and the regularized damage state variable from the previous increment weighed by η:

$$d_v|_{t_0+\Delta t} = \frac{\Delta t}{\eta + \Delta t} d|_{t_0+\Delta t} + \frac{\eta}{\eta + \Delta t} d_v|_{t_0} \tag{8.7}$$

To assess what effects varying η had on the number of iterations required to complete a simulation and the consistency of solutions, a parametric study using the local FE model of panel CP5 was conducted with five different values of η, varying from 0.0001 to 0.01. The local model was solved using a maximum strain failure criterion and represented fiber fractures as perfectly brittle, with the internal pressure and hoop loads being increased to the panel fracture load over a period of 0.90. As expected, prior to the initiation of damage, η had no effect on the solution. While damage was progressing from the notch tip, however, a marked difference was observed in the number of iterations required to complete the simulation, Figure 8.25a. This, in turn, indicates that the maximum achievable load increments decreased with increasingly severe states-of-damage. A roughly exponential relationship was observed between the total number of iterations required to complete the simulation and η, Figure 8.25b. Therefore, η should be set as high as possible while ensuring that its influence over the final state-of-damage is minimal.

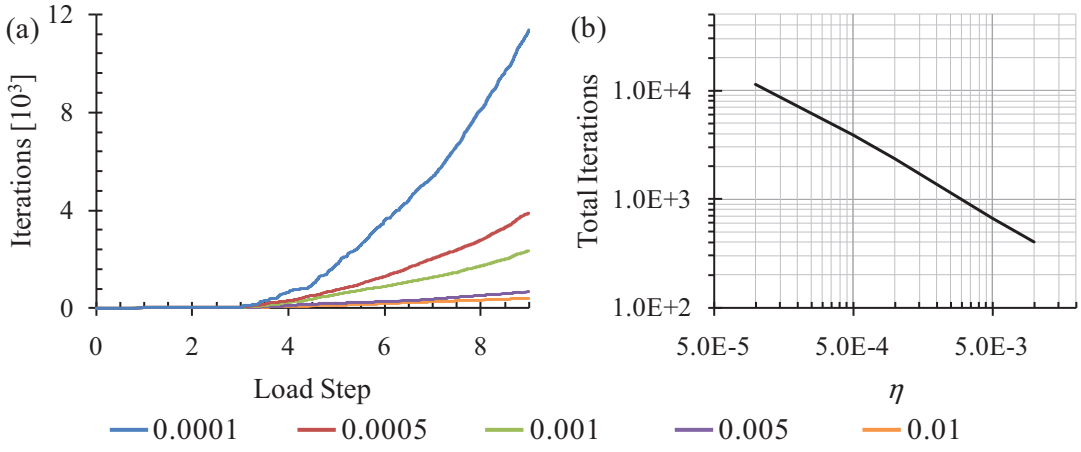

Figure 8.25. Effect of viscous regularization on the required iterations to solve the local FE model of panel CP5 using the maximum strain failure criteria and perfectly brittle fiber fracture behavior, showing (a) the iterations required with increasing hoop loads for various η values, and (b) the total iterations as a function of η.

The influence of η on the overall state-of-damage of a model can be roughly quantified by the amount of strain energy lost due to viscous regularization. The strain energy lost is defined as being the difference between the strain energies calculated based on the state-of-stress using the non-regularized damage state variables and that using the regularized damage state variables. Excessively large η values may cause an inordinate amount of energy to be lost, causing unacceptably large errors as damage propagates through the model. Figure 8.26 shows the energy lost due to viscous regularization using the same range of η values for the panel CP5 local FE model study. The influence of η on the cumulative energy lost (Figure 8.26) is less pronounced compared to the iterations required to complete the solution, Figure 8.25a. It was observed that the maximum load increments achieved by the solver approached the selected η value during the solution, after the initiation of damage. Consequently, the propagation of damage was arrested at similar rates while using a wide range of η values, diminishing the influence of η on the state-of-damage. As a compromise between accuracy and efficiency, η was set to 0.0005 for all local FE models.

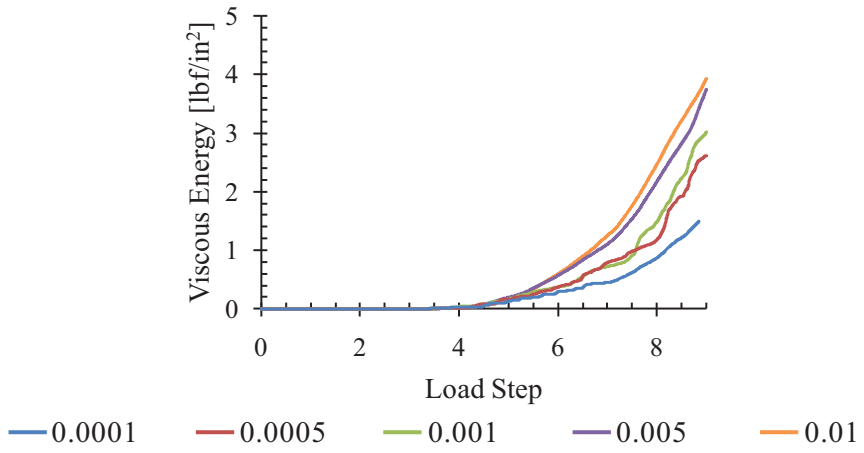

Figure 8.26. Energy lost due to viscous regularization with varying values for η for the local FE model of panel CP5 using the maximum strain failure criteria and perfectly brittle fiber fracture behavior.

A UMAT user subroutine was written based on the failure model described above and linked with the ABAQUS solver to represent the mechanical behavior of the face sheet prepreg material during the formation and progression of damage through the local FE models. The details of this subroutine are presented in Appendix B.

8.4.3. LOADING AND BOUNDARY CONDITIONS

The response of the local FE models was determined by two sets of input: internal pressurization and driven submodel boundary conditions. The entire interior surface of the local FE models was loaded with internal pressurization equivalent to that applied in the corresponding global FE model. Every node of the exposed internal cross section of the sandwich composite was driven by the results of the global FE models.

8.4.3a MODIFIED SUBMODELING DEFINITIONS

Submodeling boundary conditions can be applied via either surface-based or node-based techniques. Surface-based submodeling involves the interpolation of the stress components from the elements of selected global model surfaces onto the adjoining surfaces of the local model. This method provides an accurate transmission of the global model stresses to the local model surfaces. However, this method is only applicable for cases of solid-to-solid submodeling in ABAQUS. With shell-to-solid submodeling, such as that being adopted in this investigation, the nodal displacement and rotation results of global shell models are used to define the nodal displacements of the driven local model surfaces [8.9]. The displacements of the driven local model nodes in most FE codes are defined according to Kirchhoff plate theory:

$$u = u_0 - \frac{\partial w_0}{\partial x} z$$

$$v = v_0 - \frac{\partial w_0}{\partial y} z \tag{8.8}$$

$$w = w_0$$

where u, v, and w are the displacements applied to the local FE model nodes; and u_0, v_0 and w_0 are the interpolated mid-plane displacements from the global FE model. Here, the x-, y-, and z-directions refer to the longitudinal, hoop, and thickness directions, respectively.

When analyzing thick and/or composite shell structures subjected to internal pressurization, the effect of transverse shear strains, which are neglected in the shell-to-solid submodeling routines in ABAQUS, may become significant. In such cases, it is typically advised to avoid locating the global/local interface in regions of appreciable transverse shear strains. However, due to the presence of through-thickness damage and internal pressurization applied to the panels modeled in this investigation, the regions of interest ahead of the notch tips coincided with regions of significant transverse shear strains. Hence, it may be necessary to include the transverse shear strain in the determination of the nodal displacements of the driven local model surfaces

As mentioned, the S4R shell elements used in the global FE model adhere to Mindlin shell theory, assuming constant transverse shear strains through the thickness of the shell [8.1]. The nodal displacements along the driven boundaries of the local models were computed through:

$$u = u_0 + \left(\gamma_{xz} - \frac{\partial w_0}{\partial x}\right) z$$

$$v = v_0 + \left(\gamma_{yz} - \frac{\partial w_0}{\partial y}\right) z \tag{8.9}$$

$$w = w_0$$

where γ_{xz} and γ_{yz} are the transverse shear strains in the longitudinal-thickness and hoop-thickness planes, respectively, Figure 8.27.

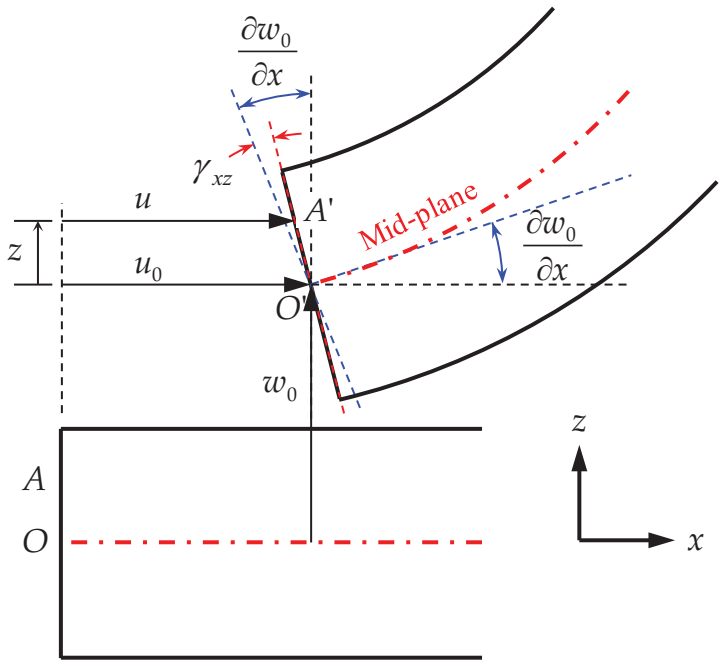

Figure 8.27. Effect of constant transverse shear strain on the displacement of points of the shell mid-plane.

To assess what influence the inclusion of transverse shear strains may have on the local model deformation, all transverse shear strains equal to at least 20% of the maximum corresponding component of nodal rotation along the global/local interface were plotted, Figure 8.28. For panels CP3 through CP5, significant transverse shear strains were observed in the plane perpendicular to the notch. For panel CP6, the significant transverse shear strains in both the longitudinal-thickness and hoop-thickness planes extended an additional 2–3 inches beyond the global/local interface. Due to the fine mesh necessary to independently represent the individual prepreg laminae, the element count for the local models would become undesirably high if the local model geometry was extended beyond these regions.

To increase the accuracy of the local FE models while maintaining computational efficiency, the transverse shear strain results from the global FE models were incorporated into the calculation of the driven local FE model boundary conditions. Along the mid-plane of the local FE model sandwich, the global nodal displacement results were interpolated onto the local

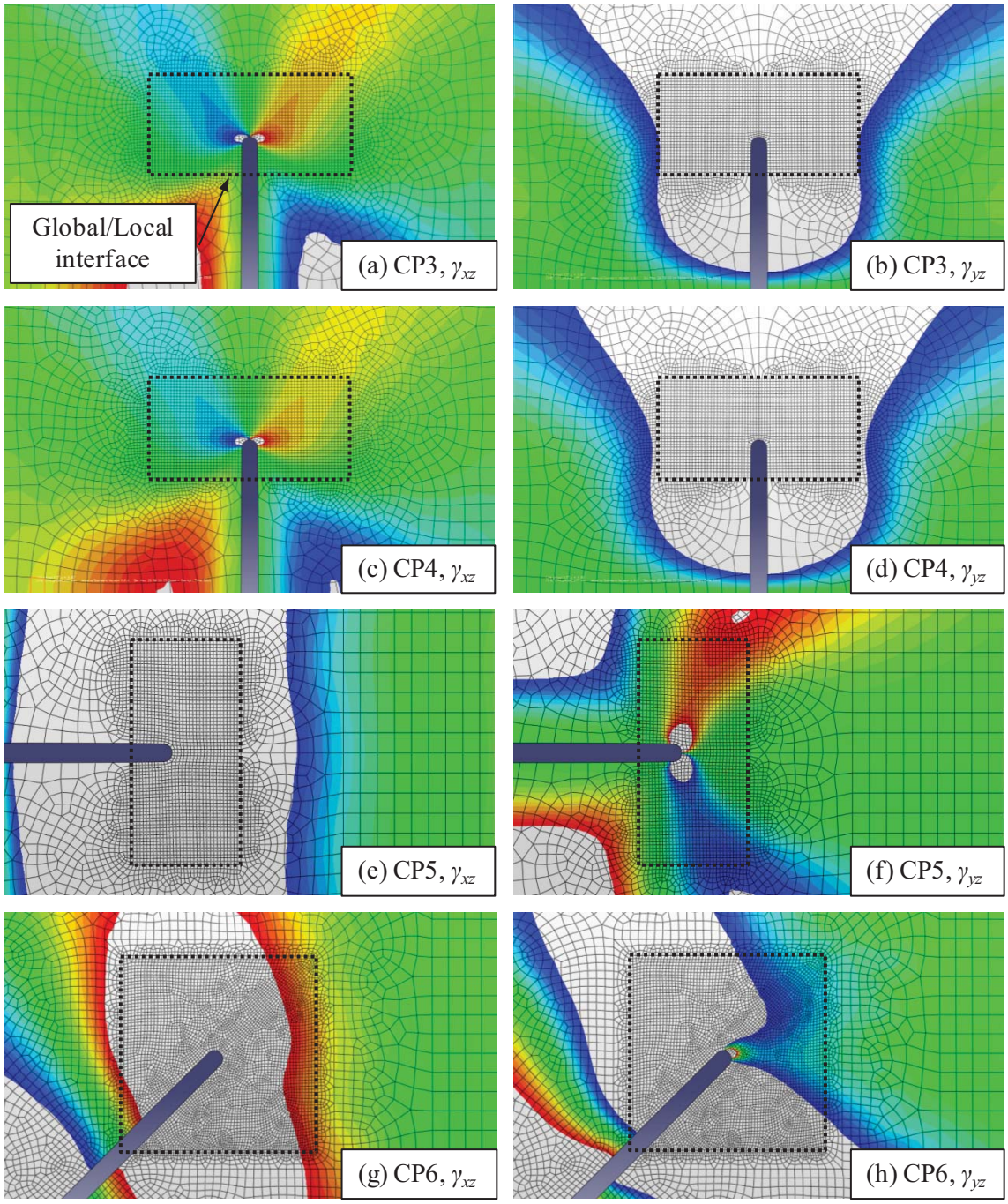

Figure 8.28. Comparison of transverse shear strain and nodal rotation results of the global FE models. The regions highlighted in white in the above transverse shear strain contour plots have magnitudes equal to at least 20% of the maximum corresponding nodal rotation along the global/local interface. The data are from the load step preceding the initiation of visual damage. The coordinate system referenced in the above plots has the *x*-, *y*-, and *z*-directions parallel to the longitudinal, hoop, and thickness directions, respectively.

mesh and directly used to drive the local boundary conditions. For any local nodes not located along the sandwich mid-plane, the nodal rotations and transverse shear strains were combined and scaled by the perpendicular distance away from the sandwich mid-plane to determine the 3-D displacement of the nodes with respect to the deformed mid-plane locations. A custom user subroutine has been developed for use with the ABAQUS solver to implement these modified submodeling boundary condition definitions.

8.4.3b ADAPTIVE BOUNDARY CONDITIONS

Central to the application of global/local submodeling is the concept that the interface between the two models is far-removed from regions of stress concentration or damage in the local model. Ideally, either the absence or detailed modeling of these regions in the global model would have a negligible effect the response of the whole structure, and the boundary conditions of the local model could be kept unchanged. This thinking is applicable where the regions of elevated stress are either stationary or confined to a small area throughout the analysis.

As was discussed in Section 4.3, however, visual damage in panels CP3 through CP5 was observed to extend up to 1.3 inches ahead of the original notch tips, as measured along the axis of the notches prior to the end of their residual strength tests. Therefore, as damage progresses and the notch length effectively extends through the local models, the error involved in using the original undamaged global solution to drive the local boundary conditions increases to undesirable levels.

In order to ensure proper driving of the local FE model boundaries with increasingly severe states-of-damage, the global mesh must be updated to roughly represent the notch tip damage extensions. Neglecting to adapt the global model solution to the changing state of the notch tip damage underestimates the notch tip opening displacement and the driving forces behind further damage extensions. As a result, a linear progression of damage would be predicted with continued loading, inaccurately predicting the eventual instability of damage

propagation. Co-simulation (i.e., simultaneously solving the global and local FE models) is a common means of addressing this issue, wherein each extension of the damage in the local model would require the remeshing and resolving of the global model so as to coincidentally locate the damage front in both the global and local models. In this study, however, the small load increments necessary to solve FE models during which the stiffness matrix is frequently updated and the ensuing large number of incremental damage extensions requires an undesirably high frequency of global solution remeshing to properly and smoothly drive the local boundary conditions.

In this study, an adaptive boundary condition scheme was developed to decrease the required number of global solutions and simultaneously maintain a smooth driving force behind damage progression. This novel numerical scheme involves generating a library of global solutions prior to beginning the local model analysis. Depending on the state-of-damage within the local FE model solution at any given load increment, the library is queried for the most appropriate global FE model solution(s).

Within this library of global solutions, the location of the effective notch tip damage front is varied. Here, the effective notch tip damage front corresponds with the locus of the elevated kidney-shaped strain field. A criterion must be established in terms of the local FE model results to define this location. The damage state variables corresponding with fiber fracture act as a good indicator of material's inability to carry significant loads. Based upon the inspection of earlier local FE model solutions, the locus of the elevated strain field was located about the element farthest from the original notch tip whose stiffness was degraded by at least 85%, Figure 8.29. Therefore, fiber damage state variables of 0.85 were used to determine the location of the effective notch tip damage front in each of the local models. It should be noted that this degradation term is likely a function of both the material properties and the specific composite lay-up under investigation, and should be determined on a case-by-case basis.

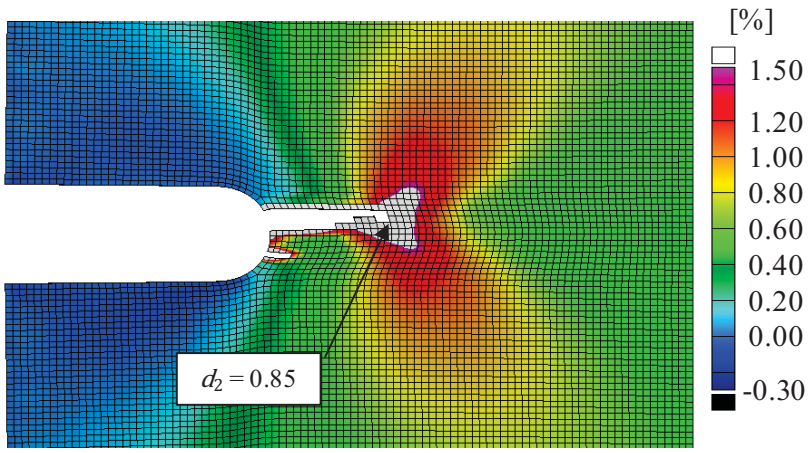

Figure 8.29. Locus of the notch tip strain field correlating with the farthest element whose fiber damage state variable was equal to at least 0.85. These results are from the local FE model of panel CP5 at 95% of the panel fracture load, showing the hoop strain field in the exterior face sheet mid-ply. Elements whose d_2 damage state variable exceeded 0.85 are removed from the figure.

While the local FE models are capable of representing a 3-D state-of-damage ahead of the original notch tips, it is assumed that the elevated strain field ahead of the notch is relatively constant through the thickness and that the global models require only the definition of a planar location for the effective notch tip. As a result, the library of global solutions would be queried for the nearest solution in terms of load increment and two spatial dimensions: the effective notch tip extension parallel to the notch and effective notch tip extension perpendicular to the notch. Each additional spatial dimension along which effective notch tip extensions must be considered greatly increases the required size of the global solution library (e.g., for ten intervals in each n spatial dimensions, 10^n global solutions must be solved). However, if knowledge of the damage propagation path exists a priori, the set of global solutions can be decreased to the number of desired intervals along the suspected path of damage propagation. For panels CP3 through CP5, the damage propagation path coincided with the original axis of the notch. Accordingly, the location of the effective notch tips were represented by separating the nodes along the notch axis in 0.1-inch increments up to 2 inches of damage extension (i.e., through the full geometry of the

local FE models). Examples of global FE models containing no additional damage extension and a one-inch damage extension are shown in Figure 8.30.

A disparity exists between the increments in which damage is represented in the global and local models. While it was chosen to represent damage in the global models in 0.1-inch increments, damage in the local models has a resolution equal to the global element size (i.e., 0.034 inch). Immediately transitioning from one global model damage increment to the next would cause an abrupt change in the driving force behind further damage propagation in the local model. Furthermore, the load increments at which the displacements and transverse shear strains of the global model solutions were reported (i.e., 0.02) are much larger than the small load increments achieved after the initiation of damage in the local models (e.g., 0.0005). To ensure smooth transitioning of the local model boundary conditions (and the driving force behind further damage propagation), the displacement and transverse shear strain results are linearly interpolated between the bounding global model load and damage increments (Section B.3). These multidimensional interpolations create intermediate global solutions used to drive the local model boundary conditions. This procedure ensured a proper and smooth driving of the driving force behind damage propagation so that the eventual instability of the notch tip damage could be represented, while avoiding remeshing and resolving an excessive number of global models.

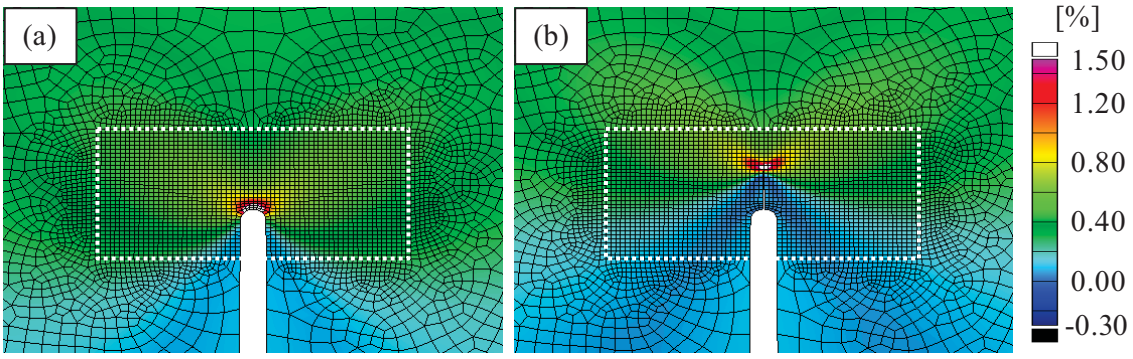

Figure 8.30. Effect of self-similar damage progression on the notch tip notch-normal strain field for panel CP3 at 74% of the panel fracture load for (a) no damage and (b) a one-inch damage extension.

Two additional custom user subroutines were developed to implement the adaptive global boundary solutions and the modified submodeling boundary condition definitions. Several additional input files are required to populate the global solution library and associate the nodes of the global and local models. The ABAQUS user subroutine DISP is used to define the local model boundary conditions while the additional input files and the global solution library interpolations are performed within the UEXTERNALDB subroutine. Each of the subroutines is presented in Appendix B.

8.5. LOCAL MODEL RESULTS

The proposed contributions to the development of local FE models capable of representing the initiation, progression, and eventual instability of damage through full-scale sandwich composite aircraft fuselage structures each merit careful consideration and examination with respect to their ability to improve the accuracy of the attained solutions. The accuracy of the modified submodel boundary condition definition is assessed by comparing the in-plane strains of the global and local models along the global/local interface in Section 8.5.1. Comparisons between the proposed submodel boundary condition formulation and the default ABAQUS formulation is presented and discussed, as well. As discussed in Section 8.4.2, the face sheet material fiber fracture toughness was an unknown input for the damage evolution laws implemented in the failure model. The details of the mentioned computational study conducted to determine an appropriate approximation the fiber fracture toughness is presented in Section 8.5.2. The notch-normal strain fields predicted ahead of the notch tip damage in the local FE models of each of the four notched panels are compared with the strain fields measured via DIC in Section 8.5.3, with the a detailed illustration of the notch tip damage progression presented in Section 8.5.4. A discussion on the effect of the selected failure criterion on the rate of damage progression is presented as well.

8.5.1. GLOBAL/LOCAL BOUNDARY CONDITIONS

An example of the strain fields predicted by the local FE models for panel CP5 is presented in Figure 8.31a. The presented strain field is of the strain in the local material 1-direction for each ply (i.e., +45° inclined above the axis of the longitudinal notch for the exterior-most ply) at 72% of the panel fracture load. No significant damage developed at the notch tip at this load level, allowing it to serve as a good basis for the discussion of any general features of the local FE model strain fields.

One apparent feature of the local model results is the waviness of the elevated, kidney-shaped strain field centered about the notch tip when compared to the smooth contours observed in the global FE model results (Section 8.3). These oscillations are most apparent along the local model edges. Along the edges of the local models, the displacements were defined by first interpolating the global model displacements and transverse shear strains, and then calculating the corresponding displacement of each local FE model node according to its perpendicular distance from the sandwich mid-plane. While the displacement contours along the local model edges were relatively smooth, discontinuities in the slope of the displacement field due to the linear interpolations along the model edges caused a more pronounced effect on the strain fields. This is similar to the increased sensitivity of the DIC strain fields to noise compared to the displacement fields (Section 4.3.1).

Differences in the modeled stiffness of the honeycomb core, as determined by the global and local models, further contributed to the observed strain contour waviness. While most apparent along the local model edges, the oscillations in the strain field remain appreciable throughout the local models. The period of the oscillations in the hoop and longitudinal directions coincides with the dimensions of the honeycomb core mesh geometry, Figure 8.31b. This behavior correlates well with the expected physical material deformation: the face sheet material is unsupported in the thickness direction within each honeycomb core cell, and may bend

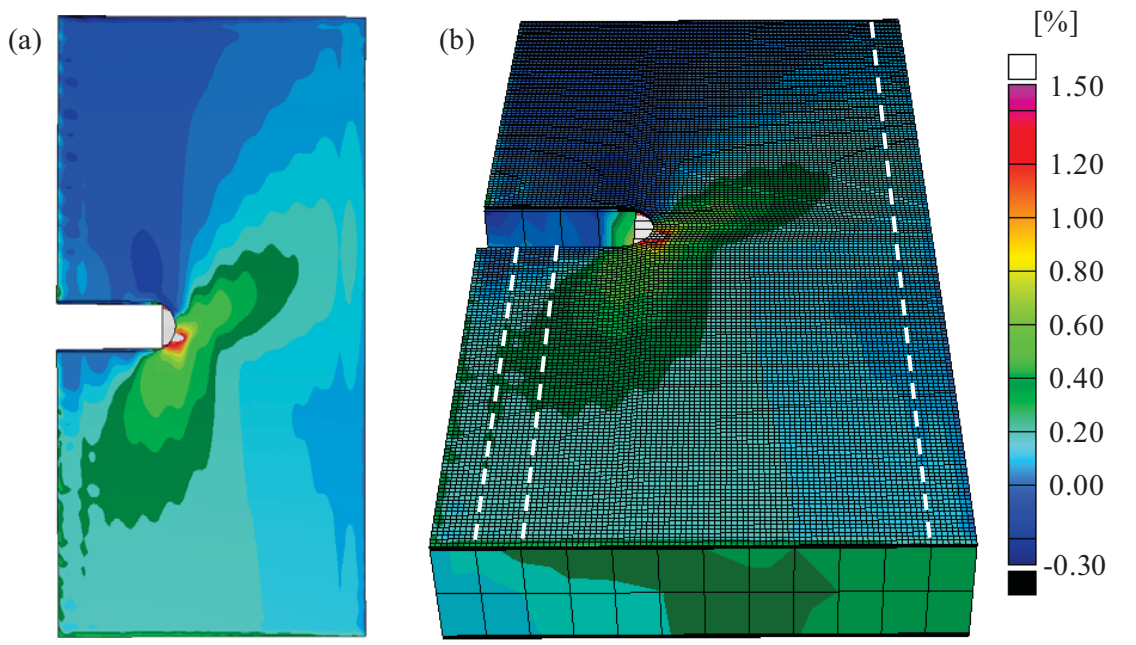

Figure 8.31. (a) Panel CP5 local FE model showing the strain in the local material 1-direction (i.e., +45° inclined above the axis of the longitudinal notch), and (b) the effect of the honeycomb core mesh geometry on the distribution of strains throughout the face sheets.

accordingly. The global models were unable to exhibit this behavior due to the uniform treatment of the transverse stiffness properties within each shell element.

An additional contributor to the observed differences between the global and local model notch tip strain fields involved the different representable strain fields of the 2-D shell elements of the global models and the 3-D solid elements of the local models. As mentioned, the global mode shell elements adhere to Mindlin shell theory, allowing for constant through-thickness transverse shear strains to develop. However, while this formulation is an improvement over that based on the Kirchhoff shell theory, where the transverse shear strains are neglected, it does not agree with either the true physical response of the sandwich composite or the transverse strain fields occurring in the 3-D local models. The several elements with different material properties used to represent the thickness of the sandwich composites in the local models allow for a more accurate representation of the transverse strain fields. While the constant transverse shear strain

values determined by the shell elements may represent well the average distribution of strain energy toward distortion of the material, such differences in the contours of the strain fields are expected to cause error in the immediate vicinity of the boundaries the 3-D local model and the 2-D global model results.

In order to assess the accuracy of the boundary conditions applied to the local FE models, the strains along the edges of the global and local models were compared. Specifically, the strains perpendicular to the hoop and longitudinal edges of the global/local interface were compared. While the displacements along the global/local interface of the two models were known to be equal, the strains resulting from the applied displacements could differ due to the differences regarding the effective stiffnesses and the representable strain fields. The strains oriented perpendicular to these edges were used because the strains parallel to the edges were fully defined by the applied displacements and offered no further information. The data from the four notched panels are presented in Figure 8.32 through Figure 8.35; the edges along which the comparisons were made in each model are shown in the accompanying schematics. Also presented for each of the notched panels are strain contour plots from the local FE model superimposed onto the results of the corresponding global FE model, qualitatively showing the continuity achieved between the two models.

Panels CP3 (Figure 8.32) and CP4 (Figure 8.33) exhibited similarly good agreement between the global and local model results. Both the panel CP3 and CP4 local model results presented here were generated using the modified submodel boundary condition formulation, the adaptive boundary conditions, and the presented failure model using the maximum stress failure criterion. The comparisons made here were between only the initial undamaged global models and the local model results up to the point of predicted damage initiation. While the discussed oscillations along the model edges were apparent in each case (particularly along edge ‘B’ indicated in the figures), the average strains along these edges correlated very well with the global model results throughout loading. The oscillations of the local model strains were generally

regular, having a constant wavelength and exhibiting gradual changes in amplitude. While some of the strains along the global/local interface oscillated by more than 50%, the magnitudes of the oscillations decreased greatly within one to two honeycomb core elements from the local model edges (i.e., Saint-Venant's principle), having a less pronounced influence over the notch tip strains. The oscillations maintained approximately constant amplitude throughout loading for panel CP3, and linearly increased with increased longitudinal load for panel CP4.

The local model of panel CP5 was solved using the same subroutines as panels CP3 and CP4 (i.e., modified submodel boundary condition formulation, adaptive boundary conditions, and the failure model using the maximum stress failure criterion), though oscillations along the global/local interface lacked the uniform nature of the earlier panels, Figure 8.34. Similar to the local model results of panel CP4, the amplitudes of the hoop strain oscillations along edge 'A' and the longitudinal strain oscillations along edge 'B' linearly increased with increased internal pressure and hoop load. Regardless, the average strains along the edges of the local FE model again tracked very well with the corresponding global model strain results.

As discussed in Section 8.4.3, the adaptive boundary conditions required an exponentially larger library of global solutions for each additional dimension which must be considered to represent the location of notch tip damage with respect to the original notch tip. The meandering path of damage progression observed in panel CP6 (Figure 4.43g) required both notch-normal and notch-axial distances to define the effective notch tip. Due to the large size of the required global model library, the local FE model of panel CP6 was solved using the default ABAQUS submodeling algorithm. This generated a local model data set with which to characterize what effects the modified submodeling routines had on the accuracy of the local model boundary condition definitions.

Throughout loading, the default ABAQUS submodeling algorithm applied to the local FE model of panel CP6 caused for the hoop strains to be consistently overestimated and for the longitudinal strains to be consistently underestimated. At 36% of the panel fracture load, the

peak hoop strain along edge ‘B’ was overestimated in the local model by almost 30%; the peak longitudinal strain along edge ‘A’ in the local model was approximately 20% less than that observed in the global model at that same load level. Despite the amplitude difference observed between the global and local strains, the overall strain distributions were similar. Furthermore, the default ABAQUS algorithm produced less pronounced strain oscillations along the local model boundaries.

In order to provide a direct comparison of local model results generated using the default and modified submodeling routines, the local model of panel CP5 was again solved under identical conditions with the sole exception that the default submodeling algorithm was used. The results of each local model solution are presented side-by-side in Figure 8.36.

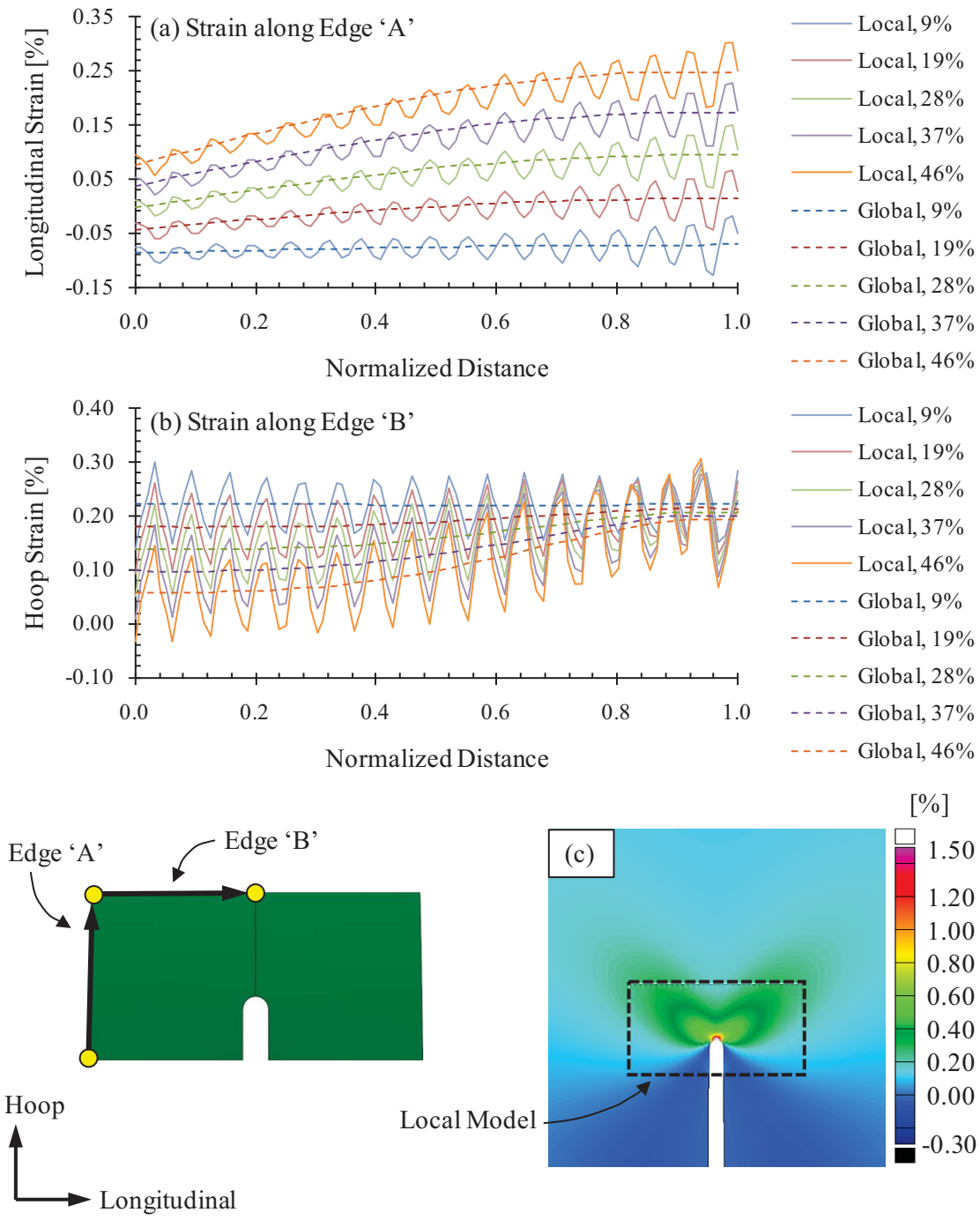

Figure 8.32. Comparison of the panel CP3 strains along the global/local interface. The strains were taken along edges 'A' and 'B' indicated in the schematic, and were oriented perpendicular to the edge along which they were located. Figure 8.32c shows the longitudinal strain contour plot at 46% of the panel fracture load, as determined by the local FE model, superimposed onto the corresponding global model results.

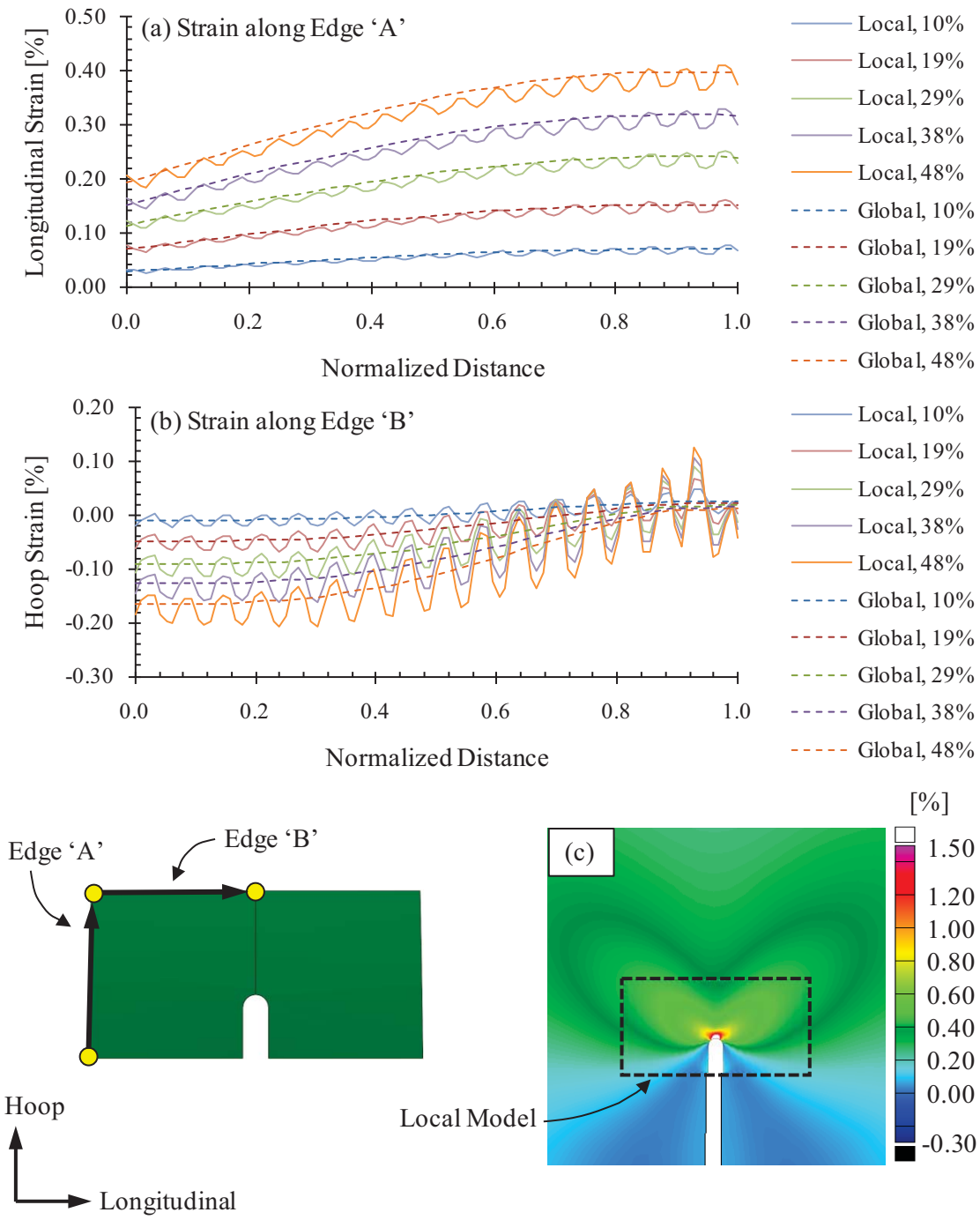

Figure 8.33. Comparison of the panel CP4 strains along the global/local interface. The strains were taken along edges 'A' and 'B' indicated in the schematic, and were oriented perpendicular to the edge along which they were located. Figure 8.33c shows the longitudinal strain contour plot at 48% of the panel fracture load as, determined by the local FE model, superimposed onto the corresponding global model results.

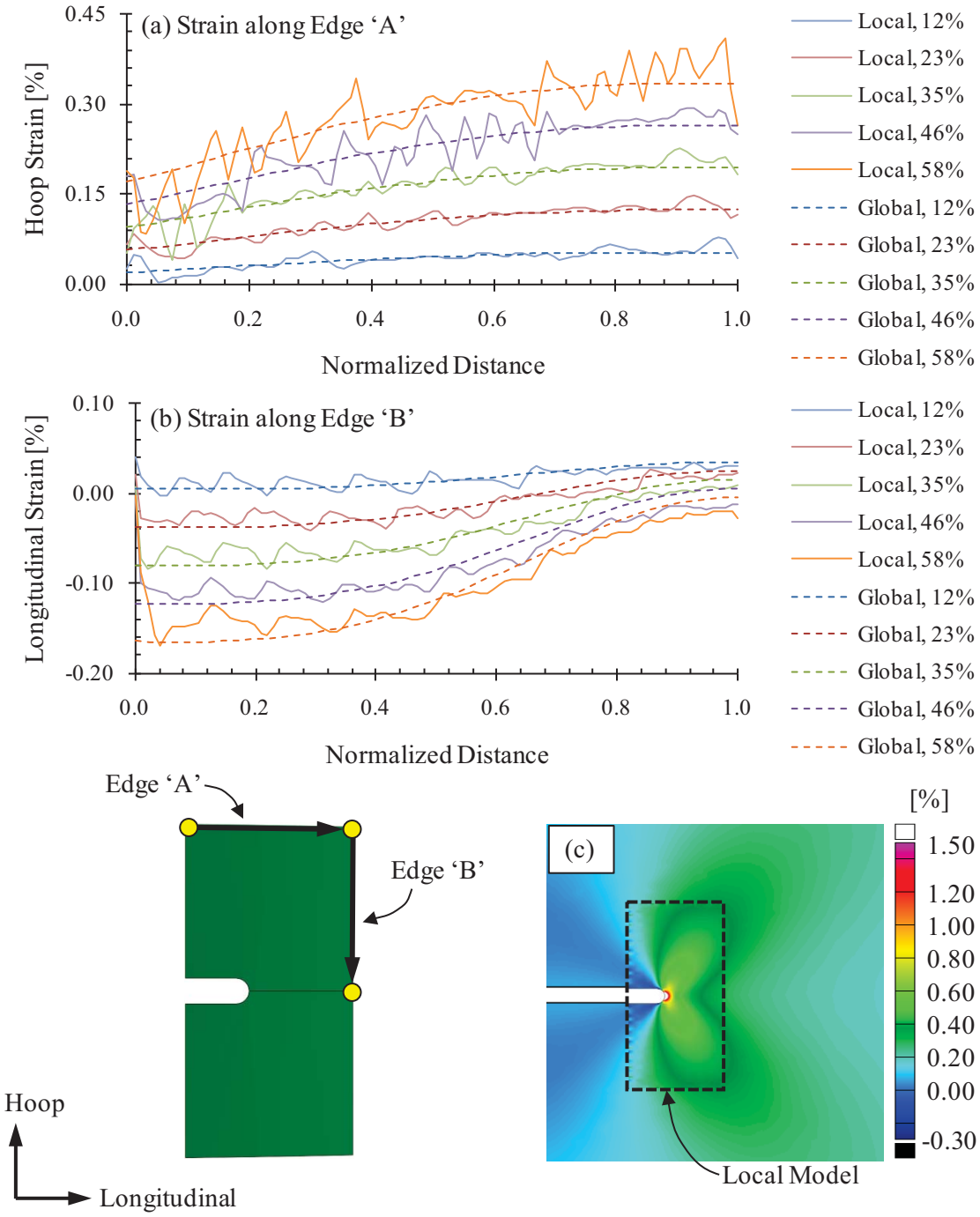

Figure 8.34. Comparison of the panel CP5 strains along the global/local interface. The strains were taken along edges 'A' and 'B' indicated in the schematic, and were oriented perpendicular to the edge along which they were located. Figure 8.34c shows the hoop strain contour plot at 58% of the maximum applied load, as determined by the local FE model, superimposed onto the corresponding global model results.

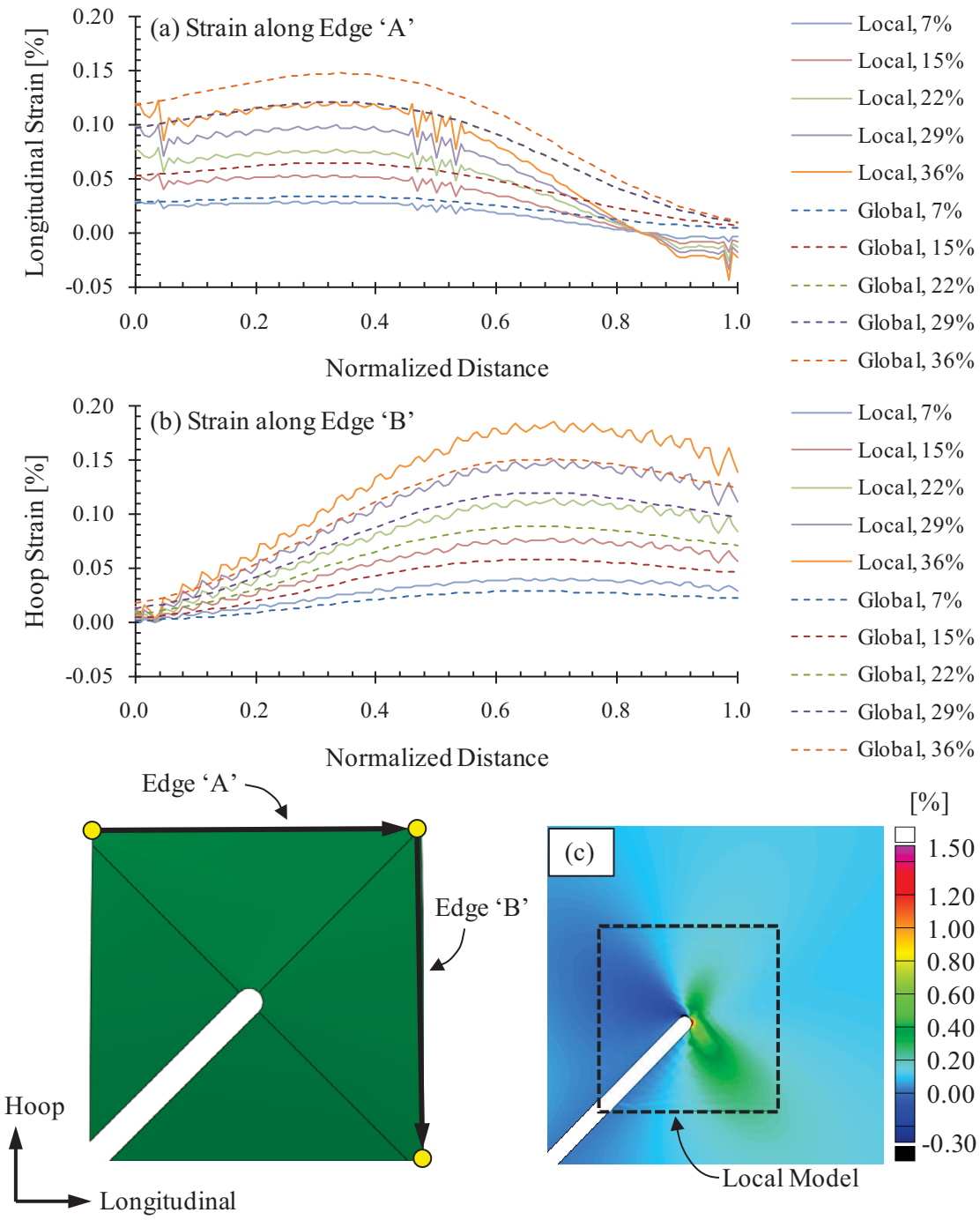

Figure 8.35. Comparison of the panel CP6 strains along the global/local interface. The strains were taken along edges 'A' and 'B' indicated in the schematic, and were oriented perpendicular to the edge along which they were located. Figure 8.35c shows the hoop strain contour at 36% of the panel fracture load, as determined by the local FE model, superimposed onto the corresponding global model results.

The panel CP5 local model results generated using the ABAQUS submodeling routine were similar to those achieved for panel CP6. Strain distributions similar to the global model results were observed, though the amplitudes did not agree. The hoop strains along edge 'A' were consistently underestimated (Figure 8.36a) and the longitudinal strains along edge 'B' were consistently overestimated (Figure 8.36c). While the oscillations produced by the ABAQUS submodeling routine were more uniform than those produced by the proposed submodeling routine, the average amplitude of the oscillations were comparable between the two cases.

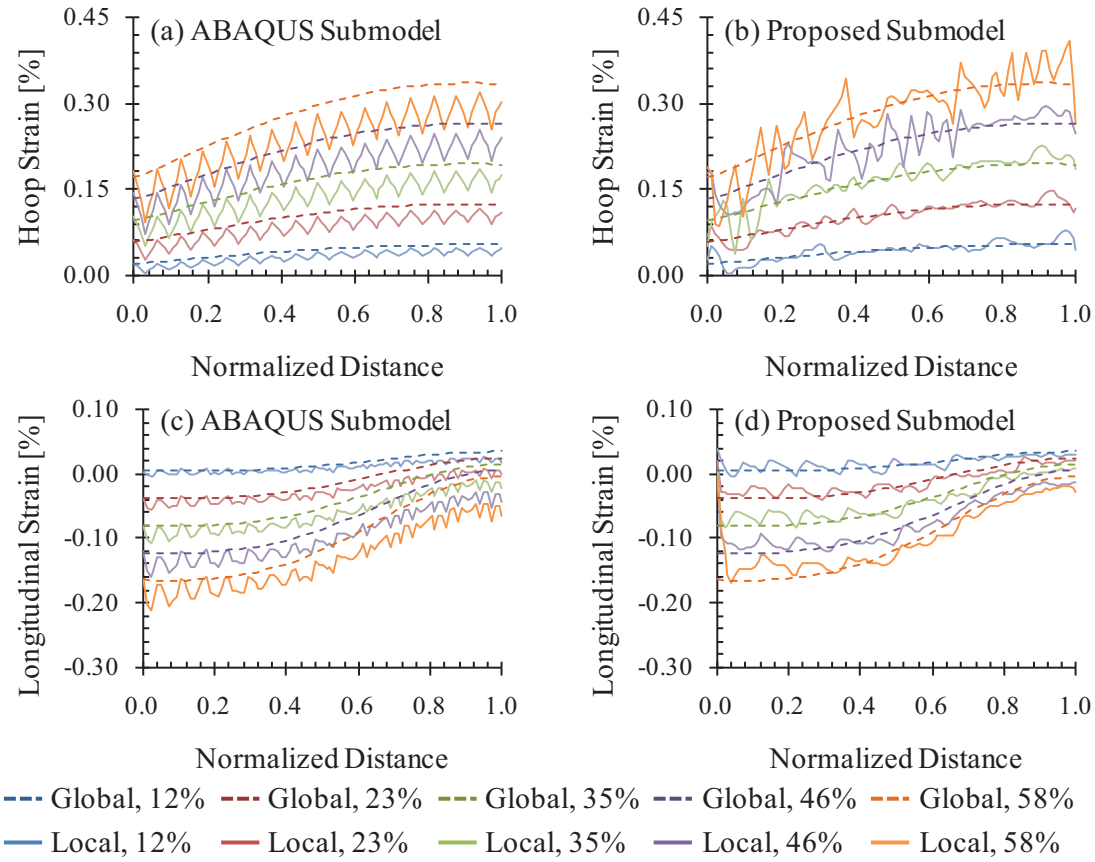

Figure 8.36. Comparison of the ABAQUS and proposed submodeling techniques for the panel CP5 strains along the global/local interface. The strains were taken along edges 'A' and 'B' indicated in the schematic in Figure 8.34, and were oriented perpendicular to the edge along which they were located.

The comparison of the two local model results in Figure 8.36 indicates that while the default routine produces less noise in the immediate vicinity of the driven edges, the inclusion of the additional transverse shear strain inputs improves the accuracy of the global/local submodeling boundary condition definition. This is expected, given that the ABAQUS documentation recommends avoiding locating the global/local interface in regions of considerable transverse shear strain [8.9]. However, for cases in which regions of considerable transverse shear strain either coincide with or extend beyond the regions of interest about which the global/local interface must be placed, the proposed submodeling approach leads to more accurate results while avoiding unnecessarily large regions to be included in the often finely meshed local models.

8.5.2. DETERMINATION OF FACE SHEET FIBER FRACTURE TOUGHNESS

As mentioned in Section 8.4.2, a fracture toughness value of 275 lbf/in was used for all damage evolution simulations in this study. Very limited data are available in open literature on the fracture toughness values for woven composites. The selected value of 275 lbf/in was chosen based on an extensive parametric study in which the fiber fracture toughness was varied from 100 to 500 lbf/in. This range of values was selected based on the work of Pinho et al. [8.8] on measuring the fracture toughness of fiber-reinforced laminated composites and its application to progressive damage modeling by Maimí et al. [8.5]. The panel CP5 local FE model was used in this parametric study with the modified submodel boundary condition formulation, adaptive boundary conditions, and the failure model using the maximum stress failure criterion.

As an input to the failure model, the fracture toughness affects the rapidity at which the state-of-damage changes with each successive exceedance of the selected failure criterion. Accordingly, some measure of the state-of-damage ahead of the notch tip had to be defined to gage the performance of the various local FE models. The available experimental data with which these comparisons could be made included measurements of the distances from the

original notch tip to where damage was furthest visible in the exterior face sheet and to the apparent center of the measured DIC notch-normal strain fields, both of which are presented in Figure 4.54c for panel CP5. The computational output most closely related to these experimental data was the extent-of-damage in the exterior face sheet, as defined by the furthest element from the original notch tip whose fiber failure damage state variable has exceeded 0.85. The results of local FE models solved using six select fiber fracture toughness values are presented in Figure 8.37 along with the experimental data originally presented in Figure 4.54c.

The predicted progression of damage with increased load was similar for each fracture toughness case. Damage progressed gradually until extending approximately 0.30 inch ahead of the original notch tip, at which point the progression of damage increased rapidly with further increases in load until either the notch tip damage extended to the limits of the local FE model geometry or unstable damage progression occurred.

While the damage progression curves were generally similar and met expectations (i.e., larger fiber fracture toughness values resulted in slower damage progression), two distinct families of curves were identified through the range of tested fracture toughness values. The first family of curves was observed in the models using fiber fracture toughness values approximately equal to or less than 300 lbf/in, and exhibited gradual damage progression up to an approximate 0.35-inch damage extension, at which point rapid damage progression was observed up until instability occurred. The second family of curves was observed in models using fiber fracture toughness values greater than 300 lbf/in, and exhibited slower damage progression up to approximately 0.25 inch ahead of the original notch tip, progressing rapidly thereafter. Based on these results shown in Figure 8.37, additional intermediate values were tested and a fracture toughness value of 275 lbf/in was chosen for all subsequent simulations as it yielded a damage progression curve most similar to that experimentally observed.

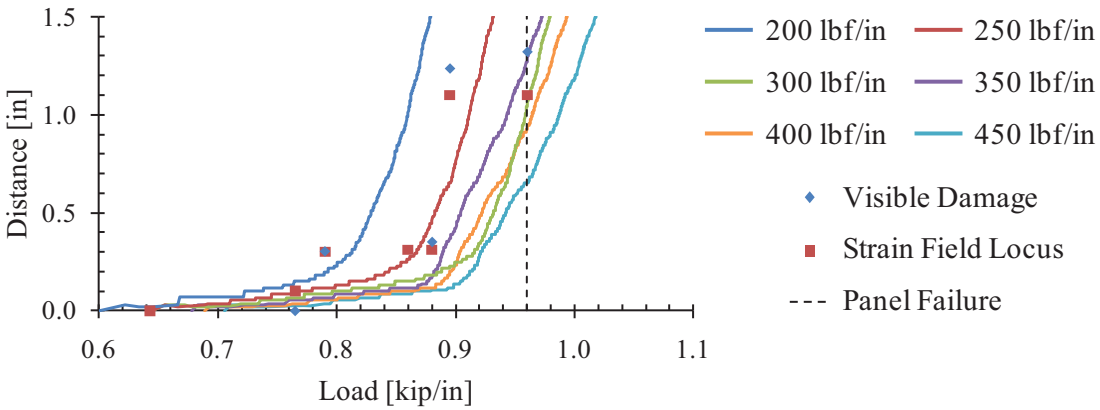

Figure 8.37. Comparison of visible notch tip damage extensions, as measured along the axis of the panel CP5 notch, the locus of the strain field ahead of the notch, as measured via DIC, and the predicted extent-of-damage in the exterior face sheet for various values of the fiber fracture toughness with the maximum stress failure criterion.

Examination of the notch tip damage progression data revealed the difference in the shape of the damage progression curves were related to different paths of damage progression through the material during the early stages of damage development. As an example, Figure 8.38 presents the development of the notch tip damage for fiber fracture toughness values of 300 and 350 lbf/in at various loads. (The notch tip damage extensions observed using the fracture toughness values from each family were similar to these representative cases, simply developing at either faster or slower rates.) The damage state variable in the figure corresponds to the local material 2-direction (i.e., oriented in the -45° direction in the exterior ply and the 90° direction in the mid-ply). Elements in which the local material 2-direction damage state variable exceeded 0.85 are removed from the figure.

Figure 8.38a shows the development of a crack along the fourth row of elements above the axis of the notch at 81% of the experimentally observed panel fracture load, using 300 lbf/in for the fiber fracture toughness. Upon loading up to 97% and 102% of the panel fracture load, the damage shifted to the third row of elements above the notch axis and extended to 0.80 and 1.30 inches, respectively. Figure 8.38d shows the development of cracks along the second and fourth

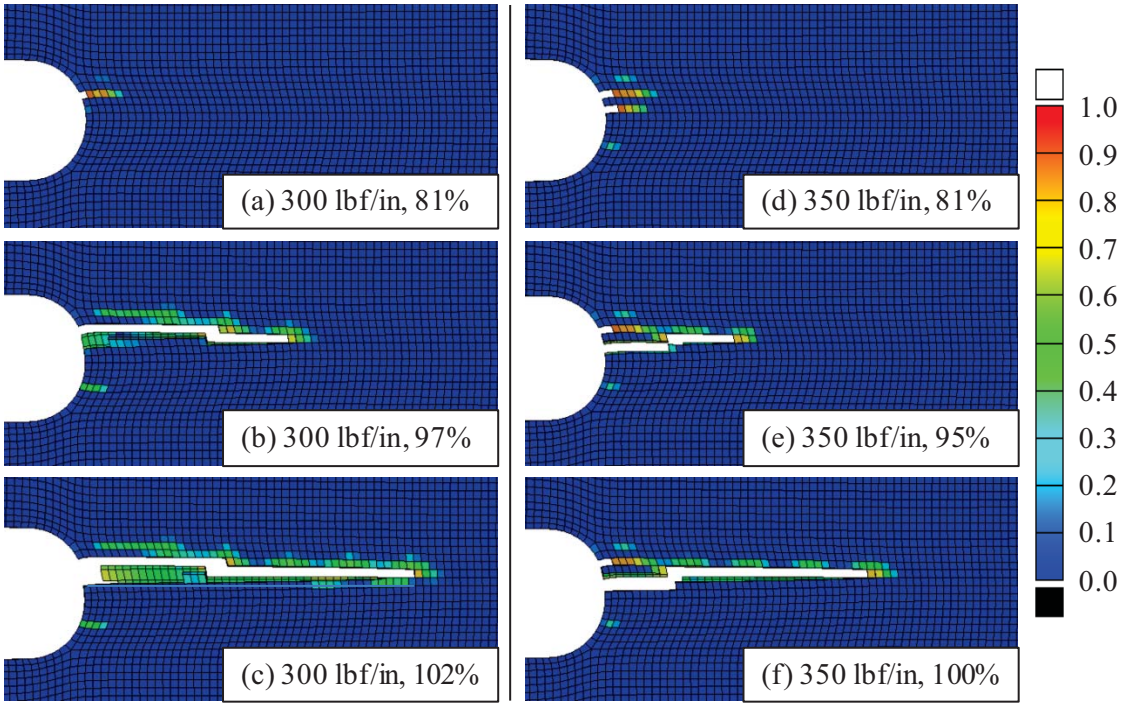

Figure 8.38. Comparison of notch tip damage progression for the local FE model of panel CP5 using the maximum stress failure criteria and fracture toughness values of 300 lbf/in and 350 lbf/in. These two fracture toughness values represent the two families of the extent-of-damage with load curves identified in Figure 8.37.

rows of elements above the axis of the notch at 81% of the panel fracture load using 350 lbf/in for the fiber fracture toughness. The notch tip crack closer to the axis of the notch developed more quickly, cutting off the second crack at 95% of the panel fracture load, shifting to the third row of elements above the notch axis, and progressing rapidly.

Clearly, the precise shape of the damage progression curve depends on the path along which damage propagated through the material. Within the context of the local FE models, the path along which damage propagates depends on the geometry of the mesh. While the effect is subtle for models through which the path of damage progression is generally straight along the axis of the original notch, for cases in which the path of damage propagation is more complex (e.g., panel CP6), the influence of the mesh geometry would have a stronger influence on the accuracy of the extent-of-damage predictions.

8.5.3. NOTCH TIP STRAIN FIELDS

While the global FE model results accurately predicted the strain fields ahead of the notch tips, the initiation and progression of additional notch tip damage through the face sheet material could not be predicted without the inclusion of an appropriate failure model. The local FE models, of course, included such a failure model and were capable of predicting the change in the state-of-damage of the material and the resulting strain field ahead of the damage. Having confirmed the validity of the local model boundary conditions in Section 8.5.1 and selected the final necessary material property input in Section 8.5.2, local FE models were solved for each of the four notched panels. For each panel, three simulations were run in which the maximum strain, the maximum stress, and the Hashin failure criteria were implemented. Since the fiber fracture toughness was selected using models which utilized the maximum stress failure criterion, the four models solved using this criterion were expected to correlate best with the experimental data. The effect of varying the failure criterion on the initiation, progression, and eventual instability of damage is discussed in Section 8.5.4. Here, the elevated strain fields ahead of the notch tips are presented as they were predicted by the local FE models using the maximum stress failure criterion.

The DIC and local FE model notch-normal strain field results for panel CP3 are presented side-by-side in Figure 8.39 at several load levels. The local FE model initially appears to overestimate the severity of the notch tip strain field at 56% of the panel fracture load. However, as mentioned in Section 4.3.1, the post-processing filtering applied to the raw DIC data diminished the apparent severity of the strains within approximately 0.3 inch of the notch tip. Therefore, only the strain contours outside this area should be used for comparative purposes, though the extent-of-damage from each data set can be directly compared. Taking this into consideration, excellent correlation is observed through 65% of the panel fracture load, prior to any indication of notch tip damage extension as per the location about which the elevated strain field was centered. At 74% of the panel fracture load (Figure 8.39c), the center of the elevated

strain field in both the DIC and FE data sets advanced approximately 0.1 inch ahead of the notch tip, though no significant visible damage is apparent in either. At 84% of the panel fracture load (Figure 8.39d), the visible notch tip damage extended 0.57 inch, with the DIC strain field advancing to approximately 0.47 inch ahead of the original notch tip. The state-of-damage and resultant strain field predicted by the local FE model advanced accordingly, showing excellent correlation.

The final visible state-of-damage prior to the catastrophic fracture of the panel occurred at 93% of the panel fracture load (Figure 8.39e), extending 1.14 inches ahead of the original notch tip and holding there until panel fracture. The local FE models cannot replicate the sudden, step-wise advancements of damage which were experimentally observed (e.g., the extension of the notch tip damage from 0.61 to 1.14 inches at 93% of the panel CP3 fracture load) due to the assumption that the modeled material is a homogeneous orthotropic continuum. Regardless, the predicted continuous advancement of the notch tip damage correlated very well with the experimentally observed results. At 93% of the panel fracture load, the local FE model predicted a notch tip damage extension of 1.09 inches in the exterior face sheet, progressing up to the global/local interface by 99% of the panel fracture load (Figure 8.39f). Hence, instability was observed in both the experimental and computational data sets at near-equal loads.

As discussed throughout Section 4.2.4, despite having a more severe loading configuration than panel CP3, panel CP4 did not exhibit a catastrophic fracture at its maximum applied load. The predictions on damage initiation and progression correlated well with experimental observations during the early stages of damage development even though the predicted instability was not observed experimentally. Nevertheless, the local FE predictions supported the initial expectation that panel CP4 would fail in a manner similar to CP3, though at lower applied longitudinal loads.

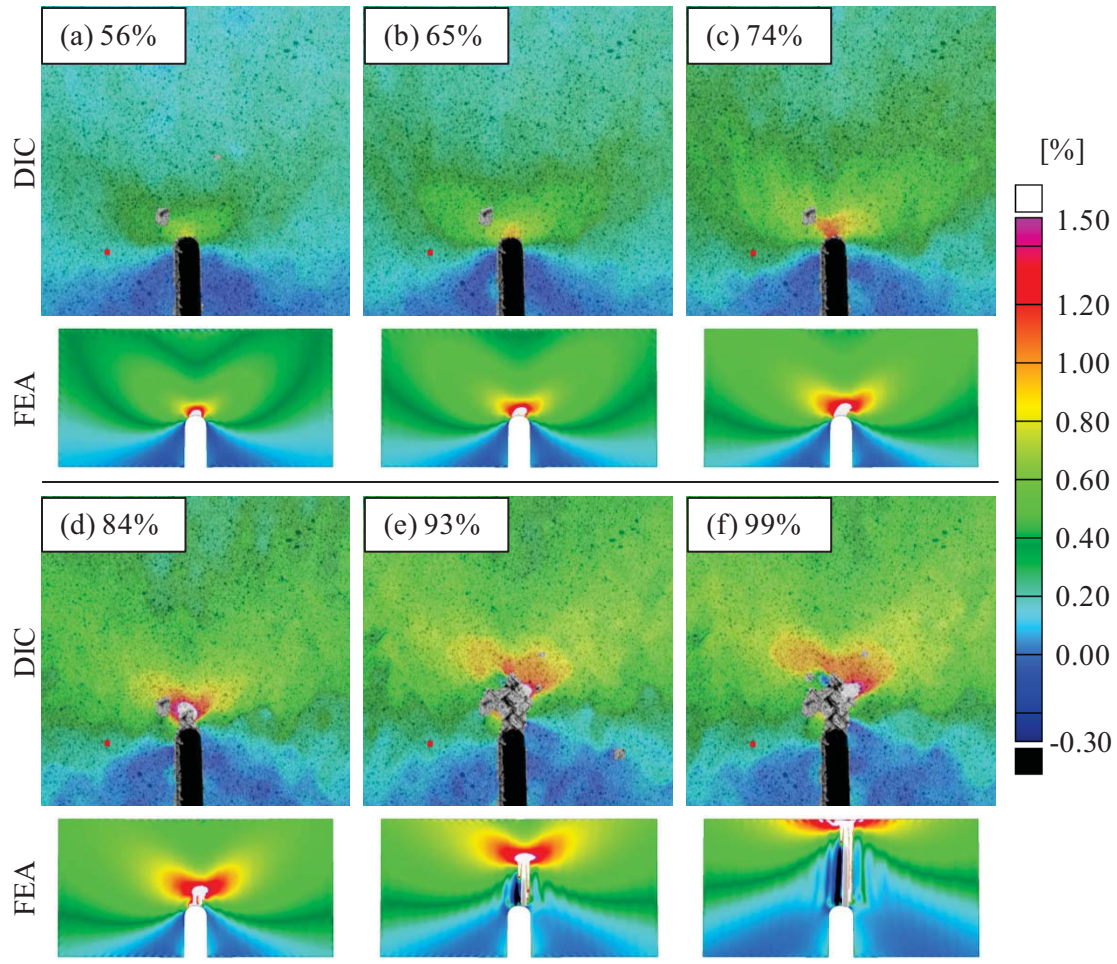

Figure 8.39. Comparison of panel CP3 notch tip longitudinal strains at various load levels as measured via DIC and as predicted by the local FE model using the maximum stress failure criterion.

The first instance of visible damage in panel CP4 was observed at 67% of the maximum applied load, Figure 8.40b. The damage was along the semicircular notch tip and was located approximately 0.1 inch to the right of the notch axis, causing a slight bias of the elevated strain field to the right. The predicted notch tip strain field showed a similar development of damage and bias of the strain field at this load level. The visible notch tip damage extended 0.41 inch at 76% of the maximum applied load, advancing the center of the strain field to 0.3 inch ahead of the original notch tip, Figure 8.40c. Again, the local FE model results correlated very well with the observed notch tip damage extension, predicting an extension of 0.29 inch in the exterior face

sheet. The strain fields in each data set continued to show a bias toward the right side of the notch. Beyond this load, the experimental observations and the computational predictions began to diverge. The local FE model results showed continued notch tip damage progression along the axis of the notch up to the global/local interface at 94% of the maximum applied load, while the strain field measured by the DIC system showed negligible notch tip damage extensions in this loading range. Examination of the DIC data during the latter stages of the test revealed that while no further axial notch tip damage extensions were observed, damage continued to develop along

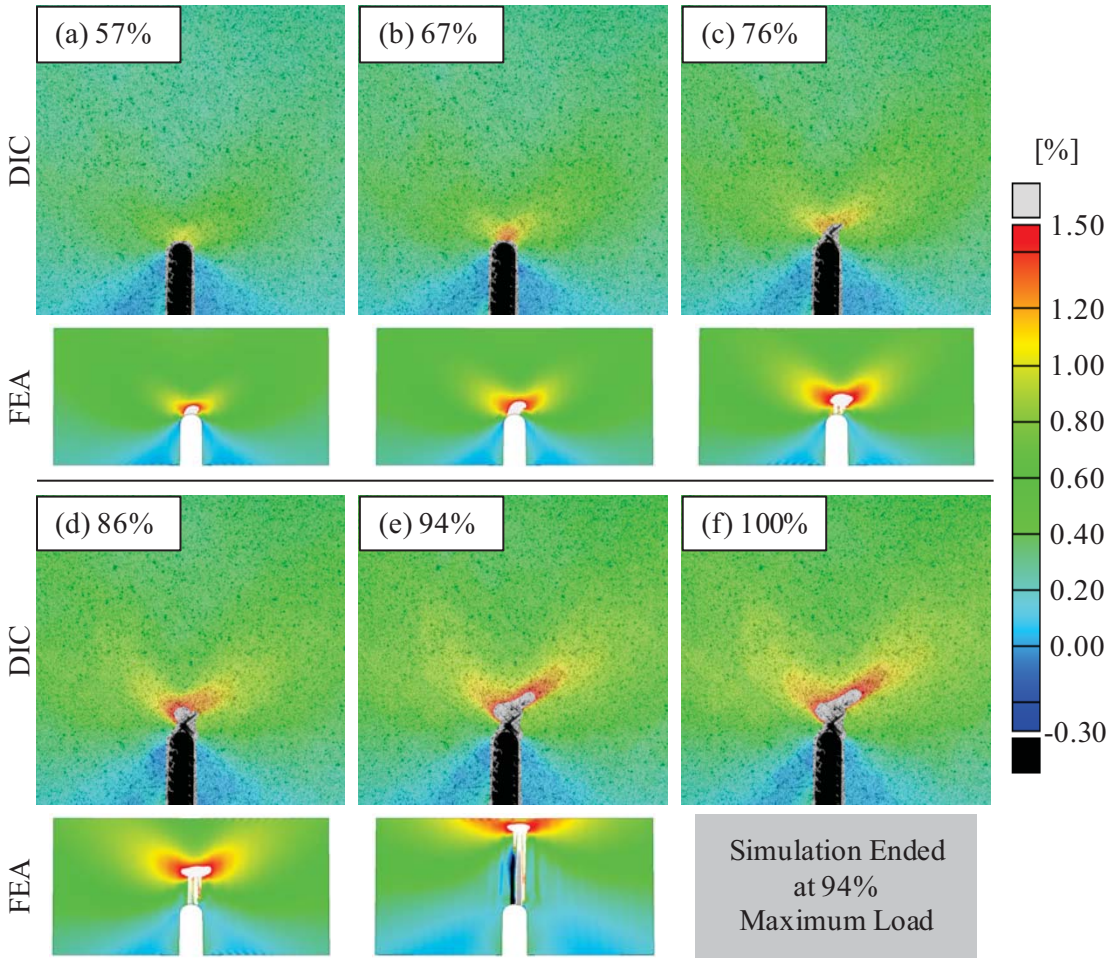

Figure 8.40. Comparison of panel CP4 notch tip longitudinal strains at various load levels as measured via DIC and as predicted by the local FE model using the maximum stress failure criterion.

the +45° fiber tow ahead of the notch tip damage, as was evident by the strains in exceedance of 1.5% along this tow (Figure 8.40f) and the NDI data presented throughout Chapter 5.

Similar to the sudden, step-wise notch tip damage extensions, the assumption to treat the face sheet laminae as orthotropic continua made the representation of the redirection of damage along the plain-weave structure of the face sheet laminae impossible. However, prior to this effect of the heterogeneous structure of the face sheet material, very good agreement was achieved between the experimental observations and the computational predictions. Therefore, assuming minimal influence of material and structural heterogeneities, the ability of the local FE models to accurately predict the advancement of damage is further supported.

Similar to the results achieved with panels CP3 and CP4, excellent correlation was observed between the experimental observations and computational predictions for panel CP5, especially during the early stages of damage development, Figure 8.41. This was expected since the fiber fracture toughness was calibrated using the experimental results of panel CP5. Regardless, the fact that the nonlinear experimental and computational damage progression curves were able to be fit for a given fracture toughness value (and that good correlation was observed with the remaining panels using the same selected value) suggests both that a fiber fracture toughness of 275 lbf/in well represents the actual material behavior and that the comparison of the two data sets is nontrivial.

As mentioned, excellent correlation was observed through the early stages of damage development between the measured and predicted notch tip strains and the states-of-damage. Similar notch tip damage extensions, in terms of both the visible notch tip damage and the center of the elevated strain field, occurred in both the DIC and local FE model strain fields at 90% of the panel fracture load, Figure 8.41d. Upon further loading to 93% of the panel fracture load, the notch tip damage suddenly extended 1.24 inches ahead of the original notch tip. While the local FE model was unable to predict the sudden change in the physical state-of-damage ahead of the notch tip, the rate at which the predicted damage progressed increased at this load level, rapidly

extending to 1.64 inches in the exterior face sheet at the panel fracture load. As discussed in Section 4.2.5, panel CP5 fractured catastrophically after holding at its maximum applied load level for 43 seconds. Similar to the panel CP3 results, while the final experimentally observed states-of-damage could not be precisely predicted due to the influence of the heterogeneous plain-weave face sheet material, the predicted rate of damage propagation through the local FE model correlated well with the step-wise experimental measurements and the final panel fracture.

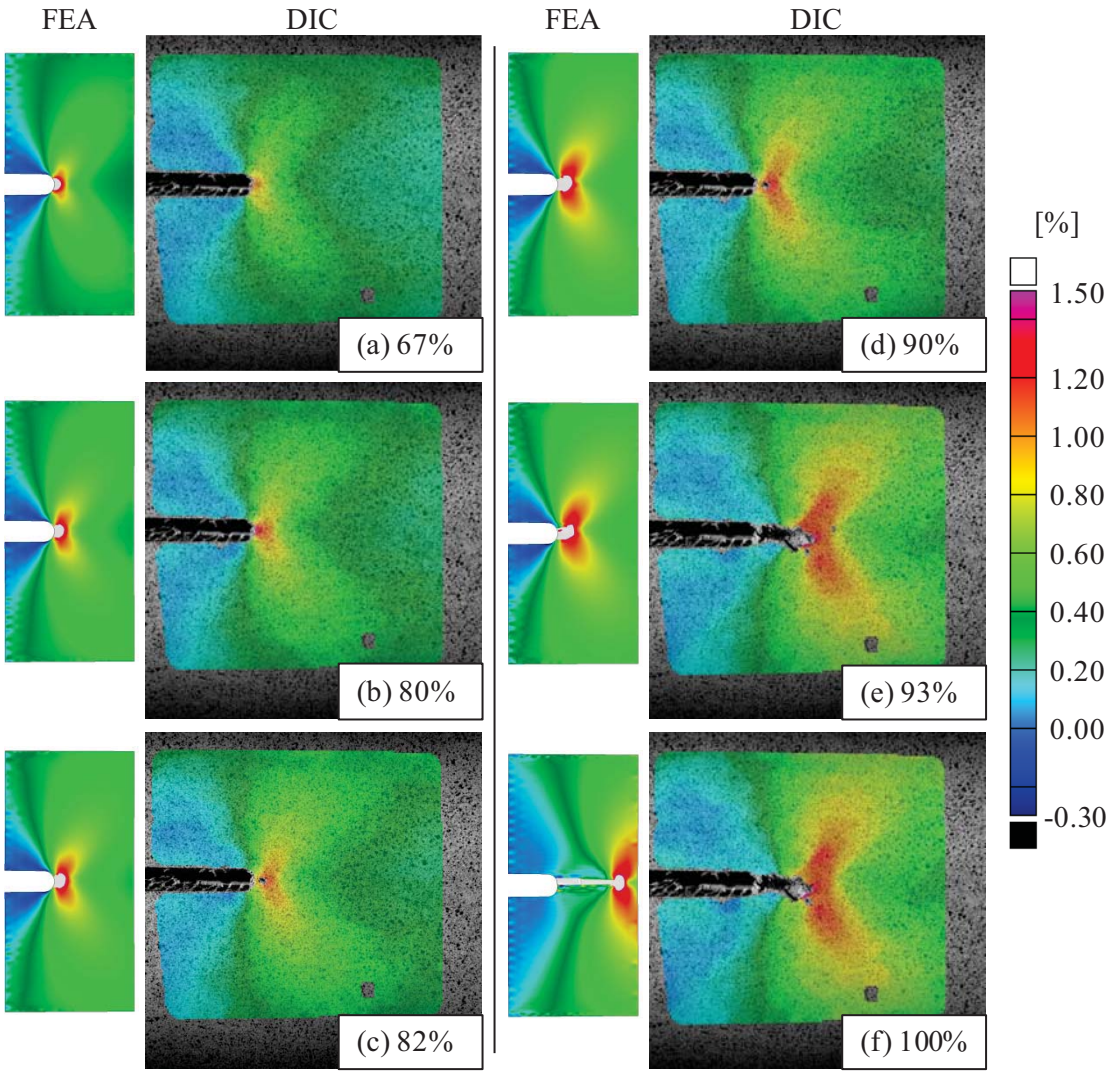

Figure 8.41. Comparison of panel CP5 notch tip hoop strains at various load levels as measured via DIC and as predicted by the local FE model using the maximum stress failure criterion.

As was discussed in Section 8.5.1, the panel CP6 local FE model was solved using the default ABAQUS submodeling algorithm. As a result, the predicted strains along the global/local interface in the local FE model differed from those in the global FE model, Figure 8.35. Regardless, generally good correlation was observed between the experimental observations and the computational predictions. The first instance of visible notch tip damage occurred along the hoop tangent of the semicircular notch tip at 65% of the panel fracture load. The damage predicted by the local FE models was approximately 0.1 inch to the right of the inclined notch axis, underestimating the observed bias of the notch tip damage and the resulting strain field, Figure 8.42b. While the damage initiation location was not accurately predicted, the orientation of the damage propagation path was well represented at 73% of the panel fracture load, proceeding along the longitudinal panel direction, Figure 8.42c. The magnitude, bias to the right of the notch, and shape of the elevated notch tip strain field correlated well with the DIC strain field results up to 77% of the panel fracture load, Figure 8.42d. Beyond this load level, several sources of error became more influential. As the damage progressed away from the original notch tip, the failure of the boundary conditions to adapt to the new strain field locus artificially decreased the driving force behind further damage progression. Furthermore, as discussed in relation to the notch tip damage of panel CP4, the heterogeneous nature of the latter stages of the panel CP6 damage progression cannot be predicted with the assumption of a homogenous face sheet material. While the center of the elevated strain field extended only in the longitudinal direction, the blunting of the notch tip damage resultant of the extensive damage to the plain-weave fabric structure could not be represented.

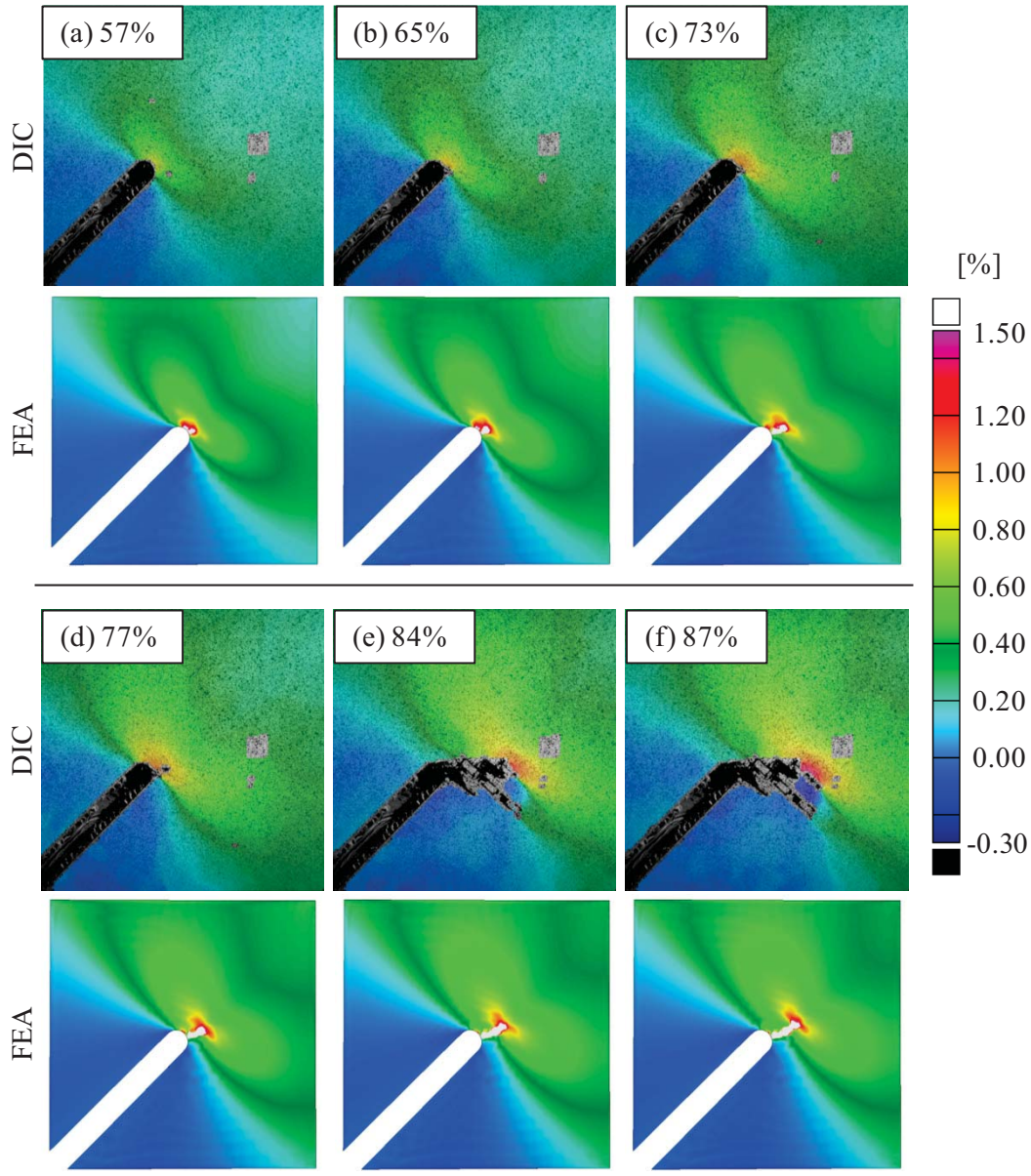

Figure 8.42. Comparison of panel CP6 notch-normal strains at various load levels as measured via DIC and as predicted by the local FE model using the maximum stress failure criterion.

8.5.4. PLY-BY-PLY DAMAGE PROGRESSION

While the local FE model notch tip strain fields provided good input for comparisons to the visible notch tip damage extensions and the centers of the elevated notch tip strain fields, the models generated much richer data regarding the initiation and further development of the states-of-damage ahead of the notch tips. Specifically, the two fiber damage state variables (representing fiber fractures in the local material 1- and 2-directions) contained information regarding the location, orientation, and ply in which damage formed and progressed. Such data are particularly useful for supporting the numerous assumptions made regarding the progression of the notch tip damage through the various prepreg plies of the honeycomb sandwich composite based on the visible states-of-damage and the measured DIC strain fields (Section 4.3.3).

Figures 8.43 and 8.44 show the state-of-damage in the local material 1- and 2-directions, respectively, in all six plies of the two face sheets for panel CP3 at the six select load levels used in the local FE model notch tip strain field figures in Section 8.5.3. The dark regions ahead of the notch tips in each figure are indicative of increasingly severe states-of-damage, with black representing a damage state variable equal to unity. It can be seen that cracks formed ahead of the notch tip in each of the three exterior face sheet plies prior to the formation of a single dominant crack. The most prominent damage development occurred in the fibers perpendicular to the notch in the exterior face sheet mid-ply. Figure 8.43a shows the initial softening of the 0° fibers ahead of the notch tip at 56% of the panel fracture load, followed by the formation of three mid-ply cracks (i.e., series of fully failed elements forming lines originating at the original notch tip) at 65% (Figure 8.43b) and 74% (Figure 8.43c) of the panel fracture load. Two of these mid-ply cracks continued to grow, propagating toward the global/local interface and becoming the center of the notch tip strain field during the later load steps. As the state-of-damage rapidly progressed during the later load steps, the area affected by the elevated notch tip strain field expanded due to the increasing loads. This resulted in fibers partially failing at increasingly large distances away from the dominant crack due to larger regions being affected by the strain field

exceeding the associated failure criterion. This behavior is apparent in the mid-plies of both the exterior and interior face sheets at 99% of the panel fracture load, Figure 8.43f.

Despite the relatively complex initial stages of damage development, only a single dominant crack results from continued damage propagation. The interactions of the three mentioned mid-ply cracks, the additional interactions of any damage which independently developed in the bounding ±45° face sheet plies, and their joint effect on the notch tip strain field defined what early notch tip damage would lead to the catastrophic fracture of the panel. As early as 56% of the panel fracture load, damage was developing in the +45° direction, along the respective +45° fiber tow tangent to the notch, Figure 8.43a. Similar damage developed in the exterior and interior plies of the exterior face sheet in the -45° direction at this load level (Figure 8.44a); the location of this damage corresponded with the location of one of the three mid-ply cracks. As a result, the independent failures in the exterior face sheet plies coalesced, forming the dominant notch tip crack which led to the catastrophic fracture of the panel. This correlates well with the failure process postulated in Section 4.3.3 regarding panel CP3.

Care must be taken while interpreting these figures, for the presence of damage at a particular location and orientation does not necessarily indicate that the material at that location failed as a result of loading, but rather as a result of either excessive distortion resultant of failure in the perpendicular fiber damage state variable or a failure in an adjacent ply. For example, throughout Figure 8.44, the major state-of-damage which developed in the exterior face sheet mid-ply was not preceded by any initial softening of the material. Furthermore, the location geometry of the failure coincide perfectly with the fully failed elements of the opposite damage state variable. Attention must be paid as to which location and orientation of failure motivated the ensuing propagation of damage through the material.

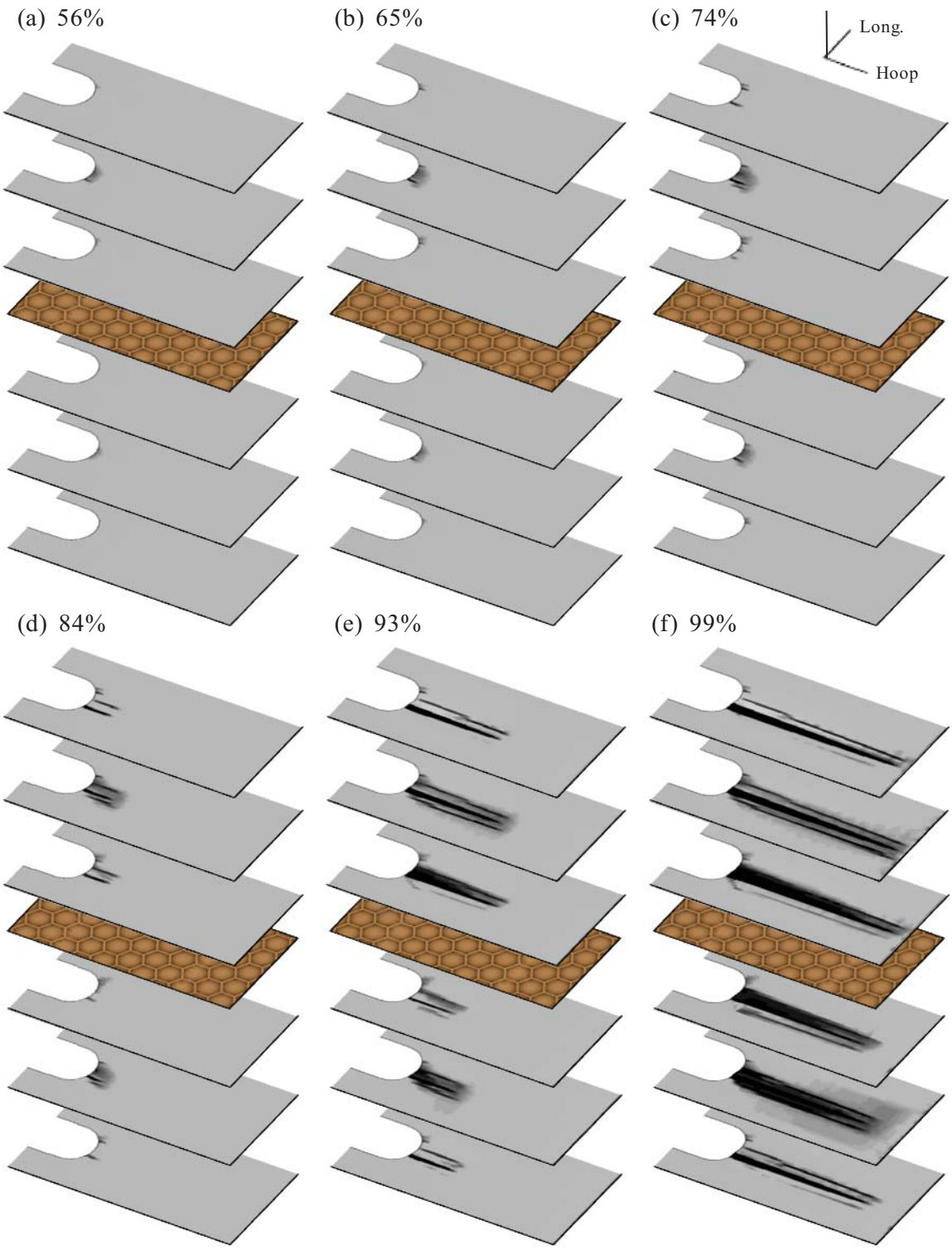

Figure 8.43. Panel CP3 local FE model notch tip damage progression as determined using the maximum stress failure criteria at various stages of loading. The dark regions ahead of the notch tip are indicative of failure in the local material 1-direction.

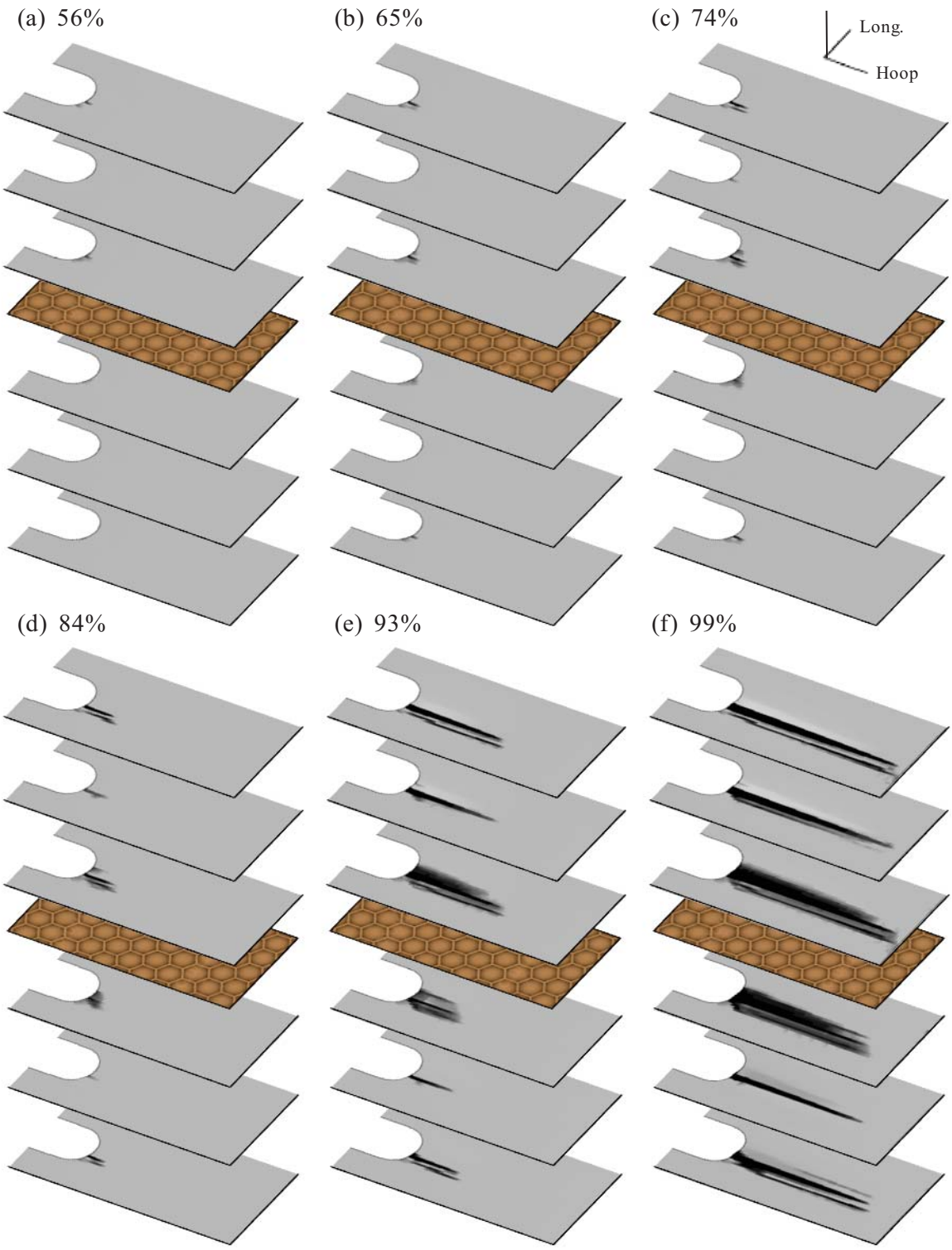

Figure 8.44. Panel CP3 local FE model notch tip damage progression as determined using the maximum stress failure criteria at various stages of loading. The dark regions ahead of the notch tip are indicative of failure in the local material 2-direction.

Similar illustrations of the ply-by-ply damage progression in panels CP4 through CP6 are shown in Figures 8.45 through 8.50. Panel CP4 (Figures 8.45 and 8.46) exhibited similar trends during the early stages of damage development as those exhibited by panel CP3. Due to the high applied longitudinal loads, the fibers oriented perpendicular to the circumferential notch were loaded most critically and were the first to fail at 56% of the maximum applied load, Figure 8.45a. This initial damage was generally symmetric about the notch axis. However, failures in the -45° fibers at 65% of the maximum applied load (Figure 8.46b) redirected the advancement of damage toward the right side of the notch, causing the bias in the notch-normal strain field discussed in the previous section. The 0° mid-ply cracks and the -45° interior and exterior ply cracks progressed together through 76% of the maximum applied load (Figures 8.45d and 8.46d, respectively), at which point the 0° mid-ply cracks became the dominant failure mechanism, driving self-similar notch tip damage progression up to predicted instability. The effect of the increasingly severe notch tip strain field is evident in both the exterior and interior face sheets at 99% of the maximum applied load, showing the increasingly large and increasingly severe states-of-damage outside the major fracture which occurred during the latter stages of rapid damage propagation, Figure 8.45f.

Like the notch tip damage progression results of panel CP3, the results of panel CP5 (Figures 8.47 and 8.48) supported the failure process postulated in Section 4.3.3 based on the visible notch tip damage and the resulting notch tip DIC strain fields. While both panels CP3 and CP5 exhibited self-similar notch tip damage progression with minimal far-reaching damage prior to the fracture of the panels, only panel CP3 exhibited extensive damage in the exterior ±45° ply upon fracture. Minimal visible damage was observed ahead of the panel CP5 notch away from the major fracture. This led to the conclusion that the panel CP5 damage process was driven by solely notch-normal fiber failures while panel CP3 involved the interaction of failures throughout the face sheet. The development of damage in the exterior and interior face sheets of panel CP5 supports this statement. Throughout loading, all damage in the ±45° directions corresponded to

damage having already occurred in the 90° mid-ply fibers (Figure 8.48). The additional components of damage presented in Figure 8.47 showed similar results. The bounding ±45° plies contained only collateral damage resulting from the high-energy mid-ply failures, and were not directly damaged by the elevated notch tip strain field.

While the local FE model results of panel CP6 are only valid during the initial stages of damage development due to the employed submodeling boundary condition algorithm, reasonably good agreement between the postulated failure process and the local FE model results was observed during this period. Examination of the local material 1- (Figure 8.49) and 2-direction (Figure 8.50) fiber damage state variable figures of panel CP6 indicates that damage initiation and propagation was driven by failures in the local material 2-direction in each ply of the sandwich composite (as is evident by the development of partially failed elements preceding the formation of defined notch tip cracks). The DIC strain fields discussed in Section 4.3.3 indicated that failures in the 90° mid-ply drove the progression of the damage along the longitudinal direction of the panel, while failures in the fibers perpendicular to the notch caused the far-reaching damage along the tows ahead of the notch tip damage. At 58% of the panel fracture load, damage was observed in each of the six plies of the sandwich composite. A defined through-thickness crack emanated from the notch in the exterior face sheet, though partially failed material in both the 90° and -45° fibers was also observed, Figure 8.50a. The partially failed elements in the various plies did correspond to more severe failures in adjacent plies, indicating that the elevated strain fields in each ply contributed to the formation of the through-thickness crack. As discussed earlier, it was not expected that the panel CP6 local FE model would represent the observed expansive states-of-damage related to the plain-weave fabric of the prepreg plies, though the indications that separate components of strain in separate plies drove the overall failure process provide further support for the ability of the model to represent the initiation and progression of damage in cases less influenced by the heterogeneous plain-weave fabric.

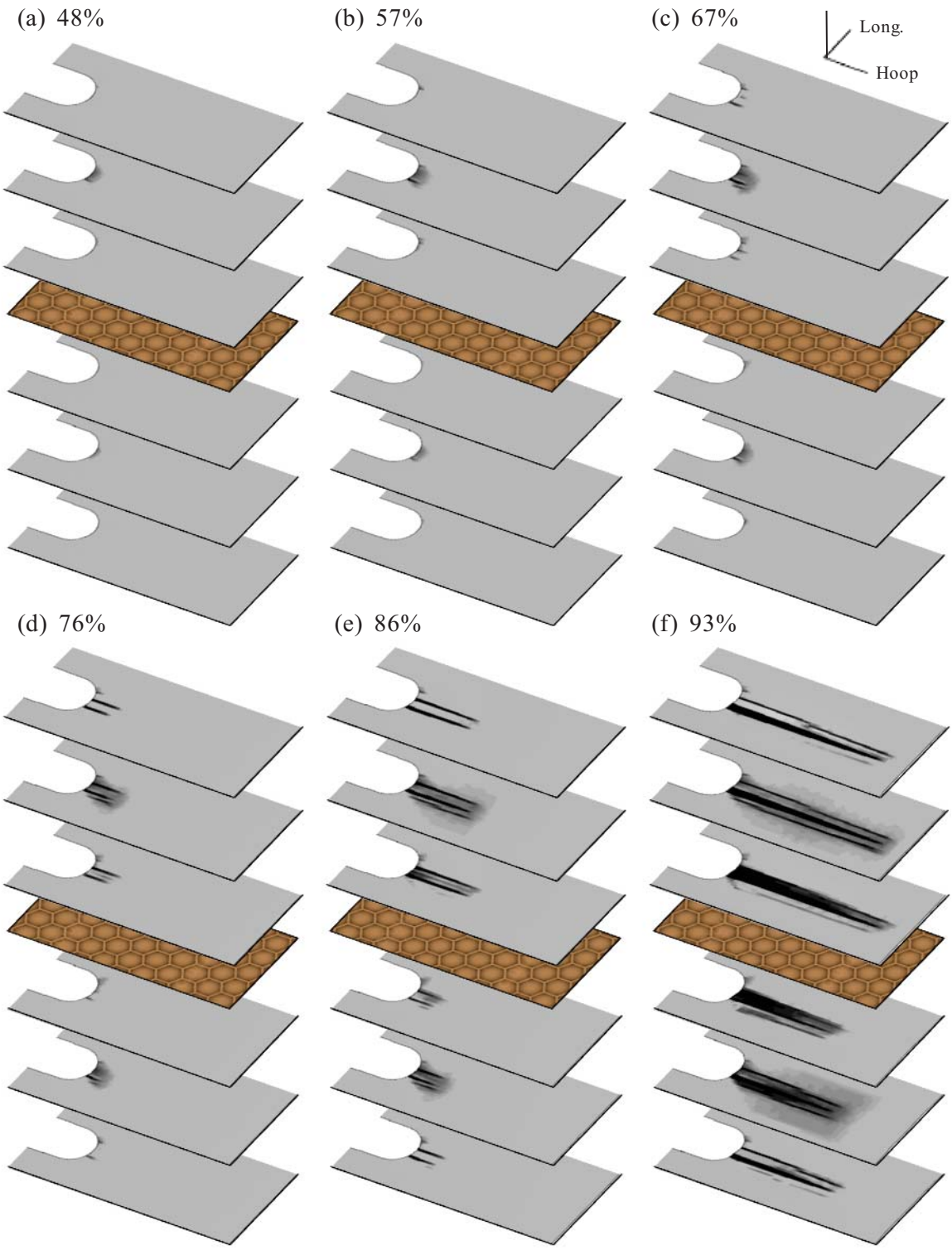

Figure 8.45. Panel CP4 local FE model notch tip damage progression as determined using the maximum stress failure criteria at various stages of loading. The dark regions ahead of the notch tip are indicative of failure in the local material 1-direction.

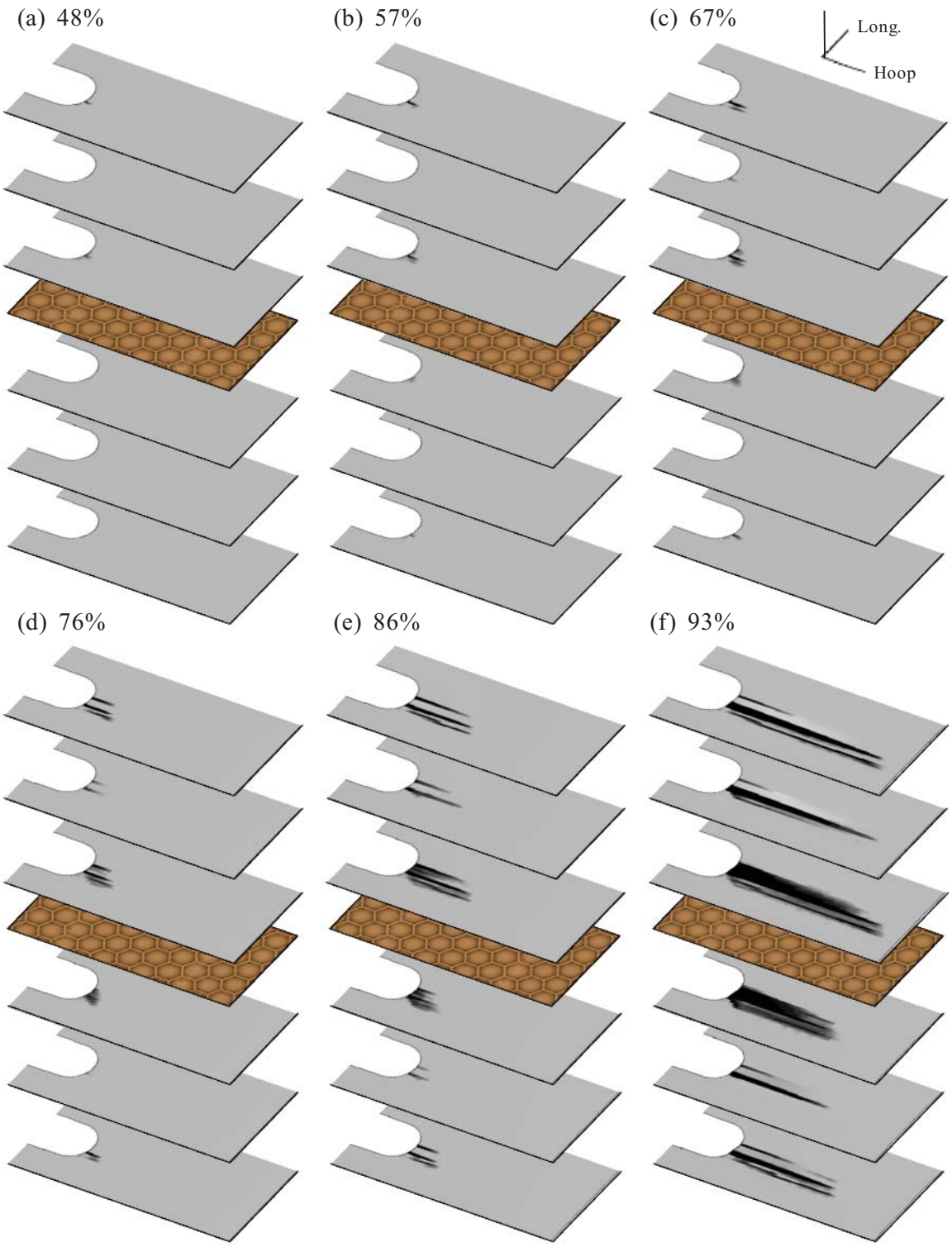

Figure 8.46. Panel CP4 local FE model notch tip damage progression as determined using the maximum stress failure criteria at various stages of loading. The dark regions ahead of the notch tip are indicative of failure in the local material 2-direction.

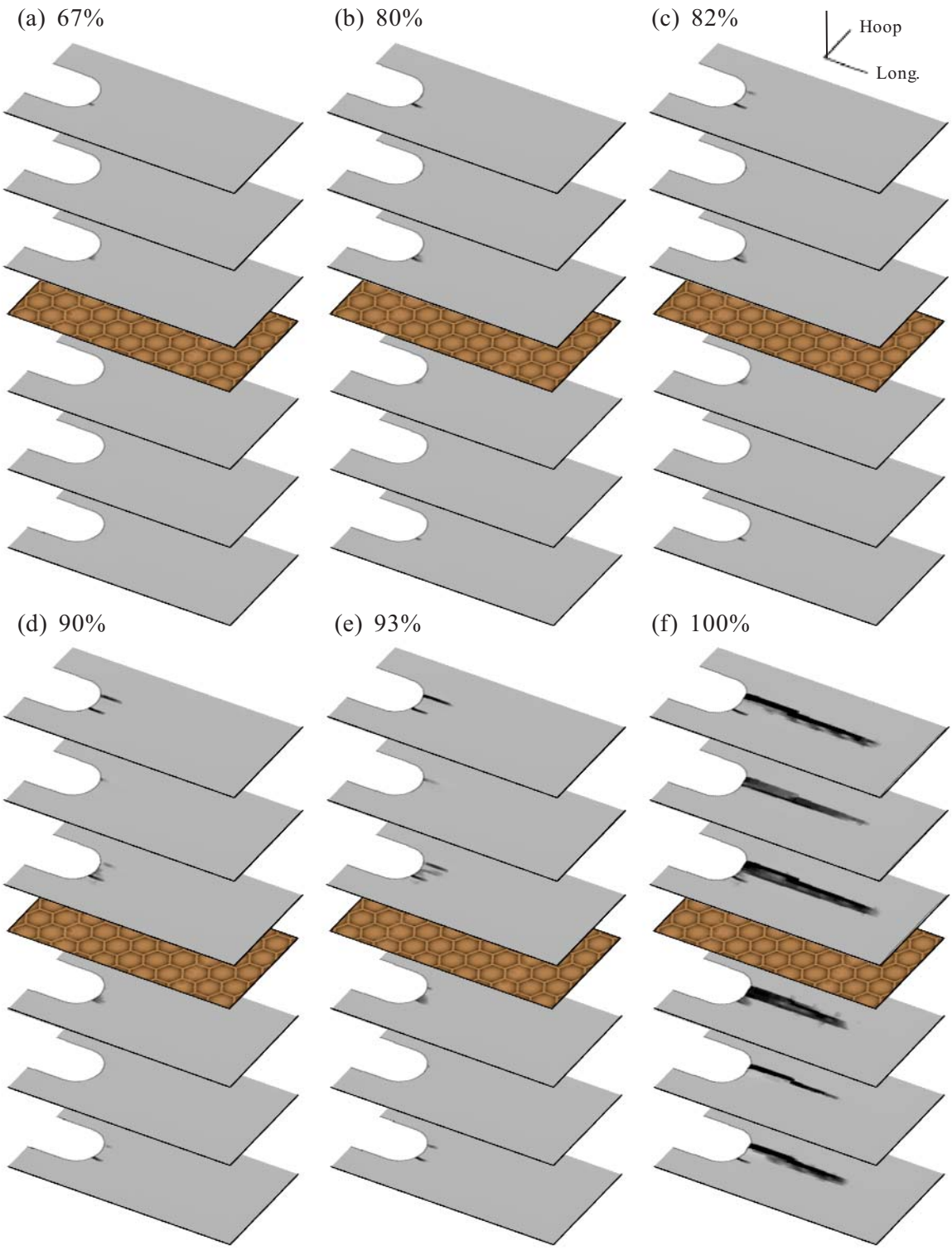

Figure 8.47. Panel CP5 local FE model notch tip damage progression as determined using the maximum stress failure criteria at various stages of loading. The dark regions ahead of the notch tip are indicative of failure in the local material 1-direction.

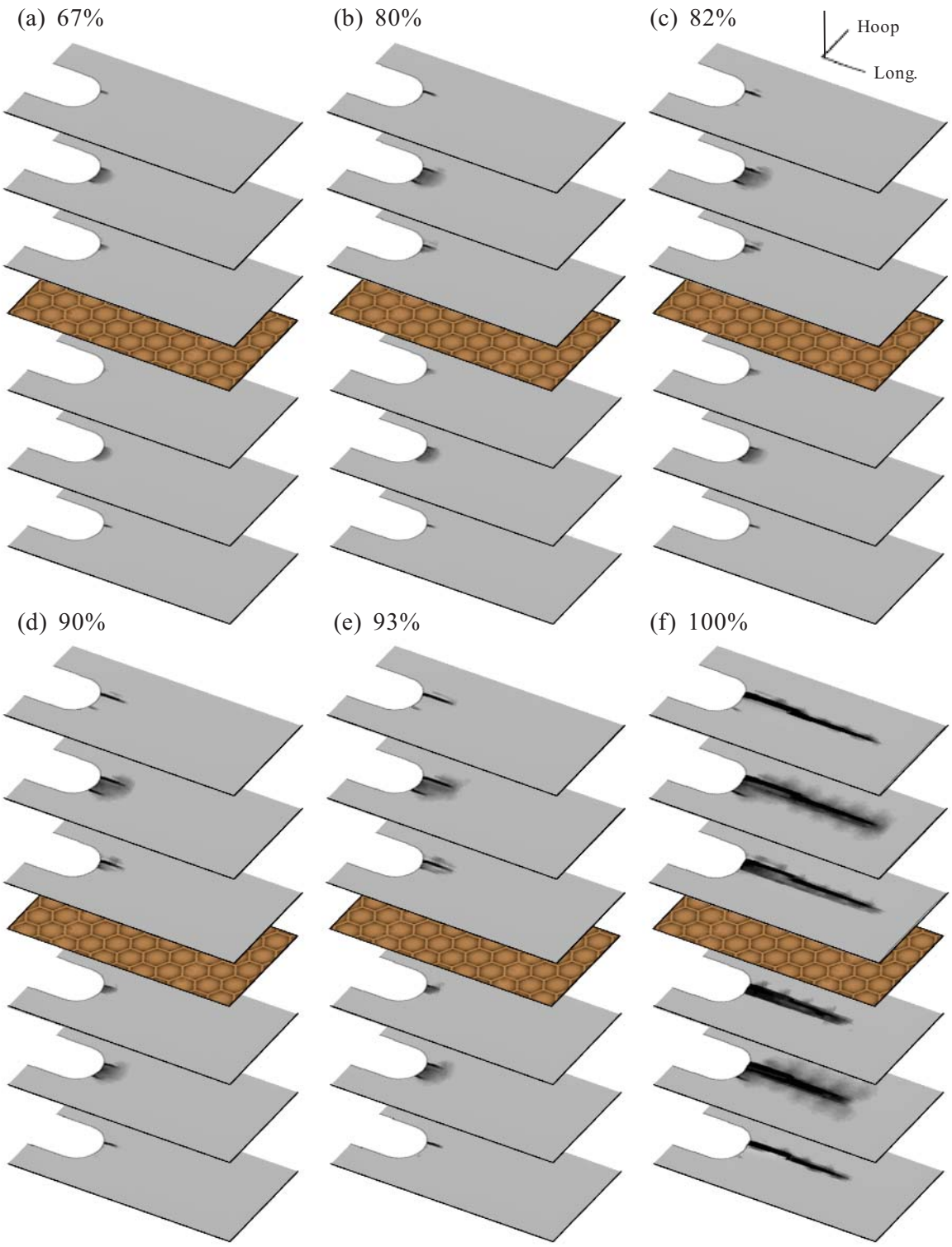

Figure 8.48. Panel CP5 local FE model notch tip damage progression as determined using the maximum stress failure criteria at various stages of loading. The dark regions ahead of the notch tip are indicative of failure in the local material 2-direction.

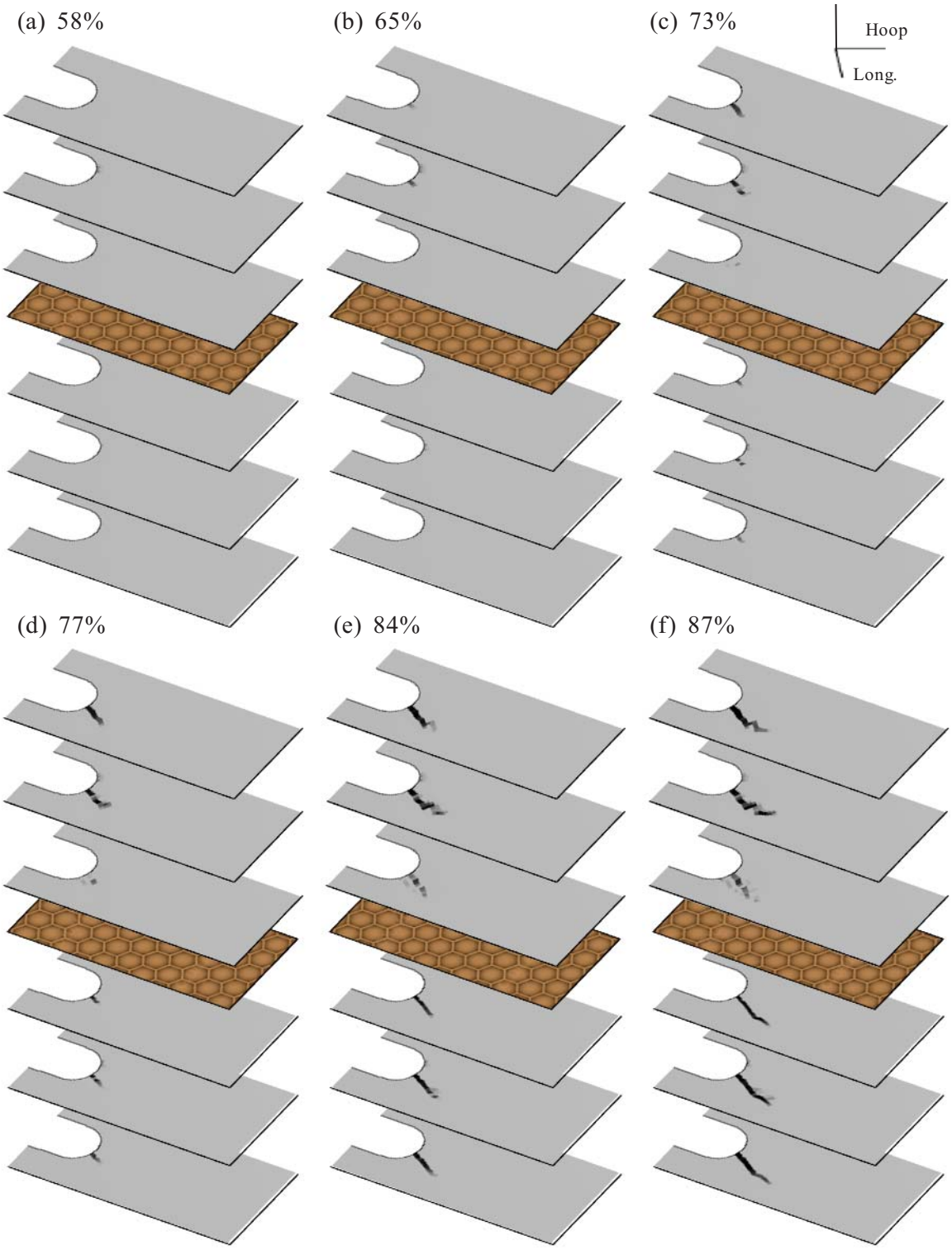

Figure 8.49. Panel CP6 local FE model notch tip damage progression as determined using the maximum stress failure criteria at various stages of loading. The dark regions ahead of the notch tip are indicative of failure in the local material 1-direction.

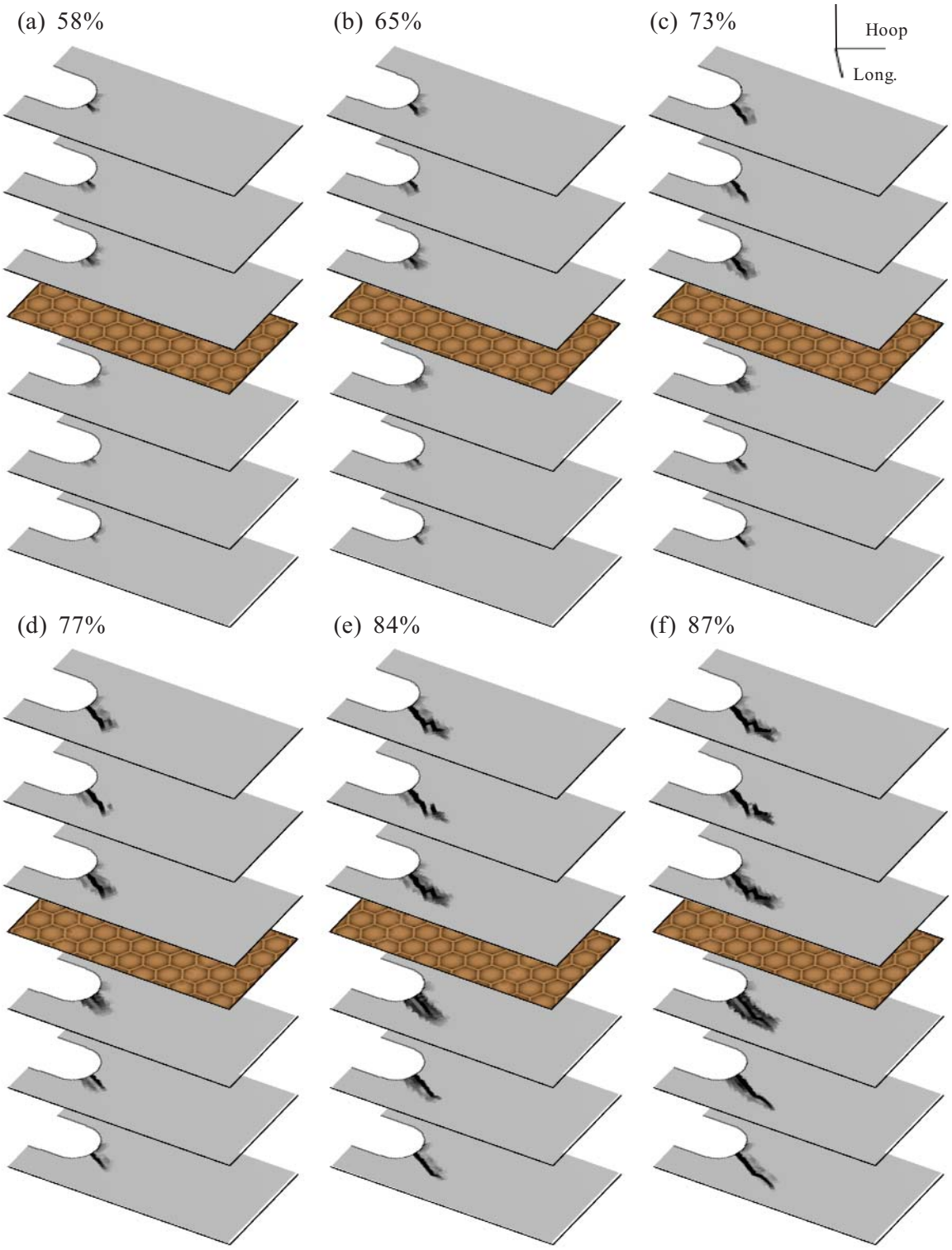

Figure 8.50. Panel CP6 local FE model notch tip damage progression as determined using the maximum stress failure criteria at various stages of loading. The dark regions ahead of the notch tip are indicative of failure in the local material 2-direction.

Notch tip damage extensions in the exterior face sheets as a function of load served as the best measure for comparisons between the experimental observations and the computational predictions. As originally presented in Figure 4.54, the measurements of the furthest reaching visible damage and the locations of the elevated notch tip strain field centers served to characterize the effective notch tip damage extensions for the three notched panels which exhibited generally self-similar damage progression (i.e., panels CP3, CP4, and CP5). The most comparable computational output was the extent-of-damage in the exterior face sheet, defined as the distance to the furthest element from the original notch tip containing at least one fiber damage state variable that exceeded 0.85.

Figure 8.51 summarizes the results discussed regarding the local FE model predictions of the notch tip strain fields and the progression of notch tip damage, comparing the computational results to the corresponding experimental data. As discussed in Section 8.4.3, the extent-of-damage was defined to correspond with the location about which the elevated strain field was centered in each face sheet. Therefore, the strain field locus data presented in Figure 8.51 should be used to assess the accuracy of the predicted notch tip damage extensions.

Excellent correlation was observed between the strain field locus data and the progression of damage as predicted by the local FE models utilizing the maximum stress failure criterion. The results obtained for panels CP3 and CP5 agreed through the early stages of damage formation, the transitions to more rapid damage propagation, and the instability of the notch tip damage. The results obtained for panel CP4 also agreed well with the experimental data during the early stages of damage formation, but, as mentioned, the heterogeneous nature of the plain-weave fabric redirected the progression of the notch tip damage away from the notch axis, arresting its progression and avoiding instability within the applied range of loading.

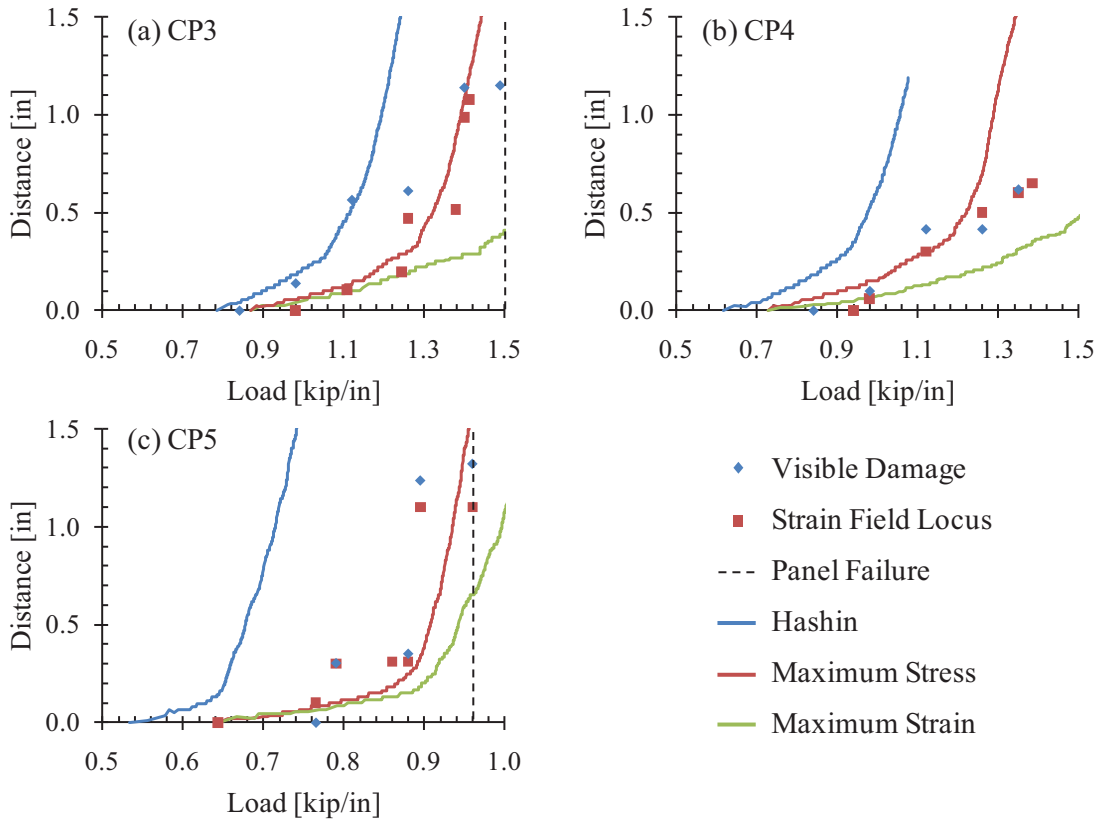

Figure 8.51. Comparison of visible notch tip damage extensions, as measured along the axis of the original notch, the locus of the strain field ahead of the notch, as measured via DIC, and the predicted extent-of-damage in the exterior face sheet for panels (a) CP3, (b) CP4, and (c) CP5.

Figure 8.51 also shows results obtained based on the maximum strain failure criterion and the Hashin failure criterion. While it is generally agreed that these three failure criteria correlate well in terms of predicting the onset of failure under both uniaxial loading and tensile-tensile combined loading conditions, investigation into the dependence of damage state variables on the selected failure criterion is absent in literature. Table 8.1 presents the loads at which fiber damage state variables of at least 0.85 were generated for each of the notched panels exhibiting self-similar damage progression for each of the evaluated failure criteria. A discussion comparing the predicted rates of damage propagation as a function of the selected failure criterion is presented here.

Table 8.1. Damage Initiation by Panel and Failure Criterion.

Panel	Failure Criterion	Percent Maximum Load at Damage Initiation
CP3	Hashin	0.54
	Max. Stress	0.59
	Max. Strain	0.59
CP4	Hashin	0.42
	Max. Stress	0.50
	Max. Strain	0.51
CP5	Hashin	0.58
	Max. Stress	0.68
	Max. Strain	0.69

For each panel, the progressions of damage as predicted by the maximum stress and the Hashin failure criteria were very similar throughout the applied loading range, with the clear exception that the local FE models utilizing the Hashin failure criterion predicted damage extensions and instability at lower loads than those utilizing the maximum stress failure criterion. The resulting damage progression curves driven by the two failure criteria were offset (in terms of load) by approximately the same amount throughout loading in each panel. Comparing equations (8.2) and (8.3), the presence of nonzero shear stresses, which are primarily due to panel bending, can cause the Hashin failure criterion to be satisfied earlier than the maximum stress criterion, as was observed. After the initiation of damage, however, the severity of the notch tip stress concentration greatly exceeded that due to panel bending, causing the change in the evaluated failure criteria to be dominated by the fiber-oriented stresses. The similar shapes of the maximum stress and Hashin damage progression curves support this statement.

The damage progression curves from the local FE models solved using the maximum strain failure criterion do not follow the same trend as those between the maximum stress and the Hashin criteria. For all three panels, the loads at which the fiber damage state variables first exceeded 0.85 were similar as predicted by both the maximum stress and maximum strain criteria, Table 8.1. However, the post-initiation behavior of the local FE models driven by the

maximum stress and maximum strain failure criteria differed notably. For panels CP3 (Figure 8.51a) and CP4 (Figure 8.51b), the progression of damage driven by the maximum strain criterion proceeded more slowly during the early stages of damage development and never reached instability. For panel CP5, both the maximum stress and maximum strain criteria again predicted the initiation of critical notch tip damage progression at the similar load levels. However, the rate at which damage progressed throughout loading was consistently lower with the maximum strain failure criterion, Figure 8.51c. The maximum strain failure criterion, as can be seen in equation (8.2), depends on the sign and magnitude of the off-axis strains (i.e., tensile off-axis strains result in earlier damage initiation, while compressive off-axis strains delay the onset of damage). As is evident by the damage progression curves in Figure 8.51, tensile off-axis strains occurred in each of the failing elements in each of panel, slowing the rapidity with which damage progressed as compared to the models driven by the maximum stress criterion.

While the initiation of damage in a particular element may be well predicted using any of several failure criteria, care must be taken to understand the expected off-axis deformation of an element whose stiffness matrix is being artificially degraded. For example, if axial failures result in a propensity to generate either tensile or compressive off-axis strains of non-negligible magnitudes, notable differences in the post-initiation behavior of the element could result, influencing both the current state-of-damage and the rate at which damage will progress through the model.

8.6. CONCLUSIONS

The primary objective of this computational study was to accurately and efficiently simulate the formation, progression, and eventual instability of damage in full-scale sandwich composite aircraft fuselage panels originating at severe artificial damage sources through use of the finite element (FE) method. A global/local analysis was performed to represent the

development of damage in the immediate vicinity of the artificial damage due to the global deformations imposed by the FASTER test fixture.

An in-depth representation of the panels was developed, taking into consideration the panel geometries, composite lay-ups, and the test fixture loading mechanisms. Excellent correlation, in terms of both the far-field and notch tip region strain responses to increasing load, was observed between the strain data recorded via the arrays of strain gages and the DIC method, and as predicted by the global FE model solutions for each of the notched panels. A thorough and accurate representation of the global deformation of full-scale sandwich composite fuselage panels due to the actual loading mechanisms of the test fixture was achieved, offering a reliable source from which to drive the boundary conditions of the progressive damage local FE models.

Considerable efforts were made regarding the details and scalability of the failure model and its application to full-scale structures. The internal pressurization applied to the panels caused significant transverse shear strains to develop in the regions of interest, invalidating the assumptions of typical shell-to-solid submodeling algorithms. To address this issue, a custom user subroutine was written to modify the algorithm used to define the local FE model boundary conditions, integrating the transverse shear strains of the global FE models. Furthermore, a set of adaptive boundary conditions was developed to ensure proper and smooth driving of the local FE model boundaries with increasingly severe states-of-damage. A library of global FE solutions with varying degrees of notch tip damage extensions was generated. Depending on the current state-of-damage and load increment in the local FE model solution, the library was queried for the most appropriate set of global FE model solutions. These global solutions were then interpolated to create an ideal global model solution set for the current state-of-damage and applied loads. This custom global FE model solution set was then used to drive the local model boundary conditions.

Excellent correlation was achieved between the experimental measurements and the computational predictions in terms of notch tip damage progression. Each of the local FE models

predicted catastrophic failure, though such large-scale failures were not experimentally observed in every case. In some instances the heterogeneous plain-weave prepreg material redirected the damage propagation path, arresting further crack growth. The treatment of the face sheet material as a homogenous orthotropic continuum prevented such predictions. In cases in which the propagation of damage was not significantly affected by the plain-weave fabric, the notch tip failure processes were well modeled from initiation through to instability.

The successful implementation of these progressive damage modeling techniques to full-scale composite aircraft structures bodes well for the scalability of more advanced methods. Proper use of the tools proposed in this chapter allow for the further testing of higher-order failure criteria and damage evolution laws. Continued advancement in this area of research will allow for more ambitious materials and structural concepts to be implemented in future aircraft design, while maintaining an understanding of the damage tolerance-related performance characteristics.

CHAPTER 9: SUMMARY AND CONCLUSIONS

9.1. SUMMARY

The research conducted during the course of this investigation consisted of in-depth experimental and computational efforts. In the experimental phase of the investigation, six full-scale sandwich composite aircraft fuselage panels were tested at the Full-Scale Aircraft Structural Test and Research (FASTER) facility at the William J. Hughes FAA Technical Center, Atlantic City International Airport, NJ. The face sheets and core of the sandwich composite consisted of plain-weave carbon/epoxy prepreg and Nomex® honeycomb materials, respectively. The panels contained artificially inserted holes and notches, representative of common failure modes, such as those resultant of impact (e.g., caused by tool drops, runway stones, etc.), debonded repair patches, and blade separation. Each panel was subjected to a combination of internal pressurization, hoop, and longitudinal loads designed to cause additional damage during loading.

Series of strain surveys and residual strength tests were conducted for each of the panels. Global and local deformation and strain fields were monitored using strain gages and a three-dimensional (3-D) digital image correlation (DIC) system. The panels were quasi-statically loaded up to either panel fracture or the maximum load capacity of the test fixture. Catastrophic fracture occurred at loads far exceeding realistic flight loading conditions. While the panels generally exhibited few stages of visible damage extension prior to catastrophic fracture, the DIC system provided comprehensive full-field data on the redistribution of the strain fields with the corresponding changes in the state-of-damage. The full-field DIC data allowed for the characterization of the elevated strain fields ahead of the damage (e.g., in terms of maximum strain, strain concentration factors, the shape of the elevated strain field, etc.) and the identification of those strain components that drove damage progression.

The state-of-damage in the panels was qualitatively and quantitatively characterized, pretest and posttest, using various nondestructive inspection (NDI) methods, including

thermography, computer-aided tap testing (CATT), ultrasound, and x-radiographic computed tomography (CT). A great deal of effort was placed on the real-time monitoring of damage initiation and progression using the acoustic emission (AE) and frequency response (FR) methods. The morphology of the ensuing fracture surfaces near the notch tips were evaluated via scanning electron microscopy (SEM).

The conventional wisdom of using AE as a nondestructive evaluation technique is that it could serve multiple purposes, namely: detecting the initiation and progression of damage, and determining when it occurs in terms of load; locating sites of failure and tracking its progression; and determining the dominant failure modes. Each of these purposes was addressed, evaluating their feasibility and the measure of their success in monitoring the formation, progression, and eventual instability of damage. Further, the AE method provided early warning of incipient failures and of imminent fracture.

The difficulties in using AE for distinguishing different failure mechanisms in complex, full-scale, composite structures that are subjected to combine loading were explored in great detail, including thorough analyses of the distributions of intensities of the accumulated AE signals and the frequency content of individual waveforms. Studies on the potential errors related to sensor failure and the saturation of AE channels were conducted as well. The FR method was used to actively monitor the severity of notch tip damage during loading. An extensive series of calibration studies were conducted to better understand the dependence of signal attenuation on the length and orientation of the wave path through the inspected material.

The primary objective of the computational phase of the research was to accurately and efficiently simulate the formation, progression, and eventual instability of damage originating at severe artificial damage in the full-scale sandwich composite fuselage panels through use of the finite element (FE) method. While several advanced computational failure models have been developed for composite materials, most of their derivations and validations have been performed on the coupon-scale in a laboratory environment, neglecting issues related to scalability and real-

world application. The modification and application of existing composite material failure concepts to full-scale fuselage structures are necessary for their use in future in-depth aircraft damage tolerance studies and certifications. Computational tools and damage models to be used toward this end were developed and applied, with their predictions validated via the experimental data obtained in this work.

The comprehensive deformation and strain data and the characterization of subsurface damage via NDI offered means of validating both the general far-field response of the panels and the evolution of damage ahead of the artificial stress risers. Due both to the large disparity in the characteristic lengths of the panels and the notches, and to the complex 3-D states-of-damage ahead of the notch tips, a global/local analysis was performed. Two-dimensional shell elements were used for the global models, representing the entire panels, while 3-D solid elements were used for the local models in the vicinity of the notch tips. The results of the global models were used to drive the boundary conditions of the local models. Custom user subroutines were developed to properly define the local model boundary conditions and to allow the formation and propagation of damage through them.

The material degradation failure method was adopted while modeling the face sheet material using three separate damage state variables, one in each principal material direction. Due to significant transverse shear strains in the vicinity of the damage, typical shell-to-solid submodeling algorithms were no longer applicable near the areas of interest. In order to both increase the accuracy of the local FE model results and maintain the efficiency of the global/local analysis, the local model submodeling boundary conditions were modified to incorporate the global model transverse shear strain results.

Furthermore, an alternative method to global/local FE model co-simulation was proposed and implemented. A set of adaptive boundary conditions was defined to ensure proper driving of the local models while damage progressed, shifting the center of the predicted elevated strain field. A library of global FE model solutions was developed. The results within this library were

queried and interpolated to produce a custom set of global model results corresponding to the applied loads and the severity of damage of the local model for each iteration throughout its solution.

9.2. CONCLUSIONS

Below are listed the major conclusions of this experimental and computational investigation. Additional detailed finding are provided in the conclusion sections of the corresponding chapters:

9.2.1. VISUAL OBSERVATIONS DURING FULL-SCALE TESTING

With regards to the visual observations of the development of damage during the full-scale testing of the composite panels, it was found that:

1. Despite the severity of the inserted artificial damage modes (e.g., 10-inch long, 0.5 inch wide, through-thickness notches), each of the panels withstood quasi-statically applied loads far exceeding realistic flight loading conditions. Four of the six tested panels were loaded up to catastrophic fracture.
2. Damage progressed in sudden bursts, tending to abruptly extend through whole fiber tows. Upon exhibiting less than 1.4 inches of damage extension (i.e., less than 2% of the full panel length) ahead of the notch tips in three of the panels, the notch tip damage suddenly extended to nearly the entire length of the panel.
3. Damage progression from the notch tips tended to be self-similar, though the precise location of the notch tips with respect to the plain-weave prepreg material influenced both the failure strain associated with damage initiation and the initial direction of damage propagation. For panels CP4 and CP6, the influence of the plain-weave geometry of the face sheets diverted the damage propagation path away from the original notch axis, either delaying or altogether avoiding the ultimate fracture of the panel.

9.2.2. STRAIN AND DEFORMATION FIELDS

With regards to the local- and far-field strain and deformation results recorded with the strain gages and the DIC system in each of the panels, it was found that:

4. The strain response to applied load was generally linear throughout loading prior to the initiation of any damage. However, nonuniformity of the hoop and longitudinal strains throughout the panels was observed. The applied longitudinal loads were consistently attracted to the load application regions of the panels due to the widespread uniformity of the panel test section. Previously tested aluminum skin fuselage panels contained skeletal substructures which provided more uniform distributions of strain within each bay.
5. Of the four panels that fractured catastrophically, indications of incipient failure processes (e.g., in terms of visual damage, strain gage readings, and DIC measurements) were observed at load levels between 56% and 67% of the panel fracture loads, offering several opportunities to characterize the development and progression of notch tip damage prior to catastrophic failure.
6. The full-field DIC measurements greatly expanded the possible analyses of notch tip damage initiation, formation, and progression. The effective notch tip damage extensions, later used for local FE model validations, were characterized by the locus of the elevated, kidney-shaped, strain fields ahead of the notch tip. The components of strain that drove damage progression were identified jointly by the DIC strain contour plots and the severity of the visual damage.

9.2.3. CHARACTERIZATION OF INTERNAL DAMAGE

With regards to the pretest and posttest NDI inspections of the panels and the examination of the fracture surface morphology at the notch tips, it was found that:

7. Thermography successfully mapped out the internal structure of the composite face sheets and detected nonvisual, subsurface defects parallel to the inspected surface. For the particular

operating conditions used in this study, the thermographic measurements were capable of locating a disbond between the inspected face sheet and the core, but could not penetrate into the core or through to the opposite face sheet. Therefore, thermography should perform well at detecting delaminations in solid laminates, but access to both the external and internal surfaces of sandwich composites is required to detect delaminations.

8. The CATT system was effective at detecting and quantifying both the extent and severity of delaminations and disbonds, successfully detecting both near- and far-side disbonds in the investigated sandwich composite material. For the high-resolution scans performed, the method proved to be time consuming when compared to thermography. However, lower-resolution scans could be performed in the field, increasing the speed at which inspections could be completed without significantly decreasing the threshold of detectability.
9. Ultrasonic inspection results were comparable to the thermographic data in terms of mapping out the internal structure of the face sheets and detecting in-plane defects. Neither the quality of the skin-to-core bond nor the integrity of the honeycomb core could be assessed with the test setup employed. The frequencies at which the panels were scanned (i.e., 10 and 15 MHz) were too high to characterize the honeycomb core, through which significant high-frequency signal attenuation is typical.
10. X-radiographic CT scans clearly visualized several structural components of the sandwich composites. However, the relatively large size of the specimens (i.e., between 20 and 30 inches in length) made any inspection of the interlaminar states-of-damage difficult to assess due to the resulting low spatial resolution of the data.
11. Fractographic examinations offered supplementary information regarding the specific failure modes, their locations, and their multiplicity. Several failure modes were observed, including matrix cracking, delamination, fiber/matrix interfacial failure, the fracture of both fiber filaments and bundles, and the pull-out of fiber tows and bundles from the weave. However, it is worth noting that these observations were made from a specimen of a panel which had

undergone catastrophic failure, and that some of the modes of damage may have not developed prior to the abrupt, high-energy fracture.

9.2.4. MONITORING ACOUSTIC EMISSION

The acoustic emission results and analyses indicated that:

12. Monitoring AE in large composite structures provides early indication for both incipient damage development and ultimate panel fracture. AE activity was first detected from the notch tip regions between 45% and 65% of the panel fracture loads while using either resonant or wideband sensors. The rate of AE event accumulation increased exponentially immediately preceding the catastrophic failure of the panels.
13. The large composite structures tested in this investigation contained several sources of extraneous emission (i.e., emission not associated with the formation of new fracture surfaces). The most predominant sources of extraneous emission were the test fixture loaders and supports and fretting among existing fracture surfaces.
14. The AE source locations associated with new failures coincided with the notch tip regions of each panel. However, the extraneous panel-wide emissions often obscured the notch tip regions. Hit-based filtering (rather than feature-based filtering) was adopted to remove the AE signals associated with extraneous emission. This decreased the dependence of the filtering scheme on the features of the first-recorded hits of locatable events. It was found that 5-hit event filtering (i.e., considering only events in which AE signals were recorded by at least 5 sensors) performed best in isolating the notch tip emissions.
15. The complexity of the large composite panels makes it, for all practical purposes, impossible to identify specific failure modes through reduction of the collected AE data. Comparisons between emissions generated from several known sources, including the notch tips, the fretting of existing fracture surfaces, and the test fixture supports, were made, revealing

similar distributions of waveform features (i.e., amplitude, duration, counts, energy, peak frequency, etc.), whether recorded by resonant or wideband sensors.

16. When the load approaches its ultimate, the rate at which AE signals are recorded increases exponentially, and the propensity for multiple stress waves to interfere with another increases, as well. Such instances of AE signal interference affect the accuracy of the determined source locations, the distributions of AE signal intensities, etc. Considering the percentage of time an AE channel spent recording data, with respect to some characteristic period of the total test time, can be used to estimate the frequency at which such instances of interference may have occurred.
17. While using resonant sensors, the average frequency (i.e., counts per duration) of an AE signal serves as a good indicator as to whether a recorded signal was caused by either a single stress wave or a train of AE signals originating from different sources.

9.2.5. MONITORING DAMAGE VIA FREQUENCY RESPONSE

The results of the frequency response testing indicated that:

18. The transmitted signals are highly sensitive to the presence of internal damage, particularly under load. Increasingly severe states-of-damage caused for markedly increased signal attenuation in the investigated material.
19. While certain frequency ranges attenuated more than others during damage progression, no significant frequency shifts of the dominant frequencies were observed.
20. The FR technique was comparable in sensitivity to the AE method in terms of detecting incipient damage. Significant FR signal attenuation was observed at 70% of the panel CP5 fracture load, while the initial indications of incipient failure by AE occurred at 57% of the fracture load; visual damage was not observed until 82% of the fracture load.
21. The FR results are highly dependent on the pulser-receiver sensor separation distance, the orientation of the monitored wave path with respect to the principal directions of the

orthotropic material, and the precise placement of the sensors with respect to the plain-weave unit cells. As a result, both the pulser and receiver should remain stationary throughout the test. Further, all FR data are applicable to a particular set of test conditions, including, input voltage, frequency input, quality of sensor coupling, etc.

22. The purpose of the FR technique is not to distinguish specific modes of failure. The effects of various modes of failure on the characteristics of the power spectrum requires testing with model specimens that exhibit a single mode of failure (e.g., matrix cracking, delamination, etc.) under loading. Due to the complex transfer function associated with wave propagation through composite materials, such testing would be required for each new combination of constituent materials and laminate configuration.

9.2.6. GLOBAL FINITE ELEMENT MODELS

With regards to the development of the global FE models and their residual strength test predictions, it was found that:

23. The nonuniform strain distributions characterized by the strain gage and DIC data sets required an in-depth representation of the panels, taking into consideration the panel geometries, composite lay-ups, and the details of test fixture loading mechanisms.
    i. The details of the panel geometry relative to the load applications points caused much of the nonuniformity of the hoop and longitudinal strain distributions.
    ii. Modeling the test fixture loading mechanisms accounted for additional panel bending and nonlinearity of strain with applied load which was otherwise neglected by simpler models.
24. Free play in the test fixture loaders often introduced a fixed offset, in terms of strain, between the experimental and computational results. Accordingly, the experimental strain data were shifted to ensure that the measured results were those due to the applied loads and not due to

free play in the loaders, and to ensure that valid comparisons could be made between the two data sets.

25. Excellent correlation, in terms of the notch tip strain distributions, the size and shape of the elevated strain field, and the notch tip strain concentration factors, was observed between the strain data recorded via the arrays of strain gages and the DIC method, and predicted via the global FE models for each of the notched panels tested in this investigation.

9.2.7. LOCAL FINITE ELEMENT MODELS

With regards to the development of the local FE models, the failure model, the modified shell-to-solid submodeling boundary conditions, the adaptive local model boundary conditions, and the predictions of notch tip damage progression, it was found that:

26. A failure model was successfully applied to predict damage, from initiation to instability, in the local FE models of the panels which experimentally exhibited self-similar notch tip damage progression throughout loading. In every panel, the initiation and early stages of notch tip damage development were well predicted. The experimental and computational damage progression results correlated well in terms of visual observations, strain gage, DIC, AE, and FR data.
27. The comparable dimensions of the notches and the plain-weave unit cell required further consideration of the heterogeneity of the plain-weave face sheet material. While the average rate of damage progression was well modeled, the experimentally observed bursts of damage could not be represented computationally.
28. The path of damage progression in two of the six tested panels was clearly affected by the geometry of the plain-weave fabric. In hindsight, meshing the face sheet plies independently, so as to be orthogonal to the principal material directions, may have better predicted this behavior.

29. The continuity of the strain field between the global and local models was improved by developing a new modified definition of submodeling boundary conditions. As a result, the interface between the local and global models could be moved closer to the areas of interest in similar shell-to-solid submodels, thus decreasing simulation times.
30. The implementation of the proposed local model adaptive boundary conditions allowed for the successful prediction of notch tip damage instability. While the sudden bursts of damage progression were not modeled, the predicted smooth progression of damage exponentially increased to coincide with the observed step-wise progression and damage instability.

9.3. FUTURE WORK RECOMMENDATIONS

Extensive work has been performed on the development and refinement of failure criteria and damage evolution laws for use in FE models capable of representing the early stages of damage progression (i.e., from the micro-scale to laminate-level severity). The scalability of such advanced failure models and concepts is an important area of research and merits further investigation. Assessing the scaling limits of specific models as they currently exist and appropriately adapting them to full-scale applications will expand the available toolset for damage tolerance studies of large composite structures. In this thesis, several modifications to the application of submodeling boundary conditions have been proposed to allow for the application of progression damage modeling concepts, which were developed on the coupon-scale, to full-scale engineering structures.

The scalability of any damage mode interactions must be investigated, determining if a characteristic scale and/or severity of damage exist where certain higher-level assumptions become negligible. For example, while the interactions of matrix cracking and delaminations are critical during the initial stages of damage development in coupon-scale specimens, these interactions may become less influential after a certain characteristic amount of damage progression, in terms of either size or severity. Assuming that characteristic scale limits exist for

the current implementations of progressive damage modeling techniques, methods to further expand the applicable limits of each should be explored. Homogenization of the detailed failure processes in small-scale models should be investigated, considering the determined limits of the detailed failure criteria and damage evolution laws in terms of both size and severity.

Convergence issues are commonplace in progressive damage models in which regular modifications to the global stiffness matrix are required. These convergence issues are rooted in the related material and structural instabilities and their interactions, and often lead to the maximum achievable load increments being several orders of magnitude below the target loads. As a result, the representation of gradual failure processes over large load ranges becomes unreasonable in terms of computational cost. Current FE solvers fail to provide any useful feedback concerning either the type or location of the instabilities, often requiring broad solutions such as the temporary artificial toughening of the damaged material to slow the rapidity of failure. While convergence issues are inherent to modifying the global stiffness matrix, improvement of solver feedback regarding the location, severity, and type of instabilities may allow for significant refinement of the mathematical devices used to overcome current convergence issues. Means of identifying the root cause of the most severe instabilities should be investigated and a useful user feedback system developed.

LIST OF REFERENCES

1.1 Deo, R.B., Starnes, J.H., & Holzwarth, R.C. (2003). Low-cost Composite Materials and Structures for Aircraft Applications. RTO-MP-069(II).

1.2 Ilcewicz, L.B., Walker, T.H., & Willden, K.S. (1991). Application of a Design-Build-Team Approach to Low Cost and Weight Composite Fuselage Structure. NASA CR 4418.

1.3 Scholz, B.B., Dost, E.F., & Flynn, B.W. (1997). Advanced Technology Composite Fuselage–Materials and Processes. NASA CR 4731.

1.4 Bitzer, T.N. (1992). Honeycomb Materials and Applications. Sandwich Constructions 2 – *Proceedings of the Second International Conference on Sandwich Construction*. pp. 681-691.

1.5 Tomblin, J., Lacy, T., & Smith, B. (1999). Review of Damage Tolerance for Composite Sandwich Airframe Structures. DOT/FAA/AR-99/49.

1.6 Gunter, L. (2005, March). The Dreamliner team unveils the historic first composite development barrel for the airplane. *Boeing Frontiers*, 3(10).

1.7 "Boeing: Commercial Airplanes - 787 Dreamliner - Background," URL: http://www.boeing.com/commercial/787family/background.html [cited 24 April 2010].

1.8 Swindeman, M.J., Brockman, R.A., & Iarve, E. (2010). Composite Failure Predication by Explicit Matrix Cracking and Delamination Networks. *Aircraft Airworthiness & Sustainment Conference*, Austin, TX.

1.9 Nikishkov, Y., Makeev, A., & Cline, C. (2010). Durability and Damage Tolerance Models for Composite Structures. *Aircraft Airworthiness & Sustainment Conference*, Austin, TX.

1.10 Composite Aircraft Structure. (2010, August). FAA Advisory Circular 20-107B.

1.11 Damage Tolerance Assessment Handbook, Volume I: Introduction, Fracture Mechanics, Fatigue Crack Propagation. DOT/FAA/CT-93/69.I, 1993.

1.12 Damage Tolerance Assessment Handbook, Volume II: Airframe Damage Tolerance Evaluation. DOT/FAA/CT-93/69.II, 1993.

1.13 Damage Tolerance and Fatigue Evaluation of Structure. (1998, April). FAA Advisory Circular 25.571-1C.

1.14 Bakuckas, J.G. Jr. (2001). Full-Scale Testing of Fuselage Structure Containing Multiple Cracks. DOT/FAA/AR-01/46.

1.15 Ahmed, A., & Bakuckas, J.G. (2005). Development of multiple site damage in fuselage structures. DOT/FAA/AR-05/38.

1.16 Mosinyi, B., Bakuckas J.G., & Steadman, D. (2007). Destructive evaluation and extended fatigue testing of retired transport aircraft, volume 4; extended fatigue testing. DOT/FAA/AR-07/22,4.

1.17 Federal Aviation Administration. (2006, April). Aging Aircraft Program: Widespread Fatigue Damage. *Federal Register*, *71*(74), 19928–19951.

1.18 Jackson, A.C., Campion, M.C., & Pei, G. (1984). Study of Utilization of Advanced Composites in Fuselage Structures of Large Transports. NASA-CR-172404.

1.19 Tomblin, J.S., Raju, K.S., & Liew, J. (2001). Impact Damage Characterization and Damage Tolerance of Composite Sandwich Airframe Structures. DOT/FAA/AR-00/44.

1.20 Tomblin, J.S., Raju, K.S., & Acosta, J.F. (2001). Impact Damage Characterization and Damage Tolerance of Composite Sandwich Airframe Structures—Phase II. DOT/FAA/AR-02/80.

1.21 Lacy, T.E., Samarah, I.K., & Tomblin, J.S. (2002). Damage Tolerance Characterization of Sandwich Composites using Response Surfaces. DOT/FAA/AR-02/101.

1.22 Shyprykevich, P., Tomblin, J.S., & Ilcewicz, L. (2003). Guidelines for Analysis, Testing, and Nondestructive Inspection of Impact-Damaged Composite Sandwich Structures. DOT/FAA/AR-02/121.

1.23 Tomblin, J.S., Raju, K.S., & Arosteguy, G. (2004). Damage Resistance and Tolerance of Composite Sandwich Panels–Scaling Effects. DOT/FAA/AR-03/75.

1.24 Tomblin, J.S., Raju, K.S., & Walker, T. (2005). Damage Tolerance of Composite Sandwich Airframe Structures–Additional Results. DOT/FAA/AR-05/33.

2.1 Tay, T.E., Liu, G., Tan, & V.B.C. (2008). Progressive Failure Analysis of Composites. *Journal of Composite Materials*, *42*(18), 1921–1966.

2.2 Daniel, I.M. (2007). Failure of Composite Materials. *Strain*, *43*, 4–12.

2.3 Jones, R.M. (1999). *Mechanics of Composite Materials, Second Edition*. Philadelphia, PA: Taylor & Francis, Inc.

2.4 Tsai, S.W. (1968). Strength Theories of Filamentary Structures. *Fundamental Aspects of Fiber Reinforced Plastic Composites*, Dayton, OH, 24–26 May 1966, New York, NY: Wiley Interscience, pp. 3–11.

2.5 Hill, R. (1950). *The Mathematical Theory of Plasticity*. London: Oxford University Press, p. 318.

2.6 Tsai, S.W., & Wu, E.M. (1971, January). A General Theory of Strength for Anisotropic Materials. *Journal of Composite Materials*, *5*, 58–80.

2.7 Hashin, Z., & Rotem, A. (1973, October). A Fatigue Criterion for Fiber Reinforced Materials. *Journal of Composite Materials*, *7*, 448–464.

2.8 Hashin, Z. (1980, June). Failure Criteria for Unidirectional Fiber Composites. *Journal of Applied Mechanics*, *47*, 329–334.

2.9 Puck, A., & Shürmann, H. (1998). Failure analysis of FRP laminates by means of physically based phenomenological models. *Composites Science and Technology*, *58*, 1045–1067.

2.10 Mohr, O. (1900). Which circumstances are causing yield limit and fracture of a material? *Civilingenieur*, *44*, 1524–1530 and 1572–1577.

2.11 Soden, P.D., Hinton, M.J., & Kaddour, A.S. (1998). A comparison of the predictive capabilities of current failure theories for composite laminates. *Composites Science and Technology*, *58*, 1225–1254.

2.12 Hinton, M.J., Kaddour, A.S., & Soden, P.D. (2002). A comparison of the predictive capabilities of current failure theories for composite laminates, judged against experimental evidence. *Composites Science and Technology*, *62*, 1725–1797.

2.13 Dávila, C.G., & Camanho, P.P. (2003). Failure Criteria for FRP Laminates in Plane Stress. *NASA/TM-2003-212663*.

2.14 Hahn, H.T., & Johannesson, T. (1983). Fracture of Unidirectional Composites: Theory and Applications. In G.J. Dvoark (Ed.) *Mechanics of Composite Materials* (pp. 135–142), AMD.

2.15 Pinho, S.T., Dávila, C.G., & Camanho, P.P. (2005). Failure Models and Criteria for FRP Under In-Plane or Three-Dimensional Stress States Including Shear Non-Linearity. *NASA/TM-2005-213530*.

2.16 Chandra, A., Huang, Y., & Hu, K.X. (1997). Crack-size dependence of overall responses of fiber-reinforced composites with matrix cracking. *International Journal of Solids and Structures*, *34*(29), 3837–3857.

2.17 Rousselier, D. (1979). Numerical treatment of crack growth problems. In L.H. Larson (Ed.) *Advances in Elasto-plastic Fracture Mechanics*, (pp. 165–189).

2.18 Bakuckas, J.G., Lau, A.C.W., & Tan, T.-M. (1995). Computational methodology to predict damage growth in unidirectional composites—I. Theoretical formulation and numerical implementation. *Engineering Fracture Mechanics*, *52*(5), 937–951.

2.19 Tay, T.E., Tan, V.B.C., & Deng, M. (2003). Element-failure concepts for dynamic fracture and delamination in low-velocity impact of composites. *International Journal of Solids and Structures*, *40*, 555–571.

2.20 Hahn, H.T., & Tsai, S.W. (1974). On the behavior of composite laminates after initial failures. *Journal of Composite Materials*, *8*(3), 288–305.

2.21 Beissel, S.R., Johnson, G.R., & Popelar, C.H. (1998). An element-failure algorithm for dynamic crack propagation in general directions. *Engineering Fracture Mechanics*, *61*, 407–425.

2.22 Tan, S.C. (1991). A Progressive Failure Model for Composite Laminates Containing Openings. *Journal of Composite Materials*, *25*, 556–577.

2.23 Nuismer, R.J., & Tan, S.C. (1988). Constitutive Relations of a Cracked Composite Lamina. *Journal of Composite Materials*, *22*, 306–321.

2.24 Matzenmiller, A., Lubliner, J., & Taylor, R.L. (1995). A constitutive model for anisotropic damage in fiber-composites. *Mechanics of Materials*, *20*, 125–152.

2.25 Lapczyk, I., & Hurtado, J.A. (2007). Progressive damage modeling in fiber-reinforced materials. *Composites: Part A*, *38*, 2333–2341.

2.26 Maimí, P., Camanho, P.P., & Mayugo, J.-A. (2006). A Thermodynamically Consistent Damage Model for Advanced Composites. *NASA/TM-2006-214282*.

2.27 Lee, J.D. (1982) Three dimensional finite element analysis of damage accumulation in composite laminate. *Computers & Structures*, *15*(3), 335–350.

2.28 Tan, S.C., & Perez, J. (1993). Progressive Failure of Laminated Composites with a Hole under Compressive Loading. *Journal of Reinforced Plastics and Composites*, *12*, 1043–1057.

2.29 Camanho, P.P., & Matthews, F.L. (1999). A Progressive Damage Model for Mechanically Fastened Joints in Composite Laminates. *Journal of Composite Materials*, *33*, 2248–2280.

2.30 Reddy, Y.S.N., Moorthy, C.M.D., & Reddy, J.N. (1995). Non-Linear Progressive Failure Analysis of Laminated Composite Plates. *International Journal of Non-Linear Mechanics*, *30*(5), 629–649.

2.31 Gama, B.A., Bogetti, T.A., & Gillespie, J.W. (2009). Progressive Damage Modeling of Plain-Weave Composites using LS-Dyna Composite Damage Model MAT162. *7th European LS-DYNA Conference*, Salzburg, Austria.

2.32 Bažant, Z.P., & Oh, B.H. (1983). Crack band theory for fracture of concrete. *Materials and Structures*, *16*, 155–177.

2.33 Dolbeer, R.A., Wright, S.E., & Weller, J. (2009, September). Wildlife Strikes to Civil Aircraft in the United States 1990–2008. FAA National Wildlife Strike Database, Serial Report Number 15.

2.34 Garrett, R.A. (1985). Effect of manufacturing defects and service-induced damage on the strength of aircraft composite structures. *National SAMPE Technical Conference*, 325–341.

2.35 Petras, A., & Sutcliffe, M.P.F. (1999). Failure mode maps for honeycomb sandwich panels. *Composite Structures*, *44*, 237–252.

2.36 Kim, R.Y., & Aoki, R.M. (1983, April). Transverse cracking and delamination in composite materials. *Fibre Science and Technology*, *18*(3), 203–216.

2.37 Stein, P.K. (2001, March). Strain Gage History and the End of the Twentieth Century. *Experimental Techniques*, *25*(2), 15–16.

2.38 Tuttle, M.E., & Brinson, H.F. (1983). Transverse sensitivity effects of strain gages on orthotropic composite materials. *Proceedings of the Society for Experimental Stress Analysis*, 6–10.

2.39 Lang, E.J., & Chou, T.-W. (1998). The effect of strain gage size on measurement errors in textile composite materials. *Composites Science and Technology*, *58*, 539–548.

2.40 Zhang, D., Miao, L., & Arola, D.D. (2006, March). Displacement/strain measurements using an optical microscope and digital image correlation. *Optical Engineering*, *45*(3).

2.41 Pan, B., Qian, K., & Xie, H., (2009). Two-dimensional digital image correlation for in-plane displacement and strain measurement: a review. *Measurement Science and Technology*, *20*, 1–17.

2.42 *ARAMIS User Manual – Software (ARAMIS v6.1 and higher)*, (2009, August). GOM mbH.

2.43 Bruck, H.A., McNeill, S.R., & Sutton, M.A. (1989). Digital Image Correlation Using Newton-Raphson Method of Partial Differential Correction. *Experimental Mechanics*, *29*(3), 261–268.

2.44 Gere, J.M., & Goodno, B.J. (2008). *Mechanics of Materials, 7th edition*. CL-Engineering.

2.45 Spencer, A.J.M. (2004). *Continuum Mechanics*, Dover Publications; Dover Ed edition.

2.46 *Nondestructive Testing Handbook, Volume 6, Acoustic Emission Testing, Third Edition* (2005). ASNT.

2.47 Spanner, J.C. (1974). *Acoustic Emission: Techniques and Applications*, Intex Publishing Company.

2.48 Stephens, R.W., & Pollock, A.A. (1971). Waveforms and Frequency Spectra of Acoustic Emission. *Journal of the Acoustical Society of America*, *50*(3), 904–910.

2.49 Groot, P.J., Wijnen, P.A.M., & Janssen, R.B.F. (1995). Real-Time Frequency Determination of Acoustic Emission for Different Fracture Mechanisms in Carbon-Epoxy Composites. *Composites Science and Technology*, *55*, 405–412.

2.50 Drouillard, T.F. (1979). *Acoustic emission: A bibliography with abstracts*. New York, NY: Plenum Publishing.

2.51 Drouillard, T.F. (1990). Anecdotal history of acoustic emission from wood. *Journal of Acoustic Emission*, *9*(3), 155–176.

2.52 Drouillard, T.F. (1996). A history of acoustic emission. *Journal of Acoustic Emission*, *14*(1), 1–34.

2.53 Fuwa, M., Bunsell, A.R., & Harris, B. (1975). Tensile failure mechanisms in carbon fibre reinforced plastics. *Journal of Materials Science*, *10*, 2062–2070.

2.54 Fuwa, M., Harris, B., & Bunsell, A.R. (1975). Acoustic emission during cyclic loading of carbon-fibre-reinforced plastics. *Journal of Physics D: Applied Physics*, *8*, 1460–1471.

2.55 Bussiba, A., Kupiec, M., & Piat, R. (2008). Fracture characterization of C/C composites under various stress modes by monitoring both mechanical and acoustic responses. *Carbon*, *46*, 618–630.

2.56 Berthelot, J.M., & Rhazi, J. (1990). Acoustic Emission in Carbon Fibre Composites. *Composites Science and Technology*, *37*, 411–428.

2.57 Awerbuch, J., & Ghaffari, S. (1986). Monitoring Progression of Matrix Splitting During Fatigue Loading Through Acoustic Emission in Notched Graphite/Epoxy Composites. *Proceedings of the Second International Symposium on Acoustic Emission from Reinforced Composites*, The Society of the Plastic Industry, Inc., Montreal, Canada, 51–58.

2.58 Eckles, W.W., & Awerbuch, J. (1986). Monitoring Acoustic Emission in Cross-Ply Graphite/Epoxy Laminates During Fatigue Loading. *Proceedings of the Second International Symposium on Acoustic Emission from Reinforced Composites*, The Society of the Plastic Industry, Inc., Montreal, Canada, 78–84.

2.59 Awerbuch, J., & Ghaffari, S. (1986). Effect of Friction Emission on Monitoring Damage in Composite Laminates Through Acoustic Emission. *Progress in Acoustic Emission III*, The Japanese Society of NDI, 638–652.

2.60 Awerbuch, J., & Ghaffari, S. (1986). Tracking Progression of Matrix Splitting During Static Loading Through Acoustic Emission in Notched Unidirectional Graphite/Epoxy Composites. *Progress in Acoustic Emission III*, The Japanese Society of NDI, 575–585.

2.61 Sypeck, D.J. (1996). *Damage evolution in titanium matrix composites* (Doctoral dissertation). Retrieved from ProQuest Dissertations and Theses Database. (AAT 9701350).

2.62 Kundu, T., Das, S., & Martin, S.A. (2007). Point of impact prediction in isotropic and anisotropic plates from the acoustic emission data. *Journal of the Acoustical Society of America*, *122*, 2057–2066.

2.63 Kundu, T., Das, S., & Martin, S.A. (2008). Locating point of impact in anisotropic fiber reinforced composite plates. *Ultrasonics*, *48*: 193–201.

2.64 Gorman, M.R. (1991). Acoustic Emission for the 1990s. *Proceedings of the 1991 Ultrasonics Symposium*, *2*, 1039–1046.

2.65 Gorman, M.R. (1991). Plate wave acoustic emission. *Journal of Acoustical Society of America*, *90*(5), 358–364.

2.66 Gorman, M.R., & Prosser, W.H. (1990). AE source orientation by plate wave analysis. *Journal of Acoustic Emission*, *9*(4), 283–288.

2.67 Surgeon, M., & Wevers, M. (1999). Modal analysis of acoustic emission signal from CFRP laminates. *NDT&E International*, *32*, 311–322.

2.68 Surgeon, M., & Wevers, M. (1999). One sensor linear location of acoustic emission events using plate wave theories. *Materials Science and Engineering*, *265*(1–2), 254–261.

2.69 Becht, J., Schwalbe, H.-J., & Eisenblaetter, J. (1976). Acoustic emission as an aid for investigating the deformation and fracture of composite materials. *Composites*, 245–248.

2.70 Barré, S., & Benzeggah (1994). One the use of acoustic emission to investigate damage mechanisms in glass-fibre-reinforced polypropylene. *Composites Science and Technology*, *52*, 369–376.

2.71 Siron, O., Chollon, G., & Tsuda, H. (2000). Microstructural and mechanical properties of filler-added coal-tar pitch-based C/C composites: the damage and fracture process in correlation with AE waveform parameters. *Carbon*, *38*, 1369–1389.

2.72 Philippidis, T.P., Nikolaidis, V.N., & Anastassopoulos, A.A. (1998). Damage characterization of carbon/carbon laminates using neural network techniques on AE signals. *NDT&E International*, *31*(5), 329–340.

2.73 Vary, A. (1982). Acousto-ultrasonic characterization of fiber reinforced composites. *Materials Evaluation*, *40*(6), 650–654.

2.74 Cartz, L., (1995, September). *Nondestructive Testing: Radiography, Ultrasonics, Liquid Penetrant, Magnetic Particle, Eddy Current*. ASM International.

2.75 Krautkramer, J., & Krautkramer, H. (1990, November). *Ultrasonic Testing of Materials, 4th/revised ed.*, Spring Verlag.

2.76 Balageas, D., Bourasseau, S., & Dupont, M. (2000). Comparison between Non-Destructive Evaluation Techniques and Integrated Fiber Optic Health Monitoring Systems for Composite Sandwich Structures. *Journal of Intelligent Material Systems and Structures*, *11*, 426–437.

2.77 Růžek, R., Lohonka, R., & Jironč, J. (2006). Ultrasonic C-Scan and shearography NDI techniques evaluation of impact defects identification. *NDT&E International*, *39*, 132–142.

2.78 Howell, P.A., Winfree, W.P., & Cramer, K.E. (2008). On-orbit passive thermography. *Nondestructive Testing and Evaluation*, *23*, 195–210.

2.79 Kroll, A., Baetz, W., & Peretzki, D. (2009, May 12–17). On Autonomous Detection of Pressurized Air and Gas Leaks Using Passive IR-Thermography for Mobile Robot Application. *IEEE International Conference on Robotics and Automation*, Kobe, Japan.

2.80 Hung, Y.Y., Chen, Y.S., & Ng, S.P. (2009). Review and comparison of shearography and active thermography for nondestructive evaluation. *Materials Science and Engineering R*, *64*, 73–112.

2.81 Avdelidis, N.P., Almond, D.P., & Dobbinson, A. (2004). Aircraft composites assessment by means of transient thermal NDT. *Progress in Aerospace Sciences*, *40*, 142–162.

2.82 Carslaw, H.S., & Jaeger, J.C. (1986). *Conduction of Heat in Solids*. Oxford: Clarendon Press.

2.83 ASTM WK12796 Draft Specification "Standard Practice for Infrared Flash Thermography of Composite Panels and Repair Patches Used in Aerospace Applications."

2.84 Hagemaier, D., & Fassbender, R. (1978, July). Nondestructive Testing of Adhesively Bonded Structure. *SAMPE Quarterly*, *9*, 36–58.

2.85 Hsu, D.K., Barnard, D.J., & Peters, J.J. (2001). *U.S. Patent No. 6,327,921 B1*. Washington, DC: U.S. Patent and Trademark Office.

2.86 Greszczuk, L.B. (1982). Damages in Composite Materials due to Low Velocity Impact. In J.A. Zukas, T. Nicholas, & H.F. Swift, *Impact Dynamics* (pp. 55–94) Krieger Publishing Company.

2.87 Hsu, D.K., Barnard, D.J., & Peters, J.J. (2000). Physical Basis of Tap Test as a Quantitative Imaging Tool for Composite Structures on Aircraft, In D.O. Thompson & D.E. Chimenti (Eds.), *Review of Progress in Quantitative NDE*, Vol. 19B (pp. 1857–1864) New York: American Institute of Physics.

3.1 Bakuckas, J. G. Jr. (2001). Full-Scale Testing of Fuselage Structure Containing Multiple Cracks. DOT/FAA/AR-01/46.

3.2 Bakuckas, J. G., Jr., Bigelow, C. A., & Tan, P. W. (1999). The FAA Full-scale Aircraft Structural Test Evaluation and Research (FASTER) Facility. *Proceedings from the International Workshop on Technical Elements for Aviation Safety,* Tokyo, Japan, pp. 158–170.

3.3 Raju, K.S., & Tomblin, J.S. (2009). Damage Tolerance Evaluation of Full-Scale Sandwich Composite Fuselage Panels. DOT/FAA/AR-09/9.

4.1 Raju, K.S., & Tomblin, J.S. (2009). Damage Tolerance Evaluation of Full-Scale Sandwich Composite Fuselage Panels, DOT/FAA/AR-09/9.

4.2 Schmidt, T. (2008). 3D ARAMIS: Sensitivity, Accuracy and Data Validity Considerations. Trilion Quality Systems LLC, West Conshohocken, PA.

6.1 Fuwa, M., Bunsell, A.R., & Harris, B. (1975). Tensile failure mechanisms in carbon fibre reinforced plastics. *Journal of Materials Science*, *10*, 2062–2070.

6.2 Hamstad, M.A. (1986). A discussion on the basic understanding of the Felicity Effect in fiber composites. *Journal of Acoustic Emission*, *5*(2), 95–102.

6.3 Barré, S., & Benzeggah (1994). One the use of acoustic emission to investigate damage mechanisms in glass-fibre-reinforced polypropylene. *Composites Science and Technology*, *52*, 369–376.

6.4 Siron, O., Chollon, G., & Tsuda, H. (2000). Microstructural and mechanical properties of filler-added coal-tar pitch-based C/C composites: the damage and fracture process in correlation with AE waveform parameters. *Carbon*, *38*, 1369–1389.

6.5 Awerbuch, J., & Ghaffari, S. (1986). Monitoring Progression of Matrix Splitting During Fatigue Loading Through Acoustic Emission in Notched Graphite/Epoxy Composites. In *Proceedings of the Second International Symposium on Acoustic Emission from Reinforced Composites*, The Society of the Plastic Industry, Inc., Montreal, Canada, pp. 51–58.

6.6 Eckles, W.W., & Awerbuch, J. (1986). Monitoring Acoustic Emission in Cross-Ply Graphite/Epoxy Laminates During Fatigue Loading. In *Proceedings of the Second International Symposium on Acoustic Emission from Reinforced Composites*, The Society of the Plastic Industry, Inc., Montreal, Canada, pp. 78–84.

6.7 Awerbuch, J., & Ghaffari, S. (1986). Effect of Friction Emission on Monitoring Damage in Composite Laminates Through Acoustic Emission. In *Progress in Acoustic Emission III*, The Japanese Society of NDI, pp. 638–652.

6.8 Awerbuch, J., & S. Ghaffari, S. (1986). Tracking Progression of Matrix Splitting During Static Loading Through Acoustic Emission in Notched Unidirectional Graphite/Epoxy Composites. In *Progress in Acoustic Emission III*, The Japanese Society of NDI, pp. 575–585.

6.9 Takemoto, M., Nishino, H., & Ono, K. (2000). Wavelet Transform-Applications to AE Signal Analysis. *Acoustic Emission - Beyond the Millennium*, Elsevier.

6.10 Prosser, W.H., & Gorman, M.R. (1997, March). Accurate Simulation of Acoustic Emission Sources in Composite Plates. *ASNT Spring Conference*, New Orleans.

7.1 NDT Resource Center. (2010). *Attenuation of Sound Waves*. Retrieved July 10, 2010 from http://www.ndt-ed.org/EducationResources/CommunityCollege/Ultrasonics/

8.1 Mindlin, R.D. (1951). Influence of rotary inertia and shear on flexural motions of isotropic, elastic plates. *Journal of Applied Mechanics*, *18*, 31–38.

8.2 Hinton, M.J., Kaddour, A.S., & Soden, P.D. (2002). A comparison of the predictive capabilities of current failure theories for composite laminates, judged against experimental evidence. *Composites Science and Technology*, *62*, 1725–1797.

8.3 Hashin, Z. (1980, June). Failure Criteria for Unidirectional Fiber Composites. *Journal of Applied Mechanics*, *47*, 329–334.

8.4 Matzenmiller, A., Lubliner, J., & Taylor, R.L. (1995). A constitutive model for anisotropic damage in fiber-composites. *Mechanics of Materials*, *20*, 125–152.

8.5 Maimí, P., Camanho, P.P., & Mayugo, J.-A. (2006). A Thermodynamically Consistent Damage Model for Advanced Composites. *NASA/TM-2006-214282*.

8.6 Lapczyk, I., & Hurtado, J.A. (2007). Progressive damage modeling in fiber-reinforced materials. *Composites: Part A*, *38*, 2333–2341.

8.7 Linde, P., Pleitner, J., & de Boer, H. (2004). Modelling and Simulation of Fibre Metal Laminates. *ABAQUS Users' Conference*, 421–439.

8.8 Pinho, S.T., Robinson, P., & Iannucci, L. (2006). Fracture toughness of the tensile and compressive fibre failure modes in laminated composites. *Composites Science and Technology*, *66*, 2069–2079.

8.9 *ABAQUS Online Documentation: Version 6.8*. (2008). Dassault Systèmes.

APPENDIX A: DIGITAL IMAGE CORRELATION DATA

Strain fields in the vicinity of the machined damage were recorded using the digital image correlation (DIC) method for each of panel, select measurements of which are presented here, Figure A.1. The full state-of-strain is represented through inclusion of several strain components, including those in the global 0°, 90°, and ±45° directions, and the principal and Tresca strains.

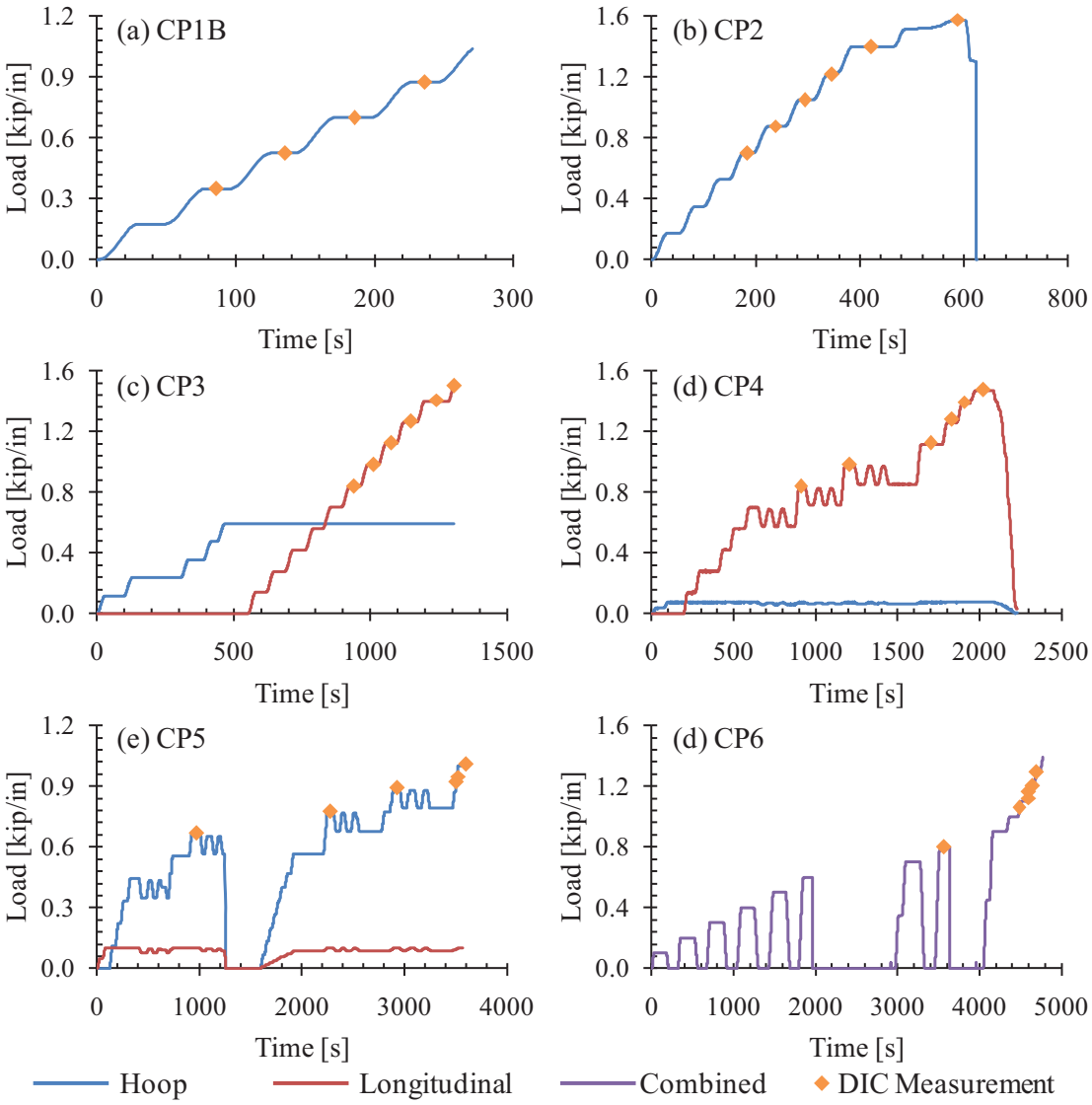

Figure A.1. Load levels at which DIC measurements for each panel are presented.

PANEL CP1B – NOTCH-NORMAL STRAIN

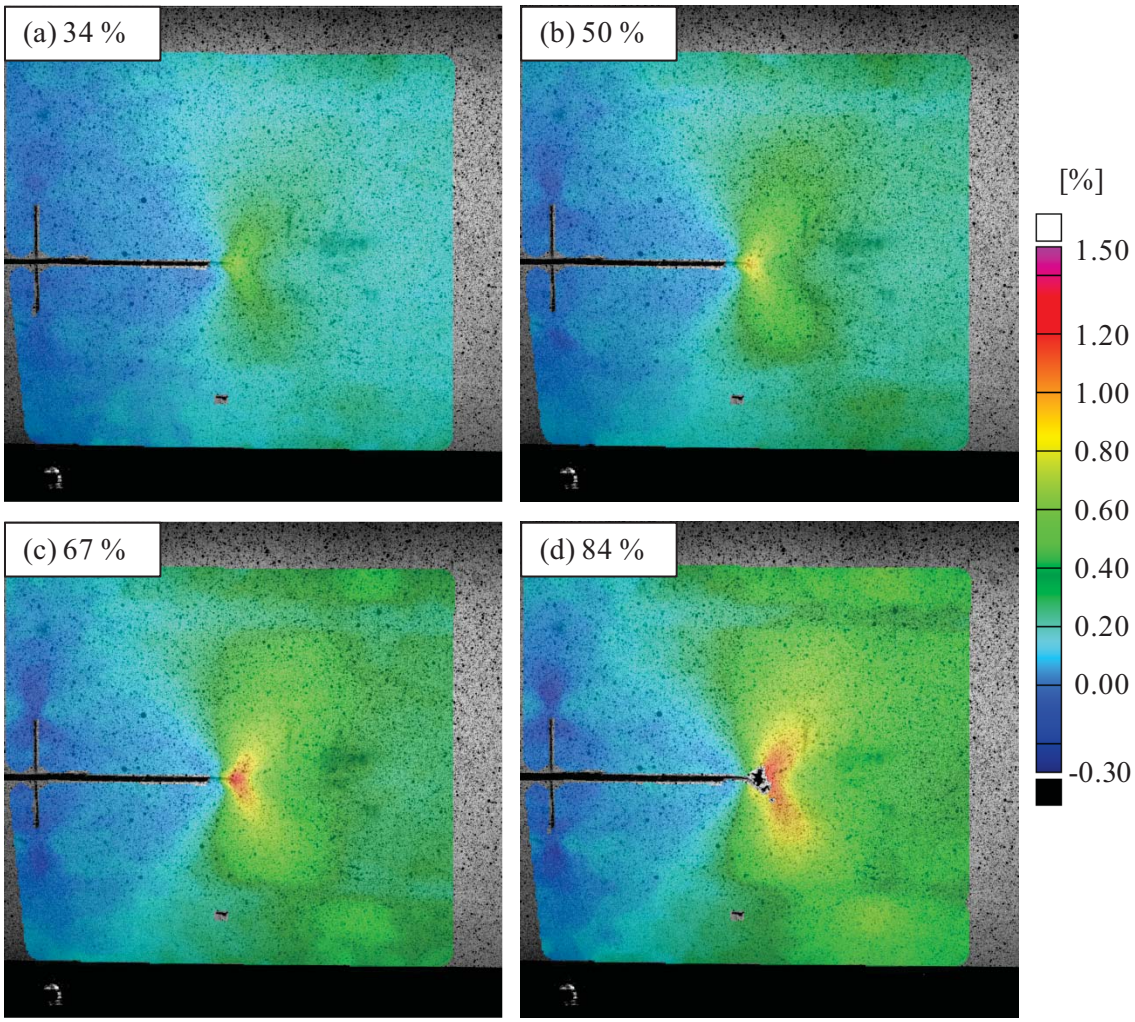

Figure A.2. Notch-normal strain for panel CP1B, run CP1B-RST-1. The panel fracture load was 14.0 psi internal pressure and 1040 lbf/in hoop load.

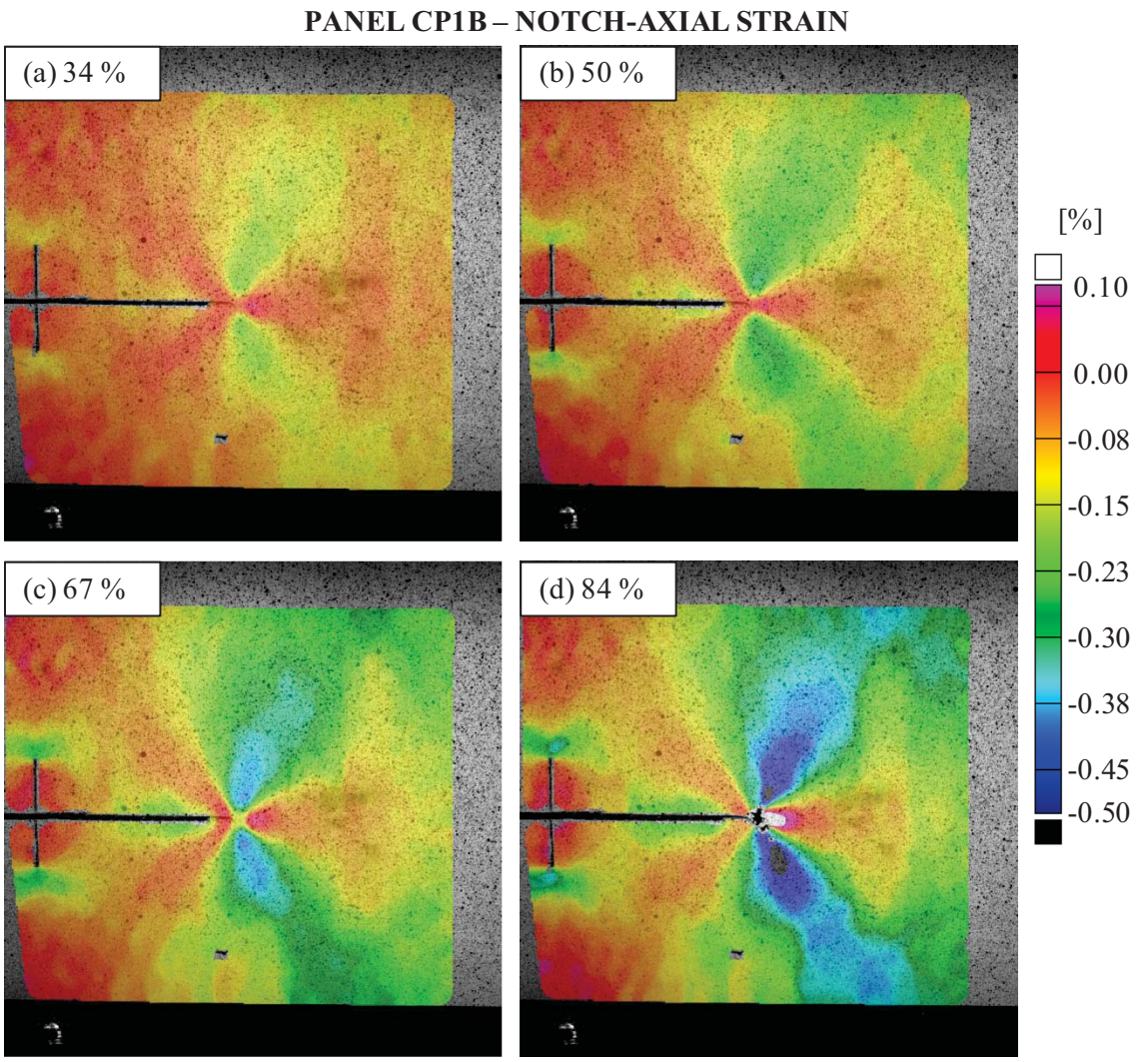

Figure A.3. Notch-axial strain for panel CP1B, run CP1B-RST-1. The panel fracture load was 14.0 psi internal pressure and 1040 lbf/in hoop load.

PANEL CP1B – STRAIN ALONG +45° DIRECTION

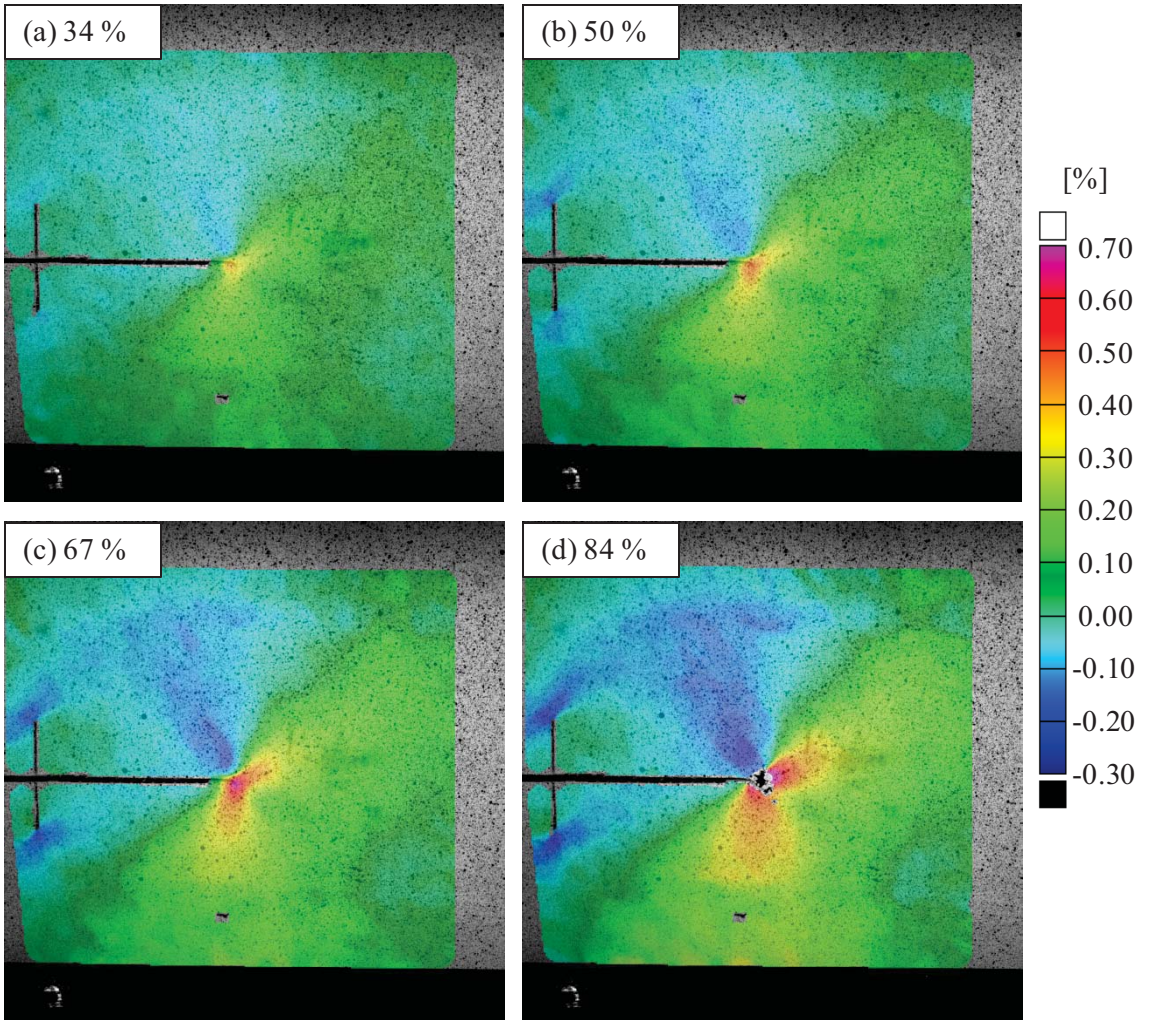

Figure A.4. Strain in the +45° direction for panel CP1B, run CP1B-RST-1. The panel fracture load was 14.0 psi internal pressure and 1040 lbf/in hoop load.

PANEL CP1B – STRAIN ALONG -45° DIRECTION

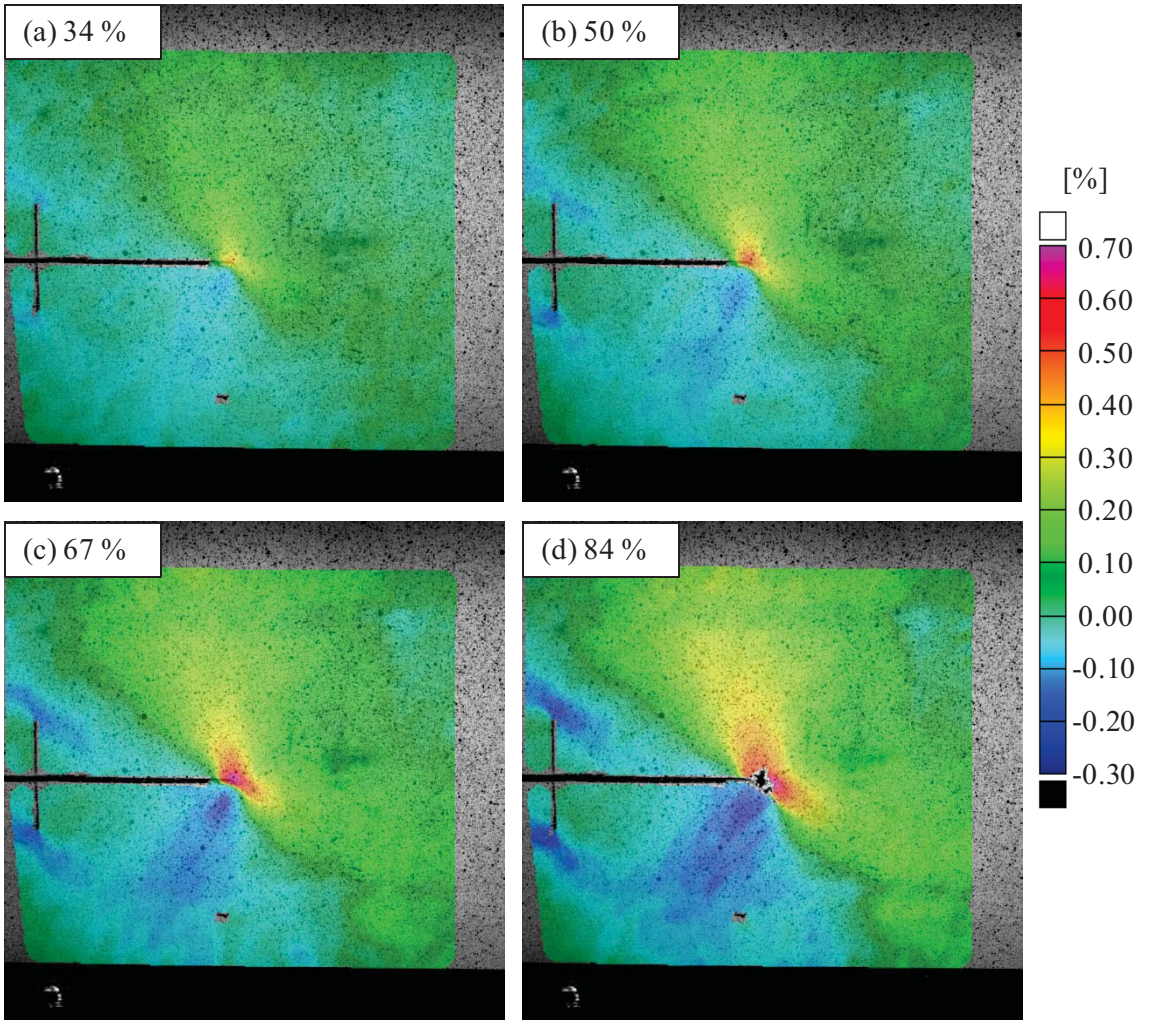

Figure A.5. Strain in the -45° direction for panel CP1B, run CP1B-RST-1. The panel fracture load was 14.0 psi internal pressure and 1040 lbf/in hoop load.

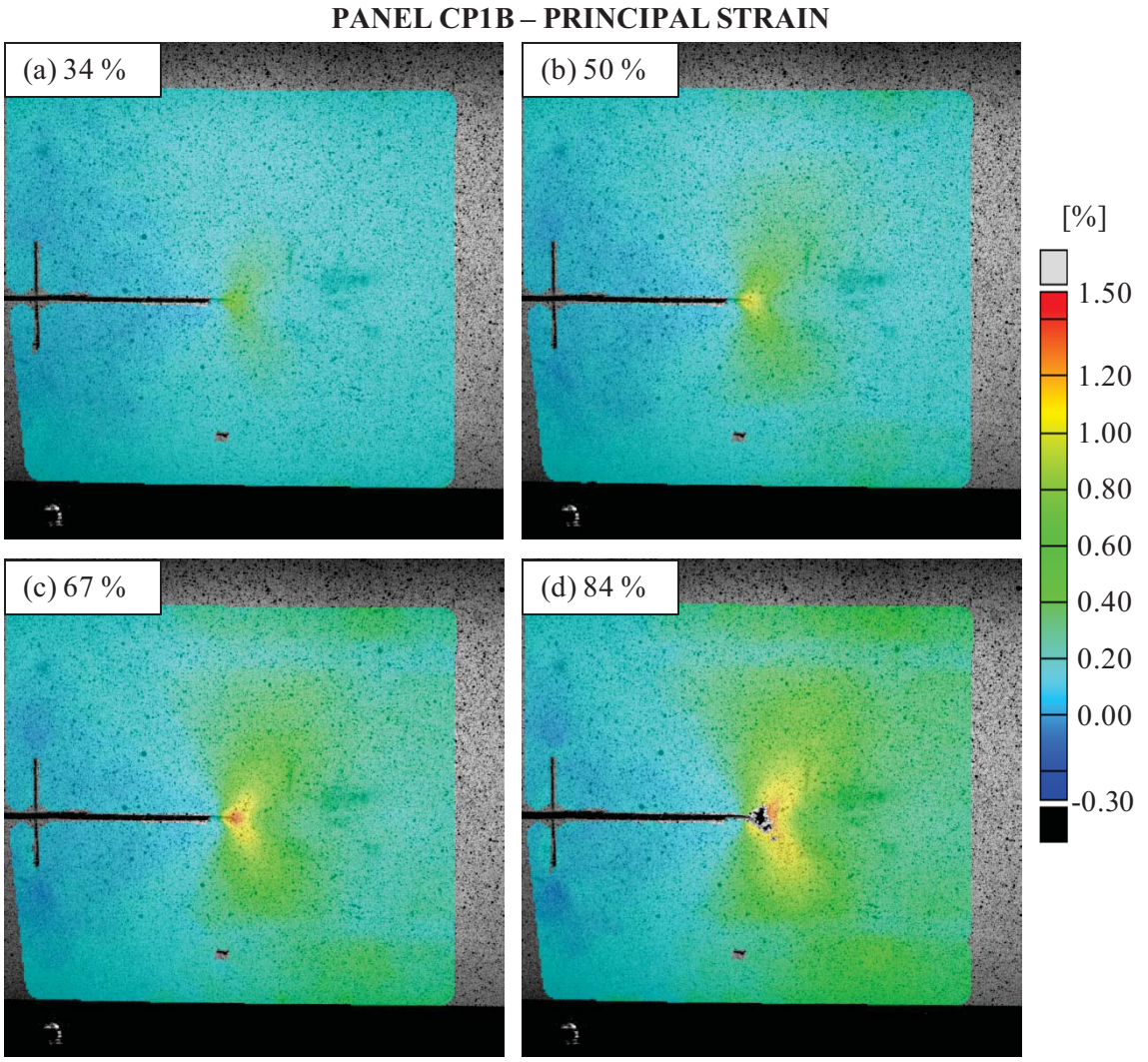

Figure A.6. Principal strain for panel CP1B, run CP1B-RST-1. The panel fracture load was 14.0 psi internal pressure and 1040 lbf/in hoop load.

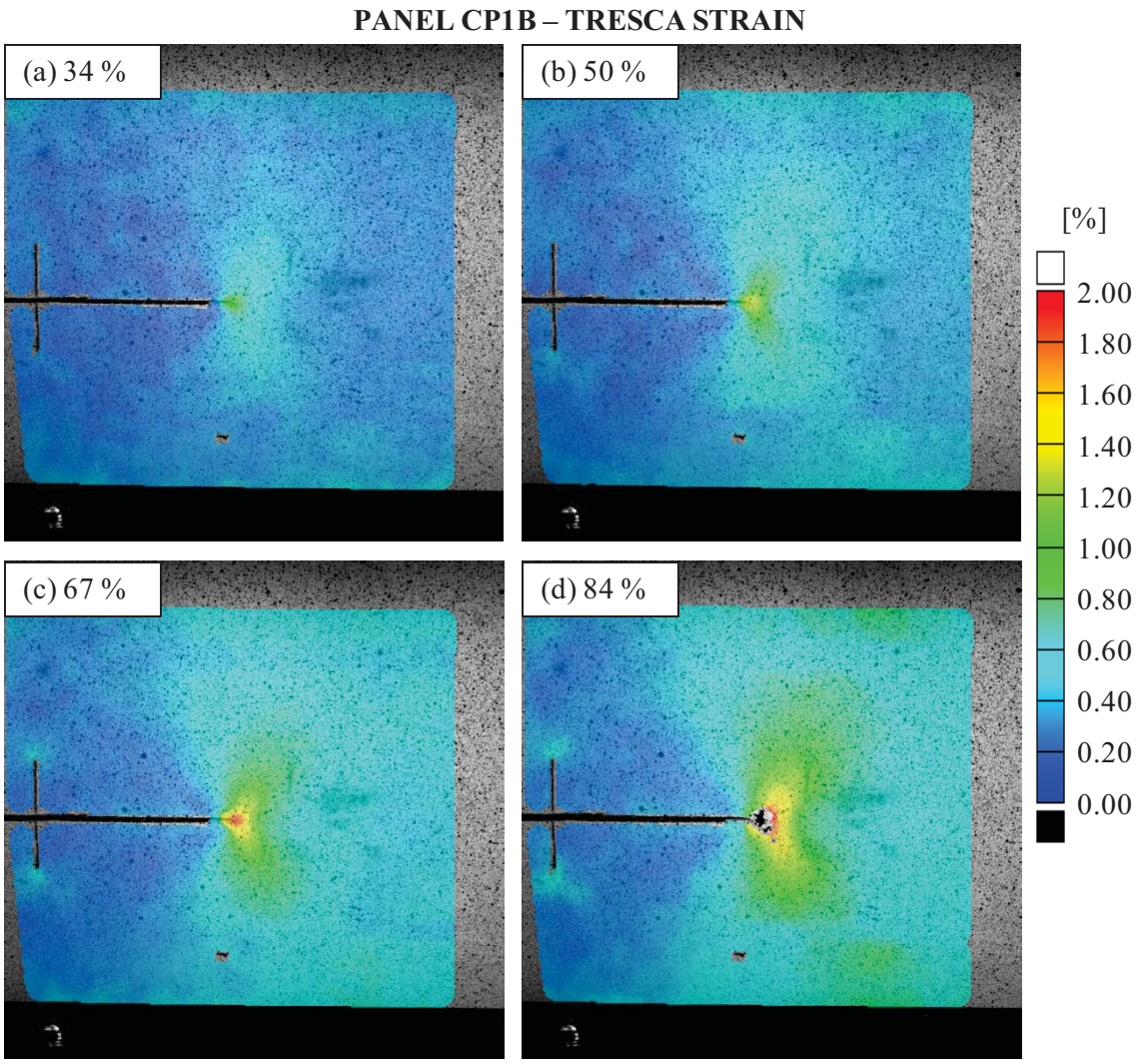

Figure A.7. Tresca strain for panel CP1B, run CP1B-RST-1. The panel fracture load was 14.0 psi internal pressure and 1040 lbf/in hoop load.

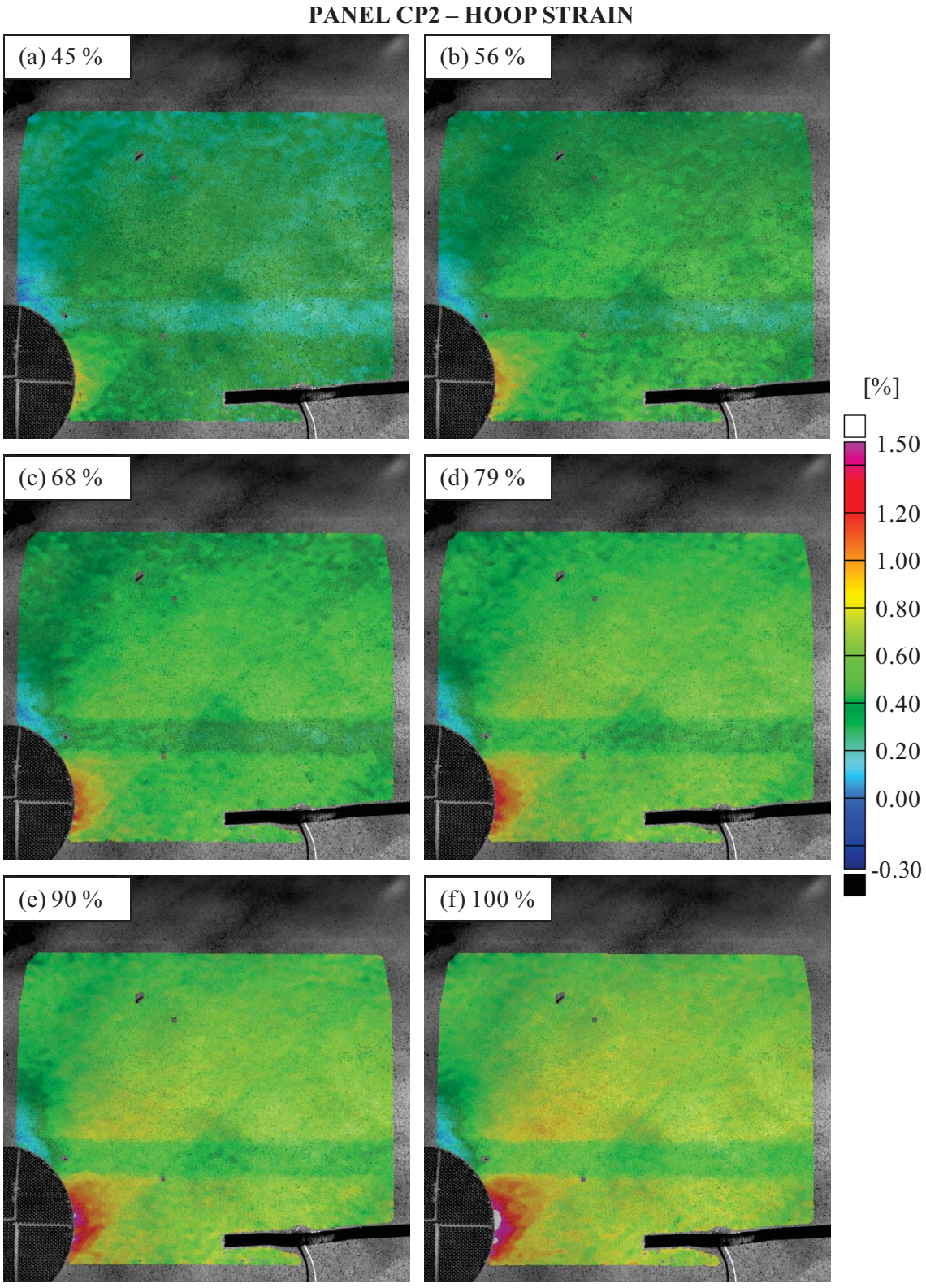

Figure A.8. Hoop strain for panel CP2, run CP2-RST-H3. The maximum applied load was 21.3 psi internal pressure and 1550 lbf/in hoop load.

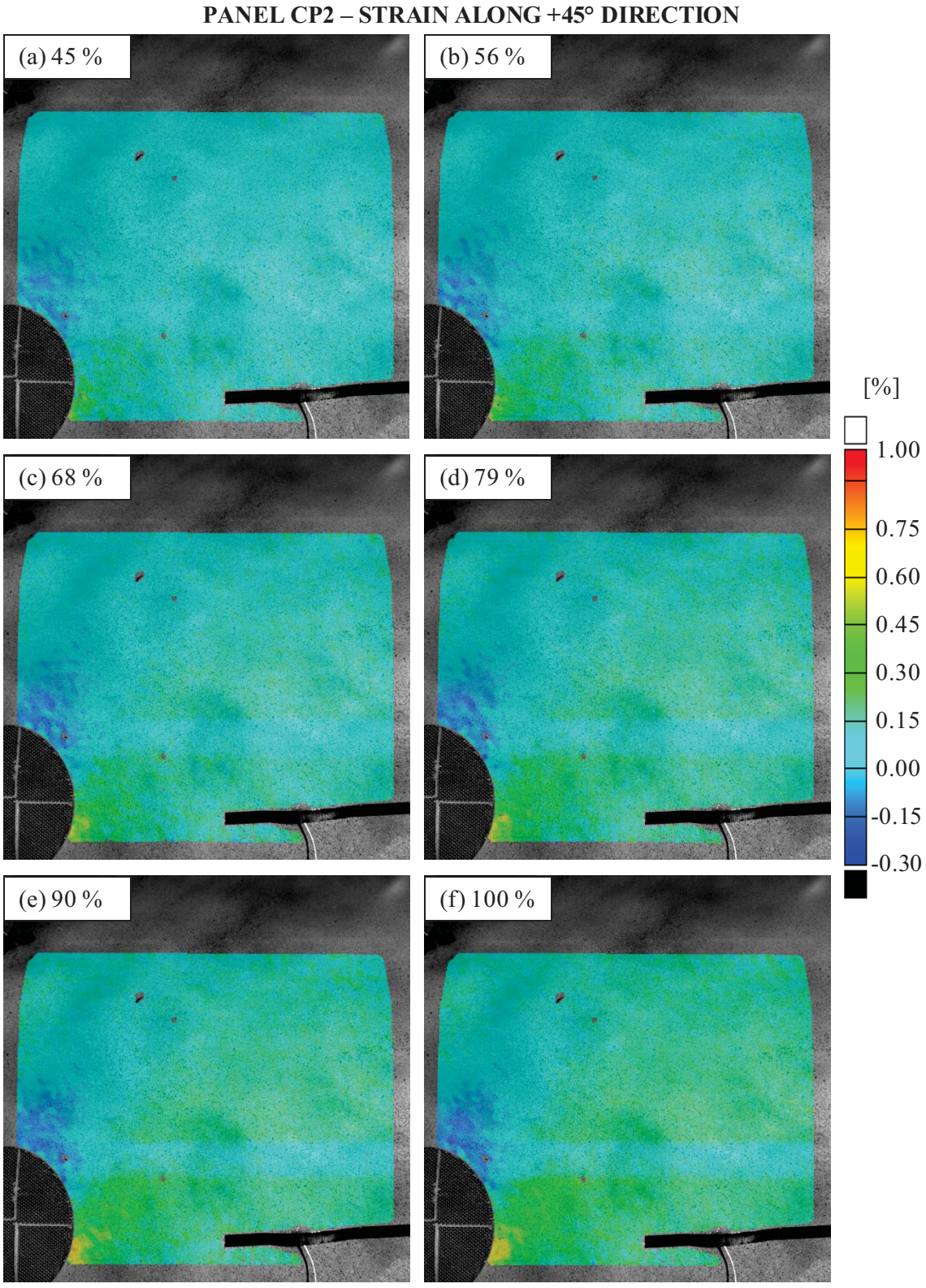

Figure A.9. Strain in the +45° direction for panel CP2, run CP2-RST-H3. The maximum applied load was 21.3 psi internal pressure and 1550 lbf/in hoop load.

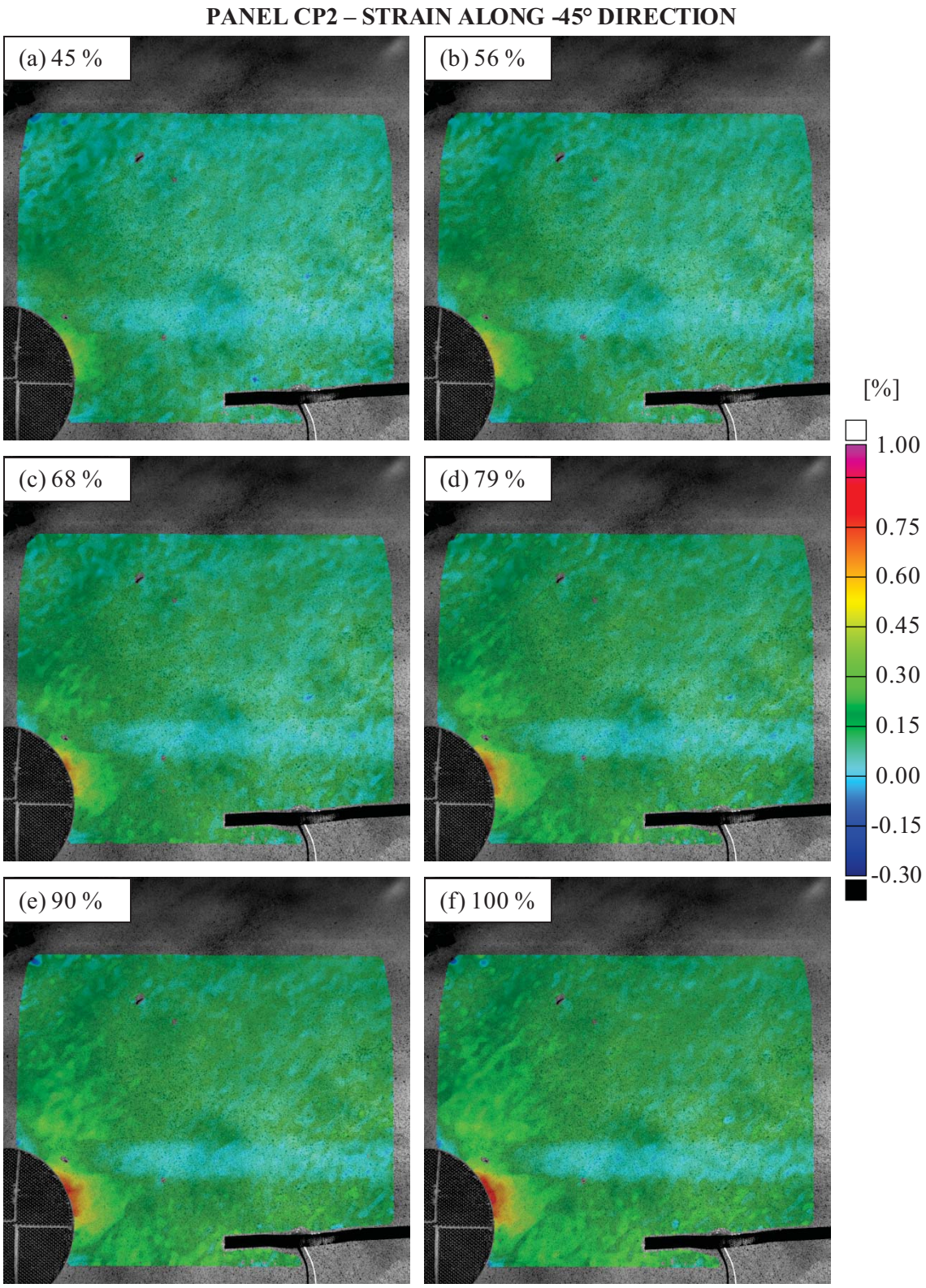

Figure A.10. Strain in the -45° direction for panel CP2, run CP2-RST-H3. The maximum applied load was 21.3 psi internal pressure and 1550 lbf/in hoop load.

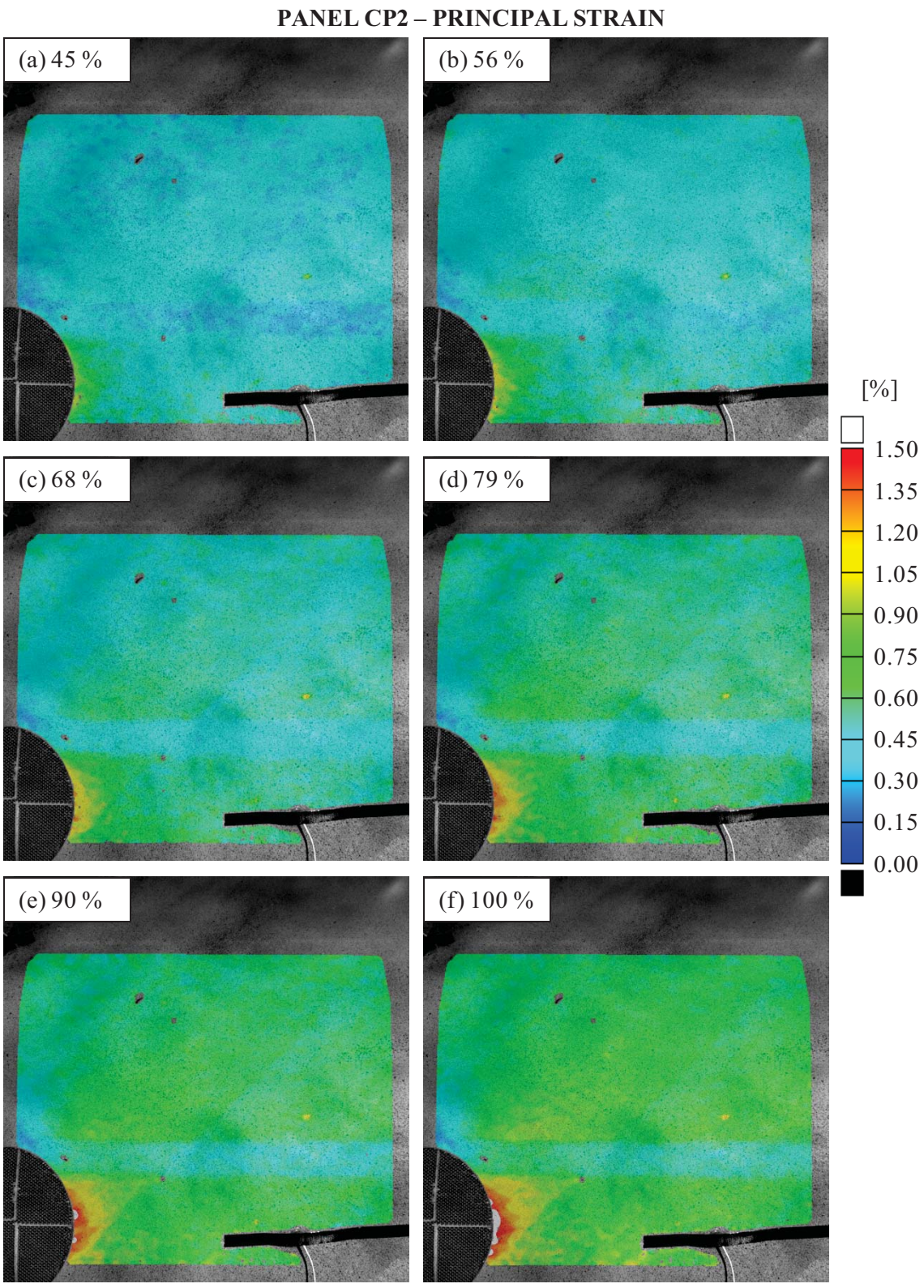

Figure A.11. Principal strain for panel CP2, run CP2-RST-H3. The maximum applied load was 21.3 psi internal pressure and 1550 lbf/in hoop load.

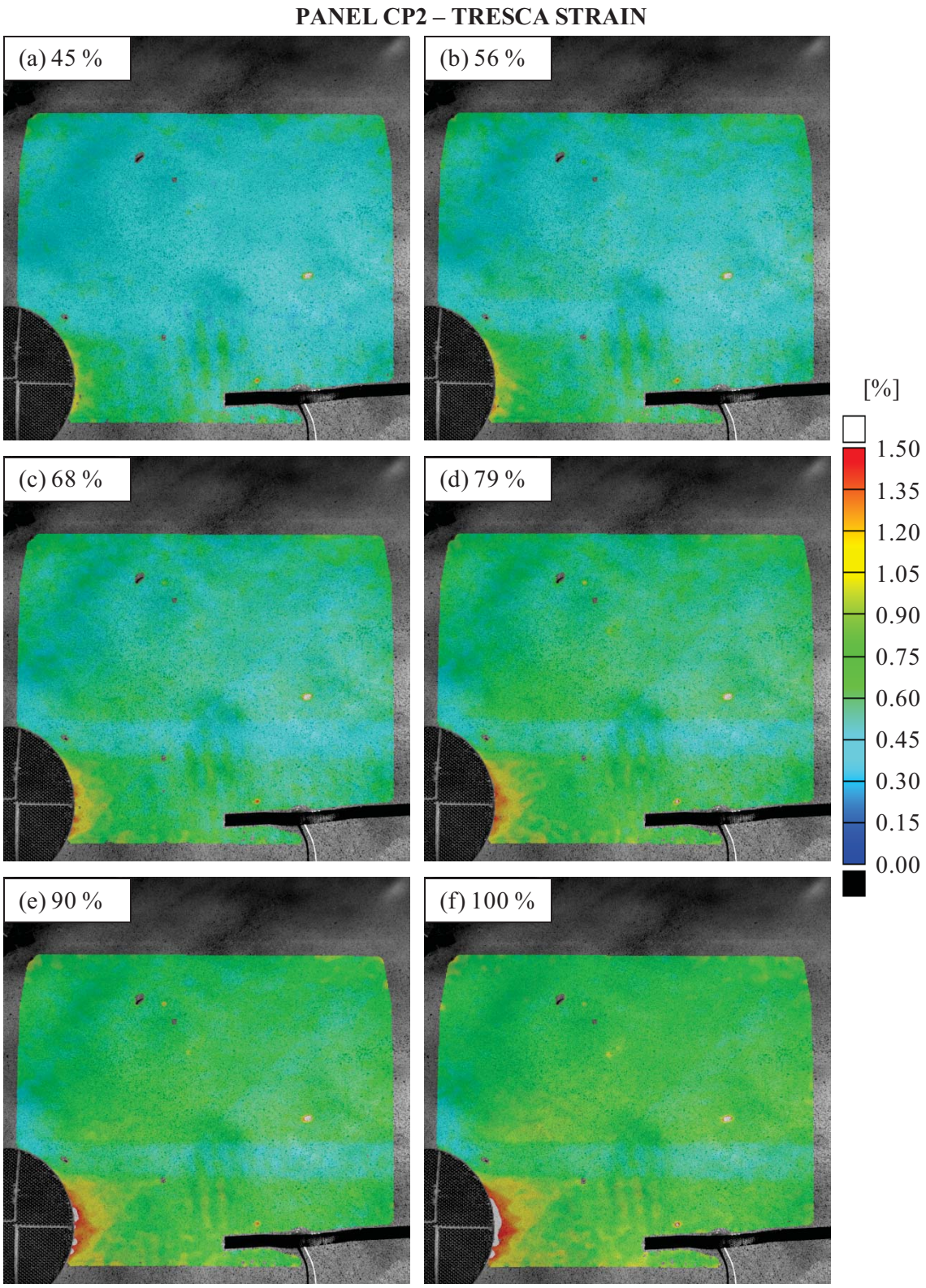

Figure A.12. Tresca strain for panel CP2, run CP2-RST-H3. The maximum applied load was 21.3 psi internal pressure and 1550 lbf/in hoop load.

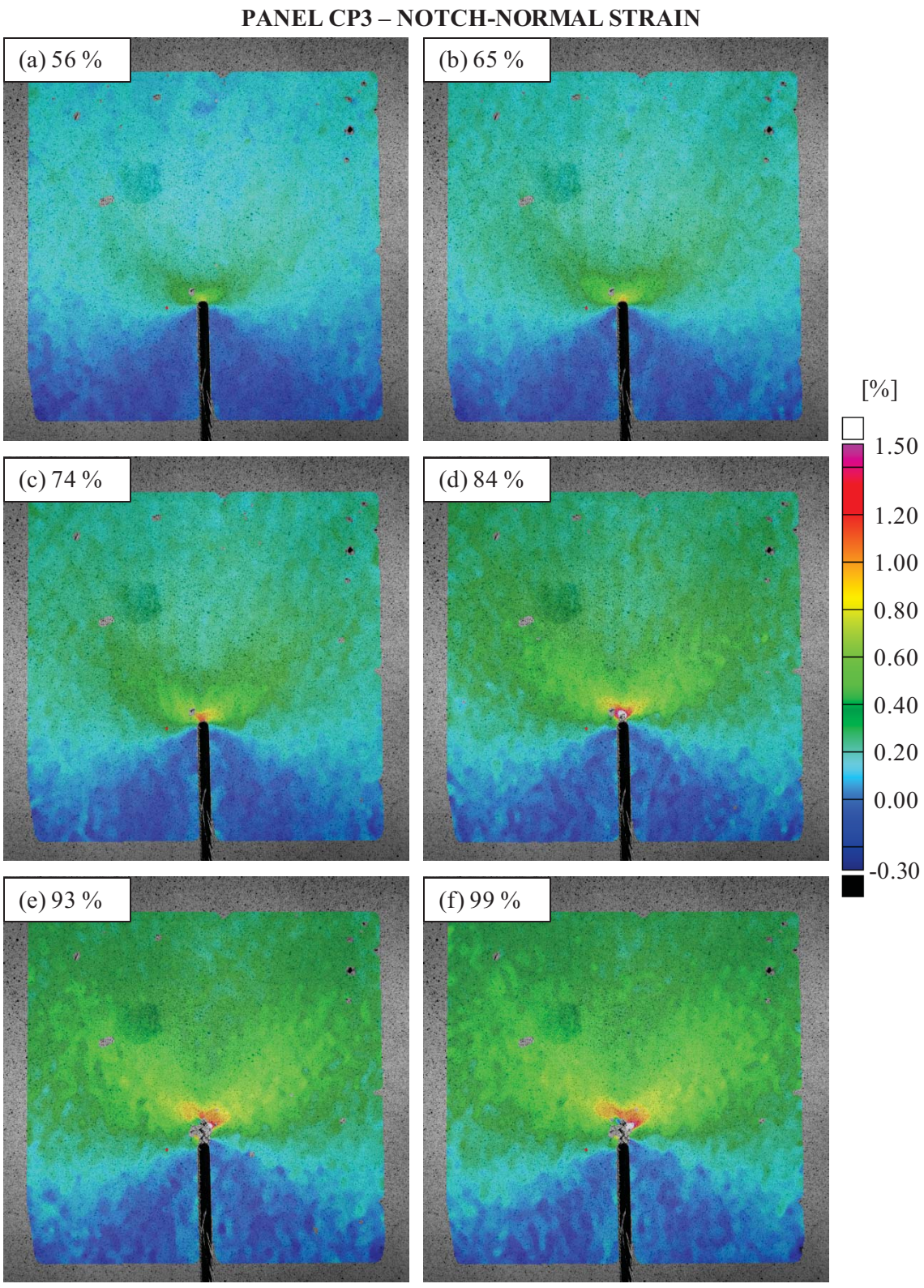

Figure A.13. Notch-normal strain for panel CP3, run CP3-RST-1. The panel fracture load was 1507 lbf/in longitudinal load, 8.0 psi internal pressure, and 592 lbf/in hoop load.

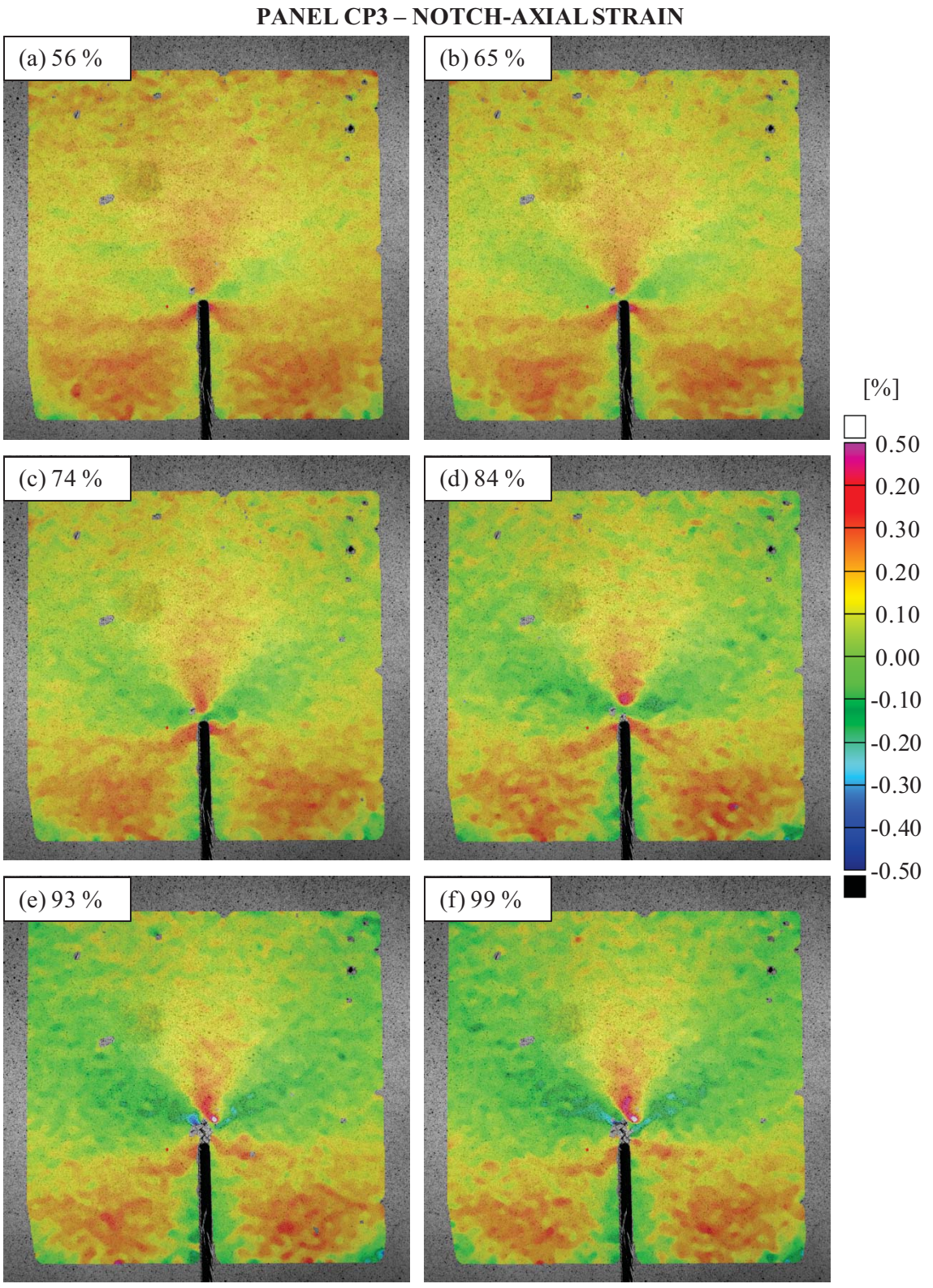

Figure A.14. Notch-axial strain for panel CP3, run CP3-RST-1. The panel fracture load was 1507 lbf/in longitudinal load, 8.0 psi internal pressure, and 592 lbf/in hoop load.

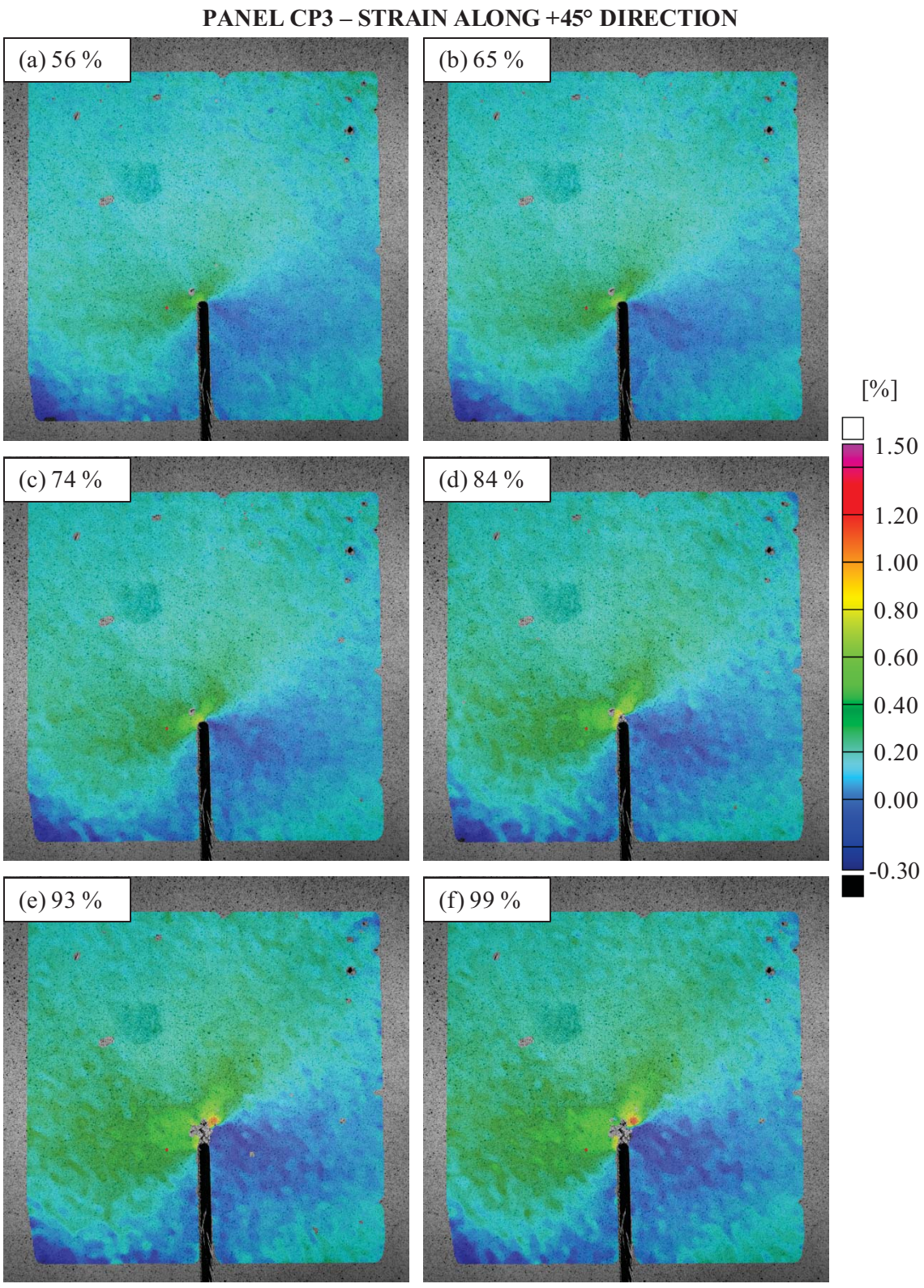

Figure A.15. Strain in the +45° direction for panel CP3, run CP3-RST-1. The panel fracture load was 1507 lbf/in longitudinal load, 8.0 psi internal pressure, and 592 lbf/in hoop load.

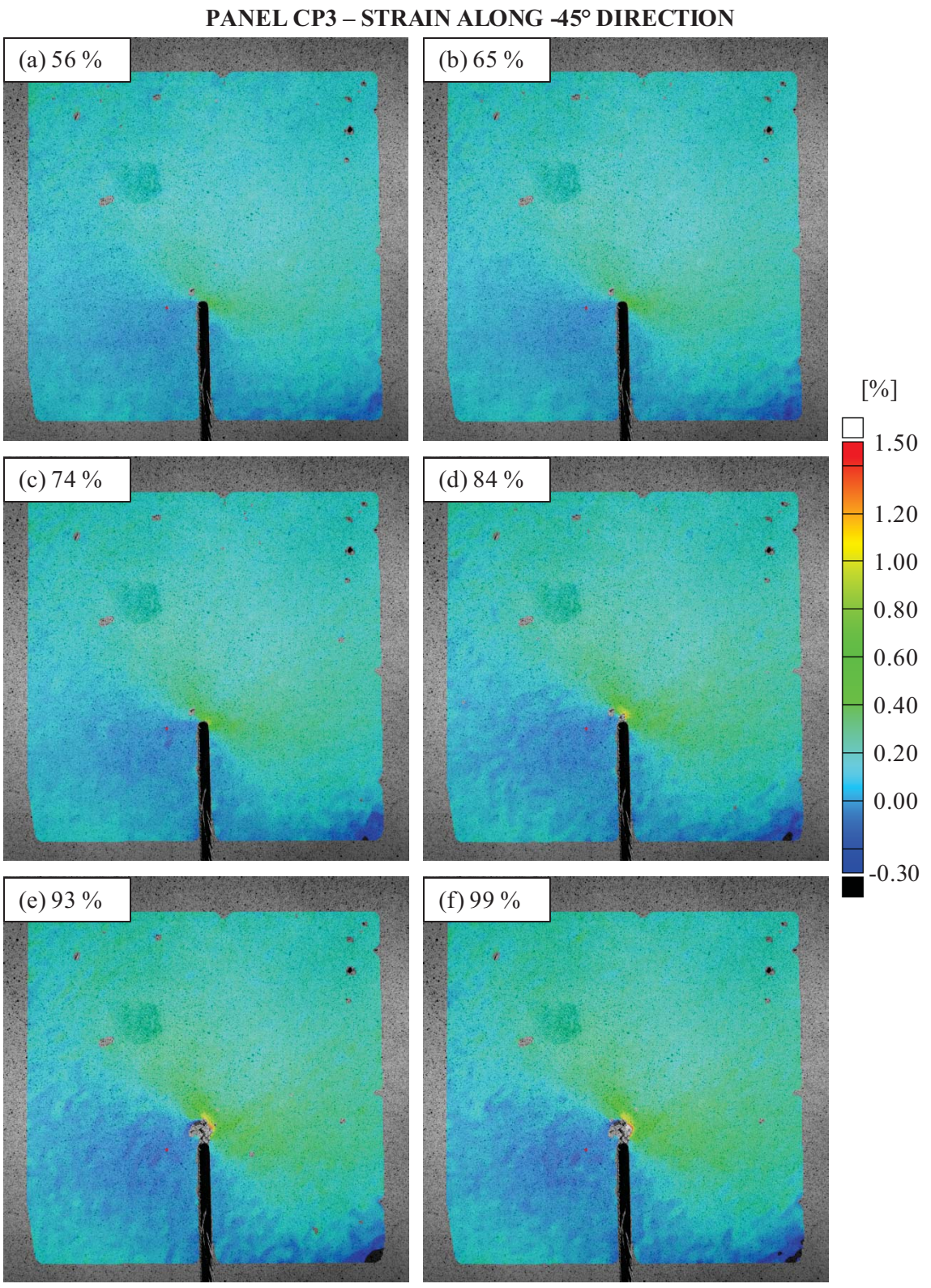

Figure A.16. Strain in the -45° direction for panel CP3, run CP3-RST-1. The panel fracture load was 1507 lbf/in longitudinal load, 8.0 psi internal pressure, and 592 lbf/in hoop load.

PANEL CP3 – PRINCIPAL STRAIN

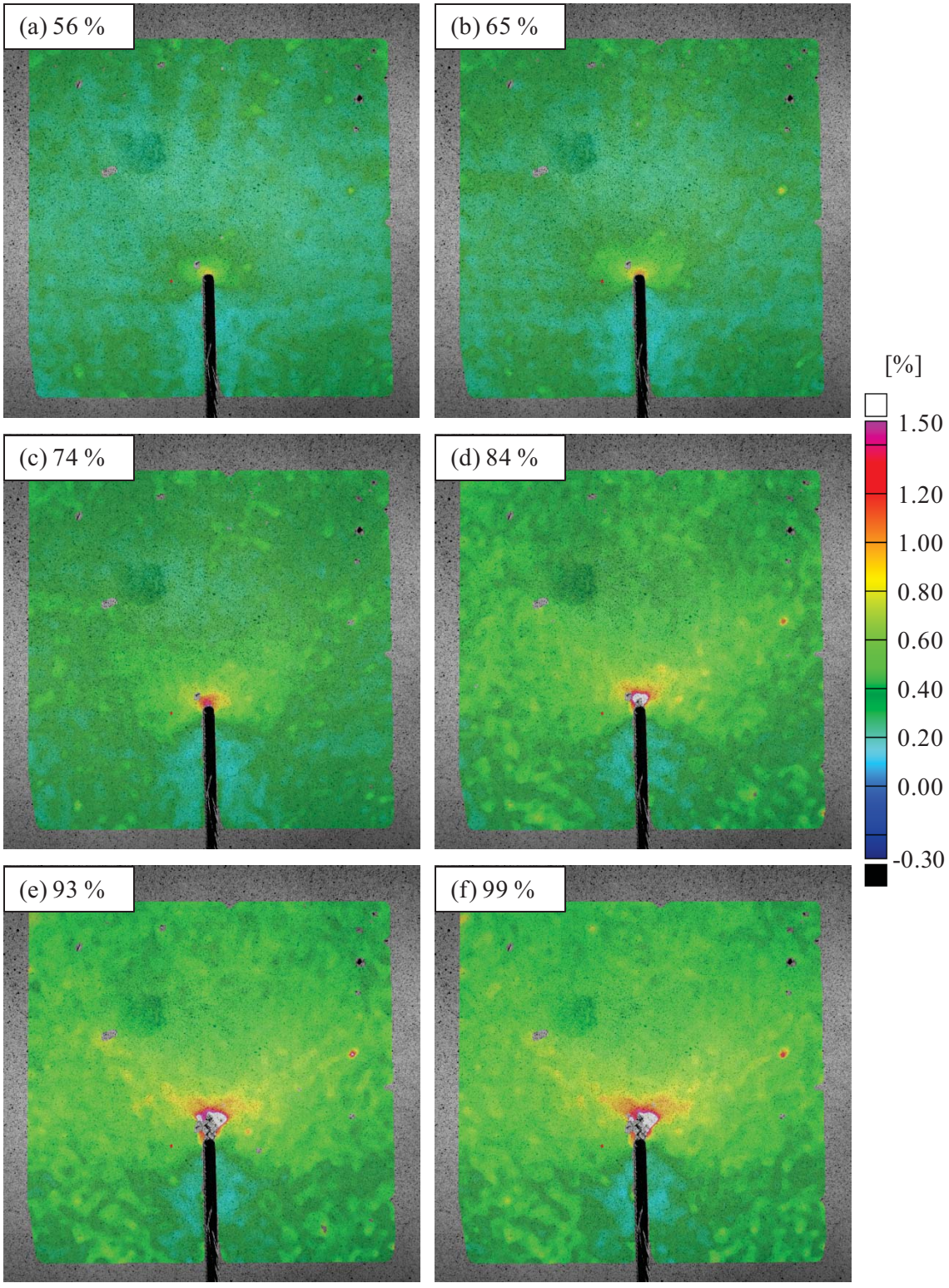

Figure A.17. Principal strain for panel CP3, run CP3-RST-1. The panel fracture load was 1507 lbf/in longitudinal load, 8.0 psi internal pressure, and 592 lbf/in hoop load.

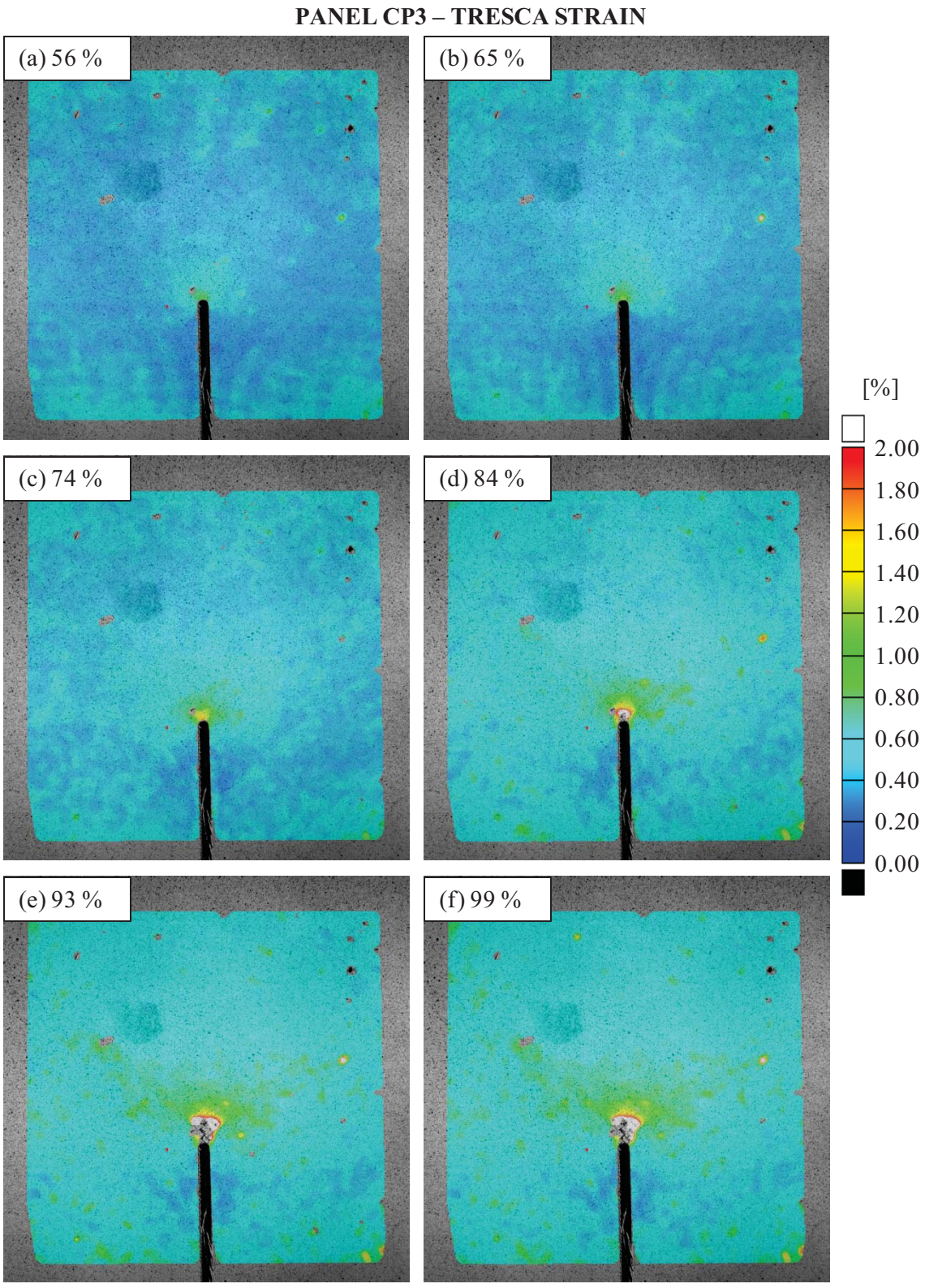

Figure A.18. Tresca strain for panel CP4, run CP4-RST-1. The panel fracture load was 1470 lbf/in longitudinal load, 1.0 psi internal pressure, and 74 lbf/in hoop load.

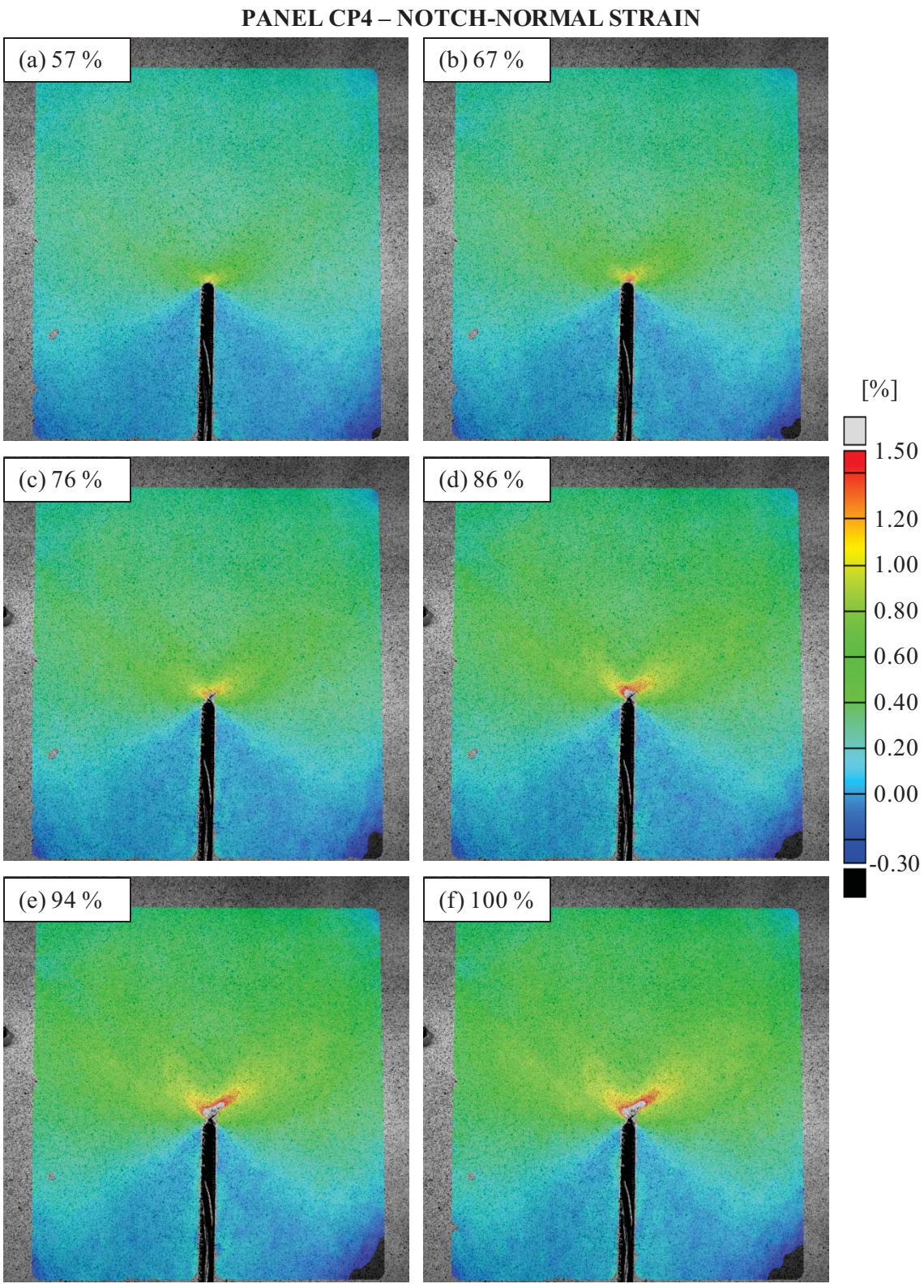

Figure A.19. Notch-normal strain for panel CP4, run CP4-RST-1. The maximum applied load was 1470 lbf/in longitudinal load, 1.0 psi internal pressure, and 74 lbf/in hoop load.

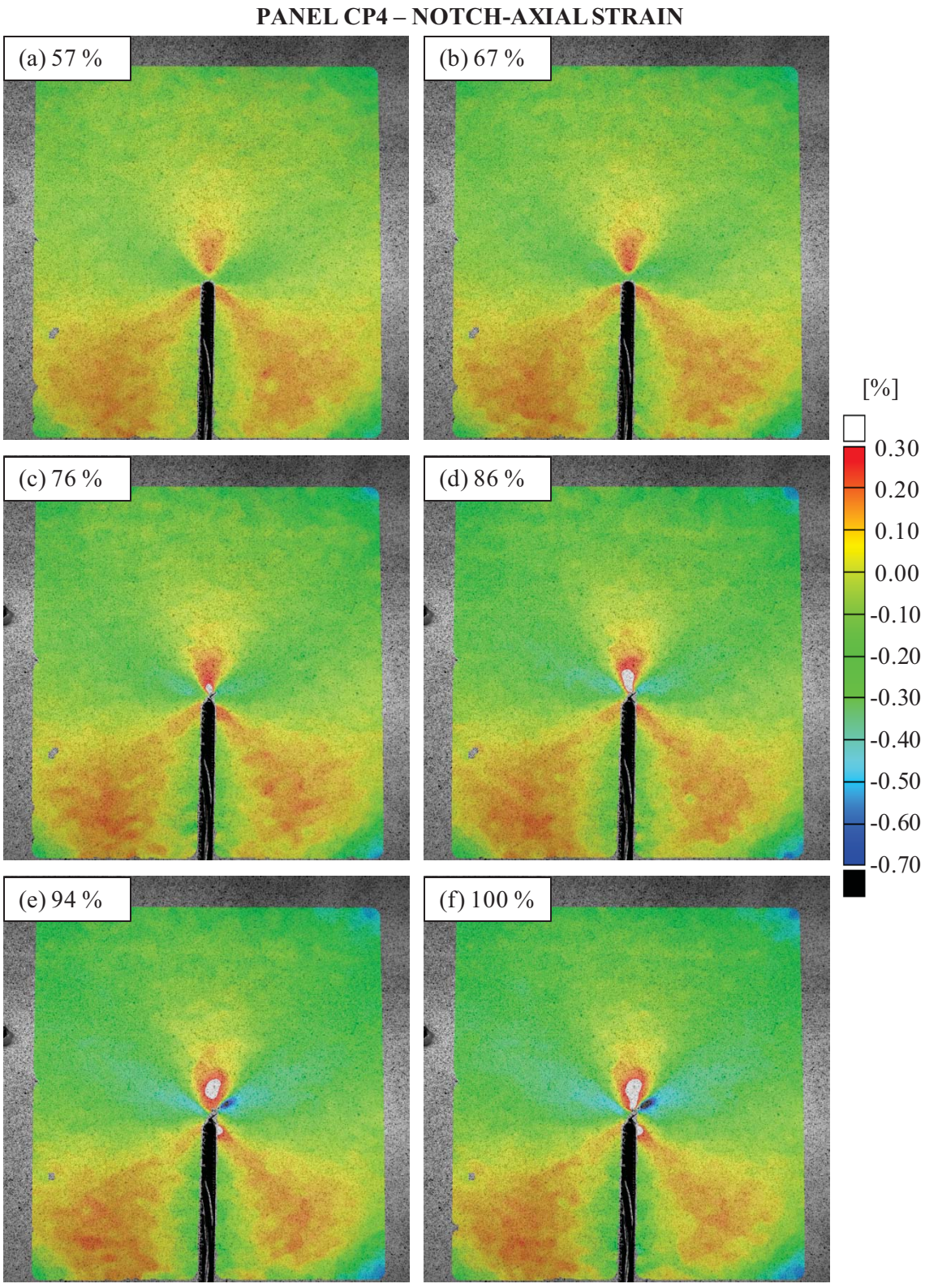

Figure A.20. Notch-axial strain for panel CP4, run CP4-RST-1. The maximum applied load was 1470 lbf/in longitudinal load, 1.0 psi internal pressure, and 74 lbf/in hoop load.

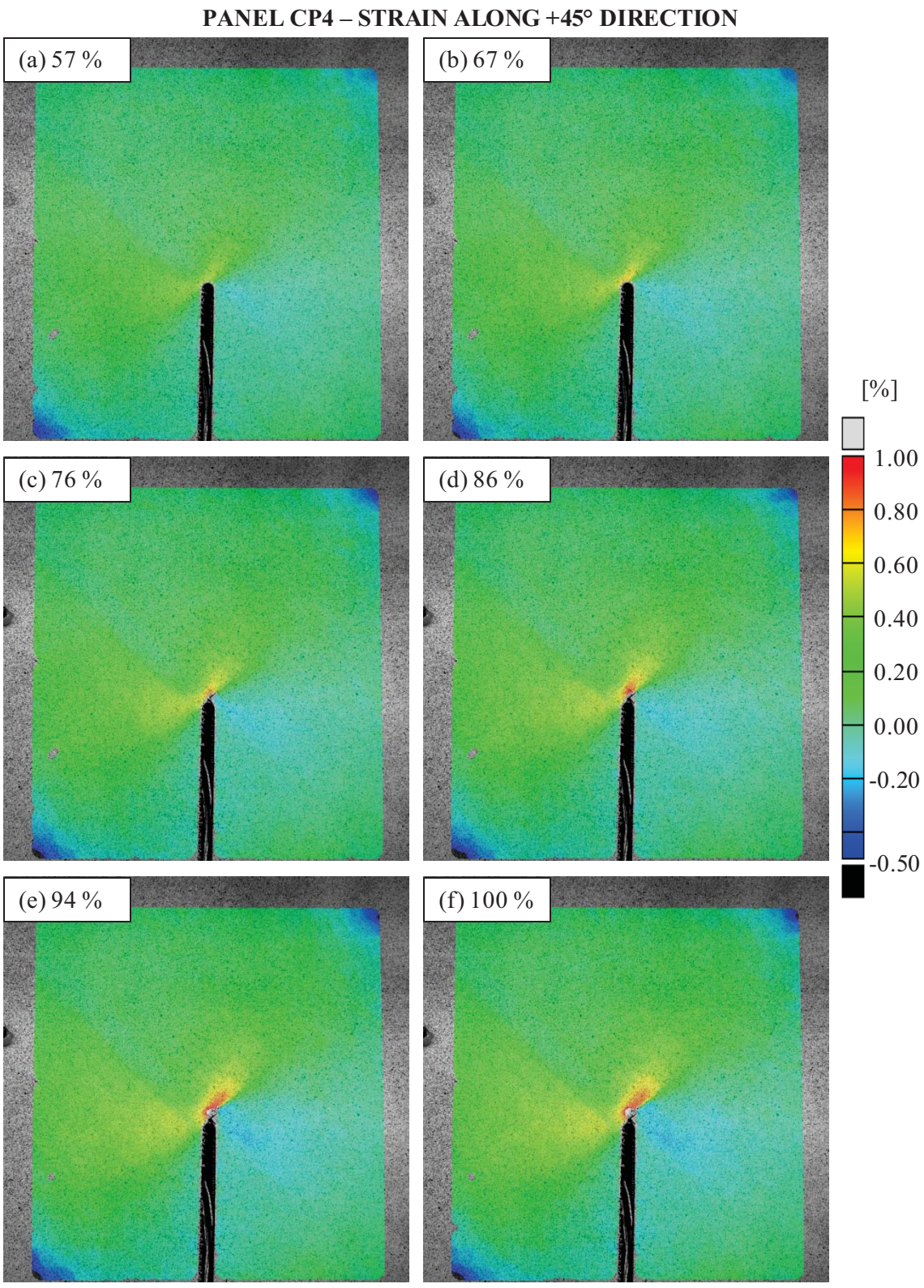

Figure A.21. Strain in the +45° direction for panel CP4, run CP4-RST-1. The maximum applied load was 1470 lbf/in longitudinal load, 1.0 psi internal pressure, and 74 lbf/in hoop load.

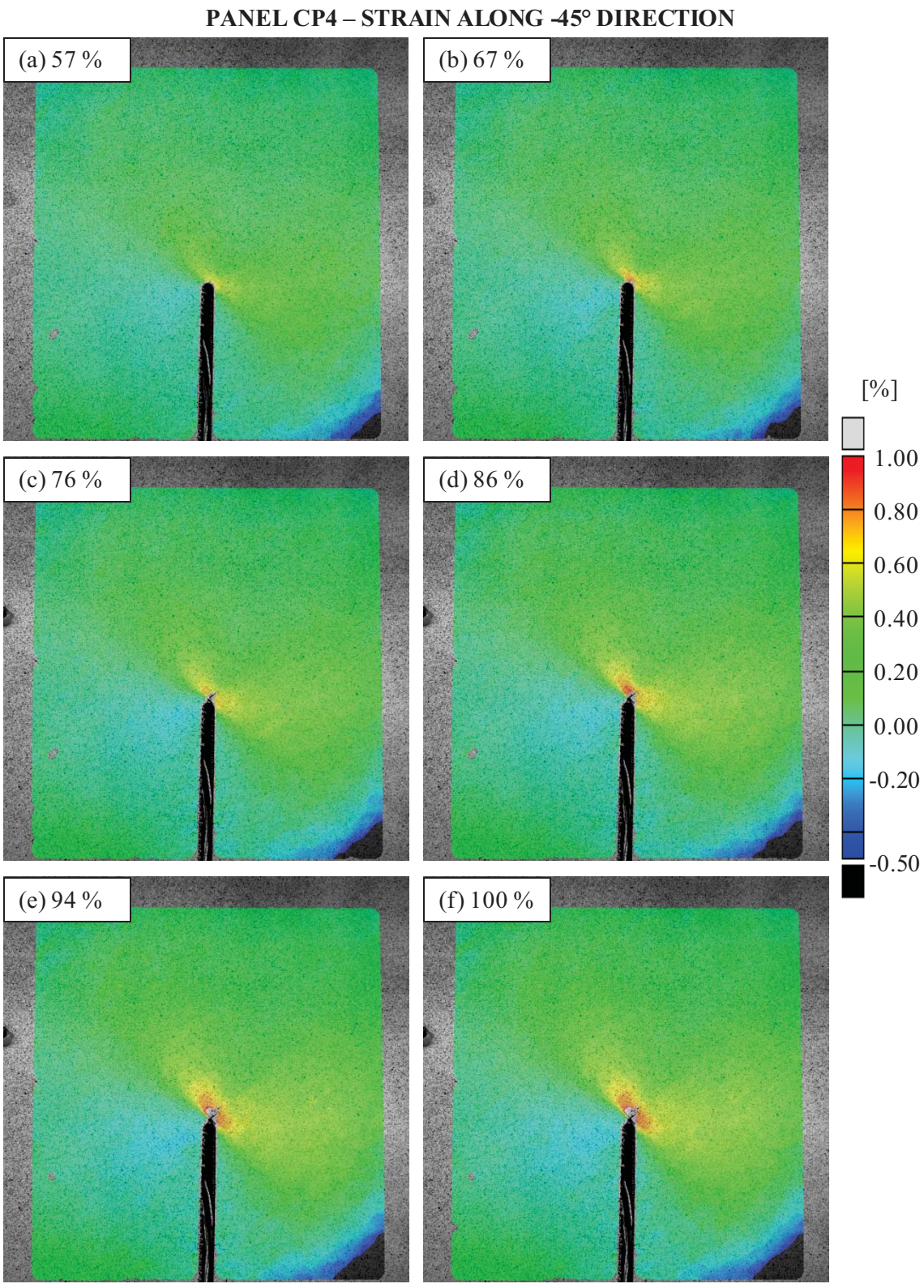

Figure A.22. Strain in the -45° direction for panel CP4, run CP4-RST-1. The maximum applied load was 1470 lbf/in longitudinal load, 1.0 psi internal pressure, and 74 lbf/in hoop load.

PANEL CP4 – PRINCIPAL STRAIN

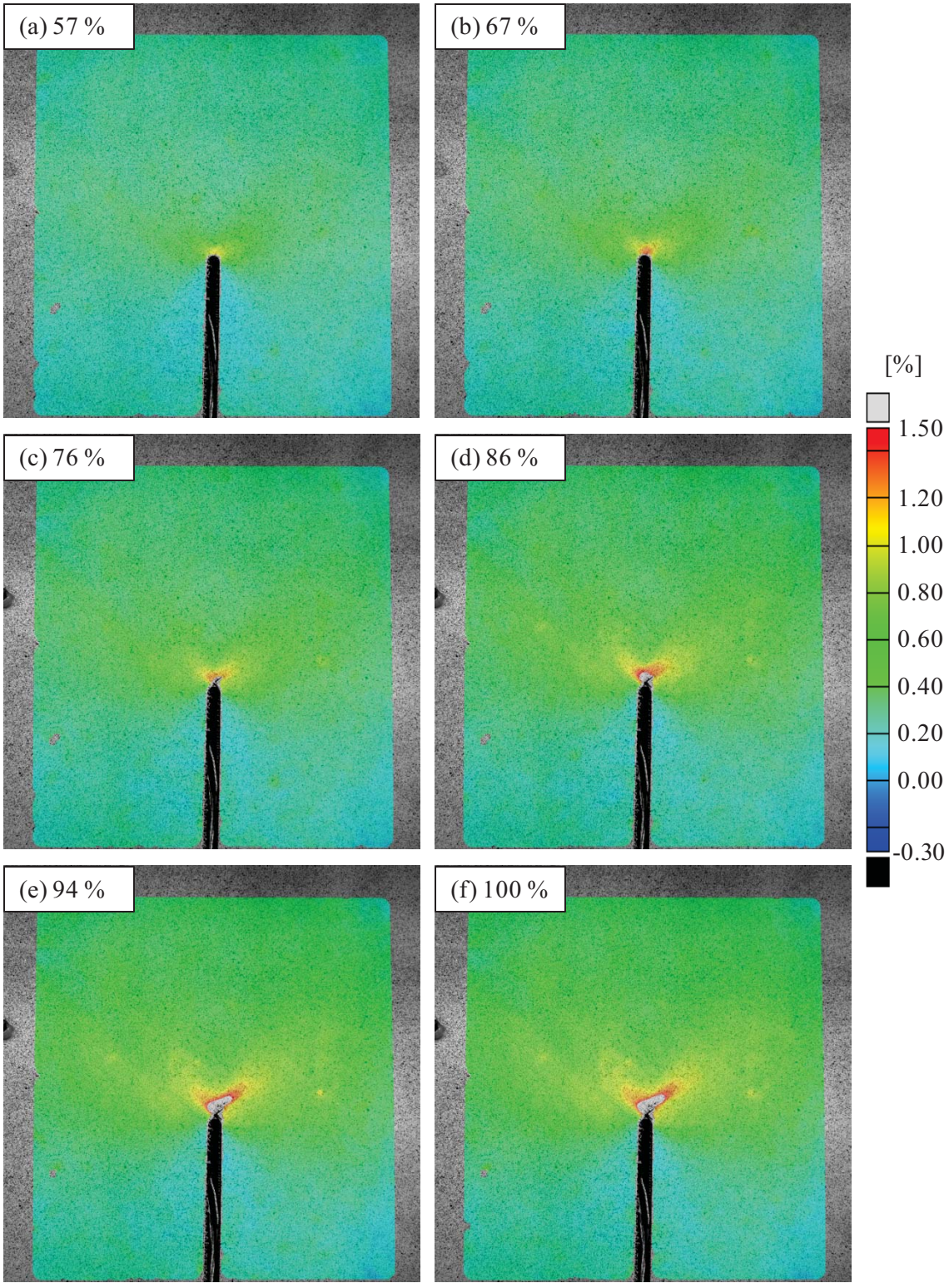

Figure A.23. Principal strain for panel CP4, run CP4-RST-1. The maximum applied load was 1470 lbf/in longitudinal load, 1.0 psi internal pressure, and 74 lbf/in hoop load.

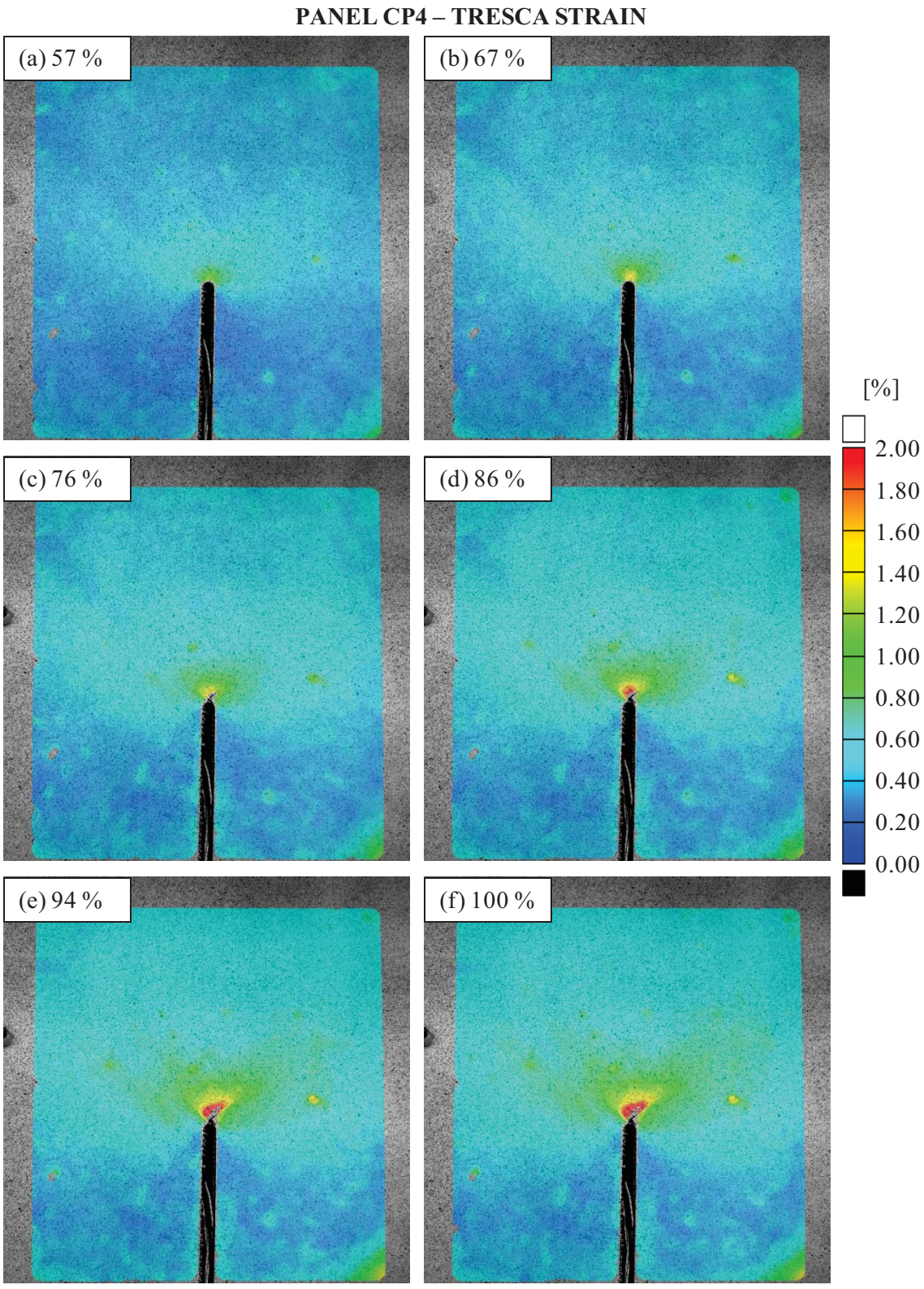

Figure A.24. Tresca strain for panel CP4, run CP4-RST-1. The maximum applied load was 1470 lbf/in longitudinal load, 1.0 psi internal pressure, and 74 lbf/in hoop load.

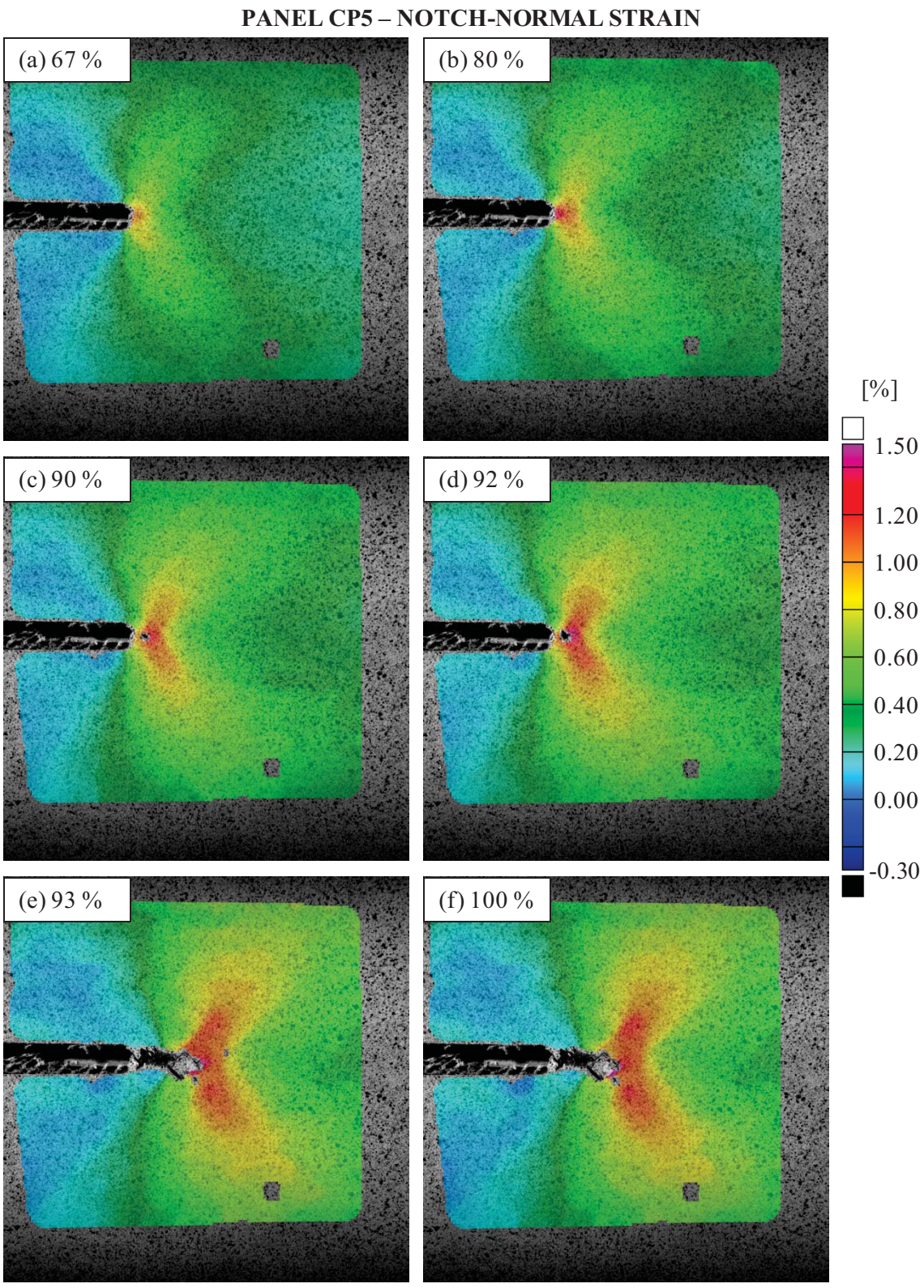

Figure A.25. Notch-normal strain for panel CP5, run CP5-RST-1. The panel fracture load was 13.5 psi internal pressure, 960 lbf/in hoop load, and 100 lbf/in longitudinal load.

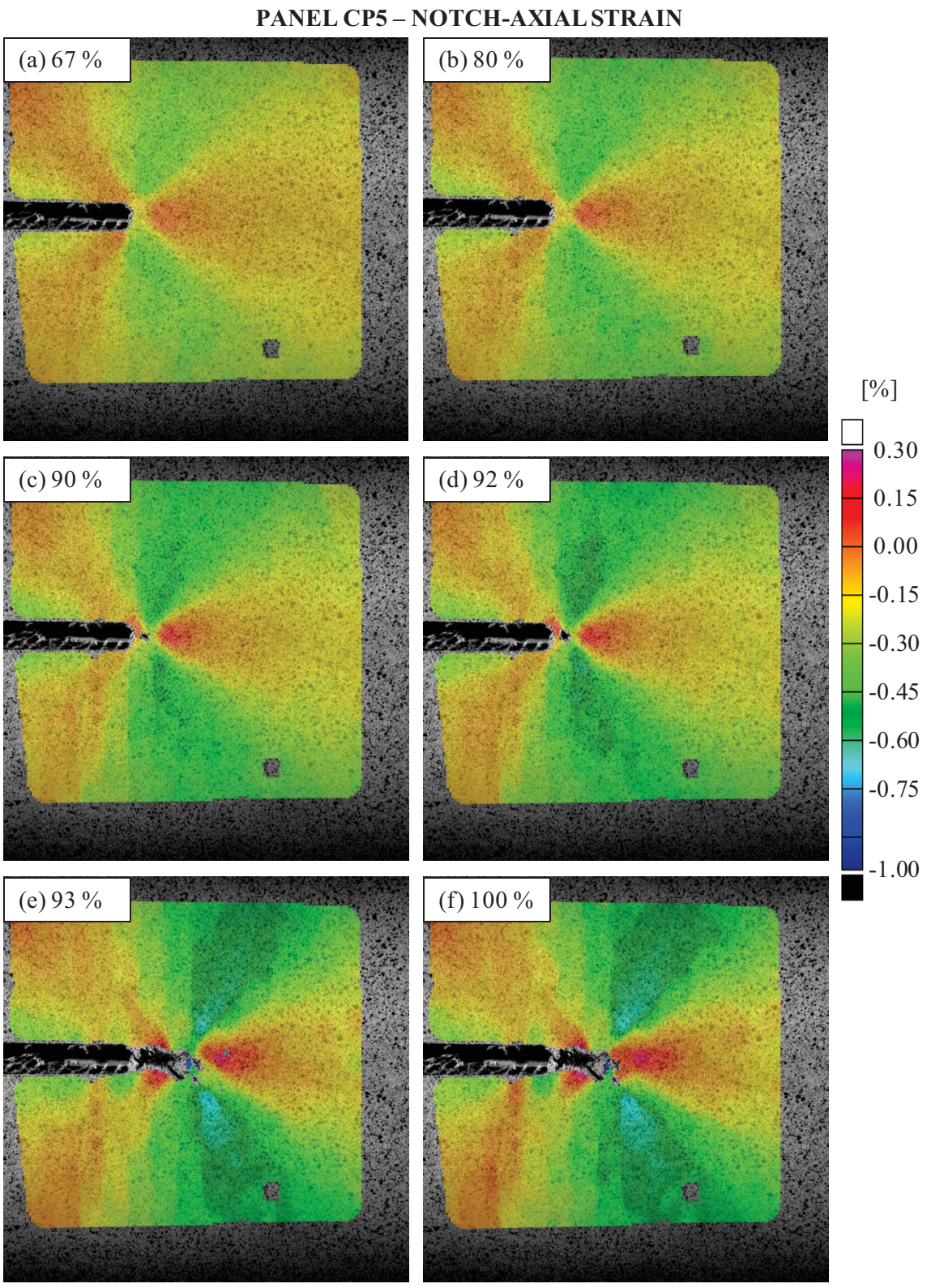

Figure A.26. Notch-axial strain for panel CP5, run CP5-RST-1. The panel fracture load was 13.5 psi internal pressure, 960 lbf/in hoop load, and 100 lbf/in longitudinal load.

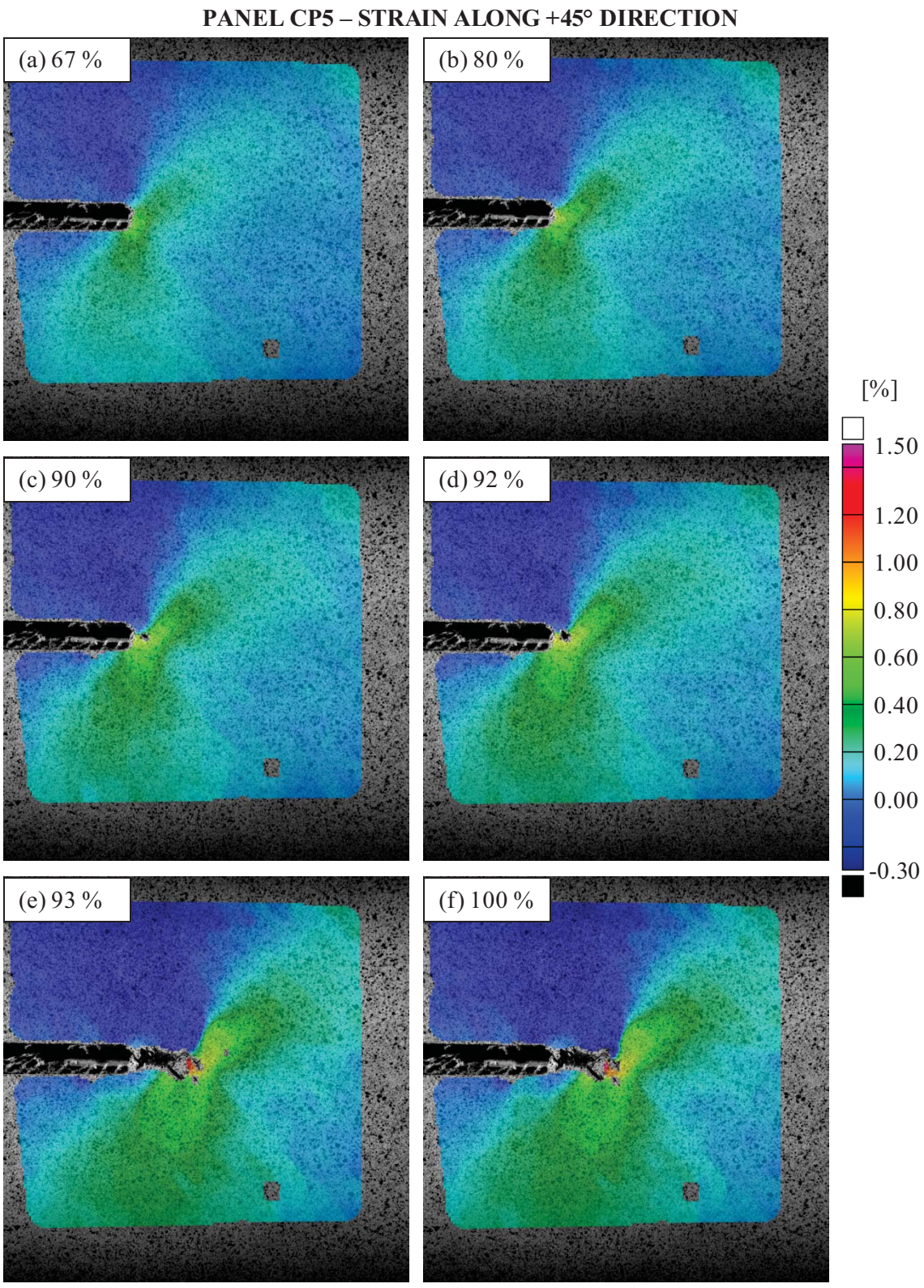

Figure A.27. Strain in the +45° direction for panel CP5, run CP5-RST-1. The panel fracture load was 13.5 psi internal pressure, 960 lbf/in hoop load, and 100 lbf/in longitudinal load.

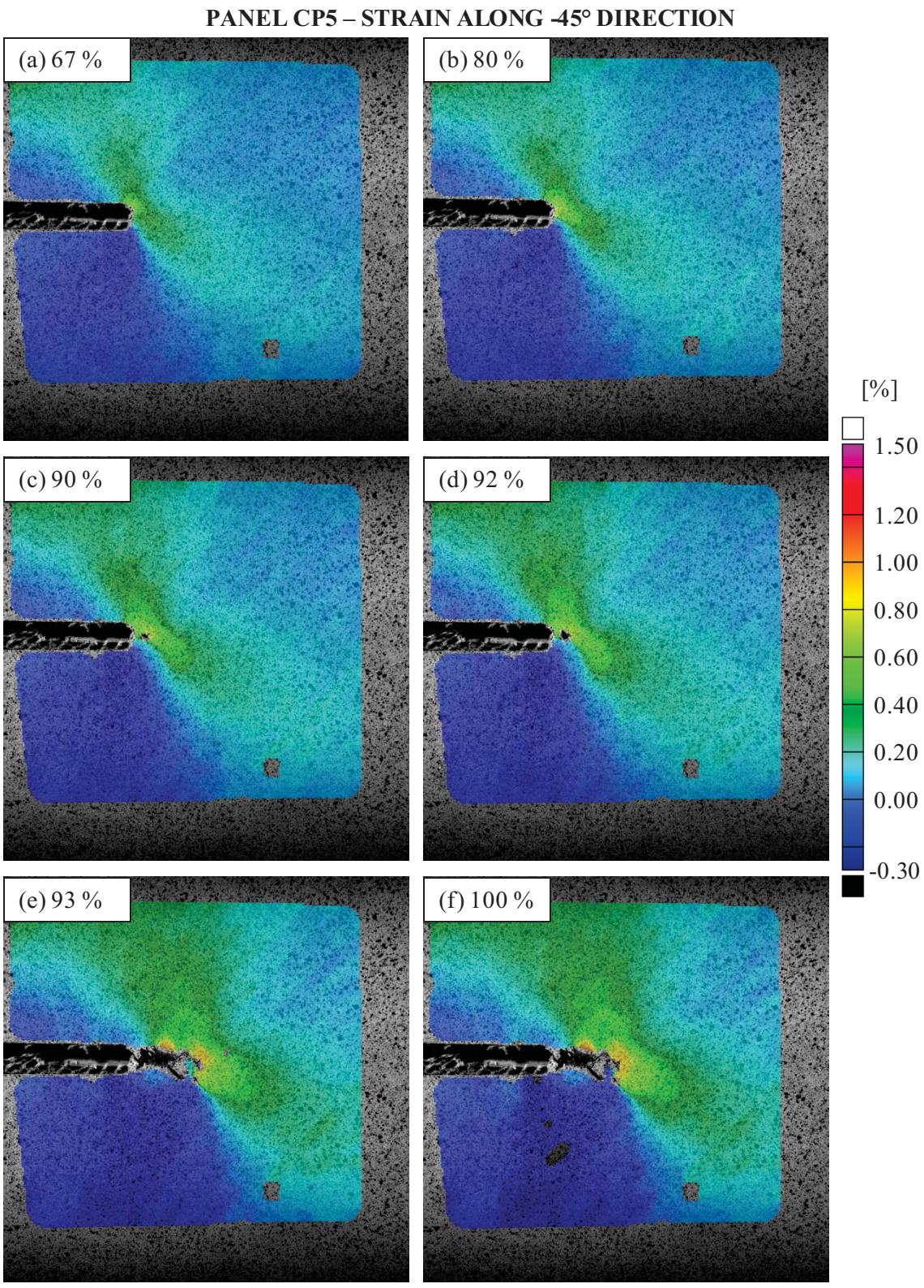

Figure A.28. Strain in the -45° direction for panel CP5, run CP5-RST-1. The panel fracture load was 13.5 psi internal pressure, 960 lbf/in hoop load, and 100 lbf/in longitudinal load.

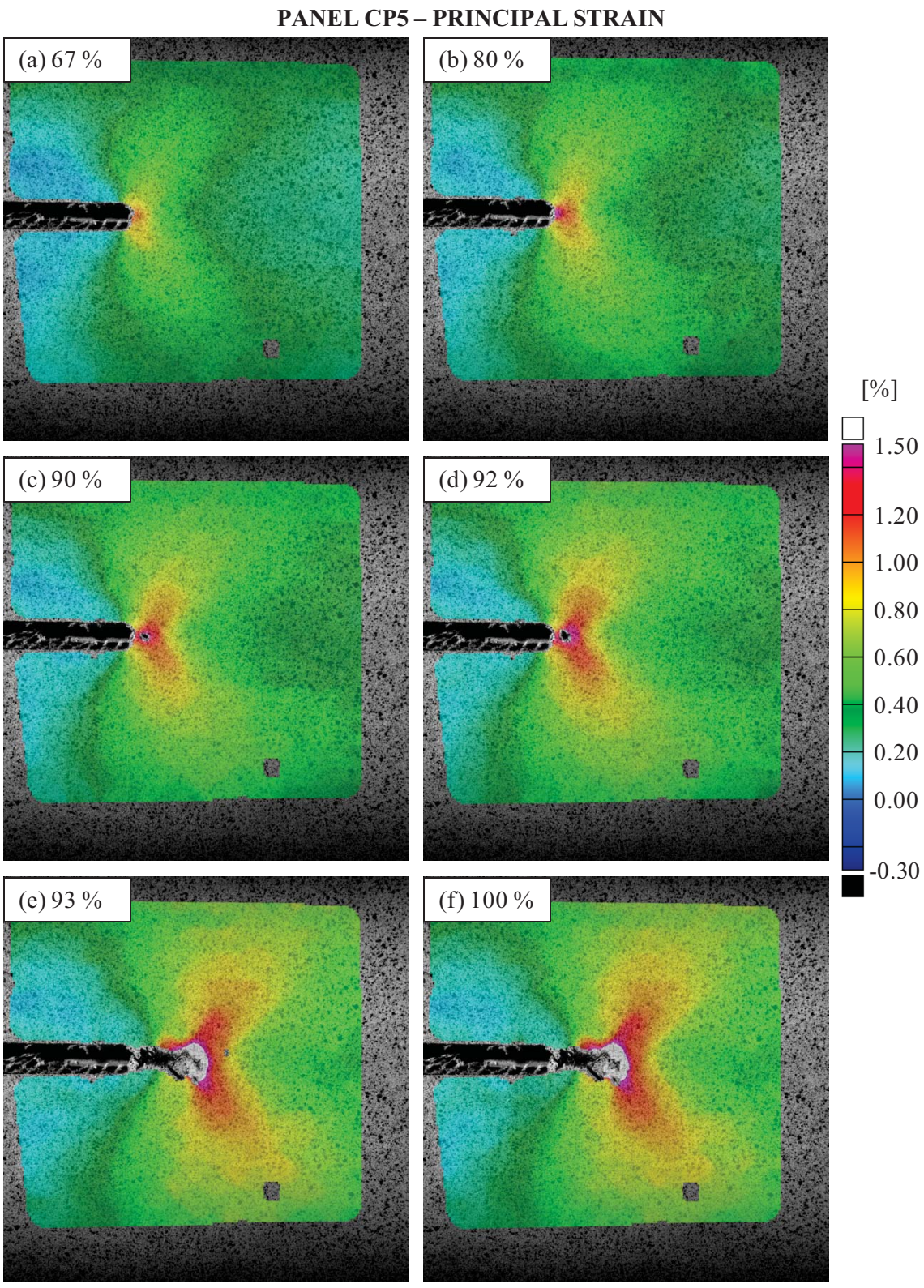

Figure A.29. Principal strain for panel CP5, run CP5-RST-1. The panel fracture load was 13.5 psi internal pressure, 960 lbf/in hoop load, and 100 lbf/in longitudinal load.

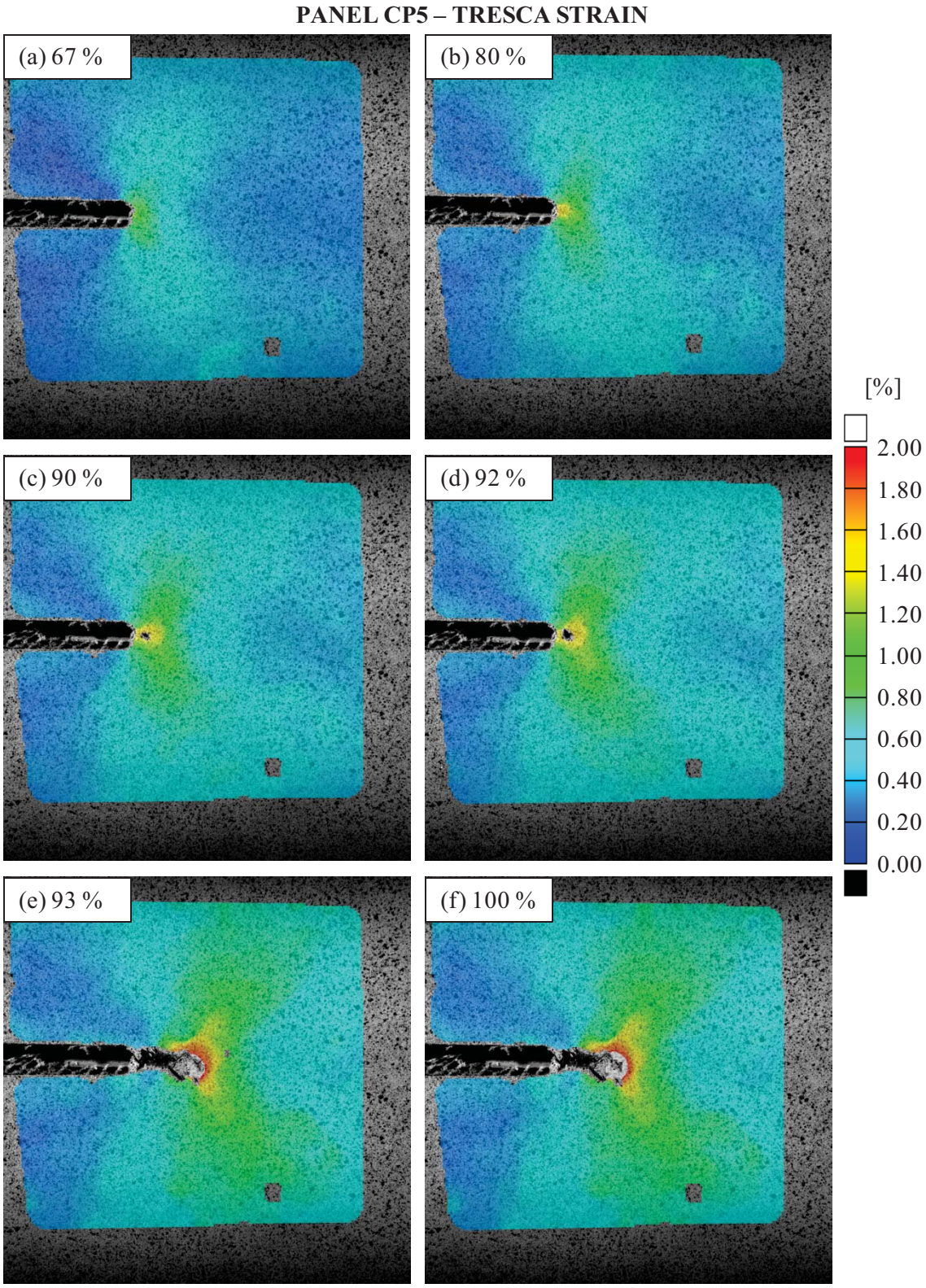

Figure A.30. Tresca strain for panel CP5, run CP5-RST-1. The panel fracture load was 13.5 psi internal pressure, 960 lbf/in hoop load, and 100 lbf/in longitudinal load.

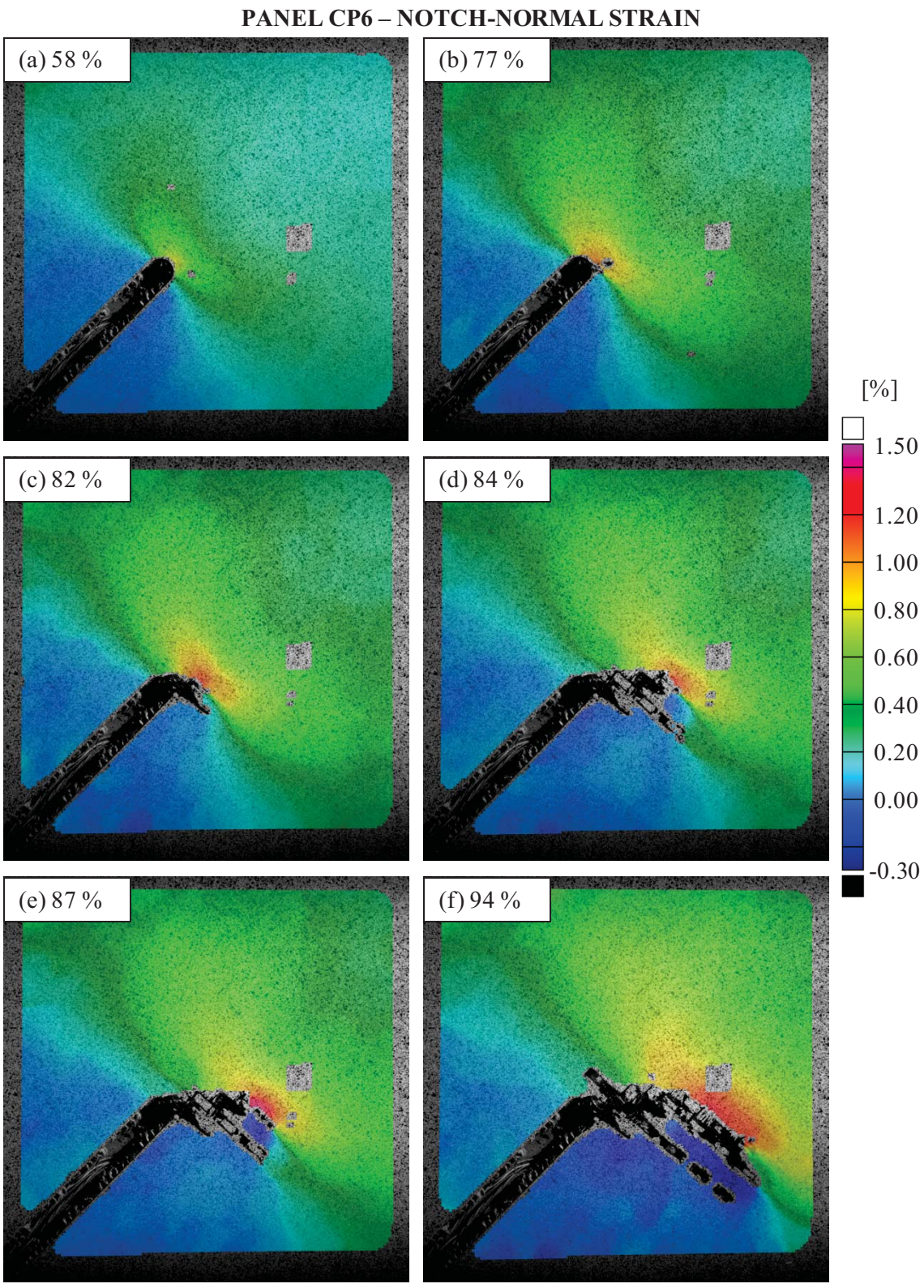

Figure A.31. Notch-normal strain for panel CP6, run CP6-RST-1. The panel fracture load was 18.8 psi internal pressure, 1375 lbf/in hoop load, and 1388 lbf/in longitudinal load.

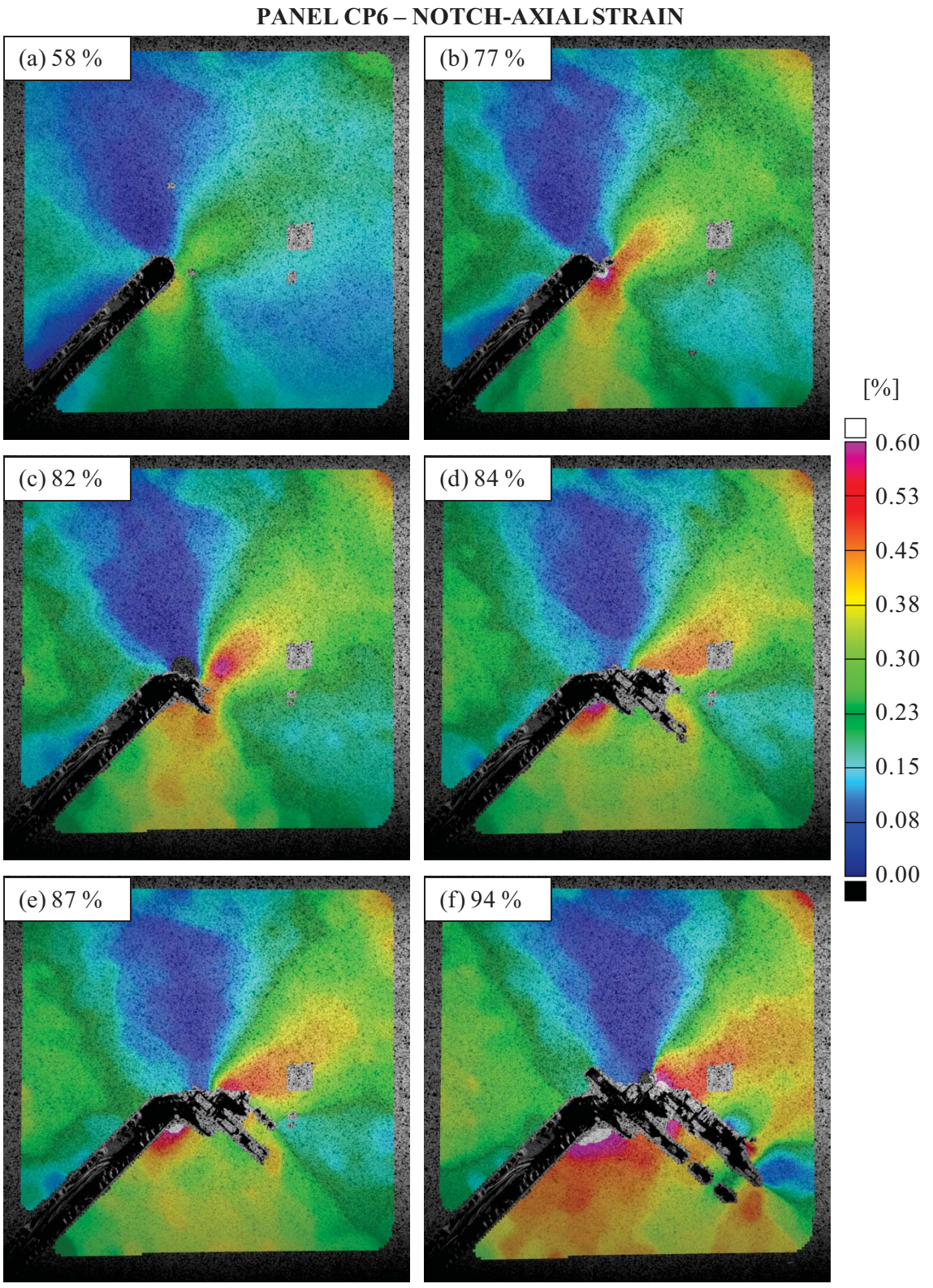

Figure A.32. Notch-axial strain for panel CP6, run CP6-RST-1. The panel fracture load was 18.8 psi internal pressure, 1375 lbf/in hoop load, and 1388 lbf/in longitudinal load.

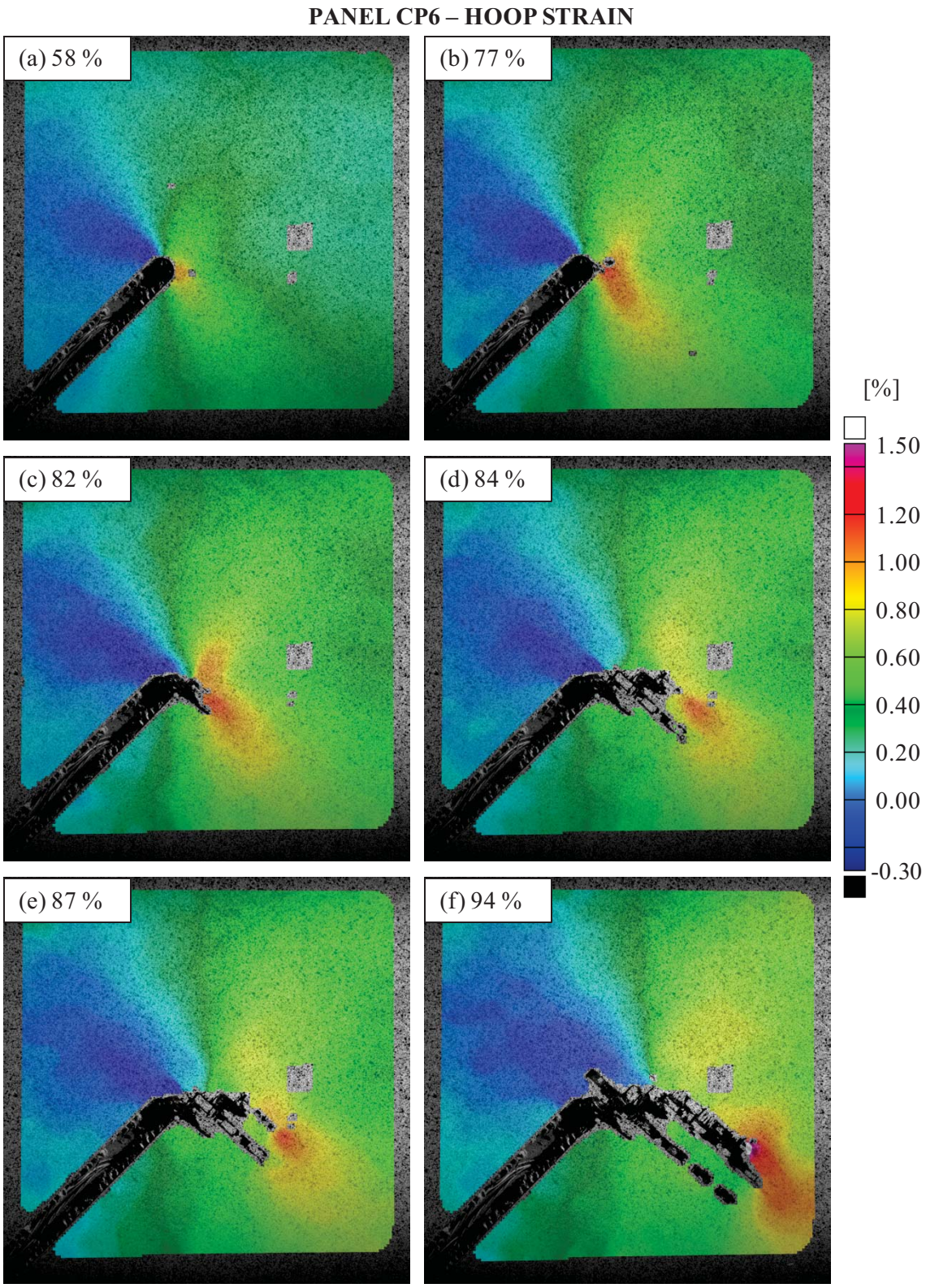

Figure A.33. Hoop strain for panel CP6, run CP6-RST-1. The panel fracture load was 18.8 psi internal pressure, 1375 lbf/in hoop load, and 1388 lbf/in longitudinal load.

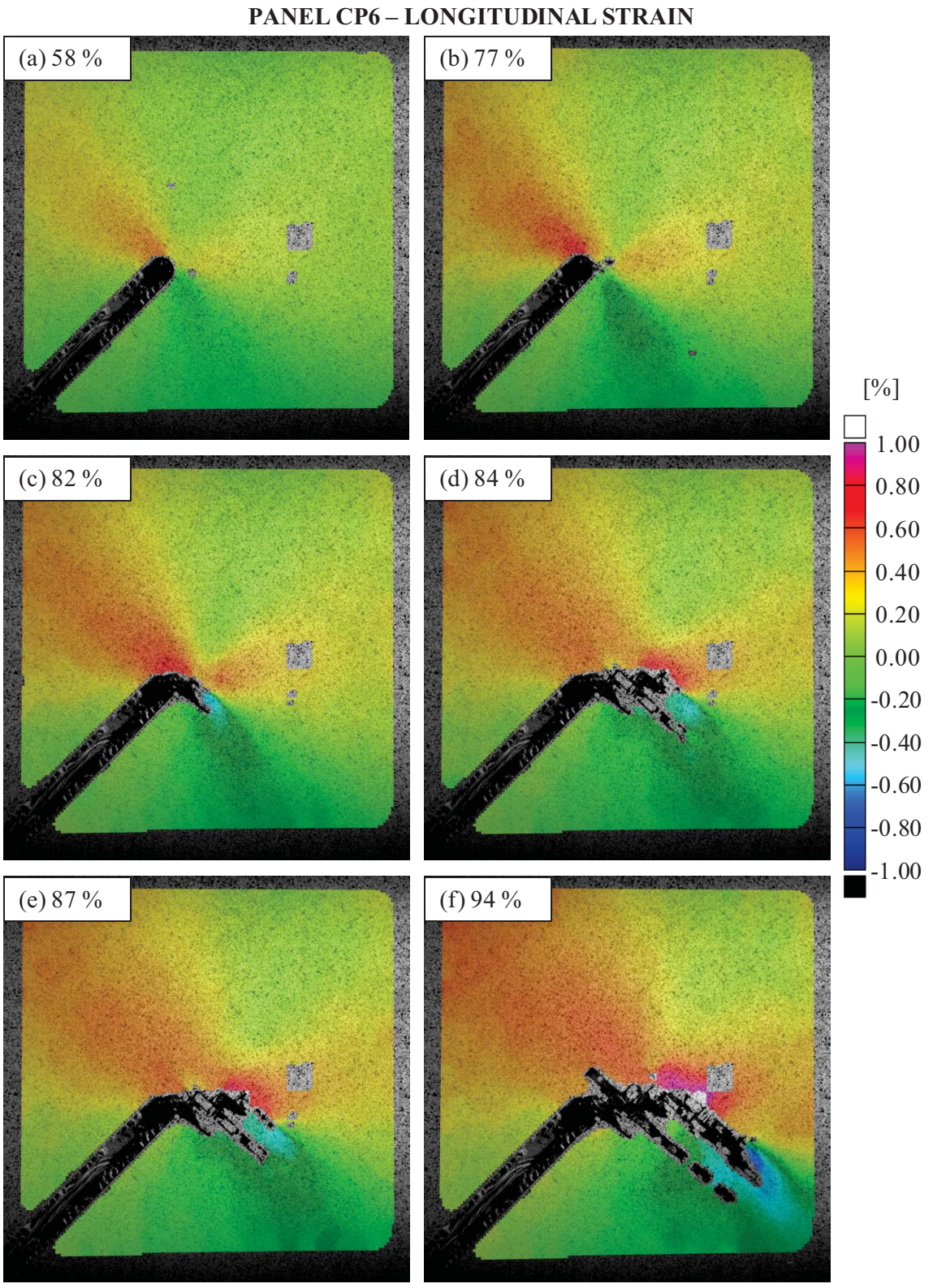

Figure A.34. Longitudinal strain for panel CP6, run CP6-RST-1. The panel fracture load was 18.8 psi internal pressure, 1375 lbf/in hoop load, and 1388 lbf/in longitudinal load.

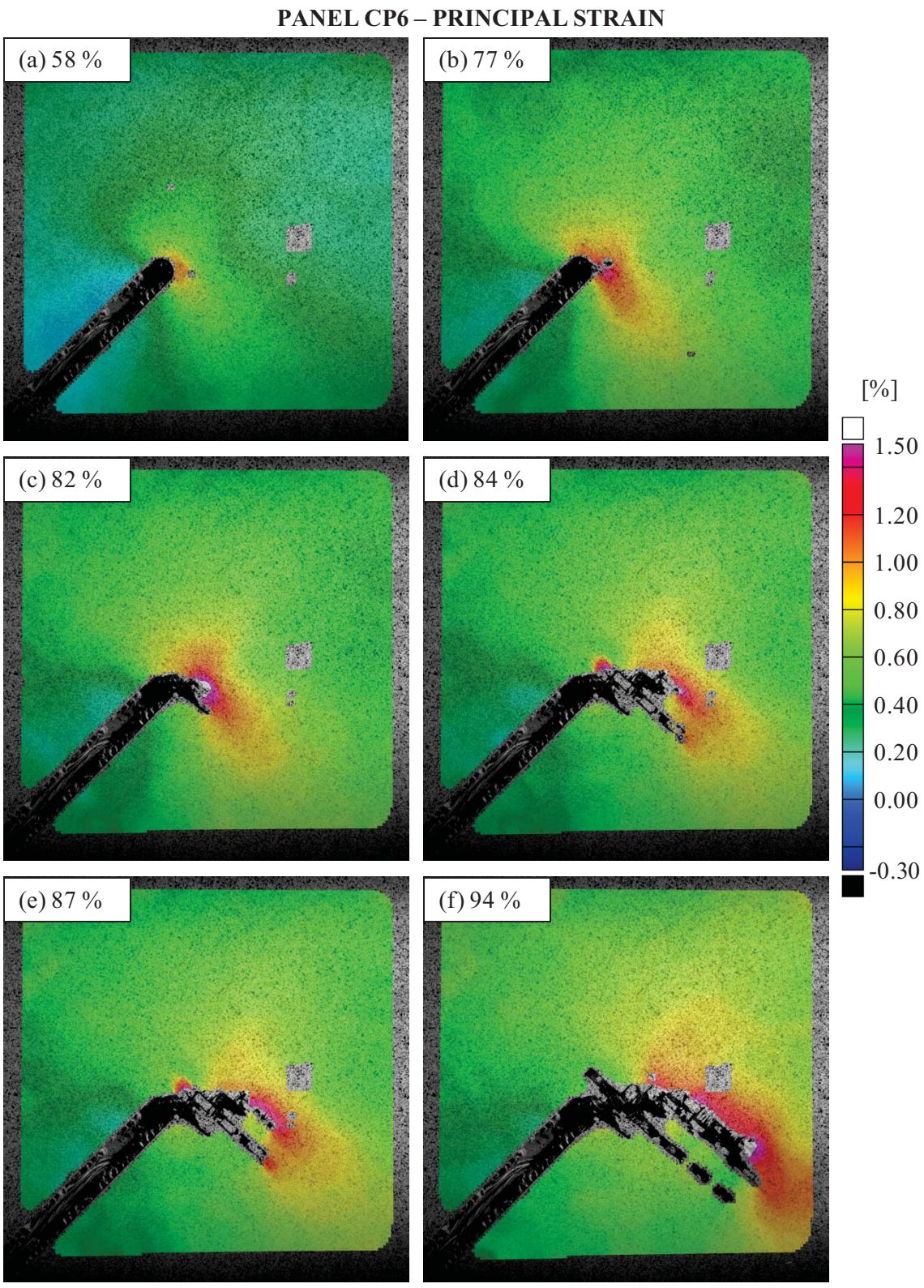

Figure A.35. Principal strain for panel CP6, run CP6-RST-1. The panel fracture load was 18.8 psi internal pressure, 1375 lbf/in hoop load, and 1388 lbf/in longitudinal load.

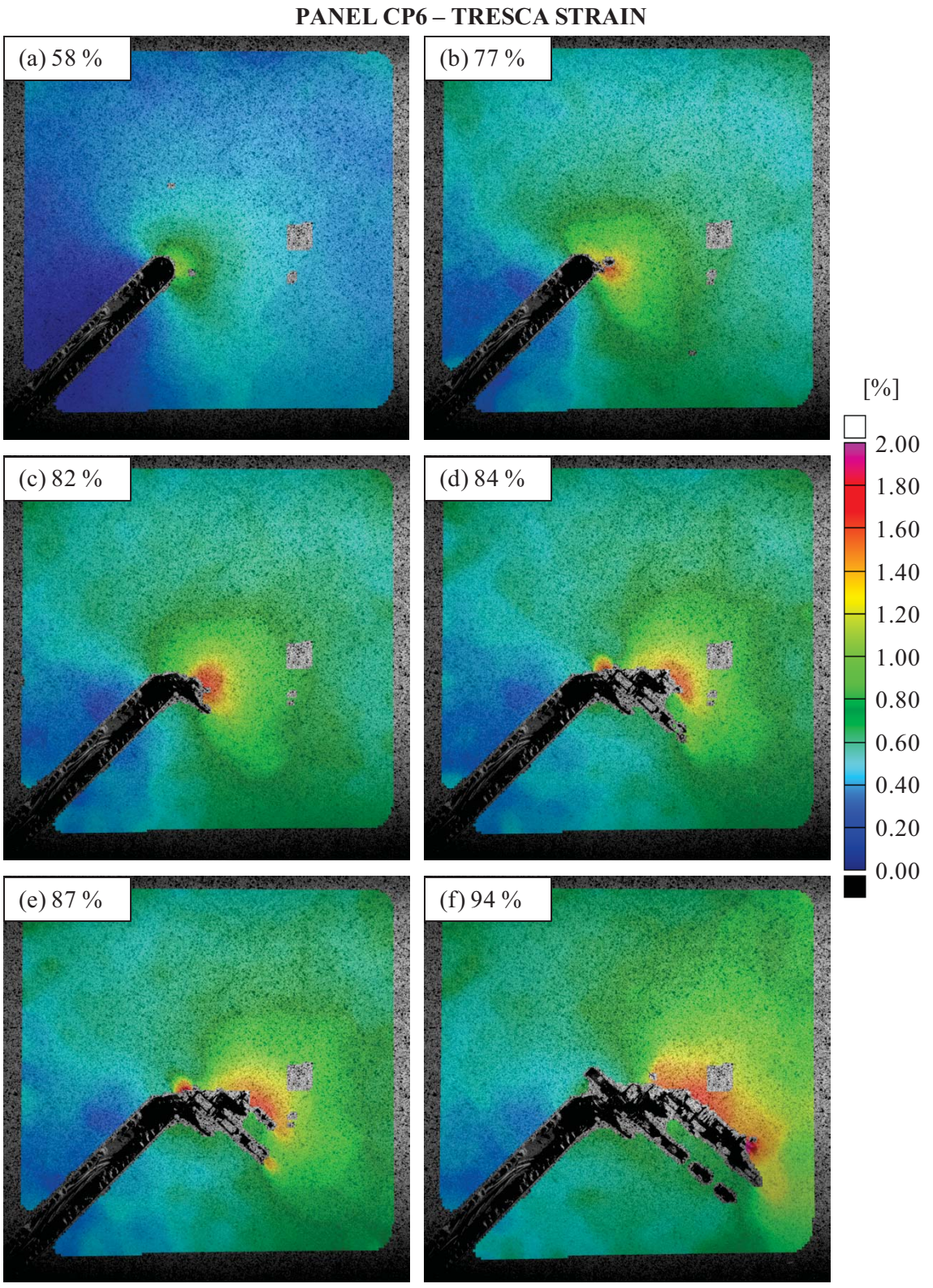

Figure A.36. Tresca strain for panel CP6, run CP6-RST-1. The panel fracture load was 18.8 psi internal pressure, 1375 lbf/in hoop load, and 1388 lbf/in longitudinal load.

APPENDIX B: FINITE ELEMENT MODEL USER SUBROUTINES

B.1. INTRODUCTION

Four custom user subroutines were written to model the propagation of damage through sandwich composite materials in regions of significant transverse shear strain. Each of the three subroutines was prepared in Fortran so as to be able to be compiled and linked with the ABAQUS 6.8-2 solver. The purpose of each of these subroutines, the uncompiled code, and an explanation of all required input files are presented in this appendix.

B.2. INPUT FILES

As detailed in Sections 8.4.2 and 8.4.3, the custom user subroutines presented in this appendix were capable of creating a customized global FE model solution set for a particular state-of-damage and load increment, applying a modified version of typical submodeling boundary conditions, and representing the gradual degradation of woven fiber-reinforced composite materials using one of three user-selectable sets of failure criteria. To accomplish these tasks, six input files in addition to the standard ABAQUS input file are required to be prepared by the user. A basic description of the data contained in each of the six input files is presented in Table B.1.

The LocalNodes.txt input file contains 3 columns. The first column contains the numbers of the local FE model nodes along the global/local interface in numerical order. In columns two and three are the global FE model nodes which bound the corresponding local node with respect to their projected position along the global/local interface mid-plane. The GlobalNodes.txt input file contains a single column with the global node numbers sorted in numerical order. The LocalPos.txt and GlobalPos.txt contains the coordinates of the local and global nodes with respect to the default global coordinate system. The coordinate systems of the global and local FE

Table B.1. Descriptions of Required User Subroutine Input Files.

Input File	Description
LocalNodes.txt	Numbers of the local nodes located along the global/local interface and the numbers of the two bounding global nodes with respect to position along the global/local interface mid-plane
GlobalNodes.txt	Numbers of the global nodes located along the global/local interface
LocalPos.txt	Locations of the local nodes, sorted by local node number
GlobalPos.txt	Locations of the global nodes, sorted by global node number
LocalData.txt	Two interpolation coefficients for each driven local node, corresponding to the two bounding global nodes
AllDisp.txt	All global FE model displacement and transverse shear strain data for all load and damage increments

models should be equal. If not, the coordinates and results of the global FE models should be transformed accordingly.

The LocalData.txt input file contains two interpolation coefficients for each local node, sorted numerically by the associated local node number. The interpolation coefficients are used to relate each local node to their two bounding global nodes, and are based on the relative position of the local nodes along the global/local interface mid-plane with respect to the two nearest global nodes.

The AllDisp.txt input file contains all the necessary displacement and transverse shear strain data from the global FE model library to drive the local nodes under any combination of extent-of-damage and load increment. As mentioned in Section 8.4.3, global FE model libraries can be constructed for multidimensional notch tip damage locations; however, the subroutines presented in this appendix are written for only two-dimensional interpolations (i.e., one physical dimension and one load increment dimension). The input file contains eight columns per time increment and rows equal to the product of the number of global nodes and the number of extent-of-damage increments. The eight columns per time increment contain the six components of displacement and rotation (i.e., u, v, w, θ_x, θ_y, and θ_z), and the two transverse shear strain terms

(i.e., γ_{13} and γ_{23}). Within each load increment, the displacement and transverse shear strain data should be sorted by associated global node number.

B.3. SUBROUTINE: UEXTERNALDB

This subroutine is designed perform specific tasks at set times during the analysis: prior to the analysis, the beginning of each time increment, and the end of each time increment. Prior to the beginning of the analysis, the six input files must be read. Vectors containing the time and damage increments corresponding to the data in AllDisp.txt must be generated, as well. At the beginning of each increment, global interpolation coefficients are generated for the current time and extent-of-damage (i.e., the maximum distance from the notch tips to damage of user-defined severity) with respect to the time and damage increment vectors. These coefficients are used to reduce the data contained in the array AllDisp to a single global model data set to be used to drive the local model. At the end of each increment, the maximum extent-of-damage is calculated and stored for later use in the DISP subroutine.

All values highlighted in red should be manually changed prior to compilation. Descriptions of any such variables can be found in the comments.

```
C**********************************************************************
      SUBROUTINE UEXTERNALDB(LOP,LRESTART,TIME,DTIME,KSTEP,KINC)
C**********************************************************************
C
      INCLUDE 'ABA_PARAM.INC'
C
      INTEGER I, J, K, L, AllEL, AllLD, AllGD, DSteps, TSteps
      DOUBLE PRECISION DFreq, TFreq
      PARAMETER (zero = 0.D0, two = 2.D0, AllEL = 109042, AllLD = 4908,
     1   AllGD = 255, DFreq = 0.1D0, TFreq = 0.02D0, DSteps = 21,
     2   TSteps = 66)
      DOUBLE PRECISION tempDmgExtent1, tempDmgExtent2, DD, TT
      DIMENSION TIME(2)
C
      COMMON LocalPos(AllLD,3), GlobalPos(AllGD,3), LocalData(AllLD,2),
     1   AllDisp(AllGD*DSteps,8*TSteps), DmgLoc(AllEL,3), DmgExtent,
     2   DmgSource1(3), DmgSource2(3), GlobalDisp(AllGD,8),
     3   GDmgInc(DSteps), GTimeInc(TSteps), LocalNodes(AllLD,3),
     4   GlobalNodes(AllGD)
      INTEGER LocalNodes, GlobalNodes
      DOUBLE PRECISION LocalPos, GlobalPos, LocalData, AllDisp, DmgLoc,
     1   DmgExtent, DmgSource1, DmgSource2, GlobalDisp, GDmgInc,
```

```
     2   GTimeInc
C
C*************************************************************************
C   DEFINITION OF VARIABLES
C*************************************************************************
C   DmgSource1     Convex face sheet notch tip location
C   DmgSource2     Concave face sheet notch tip location
C   DmgLoc         Array containing locations of all damage over
C                   preselected threshold value
C   LocalNodes     Array containing driven local node numbers and
C                   associated global nodes
C   GlobalNodes    Array containing driving global node numbers
C   LocalPos       Array containing driven local node locations
C   GlobalPos      Array containing driving global node locations
C   LocalData      Array containing driving node coefficients
C   AllDisp        Array containing global displacement and transverse
C                   shear strain data for all load and damage steps
C   GlobalDisp     Array containing current global displacement data
C   GDmgInc        Damage states contained in AllDisp
C   GTimeInc       Time steps contained in AllDisp
C   DmgExtent      Largest distance between the notch tip and an element
C                   with damage above a preselected threshold value,
C                   averaged between face sheets
C   tempDmgExtent1 Temp value used to calculate max. convex DmgExtent
C   tempDmgExtent2 Temp value used to calculate max. concave DmgExtent
C   TT             Linear interpolation term for time
C   DD             Linear interpolation term for damage
C   AllEL          Total number of elements in model*
C   AllLD          Total number of local driven nodes in model*
C   AllGD          Total number of global driving nodes in model*
C   DFreq          Interval between damage increments [length]*
C   TFreq          Interal between time steps*
C   DSteps         Number of damage incremens*
C   TSteps         Number of time increment*
C                 *These parameters should be defined in each routine
C*************************************************************************
C
C     At the beginning of the analysis:
      IF (LOP .EQ. 0) THEN
C
C     Initialize the damage location matrix.
      DmgExtent = zero
      DO I = I, 3
         DmgSource1(I) = zero
         DmgSource2(I) = zero
      END DO
      DO I = 1, AllEL
         DO J = 1, 3
            DmgLoc(I,J) = zero
         END DO
      END DO
C
C     Open all external input files...
      OPEN(unit = 101,file = 'LocalNodes.txt',
     1   status = 'old', action = 'read')
      OPEN(unit = 102,file = 'GlobalNodes.txt',
     1   status = 'old', action = 'read')
      OPEN(unit = 103,file = 'LocalPos.txt',
     1   status = 'old', action = 'read')
      OPEN(unit = 104,file = 'GlobalPos.txt',
```

```
     1   status = 'old', action = 'read')
      OPEN(unit = 105,file = 'LocalData.txt',
     1   status = 'old', action = 'read')
      OPEN(unit = 106,file = 'AllDisp.txt',
     1   status = 'old', action = 'read')
C
C     ...and write their contents to their respective arrays.
      DO I = 1, AllLD
         READ(101,*) (LocalNodes(I,J),J=1,3)
      END DO
      DO I = 1, AllGD
         READ(102,*) GlobalNodes(I)
      END DO
      DO I = 1, AllLD
         READ(103,*) (LocalPos(I,J),J=1,3)
      END DO
      DO I = 1, AllGD
         READ(104,*) (GlobalPos(I,J),J=1,3)
      END DO
      DO I = 1, AllLD
         READ(105,*) (LocalData(I,J),J=1,2)
      END DO
      DO I = 1, AllGD*DSteps
         READ(106,*) (AllDisp(I,J),J=1,8*TSteps)
      END DO
C     Close all opened external input files
      CLOSE(101)
      CLOSE(102)
      CLOSE(103)
      CLOSE(104)
      CLOSE(105)
      CLOSE(106)
C
C     Initialize GlobalDisp
      DO I = 1, AllGD
         DO J = 1, 6
            GlobalDisp(I,J) = zero
         END DO
      END DO
C
C     Populate the damage and time increment vectors
      DO I = 1, DSteps
         GDmgInc(I) = DFreq*(I-1)
      END DO
      DO I = 1, TSteps
         GTimeInc(I) = TFreq*(I-1)
      END DO
C
      END IF
C*************************************************************************
C     At the beginning of each increment:
      IF (LOP .EQ. 1) THEN
C
C     Determine the time and damage increments which bound the current
C      time and extent of damage.
      DO I = 1, TSteps-1
         IF((TIME(2)+DTIME).GE.GTimeInc(I).AND.(TIME(2)+DTIME).LT.
     1      GTimeInc(I+1)) THEN
            DO J = 1, DSteps-1
               IF(DmgExtent.GE.GDmgInc(J).AND.DmgExtent.LT.GDmgInc(J+1))
```

```
     1            THEN
                  TT = ((TIME(2)+DTIME)-GTimeInc(I))/(GTimeInc(I+1)-
     1              GTimeInc(I))
                  DD = (DmgExtent-GDmgInc(J))/(GDmgInc(J+1)-GDmgInc(J))
C
C     Interpolate AllDisp and populate GlobalDisp
                  DO K = 1+(I-1)*8, 8+(I-1)*8
                     DO L = 1+(J-1)*AllGD, AllGD+(J-1)*AllGD
      GlobalDisp(L-(J-1)*AllGD,K-(I-1)*8) = AllDisp(L,K) + TT *
     1   (AllDisp(L,K+8)-AllDisp(L,K)) + DD * ( AllDisp(L+AllGD,K) + TT*
     2   (AllDisp(L+AllGD,K+8)-AllDisp(L+AllGD,K)) - AllDisp(L,K) - TT *
     3   (AllDisp(L,K+8)-AllDisp(L,K)))
                     END DO
                  END DO
               END IF
            END DO
         END IF
      END DO
C
      END IF
C*****************************************************************
C     At the end of each increment:
      IF (LOP .EQ. 2) THEN
C
C     Initialize the temporary damage extent variables
      tempDmgExtent1 = zero
      tempDmgExtent2 = zero
      DO I = 1, AllEL
C
C     Check to see if damage has occurred
         IF (DmgLoc(I,1).NE.zero.OR.DmgLoc(I,2).NE.zero.OR.DmgLoc(I,3)
     1      .NE.zero) THEN
C
C     If damage has occurred, check which face sheet it occurred in and
C        update the corresponding temporary damage extent variable
            IF (I .LE. 54862) THEN !*
               tempDmgExtent2 = max( tempDmgExtent2, abs(DmgLoc(I,3)
     1            - DmgSource2(3)) )
            ELSEIF (I .GE. 54863) THEN !*
               tempDmgExtent1 = max( tempDmgExtent1, abs(DmgLoc(I,3)
     1            - DmgSource1(3)) )
            END IF
C     *The above values highlighted in red differentiate the local
C      elements located in the exterior and interior face sheets.
C      These should be adjusted for each model accordingly. For
C      non-sandwich structures, remove the above IF statement and
C      define DmgExtent directly.
C
C     Calculate the damage extent used to select the global solutions
C        used to drive the local model in the next step
            DmgExtent = max(DmgExtent,(tempDmgExtent1+tempDmgExtent2)
     1         /two)
         END IF
      END DO
C
      END IF
C
      RETURN
      END
C*****************************************************************
```

B.4. SUBROUTINE: DISP

The DISP subroutine is called by ABAQUS at the beginning of each load increment to define the magnitude of the displacement boundary conditions of all local nodes driven by the global model results. Using the custom displacement and transverse shear strain global FE model data set assembled by the UEXTERNALDB subroutine, the three displacement components of the driven local nodes are calculated. Because the local model nodes are more densely spaced along the global/local interface, the applied displacements must be interpolated from the two bounding global nodes. The relative location of the global and local nodes is known a priori, and these coefficients are stored in the required input file LocalData.txt, described in Section B.2.

All values highlighted in red should be manually changed prior to compilation. Descriptions of any such variables can be found in the comments.

```
C**********************************************************************
      SUBROUTINE  DISP(U,KSTEP,KINC,TIME,NODE,NOEL,JDOF,COORDS)
C**********************************************************************
C
      INCLUDE 'ABA_PARAM.INC'
C
      INTEGER I, J, K, L, AllEL, AllLD, AllGD, DSteps, TSteps
      DOUBLE PRECISION DFreq, TFreq
      PARAMETER (zero = 0.D0, two = 2.D0, AllEL = 109042, AllLD = 4908,
     1   AllGD = 255, DFreq = 0.1D0, TFreq = 0.02D0, DSteps = 21,
     2   TSteps = 66)
C
      DIMENSION U(3),TIME(2),COORDS(3)
      INTEGER GNodeL, GNodeU
      DOUBLE PRECISION GNodeLCof, GNodeUCof, GDispL(8), GPosL(3),
     1   GDispU(8), GPosU(3), LPos(3)
C
      COMMON LocalPos(AllLD,3), GlobalPos(AllGD,3), LocalData(AllLD,2),
     1   AllDisp(AllGD*DSteps,8*TSteps), DmgLoc(AllEL,3), DmgExtent,
     2   DmgSource1(3), DmgSource2(3), GlobalDisp(AllGD,8),
     3   GDmgInc(DSteps), GTimeInc(TSteps), LocalNodes(AllLD,3),
     4   GlobalNodes(AllGD)
      INTEGER LocalNodes, GlobalNodes
      DOUBLE PRECISION LocalPos, GlobalPos, LocalData, AllDisp, DmgLoc,
     1   DmgExtent, DmgSource1, DmgSource2, GlobalDisp, GDmgInc,
     2   GTimeInc
C
C**********************************************************************
C   DEFINITION OF VARIABLES
C**********************************************************************
C   GNodeL         Lower global driving node number
C   GNodeU         Upper global driving node number
C   GNodeLCof      Lower global driving node coefficient
C   GNodeUCof      Upper global driving node coefficient
```

```
C   GlobalPos      Array containing all original global positions
C   GlobalDisp     Array containing all current global displacement data
C   LocalData      Array containing global driving node coefficients
C   GDispL(6)      Global displacement of lower driving node
C   GDispU(6)      Global displacement of upper driving node
C   GPosL(3)       Original global position of lower driving node
C   GPosU(3)       Original global position of upper driving node
C   LPos(3)        Original local position of current node
C*****************************************************************
C
C     Lookup loop to read conversion parameters and original local
C        position for current node
      LocalData1: DO I = 1, AllLD
         IF (LocalNodes(I,1) .EQ. NODE) THEN
            GNodeL = LocalNodes(I,2)
            GNodeU = LocalNodes(I,3)
            GNodeLCof = LocalData(I,1)
            GNodeUCof = LocalData(I,2)
            DO J = 1, 3
               LPos(J) = LocalPos(I,J)
            END DO
            EXIT LocalData1
         END IF
      END DO LocalData1
C
C     Read current global disp. and original global position data
      GlobalLower1: DO I = 1, AllGD
         IF (GlobalNodes(I) .EQ. GNodeL) THEN
            DO J = 1, 8
               GDispL(J) = GlobalDisp(I,J)
            END DO
            DO J = 1, 3
               GPosL(J) = GlobalPos(I,J)
            END DO
            EXIT GlobalLower1
         END IF
      END DO GlobalLower1
C
      GlobalUpper1: DO I = 1, AllGD
         IF (GlobalNodes(I) .EQ. GNodeU) THEN
            DO J = 1, 8
               GDispU(J) = GlobalDisp(I,J)
            END DO
            DO J = 1, 3
               GPosU(J) = GlobalPos(I,J)
            END DO
            EXIT GlobalUpper1
         END IF
       END DO GlobalUpper1
C
C     Calculate 3 components of current local displacement
      SELECT CASE (JDOF)
      CASE (1)
         U(1) = GNodeLCof*GDispL(1) + GNodeUCof*GDispU(1) + (GNodeLCof*
     1       (GDispL(5) - GDispL(7)) + GNodeUCof*(GDispU(5) - GDispU(7)))
     2       *(LPos(3) - (GNodeLCof*GPosL(3) + GNodeUCof*GPosU(3))) -
     3       (GNodeLCof*(GDispL(6) - GDispL(8)) + GNodeUCof*(GDispU(6) -
     4       GDispU(8)))*(LPos(2) - (GNodeLCof*GPosL(2) + GNodeUCof*
     5       GPosU(2)))
      CASE (2)
```

```
            U(1) = GNodeLCof*GDispL(2) + GNodeUCof*GDispU(2) + (GNodeLCof*
     1         (GDispL(6) - GDispL(8)) + GNodeUCof*(GDispU(6) - GDispU(8)))
     2         *(LPos(1) - (GNodeLCof*GPosL(1) + GNodeUCof*GPosU(1))) -
     3         (GNodeLCof*GDispL(4) + GNodeUCof*GDispU(4))*(LPos(3) -
     4         (GNodeLCof*GPosL(3) + GNodeUCof*GPosU(3)))
          CASE (3)
            U(1) = GNodeLCof*GDispL(3) + GNodeUCof*GDispU(3) + (GNodeLCof*
     1         GDispL(4) + GNodeUCof*GDispU(4))*(LPos(2) - (GNodeLCof*
     2         GPosL(2) + GNodeUCof*GPosU(2))) - (GNodeLCof*(GDispL(5) -
     3         GDispL(7)) + GNodeUCof*(GDispU(5) - GDispU(7)))*(LPos(1) -
     4         (GNodeLCof*GPosL(1) + GNodeUCof*GPosU(1)))
          END SELECT
C
          RETURN
          END
C*******************************************************************************
```

B.5. SUBROUTINE: UMAT

The UMAT subroutine allows for custom material and failure models to be incorporated into the ABAQUS solver. The subroutine is called by the solver for each element integration point during each load increment of the solution. This particular UMAT subroutine represents an orthotropic material capable of gradually failing in its three principal material directions (i.e., warp, fill, and thickness). Failure can be determined using sets of either the maximum strain, maximum stress, or Hashin failure criteria. Upon reaching a user-specified damage threshold, the location of the damage is stored for use by the UEXTERNALDB subroutine to determine the extent-of-damage for use in defining the local model boundary conditions of the next load increment.

All values highlighted in red should be manually changed prior to compilation. Descriptions of any such variables can be found in the comments.

```
C**********************************************************************
      SUBROUTINE UMAT(STRESS,STATEV,DDSDDE,SSE,SPD,SCD,
     1     RPL,DDSDDT,DRPLDE,DRPLDT,
     2     STRAN,DSTRAN,TIME,DTIME,TEMP,DTEMP,PREDEF,DPRED,CMNAME,
     3     NDI,NSHR,NTENS,NSTATV,PROPS,NPROPS,COORDS,DROT,PNEWDT,
     4     CELENT,DFGRD0,DFGRD1,NOEL,NPT,LAYER,KSPT,KSTEP,KINC)
C**********************************************************************
C
      INCLUDE 'ABA_PARAM.INC'
C
      CHARACTER*80 CMNAME

      DIMENSION STRESS(NTENS), STATEV(NSTATV), DDSDDE(NTENS,NTENS),
     1     DDSDDT(NTENS), DRPLDE(NTENS), STRAN(NTENS), DSTRAN(NTENS),
     2     TIME(2), PREDEF(1), DPRED(1), PROPS(NPROPS), COORDS(3),
     3     DROT(3,3), DFGRD0(3,3), DFGRD1(3,3)
C
      DOUBLE PRECISION C(6,6), CD(6,6), old_stress(6), STRANT(6),
     1   dold_stress(6), d_stress(6), DCDD1(6,6), DCDD2(6,6),
     2   DCDD3(6,6), DF1DE(6), DF2DE(6), DF3DE(6), DD1DE(6), DD2DE(6),
     3   DD3DE(6), Atemp1(6), Atemp2(6), Atemp3(6)
C
      DOUBLE PRECISION zero, one, two, half, DFreq, TFreq
      INTEGER I, J, AllEL, AllLD, AllGD, DSteps, TSteps, FC
      PARAMETER (zero = 0.D0, one = 1.D0, two = 2.D0, half = 0.5D0,
     1   AllEL = 109042, AllLD = 4908, AllGD = 255, DFreq = 0.1D0,
     2   TFreq = 0.02D0, DSteps = 21, TSteps = 66)
      DOUBLE PRECISION E1,E2,E3,G12,G23,G13,nu12,nu21,nu23,nu32,nu13,
     1     nu31,Ctemp,CDtemp,DCDtempDD1,DCDtempDD2,DCDtempDD3,DD3DF3,
     2     DD2DF2,DD1DF1,AD1,AD2,AD3,F1,F2,F3
      DOUBLE PRECISION sigT1,sigC1,sigT2,sigC2,sigT3,sigC3,sigS12,
```

```
     1     epiT1,epiC1,epiT2,epiC2,epiT3,epiC3,epiS12,eta,Gf,Gm
      DOUBLE PRECISION D1,D2,D3,D1v,D2v,D3v,D1_OLD,D2_OLD,D3_OLD,
     1     D1v_OLD,D2v_OLD,D3v_OLD
C
      COMMON LocalPos(AllLD,3), GlobalPos(AllGD,3), LocalData(AllLD,2),
     1   AllDisp(AllGD*DSteps,8*TSteps), DmgLoc(AllEL,3), DmgExtent,
     2   DmgSource1(3), DmgSource2(3), GlobalDisp(AllGD,8),
     3   GDmgInc(DSteps), GTimeInc(TSteps), LocalNodes(AllLD,3),
     4   GlobalNodes(AllGD)
      INTEGER LocalNodes, GlobalNodes
      DOUBLE PRECISION LocalPos, GlobalPos, LocalData, AllDisp, DmgLoc,
     1   DmgExtent, DmgSource1, DmgSource2, GlobalDisp, GDmgInc,
     2   GTimeInc
C
C**********************************************************************
C   DEFINITION OF VARIABLES
C**********************************************************************
C   C              Undamaged stiffness tensor
C   Ctemp          Coefficient used in calculation of C
C   CD             Damaged stiffness tensor
C   CDtemp         Coefficient used in calculation of CD
C   old_stress     Stress at beginning of the increment
C   dold_stress    Stress at beginning of the increment if eta = zero
C   d_stress       Stress if eta = zero
C   FC             Failure criterion: 1 for max strain, 2 for max
C                   stress, 3 for Hashin
C   D1             Damage state variable in the 1-direction*
C   D1v            Regularized damage state variable in the 1-direction*
C   F1             Failure criterion governing 1-direction failures*
C   AD1            Coefficient used in the calculation of D1*
C   DD1DF1         1st derivative of D1 w.r.t. F1*
C   DF1DE          1st derivative of F1 w.r.t. strain*
C   DD1DE          1st derivative of D1 w.r.t. strain*
C   DCDD1          1st derivative of CD w.r.t. D1*
C   STATEV(1)      Storage space to save D1 (matrix)
C   STATEV(2)      Storage space to save D2 (fill)
C   STATEV(3)      Storage space to save D3 (warp)
C   STATEV(4)      Storage space to save D1v (matrix)
C   STATEV(5)      Storage space to save D2v (fill)
C   STATEV(6)      Storage space to save D3v (warp)
C   STATEV(7:12)   Storage space to save dold_stress between increments
C   DmgSource1     Convex face sheet notch tip location
C   DmgSource2     Concave face sheet notch tip location
C   DmgLoc         Array containing locations of all damage over
C                   preselected threshold value
C   DDSDDE         Jacobian tensor
C   Atemp1,2,3     Temporary values used in the calculations of DDSDDE
C                 *similar variables used for the 2- and 3-directions
C**********************************************************************
C
C     Read material properties from ABAQUS input file
      E1 = PROPS(1)           !Young's modulus in direction 1
      E2 = PROPS(2)           !Young's modulus in direction 2
      E3 = PROPS(3)           !Young's modulus in direction 3
      G12 = PROPS(4)          !Shear modulus in direction 12 plane
      G23 = PROPS(5)          !Shear modulus in direction 23 plane
      G13 = PROPS(6)          !Shear modulus in direction 13 plane
      nu21 = PROPS(7)         !Poisson's ratio (21)
      nu32 = PROPS(8)         !Poisson's ratio (32)
      nu31 = PROPS(9)         !Poisson's ratio (31)
```

```
      nu12 = nu21 / E2 * E1   !Poisson's ratio (12)
      nu23 = nu32 / E3 * E2   !Poisson's ratio (23)
      nu13 = nu31 / E3 * E1   !Poisson's ratio (13)
C
C     Read failure properties from ABAQUS input file
      sigT1 = PROPS(10)     !Failure Stress in 1 direction (Tension)
      sigC1 = PROPS(11)     !Failure Stress in 1 direction (Compression)
      sigT2 = PROPS(12)     !Failure Stress in 2 direction (Tension)
      sigC2 = PROPS(13)     !Failure Stress in 2 direction (Compression)
      sigT3 = PROPS(14)     !Failure Stress in 3 direction (Tension)
      sigC3 = PROPS(15)     !Failure Stress in 3 direction (Compression)
      sigS12 = PROPS(16)    !Failure Shear Stress
      eta = PROPS(17)       !Viscous regularization parameter
      Gf = PROPS(18)        !Fiber fracture toughness
      Gm = PROPS(19)        !Matrix facture toughness
C
C     Read damage progression parameters from ABAQUS input file
      FC = PROPS(20)        !Failure criterion
      DmgPrg = PROPS(21)    !Damage progression threshold
C
C     Calculate the strain at the end of the increment
      DO I = 1, NTENS
         STRANT(I) = STRAN(I) + DSTRAN(I)
      END DO
C
C     Calculate the undamaged stiffness tensor, C
      DO I = 1, 6
         DO J = 1, 6
            C(I,J) = zero
         END DO
      END DO
      Ctemp = one / (one - nu12*nu21 - nu23*nu32 - nu13*nu31 -
     1   two*nu21*nu32*nu13)
      C(1,1) = E1 * (one - nu23*nu32) * Ctemp
      C(2,2) = E2 * (one - nu13*nu31) * Ctemp
      C(3,3) = E3 * (one - nu12*nu21) * Ctemp
      C(1,2) = E2 * (nu12 + nu32*nu13) * Ctemp
      C(1,3) = E3 * (nu13 + nu12*nu23) * Ctemp
      C(2,3) = E2 * (nu32 + nu12*nu31) * Ctemp
      C(4,4) = G12
      C(5,5) = G13
      C(6,6) = G23
      DO I = 2, 6
         DO J = 1, I-1
            C(I,J) = C(J,I)
         END DO
      END DO
C
C     Calculate the failure strains
      IF (FC .EQ. 1) THEN
         epiT1 = sigT1 / C(1,1)  !Failure strain in 1 direction (T)
         epiC1 = sigC1 / C(1,1)  !Failure strain in 1 direction (C
         epiT2 = sigT2 / C(2,2)  !Failure strain in 2 direction (T)
         epiC2 = sigC2 / C(2,2)  !Failure strain in 2 direction (C)
         epiT3 = sigT3 / C(3,3)  !Failure strain in 3 direction (T)
         epiC3 = sigC3 / C(3,3)  !Failure strain in 3 direction (C)
         epiS12 = sigS12 / C(4,4)!Failure shear strain
      END IF
C
C     Read the old damage state variables
```

```
      D1_OLD = STATEV(1)
      D2_OLD = STATEV(2)
      D3_OLD = STATEV(3)
      D1v_OLD = STATEV(4)
      D2v_OLD = STATEV(5)
      D3v_OLD = STATEV(6)
C
C     Save the old stress to old_stress
      DO I = 1, NTENS
         old_stress(I) = STRESS(I)
      END DO
C
C     Read old stress without viscous regularization from state variables
      DO I = 1, NTENS
         dold_stress(I) = STATEV(I+6)
      END DO
C
C     Initialize damage state variables and their derivatives
      D1 = zero
      D2 = zero
      D3 = zero
      DD1DF1 = zero
      DD2DF2 = zero
      DD3DF3 = zero
      DO I = 1, 6
         DF1DE(I) = zero
         DD1DE(I) = zero
         DF2DE(I) = zero
         DD2DE(I) = zero
         DF3DE(I) = zero
         DD3DE(I) = zero
      END DO
C
      SELECT CASE (FC)
      CASE (1) !Maximum strain failure criterion
C*********************************************************************
C     CHECK THE WARP-DIRECTION FIBER FAILURE CRITERION
C*********************************************************************
C
C     Failure Criterion
      F3 = STRANT(3) / epiT3
C
C     Calculate D3
      IF (F3 .GT. one) THEN
         AD3 = (two*CELENT*sigT3**two)/(two*E3*Gf - CELENT*sigT3**two)
         D3 = one - (one / F3) * EXP(AD3 * (one - F3))
C
C     Calculate DD3DE
         IF (D3 .GT. D3_OLD) THEN
            DD3DF3 = (one/(F3**two))*(AD3*F3 + one)*EXP(AD3*(one - F3))
            DF3DE(3) = one / epiT3
            DD3DE(3) = DD3DF3 * DF3DE(3)
         END IF
      END IF
      D3 = MAX(D3, D3_OLD)
C*********************************************************************
C     CHECK THE FILL-DIRECTION FIBER FAILURE CRITERION
C*********************************************************************
C
C     Failure Criterion
```

```
      F2 = STRANT(2) / epiT2
C
C     Calculate D2
      IF (F2 .GT. one) THEN
         AD2 = (two*CELENT*sigT2**two)/(two*E2*Gf - CELENT*sigT2**two)
         D2 = one - (one / F2) * EXP(AD2 * (one - F2))
C
C     Calculate DD2DE
         IF (D2 .GT. D2_OLD) THEN
            DD2DF2 = (one/(F2**two))*(AD2*F2 + one)*EXP(AD2*(one - F2))
            DF2DE(2) = one / epiT2
            DD2DE(2) = DD2DF2 * DF2DE(2)
         END IF
      END IF
      D2 = MAX(D2, D2_OLD)
C*************************************************************************
C     CHECK THE MATRIX FAILURE CRITERION
C*************************************************************************
C
C     Failure Criterion
      F1 = MAX(STRANT(1) / epiT1, -STRANT(1) / epiC1)
C
C     Calculate D1 and DD1DE
      IF (F1 .GT. one) THEN
         IF (STRANT(1) .GT. zero) THEN
            AD1 = (two*CELENT*sigT1**two)/(two*E1*Gm-CELENT*sigT1**two)
            D1 = one - (one / F1) * EXP(AD1 * (one - F1))
            IF (D1 .GT. D1_OLD) THEN
               DD1DF1 = (one/(F1**two))*(AD1*F1 + one)*EXP(AD1*(one-F1))
               DF1DE(1) = one / epiT1
               DD1DE(1) = DD1DF1 * DF1DE(1)
            END IF
         ELSE
            AD1 = (two*CELENT*sigC1**two)/(two*E1*Gm-CELENT*sigC1**two)
            D1 = one - (one / F1) * EXP(AD1 * (one - F1))
            IF (D1 .GT. D1_OLD) THEN
               DD1DF1 = (one/(F1**two))*(AD1*F1 + one)*EXP(AD1*(one-F1))
               DF1DE(1) = -one / epiC1
               DD1DE(1) = DD1DF1 * DF1DE(1)
            END IF
         END IF
      END IF
      D1 = MAX(D1, D1_OLD)
C*************************************************************************
      CASE (2) !Maximum stress failure criterion
C*************************************************************************
C     CHECK THE WARP-DIRECTION FIBER FAILURE CRITERION
C*************************************************************************
C
C     Failure Criterion
      F3 = STRESS(3) / sigT3
C
C     Calculate D3
      IF (F3 .GT. one) THEN
         AD3 = (two*CELENT*sigT3**two)/(two*E3*Gf - CELENT*sigT3**two)
         D3 = one - (one / F3) * EXP(AD3 * (one - F3))
C
C     Calculate DD3DE
         IF (D3 .GT. D3_OLD) THEN
            DD3DF3 = (one/(F3**two))*(AD3*F3 + one)*EXP(AD3*(one - F3))
```

```
            DO I = 1, 3
               DF3DE(I) = C(I,3) / sigT3
            END DO
            DO I = 1, 3
               DD3DE(I) = DD3DF3 * DF3DE(I)
            END DO
         END IF
      END IF
      D3 = MAX(D3, D3_OLD)
C*********************************************************************
C     CHECK THE FILL-DIRECTION FIBER FAILURE CRITERION
C*********************************************************************
C
C     Failure Criterion
      F2 = STRESS(2) / sigT2
C
C     Calculate D2
      IF (F2 .GT. one) THEN
         AD2 = (two*CELENT*sigT2**two)/(two*E2*Gf - CELENT*sigT2**two)
         D2 = one - (one / F2) * EXP(AD2 * (one - F2))
C
C     Calculate DD2DE
         IF (D2 .GT. D2_OLD) THEN
            DD2DF2 = (one/(F2**two))*(AD2*F2 + one)*EXP(AD2*(one - F2))
            DO I = 1, 3
               DF2DE(I) = C(I,2) / sigT2
            END DO
            DO I = 1, 3
               DD2DE(I) = DD2DF2 * DF2DE(I)
            END DO
         END IF
      END IF
      D2 = MAX(D2, D2_OLD)
C*********************************************************************
C     CHECK THE MATRIX FAILURE CRITERION
C*********************************************************************
C
C     Failure Criterion
      F1 = MAX(STRESS(1) / sigT1, -STRESS(1) / sigC1)
C
C     Calculate D1 and DD1DE
      IF (F1 .GT. one) THEN
         IF (STRESS(1) .GT. zero) THEN
            AD1 = (two*CELENT*sigT1**two)/(two*E1*Gm-CELENT*sigT1**two)
            D1 = one - (one / F1) * EXP(AD1 * (one - F1))
            IF (D1 .GT. D1_OLD) THEN
               DD1DF1 = (one/(F1**two))*(AD1*F1 + one)*EXP(AD1*(one-F1))
               DO I = 1, 3
                  DF1DE(I) = C(I,1) / sigT1
               END DO
               DO I = 1, 3
                  DD1DE(I) = DD1DF1 * DF1DE(I)
               END DO
            END IF
         ELSE
            AD1 = (two*CELENT*sigC1**two)/(two*E1*Gm-CELENT*sigC1**two)
            D1 = one - (one / F1) * EXP(AD1 * (one - F1))
            IF (D1 .GT. D1_OLD) THEN
               DD1DF1 = (one/(F1**two))*(AD1*F1 + one)*EXP(AD1*(one-F1))
               DO I = 1, 3
```

```
                  DF1DE(I) = -C(I,1) / sigC1
               END DO
               DO I = 1, 3
                  DD1DE(I) = DD1DF1 * DF1DE(I)
               END DO
            END IF
         END IF
      END IF
      D1 = MAX(D1, D1_OLD)
C**********************************************************************
      CASE (3) !Hashin failure criterion
C**********************************************************************
C     CHECK THE WARP-DIRECTION FIBER FAILURE CRITERION
C**********************************************************************
C
C     Failure Criterion
      F3 = SQRT((STRESS(3)/sigT3)**two+(STRESS(5)**two+STRESS(6)**two)/
     1   sigS12**two)
C
C     Calculate D3
      IF (F3 .GT. one) THEN
         AD3 = (two*CELENT*sigT3**two)/(two*E3*Gf - CELENT*sigT3**two)
         D3 = one - (one / F3) * EXP(AD3 * (one - F3))
C
C     Calculate DD3DE
         IF (D3 .GT. D3_OLD) THEN
            DD3DF3 = (one/(F3**two))*(AD3*F3 + one)*EXP(AD3*(one - F3))
            DO I = 1, 3
               DF3DE(I) = STRESS(3)*C(I,3) / (F3 * sigT3**two)
            END DO
            DF3DE(5) = STRESS(5)*C(5,5) / (F3 * sigS12**two)
            DF3DE(6) = STRESS(6)*C(6,6) / (F3 * sigS12**two)
            DO I = 1, 6
               DD3DE(I) = DD3DF3 * DF3DE(I)
            END DO
         END IF
      END IF
      D3 = MAX(D3, D3_OLD)
C**********************************************************************
C     CHECK THE FILL-DIRECTION FIBER FAILURE CRITERION
C**********************************************************************
C
C     Failure Criterion
      F2 = SQRT((STRESS(2)/sigT2)**two + (STRESS(4)**two + STRESS(6)**two)
/
     1   sigS12**two)
C
C     Calculate D2
      IF (F2 .GT. one) THEN
         AD2 = (two*CELENT*sigT2**two)/(two*E2*Gf - CELENT*sigT2**two)
         D2 = one - (one / F2) * EXP(AD2 * (one - F2))
C
C     Calculate DD2DE
         IF (D2 .GT. D2_OLD) THEN
            DD2DF2 = (one/(F2**two))*(AD2*F2 + one)*EXP(AD2*(one - F2))
            DO I = 1, 3
               DF2DE(I) = STRESS(2)*C(I,2) / (F2 * sigT2**two)
            END DO
            DF2DE(4) = STRESS(4)*C(4,4) / (F2 * sigS12**two)
            DF2DE(6) = STRESS(6)*C(6,6) / (F2 * sigS12**two)
```

```
            DO I = 1, 6
               DD2DE(I) = DD2DF2 * DF2DE(I)
            END DO
         END IF
      END IF
      D2 = MAX(D2, D2_OLD)
C**********************************************************************
C     CHECK THE MATRIX FAILURE CRITERION
C**********************************************************************
C
C     Failure Criterion
      F1 = MAX(STRESS(1) / sigT1, -STRESS(1) / sigC1)
C
C     Calculate D1 and DD1DE
      IF (F1 .GT. one) THEN
         IF (STRESS(1) .GT. zero) THEN
            AD1 = (two*CELENT*sigT1**two)/(two*E1*Gm-CELENT*sigT1**two)
            D1 = one - (one / F1) * EXP(AD1 * (one - F1))
            IF (D1 .GT. D1_OLD) THEN
               DD1DF1 = (one/(F1**two))*(AD1*F1 + one)*EXP(AD1*(one-F1))
               DO I = 1, 3
                  DF1DE(I) = C(I,1) / sigT1
               END DO
               DO I = 1, 3
                  DD1DE(I) = DD1DF1 * DF1DE(I)
               END DO
            END IF
         ELSE
            AD1 = (two*CELENT*sigC1**two)/(two*E1*Gm-CELENT*sigC1**two)
            D1 = one - (one / F1) * EXP(AD1 * (one - F1))
            IF (D1 .GT. D1_OLD) THEN
               DD1DF1 = (one/(F1**two))*(AD1*F1 + one)*EXP(AD1*(one-F1))
               DO I = 1, 3
                  DF1DE(I) = -C(I,1) / sigC1
               END DO
               DO I = 1, 3
                  DD1DE(I) = DD1DF1 * DF1DE(I)
               END DO
            END IF
         END IF
      END IF
      D1 = MAX(D1, D1_OLD)
C**********************************************************************
      END SELECT
C
C     Apply viscous regularization
      D1v = ETA / (ETA + DTIME) * D1v_OLD + DTIME / (ETA + DTIME) * D1
      D2v = ETA / (ETA + DTIME) * D2v_OLD + DTIME / (ETA + DTIME) * D2
      D3v = ETA / (ETA + DTIME) * D3v_OLD + DTIME / (ETA + DTIME) * D3
C
C     If damage threshold is exceeded, store the location of the failed
C        element (for use in UEXTERNALDB subroutine)
      IF (D2v .GT. DmgPrg .OR. D3v .GT. DmgPrg) THEN
         DO I = 1, 3
            DmgLoc(NOEL,I) = COORDS(I)
         END DO
      END IF
C
C     Save locations of exterior and interior damage sources (for use in
C        UEXTERNALDB subroutine)
```

```
      IF (NOEL .EQ. 80615 .AND. NPT .EQ. 8) THEN !*
         DO I = 1, 3
            DmgSource1(I) = COORDS(I)
         END DO
      END IF
      IF (NOEL .EQ. 8911 .AND. NPT .EQ. 4) THEN !*
         DO I = 1, 3
            DmgSource2(I) = COORDS(I)
         END DO
      END IF
C     *The above values highlighted in red are the elements and
C      integration points from which the exterior and interior
C      extent-of-damage measurements are to be made from. These
C      should be adjusted for each model accordingly.
C
C     Update the damage state variables
      STATEV(1) = D1
      STATEV(2) = D2
      STATEV(3) = D3
      STATEV(4) = D1v
      STATEV(5) = D2v
      STATEV(6) = D3v
C
C     Calculate the damaged stiffness tensor, CD, and the new stress
C        without viscous regularization
      Call Stiffness(E1,E2,E3,G12,G23,G13,nu12,nu21,nu13,nu31,nu23,nu32,
     1   D1,D2,D3,C,CD)
      DO I = 1, NTENS
         d_stress(I) = zero
         DO J = 1, NTENS
            d_stress(I) = d_stress(I) + CD(I,J) * STRANT(J)
         END DO
      END DO
C
C     Save the current stress without viscous regularization
      DO I = 1, NTENS
         STATEV(I+6) = d_stress(I)
      END DO
C
C     Calculate the damaged stiffness matrix, CD, and the new stress
C        with viscous regularization
      Call Stiffness(E1,E2,E3,G12,G23,G13,nu12,nu21,nu13,nu31,nu23,nu32,
     1   D1v,D2v,D3v,C,CD)
      DO I = 1, NTENS
         STRESS(I) = zero
         DO J = 1, NTENS
            STRESS(I) = STRESS(I) + CD(I,J) * STRANT(J)
         END DO
      END DO
C**********************************************************************
C
C     Calculate the derivative of the damaged stiffness tensor CD with
C        respect to the regularized damage variables
      DO I = 1, 6
         DO J = 1, 6
            DCDD1(I,J) = zero
            DCDD2(I,J) = zero
            DCDD3(I,J) = zero
         END DO
      END DO
```

```
C
      CDtemp = (one - nu12*nu21*(one - D1v)*(one - D2v) -
     1   nu23*nu32*(one - D2v)*(one - D3v) - nu13*nu31*(one - D1v)*(one
     2   - D3v) - two*nu12*nu23*nu31*(one - D1v)*(one - D2v)*(one-D3v))
      DCDtempDD1 = nu12*nu21*(one - D2v) + nu13*nu31*(one - D3v) +
     1   two*nu12*nu23*nu31*(one - D2v)*(one - D3v)
      DCDtempDD2 = nu12*nu21*(one - D1v) + nu23*nu32*(one - D3v) +
     1   two*nu12*nu23*nu31*(one - D1v)*(one - D3v)
      DCDtempDD3 = nu23*nu32*(one - D2v) + nu13*nu31*(one - D1v) +
     1   two*nu12*nu23*nu31*(one - D1v)*(one - D2v)
C
C     Calculate dC/dD1
      DCDD1(1,1) = (-E1*(one - nu23*nu32*(one - D2v)*(one - D3v)) -
     1   CD(1,1)*DCDtempDD1)/CDtemp
      DCDD1(2,2) = (E2*(one - D2v)*nu13*nu31*(one - D3v) - CD(2,2)*
     1   DCDtempDD1)/CDtemp
      DCDD1(3,3) = (E3*(one - D3v)*nu12*nu21*(one - D2v) - CD(3,3)*
     1   DCDtempDD1)/CDtemp
      DCDD1(1,2) = (-E1*(one - D2v)*(nu21 + (one - D3v)*nu23*nu31) -
     1   CD(1,2)*DCDtempDD1)/CDtemp
      DCDD1(2,1) = DCDD1(1,2)
      DCDD1(1,3) = (-E1*(one - D3v)*(nu31 + (one - D2v)*nu21*nu32) -
     1   CD(1,3)*DCDtempDD1)/CDtemp
      DCDD1(3,1) = DCDD1(1,3)
      DCDD1(2,3) = (-E2*(one - D2v)*(one - D3v)*nu12*nu31 -
     1   CD(2,3)*DCDtempDD1)/CDtemp
      DCDD1(3,2) = DCDD1(2,3)
      DCDD1(4,4) = -G12*(one - D2v)
      DCDD1(5,5) = -G13*(one - D3v)
C
C     Calculate dC/dD2
      DCDD2(1,1) = (E1*(one - D1v)*nu23*nu32*(one - D3v) - CD(1,1)*
     1   DCDtempDD2)/CDtemp
      DCDD2(2,2) = (-E2*(one - nu13*nu31*(one - D1v)*(one - D3v)) -
     1   CD(2,2)*DCDtempDD2)/CDtemp
      DCDD2(3,3) = (E3*(one - D3v)*nu12*nu21*(one - D1v) - CD(3,3)*
     1   DCDtempDD2)/CDtemp
      DCDD2(1,2) = (-E1*(one - D1v)*(nu21 + (one - D3v)*nu23*nu31) -
     1   CD(1,2)*DCDtempDD2)/CDtemp
      DCDD2(2,1) = DCDD2(1,2)
      DCDD2(1,3) = (-E1*(one - D1v)*(one - D3v)*nu21*nu32 - CD(1,3)*
     1   DCDtempDD2)/CDtemp
      DCDD2(3,1) = DCDD2(1,3)
      DCDD2(2,3) = (-E2*(one - D3v)*(nu32 + (one - D1v)*nu12*nu31) -
     1   CD(2,3)*DCDtempDD2)/CDtemp
      DCDD2(3,2) = DCDD2(2,3)
      DCDD2(4,4) = -G12*(one - D1v)
      DCDD2(6,6) = -G23*(one - D3v)
C
C     Calculate dC/dD3
      DCDD3(1,1) = (E1*(one - D1v)*nu23*nu32*(one - D2v) - CD(1,1)*
     1   DCDtempDD3)/CDtemp
      DCDD3(2,2) = (E2*(one - D2v)*nu13*nu31*(one - D1v) - CD(2,2)*
     1   DCDtempDD3)/CDtemp
      DCDD3(3,3) = (-E3*(one - nu12*nu21*(one - D2v)*(one - D1v)) -
     1   CD(3,3)*DCDtempDD3)/CDtemp
      DCDD3(1,2) = (-E1*(one - D1v)*(one - D2v)*(nu23*nu31) - CD(1,2)*
     1   DCDtempDD3)/CDtemp
      DCDD3(2,1) = DCDD3(1,2)
      DCDD3(1,3) = (-E1*(one - D1v)*(nu31 + (one - D2v)*nu21*nu32) -
```

```
     1   CD(1,3)*DCDtempDD3)/CDtemp
      DCDD3(3,1) = DCDD3(1,3)
      DCDD3(2,3) = (-E2*(one - D2v)*(nu32 + (one - D1v)*nu12*nu31) -
     1   CD(2,3)*DCDtempDD3)/CDtemp
      DCDD3(3,2) = DCDD3(2,3)
      DCDD3(5,5) = -G13*(one - D1v)
      DCDD3(6,6) = -G23*(one - D2v)
C**********************************************************************
C
C     Calculate the Jacobian
      DO I = 1, NTENS
         Atemp1(I) = zero
         DO J = 1, NTENS
            Atemp1(I) = Atemp1(I) + DCDD3(I,J) * STRANT(J)
         END DO
      END DO
      DO I = 1, NTENS
         Atemp2(I) = zero
         DO J = 1, NTENS
            Atemp2(I) = Atemp2(I) + DCDD2(I,J) * STRANT(J)
         END DO
      END DO
      DO I = 1, NTENS
         Atemp3(I) = zero
         DO J = 1, NTENS
            Atemp3(I) = Atemp3(I) + DCDD1(I,J) * STRANT(J)
         END DO
      END DO
      DO I = 1, NTENS
         DO J = 1, NTENS
            DDSDDE(I,J) = CD(I,J) + (Atemp1(I) * DD3DE(J)
     1           + Atemp2(I) * DD2DE(J) + Atemp3(I) * DD1DE(J)) *
     2           DTIME / (DTIME + ETA)
         END DO
      END DO
C
C     Calculate the strain energy
      DO I = 1, NDI
         SSE = SSE + half * (STRESS(I) + old_stress(I)) * DSTRAN(I)
      END DO
      DO I = NDI+1, NTENS
         SSE = SSE + (STRESS(I) + old_stress(I)) * DSTRAN(I)
      END DO
C
C     Calculate the energy associated with viscous regularization
      DO I = 1, NDI
         SCD = SCD + half * (STRESS(I) + old_stress(I)
     1       - d_stress(I) - dold_stress(I)) * DSTRAN(I)
      END DO
      DO I = NDI+1, NTENS
         SCD = SCD + (STRESS(I) + old_stress(I)
     1       - d_stress(I) - dold_stress(I)) * DSTRAN(I)
      END DO
      RETURN
      END
C**********************************************************************
```

B.6. SUBROUTINE: STIFFNESS

This subroutine, called by the UMAT subroutine, calculates the damaged stiffness tensor.

```
C**********************************************************************
      SUBROUTINE Stiffness(E1,E2,E3,G12,G23,G13,nu12,nu21,nu13,nu31,
     1   nu23,nu32,D1,D2,D3,C,CD)
C**********************************************************************
C
      INCLUDE 'ABA_PARAM.INC'
C
      DOUBLE PRECISION C(6,6), CD(6,6)
      DOUBLE PRECISION zero, one, two
      PARAMETER (zero = 0.D0,one = 1.D0,two = 2.D0)
      DOUBLE PRECISION E1,E2,E3,G12,G23,G13,nu12,nu21,nu23,nu32,nu13,
     1   nu31,CDtemp
      DOUBLE PRECISION D1,D2,D3
      INTEGER I,J
C
      DO I = 1, 6
         DO J = 1, 6
            CD(I,J) = C(I,J)
         END DO
      END DO
C
      IF ((D1 .NE. zero) .OR. (D2 .NE. zero) .OR. (D3 .NE. zero)) THEN
         CDtemp = (one - nu12*nu21*(one - D1)*(one - D2) -
     1      nu23*nu32*(one - D2)*(one - D3) - nu13*nu31*(one - D1)*(one
     2      - D3) - two*nu12*nu23*nu31*(one - D1)*(one - D2)*(one - D3))
C
         CD(1,1) = (E1*(one - D1)*(one - nu23*nu32*(one - D2)*(one -
     1               D3)))/CDtemp
         CD(2,2) = (E2*(one - D2)*(one - nu13*nu31*(one - D1)*(one -
     1               D3)))/CDtemp
         CD(3,3) = (E3*(one - D3)*(one - nu12*nu21*(one - D2)*(one -
     1               D1)))/CDtemp
         CD(1,2) = (E1*(one - D1)*(one - D2)*(nu21 + (one - D3)*nu23*
     1               nu31))/CDtemp
         CD(2,1) = CD(1,2)
         CD(1,3) = (E1*(one - D1)*(one - D3)*(nu31 + (one - D2)*nu21*
     1               nu32))/CDtemp
         CD(3,1) = CD(1,3)
         CD(2,3) = (E2*(one - D2)*(one - D3)*(nu32 + (one - D1)*nu12*
     1               nu31))/CDtemp
         CD(3,2) = CD(2,3)
         CD(4,4) = G12*(one - D1)*(one - D2)
         CD(5,5) = G13*(one - D1)*(one - D3)
         CD(6,6) = G23*(one - D2)*(one - D3)
      END IF
C
      RETURN
      END
C**********************************************************************
```

VITA

Frank Leone was born in Abington, Pennsylvania in 1984. He obtained his Bachelor's and Master's degrees from the Department of Mechanical Engineering & Mechanics at Drexel University in Philadelphia, Pennsylvania in 2007. In September 2007, he was awarded the FAA-Drexel Research Fellowship to study the damage processes of full-scale sandwich composite aircraft fuselage structure at the FAA William J. Hughes Technical Center at the Atlantic City International Airport. As an FAA-Drexel fellow, he conducted research toward his Doctorate degree developing finite element-based progressive damage models to predict the formation, progression, and instability of damage. In October 2010, he accepted a postdoctoral research position with the National Institute of Aerospace at the NASA Langley Research Center in Hampton, Virginia.